

Molecular-Level Engineering of Stress-Responsive Materials

by

Yangju Lin

Department of Chemistry  
Duke University

Date: \_\_\_\_\_

Approved:

\_\_\_\_\_  
Stephen L. Craig, Advisor

\_\_\_\_\_  
Kevin D. Welsler

\_\_\_\_\_  
Piotr E. Marszalek

\_\_\_\_\_  
Ross A. Widenhoefer

Dissertation submitted in partial fulfillment of  
the requirements for the degree of Doctor  
of Philosophy in the Department of  
Chemistry in the Graduate School  
of Duke University

2020

ABSTRACT

Engineering of Stress-Responsive Behaviors in Polymers and Elastomers

by

Yangju Lin

Department of Chemistry  
Duke University

Date: \_\_\_\_\_

Approved:

\_\_\_\_\_  
Stephen L. Craig, Advisor

\_\_\_\_\_  
Kevin D. Welsler

\_\_\_\_\_  
Piotr E. Marszalek

\_\_\_\_\_  
Ross A. Widenhoefer

An abstract of a dissertation submitted in partial  
fulfillment of the requirements for the degree  
of Doctor of Philosophy in the Department of  
Chemistry in the Graduate School of  
Duke University

2020

Copyright by  
Yangju Lin  
2020

## Abstract

The insertion of force-sensitive motifs (mechanophores) into polymer backbones provides a mechanism to induce forbidden reactions, stabilize transition state, and build intrinsic stress-responsive materials. Although polymer mechanochemistry has provided the basis for a variety of stress-responsive materials (e.g., those that are mechanochromic, mechanoluminescent, and mechanocatalytic, or that release small molecules or generate novel chemical reactions), many desirable stress-responsive behaviors have yet to be realized. We applied molecular-level design and synthesis to engineer stress-responsive materials that address several gaps in the prior polymer mechanochemistry toolbox:

Chapter 2 presents four studies of structure-reactivity relationships. First, regiochemical effects on mechanophore reactivity is quantified in the context of three spiropyran (SP) derivatives that are incorporated into polydimethylsiloxane (PDMS) elastomers. Under thermodynamic control, we find that the relative activation of the regioisomers is well correlated with the extent of mechanochemical coupling between the equilibrium reaction coordinate and the applied force, as quantified by computational modeling. Second, subtle differences in stereochemistry between two *gem*-monochlorocyclopropane (*gMCC*) stereoisomers (i.e., *syn* and *anti*, relative to the polymer attachment points through which force is delivered) lead to dramatic differences in reactivity and reactivity outcomes. The two *gMCC*s were embedded along a polymer backbone and their mechanochemical reactivities were quantified using single molecule force spectroscopy (SMFS). The mechanical ring-opening of *syn-gMCC* proceeds along an

anti-Woodward-Hoffmann-Depuy pathway and exhibits significantly lower reactivity than *anti-gMCC*. Further, under tension applied through ultrasonication, the *syn-gMCC* isomer generates about 0.25 equivalents of HCl per ring-opening event, whereas ring opening of the *anti-gMCC* led to no detectable HCl under identical conditions. Third, we report the dependence of the mechanical strength of a C-S bond on the oxidation state of the S atom (i.e., the relative mechanical strength of sulfide, sulfoxide and sulfone). Ultrasonication of *gem*-dichlorocyclopropane (gDCC) copolymers of each sulfur-containing group reveals that their relative mechanical strengths follow the order: polysulfide ~ polysulfone > polysulfoxide. Finally, we demonstrate the effect of cyclic polymer structure/architecture on mechanophore activation along a polymer backbone. A multi-mechanophore, cyclic gDCC copolymer was prepared via ring expansion metathesis polymerization (REMP), and its mechanochemical response to ultrasonication was compared to a linear analog prepared using ring opening metathesis polymerization (ROMP). The cyclic polymer experiences less gDCC activation per fragmentation along its backbone than does the linear analog. This observation suggests conformational memory effects in the nascent cyclic polymer during elongation and fragmentation.

Chapter 3 introduces two new mechanophores that convert mechanical input into potentially useful chemical signals, enriching the available toolkit of stress-responsive behaviors. The first mechanophore is a 1,2-diaitidinone (DAO) based four-member ring that generates reactive isocyanate upon mechanical activation via pulsed ultrasonication; evidence for the generation of isocyanate is acquired by <sup>1</sup>H NMR analysis and trapping

experiments. We anticipate that this latent reactive isocyanate might lead to materials that heal or strengthen in response to a mechanical load. A second mechanophore is a new thermally stable and non-scissile mechanoacid that is based on a methoxy-substituted gDCC and that overcomes drawbacks present in previously reported mechanoacids. The introduction of the methoxy substituent not only facilitates the release of HCl as a result of gDCC ring opening (0.58 equivalents per activation), it significantly lowers the force necessary to trigger rapid ring opening, as evidenced by SMFS studies. The utility of this new mechanoacid is demonstrated in PDMS elastomers, where its mechanical activation leads to a strain-triggered color change in a pH-sensitive dye prior to fracture of the elastomer. The post-activation kinetics of coloration are used to demonstrate a new concept in mechanochromism, namely not only a spectroscopic indicator of whether and where a mechanical event has occurred, but when it occurred.

Chapter 4 describes how the well-known photoswitch azobenzene, when embedded into PDMS elastomers, can be used as a mechanochromic probe of the molecular forces present in strained bulk materials. Specifically, the *cis-to-trans* isomerization of azobenzene is accelerated under uniaxial tension. The kinetics are cleanly described by a single exponential first-order process ( $k = 2.7 \times 10^{-5} \text{ s}^{-1}$ ) in the absence of tension, but they become multi-exponential under constant strains of 40-90%. The complex kinetics can be reasonably modeled as a two-component process. The majority (~92%) process is slower and occurs with a rate constant that is similar to that of the unstrained system ( $k = 2.3\text{--}2.7 \times 10^{-5} \text{ s}^{-1}$ ), whereas the rate constant of the minority (~8%)

process increases from  $k = 10.1 \times 10^{-5} \text{ s}^{-1}$  at 40% strain to  $k = 21.3 \times 10^{-5} \text{ s}^{-1}$  at 90% strain. Simple models of expected force-rate relationships suggest that the average force of tension per strand in the minority component ranges from 28 pN to 44 pN across strains of 40-90%.

Finally, in Chapter 5, polymer mechanochemistry is integrated into two degradable polymers to demonstrate new concepts in mechanically coupled degradable polymers. The unintentional scission of chemical degradable functionalities on the polymer backbone can diminish polymer properties, and we report a strategy that combats unintended degradation in polymers by combining two common degradation stimuli—mechanical and acid triggers—in an “AND gate” fashion. A cyclobutane (CB) mechanophore is used as a mechanical gate to regulate an acid-sensitive ketal that has been widely employed in acid degradable polymers. This gated ketal is further incorporated into the polymer backbone. In the presence of acid trigger alone, the pristine polymer retains its backbone integrity, and delivering high mechanical forces alone by ultrasonication degrades the polymer to an apparent limiting molecular weight of 28 kDa. The sequential treatment of ultrasonication followed by acid, however, leads to a further 11-fold decrease in molecular weight to 2.5 kDa. Experimental and computational evidence further indicate that the ungated ketal possesses mechanical strength that is commensurate with the conventional polymer backbones. Single molecule force spectroscopy (SMFS) reveals that the force necessary to activate the CB molecular gate on the timescale of 100 ms is approximately 2 nN. With this success in hand, we noted that

mechanical-only polymer degradation is intrinsically limited to one chain scission per stretching event. To overcome this drawback, we integrate multiple copies of a [4.2.0]bicyclooctene (BCOE) based mechanophore into the polymer backbone. Mechanochemical remodeling of the polymer backbone occurs through the force-promoted forbidden ring-opening of BCOE, the product of which undergoes a subsequent, slower cascade lactonization that leads to a spontaneous, force-free decrease in average molecular weight to 4.4 kDa (from an initial molecular weight of over 120 kDa) over the course of 9 days.

# Contents

|  |      |
|--|------|
| Abstract.....  | iv   |
| List of Tables.....  | xiv  |
| List of Figures.....   | xvi  |
| Acknowledgements .....   | xxxi |
| 1. Introduction.....   | 1    |
| 1.1 A brief introduction to polymer mechanochemistry.....                    | 1    |
| 1.2 Principles of mechanophore design.....                                   | 3    |
| 1.3 Techniques for coupling mechanical force.....                            | 8    |
| 2. Structure-reactivity relationships in polymer mechanochemistry .....      | 14   |
| 2.1 Regiochemical effects on mechanophore activation in bulk materials ..... | 14   |
| 2.1.1 Introduction.....  | 15   |
| 2.1.2 Experimental section.....  | 17   |
| 2.1.2.1 Preparation of SP regioisomers.....                                  | 17   |
| 2.1.2.2 Network preparation.....   | 18   |
| 2.1.2.3 Tensile tests.....   | 18   |
| 2.1.3 Results and discussion.....  | 19   |
| 2.1.3.1 Relative activation.....   | 19   |
| 2.1.3.2 Onset of activation .....  | 20   |
| 2.1.3.4 Ratiometric activation as a function of strain .....                 | 22   |
| 2.1.3.5 Molecular origins of differential activation.....                    | 24   |
| 2.1.4 Conclusion.....  | 25   |
| 2.1.5 Synthetic and general procedures.....                                  | 27   |

|   |     |
|---|-----|
| 2.1.5.1 Materials and characterization.....                                 | 27  |
| 2.1.5.2 Synthetic procedures .....  | 28  |
| 2.1.5.3 Mechanical activation of SP regioisomers.....                       | 34  |
| 2.1.5.4 Kinetic and thermodynamic parameters.....                           | 41  |
| 2.1.5.5 CoGEF modeling .....  | 46  |
| 2.2 Stereochemical effects on a mechanochemical reaction.....               | 58  |
| 2.2.1 Introduction.....   | 58  |
| 2.2.2 Results and discussion.....   | 60  |
| 2.2.3 Experimental section.....   | 68  |
| 2.2.3.1 Materials and characterization.....                                 | 68  |
| 2.2.3.2 Synthetic details .....   | 70  |
| 2.2.3.3. Sonication experiment .....  | 73  |
| 2.2.3.4 SMFS analysis.....  | 82  |
| 2.2.3.5 CoGEF modeling.....   | 92  |
| 2.3 Redox-regulation of the mechanical strength of a C-S bond .....         | 97  |
| 2.3.1 Introduction.....   | 97  |
| 2.3.2 Results and discussion.....   | 99  |
| 2.3.3 Experimental section.....   | 106 |
| 2.3.3.1 General procedures.....   | 106 |
| 2.3.3.2 Synthesis procedures .....  | 107 |
| 2.3.3.3 Sonication experiment .....   | 110 |
| 2.3.3.4 Relative mechanical strength analysis.....                          | 119 |
| 2.3.3.5 GoGEF modeling.....   | 120 |
| 2.4 Dynamic memory effects in the mechanochemistry of cyclic polymers ..... | 123 |

|   |     |
|---|-----|
| 2.4.1 Introduction.....   | 123 |
| 2.4.2 Results and discussion.....   | 125 |
| 2.4.3 Experimental section.....   | 134 |
| 2.4.3.1 Materials and characterization.....   | 134 |
| 2.4.3.2 Synthetic procedures .....  | 136 |
| 2.4.3.3 Intrinsic viscosity .....   | 143 |
| 2.4.3.4 Sonication experiment .....   | 144 |
| 2.4.3.5 Ozonolysis experiment.....  | 151 |
| 3. Development of mechanophores with novel stress-responsive behaviors.....   | 158 |
| 3.1 Mechanical Generation of Isocyanate by Mechanically Induced Retro [2+2]<br>Cycloaddition of a 1,2-Diazetidione Mechanophore ..... | 158 |
| 3.1.1 Introduction.....   | 159 |
| 3.1.2 Results and discussion.....   | 161 |
| 3.1.3 Experimental section.....   | 169 |
| 3.1.3.1 Materials and chracterization.....  | 169 |
| 3.1.3.2 Synthetic procesures .....  | 170 |
| 3.1.3.3 Sonication experiment .....   | 175 |
| 3.1.3.4 Determination of mechanophore activation rate under sonication .....  | 179 |
| 3.2 A Latent Mechanoacid for Time-Stamped Mechanochromism and Chemical<br>Signaling in Polymeric Materials .....                      | 185 |
| 3.2.1 Introduction.....   | 186 |
| 3.2.2 Results and discussion.....   | 187 |
| 3.2.3 Experimental section.....   | 196 |
| 3.2.3.1 Materials and chracterizatoin.....  | 196 |

|  |     |
|--|-----|
| 3.2.3.2 Synthetic procedures .....   | 200 |
| 3.2.3.3 Thermal stability of mechanoacid.....  | 209 |
| 3.2.3.4 Sonication experiment .....  | 211 |
| 3.2.3.5 SMFS analysis.....   | 213 |
| 3.2.3.6 Generation and labeling of mechanoacid in PDMS elastomer .....                                 | 220 |
| 3.2.3.7 CoGEF modeling.....  | 224 |
| 4. Force distribution in the strained bulk materials.....  | 230 |
| 4.1 Strain-dependent Kinetics in the cis-to-trans Isomerization of Azobenzene in Bulk Elastomers ..... | 230 |
| 4.1.1 Introduction.....  | 230 |
| 4.1.2 Experimental section.....  | 232 |
| 4.1.3 Results and discussion.....  | 234 |
| 4.1.4 Synthetic and general procedures.....  | 243 |
| 4.1.4.1 Materials and characterization.....  | 243 |
| 4.1.4.2 Small molecule synthesis.....  | 244 |
| 4.1.4.3 Preparation of azobenzene incorporated PDMS bulk material.....                                 | 245 |
| 4.1.4.4 UV-vis characterization .....  | 245 |
| 4.1.4.5 <sup>1</sup> H NMR determination of the photostationary state .....                            | 247 |
| 4.1.4.6 Kinetic study of strained PDMS-AB film .....   | 248 |
| 4.1.4.7 CoGEF modeling.....  | 253 |
| 5. Mechanically integrated degradable polymers.....  | 257 |
| 5.1 Mechanically gated degradable polymers .....   | 257 |
| 5.1.1 Introduction.....  | 258 |
| 5.1.2 Results and discussion.....  | 261 |

|   |     |
|---|-----|
| 5.1.3 Experimental section.....   | 268 |
| 5.1.3.1 Materials and chracterization.....  | 268 |
| 5.1.3.2 Synthesis .....   | 271 |
| 5.1.3.3 Ultrasonication.....  | 275 |
| 5.1.3.4 SMFS analysis.....  | 286 |
| 5.1.3.5 Comparison of ring strain .....   | 290 |
| 5.1.3.6 CoGEF modeling.....   | 291 |
| 5.2 Enhanced polymer mechanical degradation through mechanochemically<br>unveiled lactonizatoin ..... | 297 |
| 5.2.1 Introduction.....   | 297 |
| 5.2.2 Results and discussion.....   | 300 |
| 5.2.3 Experimental section.....   | 312 |
| 5.2.3.1 Materials and chracterization.....  | 312 |
| 5.2.3.2 Synthesis details .....   | 315 |
| 5.2.3.3 Sonication experiment .....   | 321 |
| 5.2.3.4 SMFS analysis.....  | 327 |
| 5.2.3.5 CoGEF modeling.....   | 334 |
| 6. Conclusions .....  | 336 |
| 7. Reference.....   | 339 |
| Biography .....   | 373 |

## List of Tables

|  |     |
|--|-----|
| Table 1 : Representative data from analysis of image set of SP( <i>o</i> )-PDMS specimen.....  | 39  |
| Table 2 : Estimated equilibrium constants of SP( <i>o</i> ), SP( <i>m</i> ) and SP( <i>p</i> ) from SP( <i>o</i> )-NO <sub>2</sub> ..... | 42  |
| Table 3 : Backward reaction rate of SP( <i>o</i> ), SP( <i>m</i> ) and SP( <i>p</i> ) .....  | 45  |
| Table 4 : Kinetic and thermodynamic parameters of SP( <i>o</i> ), SP( <i>m</i> ) and SP( <i>p</i> ).....                                 | 45  |
| Table 5 : Summary of contour length of MC isomers from SP( <i>o</i> ) (unit: Å).....   | 49  |
| Table 6 : Summary of contour length of MC isomers from SP( <i>m</i> ) (unit: Å) .....  | 53  |
| Table 7 : Summary of contour length of MC isomers from SP( <i>p</i> ) (unit: Å) .....  | 57  |
| Table 8. Force-Free Activation Energies, Mechanical Coupling $\Delta x^\ddagger$ , and Transition Force of gDCC and gMCC isomers. ....   | 66  |
| Table 9 : List of results from SMFS curves analysis.....   | 89  |
| Table 10 : Summary of results from SMFS fitting.....   | 90  |
| Table 11 : Effect of sonication and subsequent ozonolysis on L2 and C2 homopolymers .....  | 132 |
| Table 12 : Summary of residual ruthenium amounts in C1 polymer.....  | 140 |
| Table 13 : List of data for measurement of intrinsic viscosity.....  | 143 |
| Table 14 : DAO-PMA activation rate constants obtained from various methods.....  | 167 |
| Table 15 : A representative data set of molecular degradation during sonication .....  | 180 |
| Table 16 : Summary of obtained activation rate from different reported method. ....  | 184 |
| Table 17 : Force-free activation energies, mechanical coupling $\Delta x^\ddagger$ , and transition force of gDCC and MeO-gDCC. ....     | 192 |
| Table 18 : Kinetically regulated “time stamp” calculations of the occurrence of a triggering mechanical event.....                       | 195 |
| Table 19 : List of results from SMFS curves analysis.....  | 218 |
| Table 20 : Summary of modeling contour length (unit: Å) .....  | 227 |

|  |     |
|--|-----|
| Table 21 : Summary of contour length for epoxide repeating unit (unit: Å).....                     | 229 |
| Table 22 : Summary of rate constants obtained from two-phase fitting of strained PDMS-AB film..... | 239 |
| Table 23 : Fitting result with $A_0$ and $A_\infty$ constrained/unconstrained .....                | 249 |
| Table 24 : Two-phase fitting of obtained isomerization rate constants under various strains.....   | 250 |
| Table 25 : Parameters obtained form one-phase fitting.....   | 251 |
| Table 26 : Summary of CoGEF modeling if azobenzene.....  | 256 |
| Table 27 : List of results from SMFS analysis.....   | 287 |
| Table 28 : Contour length of each repeating unit obtained from CoGEF modeling .....                | 296 |
| Table 29 : List of results from SMFS curves analysis.....  | 333 |

## List of Figures

|  |    |
|--|----|
| Figure 1 : Mechanically induced ring-opening of <i>cis</i> and <i>trans</i> benzocyclobutene (BCB) yields single <i>E, E</i> -isomer as product.....                                   | 2  |
| Figure 2 : Characterization of available mechanophores as of early 2020, with apologies for any omissions..  | 7  |
| Figure 3 : Mechanism of ultrasound-induced stretching of polymer chains in the solution. ....  | 9  |
| Figure 4 : Schematic of pulling a multi-mechanophore polymer using SMFS and the corresponding force-extension curve. ....  | 10 |
| Figure 5 : Schematic of a stress-strain curve that might be obtained from a mechanophore embedded polymer. The optical response versus stress/strain is recorded <i>in situ</i> . .... | 12 |
| Figure 6 : a) Mechanical conversion of spiropyran (SP) into colored merocyanine (MC); b) Spiropyran regioisomers, with the locations of the force handles indicated by arrows...       | 16 |
| Figure 7 : Synthesis of SP regioisomers and illustrated incorporation of SP regioisomers into PDMS polymer network. ....   | 17 |
| Figure 8 : a) Representative image set of SP-PDMS under quasi-static tensile test; b) Stress-strain curve and corresponding B/G value from image analysis .....                        | 20 |
| Figure 9 : a) Change in B:G ratio of three SP regioisomers; b) data in (a) normalized to the value at 135% strain. ....  | 22 |
| Figure 10 : Mechanical activation of SP regioisomers by manual stretch of PDMS strips  | 34 |
| Figure 11 : Additional stress-strain curves of SP( <i>o</i> ), SP( <i>m</i> ) and SP( <i>p</i> ) specimen.....   | 34 |
| Figure 12 : UV-vis spectra of mechanical activated SP( <i>o</i> ), SP( <i>m</i> ) and SP( <i>p</i> ). All show a broad absorption peak between 460~700 nm.....                         | 35 |
| Figure 13 : Plot of stress and (A580 nm – A780 nm) value against time for SP( <i>o</i> )-PDMS at constant 106% strain. ....  | 36 |
| Figure 14 : Representative image montage of SP( <i>o</i> )-PDMS specimen in red channel.....   | 37 |
| Figure 15 : Representative image montage of SP( <i>o</i> )-PDMS specimen in green channel. .   | 37 |
| Figure 16 : Representative image montage of SP( <i>o</i> )-PDMS specimen in blue channel.....  | 38 |

|  |    |
|--|----|
| Figure 17 : Image analysis from red, green and blue channels using FIJI software. The length of sample is measured and pixel values are retrieved. ....  | 38 |
| Figure 18 : The intensity in each channel was analyzed in B/G, B/R and R/G versus strain to determine the activation.....                                | 40 |
| Figure 19 : Additional B/G versus strain pots of SP( <i>o</i> ), SP( <i>m</i> ) and SP( <i>p</i> ) specimen .....  | 40 |
| Figure 20 : Representative frame montage from video of locally compressed SP( <i>o</i> )-PDMS film in red channel. ....                                  | 43 |
| Figure 21 : Representative frame montage from video of locally compressed SP( <i>o</i> )-PDMS film in green channel. ....                                | 43 |
| Figure 22 : presentative frame montage from video of locally compressed SP( <i>o</i> )-PDMS film in blue channel. ....                                   | 44 |
| Figure 23 : Representative frame analysis of locally compressed SP( <i>o</i> )-PDMS film in red, green and blue channels. ....                           | 44 |
| Figure 24 : Fading rate fitting of mechanically activated SP( <i>o</i> ). ....   | 45 |
| Figure 25 : Quadratic fit of energy vs. distance curve (green); force vs. distance curve (orange). End-to-end distance of SP( <i>o</i> ): 22.733 Å.....  | 47 |
| Figure 26 : Quadratic fit of energy vs. distance curve (green); force vs. distance curve (orange). End-to-end distance of CTT: 25.173 Å.....             | 47 |
| Figure 27 : Quadratic fit of energy vs. distance curve (green); force vs. distance curve (orange). End-to-end distance of CTC: 26.319Å .....             | 48 |
| Figure 28 : Quadratic fit of energy vs. distance curve (green); force vs. distance curve (orange). End-to-end distance of TTC: 25.110 Å.....             | 48 |
| Figure 29 : Quadratic fit of energy vs. distance curve (green); force vs. distance curve (orange). End-to-end distance of TTT: 27.246 Å.....             | 49 |
| Figure 30 : Quadratic fit of energy vs. distance curve (green); force vs. distance curve (orange). End-to-end distance of TCC: 26.158 Å .....            | 49 |
| Figure 31 : Quadratic fit of energy vs. distance curve (green); force vs. distance curve (orange). End-to-end distance of SP( <i>m</i> ): 26.839 Å ..... | 50 |
| Figure 32 : Quadratic fit of energy vs. distance curve (green); force vs. distance curve (orange). End-to-end distance of CTT: 27.254 Å.....             | 51 |

|   |    |
|---|----|
| Figure 33 : Quadratic fit of energy vs. distance curve (green); force vs. distance curve (orange). End-to-end distance of CTC: 27.796 Å .....                           | 51 |
| Figure 34 : Quadratic fit of energy vs. distance curve (green); force vs. distance curve (orange). End-to-end distance of TTC: 27.277 Å.....                            | 52 |
| Figure 35 : Quadratic fit of energy vs. distance curve (green); force vs. distance curve (orange). End-to-end distance of TCC: 28.440 Å .....                           | 52 |
| Figure 36 : Quadratic fit of energy vs. distance curve (green); force vs. distance curve (orange). End-to-end distance of TCC: 26.905 Å .....                           | 53 |
| Figure 37 : Quadratic fit of energy vs. distance curve (green); force vs. distance curve (orange). End-to-end distance of SP( <i>p</i> ): 25.062 Å .....                | 54 |
| Figure 38 : Quadratic fit of energy vs. distance curve (green); force vs. distance curve (orange). End-to-end distance of CTT: 26.190 Å.....                            | 55 |
| Figure 39 : Quadratic fit of energy vs. distance curve (green); force vs. distance curve (orange). End-to-end distance of CTC: 25.185 Å .....                           | 55 |
| Figure 40 : Quadratic fit of energy vs. distance curve (green); force vs. distance curve (orange). End-to-end distance of TTC: 25.622 Å.....                            | 56 |
| Figure 41 : Quadratic fit of energy vs. distance curve (green); force vs. distance curve (orange). End-to-end distance of TTT: 25.271 Å.....                            | 56 |
| Figure 42 : Quadratic fit of energy vs. distance curve (green); force vs. distance curve (orange). End-to-end distance of TCC: 25.987 Å .....                           | 57 |
| Figure 43 : Schematic presentation of reactions that follow a WHD pathway and mechanically induced reactions that proceed through an anti-WHD pathway. ....             | 60 |
| Figure 44 : Mechanochemical activation of polymers 3 and 5 using ultrasonication treatment, and their corresponding <sup>1</sup> H NMR post sonication.. ....           | 63 |
| Figure 45 : Representative force-extension curve of polymer 4. Retraction velocity: 300 nm/s.....   | 64 |
| Figure 46 : Proposed radical and cation mechanisms for mechanical generation of HCl, and experimental demonstration of nonradical mechanism. ....                       | 67 |
| Figure 47 : GPC traces of polymer 3 (M <sub>n</sub> = 171.3 kDa, PDI = 1.686) (left) and corresponding M <sub>n</sub> evolution (right) at various sonication time..... | 74 |

|  |    |
|--|----|
| Figure 48 : Stack of $^1\text{H-NMR}$ ( $\text{CDCl}_3$ , 500 MHz) spectra of polymer 3 at various sonication time.....  | 75 |
| Figure 49 : Left: ring-opening percentage of each gMCC stereoisomers; Right: percentage of HCl release in polymer 3.....   | 76 |
| Figure 50 : GPC traces of polymer 5 ( $M_n = 103.7$ kDa, PDI = 1.529) (left) and corresponding $M_n$ evolution (right) at various sonication time.....                           | 76 |
| Figure 51 : Stack of $^1\text{H-NMR}$ ( $\text{CDCl}_3$ , 500 MHz) spectra of sonicated polymer 5 at various sonication time. ....   | 77 |
| Figure 52 : Ring-opening percentage of <i>syn</i> -gMCC (left axis) and percentage of HCl release (right axis) in polymer 5 at various sonication time. ....                     | 78 |
| Figure 53 : Mechanically generated HCl from polymers 3 and 5 turn on rhodamine B base indicator. ....  | 79 |
| Figure 54 : GPC traces of sonication of polymer 5 in the presence of radical scavenger CT (left) and corresponding plot of molecular weight versus sonication time (right). .... | 80 |
| Figure 55 : The concentration of generated new chains at various sonication time. ....   | 80 |
| Figure 56 : GPC UV332 nm signal of polymer 5 at various sonication time (left); integration of GPC UV332 nm signal at various sonication time. ....                              | 81 |
| Figure 57 : The concentration of incorporated CT in polymer 5 at various sonication time. ....   | 81 |
| Figure 58 : The concentration of incorporated CT as a function of concentration of generated new chains in sonicated polymer 5.....  | 82 |
| Figure 59 : The concentration of incorporated CT as a function of amount of generated new chains from sonication of different polymers. ....                                     | 82 |
| Figure 60 : $^1\text{H NMR}$ ( $\text{CDCl}_3$ , 500 MHz) spectra overlay of thermolysis of polymer 3 at 180 °C in diphenyl ether. ....  | 83 |
| Figure 61 : Retrieving thermal ring-opening rate of <i>anti</i> -gMCC (left); <i>syn</i> -gMCC (right) kept intact under 180 °C for 3 h.....                                     | 84 |
| Figure 62 : $^1\text{H NMR}$ ( $\text{CDCl}_3$ , 500 MHz) spectra overlay of thermolysis of polymer 3 at 220 °C in diphenyl ether.2.2.3.4.2 SMFS curve analysis .....            | 85 |

|  |     |
|--|-----|
| Figure 63 : Extended FJC model fitting (pre- and post- first transition) of the force-extension curve of polymer 4.....  | 86  |
| Figure 64 : Extended FJC model fitting (pre- and post- second transition) of the force-extension curve of polymer 4.....   | 87  |
| Figure 65 : BE model fitting of the first transition in the force-extension curve of polymer 4. $\Delta x^\ddagger = 1.02 \text{ \AA}$ .....   | 87  |
| Figure 66 : BE model fitting of the second transition in the force-extension curve of polymer 4. $\Delta x^\ddagger = 0.99 \text{ \AA}$ .....  | 88  |
| Figure 67 : Cusp model fitting of the first transition in the force-extension curve of polymer 4. $\Delta x^\ddagger = 1.25 \text{ \AA}$ .....   | 88  |
| Figure 68 : Cusp model fitting of the second transition in the force-extension curve of polymer 4. $\Delta x^\ddagger = 1.26 \text{ \AA}$ .....  | 89  |
| Figure 69 : Quadratic fit of energy vs. distance curve (green); force vs. distance plot (orange). End-to-end distance of repeating unit <i>syn</i> -gMCC: $4.802 \text{ \AA}$ .....                        | 93  |
| Figure 70 : Quadratic fit of energy vs. distance curve (green); force vs. distance plot (orange). End-to-end distance of repeating unit <i>anti</i> -gMCC: $4.814 \text{ \AA}$ .....                       | 93  |
| Figure 71 : Quadratic fit of energy vs. distance curve (green); force vs. distance plot (orange). End-to-end distance of repeating unit <i>cis</i> -alkene: $4.485 \text{ \AA}$ .....                      | 94  |
| Figure 72 : Quadratic fit of energy vs. distance curve (green); force vs. distance plot (orange). End-to-end distance of repeating unit <i>trans</i> -alkene: $4.879 \text{ \AA}$ .....                    | 94  |
| Figure 73 : Quadratic fit of energy vs. distance curve (green); force vs. distance plot (orange). End-to-end distance of repeating unit <i>cis</i> -epoxide: $4.809 \text{ \AA}$ .....                     | 95  |
| Figure 74 : Quadratic fit of energy vs. distance curve (green); force vs. distance plot (orange). End-to-end distance of repeating unit <i>trans</i> -epoxide: $4.856 \text{ \AA}$ .....                   | 95  |
| Figure 75 : Quadratic fit of energy vs. distance curve (green); force vs. distance plot (orange). End-to-end distance of repeating unit 3-chloroalkene: $6.248 \text{ \AA}$ .....                          | 96  |
| Figure 76. Illustration of competition between gDCC ring opening and C-S bond scission on polymer backbone under sonication.....   | 99  |
| Figure 77 : a) Normalized GPC traces of PE-S, PE-SO and PE-SO <sub>2</sub> polymers. b) <sup>1</sup> H NMR (500 MHz, CDCl <sub>3</sub> ) spectra stacking of PE-S, PE-SO, PE-SO <sub>2</sub> polymers..... | 102 |

|   |     |
|---|-----|
| Figure 78 : a) The evolution of $M_n$ and gDCC ring opening in PE-S. b) The fraction of gDCC ring opening vs. scission cycle for each C-S containing polymer..... | 103 |
| Figure 79 : DFT calculation of the mechanical strength of C-S in each sulfur containing species using CoGEF method on the theory level of B3LYP/6-31G* .....      | 105 |
| Figure 80 : $^1\text{H}$ NMR ( $\text{CDCl}_3$ , 500 MHz) spectrum of PE-S polymer .....  | 108 |
| Figure 81 : $^1\text{H}$ NMR ( $\text{CDCl}_3$ , 500 MHz) spectrum of PE-SO polymer .....   | 109 |
| Figure 82 : $^1\text{H}$ NMR ( $\text{CDCl}_3$ , 500 MHz) spectrum of PE-S polymer .....  | 110 |
| Figure 83 : Evolution of GPC traces during sonication of PE-S polymer (left) and corresponding plot of molecular weight versus sonication (right).....            | 111 |
| Figure 84 : Scission cycle (SC) of PE-S polymer at various sonication time .....  | 112 |
| Figure 85 : Stack of $^1\text{H}$ -NMR ( $\text{CDCl}_3$ , 500 MHz) spectra of sonicated PE-S polymer at various sonication time.....                             | 112 |
| Figure 86 : Ring-opening percentage of gDCC in PE-S polymer versus sonication time. ....  | 113 |
| Figure 87 : Percentage of gDCC ring opening versus scission cycle plot for PE-S polymer. The slope of linear fitting through origin gives $\Phi = 0.334$ .....    | 113 |
| Figure 88 : Evolution of GPC traces during sonication of PE-SO polymer (left) and corresponding plot of molecular weight versus sonication (right).....           | 114 |
| Figure 89 : Scission cycle (SC) of PE-SO polymer at various sonication time .....   | 114 |
| Figure 90 : Stack of $^1\text{H}$ -NMR ( $\text{CDCl}_3$ , 500 MHz) spectra of sonicated PE-SO polymer at various sonication time.....                            | 115 |
| Figure 91 : Ring-opening percentage of gDCC in PE-SO polymer versus sonication time. ....   | 116 |
| Figure 92 : Percentage of gDCC ring opening versus scission cycle plot for PE-SO polymer. The slope of linear fitting through origin gives $\Phi = 0.125$ .....   | 116 |
| Figure 93 : Evolution of GPC traces during sonication of PE-SO polymer (left) and corresponding plot of molecular weight versus sonication (right).....           | 117 |
| Figure 94 : Scission cycle (SC) of PE-SO polymer at various sonication time .....   | 117 |

|   |     |
|---|-----|
| Figure 95 : Stack of <sup>1</sup> H-NMR (CDCl <sub>3</sub> , 500 MHz) spectra of sonicated PE-SO <sub>2</sub> polymer at various sonication time.....                             | 118 |
| Figure 96 : Ring-opening percentage of gDCC in PE-SO <sub>2</sub> polymer versus sonication time. ....  | 118 |
| Figure 97 : Force distribution of polymer backbone under sonication. ....   | 119 |
| Figure 98 : CoGEF modeling of sulfide containing unit. The evolution of energy (left) and the length of C-S bond (right) over increasement in end-to-end distance.....            | 121 |
| Figure 99 : CoGEF modeling of sulfoxide containing unit. The evolution of energy (left) and the length of C-S bond (right) over increasement in end-to-end distance. ....         | 121 |
| Figure 100 : CoGEF modeling of sulfone containing unit. The evolution of energy (left) and the length of C-S bond (right) over increasement in end-to-end distance. ....          | 122 |
| Figure 101 : Overlay of lengths of breaking C-S bonds for at various constrained distance. ....   | 122 |
| Figure 102 : Depiction of mechanical scission of a cyclic polymer to give a linear intermediate that subsequently fragments into two linear daughter polymers .....               | 125 |
| Figure 103 : a) Overlay of normalized GPC traces of C1 (orange) and L1 (blue). b) Evolution of M <sub>n</sub> (top) and gDCC ring opening (bottom) in C1 (orange) and L1 (blue).. | 128 |
| Figure 104 : gDCC ring opening as a function of fragmentation cycle (FC) for C1 and L1 polymers in this study. Solid lines are linear fits through the origin; slope = Φ. ....    | 130 |
| Figure 105 : Huggins-Kraemer plot for C1 (left) and L1 (right).....   | 144 |
| Figure 106 : Overlay of Huggins plot for C1 and L1. ....  | 144 |
| Figure 107 : Sonication of C1 polymer: evolution of GPC traces (left) and M <sub>n</sub> (right) during sonication (left).....  | 145 |
| Figure 108 : Fragmentation cycle (FC) of 167 kDa C1 vs. sonication time.....  | 145 |
| Figure 109 : . <sup>1</sup> H-NMR (CDCl <sub>3</sub> , 400 MHz) spectra stack of sonicated 167 kDa C1 at various sonication time. ....  | 146 |
| Figure 110 : Ring opening percentage of gDCC in 167 kDa C1 at different sonication time. ....   | 147 |

|  |     |
|--|-----|
| Figure 111 : gDCC ring opening vs. fragmentation cycle (FC) plot of 167 kDa and 98 kDa C1 polymers. $\Phi = 0.38$ and $0.44$ , respectively.....                                     | 147 |
| Figure 112 : Sonication of a 9 kDa C1: evolution of GPC traces during sonication (left); molecular weight vs. sonication time plot (right).....                                      | 148 |
| Figure 113 : gDCC ring opening percentage of 9 kDa C1 polymer at different sonication time.....  | 148 |
| Figure 114 : CT labeling of C1 polymer under sonication. $M_n$ reduced from 181 kDa to 164 kDa after 6 min sonication.....   | 149 |
| Figure 115 : g Sonication of L1: evolution of GPC traces (left) and $M_n$ (right) during sonication.....   | 149 |
| Figure 116 : Fragmentation cycle (FC) of 158 kDa L1 vs. sonication time. ....  | 150 |
| Figure 117 : Ring opening percentage of gDCC in 158 kDa L1 at different sonication time. ....  | 150 |
| Figure 118 : gDCC ring opening vs. fragmentation cycle plot of 158 kDa and 94 kDa L1. The slope of linear fitting through origin gives $\Phi = 0.62$ and $0.70$ , respectively. .... | 151 |
| Figure 119 : GPC traces of C2 ( $M_n = 245$ kDa, PDI = 1.21) before (gray) and after (dotted orange) 12 min sonication and ozonolyzed polymer (solid orange).....                    | 152 |
| Figure 120 : $^1\text{H}$ NMR overlay of C2 polymer before and after 12 min sonication and subsequent ozonolysis.....  | 152 |
| Figure 121 : GPC traces of L2 homopolymer ( $M_n = 253$ kDa, PDI = 1.29) before (gray) and after (dotted blue) 10 min sonication and ozonolyzed polymer (solid blue). ....           | 155 |
| Figure 122 : $^1\text{H}$ NMR overlay of L2 polymer before and after 10 min sonication and subsequent ozonolysis.....  | 155 |
| Figure 123 : a) Mechanical generation of ketene or isocyanate from $\beta$ -lactam mechanophore; b) 1,2-azetidinone as mechanophore to produce isocyanate.....                       | 160 |
| Figure 124 : Mechanical activation of DAO mechanophore and characterization of generated imine and isocyanate species.....   | 163 |
| Figure 125 : $^1\text{H}$ NMR spectra (DMSO- $d_6$ , 500 MHz) comparison of model molecules SMM1 and SMM2 and MAMA labelled DAO-PMA polymer after purification.....                  | 164 |

|  |     |
|--|-----|
| Figure 126 : The evolution of molecular weight ( $M_n$ ) and integration of GPC-UV356nm signal of DAO-PMA polymer during sonication.....                           | 166 |
| Figure 127 : $^1\text{H}$ NMR (400 MHz, $\text{DMSO-}d_6$ ) overlay of raw and sonicated DAO-PMA polymer and compound SMM1.....                                    | 177 |
| Figure 128 : UV-vis spectra of SMM1 and SMM2 in THF.....   | 177 |
| Figure 129 : $^1\text{H}$ NMR overlay of raw and MAMA labelled DAO-PMA polymer, compound SMM1 and SMM2. ....   | 178 |
| Figure 130 : 3D UV-vis signal of DAO-PMA, MAMA and DBTDL after 60 min physical mixing. ....  | 179 |
| Figure 131 : Zoom-in view of Figure 130 shows 12~14 min polymer retention time region. ....  | 179 |
| Figure 132 : The rate of $M_n$ degradation rate. The linear fitting was applied on first 15 min sonication that lies in the first scission cycle.....              | 181 |
| Figure 133 : Mechanophore activation rate was obtained using integration of UV 356 nm signal form GPC traces. The data was fitted with one-phase association. .... | 182 |
| Figure 134 : GPC RI signal of parent polymer at 13.20 min retention time decreased when subjected to sonication.....   | 182 |
| Figure 135 : Mechanophore activation rate was obtained by fitting the evolution of RI signal at 13.20 min retention time.....                                      | 183 |
| Figure 136 : Deconvolution of GPC RI traces using Microsoft excel solver. ....   | 183 |
| Figure 137 : Evaluation of mechanophore activation rate from deconvolution of GPC RI traces.. ....   | 184 |
| Figure 138 : Previously reported mechanoacids and new design in this work.....   | 186 |
| Figure 139 : Ultrasonication treatment of polymer P and $^1\text{H}$ NMR chracterization of activated species.....   | 189 |
| Figure 140 : Representative force-extension curve of MeO-gDCC containing ROMP copolymer P in toluene (MeO-gDCC content: 47 mol%). ....                             | 191 |
| Figure 141 : Demonstration of using mehcanoacid to indicate mechanical load under stretch, compression and localized compression in PDMS elastomer .....           | 193 |

|  |     |
|--|-----|
| Figure 142 : Bimolecular reaction between mechanoacid and rhodamine leads to a delayed coloration. ....  | 194 |
| Figure 143 : Thermal stability test: $^1\text{H}$ NMR of compound 5 in toluene- $d_6$ heated at 110 $^\circ\text{C}$ for different periods of time. ....   | 210 |
| Figure 144 : New species appeared after thermolysis of compound 5 in diphenyl ether at 138.5 $\pm$ 0.5 $^\circ\text{C}$ . ....                             | 210 |
| Figure 145 : Primary GPC elugrams of polymer P as a function of sonication time. ....  | 211 |
| Figure 146 : Overlay of $^1\text{H}$ NMR ( $\text{CDCl}_3$ , 500 MHz) spectra of sonicated polymer P at various sonication times. ....                     | 212 |
| Figure 147 : Polymer P solution was subjected to sonication for various times and added with rhodamine B base solution. ....                               | 213 |
| Figure 148 : Protonation of rhodamine by mechanoacid leads to active signals from UV-vis spectra. ....   | 213 |
| Figure 149 : Calculation of transition state for gDCC and MeO-gDCC. ....   | 214 |
| Figure 150 : Representative fitting of pre- and post-transition curves using an extended-FJC model. ....   | 215 |
| Figure 151 : Representative fitting of SMFS curve using a Cusp model. The mechanical coupling was retrieved: $\Delta x^\ddagger = 1.07 \text{ \AA}$ . .... | 215 |
| Figure 152 : Determination of characteristic transition force using first and second derivative of SMFS curve. ....  | 216 |
| Figure 153 : UV-vis spectra of active PDMS cylinder before and after compression. The corresponding absorption at 560 nm is 0.182 and 0.610. ....          | 220 |
| Figure 154 : Results of control 1 sample (rhodamine 9) under different models of mechanical load. ....   | 221 |
| Figure 155 : Results of control 2 sample (rhodamine 9 and control 7) under different models of mechanical load. ....                                       | 221 |
| Figure 156 : Four different runs of $A_{560}$ evolution in active PDMS cylinder after hammer strike. ....  | 222 |
| Figure 157 : Overlay of normalized turn-on kinetics. These data are treated as standard curves. ....   | 223 |

|   |     |
|---|-----|
| Figure 158 : The time point of mechanical load was extrapolated by fitting of kinetics data. The actual time for each sample is 6, 26, 12 min, respectively.....                          | 224 |
| Figure 159 : Quadratic fit of energy vs. distance curve (green); force vs. distance plot (orange). End-to-end distance of MeO-gDCC: 18.811 Å .....  | 225 |
| Figure 160 : Quadratic fit of energy vs. distance curve (green); force vs. distance plot (orange). End-to-end distance of P1: 20.394 Å .....  | 226 |
| Figure 161 : Quadratic fit of energy vs. distance curve (green); force vs. distance plot (orange). End-to-end distance of P2: 20.443 Å .....  | 226 |
| Figure 162 : Quadratic fit of energy vs. distance curve (green); force vs. distance plot (orange). End-to-end distance of P3: 20.556 Å .....  | 227 |
| Figure 163 : Quadratic fit of energy vs. distance curve (green); force vs. distance plot (orange). End-to-end distance of epoxide repeating unit with <i>cis</i> -olefin: 9.124 Å .....   | 228 |
| Figure 164 : Quadratic fit of energy vs. distance curve (green); force vs. distance plot (orange). End-to-end distance of epoxide repeating unit with <i>trans</i> -olefin: 9.609 Å ..... | 228 |
| Figure 165 : Mechanical isomerization of azobenzene in strained PDMS elastomer.....   | 232 |
| Figure 166 : A representative stress-strain curve (gray curve, left axis) of PDMS-AB elastomer and corresponding evolution in $A_{355}/A_{318}$ value (blue curve, right axis).....       | 237 |
| Figure 167 : a) Overlay of normalized kinetics of PDMS-AB film under various strains. b) Illustration of two isomerization kinetics in the stretched PDMS-AB film .....                   | 238 |
| Figure 168 : Derived $k_F$ and apparent average force $\langle F \rangle$ in PDMS-AB at different uniaxial strains.....   | 240 |
| Figure 169 : Photoswitch of PDMS-AB film under UV 365 nm (left) and white light (right). An isosbestic point at 318 nm was observed during photoswitching.....                            | 246 |
| Figure 170 : $A_{355}/A_{318}$ evolution of PDMS-AB film that was stretched on a TA Instruments RSA III Dynamic Mechanical Analyzer under ambient light (orange line) .....               | 246 |
| Figure 171 : <i>cis</i> -azobenzene predominant PDMS-AB film was set in dark to track the isomerization under room temperature.....   | 247 |
| Figure 172 : $^1\text{H}$ NMR overlay of UV 365 nm irradiated solution of azobenzene diene in $\text{CDCl}_3$ . The $^1\text{H}$ NMR at each time interval was recorded.....              | 247 |

|  |     |
|--|-----|
| Figure 173 : Evolution of integration and percentage of <i>trans</i> - and <i>cis</i> - azobenzenes over increasing UV irradiation time.....                                       | 248 |
| Figure 174 : Representative kinetics of <i>cis</i> -to- <i>trans</i> isomerization in PDMS-AB film at various strains. ....  | 250 |
| Figure 175 : <i>Cis</i> -to- <i>trans</i> isomerization rate of fast-phase azobenzene in PDMS-AB film at various strains. ....   | 251 |
| Figure 176 : <i>Cis</i> -to- <i>trans</i> isomerization rate of azobenzene in PDMS-AB film at various strains.....   | 252 |
| Figure 177 : Average force calculated from one- and two-phase fitting analysis .....   | 253 |
| Figure 178 : CoGEF modeling of <i>cis</i> -AB .....  | 254 |
| Figure 179 :s CoGEF modeling of TS.....  | 255 |
| Figure 180 : CoGEF modeling of <i>trans</i> -AB .....  | 256 |
| Figure 181 : Polymer degradation under typical extenal stimuli and mechanical force. The design of mechancially gated degradable polymers. ....                                    | 259 |
| Figure 182. <sup>1</sup> H NMR and GPC chracterization of acid resistance of P1 polymer.....   | 262 |
| Figure 183. Mechanically regulated degradability of P1 polymer backbone. ....  | 263 |
| Figure 184. <sup>1</sup> H NMR and GPC chracterization of fragmentation of sonicated P4 polymer. ....  | 265 |
| Figure 185 : Representative force-extension curve of P2 polymer and probability distribution of survival time at transition force.....   | 267 |
| Figure 186 : <sup>1</sup> H NMR of P1 and P3 polymers. The disappearance of proton A signals and shifts of a, b and c protons suggest full cleavage of ketal functionalities. .... | 275 |
| Figure 187 : GPC RI signals (Left) and molecular weight (right) of P3 polymer (M <sub>n</sub> = 153.7 kDa) at various sonication times.....  | 276 |
| Figure 188 : <sup>1</sup> H NMR (CDCl <sub>3</sub> ) spectrum overlay of P3 polymer with various sonication times.....   | 276 |
| Figure 189 : Percentage of gDCC ring opening in P3 polymer at different sonication times. ....   | 277 |

|   |     |
|---|-----|
| Figure 190 : $^1\text{H}$ NMR ( $\text{CDCl}_3$ ) spectrum analysis of CB activation in P3 polymer after 4 h sonication.....  | 278 |
| Figure 191 : GPC RI signals (Left) and molecular weight (right) of P1 polymer ( $M_n = 153.7$ kDa) at various sonication times.....   | 280 |
| Figure 192 : $^1\text{H}$ NMR ( $\text{CDCl}_3$ ) spectrum evolution of TFA treated P4 polymer (P1 polymer after 4 h sonication).....   | 281 |
| Figure 193 : GPC RI signals (Left) and molecular weight (right) of TFA treated P4 polymer. ....   | 281 |
| Figure 194 : Percentages of gDCC ring opening and CB activation in P4 at different sonication times.....  | 282 |
| Figure 195 : $^1\text{H}$ NMR spectrum ( $\text{CDCl}_3$ ) overlay of TFA treated P4 polymer with various sonication times.....   | 283 |
| Figure 196 : GPC RI signals (Left) and molecular weight (right) of P1 polymer ( $M_n = 128.9$ kDa) at various sonication time. The $M_n$ reduces to 61.3 kDa after 30 min sonication... | 284 |
| Figure 197 : Percentages of gDCC ring opening and CB activation in P1 polymer at different sonication times. ....   | 284 |
| Figure 198 : $^1\text{H}$ NMR ( $\text{CDCl}_3$ ) of P1 polymer after subjection to sonication for various time. ....   | 285 |
| Figure 199 : Evolution of GPC RI signals (Left) and molecular weight (right) for sonicated P1 polymer after treated with TFA.....   | 285 |
| Figure 200 : Fitting of force-extension curve with extended FJC model to give polymer contour length before transition ( $L_i = 389.4$ nm).....   | 286 |
| Figure 201 : Estimation of extra extension from plateau ( $\Delta x = x_2 - x_1 = 438.4 - 417.8 = 20.6$ nm). ....   | 287 |
| Figure 202 : Probability distribution of extra extension% ( $EE\%$ ) observed from SMFS experiment.....   | 288 |
| Figure 203 : CoGEF modeling of cyclobutane indicates reto-[2+2] cycloaddition under extension.....  | 292 |
| Figure 204 : CoGEF modeling of ketal containing product under extension. The C-O bond of methyl ester cleaves under high extension.....   | 292 |

|  |     |
|--|-----|
| Figure 205 : First derivative of quadratic fitting gives force-distance relation. The contour length of cyclobutane repeating unit is the intercept at x axis ( $x_0 = 12.946 \text{ \AA}$ ) ..... | 293 |
| Figure 206 : First derivative of quadratic fitting gives force-distance relation. The contour length of <i>E</i> alkene segment in ring-opened cyclobutane is $x_0 = 10.640 \text{ \AA}$ .....     | 294 |
| Figure 207 : First derivative of quadratic fitting gives force-distance relation. The contour length of <i>Z</i> alkene segment in ring-opened cyclobutane is $x_0 = 10.369 \text{ \AA}$ .....     | 294 |
| Figure 208 : First derivative of quadratic fitting gives force-distance relation. The contour length of <i>trans</i> alkene containing epoxide repeating unit is $x_0 = 10.583 \text{ \AA}$ .....  | 295 |
| Figure 209 : First derivative of quadratic fitting gives force-distance relation. The contour length of <i>cis</i> alkene containing epoxide repeating unit is $x_0 = 10.426 \text{ \AA}$ .....    | 295 |
| Figure 210 : Illustration of mechanically induced chain scission and design of enhanced mechanical degradation.. .....   | 299 |
| Figure 211 : Synthesis of pachylactone from a BCOE derivative and thermodynamics of lactonization. ....  | 301 |
| Figure 212 : Ultrasonication study of polymer P2 and characterization of activated backbone. ....  | 303 |
| Figure 213 : Ultrasonication study of polymer P3 and characterization of activated backbone. ....  | 305 |
| Figure 214 : Mechanical degradation of P2 and P3, and mechanically regulated degradability of P2. ....   | 307 |
| Figure 215 : Representative force-extension curves of P1. ....   | 308 |
| Figure 216 : GPC traces of P2 polymer (left) and corresponding $M_n$ evolution (right) at various sonication time. ....  | 321 |
| Figure 217 : Scission cycles of P2 polymer at various sonication times. ....   | 322 |
| Figure 218 : Stack of $^1\text{H-NMR}$ ( $\text{CDCl}_3$ , 500 MHz) spectra of sonicated P2 polymer at various sonication time. ....   | 322 |
| Figure 219 : Ring-opening percentage of gMCC (left) and HCl release (right) in polymer 3 at various sonication time. ....  | 323 |
| Figure 220 : Ring opening% of gDCC and BCOE vs. scission cycles. gDCC: $\Phi = 0.48$ ; BCOE: $\Phi = 0.39$ . ....  | 323 |

|  |     |
|--|-----|
| Figure 221 : The stability of sonicated P2 polymer backbone.....   | 324 |
| Figure 222 : GPC traces of P3 polymer (left) and corresponding $M_n$ evolution (right) at various sonication time. GPC analysis was performed right after sonication. ....   | 324 |
| Figure 223 : GPC traces of P3 polymer (left) and corresponding $M_n$ evolution (right) at various sonication time. GPC analysis was performed after 17d of standing.....     | 325 |
| Figure 224 : Molecular weight (MW) analysis of P3-17d polymer.....   | 325 |
| Figure 225 : GPC traces of pristine P3 polymer at various standing time. ....  | 326 |
| Figure 226 : $^1\text{H-NMR}$ ( $\text{CDCl}_3$ , 500 MHz) spectra stack of sonicated P3 polymer at various standing time.....   | 326 |
| Figure 227 : HRMS analysis of P3 polymer after 60 min sonication and further 20 days of standing. ....   | 327 |
| Figure 228 : $^1\text{H NMR}$ ( $\text{CDCl}_3$ , 500 MHz) spectra stack of compound 3 in diphenyl ether after heated at 150 °C for various time. ....                       | 328 |
| Figure 229 : Percentage of ring closed BCOE over time at 150 °C in diphenyl ether. ....  | 329 |
| Figure 230 : Fitting of pre and post transition in force-extension curve with extended FJC model. ....   | 330 |
| Figure 231 : Fitting of force-extension curve with BE model. Mechanical coupling $\Delta x^\ddagger = 0.87 \text{ \AA}$ . ....   | 331 |
| Figure 232 : Fitting of force-extension curve with Cusp model. Mechanical coupling $\Delta x^\ddagger = 1.06 \text{ \AA}$ . ....   | 331 |
| Figure 233 : Quadratic fit of energy vs. distance curve (blue); force vs. distance plot (orange). End-to-end distance of ring closed BCOE: $x_0 = 13.846 \text{ \AA}$ . .... | 334 |
| Figure 234 : Quadratic fit of energy vs. distance curve (blue); force vs. distance plot (orange). End-to-end distance of ring closed BCOE: $x_0 = 16.022 \text{ \AA}$ . .... | 335 |

## Acknowledgements

Looking back into my journey of pursuing a Ph.D. degree in Chemistry, I would like to first thank my family. They always support my decisions and choices without any doubt over the last 12 years, since when I started to study chemistry in Xiamen University. During the early study of chemistry, I specially thanked my mentor Dr. Guanning Hong and advisor Dr. Wengui Weng, who led me to the wonderful world of polymer science.

The last 5 years Ph.D. research experience with Dr. Stephen Craig really shaped the way how I think about and approach scientific questions. I really appreciate his patient mentoring and what he had taught me. His enthusiasm and wisdom have inspired me to continue along my academia pathway.

I thank Junpeng and Gregory for their early guidance in Craig Lab. For those colleagues I have been worked with, I want to say thanks, Tatiana, Cameron, Meredith, Yudi, Brandon, Patricia, Zi, Cary, Liqi, Shu, Yichen, Emily, Anthony, George, Anton and Tetsu. I appreciate those wonderful experience we had. I also want to thank those support I have received from chemistry department. Thank you, Michael, Janet, Chrisy, Tina, Trish, and Meg! Their support makes my research and life easier!

Last, I want to give my special thanks to my girlfriend Jiyan Ma, who has shared happiness and sadness with me over the last 3 years. She is the reason I worked so hard for this Ph.D. and the future.

# 1. Introduction

## ***1.1 A brief introduction to polymer mechanochemistry***

A century ago, the foundational work of Hermann Staudinger<sup>1</sup> revealed the covalent bonding character that links the repeating chemical units of high polymers. Soon thereafter, he and co-workers<sup>2-4</sup> noticed the reduction of polymer molecular weight that occurs as a result of mastication, and this molecular weight degradation was attributed to the mechanically induced cleavage of covalent bonds along the polymer backbone. Although a considerable amount of attention was thereafter paid to the investigation of polymer mechanochemical degradation, the experimental observation of carbon radical generation from mechanically induced homolytic C-C bond cleavage was not realized until 1989 by Sohma and coworkers,<sup>5</sup> who utilized electron spin resonance to characterize the generated radicals. For a long time, the investigation of mechanochemical polymer degradation was limited to the random cleavage of strong C-C bonds within 15% of the polymer midchain.<sup>6</sup> Selective chain scission was then realized by the incorporation of relative weak bonds, such as peroxide (1980),<sup>7</sup> metal-ligand (2004),<sup>8</sup> and carbon-azo (2005)<sup>9</sup> bonds, along the polymer backbone. These studies paved the way for the rational design of functional motifs that are especially sensitive to mechanically triggered chemical reactions – motifs that are now known as mechanophores.

In 2007, benchmark work by Moore and coworkers<sup>10</sup> demonstrated that the same mechanical forces commonly associated with the destructive response of bond scission

could be used to trigger a potentially constructive response. They observed accelerated ring-opening reaction of *cis*- and *trans*-benzocyclobutene (BCB) and found that both isomers yield the same ring-opened *E,E*-isomer product under the mechanical forces generated by pulsed ultrasonication of polymer solutions (Figure 1), establishing the utility of directional mechanical force to bias reaction pathways and induce forbidden (in the context of orbital symmetry rules) reactions. This pioneering report captured the attention of many researchers and facilitated a “boom” in modern polymer mechanochemistry.

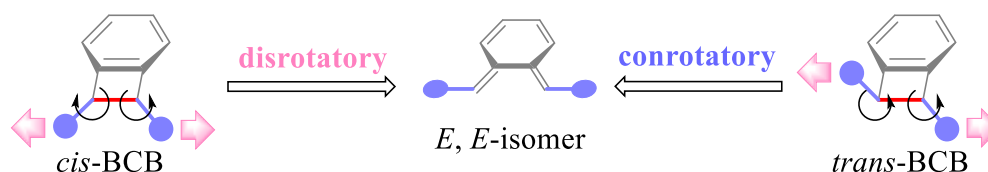


**Figure 1 : Mechanically induced ring-opening of *cis* and *trans* benzocyclobutene (BCB) yields single *E, E*-isomer as product.**

The theoretical interpretation of force-induced covalent bond cleavage was first reported by Kauzmann and Eyring<sup>11</sup> in 1940, who proposed a modified Morse potential for bond cleavage under force:  $U'(r) = U(r) - W(r)$ , where  $U(r)$  is the force-free Morse potential and  $W(r)$  is the work input that results from the applied force coupling to the reaction coordinate. This picture of force-coupled reactivity was refined by Bell (1978)<sup>12</sup> and Evans (1997),<sup>13-14</sup> who assumed a force-independent reaction length  $\Delta x^\ddagger$ , or the change in length along the reaction coordinate on going from reactant to transition state. The rate constant of force coupled reactions ( $k(F)$ ) under an external force  $F$  was expressed as:

$$k(F) = k_0 e^{F\Delta x^\ddagger/k_B T}$$

where  $k_0$  is the force-free rate constant,  $k_B$  is the Boltzmann constant, and  $T$  is temperature. Other models of modified potential energy surfaces have since been proposed, with Dudko and coworkers (2006)<sup>15</sup> deriving the following unified equation:

$$k(F) = k_0 (1 - vF\Delta x^\ddagger / \Delta G^\ddagger)^{\frac{1}{v}-1} e^{-\frac{\Delta G^\ddagger}{k_B T} \left[ 1 - \left( 1 - \frac{vF\Delta x^\ddagger}{\Delta G^\ddagger} \right)^{\frac{1}{v}} \right]}$$

where  $v = 1/2$  and  $v = 2/3$  correspond to the so-called Cusp and Cubic potential energy surfaces. Note that the equation is exactly the same as Bell-Evans expression when  $v = 1$ . More recently, Makarov<sup>16</sup> proposed the extended Bell theory (2011), and Boulatov<sup>17</sup> further considered the force-dependent coordinate in reactant and product and rewrote the equation by inserting a secondary term from Taylor expansion (2011). Lastly, potential energy obtained from first-principle methods was also reported by Martinez (2009)<sup>18</sup> and Marx (2009).<sup>19</sup>

The above brief introduction regarding the experimental and theoretical evolution of polymer mechanochemistry is presented to track the timeline of the increasing interest in polymer mechanochemistry. A more detailed history and state-of-the-art of polymer mechanochemistry can be found in some reported reviews.<sup>20-28</sup>

## **1.2 Principles of mechanophore design**

The design of mechanophores plays a crucial role in developing stress-responsive polymers, as both the latent function and the ease with which it is released by a mechanical trigger are encoded within the mechanophore structure. To date, a wide range of mechanophores have been incorporated into polymers, including those that change color/fluorescence,<sup>29-37</sup> chemiluminesce,<sup>38-39</sup> catalyze reactions,<sup>40-41</sup> release chemical

cargos,<sup>42-47</sup> and generate reactive units.<sup>36, 48-53</sup> Nevertheless, developing mechanophores with novel functionality remains an ongoing and important topic, as it enriches the scope and utility of stress-responsive polymers. Mechanophores that have been reported as of the time of this dissertation are summarized in Figure 2. As can be seen, the mechanophores can be categorized into five groups based on their mechanically coupled reactivity: homolytic/heterolytic cleavage, cycloreversion, dative bond dissociation, electrocyclic ring opening, and flex activation.

Initial mechanophores were based on the inclusion of relatively weak bonds, so that mechanical force selectively cleaves a specific bond along the polymer chain. These examples comprise relatively weak bonds that are thermally scissile, such as free radical initiators. Similarly, metal complexes that include dative bonds that are similarly weak (or weaker) relative to those weak covalent bonds proved to be popular early on.

Another judicious class of mechanophore comprises the cycloaddition adducts, which can undergo selective cyclo-reversion upon application of sufficient mechanical force. Currently reported retro-cycloadditions include retro [2+2], [4+2], and [4+4] cycloadditions, with considerable attention paid to the retro [2+2] cycloaddition as four-member rings (cyclobutanes, or CBs) are highly strained and thus are susceptible to dissociation. Investigations of CB-core mechanophores have spanned: 1) the effect of substituents on mechanochemical reactivity; 2) non-scissile CBs with stored length that provides a potential mechanism for energy dissipation; 3) fluorophore/chromophore integrated CBs that enable reversible activation-regeneration and detection of

stress/damage; 4) generation of reactive species that heal or strengthen the material under stress; and, 5) the use of CB as a molecular “gate” to regulate the chromophore photoreactivity and polymer degradability. Other [4+2] and [4+4] cycloaddition adducts are mainly based on anthracene dimer and anthracene-maleimide adducts. These mechanophores are generally designed as scissile types because the introduction of a bridge would be synthetically tedious. Nevertheless, activation produces fluorescent anthracene that can be observed and quantified easily. The photophysical properties of anthracene can be chemically modified to meet specific demand of detection, for example by extending the conjugation of anthracene to improve its fluorescence quantum yield.<sup>54</sup>

Another heavily investigated group of mechanophores is based on electrocyclic ring-opening reactions. These mechanophores can be divided further into two subgroups depending on whether the ring-opening reactions are irreversible or reversible. The former (irreversible) type includes (benzo)cyclobutene, dihalocyclopropanes, ladderane, and aziridine, while the latter (reversible) includes pyrans and rhodamines that are usually both non-scissile and photo/thermochromic. The study of the irreversible ring-opening mechanophores has mainly focused on their force-coupled kinetics and mechanisms, or use in stress-responsive mechanical properties, whereas most reversible mechanophores have been used as force probes to investigate force transduction, force distribution and damage in strained bulk polymers and polymer composites.



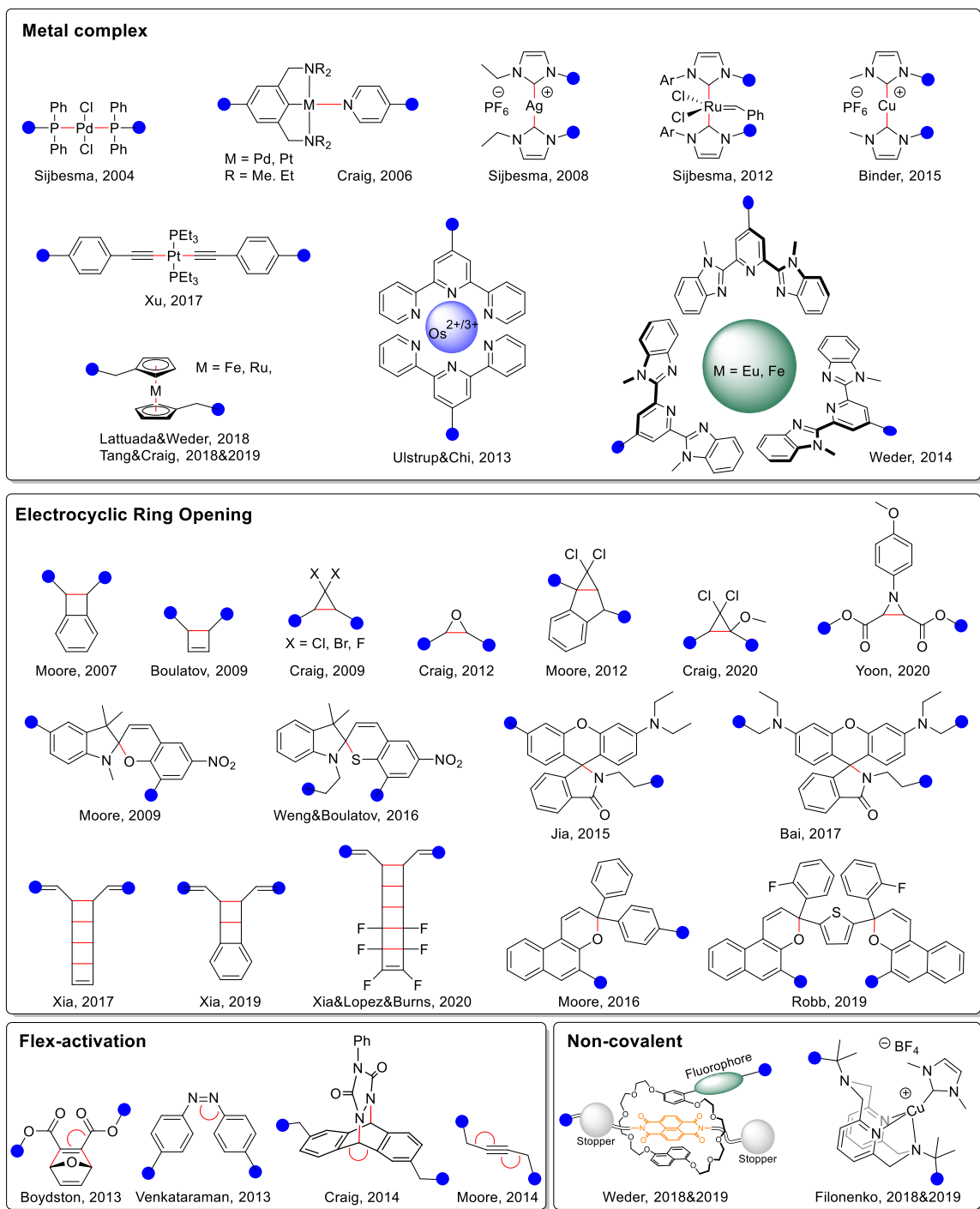


**Figure 2 : Characterization of available mechanophores as of early 2020, with apologies for any omissions. The blue dots are the attachments where force is coupled, and the red bonds indicate breaking bonds.**

Flex-activated mechanophores make up an interesting category that has received less attention, probably because the relatively poor coupling between mechanical force and the reaction coordinate leads to a relatively low mechanical reactivity. A promising exception was reported recently by Boulatov and coworkers,<sup>55</sup> who coupled force to the unreactive positions in a phosphotriester substrate to accelerate the  $S_N2$  reaction by a factor of  $> 10^4$ . Relative to other mechanochemical motifs, developing new flex-activated mechanophores requires a more careful design of molecular structures to ensure desirable mechanical reactivity.

In general, there is a trade-off between the mechanical reactivity of thermal stability in mechanophores. One needs to consider proper stability in mechanophores that is stable enough to give high mechanical reactivities. Notably, metallocene-based mechanophores reported by Lattuada and Weder,<sup>47</sup> Tang and Craig<sup>45, 56</sup> are both highly thermally stable and mechanically active. Finally, exceptions to the above categorizations exist. For example, Weder et al.<sup>31, 57</sup> recently reported a rotaxane-based mechanophore that functions as a reversible force probe, in which mechanical force is used to overcome a host-guest interaction that is weaker than the (relatively) large energy barriers associated with covalent chemical reactions.

### ***1.3 Techniques for coupling mechanical force***

This dissertation reports obtained through the use of three main techniques to trigger mechanochemical responses: ultrasonication, single molecule force spectroscopy, and bulk mechanical tests. Other industrial processes, such as extrusion and mastication

et al., are not employed in the studies reported here and therefore are not described in this section. A recent review highlights how polymer mechanochemistry can be conducted on an industrial scale and discusses several related mechanical processes.<sup>58</sup>

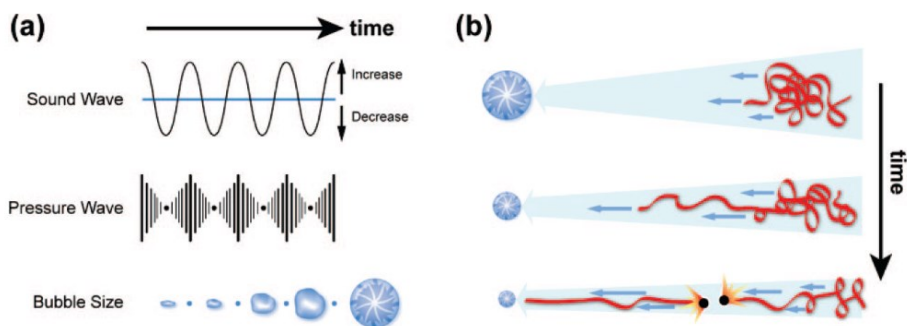


**Figure 3 : Mechanism of ultrasound-induced stretching of polymer chains in the solution.**

Ultrasonication is used to apply mechanical force to polymers in solution, and it can be applied on a scale (tens of mg) that allows for the ready identification and quantification of mechanically activated species. Despite uncertainty regarding the exact mechanisms by which forces are generated and the magnitude and distribution of those forces, it is generally accepted that the extensional flows originate from cavities that form and grow in solution in response to the pressure waves that accompany sonication. Once it grows to a certain size, the cavity will collapse, and the rush of surrounding solvent to fill that void occurs with a velocity gradient in the direction of the flow (extensional or elongational flow). That flow field stretches and pulls the polymer coil toward the cavity center (Figure 3), leading to an expected parabolic force distribution along the stretched polymer backbone with a maximum force near the polymer midchain. The peak force depends on polymer contour length (long polymers = higher forces), and when the

polymer is long enough it becomes large enough to break conventional C-C (or other) covalent bonds, leading to chain scission and a reduction in molecular weight. The collapse of the cavity (and any associated mechanochemistry) occurs on the time scale of microseconds, and the generated tension has been used to “trap” high energy reactive intermediates and even force-free transition state structures on that time scale.<sup>59</sup> The description of ultrasound here is also brief, and a more detailed discussion can be found in prior reviews.<sup>60-61</sup>

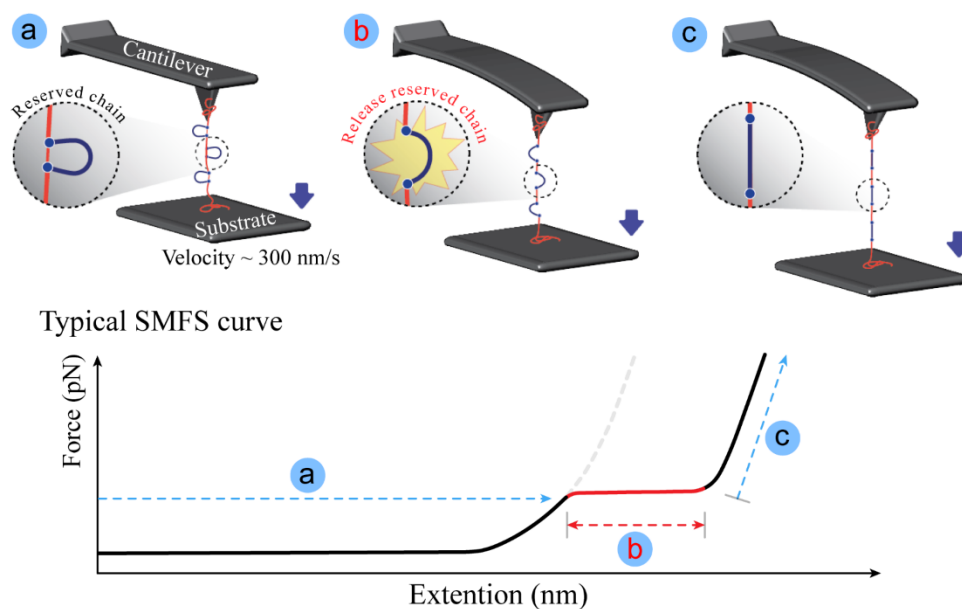


**Figure 4 :** Schematic of pulling a multi-mechanophore polymer using SMFS and the corresponding force-extension curve. Mechanophores can be viewed as loops that are bridged by weak bonds along the polymer main chain. As the polymer is stretched and the force along its backbone increases, its response can be broken into three stages: (a) The single polymer is uncoiled and extended until (b) the force becomes large enough that bridge bonds start to break and stored length in the loops is released. This release of stored length leads to a characteristic plateau in the force-extension curve. (c) Further extension of the polymer chain after mechanophore consumption continues until the polymer breaks or detaches from one of the surfaces.

Single molecule force spectroscopy (SMFS) can be used to quantify the force-dependent reactivity of mechanophores, especially those that are non-scissile in the context of the polymer backbone. A productive strategy, used extensively by Craig and co-workers, is illustrated in Figure 4. A multi-mechanophore polymer chain is anchored to the cantilever of an atomic force microscope and to an opposing substrate. The non-scissile mechanophores are depicted as bridged loops along the polymer chain. When the substrate is moved away from the cantilever, the polymer chain will first be uncoiled, which corresponds to the stage (a) in a typical force-extension curve. Eventually, the force reaches a sufficiently high value to trigger meaningful reactions, and the activation of the mechanophores releases stored length that gives the polymer chain additional extension. This process corresponds to the characteristic plateau (b) on the force-extension curve. After all mechanophores have reacted, the polymer chain will be further stretched until it breaks or detaches from the cantilever or substrate. Instead of a typical sawtooth feature as observed in SMFS pulls of multi-domain proteins, an apparently “flat” plateau is often observed on the force-extension curve. The lack of individual feature as observed in SMFS pulls of multi-domain proteins,<sup>62</sup> an apparently “flat” plateau is often observed on the force-extension curve. The lack of individual features is due to the fact that the instrument does not possess sufficiently high resolution to resolve individual events ( $\sim \text{\AA}$  of stored length). This behavior is reminiscent of some polysaccharides and DNAs,<sup>63-65</sup> in which the smooth transition plateau is ascribed to a large number of mechanically coupled conformational changes. Further, the characteristic plateau gives a measure of the force

required to achieve activation on the time scale of the SMFS test, which is typically on the order of 10-100 ms for standard experimental conditions. Analysis of SMFS curves using an extended freely jointed chain model (eFJC) and Bell-Evans or Cusp models of force-coupled potential energy surfaces and kinetics allows us to retrieve the reaction parameters  $\Delta x^\ddagger$ , which is attributed to the difference in polymer contour length at the transition state relative to the ground state of an individual reaction center embedded along the polymer main chain.

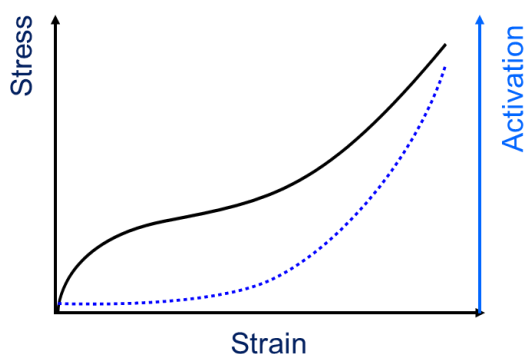


**Figure 5 : Schematic of a stress-strain curve that might be obtained from a tensile test of a mechanophore embedded polymer. The optical response versus stress/strain is recorded *in situ*.**

Mechanical tests, including tensile, shear, and compression tests, are generally employed to study the mechanochemical behavior in bulk polymeric materials. For these studies, optically active mechanophores are often embedded into the bulk materials, as their activation can be monitored *in situ* and often in real time. Typical data is illustrated in Figure 5. As the polymer bulk is subjected to tensile tests, the evolution in optical properties is recorded over time. The relative activation can be quantified from the optical signals and further correlated with stress-strain behavior. For non-crosslinked bulk

materials, there are fewer restrictions on the choice of embedded mechanophores, because their activation can be monitored either *in situ* or by using post-event, conventional solution-based analysis (e.g.,  $^1\text{H}$  NMR, mass spectroscopy). The combination of bulk studies with ultrasonication and SMFS provides an opportunity to characterize and connect mechanochemical response on different length and time scales, and the following chapters in this dissertation draw on these techniques – sometimes individually, but more often in combination – in an attempt to help make that very connection.

## 2. Structure-reactivity relationships in polymer mechanochemistry

### 2.1 Regiochemical effects on mechanophore activation in bulk materials <sup>1</sup>

Mechanochromic force probes, including spiropyran derivatives, have proven to be useful in visualizing the stress/strain distribution and fracture behavior in polymeric materials. Here, we report the macroscopic response of silicone elastomers including cross-links made up of three spiropyran (SP) regioisomers. The SP derivatives **SP(o)**, **SP(m)** and **SP(p)** are connected to the network through an identical attachment point on the indoline fragment and regioisomeric attachments *ortho*, *meta*, and *para* to the spirocyclic C-O bond on the benzaldehyde fragment, respectively. The relative colorimetric response of these regioisomers under quasi-static uniaxial tensile load is: **SP(o) > SP(m) > SP(p)**, consistent with the expected mechanical sensitivity of the regioisomers obtained from molecular modeling. The extrapolated strain onset for detectable activation of all three regioisomers, however, is indistinguishable and occurs at ~90% uniaxial strain. Finally, the ratiometric response of the three isomers is constant across the strains investigated (90% - 135% uniaxial strain), in contrast to expectations based on simulations of strained intact polymer networks.

---

<sup>1</sup> This chapter is adopted from: Lin, Y.; Barbee, M. H.; Chang, C. C.; Craig, S. L. Regiochemical Effects on Mechanophore Activation in Bulk Materials. *J. Am. Chem. Soc.* **2018**, *140*, 15969-15975.

### 2.1.1 Introduction

At the molecular level, high strains in polymeric materials, including elastomers, leads to increasing tension along the polymer chains. At sufficiently high strains, that escalating tension induces polymer chain scission and microcrack formation.<sup>60</sup> The insertion of mechanically active moieties (mechanophores) into polymer structures provides the opportunity to transduce typically destructive mechanical force into constructive chemical responses<sup>20, 60</sup> that complements mechanically coupled supramolecular responses in other systems.<sup>66-67</sup> By incorporating different mechanophores, a variety of mechanically active polymer materials can be prepared, including those that are mechanochromic,<sup>29, 54, 68-73</sup> mechanoluminescent,<sup>38, 74-75</sup> or mechanocatalytic,<sup>40, 76-77</sup> and others that release small molecules<sup>42-43, 78-79</sup> or generate novel chemical reactions.<sup>10, 80-85</sup> Not surprisingly, this rich range of mechanophores spans a similarly wide range of force-rate relationships that guide their activation at the molecular level. For example, the forces required to induce ring-opening reactions of previously studied spiropyran (SP) and *gem*-dihalocyclopropane (gDHC) derivatives so that they occur on the time scale of 0.1 s have been quantified using single molecule force spectroscopy (SMFS) to be 240~260 pN and 0.8~2.3 nN, respectively.<sup>83-88</sup>

The disparate activities of mechanophores highlight the importance of expanding the structure-activity relationships that guide mechanochemical response in bulk materials. Although many mechanophores have been quantified and evaluated using SMFS, little is known about the relative responsiveness of different mechanophores as a

function of strain in bulk materials. In order to rationally design stress-responsive materials based on mechanophores, the interplay between mechanophore and polymer network structure needs to be established. Among the various structure-activity relationships that have been investigated to date, the effect of regiochemistry on mechanophore activity, which determines the distance over which force is applied in a force-coupled transformation, hereafter  $\Delta x^\ddagger$  in kinetically determined processes, or  $\Delta L_{rxn}$  for force-coupled equilibria, has been studied from sonication and quantified at the single molecule level using SMFS.<sup>87, 89-91</sup> In bulk materials, Robb et al.<sup>92</sup> recently reported the regio-specific mechanical activation of naphthopyran mechanophores in a silicone elastomer. Of the three naphthopyran regioisomers studied, however, two displayed no detectable mechanical activity, which prevents a more detailed evaluation of regiochemical effects on mechanophore activation in the bulk materials. A more systematic comparison of mechanically active force probes would allow important structure-activity relationships to be ascertained.

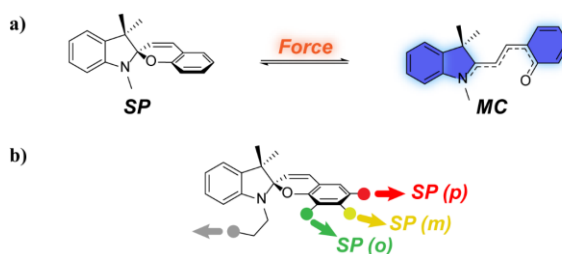


**Figure 6 : a) Spiropyran (SP) ring-opens to the highly colored merocyanine (MC) under mechanical force; b) Spiropyran regioisomers prepared for this study, with the locations of the force handles indicated by arrows.**

SP derivatives (Figure 6a) are well suited for this purpose. A range of SPs have been widely employed as mechanochromic force probes in various polymer matrices,

revealing the impact of chain mobility<sup>93-95</sup>, chain orientation<sup>96-98</sup> and chain relaxation<sup>99-100</sup> on macroscopic-to-molecular force transduction. The compatibility of SP with numerous polymeric materials (e.g. PMA<sup>29</sup>, PMMA<sup>99</sup>, PCL<sup>101</sup>, PS<sup>100</sup>, PU<sup>93, 102</sup>, PDMS<sup>79</sup>, hydrogel<sup>103</sup> and latex<sup>104</sup>) and the robust chemistry of SP preparation motivated us to explore the activity of various SP regioisomers (Figure 6b) as a function of strain in bulk materials.

## 2.1.2 Experimental section

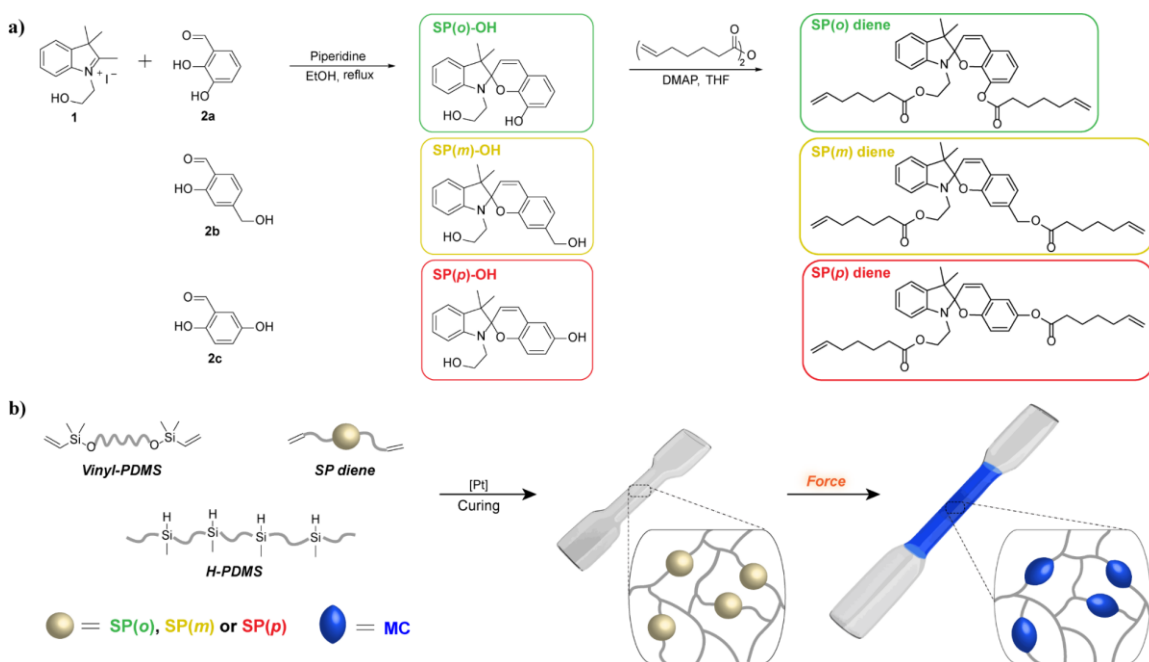


**Figure 7 :** a) Synthesis of SP regioisomers and subsequent modification with diene ‘handles’; b) Illustrated incorporation of SP regioisomers into PDMS polymer network via platinum catalyzed hydrosilylation and following mechanical activation of SP into blue color MC.

### 2.1.2.1 Preparation of SP regioisomers

SP regioisomers are named based on the relative position of alkene ‘handle’ in the benzaldehyde-based half of the SP to the labile spirocyclic C-O bond, whose scission leads to a colorimetric response. Three derivatives, **SP(o)**, **SP(m)**, and **SP(p)** were synthesized

from the well-known condensation of indoline and benzaldehyde as shown in Figure 7a, where the *o*, *m* and *p* refer to *ortho*, *meta* and *para* attachments, respectively. Indoline was prepared according to a previously reported procedure,<sup>79</sup> and by simply changing the regiochemistry of the benzaldehyde building block, different SP regioisomers are obtained. Unlike **SP(o)-OH** and **SP(p)-OH**, **SP(m)-OH** was prepared from 2-hydroxy-4-(hydroxymethyl)benzaldehyde instead of 2,4-dihydroxybenzaldehyde, because the relatively more electron-rich aldehyde results in low reactivity in the condensation reaction.<sup>105-106</sup> All SP-OH regioisomers were obtained in good yield (for details see section 2.1.5), and their subsequent esterification installs alkene ‘handles’ that allow their covalent incorporation into the silicone *via* platinum catalyzed hydrosilylation (Figure 7b), as described previously.

#### 2.1.2.2 Network preparation

**SP(o)**, **SP(m)**, or **SP(p)** diene (22 mg, 0.5 wt %) was dissolved in 0.4 mL xylene, and 4.0 g pre-mixed Sylgard 184 part A was added to the solution. The resulting pale mixture was vortex mixed for 3 min to give a clear blend. 0.4 g Sylgard 184 part B was then added and the final mixture was further mixed for 3 min. After degassing under house vacuum, the obtained mixture was poured onto a freshly cut polypropylene film. Curing at 65 °C overnight gave a clear, cross-linked PDMS film with thickness of about 0.30-0.45 mm.

#### 2.1.2.3 Tensile tests

Films were cut into ‘dog-bone’ shapes using a die with modified dimensions of ASTM Die D. Tensile tests were performed on a TA Instruments RSA III Dynamic

Mechanical Analyzer at strain rate of  $0.5 \text{ mm s}^{-1}$ , and color images were captured on a Canon EOS RebelTM xsi camera.

### 2.1.3 Results and discussion

Because of the absence of the familiar nitro group at the *para* position to the labile spirocyclic C-O bond, we anticipated that the SP-MC equilibrium would strongly favor the colorless SP due to lack of stabilization of the negative charge on the merocyanine product. As expected, all prepared SP embedded PDMS films were clear and colorless and had similar mechanical properties, as verified from uniaxial tensile testing (Figure 11). The lack of a nitro substituent also meant that the samples had negligible UV driven photoswitching, which facilitated the studies.

#### 2.1.3.1 Relative activation

As an initial evaluation of mechanical responsiveness, a specimen of each SP-PDMS film was cut into a  $\sim 3 \text{ mm}$  wide strip. For all prepared SP-PDMS samples, we clearly observed mechanical activation of SP into a blue color consistent with the expected formation of the more highly conjugated merocyanine (MC) when the strip was manually stretched (Figure 10). For more quantitative characterization of mechanochromism, the SP-PDMS films were cut into 'dog-bone' shaped samples and subjected to a uniaxial tensile test while images were recorded. A typical set of images of each of the three types of SP-PDMS specimen during tensile testing is shown in Figure 8a. The increasing blue color with strain is most obvious in **SP(o)**-PDMS, while a less intense blue color is

observed for **SP(m)**-PDMS, and less again for **SP(p)**-PDMS. In the latter case, the blue color is barely visible to the naked eye even at a uniaxial strain of 135%.

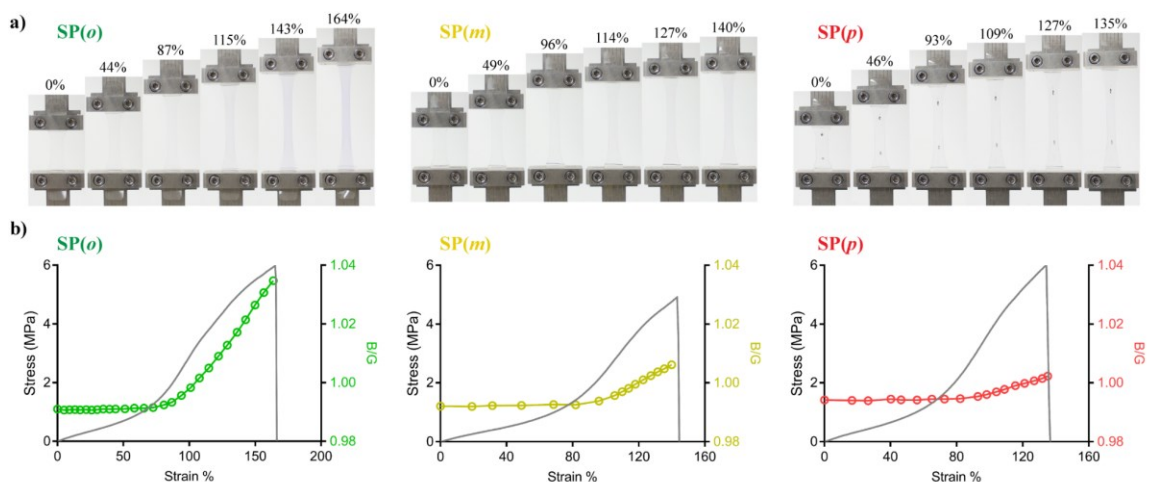


**Figure 8 :** a) Representative image set of SP-PDMS under quasi-static tensile test; b) Stress-strain curve and corresponding B/G value from image analysis, where B is the blue channel intensity and G is the green channel intensity; **SP(o)** (left), **SP(m)** (middle) and **SP(p)** (right). The blue dots in the **SP(p)** images of (a) are labels made by marker and used to verify the strain; they are not included in the image analysis.

### 2.1.3.2 Onset of activation

To quantify the onset of color change and the relative strain-dependent activation of each regioisomer, we collected RGB images using a previous developed procedure.<sup>79</sup> Analysis of these RGB images provides the intensity in red, green and blue channels. In order to correct for the effect of any subtle changes in ambient light due to the movement of the film under extension, the ratio of intensity in different channels was used; the best signal-to-noise ratio was found for the ratio of the B and G channels (Figure 18). We therefore used the B/G ratio to evaluate the mechanophore activation. As illustrated in Figure 8b, the B/G value of **SP(o)**-PDMS remains unchanged at about 0.991 from 0% to

~90% strain. Further increases in strain, however, lead to a linearly increasing B/G value that reaches 1.035 at a strain of 164%.

The linear B/G response can be extrapolated back to its baseline value to give an apparent strain at onset for detectable activation of 90%, which corresponds well with the onset detected by the naked eye. The corresponding point on the stress-strain curve indicates that the polymer network starts to enter the strain hardening section at this same value of 90% strain. The correlation between macroscopic colorimetric response and macroscopic strain hardening is intuitively reasonable, since the single molecule tension required for SP activation involves forces that are in the non-linear (strain hardening) deformation regime of the single molecule.<sup>87</sup> That enough strands are activated to observe macroscopic coloration suggests a likelihood that enough strands might also be deforming non-linearly to result in macroscopic strain hardening.

Somewhat unexpectedly to us, the onset behavior in the mechanochromic response of **SP(*m*)** and **SP(*p*)** is indistinguishable from that of **SP(*o*)**. The B/G value for **SP(*m*)** is 0.992 at 0% and increases to 1.006 at 140% whereas it is 0.994 for **SP(*p*)** at 0% and 1.002 at 135%. Extrapolation of B/G to baseline again gives apparent strains at color onset of ~90%. While subtle differences beyond the precision of the measurements employed here might exist, these results suggest that mechanochemical activation in these force probes is determined more by the network structure and strain hardening physics than the isolated molecular characteristics of the mechanophore.

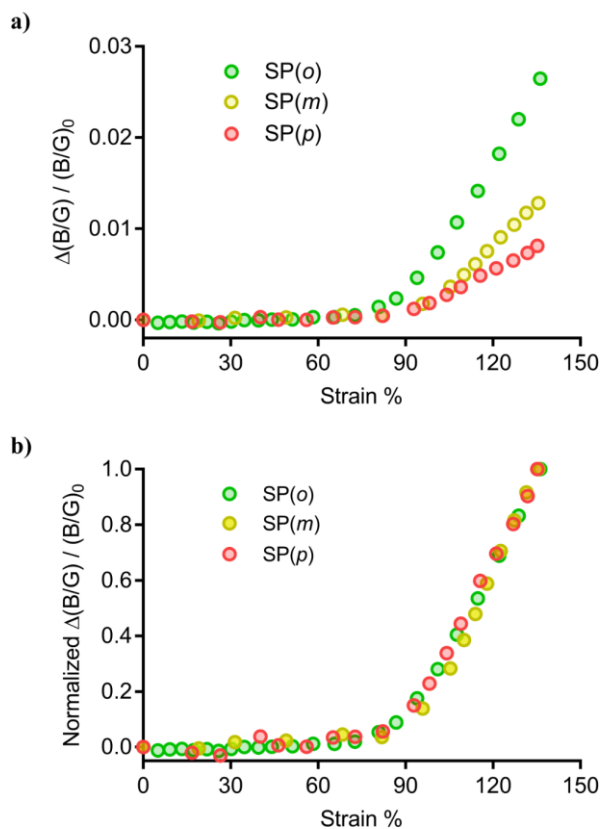


**Figure 9 : a) Change in B:G intensity ratio of three SP regioisomers, where  $\Delta(B/G) = (B/G) - (B/G)_0$ , and  $(B/G)_0$  is the value at 0% strain; b) data in (a) normalized to the value at 135% strain.**

#### 2.1.3.4 Ratiometric activation as a function of strain

We next considered the possibility of differential response at higher strains. The total response of a mechanophore within a strained network can be broken down into a function of: (i) the strain at which response begins; and, (ii) how the activation grows as a function of increasing strain from that point forward. As all three SP derivatives are effectively indistinguishable with respect to their strains at color onset, we therefore considered the relative strain dependence of their colorimetric response. A straightforward comparison of relative mechanical activation can be seen in Figure 9a, by

normalizing the increase in B/G to its initial (unstrained) value. All three derivatives show a linear change in B/G as a function of increasing strain up to the limiting strain at break. The normalized increase in B/G values at ~135% strain are 0.026, 0.013 and 0.008 for **SP(o)**, **SP(m)** and **SP(p)**, respectively. One corollary of the nearly linear response in the individual regioisomers is that the relative activation of the SPs stays constant across the accessible strain window. In other words, **SP(o)** is always more activated than **SP(m)** and more activated again than **SP(p)**, but the ratio of MC derived from any isomer to another does not change.

Quantifying the exact extent of activation of each isomer is problematic, as the extinction coefficients are not known, and the MCs cannot be generated photochemically or by another means in order to get them accurately. Since the UV-vis absorption spectra for all SP regioisomers are similar when mechanically activated to MC (Figure 12), however, one could assume that the molar absorptivities and change in B/G ratio are identical for purposes of estimating the relative activation. In this limit, the relative activation of **SP(o):SP(m):SP(p)** is 3.2:1.6:1. These numbers are necessarily approximate, and they are likely to be revised (perhaps substantially) if/as accurate extinction coefficients become available. Interestingly, however, the *ratiometric* response (regardless of the exact value of the ratios) of the three isomers is strain independent across the strains accessed (90%-135%, Figure 9b), and this result does not depend on the extinction coefficients of the three merocyanine regioisomers.

### 2.1.3.5 Molecular origins of differential activation

The relative color change of the three SP isomers (**SP(o)** > **SP(m)** > **SP(p)**) is consistent with the expected relative response of the isolated isomers. Previous studies<sup>82, 84, 86-89, 107-108</sup> have showed the significance of mechanical coupling ( $\Delta x^\ddagger$ ) – the change in contour length of a stretched polymer as an embedded mechanophore goes from its ground to transition state – on the kinetically limited activation of mechanophores. Even subtle modifications in the attachment site and/or the structure of the groups connecting the mechanophore to the polymer can significantly affect the activation length and the resulting mechanical susceptibility.

In the case of the quasi-static loading of the SP-PDMS films studied here, the extent of activation is thermodynamically, rather than kinetically, determined (equilibration times of  $\sim 1$  s; see Figure 13). Although the mechanochromism is thermodynamically determined, the considerations are similar as to the kinetically controlled cases. Namely, the greater the change in length on going from reactant to product ( $\Delta L_{\text{rxn}}$ ), the more mechanically responsive the force-coupled equilibrium will be. Because the electronic effects of these substituents on the force-free SP-MC equilibrium are relatively modest,<sup>109</sup> it is the geometric effect that likely dominates the behavior here. This picture is consistent with the relative activation observed in the SP-PDMS films. Molecular modeling (Figure 25-42) shows that the expected trend in  $\Delta L_{\text{rxn}}$  for these mechanophores corresponds to the trend observed in the relative extent of activation: **SP(o)** > **SP(m)** > **SP(p)**.

## 2.1.4 Conclusion

The results presented here provide some important insights into the molecular mechanochromic response associated with deformation of the bulk elastomer. Comparisons to single molecule behavior are illustrative. The extent of color as a function of force at the molecular level depends on the force-coupled SP-to-MC equilibrium constant:

$$K_{eq}(F) = e^{\frac{-(\Delta G^{\circ} - N_A F^* \Delta L)}{RT}} \quad (1)$$

In cases such as the SP-PDMS films employed here, where  $\Delta G^{\circ}$  is roughly constant, therefore, the reaction with the largest  $\Delta L$  should reach a detectable limit at the lowest force – and therefore the lowest strain. In other words, stretching an individual molecule would lead to detectable **SP(o)** opening before **SP(m)**, which would open before **SP(p)**. In the bulk elastomer, however, the activation of all three isomers is triggered at the same strain. It is very possible that the differences in onset strain for the mechanophores employed here are simply too small for us to detect, but at a minimum the observations here motivate further experimental and theoretical work to better understand the onset behavior.

Even more interesting is the constant ratiometric response after the onset of detectable mechanochromism. Referring to eq. 1, in systems that are characterized by a single effective force, the mechanophore with the largest  $\Delta L$  is expected to respond more strongly with increasing force than those with smaller  $\Delta L$ . This behavior is not observed

in the SP regioisomers here, nor is it observed in a similar study involving different SP force probes by Kim et al.<sup>110</sup>

In the elastomers, of course, there is a distribution of forces rather than a single force across the elastically active strands when the polymer is strained. Little is known about the details of molecular tension distributions in strained polymer networks. Recent computational work by Makarov<sup>111</sup> suggests an exponential distribution for the high tension portion of the strands in a network (those that would be responsible for any mechanochemical response). Our attempts to rectify our observations with the theory have so far been unsuccessful; Makarov's exponential distribution becomes increasingly stretched with strain, so that the ratio of high force (i.e., **SP(p)**) mechanophore activation to low force (i.e., **SP(o)**) activation should increase with strain. One possible contributor to the lack of agreement might be the contributions from chain scission events, which have been detected at the same strains (> 90%) at which mechanochromism is observed here.<sup>112</sup> For example, such events might create a high-force "ceiling" on the force distribution, leading to an accumulation of active strands that dominate the mechanochromic response, but whose force distribution changes little with strain.

Looking forward, the observations reported here motivate a closer look at the molecular tension details within strained networks. For example, careful characterization of these and other force probes by SMFS<sup>109</sup> might allow for actual tension distributions to be experimentally determined. In addition, work on other polymer networks would test the generality of these findings and potentially reveal possible interplays between the

structure of the mechanophore and the network in which it is embedded. Finally, further theoretical advances are likely to be critical. The ability to directly probe molecular behavior in necessarily heterogeneous polymer networks, through methods similar to those employed here, are likely to provide an important empirical anchor to such future investigations.

## **2.1.5 Synthetic and general procedures**

### **2.1.5.1 Materials and characterization**

Materials: Lab general solvents (dichloromethane, chloroform, hexane, ethyl acetate, acetone, xylene, tetrahydrofuran, ethanol) were purchased from VWR or Sigma Aldrich. 2,3,3-Trimethylindolenine, 2-iodoethanol, piperidine, 2,3-dihydroxybenzaldehyde, 2,5-dihydroxybenzaldehyde, 3-hydroxymethylphenol, 6-pentenoic acid, triethyl amine and 4-dimethylaminopyridine were purchased from Sigma Aldrich or Alfa Aesar and used without further purification. Sylgard®184 was purchased from Ellsworth Adhesives, Germantown, WI. Flash chromatography was performed on CombiFlash®200 auto-column system from Teledyne ISCO.

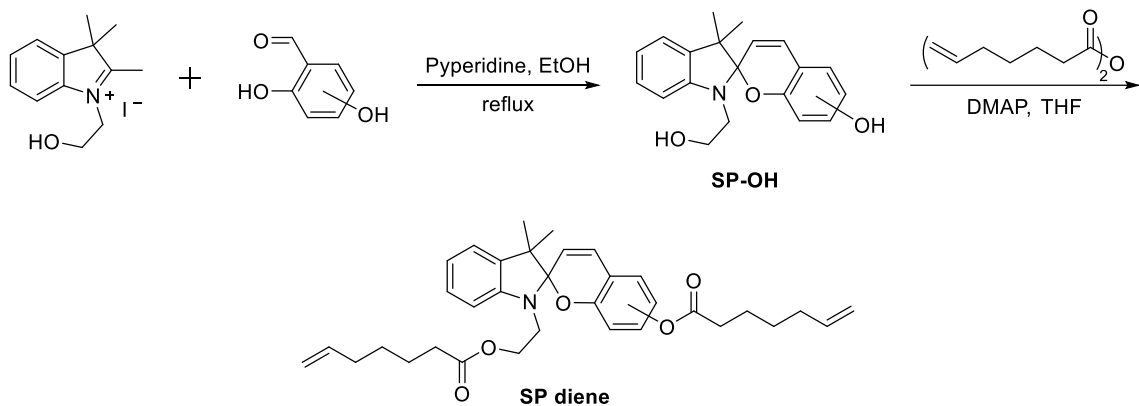
Characterization: <sup>1</sup>H NMR spectra were collected on a 400 MHz Varian INOVA spectrometer and <sup>13</sup>C NMR spectra were collected on a 500 MHz Varian UNITY spectrometer. Chemical shifts are given in *ppm* ( $\delta$ ) and referenced to the residual <sup>1</sup>H peak at 7.26 ppm or <sup>13</sup>C peak at 77.16 ppm in CDCl<sub>3</sub>. <sup>1</sup>H shifts are reported as chemical shift, multiplicity, coupling constant if applicable, and relative integral. Multiplicities are reported as: singlet (s), doublet (d), doublet of doublets (dd), doublet of triplets (dt),

doublet of doublet of doublets (ddd), doublet of doublet of triplets (ddt), triplet (t), triplet of doublets (td), quartet (q), multiplet (m), or broad (br). Coupling constants (J) are reported in Hertz. High-resolution mass spectra were collected on an Agilent LCMS-TOF-DART at Duke University's Mass Spectrometry Facility. UV-vis spectra were collected on a SI Photonics Model 440 UV/Visible Spectrophotometer while the film strips were maintained at certain strain with a homebuilt stretcher. Images were recorded using a Canon EOS Rebel™ xsi with a Canon EF-S 18-55 mm f/3.5-5.6 IS SLR lens. Images were obtained without flash and with exposure parameters set to 1/15 sec, *f*/5.6, ISO 100.

Tensile test: Prepared films were cut into 'dog-bone' shaped specimen with a modified ASTM Die D dimension. Uniaxial tensile tests were performed on a TA Instruments RSA III Dynamic Mechanical Analyzer (Force resolution: 0.0001 N, strain resolution: 1 nm) at Duke University's Shared Material Instrument Facility (SMIF). To prevent force constrained at the clamped position of the sample that may result in premature sample break, additional two small pieces of films were placed on each side of the sample film. The PDMS sandwich structure provided increased friction and prevented slipping at high strains.

### **2.1.5.2 Synthetic procedures**

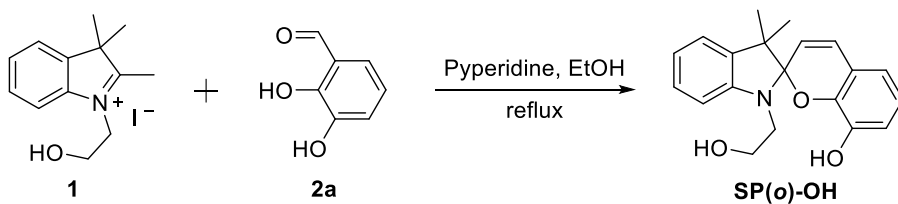
General synthesis scheme



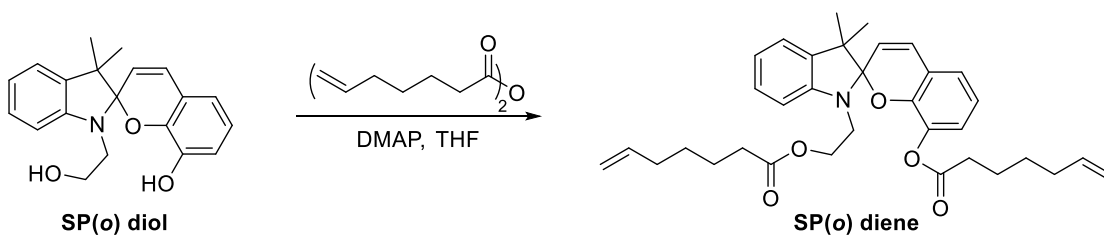
### 2.1.5.2.1 Synthesis of SP(o) derivative

The synthesis of **SP(o)-OH**<sup>113</sup>, **SP(o) diene**<sup>109</sup> and hept-6-enoic anhydride<sup>87</sup> have been reported previously.

#### *Synthesis of SP(o)-OH*

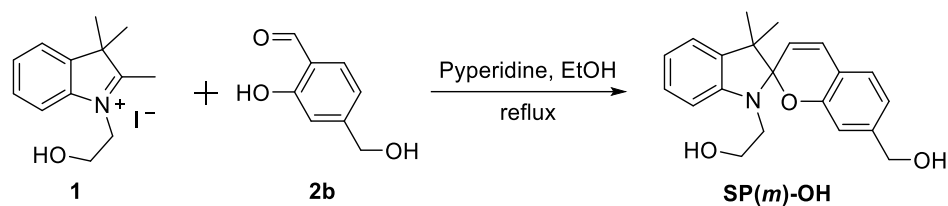


#### *Synthesis of SP(o) diene*



### 2.1.5.2.2 Synthesis of SP(m) derivative

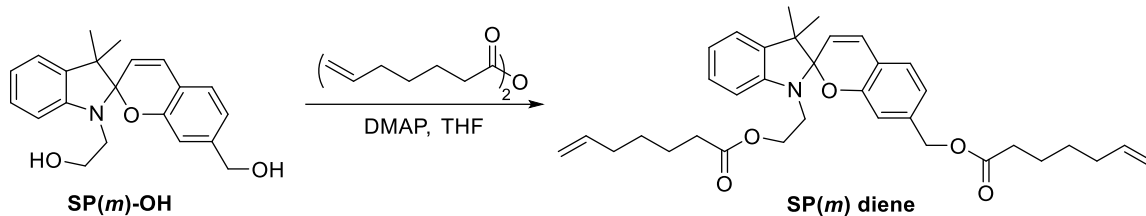
#### *Synthesis of SP(m)-OH*



2-Hydroxy-4-hydroxymethylbenzaldehyde **2b** was synthesized according to reported procedure<sup>14</sup>.

To a solution of **1** (662.4 mg, 2 mmol) and **2b** (304 mg, 2 mmol) in 10 mL ethanol, added xml piperidine (394  $\mu$ L, 4 mmol). The solution was then refluxed for overnight. After cooling down, ethanol was removed under reduced pressure to give brown oil. The oil was then dissolved in 100 mL ethyl acetate and washed with 3 $\times$ 100 mL DI water and 100 mL brine. Organic phase was further dried with MgSO<sub>4</sub>. After evaporation under reduced pressure, a light brown foam solid **SP(m)-OH** was obtained (658 mg 88.1%). An analytical product was obtained by further purification from column chromatography (0% ~ 50% EtOAc/Hexane gradient). <sup>1</sup>H NMR (400 MHz, CDCl<sub>3</sub>)  $\delta$  7.16 (td, J = 7.7, 1.4 Hz, 1H), 7.08 (dd, J = 7.3, 1.3 Hz, 1H), 7.03 (d, J = 7.6 Hz, 1H), 6.91 – 6.79 (m, 3H), 6.71 (d, J = 1.5 Hz, 1H), 6.63 (d, J = 7.7 Hz, 1H), 5.67 (d, J = 10.3 Hz, 1H), 4.57 (s, 2H), 3.74 (m, 4H), 3.50 (m, 1H), 3.33 (m, 1H), 1.30 (s, 3H), 1.17 (s, 3H). <sup>13</sup>C NMR (125 MHz, CDCl<sub>3</sub>)  $\delta$  153.89, 147.27, 143.31, 136.38, 129.23, 127.60, 126.96, 121.84, 119.35, 119.28, 118.87, 117.76, 113.34, 106.56, 104.67, 64.64, 60.65, 52.25, 45.93, 25.87, 20.37. HRMS-ESI (m/z): calculated [M + H]<sup>+</sup> for C<sub>21</sub>H<sub>24</sub>NO<sub>3</sub>, calculated 338.17507, found 338.17569.

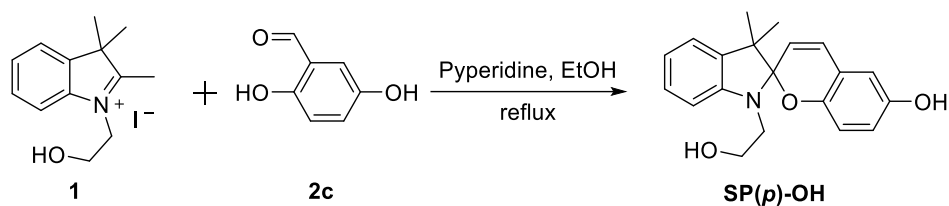
#### *Synthesis of SP(m) diene*



To a solution of **SP(m)-OH** (0.5 g, 1.48 mmol, 1.0 eq.) in 12 mL dry THF, added hept-6-enoic anhydride (740 mg, 3.11 mmol, 2.1 eq.) and DMAP catalyst (18 mg, 0.148 mmol, 0.1 eq.). The solution was allowed to stir at room temperature for overnight. After the reaction completed, 0.5 mL Et<sub>3</sub>N was added to the solution and stirred for additional 30 min. Then the solvent was removed under reduced pressure. Further flash chromatography (0% to 25% EtOAc/hexane gradient eluent) gave **SP(m) diene** as a light orange oil (704 mg, 85.4%). <sup>1</sup>H NMR (400 MHz, CDCl<sub>3</sub>) δ 7.17 (t, *J* = 7.6 Hz, 1H), 7.07 (d, *J* = 7.1 Hz, 1H), 7.02 (d, *J* = 7.7 Hz, 1H), 6.92 – 6.73 (m, 3H), 6.73 – 6.61 (m, 2H), 5.77 (m, 2H), 5.70 (d, *J* = 10.2 Hz, 1H), 4.98 (s, 2H), 4.97 – 4.90 (m, 4H), 4.25 (dt, *J* = 11.0, 6.4 Hz, 1H), 4.16 (dt, *J* = 11.5, 6.3 Hz, 1H), 3.51 (m, 1H), 3.38 – 3.29 (m, 1H), 2.34 (t, *J* = 7.5 Hz, 2H), 2.26 (t, *J* = 7.5 Hz, 2H), 2.03 (p, *J* = 7.3 Hz, 4H), 1.62 (m, 4H), 1.39 (m, 4H), 1.28 (s, 3H), 1.14 (s, 3H). <sup>13</sup>C NMR (126 MHz, cdcl<sub>3</sub>) δ 173.59, 173.50, 154.32, 147.30, 138.45, 138.15, 136.34, 129.19, 127.68, 126.96, 121.82, 119.84, 119.58, 119.42, 118.30, 114.81, 114.40, 106.57, 104.73, 65.71, 62.79, 52.38, 42.57, 34.18, 34.14, 33.44, 28.41, 25.96, 24.46, 24.40, 20.1. HRMS-ESI (*m/z*): calculated [M + H]<sup>+</sup> for C<sub>35</sub>H<sub>43</sub>NO<sub>5</sub>, calculated 558.32140, found 558.32161.

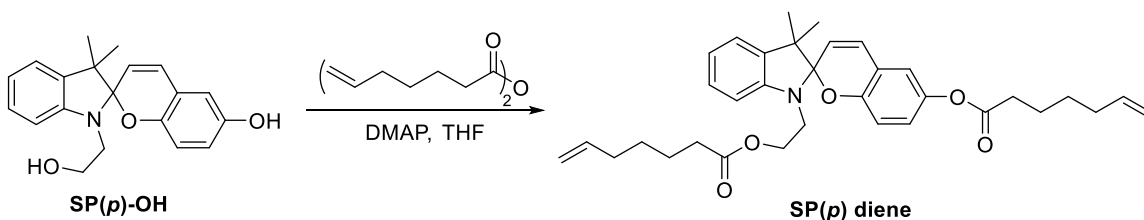
### 2.1.5.2.3 Synthesis of **SP(p)** derivative

#### *Synthesis of SP(p)-OH*



Piperidine was added to a solution of **1** (1.656 g, 5 mmol) and **2c** (0.691 g, 5 mmol) in 40 mL ethanol. The solution was then refluxed for overnight. After cooled down to room temperature, ethanol was removed. The obtained brown oil was further purified by column chromatography (0% to 70% EtOAc/Hexane gradient eluent) to give **SP(p)-OH** as a brown solid (703 mg, 43.5%). <sup>1</sup>H NMR (400 MHz, CDCl<sub>3</sub>) δ 7.16 (td, *J* = 7.7, 1.4 Hz, 1H), 7.07 (dd, *J* = 7.3, 1.4 Hz, 1H), 6.85 (t, *J* = 7.4 Hz, 1H), 6.74 (d, *J* = 10.2 Hz, 1H), 6.61 (d, *J* = 7.8 Hz, 1H), 6.56 (t, *J* = 1.9 Hz, 2H), 6.52 (dt, *J* = 2.7, 1.5 Hz, 1H), 5.68 (d, *J* = 10.2 Hz, 1H), 3.83 – 3.69 (m, 2H), 3.59 – 3.46 (m, 1H), 3.36 (m, 5.4 Hz, 1H), 1.30 (s, 3H), 1.15 (s, 3H). <sup>13</sup>C NMR (125 MHz, acetone-*d*<sub>6</sub>) δ 206.26, 151.40, 148.48, 147.95, 137.09, 129.70, 127.92, 122.08, 121.38, 119.83, 119.22, 116.86, 115.65, 113.55, 106.91, 104.70, 60.82, 52.45, 46.75, 30.12, 29.96, 29.81, 29.66, 29.50, 29.35, 29.19, 26.01, 20.33. HRMS-ESI (*m/z*): [*M* + *H*]<sup>+</sup> for C<sub>20</sub>H<sub>21</sub>NO<sub>3</sub>, calculated 324.15942, found 324.15962.

#### Synthesis of **SP(p) diene**



To a solution of **SP(p)-OH** (0.5 g, 1.55 mmol, 1.0 eq.) in 12 mL dry THF, added hept-6-enoic anhydride (774 mg, 3.26 mmol, 2.1 eq.) and DMAP catalyst (19 mg, 0.155

mmol, 0.1 eq.). The solution was allowed to stir at room temperature for overnight. After the reaction completed, 0.5 mL Et<sub>3</sub>N was added to the solution and stirred for additional 30 min. Then the solvent was removed under reduced pressure. Further flash chromatography (0% to 25% EtOAc/hexane gradient eluent) gave **SP(p) diene** as a light yellow oil (777 mg, 92.5%). <sup>1</sup>H NMR (400 MHz, CDCl<sub>3</sub>) δ 7.17 (td, *J* = 7.7, 1.3 Hz, 1H), 7.07 (dd, *J* = 7.2, 1.2 Hz, 1H), 6.85 (t, *J* = 7.4 Hz, 1H), 6.79 (m, 2H), 6.77 (d, *J* = 1.6 Hz, 1H), 6.66 (dd, *J* = 8.7, 3.2 Hz, 2H), 5.88 – 5.70 (m, 2H), 5.74 (d, *J* = 10.3 Hz, 1H), 5.09 – 4.90 (m, 4H), 4.30 – 4.12 (m, 2H), 3.52 (dt, *J* = 15.0, 6.4 Hz, 1H), 3.36 (dt, *J* = 15.1, 6.4 Hz, 1H), 2.54 (t, *J* = 7.4 Hz, 2H), 2.27 (t, *J* = 7.5 Hz, 2H), 2.12 (q, *J* = 7.2 Hz, 2H), 2.03 (q, *J* = 7.2 Hz, 2H), 1.80 – 1.70 (m, 2H), 1.55 (dp, *J* = 32.5, 7.4 Hz, 4H), 1.38 (p, *J* = 7.6 Hz, 2H), 1.29 (s, 3H), 1.14 (s, 3H). <sup>13</sup>C NMR (125 MHz, CDCl<sub>3</sub>) δ 173.56, 172.53, 151.64, 147.22, 143.74, 138.44, 138.35, 136.27, 128.99, 127.67, 122.57, 121.80, 120.54, 119.44, 119.39, 118.84, 115.69, 114.94, 114.79, 106.55, 104.70, 77.41, 77.16, 76.91, 62.71, 52.40, 42.51, 34.21, 34.11, 33.42, 28.37, 25.94, 24.48, 24.38, 20.19. HRMS-ESI (*m/z*): [M + H]<sup>+</sup> for C<sub>34</sub>H<sub>41</sub>NO<sub>5</sub>, calculated 544.30575, found 544.30596.

#### 2.1.5.2.4 Preparation of SP incorporated PDMS film

PDMS film was prepared using modified procedure according to previous literature<sup>113, 115</sup>.

To a 20 mL scintillation vial, **SP diene** (22 mg, 0.5 wt%) was dissolved in 0.4 mL xylene. Sylgard®184 PDMS base (4.0 g) was added and mixed completely with Votex. Then PDMS curing (0.4 g) was added and further mixed to form a clear homogenous mixture. The viscous mixture was casted on a Teflon mold and cured at 65 °C for overnight.

The cured PDMS was then cut with a 'dog-bone' shape die to give specimen for tensile test.

### 2.1.5.3 Mechanical activation of SP regioisomers

#### 2.1.5.3.1 Manual stretch of SP-PDMS strip

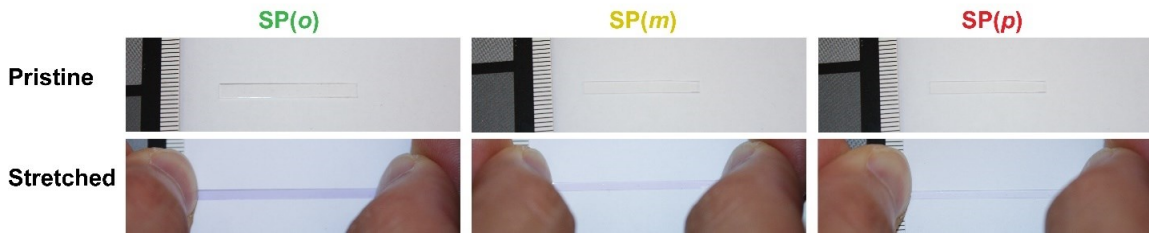


Figure 10 : Mechanical activation of SP regioisomers by manual stretch of PDMS strips

#### 2.1.5.3.2 Quasi-static tensile test

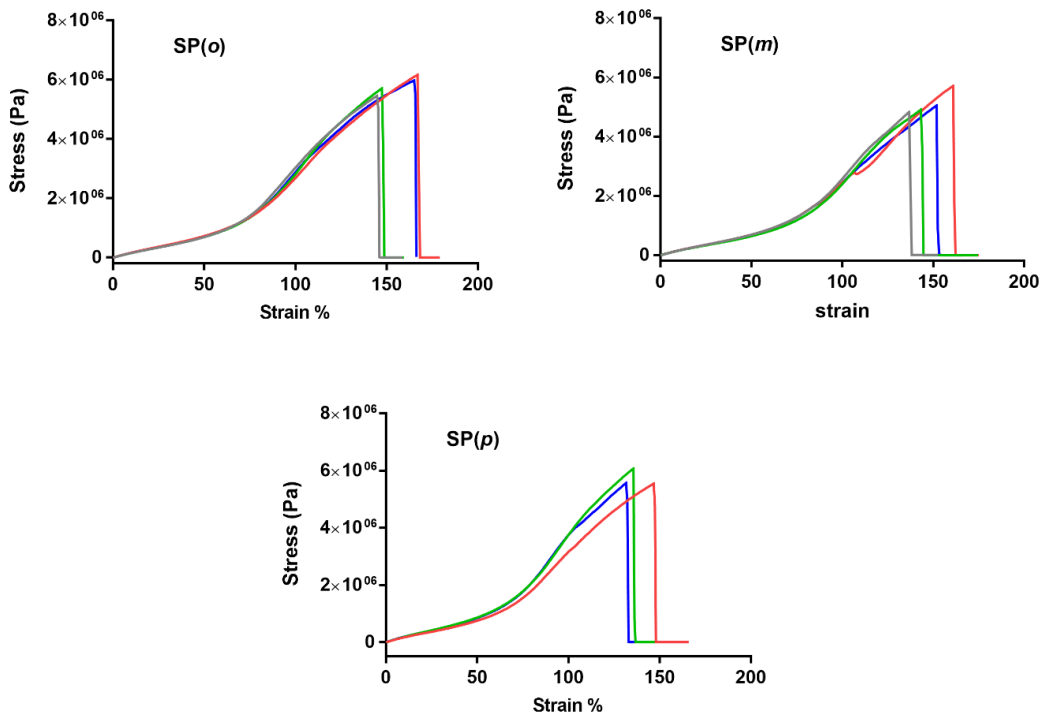


Figure 11 : Additional stress-strain curves of SP(o), SP(m) and SP(p) specimen

'Dog-bone' shape specimen was subjected to the tensile test. Notice: The head section of 'dog-bone' shape sample was sandwiched with two small pieces of PDMS to prevent premature break due to force constrained at the clamping position.

### 2.1.5.3.3 UV-vis spectra of SP(o), SP(m) and SP(p) under mechanical force

The film was fixed at a constant strain while the UV-vis spectrum was collected.

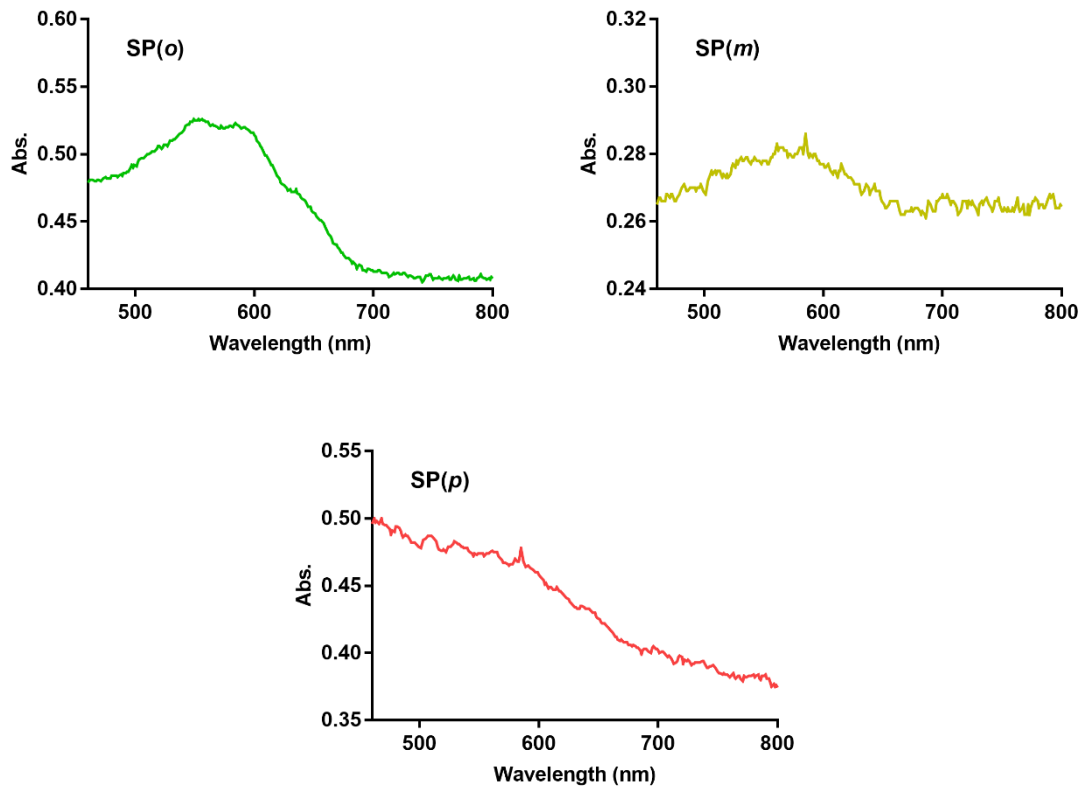
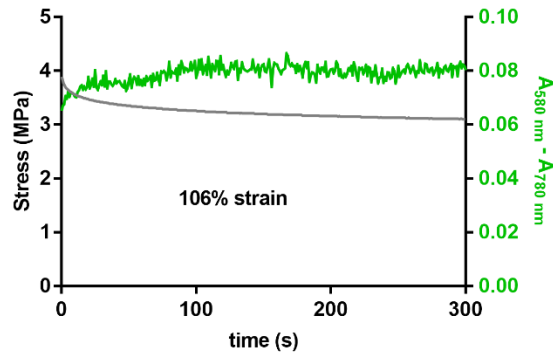


Figure 12 : UV-vis spectra of mechanical activated SP(o), SP(m) and SP(p). All show a broad absorption peak between 460~700 nm.

### 2.1.5.3.4 Time-dependent test for activation of SP(o) at constant strain

A specimen of SP(o)-PDMS was maintained at 105% strain and the evolution of absorption at 580 nm and 780 nm were monitored. The differential value of  $A_{580\text{nm}}$  and  $A_{780\text{nm}}$  was applied to track the activation.



**Figure 13 : Plot of stress and (A580 nm – A780 nm) value against time for SP(o)-PDMS at constant 106% strain.**

#### **2.1.5.3.5 Image recording and analysis for specimen under tensile test**

Image is recorded using a Canon EOS Rebel™ xsi (with a Canon EF-S 18-55 mm f/3.5-5.6 IS SLR lens) camera while the SP-PDMS specimen is subjected to tensile test. The images were taken at manual mode with exposure parameters set to 1/15 sec, f/5.6, ISO 100. Recorded .CR2 format raw files are further imported into Adobe Lightroom Classic CC to perform camera lens calibration and white balance (based on a Opteka™ Digital Color & White Balance Card in the background). Those unmodified images are then saved as .tiff format files. The image sequence is imported to Fiji image J and split into red, green and blue channels. A representative image sequence in three channels is shown here:



Figure 14 : Representative image montage of SP(o)-PDMS specimen in red channel.

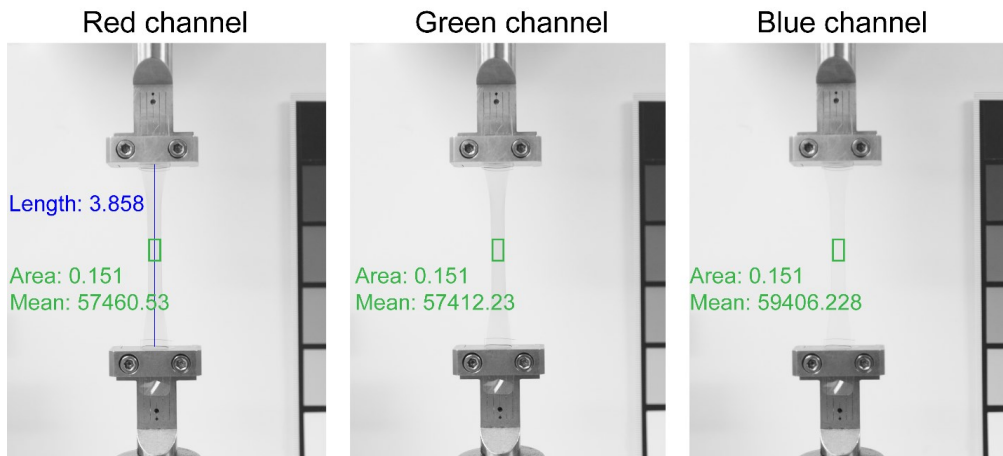


Figure 15 : Representative image montage of SP(o)-PDMS specimen in green channel.



**Figure 16 : Representative image montage of SP(o)-PDMS specimen in blue channel.**

The length of stretched specimen in the image was measured to calculate the strain and intensity in each channel are retrieved. A same size region near the center of the SP-PDMS specimen is set as region of interest in FIJI.



**Figure 17: Image analysis from FIJI in red, green and blue channels. The length of sample is measured in arbitrary unit (blue line in red channel) and the analyzed region is indicated with green square in the image.**

**Table 1 : Representative data from analysis of image set of SP(o)-PDMS specimen**

| #  | Length | Strain % | Area  | Channel   |           |           |
|----|--------|----------|-------|-----------|-----------|-----------|
|    |        |          |       | Red       | Green     | Blue      |
| 1  | 1.463  | 0.0      | 0.151 | 59980.9   | 60121.202 | 59577.523 |
| 2  | 1.537  | 5.1      | 0.151 | 59928.521 | 60095.926 | 59533.716 |
| 3  | 1.597  | 9.2      | 0.151 | 59946.153 | 60106.073 | 59549.321 |
| 4  | 1.658  | 13.3     | 0.151 | 60038.45  | 60197.243 | 59642.978 |
| 5  | 1.716  | 17.3     | 0.151 | 59991.111 | 60145.073 | 59583.864 |
| 6  | 1.783  | 21.9     | 0.151 | 60044.083 | 60193.48  | 59637.408 |
| 7  | 1.842  | 25.9     | 0.151 | 60035.986 | 60192.003 | 59626.348 |
| 8  | 1.905  | 30.2     | 0.151 | 60026.877 | 60178.846 | 59624.248 |
| 9  | 1.971  | 34.7     | 0.151 | 60011.316 | 60168.837 | 59624.596 |
| 10 | 2.042  | 39.6     | 0.151 | 59837.485 | 59990.653 | 59446.02  |
| 11 | 2.108  | 44.1     | 0.151 | 59910.715 | 60060.51  | 59519.824 |
| 12 | 2.212  | 51.2     | 0.151 | 59889.355 | 60043.986 | 59505.048 |
| 13 | 2.316  | 58.3     | 0.151 | 59942.378 | 60089.165 | 59564.032 |
| 14 | 2.423  | 65.6     | 0.151 | 59866.176 | 60014.083 | 59490.138 |
| 15 | 2.525  | 72.6     | 0.151 | 59794.162 | 59938.24  | 59426.759 |
| 16 | 2.645  | 80.8     | 0.151 | 59979.734 | 60115.186 | 59656.051 |
| 17 | 2.733  | 86.8     | 0.151 | 59940.014 | 60079.15  | 59676.039 |
| 18 | 2.838  | 94.0     | 0.151 | 59710.905 | 59816.056 | 59549.951 |
| 19 | 2.941  | 101.0    | 0.151 | 59453.145 | 59534.44  | 59433.084 |
| 20 | 3.038  | 107.7    | 0.151 | 59213.888 | 59263.406 | 59355.808 |
| 21 | 3.142  | 114.8    | 0.151 | 59086.173 | 59101.04  | 59395.773 |
| 22 | 3.25   | 122.1    | 0.151 | 58854.014 | 58857.097 | 59388.06  |
| 23 | 3.347  | 128.8    | 0.151 | 58667.683 | 58659.985 | 59409.841 |
| 24 | 3.456  | 136.2    | 0.151 | 58389.335 | 58367.999 | 59370.503 |
| 25 | 3.551  | 142.7    | 0.151 | 58187.5   | 58160.914 | 59406.949 |
| 26 | 3.654  | 149.8    | 0.151 | 57876.056 | 57834.783 | 59363.246 |
| 27 | 3.752  | 156.5    | 0.151 | 57648.563 | 57606.686 | 59373.012 |
| 28 | 3.858  | 163.7    | 0.151 | 57460.53  | 57412.234 | 59406.228 |

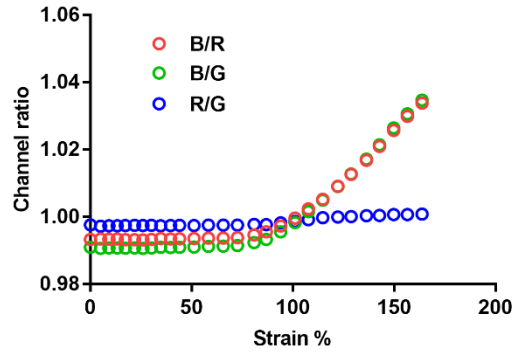


Figure 18 : The intensity in each channel was analyzed in B/G, B/R and R/G versus strain to determine the activation. The B/G provides best signal to noisy ratio, therefore, is selected to analyzed and compare all other results.

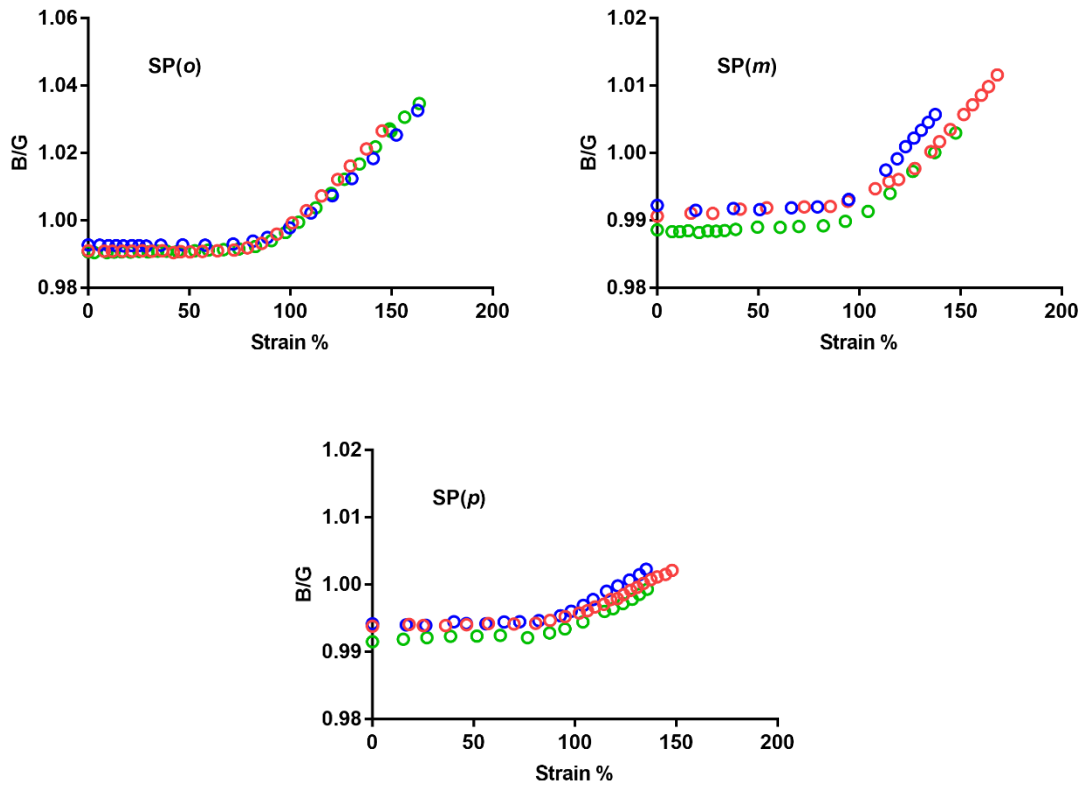
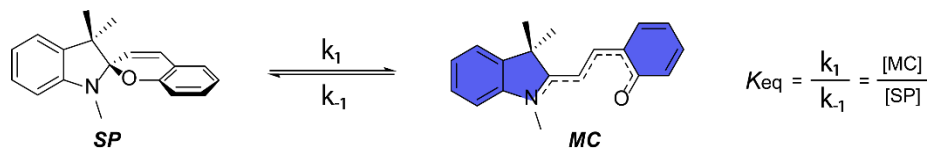


Figure 19 : Additional B/G versus strain pots of  $SP(o)$ ,  $SP(m)$  and  $SP(p)$  specimen

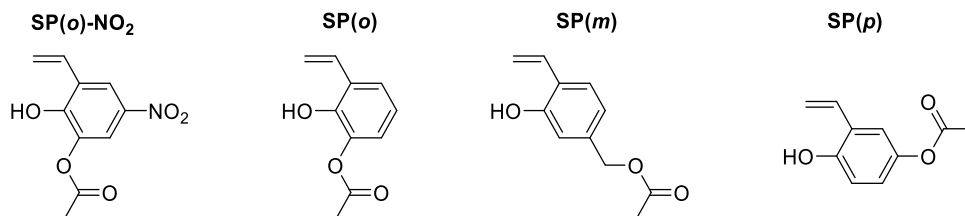
### 2.1.5.4 Kinetic and thermodynamic parameters



Due to the UV inactive nature of **SP(o)**, **SP(m)** and **SP(p)**, the forward reaction rate  $k_1$  could not be determined using reported procedures. An estimation method was applied here. The equilibrium constant  $K_{eq}$  was estimated from phenol part in the MC form while the backward reaction rate  $k_{-1}$  can be determined experimentally.

#### 2.1.5.3.1 Estimation of equilibrium constant

The  $K_{eq}$  of these spiropyran derivatives were estimated from corresponding benzaldehyde part as follows:



The  $pK_a$  of phenols describes the ability of phenol to give deprotonated form, which could be used to estimate the ability of spiropyran to stay at MC form. Hence, the following equation for two different spiropyrans was applied:

$$\frac{K_{eq1}}{K_{eq2}} \approx 10^{-(pK_{a1} - pK_{a2})}$$

The  $pK_a$  values of phenols were roughly obtained using tools from ChemAxon website. Since  $K_{eq}$  of **SP(o)-NO<sub>2</sub>** has been obtained experimentally<sup>87</sup>, the  $K_{eq}$  of other spiropyran derivatives could then be calculated. Obtained equilibrium constants were summarized in Table 2.

**Table 2 : Estimated equilibrium constants of SP(o), SP(m) and SP(p) from SP(o)-NO<sub>2</sub>**

|                 | SP(o)-NO <sub>2</sub> | SP(o)                 | SP(m)                 | SP(p)                 |
|-----------------|-----------------------|-----------------------|-----------------------|-----------------------|
| pK <sub>a</sub> | 7.86                  | 10.22                 | 9.37                  | 9.49                  |
| K <sub>eq</sub> | 3.46×10 <sup>-5</sup> | 1.82×10 <sup>-7</sup> | 1.51×10 <sup>-6</sup> | 1.07×10 <sup>-6</sup> |

### 2.1.5.3.2 Fading rate of activated SP(o), SP(m) and SP(p)

Although **SP(o)**, **SP(m)** and **SP(p)** are all UV inactive, the SP can be mechanically active to form MC. The backward reaction rate can be further retrieved from fading rate since the forward reaction rate is negligible compared to backward reaction rate. The fading rates of **SP(o)**, **SP(m)** and **SP(p)** are fast. The activated MC goes away fast (~2 seconds) when applied force is removed. A video was recorded while the SP incorporated film was compressed locally with an iron cylinder to obtain color, and then the compressive force was removed. The force-free ring-closing rate was then retrieved by monitoring the intensity change of mechanically activated region. A representative procedure for analyzing the fading rate of mechanically activated **SP** was described here. A video was recorded while **SP(o)** incorporated PDMS film was compressed with an iron cylinder. The .MTS format video file was then converted into .MP4 file using Lightroom classic CC software. Further, frames in the .MP4 video file were retrieved using Matlab R2016a. The time interval between each frame is 1/60 s. Then, the intensity of compressed region in each image was analyzed with Fiji software. The fading in intensity as a function of time gives the fading rate.

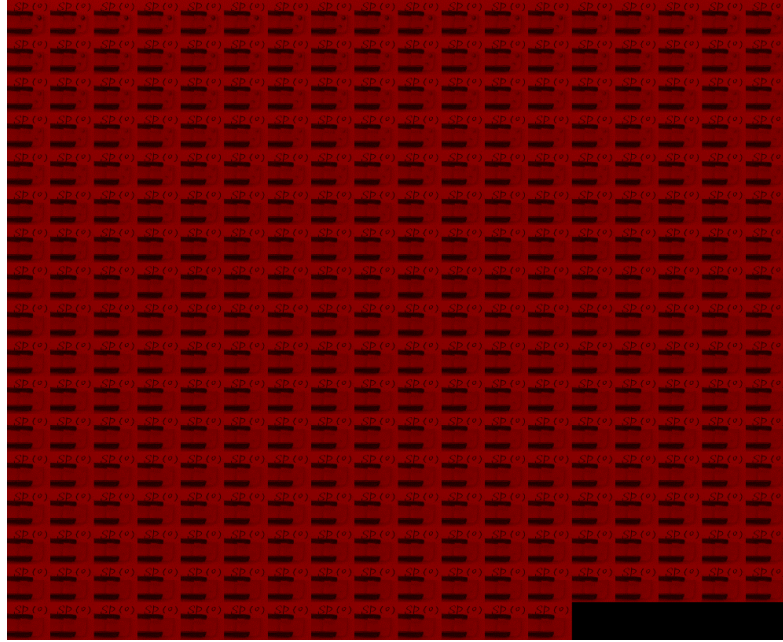


Figure 20 : Representative frame montage from video of locally compressed SP(o)-PDMS film in red channel.

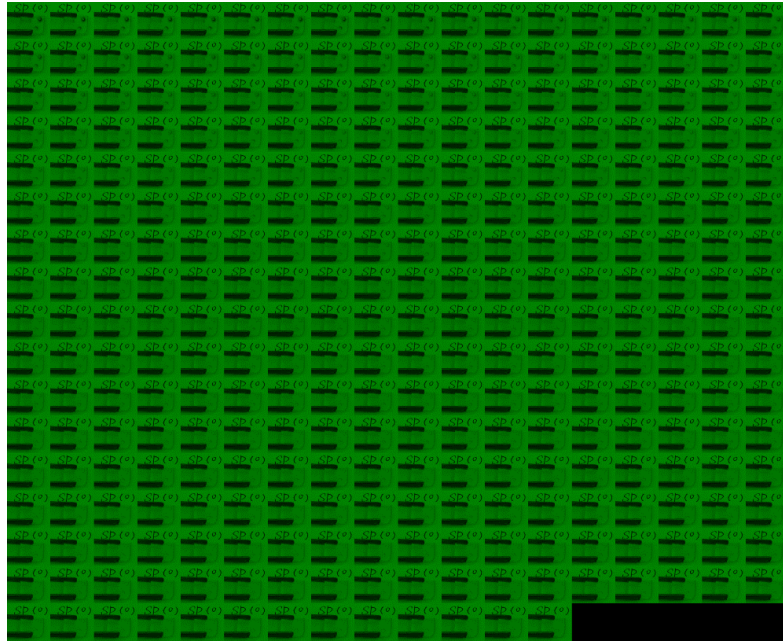


Figure 21 : Representative frame montage from video of locally compressed SP(o)-PDMS film in green channel.

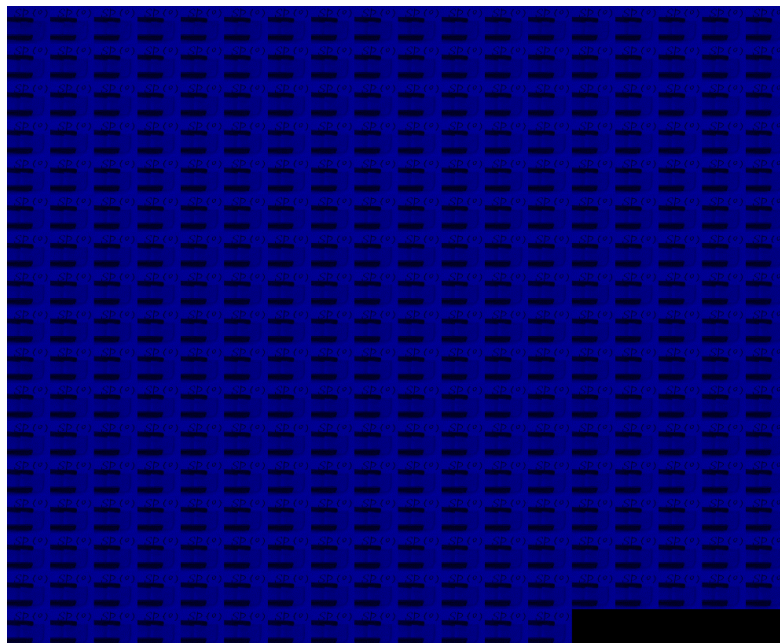


Figure 22 : presentative frame montage from video of locally compressed SP(o)-PDMS film in blue channel.



Figure 23 : Representative frame analysis of locally compressed SP(o)-PDMS film in red, green and blue channels. The mechanically activated region was indicated with yellow circle.

The intensities in red, green and blue channels were retrieved and were plot as B/R or B/G as a function of time. Further fitting with one phase decay gives the fading rate.

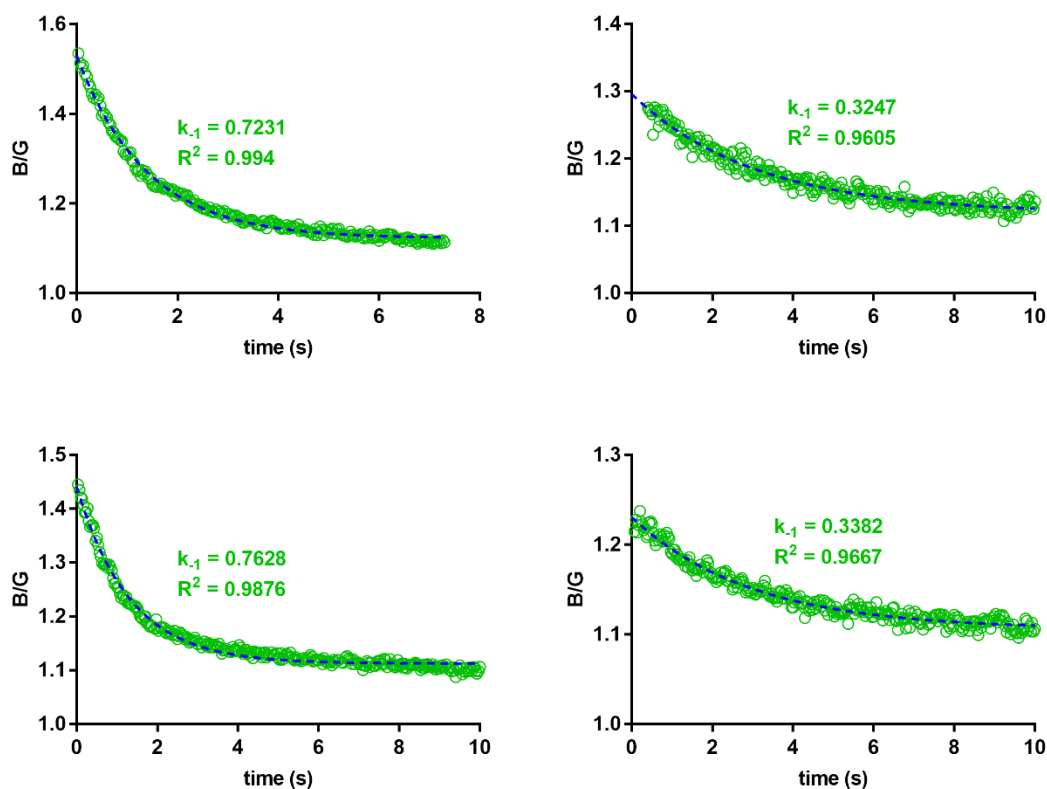


Figure 24 : Fading rate fitting of mechanically activated SP(o).

The fading rate of SP(*m*) and SP(*p*) were obtained using the same way as described above.

Table 3 : Backward reaction rate of SP(o), SP(*m*) and SP(*p*)

|                             | SP(o) | SP( <i>m</i> ) | SP( <i>p</i> ) |
|-----------------------------|-------|----------------|----------------|
| $k_{-1}$ (s <sup>-1</sup> ) | 0.537 | 0.364          | 0.575          |
| SD. (s <sup>-1</sup> )      | 0.238 | 0.102          | 0.107          |

Table 4 : Kinetic and thermodynamic parameters of SP(o), SP(*m*) and SP(*p*)

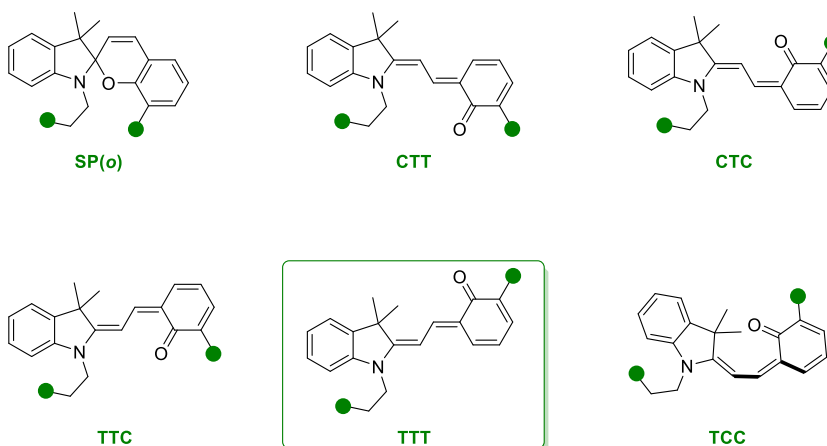
| Probe          | $K_{eq}$              | $k_1$ (s <sup>-1</sup> ) | $k_{-1}$ (s <sup>-1</sup> ) | $\Delta G^\ddagger$ (kcal/mol) | $\Delta G^\circ$ (kcal/mol) |
|----------------|-----------------------|--------------------------|-----------------------------|--------------------------------|-----------------------------|
| SP(o)          | $1.82 \times 10^{-7}$ | $9.81 \times 10^{-8}$    | 0.54                        | 27.20                          | 9.19                        |
| SP( <i>m</i> ) | $1.51 \times 10^{-6}$ | $5.44 \times 10^{-7}$    | 0.36                        | 26.18                          | 7.94                        |
| SP( <i>p</i> ) | $1.07 \times 10^{-6}$ | $6.09 \times 10^{-7}$    | 0.57                        | 26.11                          | 8.14                        |

### 2.1.5.5 CoGEF modeling

CoGEF modeling of ring-opening and ring-closed form for SP derivatives were performed on Spartan'16 V2.0.7 version at Molecular Mechanics/MMFF theory level. The end-to-end distance of the molecule was constrained to a notice distortion when the energy reached  $\sim 500$  kcal more than the unconstrained state. The constrained end-to-end distance was then reduced gradually with an interval of  $0.1 \text{ \AA}$ . The energy at each step was plotted vs. distance. This plot was further fitted with a quadratic equation, of which the first derivative gave force vs. extension as a linear function. The extrapolation of force vs. extension curve at zero force ( $x_0$ ) gave the contour length of repeating unit.

#### 2.1.5.4.1 CoGEF modeling of SP(o)

Chemical structures of **SP(o)** and corresponding ring-opening MC forms: **CTT**, **CTC**, **TTC**, **TTT** and **TCC**.<sup>87</sup>



**SP(o)**



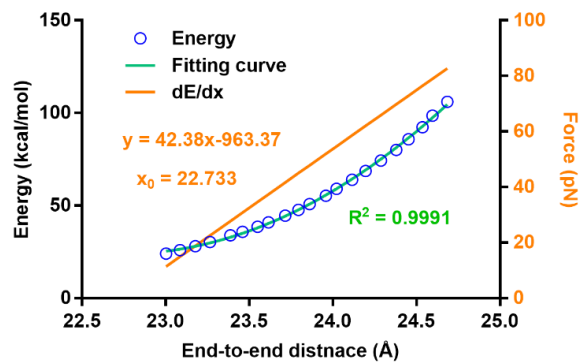


Figure 25 : Quadratic fit of energy vs. distance curve (green); force vs. distance curve (orange). End-to-end distance of SP(o): 22.733 Å

CTT

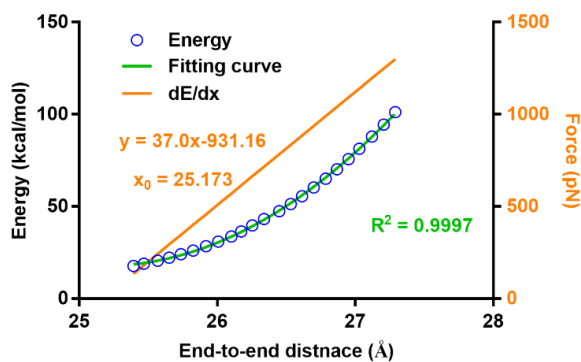
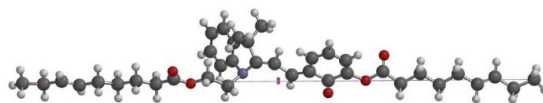
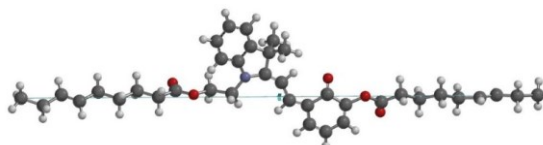


Figure 26 : Quadratic fit of energy vs. distance curve (green); force vs. distance curve (orange). End-to-end distance of CTT: 25.173 Å

CTC



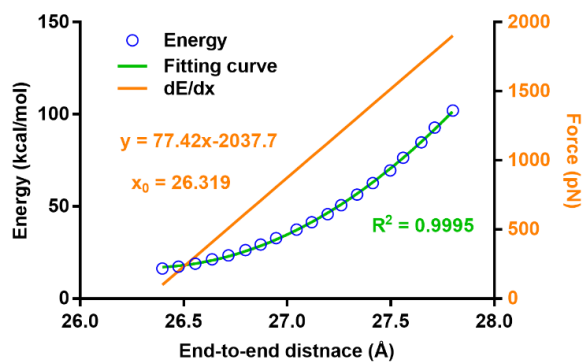


Figure 27 : Quadratic fit of energy vs. distance curve (green); force vs. distance curve (orange). End-to-end distance of CTC: 26.319 Å

TTC

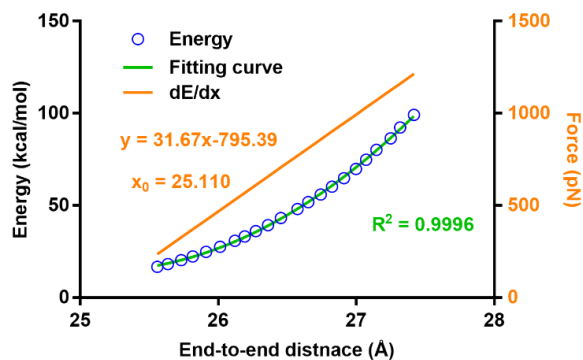
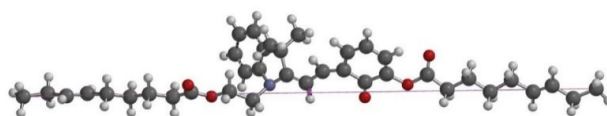


Figure 28 : Quadratic fit of energy vs. distance curve (green); force vs. distance curve (orange). End-to-end distance of TTC: 25.110 Å

TTT



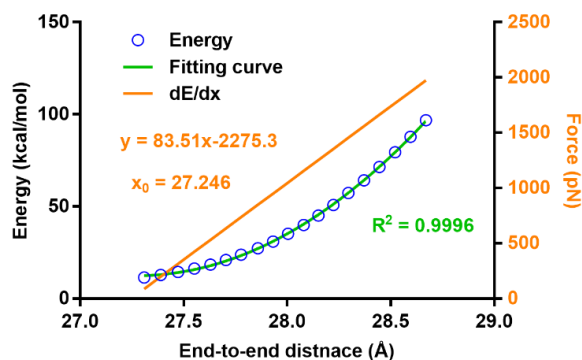


Figure 29 : Quadratic fit of energy vs. distance curve (green); force vs. distance curve (orange). End-to-end distance of TTT: 27.246 Å

TCC

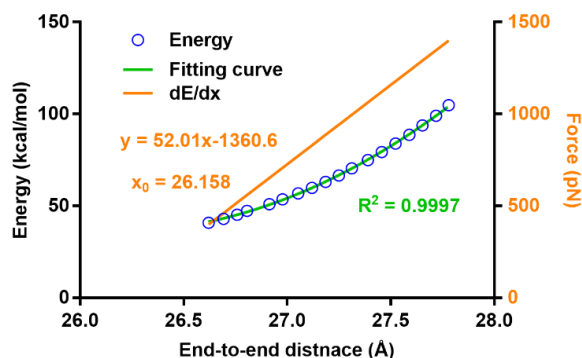
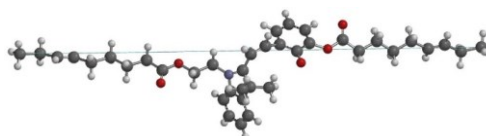


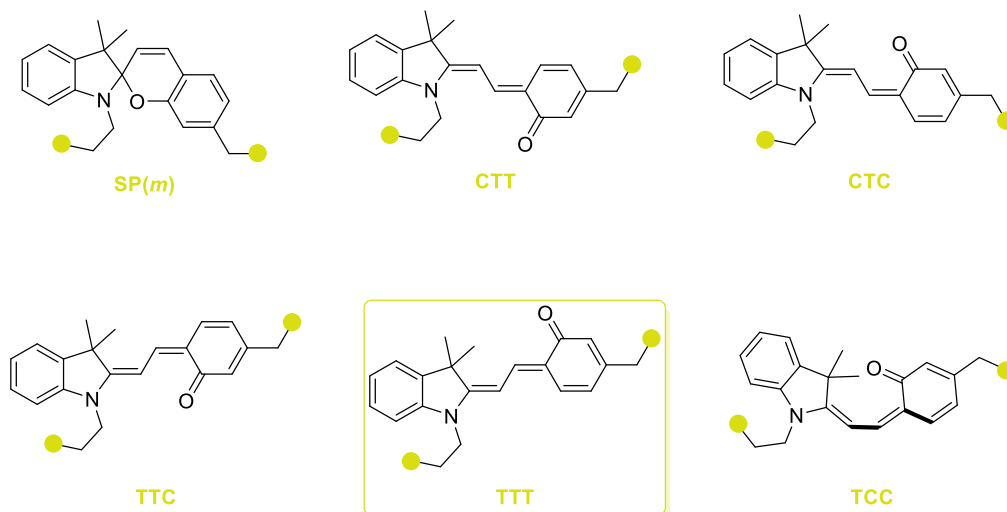
Figure 30 : Quadratic fit of energy vs. distance curve (green); force vs. distance curve (orange). End-to-end distance of TCC: 26.158 Å

Table 5 : Summary of contour length of MC isomers from SP(*o*) (unit: Å)

|         | SP( <i>o</i> ) | CTT    | CTC    | TTC    | TTT    | TCC    |
|---------|----------------|--------|--------|--------|--------|--------|
| Trial 1 | 22.792         | 25.173 | 26.389 | 25.089 | 27.305 | 26.158 |
| Trial 2 | 22.733         | 25.243 | 26.319 | 25.110 | 27.239 | 26.370 |
| Trial 3 | 22.680         | 25.057 | 26.306 | 25.136 | 27.246 | 26.217 |
| Avg.    | 22.735         | 25.158 | 26.338 | 25.112 | 27.263 | 26.248 |
| SD.     | 0.056          | 0.094  | 0.044  | 0.023  | 0.036  | 0.110  |
| ΔL      | /              | 2.423  | 3.603  | 2.377  | 4.528  | 3.513  |

### 2.1.5.4.2 CoGEF modeling of SP(*m*)

Chemical structures of SP(*m*) and corresponding ring-opening MC forms:



SP(*m*)

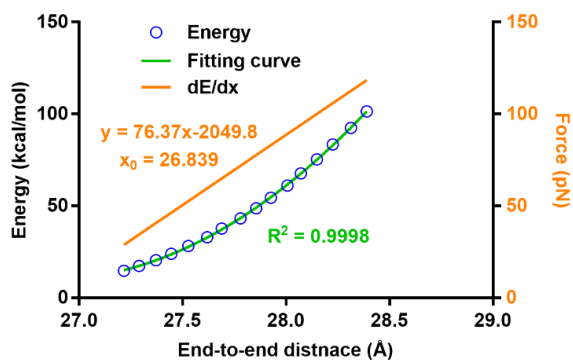
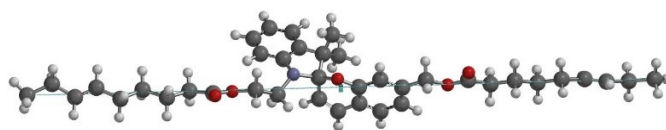


Figure 31 : Quadratic fit of energy vs. distance curve (green); force vs. distance curve (orange). End-to-end distance of SP(*m*): 26.839 Å

CTT

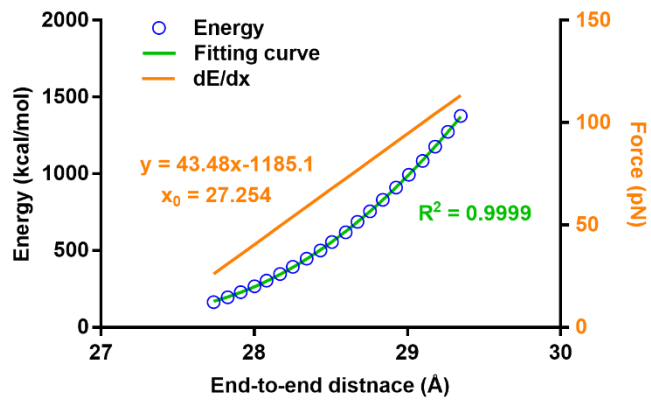
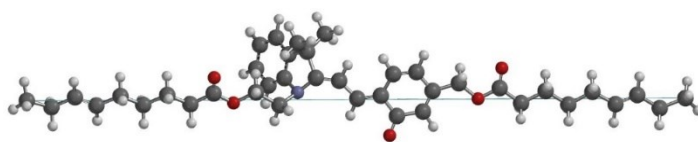


Figure 32 : Quadratic fit of energy vs. distance curve (green); force vs. distance curve (orange). End-to-end distance of CTT: 27.254 Å

CTC

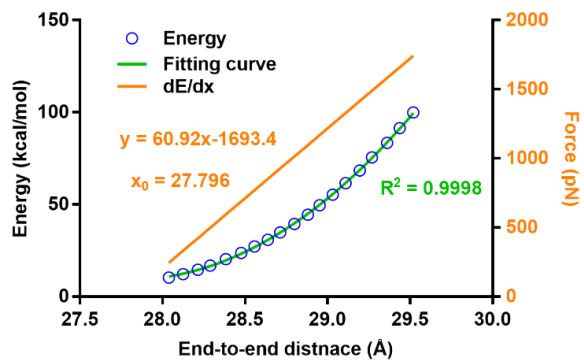
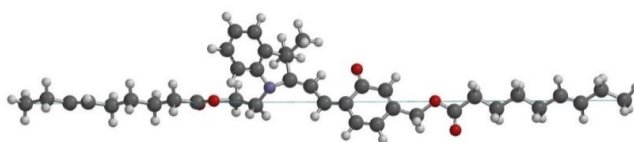


Figure 33 : Quadratic fit of energy vs. distance curve (green); force vs. distance curve (orange). End-to-end distance of CTC: 27.796 Å

TTC

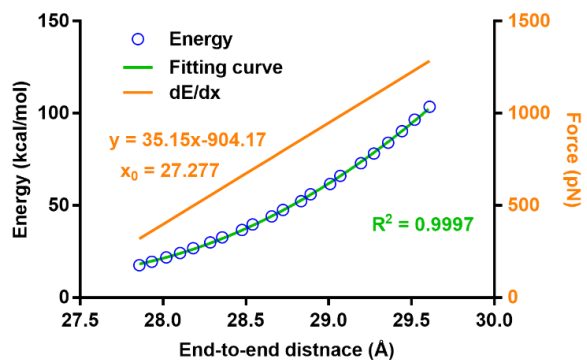
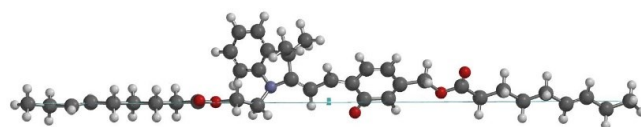


Figure 34 : Quadratic fit of energy vs. distance curve (green); force vs. distance curve (orange). End-to-end distance of TTC: 27.277 Å

TTT

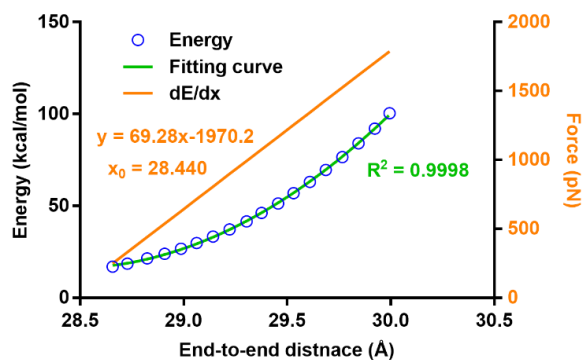
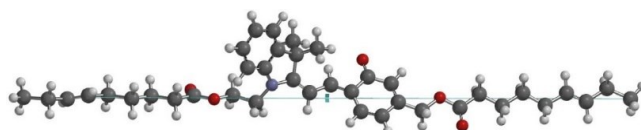


Figure 35 : Quadratic fit of energy vs. distance curve (green); force vs. distance curve (orange). End-to-end distance of TCC: 28.440 Å

TCC

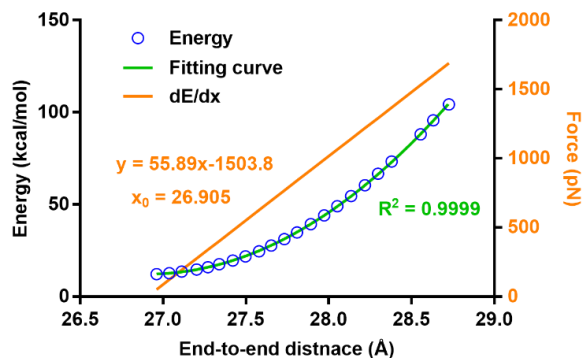
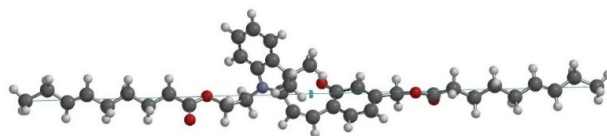


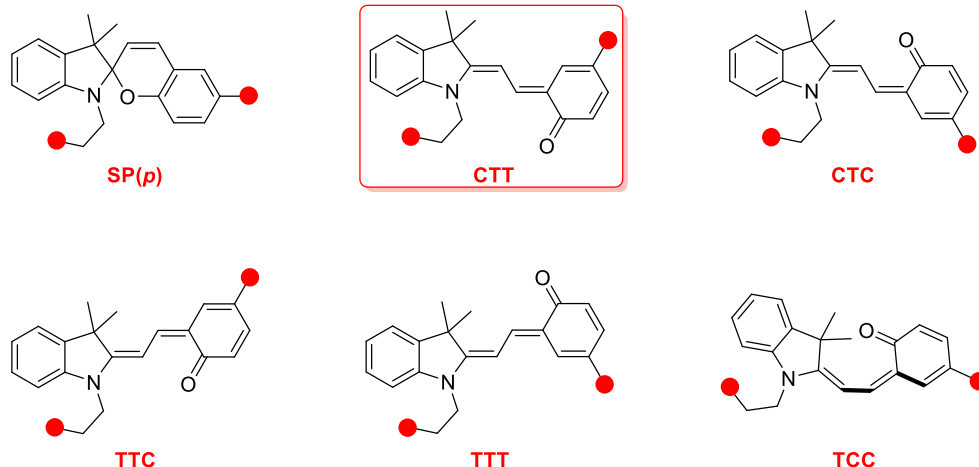
Figure 36 : Quadratic fit of energy vs. distance curve (green); force vs. distance curve (orange). End-to-end distance of TCC: 26.905 Å

Table 6 : Summary of contour length of MC isomers from SP(*m*) (unit: Å)

|         | SP( <i>m</i> ) | CTT    | CTC    | TTC    | TTT    | TCC    |
|---------|----------------|--------|--------|--------|--------|--------|
| Trial 1 | 26.788         | 27.254 | 27.816 | 27.311 | 28.456 | 26.905 |
| Trial 2 | 26.839         | 27.261 | 27.796 | 27.277 | 28.440 | 26.876 |
| Trial 3 | 26.891         | 27.225 | 27.773 | 27.264 | 28.415 | 26.908 |
| Avg.    | 26.839         | 27.247 | 27.795 | 27.284 | 28.437 | 26.896 |
| SD.     | 0.051          | 0.019  | 0.022  | 0.025  | 0.021  | 0.018  |
| ΔL      | /              | 0.407  | 0.956  | 0.445  | 1.598  | 0.057  |

### 2.1.5.3.3 CoGEF modeling of SP(*p*)

Chemical structures of SP(*p*) and corresponding ring-opening MC forms:



SP(p)

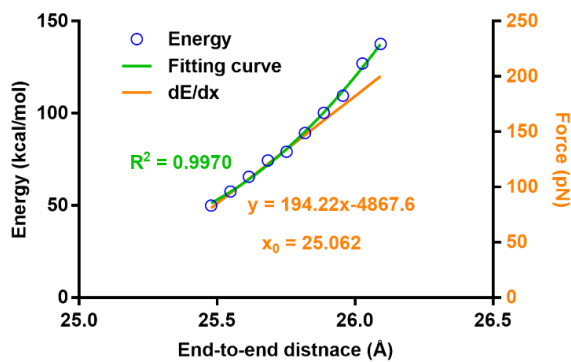
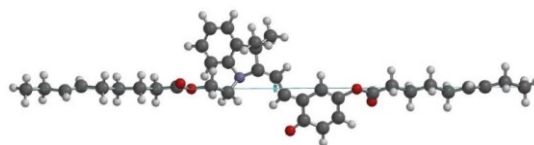


Figure 37 : Quadratic fit of energy vs. distance curve (green); force vs. distance curve (orange). End-to-end distance of SP(p): 25.062 Å

CTT



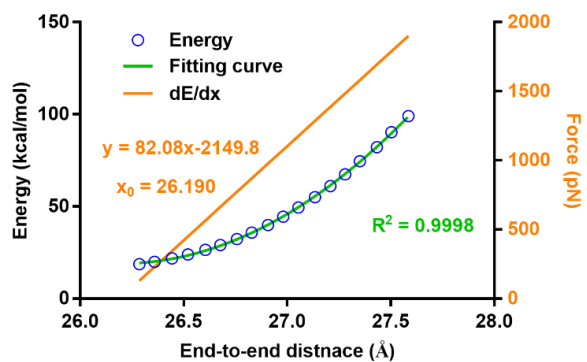


Figure 38 : Quadratic fit of energy vs. distance curve (green); force vs. distance curve (orange). End-to-end distance of CTT: 26.190 Å

CTC

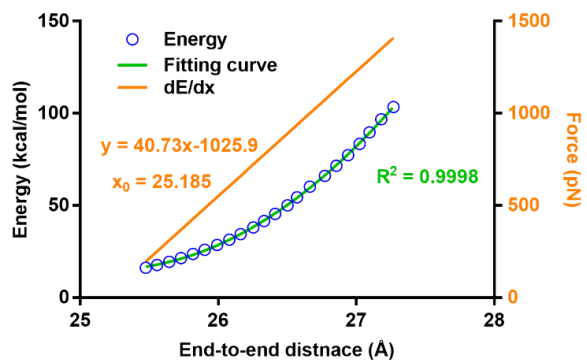
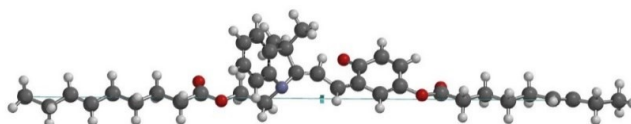


Figure 39 : Quadratic fit of energy vs. distance curve (green); force vs. distance curve (orange). End-to-end distance of CTC: 25.185 Å

TTC



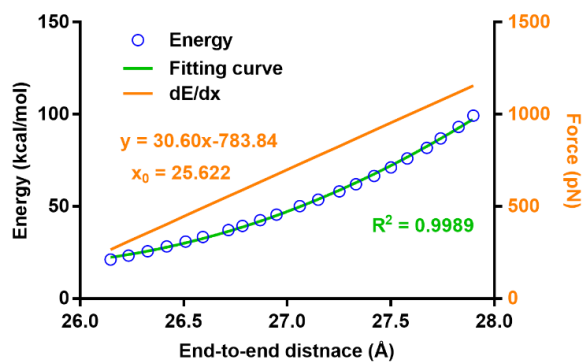


Figure 40 : Quadratic fit of energy vs. distance curve (green); force vs. distance curve (orange). End-to-end distance of TTC: 25.622 Å

TTT

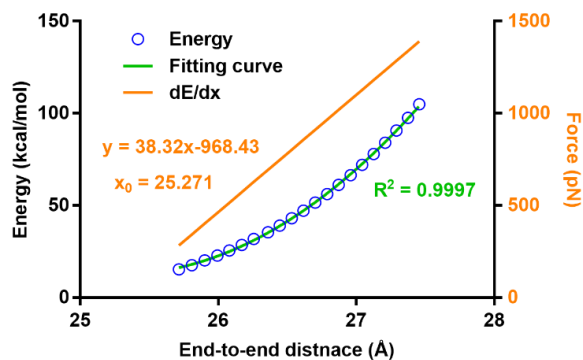
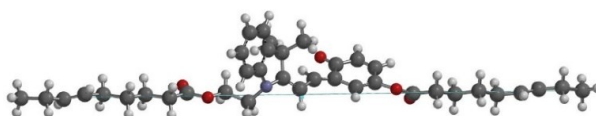


Figure 41 : Quadratic fit of energy vs. distance curve (green); force vs. distance curve (orange). End-to-end distance of TTT: 25.271 Å

TCC



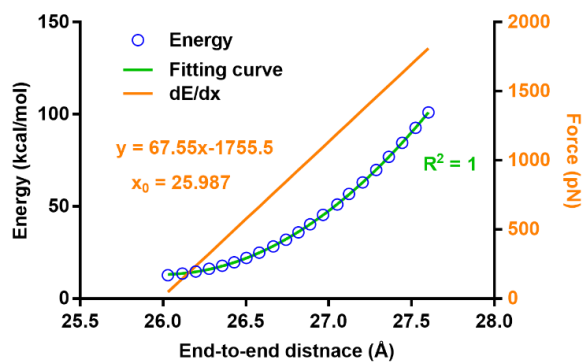


Figure 42 : Quadratic fit of energy vs. distance curve (green); force vs. distance curve (orange). End-to-end distance of TCC: 25.987 Å

Table 7 : Summary of contour length of MC isomers from SP( $p$ ) (unit: Å)

|            | SP( $p$ ) | CTT    | CTC    | TTC    | TTT    | TCC    |
|------------|-----------|--------|--------|--------|--------|--------|
| Trial 1    | 25.032    | 26.192 | 25.205 | 25.622 | 25.271 | 25.987 |
| Trial 2    | 25.062    | 26.181 | 25.183 | 25.654 | 25.272 | 25.974 |
| Trial 3    | 25.074    | 26.190 | 25.185 | 25.572 | 25.232 | 26.011 |
| Avg.       | 25.056    | 26.099 | 25.184 | 25.637 | 25.258 | 25.991 |
| SD.        | 0.022     | 0.010  | 0.021  | 0.016  | 0.023  | 0.018  |
| $\Delta L$ | /         | 1.132  | 0.135  | 0.560  | 0.203  | 0.935  |

## 2.2 Stereochemical effects on a mechanochemical reaction

In recent years, mechanical forces in polymers have been used to direct electrocyclic ring-opening reactions that violate orbital symmetry rules. Here, we show that differences in stereochemistry between two *gem*-monochlorocyclopropane (*gMCC*) stereoisomers (i.e., *syn* and *anti*, relative to the polymer attachment points through which force is delivered) lead to dramatic differences in reactivity and reactivity outcomes. The mechanochemical ring opening reactivities of *gMCC*s embedded along a polymer backbone are quantified using single molecule force spectroscopy (SMFS). As expected, the anti-Woodward-Hoffmann-Deputy ring-opening of *syn-gMCC* requires significantly higher forces to achieve force-coupled rate constants of  $\sim 100 \text{ s}^{-1}$  than does its *anti-gMCC* isomer (2100 vs. 1300 pN). When tension is applied vs. ultrasonication, the *anti-gMCC* ring opens to the expected allylic chloride product, whereas the *syn-gMCC* isomer generates roughly 0.75 equivalents of the allyl chloride and 0.25 equivalents the diene formed from subsequent elimination of HCl.

### 2.2.1 Introduction

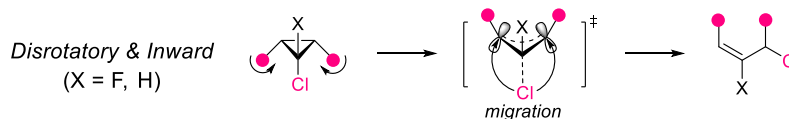
The integration of mechanophores into polymeric materials has afforded an ever-increasing range of force-activated responses, including: reporting stress/damage,<sup>32, 35, 37, 57, 116-119</sup> catalyzing reactions,<sup>41, 120-121</sup> releasing chemical cargo,<sup>43-47, 78</sup> and stress-responsive strengthening or healing.<sup>36, 51, 122-123</sup> The rational design of mechanophores has been fueled by mechanistic studies of mechanochemical reactions, which have revealed the roles of tension-stabilized reactive intermediates,<sup>59</sup> promoted<sup>82, 86, 124-127</sup> and suppressed<sup>55, 89</sup> reaction

kinetics, and reactions that proceed along pathways that are forbidden on the basis of orbital symmetry.<sup>10, 83-84, 128</sup> The first example of this latter class of mechanochemical reactions was reported by Moore and coworkers,<sup>10</sup> who demonstrated that at high forces, the mechanically induced ring-opening of *cis*- and *trans*-benzocyclobutenes (BCB) yields the same *E,E*-isomer products; computational<sup>18-19, 129</sup> and experimental<sup>84, 107</sup> work supported the hypothesis that the ring opening of *cis*-BCB proceeds through a disrotatory mechanism that is forbidden by classical orbital symmetry (i.e., Woodward-Hoffmann) arguments.<sup>130-131</sup> Subsequent examples of mechanochemical reactions of this type include the conrotatory ring-opening of *trans-gem*-dihalocyclopropanes (*g*DHCs)<sup>84</sup> and the disrotatory ring-opening of *cis*-dialkyl epoxides.<sup>128</sup> Recently, Wang et al.<sup>83</sup> considered another interplay of mechanochemical reactivity and orbital symmetry in the ring opening of *syn*-chloro-*gem*-chlorofluorocyclopropane (*syn-g*CFC) mechanophores (Figure 43). Pulling on substituents that are *syn* to the leaving group preserves orbital symmetry through the disrotatory pathway, but violates the allowed, Woodward-Hoffmann-Depuy (WHD) orbital mixing into the  $\sigma^*_{(C-Cl)}$  orbital associated with the chloride leaving group.<sup>130, 132</sup> A series of observations suggested that the anti-WHD reaction proceeds through a transition state with diradicaloid character, in contrast to a cationic transition state in the WHD-allowed analogue.

Against this backdrop, we report here that the mechanochemical anti-WHD electrocyclic ring opening reaction of *anti*-monochlorocyclopropanes (*anti-g*MCC) yields

an unanticipated diene product that is distinct from the analogous reaction of the *syn* isomer.

**Woodward-Hoffmann-Depuy rule:**



**Mechanically Induced Anti-Woodward-Hoffmann-Depuy Reactions:**

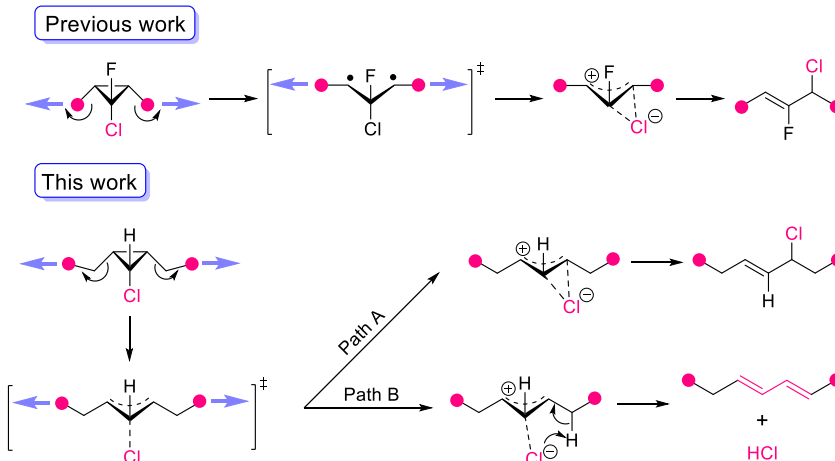


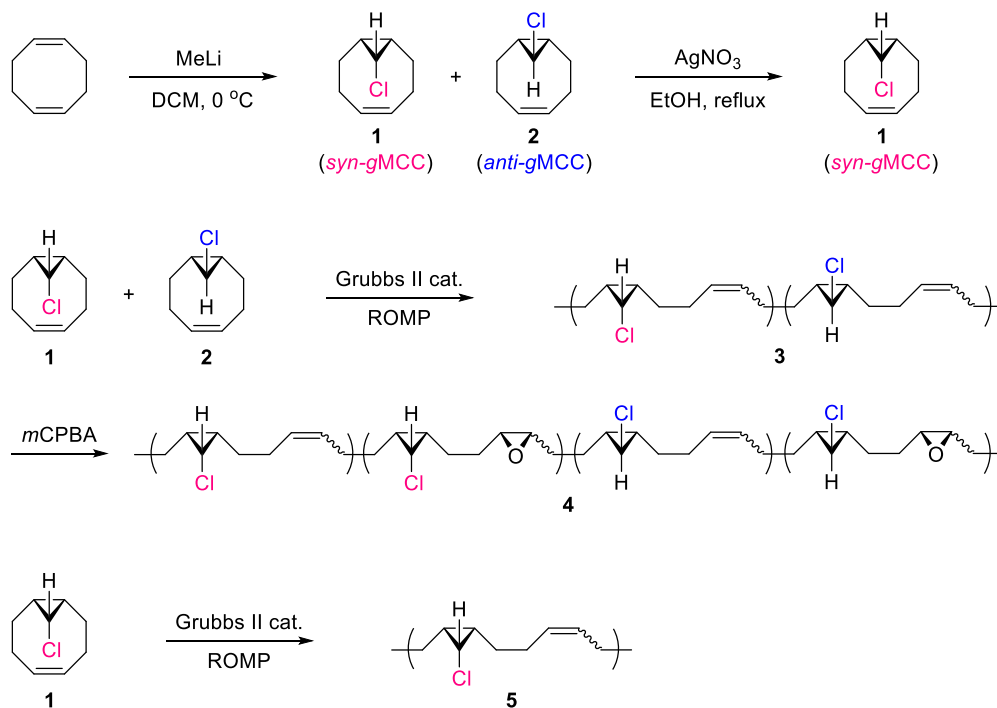
**Figure 43 :** Schematic presentation of reactions that follow a WHD pathway and mechanically induced reactions that proceed through an anti-WHD pathway. Force-activated anti-WHD ring opening of *syn*-gCFC undergoes with a diradicaloid intermediate, and a gMCC analog in this study proceeds through a cationic transition state and generates distinct reaction outcome, i.e., HCl.

## 2.2.2 Results and discussion

To quantify the mechanical reactivity, we prepared multi-mechanophore containing polymers using reported strategy.<sup>82-84, 87-88</sup> As shown in Scheme 1, gMCC monomer was first obtained as a mixture of *syn* and *anti* stereoisomers (**1** and **2**) in a ratio of 3:1. Following kinetic resolution in the presence of AgNO<sub>3</sub> allows to isolate *syn*-gMCC **1** as a pure monomer.<sup>133</sup> Further entropy-driven ring opening metathesis polymerization (ED-ROMP) of gMCC mixtures (**1** and **2**) and **1** gave polymers **3** and **5**, respectively. Polymer **3** was then subjected to epoxidation to incorporate epoxide units along backbone,

which enhance the adhesion of polymer to cantilever.<sup>82</sup> SMFS study of polymer **4** enables to quantify mechanical reactivities of both anti-gMCC and syn-gMCC isomer at the same time.

**Scheme 1 : Synthesis of gMCC stereoisomers 1 and 2, and polymers 3, 4, and 5 investigated in this study.**



To empower the quantitative study of mechanochemical activation, a multi-gMCC polymer was prepared using a reported strategy.<sup>82-84, 87-88</sup> As shown in Scheme 1, *gem*-monochlorocyclopropane (gMCC) monomer was first obtained as a mixture of *syn* and *anti* stereoisomers (**1** and **2**) in a ratio of 3:1. Following kinetic resolution in the presence of AgNO<sub>3</sub> allows to isolate *syn*-gMCC **1** as a pure monomer.<sup>133</sup> The entropy-driven ring opening metathesis polymerization (ED-ROMP) of gMCC mixture (**1** and **2**) and **1** gave polymers **3** and **5**, respectively. Polymer **4** was obtained after subjecting **3** to epoxidation

reactions, which install epoxide units along the backbone to improve the adhesion of polymer to cantilever.<sup>82</sup> SMFS study of polymer **4** allows to quantify the mechanochemical reactivities of both *anti*- and *syn*-gMCC isomers at the same time.

The mechanochemical activation of gMCC mechanophores was investigated through ultrasonication treatment. A solution (2 mg/mL) of polymer **3** in tetrahydrofuran (THF) was subjected to pulsed ultrasonication (1s on and 1s off, ice bath) for 20 min, and the activation of backbone gMCC mechanophores was analyzed from <sup>1</sup>H NMR. As shown in Figure 44a, in addition to expected 3-chloroalkene species, we surprisingly observed the generation of 1, 3-diene products, which are obtained after elimination of HCl, as evidenced by a rhodamine indicator (Figure 53). Because mechanochemical activation of *anti*-gMCC follows the WHD pathway and so produces commonly anticipated 3-chloroalkene products,<sup>134</sup> we postulated that activation of *syn*-gMCC, which proceeds along the anti-WHD pathway, is accounted for the unexpected 1,3-diene products. The <sup>1</sup>H NMR integration suggested that the activation of *anti*- and *syn*-gMCC isomers reaches 50% and 36%, respectively, and that the fraction of unexpected 1,3-diene products is ~24% of activated *syn*-gMCC.

To validate our postulation, polymer **5**, which contains only *syn*-gMCC mechanophore, was treated with similar ultrasonication conditions for 30 min. As revealed, both 3-chloroalkene and 1,3-diene species presented in the <sup>1</sup>H NMR after sonication (Figure 44b), and the release of HCl is validated by the rhodamine indicator as well (Figure 53). Further, the integration analysis indicated that the fraction of 1,3-diene

over activated *syn*-gMCC is 25%, which is consistent with that in polymer **3**. Therefore, we conclude that the generation of HCl originates only from the mechanochemical activation of *syn*-gMCC (anti-WHD reaction) and that the probability of HCl release is  $\sim 0.25$  per *syn*-gMCC activation.

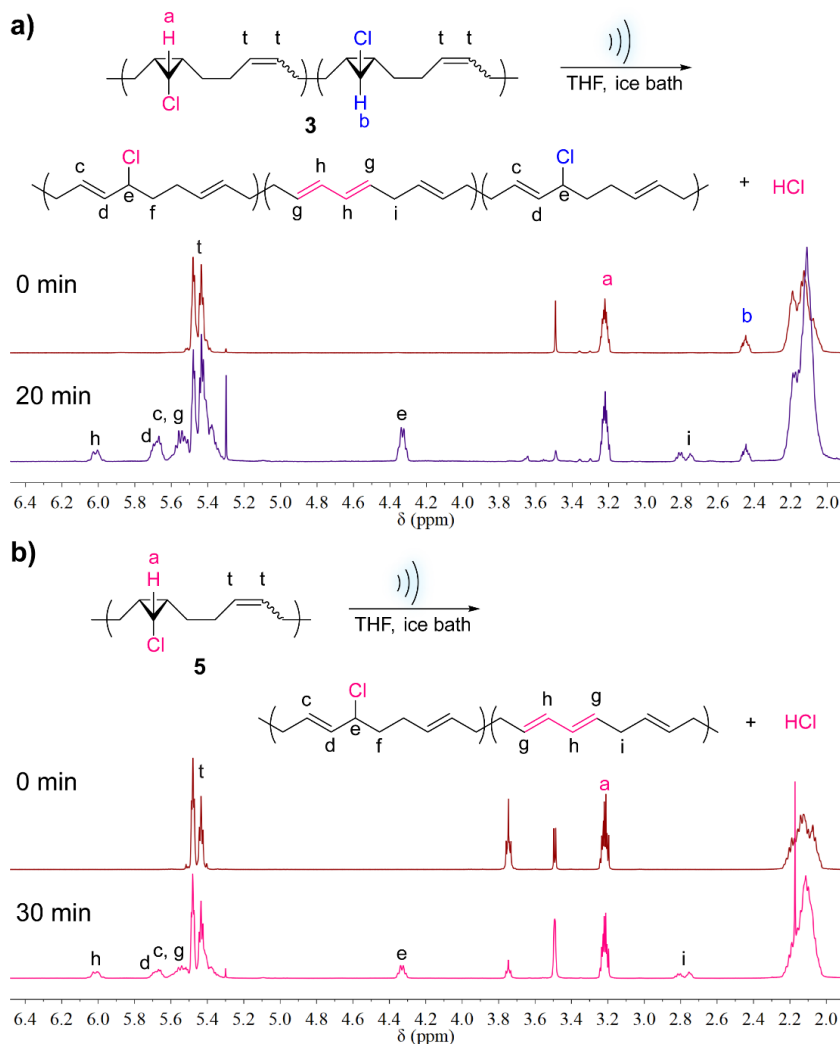


**Figure 44:** a) Subjection of polymer **3** to ultrasonication activates gMCC isomers into 3-chloroalkene and 1,3-diene.  $^1\text{H}$  NMR spectrum of polymer **3** before and after 20 min sonication. The integration of peaks from 1,3-diene species indicates that generated HCl is about 24% of activated *syn*-gMCC isomer. b) Polymer **5** was treated with ultrasonication for 30 min to generate 3-chloroalkene, 1,3-diene, and HCl. Integration analysis from  $^1\text{H}$  NMR suggests that 25% of activated *syn*-gMCC release HCl.

Single molecule force spectroscopy (SMFS) has been demonstrated useful in quantifying mechanochemical reactions and retrieving force-coupling parameters associated with transition states.<sup>82-84, 87-88, 109</sup> Several forbidden reactions have been studied using SMFS.<sup>83-84, 107</sup> We then applied SMFS to quantitatively evaluate the mechanochemical reactivities of two gMCC mechanophores and to unveil the mechanism of anti-WHD pathway.

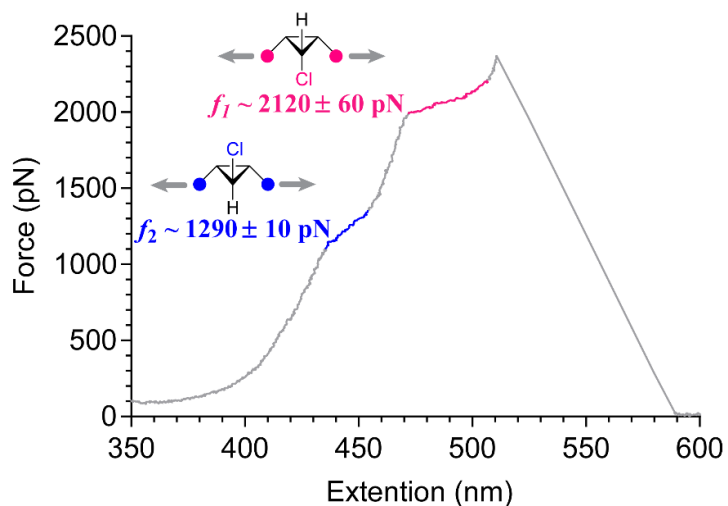


**Figure 45 : Representative force-extension curve of polymer 4. Retraction velocity: 300 nm/s.**

A representative force-extension curve of polymer 4 is provided in Figure 45. Two characteristic plateaus appear at transition forces of  $f_2 \sim 1290 \pm 10$  pN and  $f_1 \sim 2120 \pm 60$  pN, and they are ascribed to the mechanochemically activation of *anti*-gMCC and *syn*-gMCC, respectively. The apparent relative length of these two plateaus matches well with the ratio of two gMCCC isomers in polymer 4. To confirm that the transition is a consequence of gMCCs activation along the polymer chain, we calculated the theoretical additional extension using CoGEF modeling<sup>135</sup> and compared it with result obtained from SMFS

curve fitting. Activation of *anti*- and *syn*-gMCC are determined to give sequential additional extensions of 4% and 11%, respectively, which agrees well with results from curve analysis ( $5\pm 1\%$  and  $11\pm 3\%$ , details see section 2.3.3.5). Therefore, the plateau at  $1290\pm 10$  pN force was assigned to activation of *anti*-gMCC isomer; the plateau at  $1290\pm 10$  pN force, activation of *syn*-gMCC. In comparison to previously quantified *gem*-dichlorocyclopropane (gDCC) ( $\sim 1330$  pN),<sup>82, 84</sup> the slightly lower transition force in *anti*-gMCC is attributed to the absence of a second chlorine, which destabilizes the cationic transition state and increases the activation barrier. On the other hand, the  $\sim 800$  pN more force in *syn*-gMCC activation suggests a significant lower mechanochemical reactivity than *anti*-gMCC. As a result, the reactivity difference between WHD and anti-WHD reactions is more prominent than that of gCFC isomers, as quantified previously.<sup>83</sup> This more profound difference is probably due to the cationic transition state in the anti-WHD ring opening of *syn*-gMCC, in contrast to the diradicaloid transition state in *syn*-gCFC.

To draw some insights in the reaction mechanism, a model based on cusp-like potential surface<sup>15</sup> was applied to analyze the force-coupled reaction kinetics. The force-free activation energy of WHD ring opening of *anti*-gMCC and *syn*-gMCC were estimated to be 35 kcal/mol and 42 kcal/mol, respectively (details see section 2.2.3.4.1). Because the anti-WHD pathway possesses an activation energy that is at least 4 kcal/mol more than that of WHD pathway,<sup>83</sup> the activation energy of anti-WHD ring opening of *syn*-gMCC is  $> 46$  kcal/mol. Obtained activation energy parameters were then applied in the model to retrieve mechanical coupling  $\Delta x^\ddagger$ , which denotes to the change of chain length from

reaction ground state to transition state. As shown in Table 8, analysis of *anti-gMCC* activation provides  $\Delta x^\ddagger = 1.28 \pm 0.07 \text{ \AA}$ , which is identical to that of *gDCC*,<sup>82, 84</sup> and suggests a same cationic transition state in the ring opening reactions. In the similar analysis of *syn-gMCC* activation, the  $\Delta x^\ddagger$  value is determined to be  $1.29 \pm 0.04 \text{ \AA}$ . This  $\Delta x^\ddagger$  value is comparable to *anti-gMCC* and *gDCC*, but substantially lower than *syn-gCFC* ( $1.52 \text{ \AA}$ ),<sup>83</sup> in terms of anti-WHD pathway. Therefore, the anti-WHD ring opening of *syn-gMCC* proceeds through a cationic transition state, instead of a diradicaloid one, as observed in *syn-gCFC*. We reasoned that the absence of fluorine substituent, which otherwise stabilizes the diradical intermediate, leads to a more cationic character in the intermediate.

**Table 8. Force-Free Activation Energies, Mechanical Coupling  $\Delta x^\ddagger$ , and Transition Force of *gDCC* and *gMCC* isomers.**

|                  | $\Delta G^\ddagger$ (kcal/mol) | $\Delta x^\ddagger$ (Cusp) ( $\text{\AA}$ ) | $f$ (pN)      |
|------------------|--------------------------------|---|---------------|
| <i>gDCC</i> *    | 36                             | $1.28 \pm 0.05$                             | $1330 \pm 90$ |
| <i>anti-gMCC</i> | 35                             | $1.28 \pm 0.07$                             | $1290 \pm 10$ |
| <i>syn-gMCC</i>  | 46                             | $1.29 \pm 0.04$                             | $2120 \pm 60$ |

\*Data were retrieved from report by Wang et al.<sup>84</sup>

The mechanical generation of HCl was previously observed in an indene derived *gDCC*<sup>43</sup>, which spontaneously aromatizes after ring opening, and a methoxy-substituted *gDCC* derivative.<sup>46</sup> The simultaneous release of HCl in the latter case is due to resonance stabilization of cationic transition state by methoxy group. The SFMS analysis suggested a cationic transition state, we therefore hypothesized that the force assisted anti-WHD reaction increases the possibility of HCl elimination in the cationic transition state (Figure 46a). To rule out the radical mechanism, we further subjected polymer **5** to ultrasonication in the presence of coumarin-2,2,6,6-tetramethylpiperidine-1-oxyl (CT), which is an

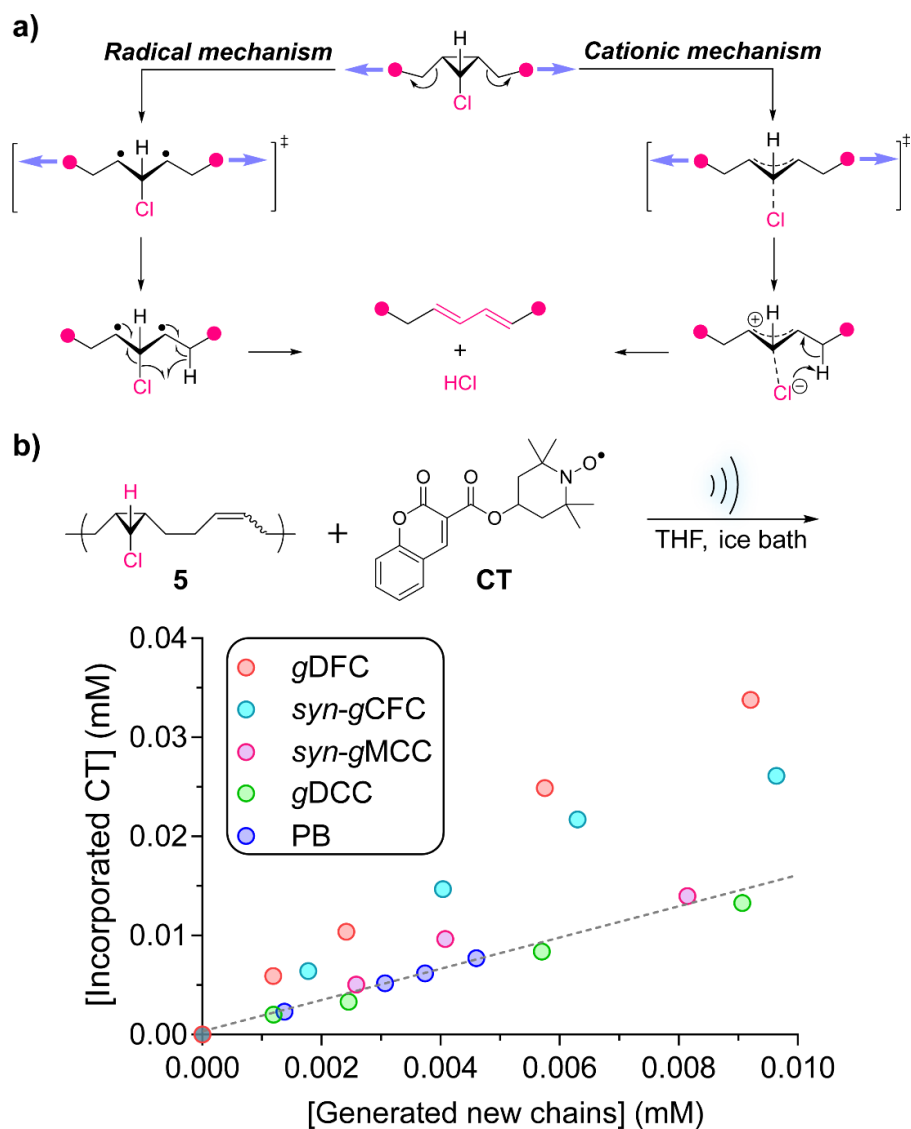


Figure 46 : a) Proposed radical and cation mechanisms for mechanical generation of HCl from syn-gMCC. b) Ultrasonication of polymer 5 in the presence of radical scavenger CT. The concentration of incorporated CT was plotted against concentration of generated new chains. The result was compared with that of previous studied gDFC, syn-gCFC, gDCC containing polymers and PB polymer.

efficient radical scavenger for trapping diradical transition state under ultrasonication.<sup>59</sup>

Addition of UV-active CT to polymer backbone was quantified and compared to some reported polymers that possess either radical or cationic transition states.<sup>83</sup> As shown in

Figure 46b, the amount of incorporated CT is lower than that of *gem*-difluorocyclopropane

(gDFC) and *syn*-gCFC but similar to that of polybutadiene (PB) and gDCC, indicating a nonradical transition state. To better understand the driving force for the elimination of HCl under mechanical force, computational modeling is necessary.

Compared with gCFC isomers, the WHD and anti-WHD ring opening of gMCC isomers reveals a more significant gap in mechanochemical reactivities, which we attribute to the absence of fluorine group that transforms the reaction from proceeds through a diradicaloid intermediate to undergoes with a cationic transition state. Further, the anti-WHD ring opening of *syn*-gMCC generates unexpected 0.25 HCl per activation. This distinct mechanochemical outcome indicates a unique intermediate under force and expands the investigation purpose of forbidden reactions. In complement to previous mechanically coupled proton (mechanoacid), the generation of mechanoacid here requires a higher force (2120 pN vs. 880 pN) and enriches the mechanoacid tool kit. The utility of mechanoacids that span a wide range of force allows for probing force distribution in the strained bulk and triggering responses (e.g., crosslinking, polymerization/depolymerization, degradation) at different level of mechanical impact.

## **2.2.3 Experimental section**

### **2.2.3.1 Materials and characterization**

Materials: Lab general solvents (dichloromethane, ethanol, acetone, toluene, tetrahydrofuran, methanol) were purchased from VWR or Sigma Aldrich. Methyl lithium solution (1.6 M in Et<sub>2</sub>O), cyclooctadiene, silver nitrate, Grubbs II catalyst, and *meta*-

chloroperoxybenzoic acid (mCPBA) were purchased from Sigma Aldrich, Alfa Aesar or TCI and used without further purification.

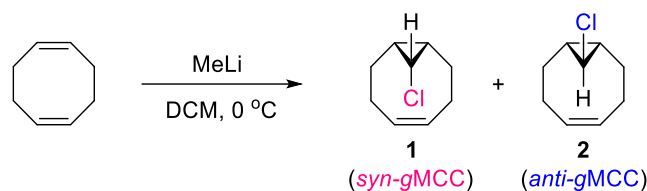
Characterizations:  $^1\text{H}$  NMR spectra were collected on a Bruker Advance Neo-500 MHz multinuclear NMR spectrometer. Chemical shifts are provided in *ppm* ( $\delta$ ) and referenced to the residual  $^1\text{H}$  peak at 7.26 ppm in  $\text{CDCl}_3$ .  $^1\text{H}$  shifts are reported as chemical shift, multiplicity, coupling constant if applicable, and relative integral. Multiplicities are reported as: singlet (s), doublet (d), doublet of doublets (dd), doublet of triplets (dt), doublet of doublet of doublets (ddd), doublet of doublet of triplets (ddt), triplet (t), triplet of doublets (td), quartet (q), pentet (p), multiplet (m), or broad (br). Coupling constants (J) are reported in Hertz. Gel permeation chromatography (GPC) was performed on two Agilent PLgel mixed-C columns ( $10^5 \text{ \AA}$ ,  $7.5 \times 300 \text{ mm}$ ,  $5 \text{ \mu m}$ , part number PL1110-6500) using THF (stabilized with 100 ppm BHT) as the eluent. Molecular weights were calculated using a Wyatt Dawn EOS multi-angle light scattering (MALS) detector and Wyatt Optilab DSP Interferometric Refractometer (RI). The refractive index increment ( $dn/dc$ ) values were determined by online calculation based on injections of known concentration and mass.

Single molecule force spectroscopy: Sharp Microlever silicon probes (MSNL) and Silicon Nitride AFM Probes (PNP-DB) were correspondingly purchased from Bruker (Camarillo, CA) and NanoAndMore (Watsonville, CA). All of the SMFS studies were conducted at ambient temperature ( $\sim 23 \text{ }^\circ\text{C}$ ) using a homemade AFM, which was constructed using a Digital Instruments scanning head mounted on top of a piezoelectric

positioner, similar to the one described in detail previously.<sup>82, 84</sup> The AFM pulling experiments were conducted in a solution of toluene. The spring constant of each cantilever was calibrated in air, using the thermal noise method, based on the energy equipartition theorem as described previously.<sup>82, 84</sup> Measurements were carried out in a closed fluid cell with a scanning set for a series of approaching/retracting cycles. Probes were prepared by immersing in piranha solution ( $\text{H}_2\text{SO}_4$ :  $\text{H}_2\text{O}_2$  = 3:1) for 15 minutes at room temperature and then immersing in deionized water and dried by touching them against a borohydride. Silicon substrates were prepared by first allowing each to soak in hot piranha solution for 30 minutes and then washed with deionized water and dried under a stream of nitrogen. Caution should be used when handling piranha solution: it has been reported to detonate unexpectedly. The substrate and the cantilever were then placed in a UVO cleaner (ozone produced through UV light) for 15 minutes. After ozonolysis, the cantilever was mounted in the fluid cell. 20  $\mu\text{L}$  of a 0.05-0.1 mg/mL polymer solution was added to the silicon substrate surface and allowed to dry. The silicon substrate was then placed on the piezoelectric stage of the AFM. Force curves were collected in dSPACE (dSPACE Inc. Wixom, MI) and analyzed using Matlab (The MathWorks, Inc., Natick, MA). All data were filtered during acquisition at 500 Hz. After acquisition, the data were calibrated and plotted by using homemade software written in Matlab language.

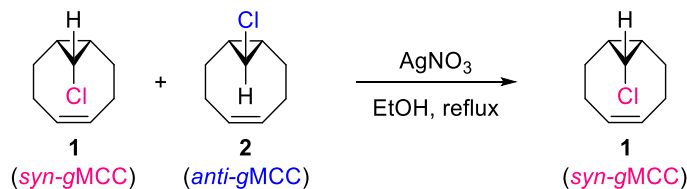
### 2.2.3.2 Synthetic details

Synthetic of (Z)-9-chloro-bicyclo[6.1.0]non-4-ene (gMCC, *syn*-Cl (1) and *anti*-Cl (2)):<sup>136</sup>



To an ice-cold solution of cyclooctadiene (10.8 g, 100 mmol) in 25 mL DCM, slowly added Methyl lithium solution (31 mL, 1.6 M in Et<sub>2</sub>O, 50 mmol) for 1h using a syringe pump. After the addition was completed, the reaction was slowly warmed to room temperature and further stirred for overnight. A white suspension was obtained. DCM phase was washed with 30 mL DI water and dried with MgSO<sub>4</sub>. After DCM was removed, the desired product was obtained by distillation under reduced pressure (49~52 °C/2 mmHg) and gave **1** and **2** stereoisomers as a mixture (2.32 g, 29.6% yield based on MeLi). <sup>1</sup>H NMR (500 MHz, CDCl<sub>3</sub>) δ: 5.72-5.55 (m, 2.69H), 3.28 (t, *J* = 7.4 Hz, 1H), 2.55 (t, *J* = 3.8 Hz, 0.33H), 2.48-2.34 (m, 2H), 2.32-2.20 (m, 1.38H), 2.17-2.06 (m, 2H), 2.06-2.00 (m, 0.69H), 1.99-1.78 (m, 4H), 1.49-1.37 (m, 0.71H), 1.35-1.28 (m, 0.68H), 1.13-1.03 (m, 2H). The ratio of stereoisomers **1** and **2** is determined from <sup>1</sup>H NMR: **1:2** = 1/0.33=3:1. <sup>13</sup>C NMR (125 MHz, CDCl<sub>3</sub>) δ: 130.07, 129.64, 39.74, 38.74, 28.05, 27.70, 26.88, 26.42, 23.72, 19.14.

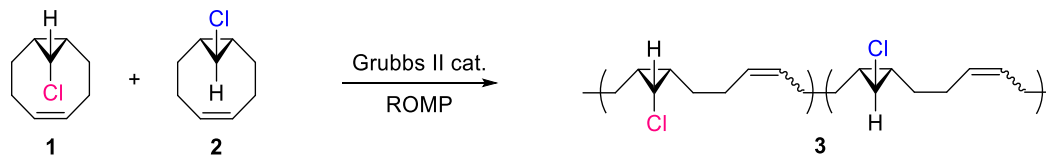
Isolation of stereoisomer **1** (*syn-gMCC*):



To a solution of **1** and **2** mixture (468 mg, 3 mmol) in 12 mL ethanol, added silver nitrate (153 mg, 0.9 mmol). The reaction was then stirred under reflux. <sup>1</sup>H NMR indicated

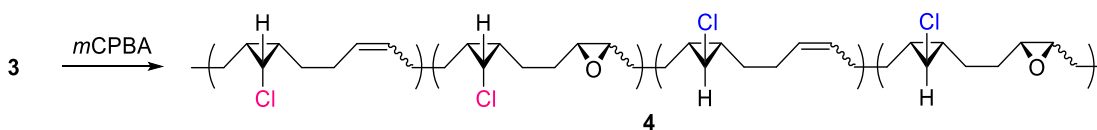
that the isomer **2** was completely consumed after 1h. The reaction was cooled down to room temperature and quenched with water. After ethanol was removed, product was extracted with 3×15 mL hexane. The combined hexane was washed with 30 mL brine and dried with MgSO<sub>4</sub>. After hexane was removed, the product was purified by column chromatography with hexane as eluent (327 mg, 71.4%). <sup>1</sup>H NMR (500 MHz, CDCl<sub>3</sub>) δ: 5.72-5.55 (m, 2H), 3.28 (t, *J* = 7.4 Hz, 1H), 2.48-2.34 (m, 2H), 2.17-2.06 (m, 2H), 1.99-1.78 (m, 4H), 1.13-1.03 (m, 2H). <sup>13</sup>C NMR (125 MHz, CDCl<sub>3</sub>) δ: 129.64, 38.74, 26.88, 23.72, 19.14.

Synthesis of polymer **3**:



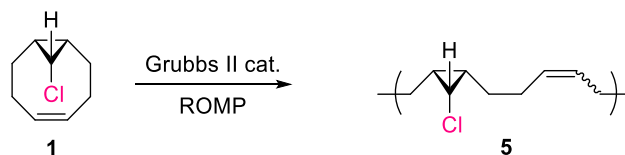
Monomer **1** and **2** mixture (156 mg, 1 mmol) was weighted in a frame dried scintillation vial and kept under N<sub>2</sub>. To another frame dried scintillation vial, added Grubbs II catalyst (1.7 mg) and 2 mL dry DCM. The solution was then sparged with N<sub>2</sub> for 3 min. Then, 0.5 mL of catalyst solution was added to the monomer vial. The vial was then sealed and stirred under room temperature for 1h, after which several drops of ethyl vinyl ether was added to quench the polymerization. After further stirred for 30min, the viscous solution was precipitated from MeOH thrice to give a white polymer (93 mg, 60%). The polymer was analyzed from GPC: *M<sub>n</sub>* = 171.3 kDa. PDI = 1.686, dn/dc = 0.127.

Synthesis of polymer **4**:



Polymer **3** (31 mg, 0.2 mmol) was dissolved in 2 mL DCM, and mCPBA (50 mg, 70%-75%, 0.2 mmol) was added to the solution in portions. After stirred at room temperature for 15 min, the solution was condensed and precipitated from methanol. Additional round of precipitation was performed. Then, the polymer was dissolved in 2 mL DCM, methanol was slowly added to the solution. When the solution turned cloudy, the vial was capped and subjected to centrifuge to give a thin layer of polymer with high molecular weight at the bottom. This polymer was used for single molecule force spectroscopy (SMFS) study.

Synthesis of polymer **5**:



Monomer **1** (78 mg, 0.5 mmol) was weighted in a flame dried scintillation vial and kept under N<sub>2</sub>. 0.3 mL of N<sub>2</sub> sparged Grubbs II catalyst solution (1.7 mg in 2.4 mL DCM) was added. The polymerization underwent for 1h, after which several drops of ethyl vinyl ether was added. The viscous solution was further stirred for 30min. After three rounds of precipitation from methanol, a white polymer was obtained (74 mg, 95%). The polymer was analyzed from GPC: M<sub>n</sub> = 103.7 kDa. PDI = 1.529, dn/dc = 0.109.

### 2.2.3.3. Sonication experiment

General sonication procedures: A solution of 36 mg polymer (**3** or **5**) in 18 mL dry THF was transferred into a dry Suslick cell. The solution was sparged with N<sub>2</sub> for 10 min while cooled with an ice bath. Pulsed ultrasound was applied (1s on, 1s off) at 30%

amplitude. Aliquots of 0.8 mL sample were draw out for GPC analysis at each sonication time. Each of these samples was further rotavaped in a 10 ml scintillation vial to give a thin layer of polymer at the bottom. The polymer was washed with methanol and further dried under high vacuum. Obtained polymers were further subjected to  $^1\text{H}$  NMR analysis.

### 2.2.3.3.1 Analysis of mechanical activation

gMCC activation in polymer 3:

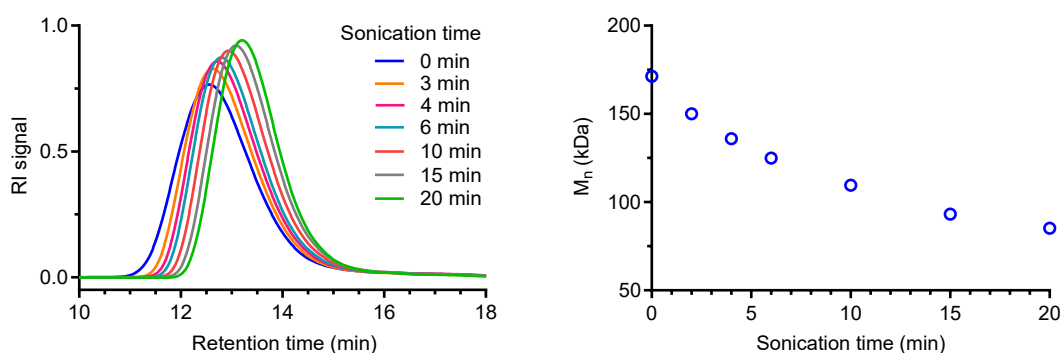


**Figure 47 : GPC traces of polymer 3 ( $M_n = 171.3$  kDa, PDI = 1.686) (left) and corresponding  $M_n$  evolution (right) at various sonication time.**

The activation of gMCC was analyzed from  $^1\text{H}$  NMR. Due to the slight overlap of peak d, c, g and t, the integration of total alkene was calculated as:  $\int H_{c,g} + \int H_d + \int H_t - 2 \times \int H_e - \int H_i$

The ring-opening (RO) percentage of *syn*-gMCC:

$$\text{RO}(\textit{syn}\text{-gMCC}) \% = \left[ 1 - \frac{\int H_a}{(\int H_{c,g} + \int H_d + \int H_t - 2 \times \int H_e - \int H_i) \times 0.75/2} \right] \times 100\%$$

The ring-opening percentage of *anti*-gMCC:

$$\text{RO}(\textit{anti}\text{-gMCC}) \% = \left[ 1 - \frac{\int H_b}{(\int H_{c,g} + \int H_d + \int H_t - 2 \times \int H_e - \int H_i) \times 0.25/2} \right] \times 100\%$$

Percentage of released HCl relative o total gMCC mechanophores:

$$(\text{HCl}) \% = \frac{\int H_i}{\int H_{c,g} + \int H_d + \int H_t - 2 \times \int H_e - \int H_i} \times 100\%$$

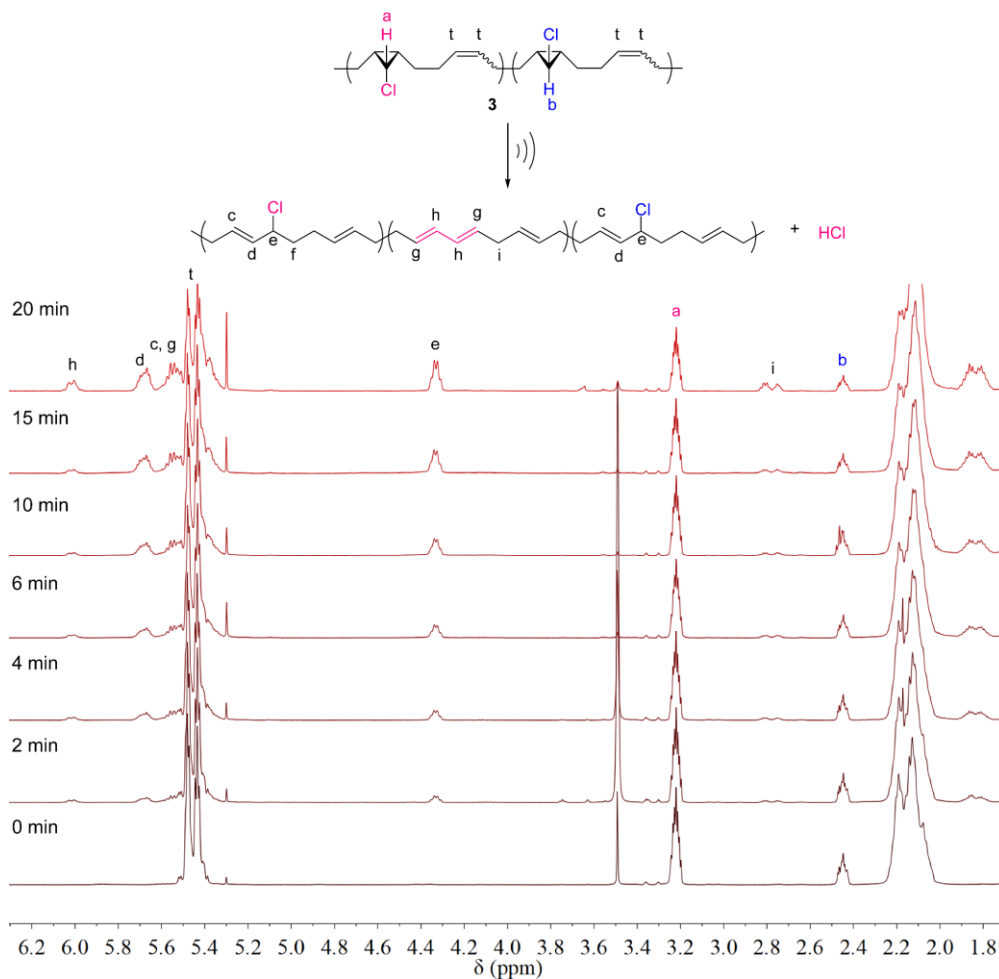


**Figure 48 : Stack of <sup>1</sup>H-NMR (CDCl<sub>3</sub>, 500 MHz) spectra of polymer 3 at various sonication time.**

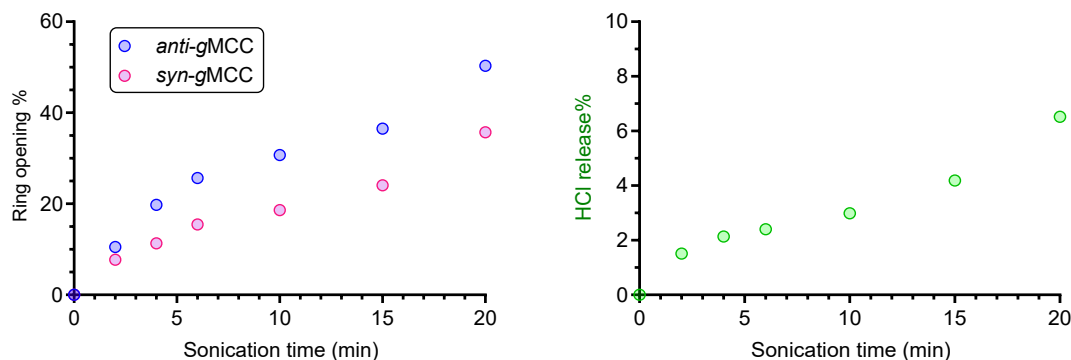


**Figure 49 : Left: ring-opening percentage of each gMCC stereoisomer relative to its initial content; Right: percentage of HCl release in polymer 3 relative to total gMCC content at various sonication time. The HCl release reaches 6.5 % after 20 min sonication**

gMCC activation in polymer 5:

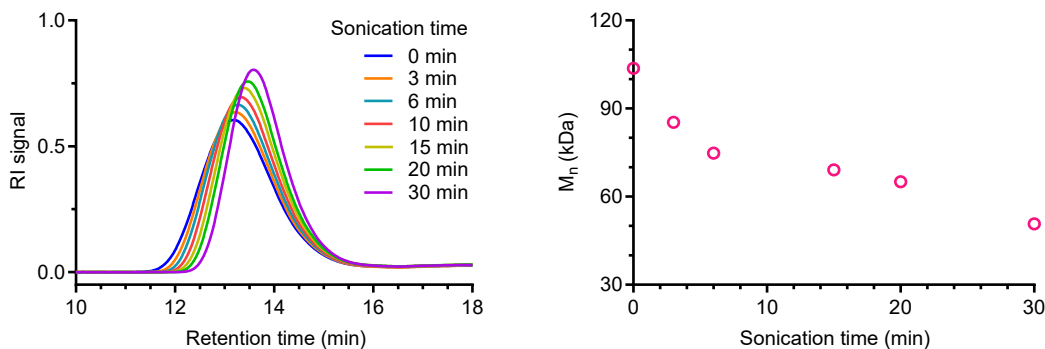


**Figure 50 : GPC traces of polymer 5 ( $M_n = 103.7$  kDa, PDI = 1.529) (left) and corresponding  $M_n$  evolution (right) at various sonication time.**

The activation of gMCC was analyzed from  $^1\text{H}$  NMR. Due to the slight overlap of peak c, g and t, the integration of total alkene was calculated as  $\int H_{c,g} + \int H_t - \int H_h - \int H_d$ .

The ring-opening (RO) percentage of *syn*-gMCC:

$$\text{RO}(\text{syn-gMCC}) \% = \left[ 1 - \frac{\int H_a}{(\int H_{c,g} + \int H_d + \int H_t - 2 \times \int H_e - \int H_i)/2} \right] \times 100\%$$

Percentage of HCl release:

$$(\text{HCl}) \% = \frac{\int H_i}{(\int H_{c,g} + \int H_d + \int H_t - 2 \times \int H_e - \int H_i)/2} \times 100\%$$

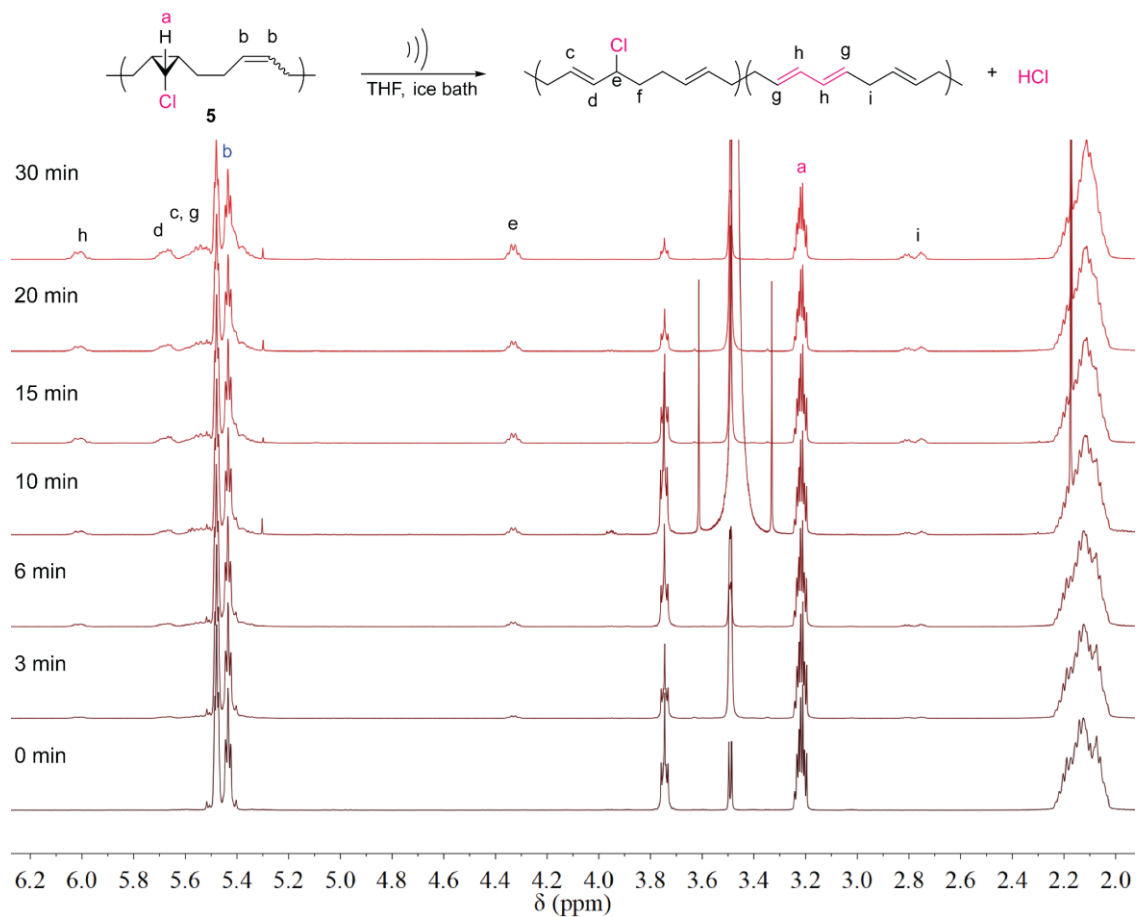


**Figure 51 : Stack of <sup>1</sup>H-NMR (CDCl<sub>3</sub>, 500 MHz) spectra of sonicated polymer 5 at various sonication time.**

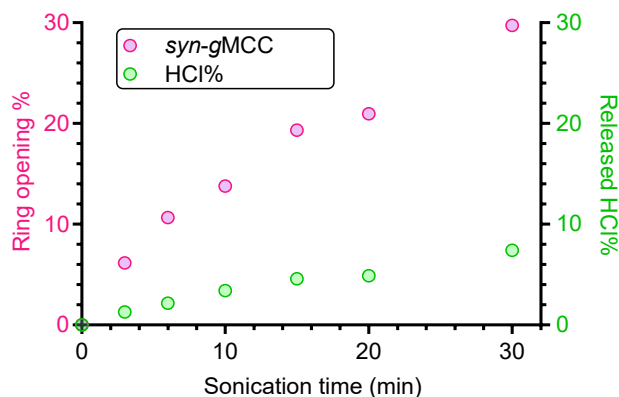


**Figure 52 : Ring-opening percentage of *syn-gMCC* (left axis) and percentage of HCl release (right axis) in polymer 5 at various sonication time. The HCl release reaches 7.4% after 30 min sonication and the ratio of HCl generation to activated *syn-gMCC* is ~ 1:4.**

#### 2.2.3.3.2 Analysis of HCl generation

For detection of generated HCl, 0.5 mL rhodamine B base solution (1 mg/mL in THF) was added to 0.5 mL of sonicated polymer (3 or 5) solution. The sonicated solution turned pink instantaneously whereas pristine solution remained colorless, establishing the generation of HCl after sonication. As can be calculated from Figure 49, the ratio of released HCl to activated *syn-gMCC* is:  $6.5\% / (35.7 \times 0.75) \sim 1:4$ , which is consistent with the number obtained from sonication of *syn-gMCC* containing polymer 5 (Figure 52) and suggests that the generation of HCl merely originates from mechanical activation of *syn-gMCC*. Averagely,  $\frac{1}{4}$  HCl will be released per *syn-gMCC* activation.

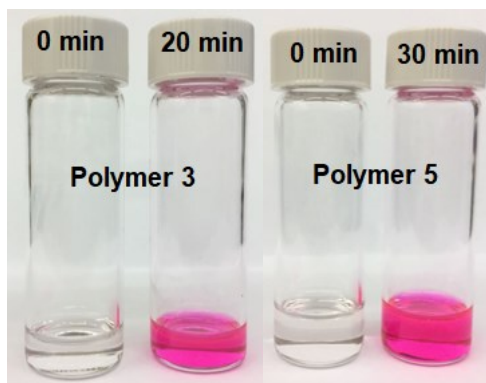
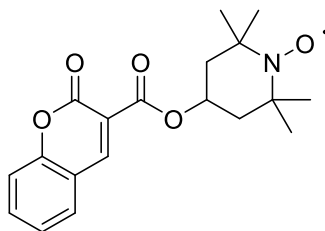


**Figure 53 : Subjection of polymer 3 and polymer 5 to sonication lead to HCl generation, which was indicated by pink color after adding rhodamine B base solution to sonicated samples. The pristine polymer solutions remain colorless.**

### 2.2.3.3.3 Trapping of radicals

To verify if the ring opening of the *syn-g*MCC involves a diradical transition state, polymer 5 was subjected to sonication in the presence of coumarin-2,2,6,6-tetramethylpiperidine-1-oxyl (CT) as radical scavenger.<sup>59, 83, 137</sup> A solution of 16 mg polymer 5 and 176 mg CT (32 mM solution) in 16 mL dry THF was transferred into a dry Suslick cell. The solution was sparged with N<sub>2</sub> for 10 min while cooled with ice bath. Pulsed ultrasound was applied (1s on, 1s off) at 30% amplitude. Aliquots of 0.8 mL sample were draw out for GPC analysis at each sonication time. The addition of CT to sonicated polymer 5 was monitored by UV-vis detector from GPC.

Radical scavenger: coumarin-2,2,6,6-tetramethylpiperidine-1-oxyl (CT)



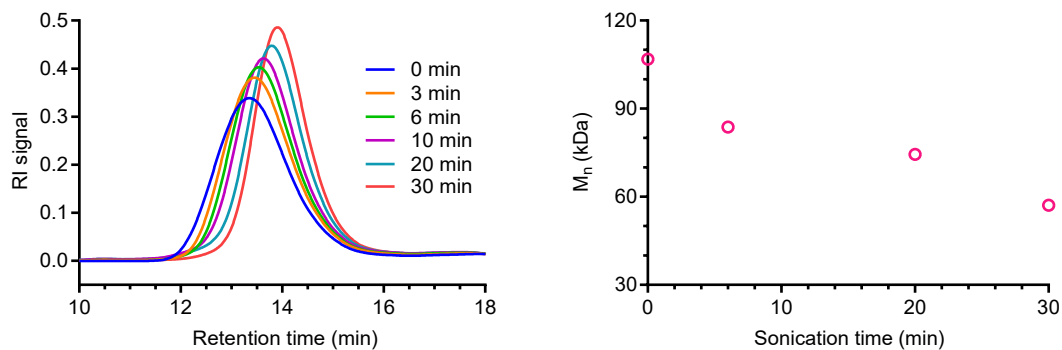


**Figure 54 : GPC traces of sonication of polymer 5 in the presence of radical scavenger CT (left) and corresponding plot of molecular weight versus sonication time (right).**

The concentration of generated new chains can be obtained according to the following relations:

$$[\text{Generated new chains}] = \frac{1}{M_n} - \frac{1}{M_{n(0)}} \text{ (mg}\cdot\text{mL)}$$

$M_{n(0)}$  is the initial molecular weight of the polymer, and  $M_n$  is the molecular weight after sonication.

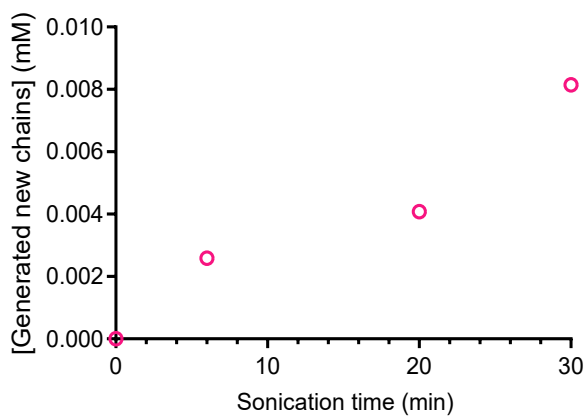


**Figure 55 : The concentration of generated new chains at various sonication time.**

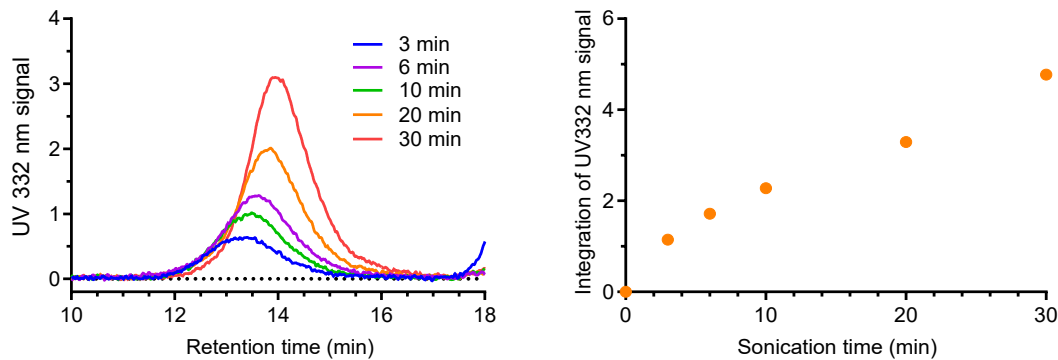


**Figure 56 : GPC UV332 nm signal of polymer 5 at various sonication time (left); integration of GPC UV332 nm signal at various sonication time.**

The concentration of incorporated CT is calculated using the following relation:

$$[CT] = \frac{\int UV_{332nm} (mV \cdot min) * [Flow rate] (mL \cdot min^{-1})}{P(mV) * \epsilon (L \cdot mol^{-1} \cdot cm^{-1}) * l(cm)}$$

The extinction coefficient of CT at 332 nm is  $\epsilon \sim 7240 \text{ L} \cdot \text{mol}^{-1} \cdot \text{cm}^{-1}$  (retrieved from previous literature),<sup>59</sup> the GPC flow rate is  $1.0 \text{ mL} \cdot \text{min}^{-1}$ , the cell length  $l$  is 1 cm and  $P$  is a pre-factor to convert signal intensity from GPC UV-vis to UV-vis spectrometer ( $P = 47.2$ ).

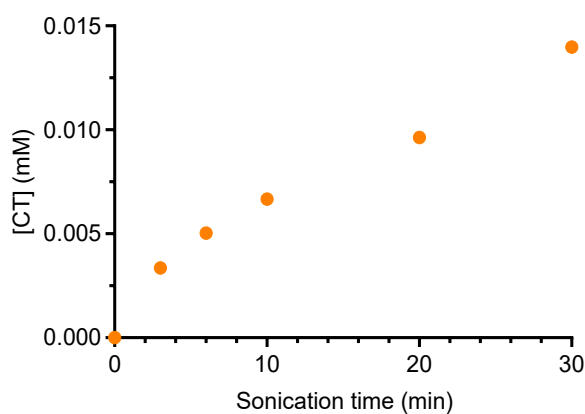


**Figure 57 : The concentration of incorporated CT in polymer 5 at various sonication time.**

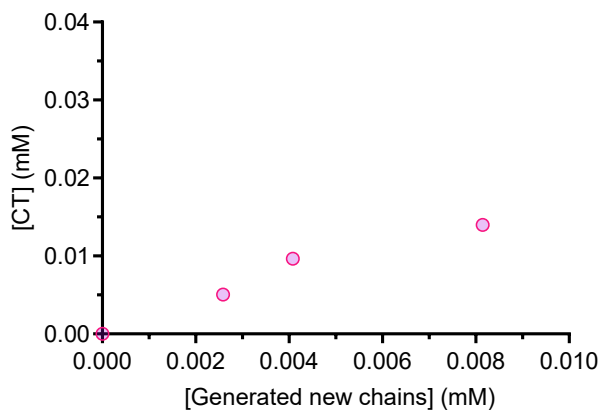


**Figure 58 : The concentration of incorporated CT as a function of concentration of generated new chains in sonicated polymer 5.**

The CT trapping result was further compared with data from previous study of different polymers.<sup>83</sup>

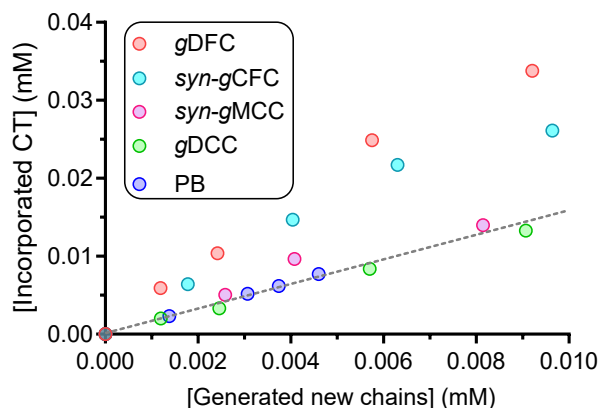


**Figure 59 : The concentration of incorporated CT as a function of amount of generated new chains from sonication of different polymers.**

#### 2.2.3.4 SMFS analysis

##### 2.2.3.4.1 Determination of thermal activation energy

A solution of 40 mg polymer 3 in 2 mL diphenyl ether was transferred into a 25 mL dried Schlenk flask. The flask was filled with N<sub>2</sub> and heated at 180 °C. Aliquots of 100

$\mu\text{L}$  solution was taken out for  $^1\text{H}$  NMR analysis at each time point (0, 0.5, 1, 1.5, 2, 3 h). Peak *b* in Figure 59 corresponds to *anti*-gMCC while peak *a* refers to *syn*-gMCC. New generated peaks *c* and *d* denote to product from ring-opening of *anti*-gMCC and subsequent elimination of HCl. The product of *anti*-gMCC after thermal ring opening is different from mechanical activation that gives 3-chloroalkene. Peak *a* kept intact after 3 h heating at 180  $^\circ\text{C}$ .

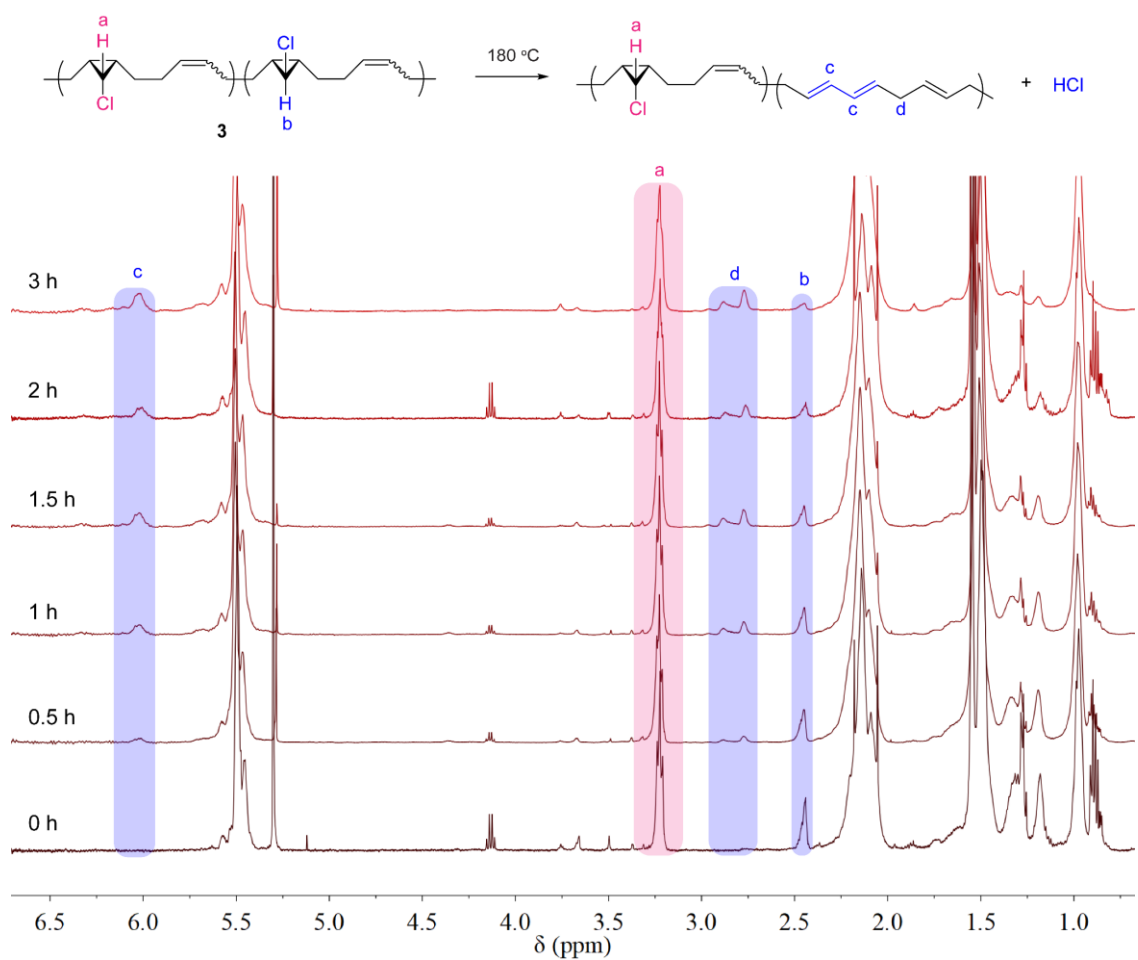


**Figure 60:**  $^1\text{H}$  NMR ( $\text{CDCl}_3$ , 500 MHz) spectra overlay of thermolysis of polymer 3 at 180  $^\circ\text{C}$  in diphenyl ether.

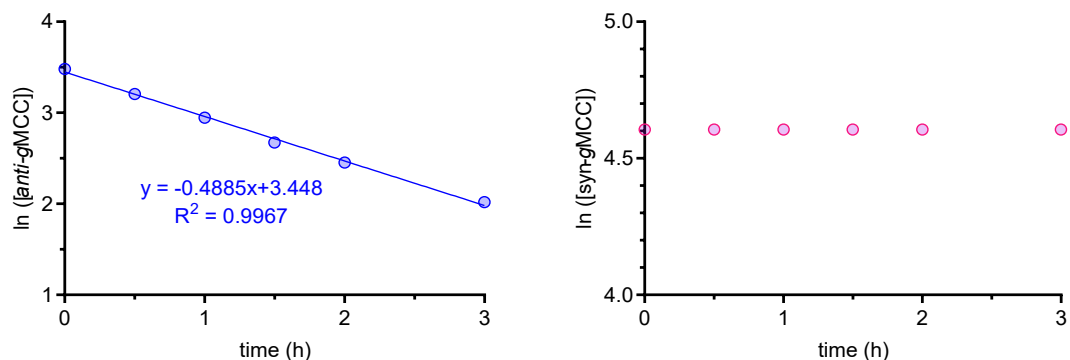


**Figure 61 : Retrieving thermal ring-opening rate of *anti*-gMCC (left): linear fitting of ln [*anti*-gMCC] vs time plot gives rate constant  $r = 0.4885 \text{ h}^{-1}$ . *syn*-gMCC (right) kept intact under 180 °C for 3 h.**

The ring-opening rate constant of *anti*-gMCC at 180 °C is:

$$r = 0.4885 \text{ h}^{-1} = 1.34 \times 10^{-4} \text{ s}^{-1}$$

Thermal activation energy of *anti*-gMCC was calculated according to transition state theory:

$$\begin{aligned} \Delta G^\ddagger &= -RT \ln \frac{kh}{k_B T} = -8.314 \times 411.5 \times \ln \frac{1.34 \times 10^{-4} \times 6.626 \times 10^{-34}}{1.38 \times 10^{-24} \times 411.5} \text{ J/mol} \\ &= 146060 \text{ J/mol} = 34.9 \text{ kcal/mol} \end{aligned}$$

Polymer **3** solution was further heated to 220 °C for 1.5 and 3 h. Resulted solution was analyzed from <sup>1</sup>H NMR. As shown in Figure 61, no ring opening of *syn*-gMCC but peak broadening was observed after 3 h. Therefore, the thermal activation energy of *syn*-gMCC was estimated using data from reported literature.<sup>133</sup> The thermolysis of *anti*-gMCC in the presence of AgNO<sub>3</sub> provided relative rate of  $r_{anti} = 154$  while  $r_{syn} < 0.04$ . The ring opening rate of *syn*-gMCC at 180 °C can be estimated:  $r < 1.34 \times 10^{-4} \div 154 \times 0.04 \text{ s}^{-1} = 3.64 \times 10^{-8} \text{ s}^{-1}$

Thermal activation energy of *syn*-gMCC was estimated:

$$\Delta G^\ddagger > -RT \ln \frac{kh}{k_B T} = -8.314 \times 411.5 \times \ln \frac{3.64 \times 10^{-8} \times 6.626 \times 10^{-34}}{1.38 \times 10^{-24} \times 411.5} \text{ J/mol}$$

$$= 177030 \text{ J/mol} = 42.3 \text{ kcal/mol}$$

The force induced disrotatory outward ring opening of *syn-g*MCC is thermal forbidden reaction. Hence, the activation energy of forbidden reaction should be > 4 kcal/mol more than thermal allowed disrotatory inward reaction.<sup>83</sup> The activation energy of disrotatory outward ring opening of *syn-g*MCC is:

$$\Delta G^\ddagger > 42.3 + 4 \text{ kcal/mol} = 46.3 \text{ kcal/mol}$$

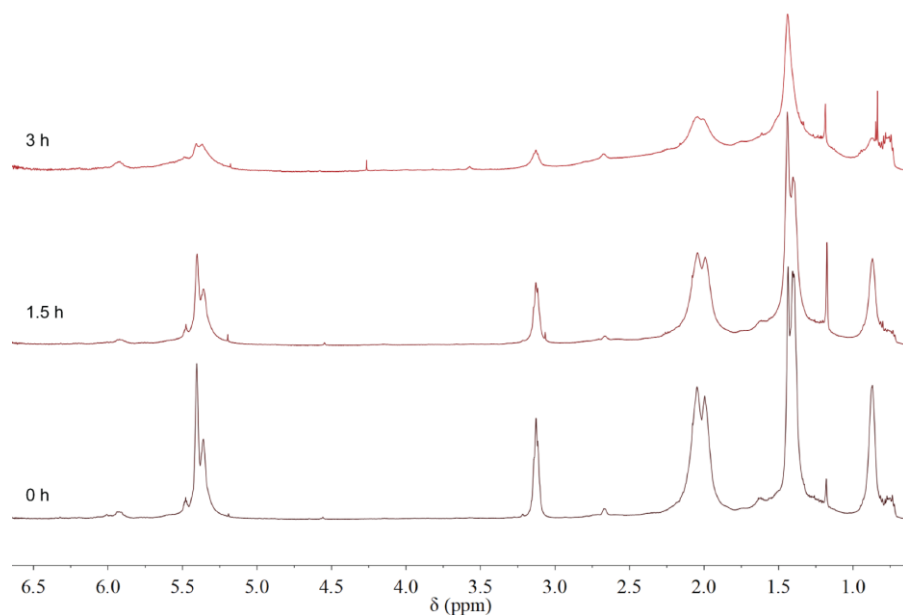


**Figure 62:**  $^1\text{H}$  NMR ( $\text{CDCl}_3$ , 500 MHz) spectra overlay of thermolysis of polymer **3** at 220 °C in diphenyl ether.

### 2.2.3.4.2 SMFS curve analysis

Force-extension curves of polymer **4** were analyzed using reported method.<sup>138</sup> Pre- and post- transition force curves were fitted with extended freely jointed chain (FJC) model<sup>63</sup> (shown in the following equation) to give the contour lengths before and after transition. Further analysis with Bell-Evans (BE) or Cusp models (see section 1.1) provided  $\Delta x^\ddagger$  information.

Extended freely jointed chain (FJC) model:

$$r(F) = L \left[ \coth \left( \frac{Fa}{k_B T} \right) - \frac{k_B T}{Fa} \right] \left( 1 + \frac{F}{KL} \right)$$

Where  $L$  is the contour length,  $a$  is Kuhn length, and  $K$  is the chain segment elasticity;  $k_B$  refers to Boltzmann constant and  $T$  denotes to temperature. The fitting was conducted without constraining  $a$  and  $K$  values.

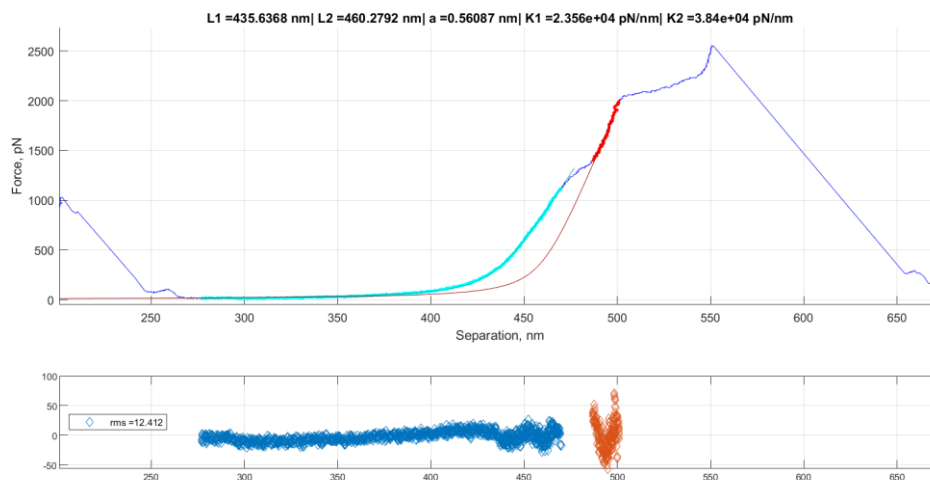


**Figure 63 : Extended FJC model fitting (pre- and post- first transition) of the force-extension curve of polymer **4**. The contour length before and after first transition are  $L_1 = 435.6$  nm and  $L_2 = 460.3$  nm, respectively.**

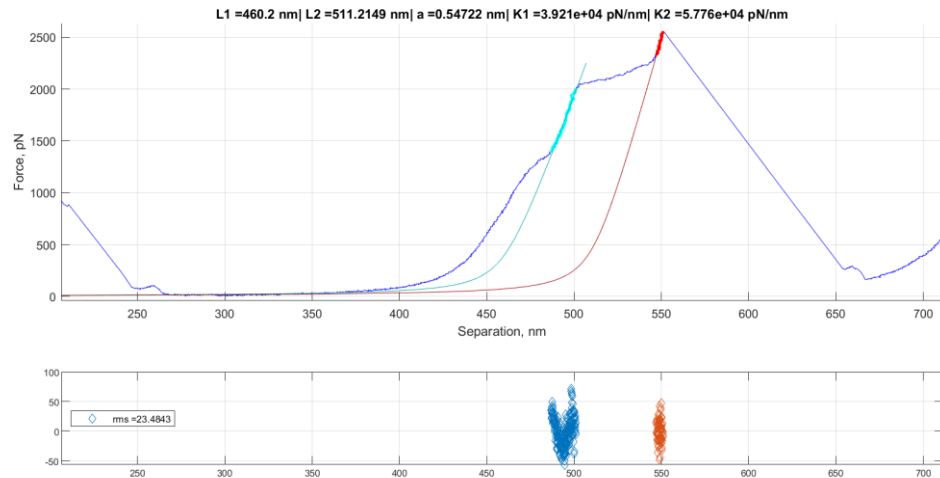


Figure 64 : Extended FJC model fitting (pre- and post- second transition) of the force-extension curve of polymer 4. The contour length before and after first transition are  $L_1 = 460.2 \text{ nm}$  and  $L_2 = 511.2 \text{ nm}$ , respectively.

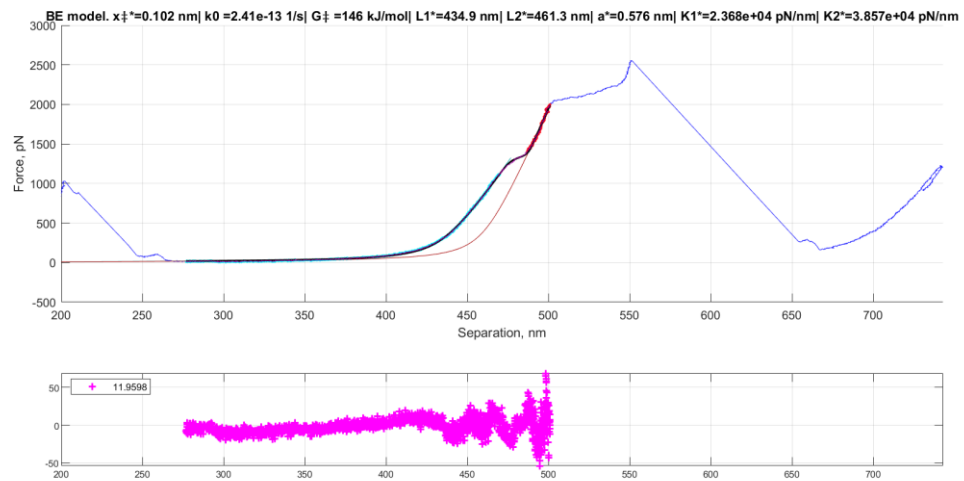


Figure 65 : BE model fitting of the first transition in the force-extension curve of polymer 4.  $\Delta x^\ddagger = 1.02 \text{ \AA}$ .

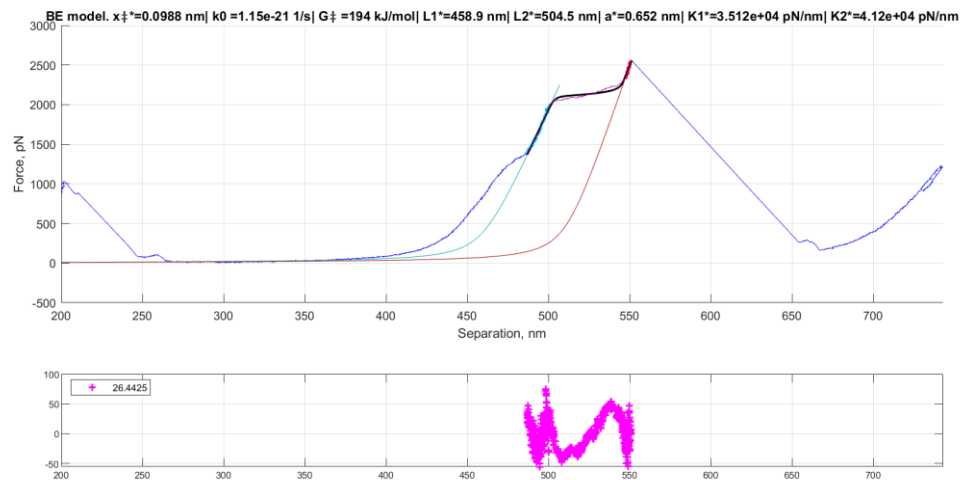


Figure 66 : BE model fitting of the second transition in the force-extension curve of polymer 4.  $\Delta x^\ddagger = 0.99$  Å.

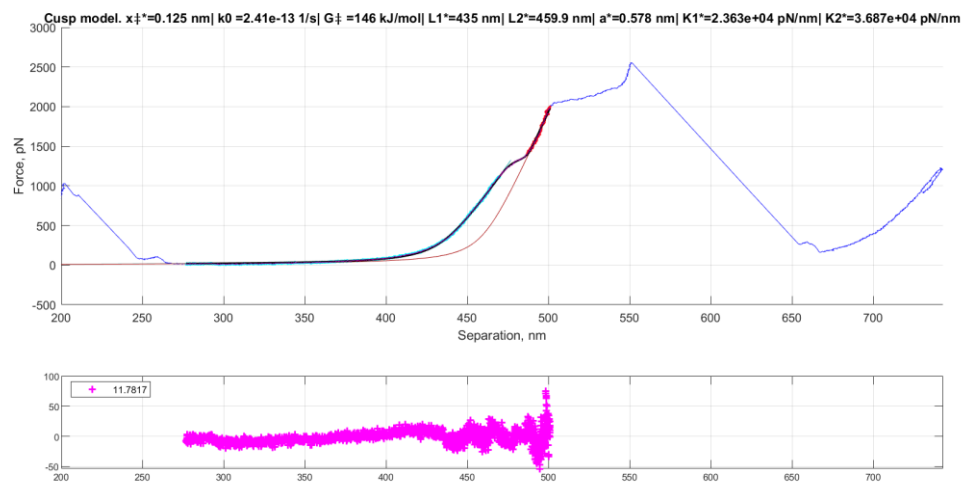


Figure 67 : Cusp model fitting of the first transition in the force-extension curve of polymer 4.  $\Delta x^\ddagger = 1.25$  Å.

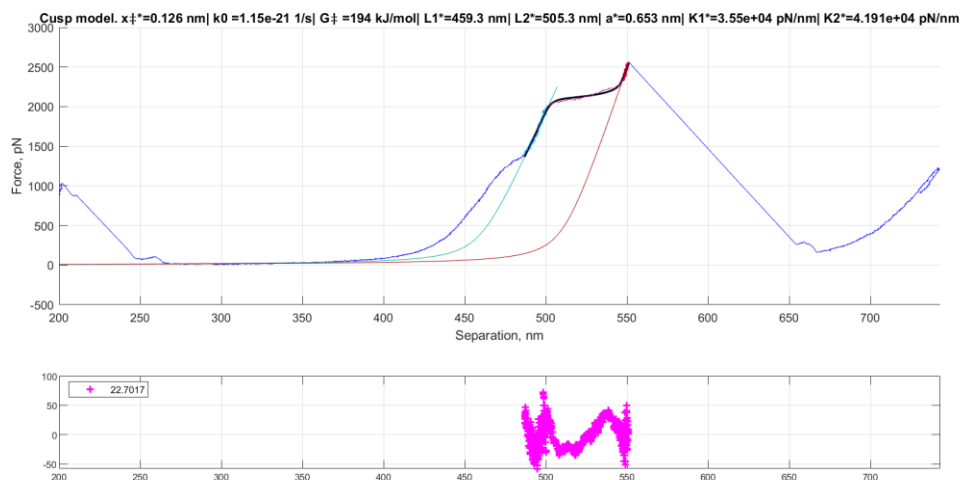


Figure 68 : Cusp model fitting of the second transition in the force-extension curve of polymer 4.  $\Delta x^\ddagger = 1.26 \text{ \AA}$ .

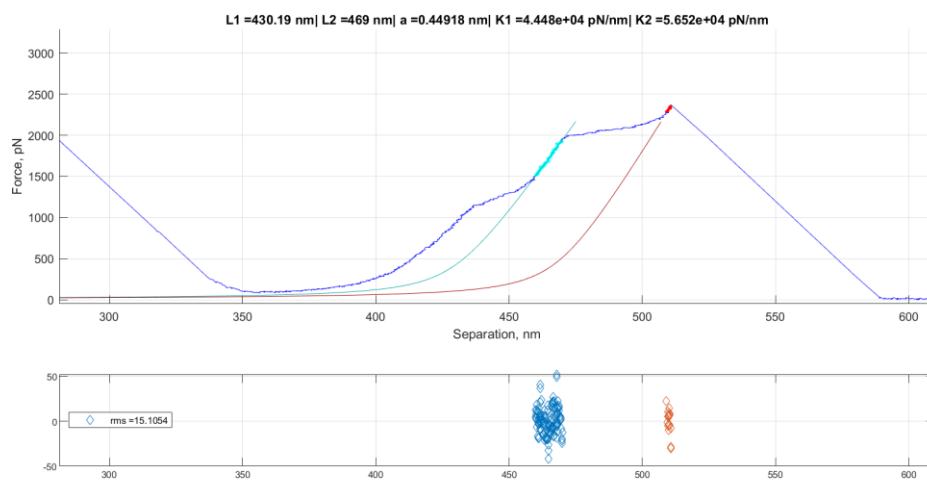
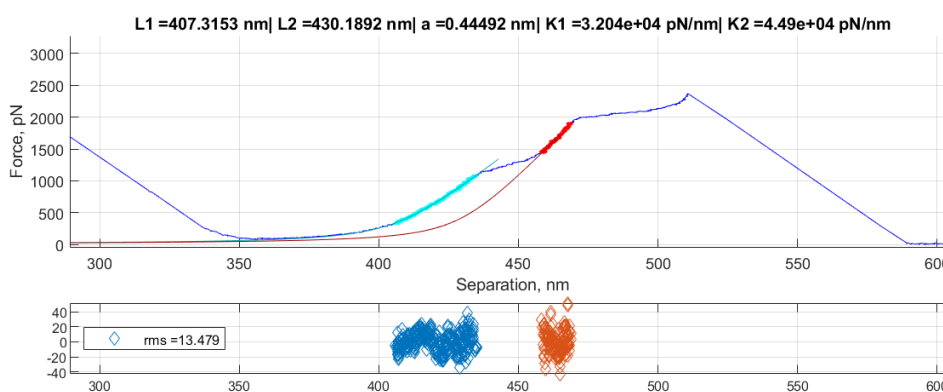
Table 9 : List of results from SMFS curves analysis

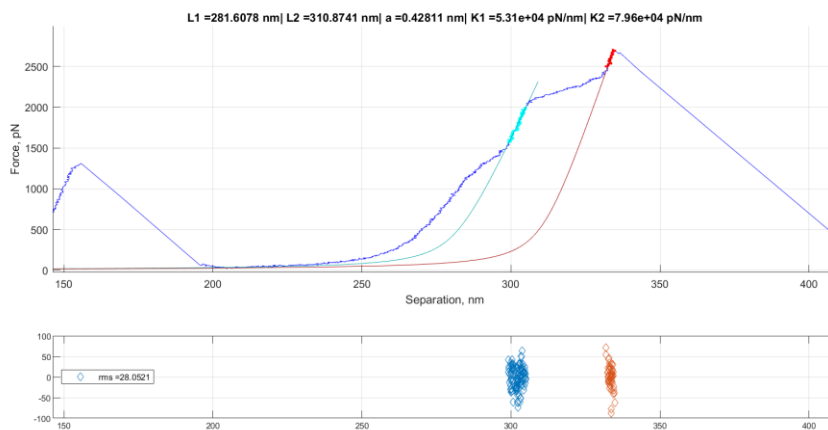
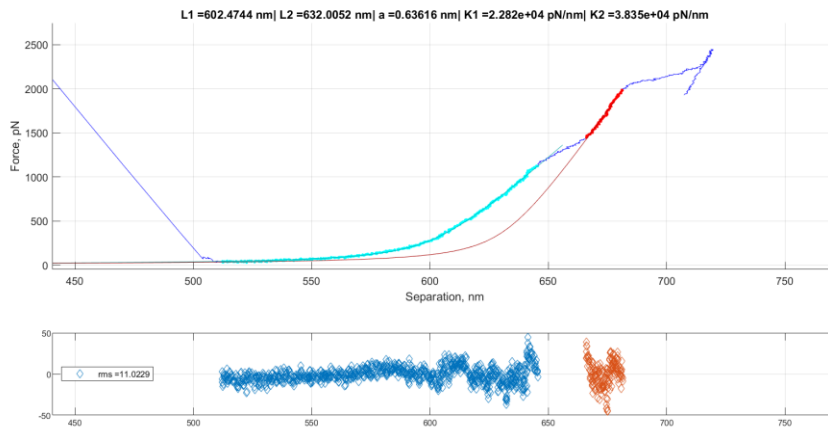
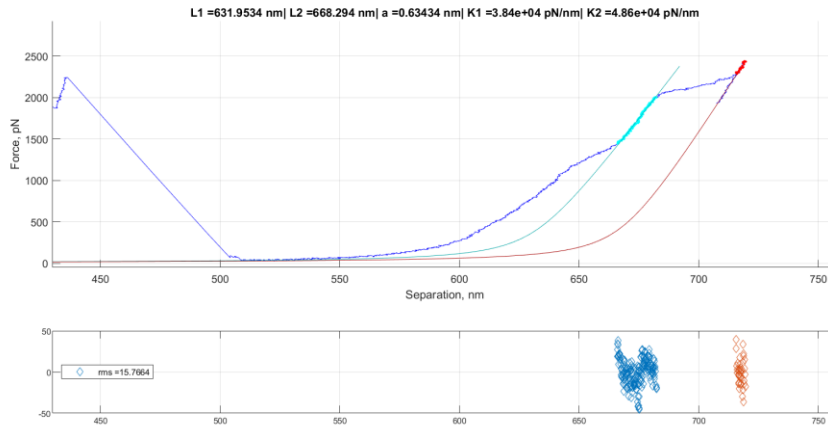
| # | L <sub>1</sub><br>(nm) | L <sub>2</sub><br>(nm) | L <sub>3</sub><br>(nm) | L <sub>2</sub> /L <sub>1</sub> | L <sub>3</sub> /L <sub>2</sub> | Kuhn<br>length<br>(nm) | K <sub>1</sub><br>(pN/nm) | K <sub>2</sub><br>(pN/nm) | $\Delta x^\ddagger$ (Å) |      | $f^*$<br>(pN) |
|---|------------------------|------------------------|------------------------|--------------------------------|--------------------------------|------------------------|---------------------------|---------------------------|-------------------------|------|---------------|
|   |                        |                        |                        |                                |                                |                        |                           |                           | BE                      | Cusp |               |
| 1 | 407.3                  | 430.2                  |                        | 1.056                          |                                | 0.445                  | 3.20E+04                  | 4.49E+04                  | 1.07                    | 1.31 | 1282          |
|   |                        | 430.2                  | 469.0                  |                                | 1.090                          | 0.449                  | 4.45E+04                  | 5.65E+04                  | 1.04                    | 1.3  | 2092          |
| 2 | 254.0                  | 266.5                  |                        | 1.049                          |                                | 0.589                  | 2.31E+04                  | 3.27E+04                  | 1.06                    | 1.3  | 1283          |
|   |                        | 266.5                  | 302.8                  |                                | 1.136                          | 0.588                  | 3.27E+04                  | 6.12E+04                  | 1.03                    | 1.32 | 2068          |
| 3 | 435.6                  | 460.3                  |                        | 1.057                          |                                | 0.561                  | 2.36E+04                  | 3.84E+04                  | 1.02                    | 1.25 | 1286          |
|   |                        | 460.2                  | 511.2                  |                                | 1.111                          | 0.547                  | 3.92E+04                  | 5.78E+04                  | 0.988                   | 1.26 | 2135          |
| 4 | 120.9                  | 126.2                  |                        | 1.044                          |                                | 0.510                  | 2.63E+04                  | 3.37E+04                  | 1.1                     | 1.34 | 1279          |
|   |                        | 126.3                  | 140.8                  |                                | 1.115                          | 0.511                  | 3.37E+04                  | 4.56E+04                  | 1.08                    | 1.38 | 2000          |
| 5 | 397.8                  | 414.3                  |                        | 1.041                          |                                | 0.629                  | 2.35E+04                  | 3.79E+04                  | 0.981                   | 1.19 | 1296          |
|   |                        | 414.3                  | 453.8                  |                                | 1.095                          | 0.629                  | 3.79E+04                  | 5.12E+04                  | 0.998                   | 1.28 | 2125          |
| 6 | 602.5                  | 632.0                  |                        | 1.049                          |                                | 0.636                  | 2.28E+04                  | 3.84E+04                  | 1                       | 1.22 | 1295          |
|   |                        | 632.0                  | 668.3                  |                                | 1.058                          | 0.634                  | 3.84E+04                  | 4.86E+04                  | 0.992                   | 1.27 | 2136          |
| 7 | 120.2                  | 123.0                  |                        | 1.023                          |                                | 0.807                  | 1.69E+04                  | 1.89E+04                  | 1.16                    | 1.42 | 1261          |
|   |                        | 123.0                  | 142.4                  |                                | 1.157                          | 0.808                  | 1.89E+04                  | 4.41E+04                  | 1.11                    | 1.43 | 1951          |
| 8 | 96.5                   | 101.6                  |                        | 1.053                          |                                | 0.189                  | 1.08E+05                  | 1.94E+05                  | 1                       | 1.22 | 1396          |
|   |                        | 99.4                   | 110.5                  |                                | 1.113                          | 1.226                  | 2.35E+04                  | 3.88E+04                  | 1.02                    | 1.31 | 2110          |
| 9 | 265.9                  | 281.9                  |                        | 1.060                          |                                | 0.434                  | 3.21E+04                  | 5.31E+04                  | 1.01                    | 1.23 | 1302          |
|   |                        | 281.6                  | 310.9                  |                                | 1.104                          | 0.428                  | 5.31E+04                  | 7.96E+04                  | 0.96                    | 1.23 | 2231          |

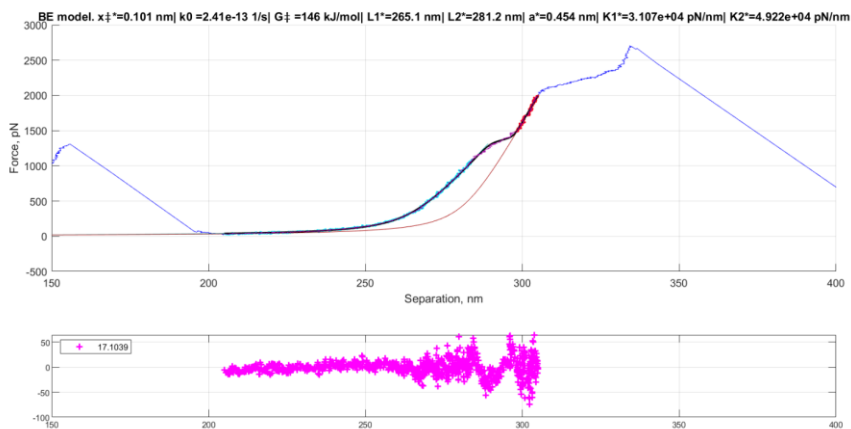
**Table 10 : Summary of results from SMFS fitting**

| Isomer        | <i>anti-gMCC</i>               |                         |             |             | <i>syn-gMCC</i>                |                         |             |             |
|---------------|--------------------------------|-------------------------|-------------|-------------|--------------------------------|-------------------------|-------------|-------------|
|               | L <sub>2</sub> /L <sub>1</sub> | $\Delta x^\ddagger$ (Å) |             | $f^*$ (pN)  | L <sub>3</sub> /L <sub>2</sub> | $\Delta x^\ddagger$ (Å) |             | $f^*$ (pN)  |
| BE            |                                | Cusp                    | BE          |             |                                | Cusp                    |             |             |
| <b>Avg.</b>   | 1.048                          | 1.05                    | 1.28        | 1290        | 1.109                          | 1.01                    | 1.29        | 2120        |
| <b>SD.</b>    | 0.011                          | 0.06                    | 0.07        | 10          | 0.028                          | 0.04                    | 0.04        | 60          |
| <b>Report</b> | <b>1.048</b>                   | <b>1.05</b>             | <b>1.28</b> | <b>1290</b> | <b>1.109</b>                   | <b>1.01</b>             | <b>1.29</b> | <b>2120</b> |
|               | $\pm 0.011$                    | $\pm 0.06$              | $\pm 0.07$  | $\pm 10$    | $\pm 0.028$                    | $\pm 0.04$              | $\pm 0.04$  | $\pm 60$    |

### 2.2.3.4.2 Additional SMFS curves

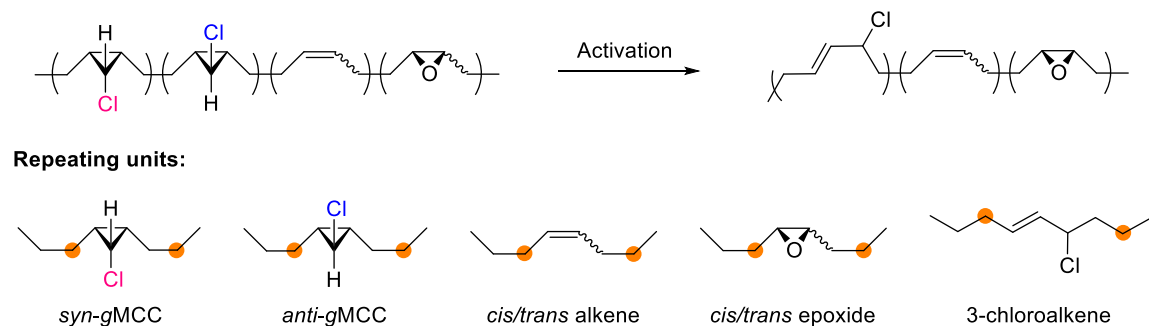






### 2.2.3.5 CoGEF modeling

The chemical structure of polymer **4** was rewritten as four components, and the corresponding activated polymer contains three components, as shown in the following:



The contour length of each repeating unit (end-to-end distance between two orange dots) was calculated from CoGEF modeling using Spartan'16 V2.0.7 on the theory level of Molecular Mechanics/MMFF. The two end carbons of each repeating unit were constrained and relaxed and the energy at each relaxed step was plotted as a function of distance. Following fitting with a quadratic equation and further analysis from the first derivative gave force vs. extension as a linear relation. Extrapolation of linear curve at zero force provided the contour length ( $x_0$ ).

Contour length of *syn*-gMCC:

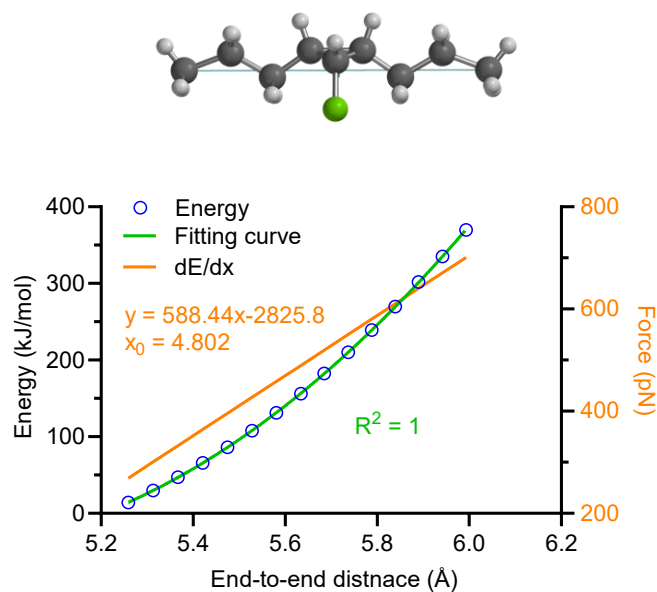


**Figure 69 : Quadratic fit of energy vs. distance curve (green); force vs. distance plot (orange). End-to-end distance of repeating unit *syn*-gMCC: 4.802 Å**

Contour length of *anti*-gMCC:

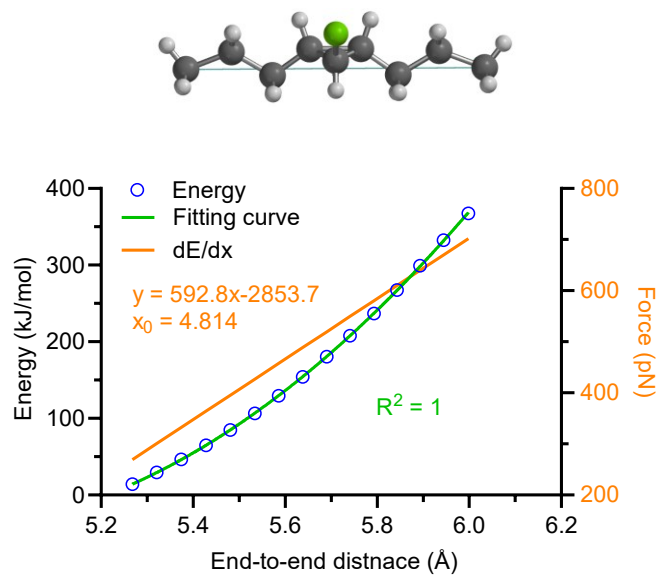


**Figure 70 : Quadratic fit of energy vs. distance curve (green); force vs. distance plot (orange). End-to-end distance of repeating unit *anti*-gMCC: 4.814 Å**

Contour length of *cis*-alkene:

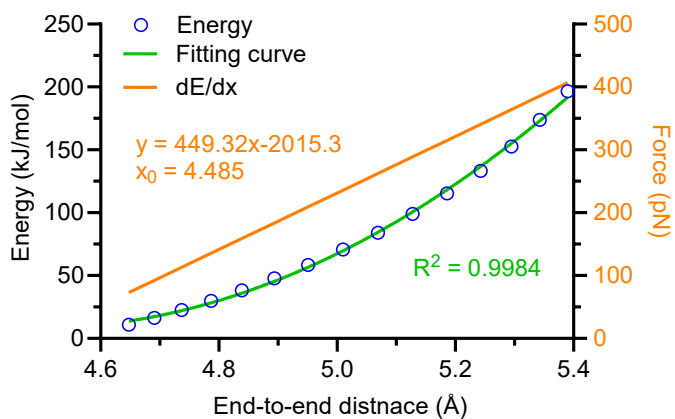
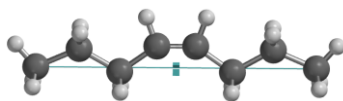


Figure 71 : Quadratic fit of energy vs. distance curve (green); force vs. distance plot (orange). End-to-end distance of repeating unit *cis*-alkene: 4.485 Å

Contour length of *trans*-alkene:

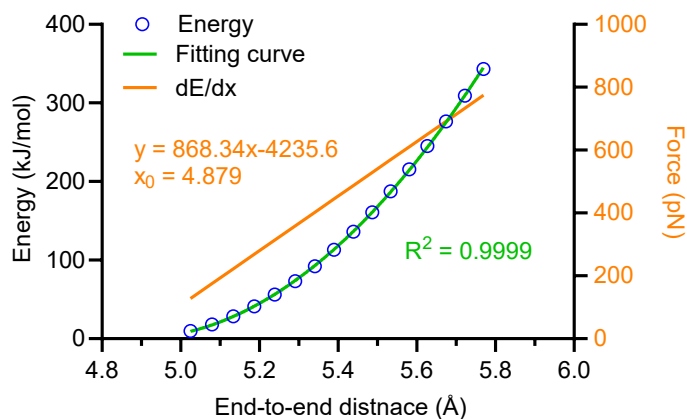
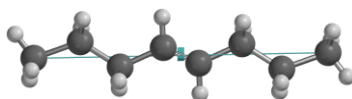


Figure 72 : Quadratic fit of energy vs. distance curve (green); force vs. distance plot (orange). End-to-end distance of repeating unit *trans*-alkene: 4.879 Å

Contour length of *cis*-epoxide:

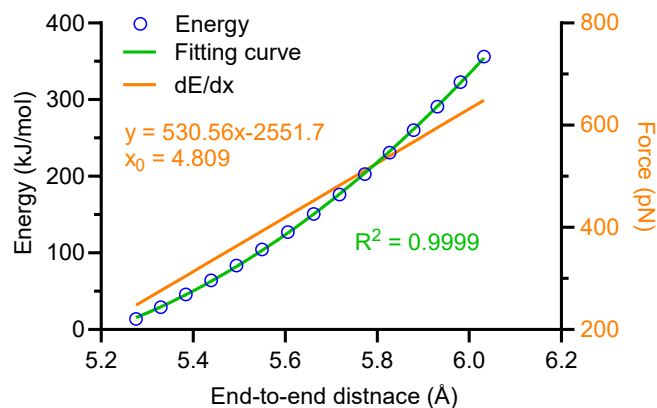
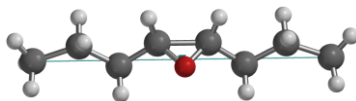


Figure 73 : Quadratic fit of energy vs. distance curve (green); force vs. distance plot (orange). End-to-end distance of repeating unit *cis*-epoxide: 4.809 Å

Contour length of *trans*-epoxide:

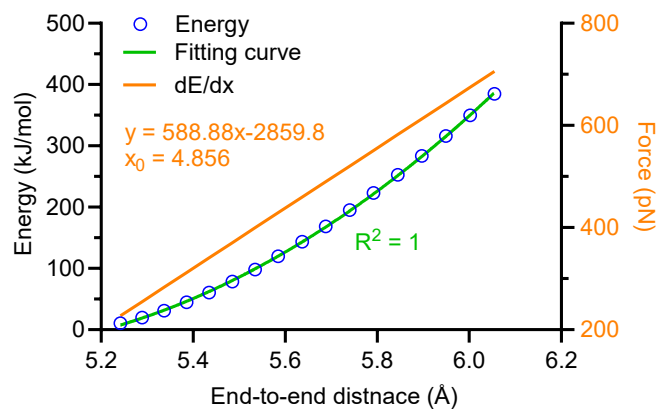
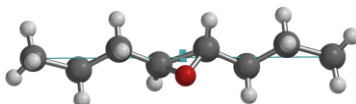
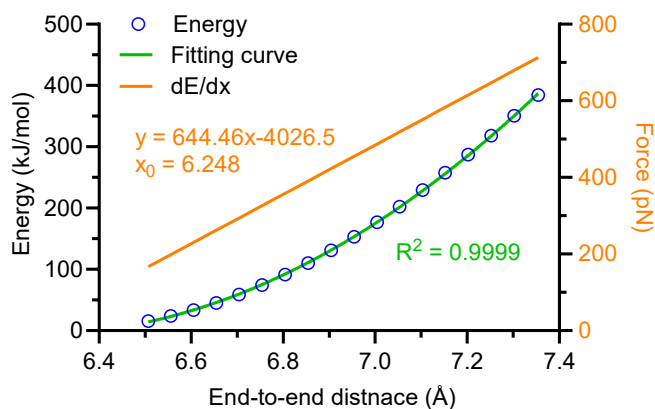


Figure 74 : Quadratic fit of energy vs. distance curve (green); force vs. distance plot (orange). End-to-end distance of repeating unit *trans*-epoxide: 4.856 Å

Contour length of 3-chloroalkene:



**Figure 75 : Quadratic fit of energy vs. distance curve (green); force vs. distance plot (orange). End-to-end distance of repeating unit 3-chloroalkene: 6.248 Å**

Calculation of extra extension:

Integration analysis from the <sup>1</sup>H NMR of polymer 4 gives the epoxide unit content as 19.5% relative to total gMCC mechanophore. Therefore, the content of alkene is 80.5%. The ratio of syn-gMCC to anti-gMCC is 3:1 in polymer 4. Hence, if we assume all gMCC mechanophores produce 3-chloroalkene product, we can calculate the theoretical extra extensions after activation of anti-gMCC and syn-gMCC, respectively.

Extra extension after activation of anti-gMCC:

$$\frac{L_f}{L_i} = \frac{6.248 \cdot 0.25 + 4.802 \cdot 0.75 + (4.485 + 4.878)/2 \cdot 0.805 + (4.809 + 4.856)/2 \cdot 0.195}{4.814 \cdot 0.25 + 4.802 \cdot 0.75 + (4.485 + 4.878)/2 \cdot 0.805 + (4.809 + 4.856)/2 \cdot 0.195} = 1.038$$

Extra extension after activation of syn-gMCC:

$$\frac{L_f}{L_i} = \frac{6.248 \cdot 0.25 + 6.248 \cdot 0.75 + (4.485 + 4.878)/2 \cdot 0.805 + (4.809 + 4.856)/2 \cdot 0.195}{6.248 \cdot 0.25 + 4.802 \cdot 0.75 + (4.485 + 4.878)/2 \cdot 0.805 + (4.809 + 4.856)/2 \cdot 0.195} = 1.110$$

## 2.3 Redox-regulation of the mechanical strength of a C-S bond

The mechanical strength of individual polymer chains is believed to underlie a number of performance metrics in bulk materials, including adhesion and fracture toughness. Methods by which the intrinsic molecular strength of the constituents of a given polymeric material might be switched are therefore potentially useful both for applications in which triggered property changes are desirable, and as tests of molecular theories for bulk behaviors. Here we report that the sequential oxidation of sulfide containing polyesters (PE) to the corresponding sulfoxide and then sulfone first weakens (sulfoxide), and then enhances (sulfone), the effective mechanical integrity of the polymer backbone;  $\text{PE-S} \sim \text{PE-SO}_2 > \text{PE-SO}$ . The relative mechanical strength as a function of oxidation state is revealed through the use of *gem*-dichlorocyclopropane (gDCC) noncissile mechanophores as an internal standard, and the observed order agrees well with the reported bond dissociation energies of C-S bonds in each species and with the results of CoGEF modeling.

### 2.3.1 Introduction

The mechanochemical scission of individual polymer chains limits their individual toughness, and it is also hypothesized to directly impact macroscopic material properties including, in some cases, the critical performance metrics of fracture toughness and adhesion.<sup>139</sup> Strategies for the *in situ* switching of the intrinsic molecular strength of a given polymeric material are therefore attractive on two fronts: (i) as a mechanism through which stimuli-responsive mechanical properties might be achieved; and, (ii) as a

direct probe to test long-held molecular theories for bulk behaviors (e.g., the Lake-Thomas theory<sup>140</sup>). To date, the external regulation of mechanochemical scission has been achieved using a photo-adaptable diarylethene-conjugated Diels–Alder adduct.<sup>91</sup> Inspired by this report, we sought an externally switchable mechanophore, with the following design parameters in mind: (i) minimal size; (ii) ease of synthesis; (iii) preceding use in bulk materials synthesis; (iv) responsiveness to stimuli other than light, in order to complement the prior work.

To this end, we hypothesized that controlling the oxidation of sulfide, which can be conveniently incorporated into polymers, provides an opportunity to achieve redox-regulation of the mechanical strength of C-S bond. Relative to polymeric systems that respond to light,<sup>141</sup> heat,<sup>142</sup> pH,<sup>143</sup> force,<sup>20</sup> and other stimuli,<sup>144-146</sup> redox-responsive polymers play remarkable roles in controlled assembly,<sup>147</sup> self-healing ability,<sup>148</sup> adjusting gel volume,<sup>149</sup> and drug delivery.<sup>150-152</sup> Construction of redox-responsive polymers is achieved through incorporation of oxidizable/reduceable chemical functional units, including ferrocene,<sup>153</sup> selenide/diselenide,<sup>154-155</sup> platinum complexes, sulfide, aryl oxalate esters, phenylboronic esters, thioketals, proline, etc.<sup>151</sup> Among these well-documented systems, we were drawn to sulfide containing polymers, which are easily constructed through thiol-ene “click” reactions,<sup>156</sup> Michael additions,<sup>157</sup> ring-opening of ethylene/propylene sulfide<sup>158-159</sup> and other scalable and accessible chemistry pathways.<sup>160-161</sup> Sulfide-based polymers have further proven to be useful in fabricating materials that are capable of adapting nanomorphology,<sup>162</sup> changing solubility,<sup>163-165</sup> tuning mechanical

modulus<sup>166</sup> and conductivity,<sup>167</sup> and delivering drugs when exposed to oxidants. Generally, the response is triggered by oxidizing sulfide to sulfoxide or sulfone, which is accompanied by a change in dipole moment/hydrophilicity.<sup>168</sup>

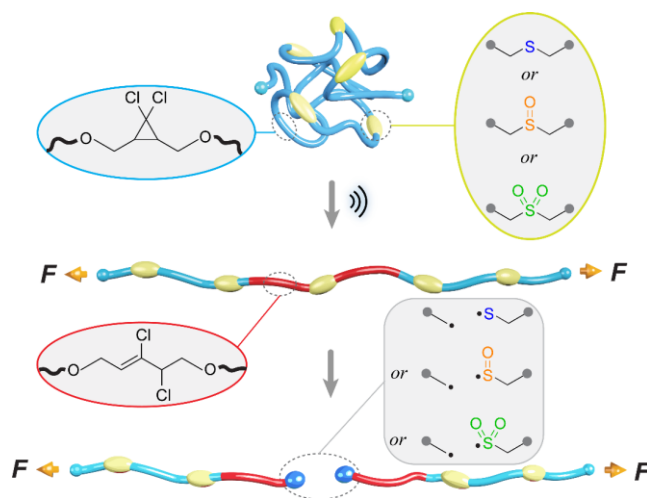


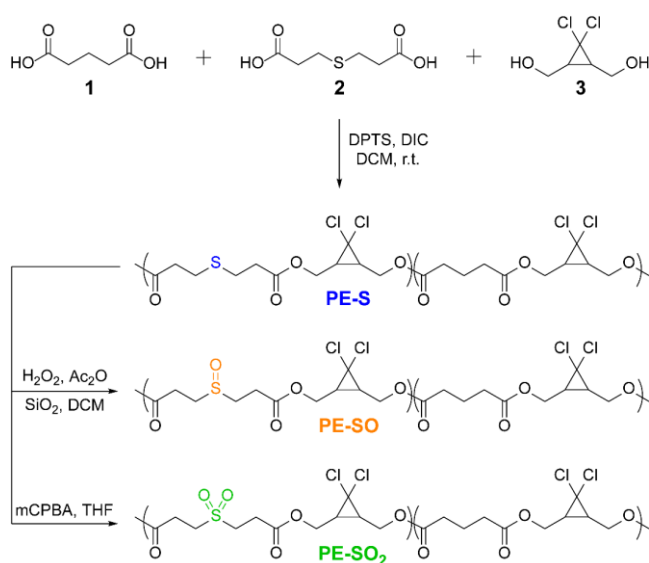
**Figure 76. Illustration of competition between gDCC ring opening and C-S bond scission on polymer backbone under sonication. Relative mechanical strength of C-S bonds in sulfide, sulfoxide and sulfone were compared.**

### 2.3.2 Results and discussion

The oxidation to sulfoxide or sulfone affects the C-S bond strength,<sup>169</sup> and we hypothesized that the corresponding mechanical strength (force required for the rapid mechanochemical scission of the corresponding C-S bond) might change similarly. The relative mechanical strengths of sulfide, sulfoxide, and sulfone can be quantified through the use of a non-scissile *gem*-dichlorocyclopropane (gDCC) mechanophore as an internal standard in pulsed sonication experiments.<sup>170</sup> As illustrated in Figure 76, there exists a competition between gDCC ring-opening and C-S bond scission, and the extent to which gDCC ring-opening could occur before chain scission depends on the mechanical strength of C-S bonds. The percentage of gDCC ring opening (gDCC RO%) per chain scission cycle

(SC, where  $SC = \ln(M_n^{(0)}/M_n^{(t)})/\ln 2$ ) is characterized by  $\Phi$ , the slope of gDCC RO% vs. SC, and it indicates the relative mechanical strength of a gDCC containing polymer. This quantification strategy has been applied to studies of the relationship between covalent bond strength and mechanical strength,<sup>83, 171</sup> the mechanochemistry of metallocenes<sup>45, 56</sup> the chain dynamics of cyclic polymers<sup>172</sup> under high strain rate elongational flows, and the subtle influence of stereochemical effects on the mechanical reactivity of Diels–Alder adducts<sup>173</sup> that are difficult to observe using more conventional chain-centered, single-mechanophore strategies.<sup>90</sup>

**Scheme 2 : Synthesis of sulfide containing polymer and corresponding oxidized sulfoxide and sulfone containing polymers.**



We prepared multi-mechanophore gDCC and sulfide containing copolymers using a polyesterification strategy (Scheme 2).<sup>50, 173</sup> Copolymerizing glutaric acid **1**, 3,3'-thiodipropionic acid **2**, and gDCC diol **3** (molar ratio,  $1/2/3 = 4:1:5$ ) monomers gave a **PE-S** polymer containing the expected 20 mol% of sulfide repeats along the backbone. **PE-S**

was further oxidized to either the corresponding polysulfoxide (**PE-SO**) using a mild oxidation protocol<sup>174</sup> or polymersulfone (**PE-SO<sub>2</sub>**) using *meta*-chloroperoxybenzoic acid (*m*CPBA) as an oxidant.

Obtained polymers were analyzed by GPC (THF mobile phase) coupled with reflective index (RI) and multi-angle light scattering (MALS) detectors. As shown in Figure 77a, oxidation of **PE-S** to **PE-SO** and **PE-SO<sub>2</sub>** leads to a shift in retention time from 13.81 min to 14.06 min, and 13.94 min, respectively. Molecular weights ( $M_n$ ) determined by MALS are consistent with the shifts in retention time;  $M_n = 72$  kDa for **PE-S** ( $D = 1.45$ ),  $M_n = 54$  kDa for **PE-SO** ( $D = 1.48$ ), and  $M_n = 60$  kDa for **PE-SO<sub>2</sub>** ( $D = 1.48$ ). We attribute the reduction in  $M_n$  on going from **PE-S** to **PE-SO** to low levels of oxidative degradation, and the increase in  $M_n$  on subsequent oxidation to **PE-SO<sub>2</sub>** to the addition of O atoms to the polymer chains.

The conversion of sulfide to sulfoxide and sulfone is verified by <sup>1</sup>H NMR spectroscopy. The protons a and b to the sulfur atom ( $H_a$  and  $H_b$ , Figure 77b) begin as clean triplets at 2.84 and 2.67 ppm in **PE-S**. Upon oxidation,  $H_a$  evolves into two coupled multiple peaks at 3.10 and 2.96 ppm, and  $H_b$  shifts to 2.91 ppm. The splitting of  $H_a$  is a result of the asymmetry of the sulfoxide, which renders the two  $H_a$  protons diastereotopic and magnetically inequivalent. Further oxidation to the symmetric sulfone restores the two triplet peaks, albeit at positions that are further downfield ( $\delta = 3.40$  ppm and 2.94 ppm). Other peaks in the spectra remain effectively unchanged. Integration of  $H_a/H_b$  relative to other backbone protons reveals that the molar content of sulfide, sulfoxide, and

sulfone stays at a constant value of  $\sim 20 \pm 1$  mol% (see section 2.3.3.2), establishing the selective oxidation of sulfide to sulfoxide and sulfone.

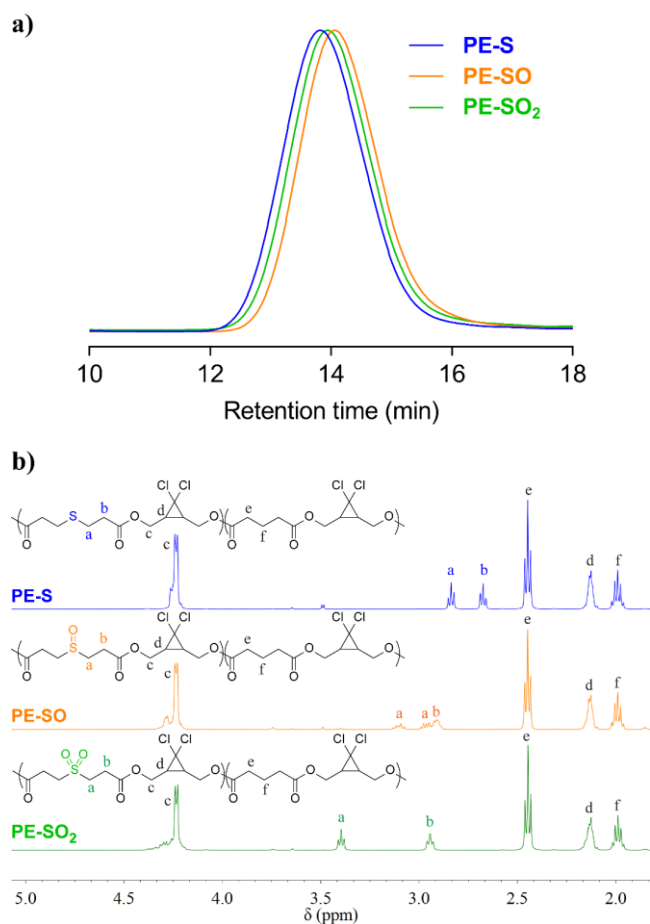


**Figure 77 : a) Normalized GPC traces (RI signal, THF eluent) of PE-S, PE-SO and PE-SO<sub>2</sub> polymers. b) <sup>1</sup>H NMR (500 MHz, CDCl<sub>3</sub>) spectra stacking of PE-S, PE-SO, PE-SO<sub>2</sub> polymers. The characteristic protons H<sub>a</sub> and H<sub>b</sub> are used to quantify the content of sulfide (20 mol%), sulfoxide (19 mol%) and sulfone (20 mol%) units on polymer backbone.**

Ultrasonication was used to quantify the relative mechanical strength of the polymer as a function of its oxidation state. In a typical experiment, a THF solution of the polymer (2 mg/mL) was treated with pulsed ultrasonication (30% amplitude, 1s on, 1s off, ice bath, N<sub>2</sub>), with aliquots removed and analyzed periodically until the  $M_n$  was reduced

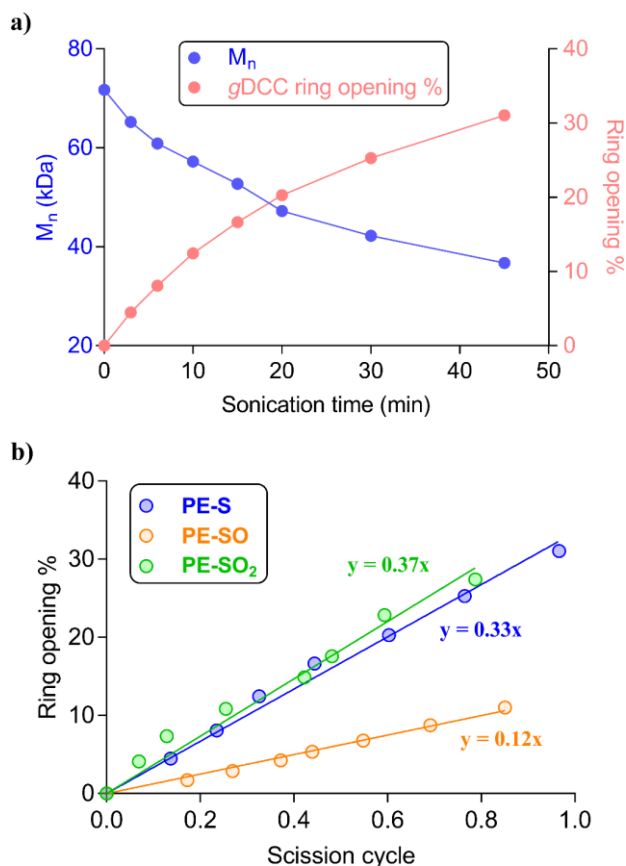


**Figure 78 : a) The evolution of  $M_n$  in PE-S and corresponding percentage of gDCC ring opening at various sonication time. b) The fraction of gDCC ring opening vs. scission cycle for each C-S containing polymer.**

to nearly half of its initial value. As the  $M_n$  decreased, the extent of gDCC ring opening increased. For example, after subjection of PE-S polymer to ultrasonication for 45 min, the  $M_n$  drops from 72 kDa to 37 kDa, and this is accompanied by 32% gDCC ring opening along the polymer backbone (Figure 78a). Here, polymer chain scission is ascribed to the selective C-S bond cleavage, based on previously evidence that C-S bond is a relative mechanical weak bond compared with other C-C and C-O bonds along the polymer backbone.<sup>170</sup> The chain scission cycle is calculated according to the following equation:

$$SC = \frac{\ln M_{n(0)} - \ln M_n}{\ln 2}$$

Where  $M_{n(0)}$  and  $M_n$  are initial and sonicated molecular weight, respectively.

The evolution of gDCC RO% vs. SC is shown in Figure 78b. The  $\Phi$  value of **PE-SO** is 0.12, and it is two-folds less than that of **PE-S** ( $\Phi = 0.33$ ). Interestingly, with further oxidized sulfone units, **PE-SO<sub>2</sub>** gave a  $\Phi$  value of 0.37. The evolution in  $\Phi$  values suggests that as the sulfide is oxidized to sulfoxide and sulfone, the relative mechanical strength of C-S bonds in each polymer follows the order: **PE-S**  $\approx$  **PE-SO<sub>2</sub>** > **PE-SO**. A rough way to evaluate this outcome is comparing the C-S bond dissociation energy, for the reason that mechanically induced bond cleavage is essentially a force-assisted bond dissociation. Some theoretical calculations suggest that the C-S bond dissociation energies of sulfide, sulfoxide, and sulfone are 74~77 kcal/mol, 53~54 kcal/mol, and ~68 kcal/mol, respectively.<sup>169</sup> This energy difference indicates a likely order of C-S bond mechanical strength: **PE-S** > **PE-SO<sub>2</sub>** > **PE-SO**. Our experimental observation of **PE-S** and **PE-SO<sub>2</sub>** is slightly in contrast to this order, and it is attributed to the difference in  $M_n$ . Previous studies<sup>171, 173</sup> indicated a dependence of  $\Phi$  value on the initial  $M_n$  in that lowering the initial  $M_n$  would increase the  $\Phi$  value. Therefore, a difference of 12 kDa in  $M_n$  between **PE-S** ( $M_n = 72$  kDa) and **PE-SO<sub>2</sub>** ( $M_n = 60$  kDa) could result in the observed similar  $\Phi$  values. A recent report by Diesendruck et al.<sup>175</sup> investigated the impact of intramolecular crosslinker on the mechanochemical fragmentation of folded polymer and found that the sulfone crosslinker is slightly mechanically weaker than sulfide. On the other hand, the lower  $\Phi$  value of **PE-**

SO ( $M_n = 54$  kDa) than that of PE-S and PE-SO<sub>2</sub> is convincing and strongly supports the conclusion that sulfoxide is the weakest among three.

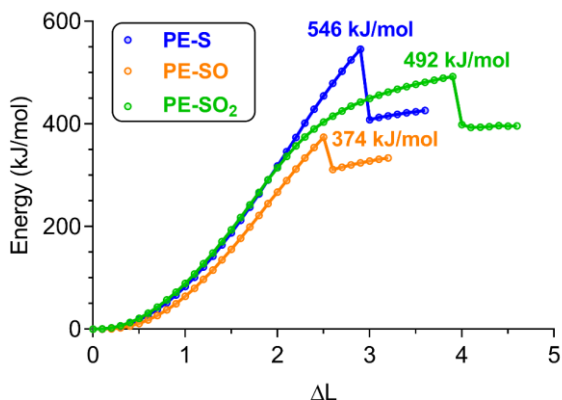


**Figure 79 : DFT calculation of the mechanical strength of C-S in each sulfur containing species using CoGEF method on the theory level of B3LYP/6-31G\*.**

The relative mechanical strength of C-S bonds was further verified using CoGEF modeling. The simulation was performed on the methyl ester forms of each C-S bond containing repeating unit. While the end-to-end distance was constrained in an increasing step of 0.1 Å, the optimal geometry energy was minimized using DFT method at the theory level of B3LYP/6-31G\*. Obtained minimal energy vs. distance ( $\Delta L$ ) profiles are shown in Figure 79. The increase in distance creates more energy input and further induces fragmentation of weak bond at sufficiently high distortion. During this process, two C-S bonds elongate symmetrically, and one C-S bond fragments while the other relaxes after reaching the maximum energy (Figure 98-100). To worth noticing, in contrast to sulfide and sulfoxide, the distortion of sulfone presented a more compliant/soft characteristic in C-S bond and provides an extra  $\sim 1$  Å elongation (0.5 Å per C-S bond, Figure 101) before break. Because the simulation mimics the stretching of molecules, the

maximum energies are indicative of bond mechanical strength. Herein, the relative mechanical strength of C-S bonds follows the order: **PE-S > PE-SO<sub>2</sub> > PE-SO**.

In conclusion, the above results suggest that the mechanical strength of C-S bond is adjustable through oxidation reactions. The wide range of strategies of embedding sulfide groups in polymers allows to facilely prepare polymeric materials with redox-regulable behaviors, where the response of C-S bonds to an external oxidant alters the polymer chain toughness and thus bulk mechanical properties. We reason that the ability to attain *in situ* switching of mechanochemical scission provides a means to exam the theoretical interpretation of polymer fracture behavior (e.g., Lake-Thomas theory), in which the energy dissipation can be correlated to single chain toughness.<sup>139</sup>

### **2.3.3 Experimental section**

#### **2.3.3.1 General procedures**

Materials: Lab general solvents (dichloromethane, ethyl acetate, acetone, toluene, tetrahydrofuran, methanol) were purchased from VWR or Sigma Aldrich. 4-Dimethylaminopyridine, *p*-toluenesulfonic acid, *N,N'*-Diisopropylcarbodiimide, 3,3'-thiodipropionic acid, glutaric acid, hydrogen peroxide, acetic anhydride, *meta*-chloroperoxybenzoic acid (mCPBA) and silica dioxide were purchased from Sigma Aldrich, Alfa Aesar or TCI and used without further purification.

Characterizations: <sup>1</sup>H NMR spectra were collected on a Bruker Advance Neo - 500 MHz multinuclear NMR spectrometer. Chemical shifts are provided in *ppm* ( $\delta$ ) and referenced to the residual <sup>1</sup>H peak at 7.26 ppm in CDCl<sub>3</sub>. <sup>1</sup>H shifts are reported as chemical

shift, multiplicity, coupling constant if applicable, and relative integral. Multiplicities are reported as: singlet (s), doublet (d), doublet of doublets (dd), doublet of triplets (dt), doublet of doublet of doublets (ddd), doublet of doublet of triplets (ddt), triplet (t), triplet of doublets (td), quartet (q), pentet (p), multiplet (m), or broad (br). Coupling constants (J) are reported in Hertz. Gel permeation chromatography (GPC) was performed on two Agilent PLgel mixed-C columns ( $10^5$  Å, 7.5x300 mm, 5  $\mu$ m, part number PL1110-6500) using THF (stabilized with 100 ppm BHT) as the eluent. Molecular weights were calculated using a Wyatt Dawn EOS multi-angle light scattering (MALS) detector and Wyatt Optilab DSP Interferometric Refractometer (RI). The refractive index increment (dn/dc) values were determined by online calculation based on injections of known concentration and mass.

### 2.3.3.2 Synthesis procedures

Synthesis of polymer PE-S:

To a 50 mL oven dried round bottom flask, added glutaric acid **1** (528.4 mg, 4.0 mmol, 0.8 eq), 3,3'-thiodipropionic acid **2** (178.2 mg, 1.0 mmol, 0.2 eq), *gem*-dichlorocyclopropane (gDCC) diol **3**<sup>176</sup> (855 mg, 5.0 mmol, 1.0 eq) and 4-(dimethylamino)pyridinium-4-toluenesulfonate (DPTS)<sup>177</sup> (588 mg, 2.0 mmol, 0.4 eq) as catalyst. 5 mL dry DCM was then added to the flask. After solids are completely dissolved, *N,N'*-Diisopropylcarbodiimide (DIC) (2.32 mL, 15 mmol, 3.0 eq) was added dropwise to the solution. White precipitate formed during the addition. The flask was then sealed and allowed to stir at room temperature for 3 days. The resulting viscous mixture was

precipitated from methanol three times. Obtained white gummy polymer **PE-S** was collected and dried under high vacuum (1.132 g, 82%). Obtained polymer was analyzed from GPC:  $M_n = 71.7$  kDa, PDI = 1.445,  $dn/dc = 0.087$ .  $^1\text{H NMR}$  (500 MHz,  $\text{CDCl}_3$ )  $\delta$ : 4.33-4.15 (m, 10H), 2.84 (t, 2H), 2.68 (t, 2H), 2.45 (t, 8H), 2.20-2.06 (m, 5H), 1.99 (p, 4H). Calculated sulfide content:  $2/10 \times 100\% = 20$  mol%.

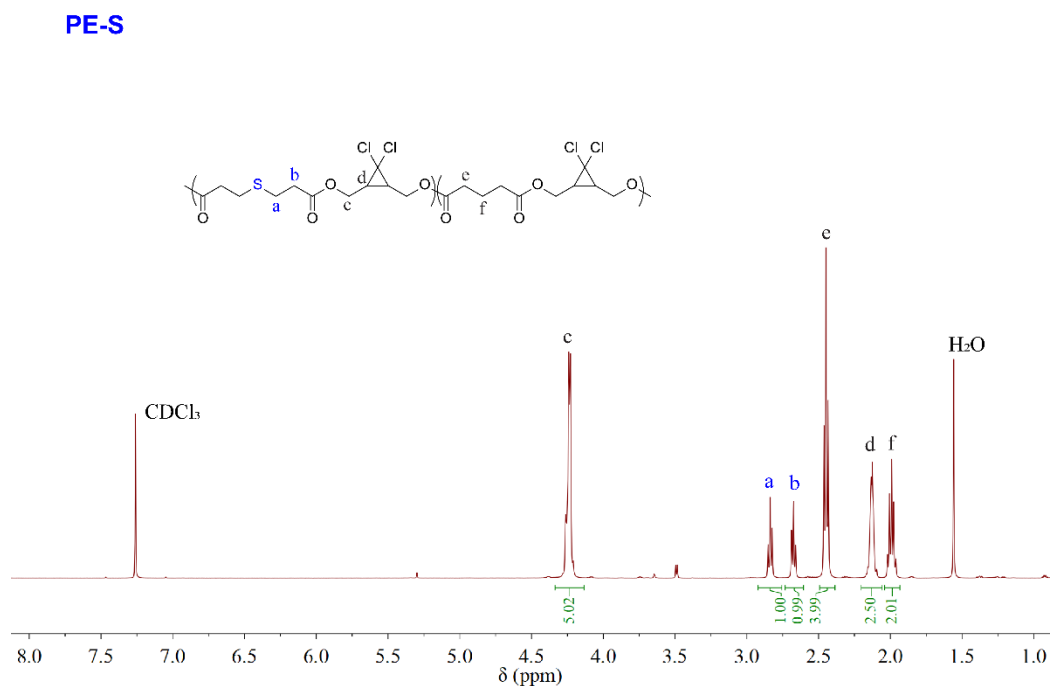


**Figure 80 :  $^1\text{H NMR}$  ( $\text{CDCl}_3$ , 500 MHz) spectrum of PE-S polymer**

Synthesis of polymer PE-SO:

The oxidation process was adapted from previous literature.<sup>178</sup>

Polymer **PE-S** (78 mg, 0.05 mmol C-S bond) was weighted in a 10 ml scintillation vial. 1 mL DCM was added to completely dissolve the polymer. Acetic anhydride (5.2  $\mu\text{L}$ , 0.055 mmol, 1.1 eq) and silica gel (50 mg) was added to the solution. Then, 30% hydrogen peroxide (57  $\mu\text{L}$ , 0.5 mmol, 10 eq) was added to the mixture. The reaction was further

stirred at room temperature for 6 h. The resulting mixture was then diluted with 2 mL DCM and silica gel was filtered using a syringe filter. Obtained DCM solution was condensed and precipitated from methanol three time to give polymer **PE-SO** (74 mg, 93.9%). GPC:  $M_n = 59.9$  kDa, PDI = 1.478,  $dn/dc = 0.090$ .  $^1\text{H NMR}$  (500 MHz,  $\text{CDCl}_3$ )  $\delta$ : 4.36-4.16 (m, 10H), 3.16-3.05 (m, 1H), 3.01-2.93 (m, 1H), 2.93-2.84 (m, 2H), 2.45 (t, 8H), 2.20-2.06 (m, 5H), 1.99 (p, 4H). Calculated sulfoxide content:  $1.9/10 \times 100\% = 19$  mol%.

### PE-SO

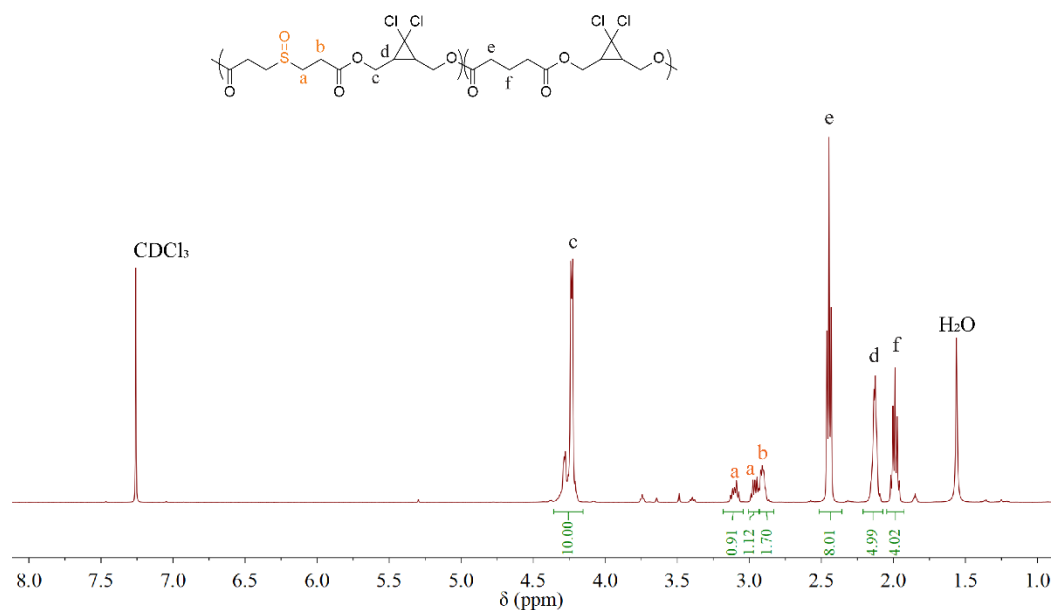


**Figure 81** :  $^1\text{H NMR}$  ( $\text{CDCl}_3$ , 500 MHz) spectrum of PE-SO polymer

Synthesis of polymer PE-SO<sub>2</sub>:

To a solution of **PE-SO** (156 mg, 0.1 mmol C-S bond) in 3 mL THF, mCPBA (74 mg, 70%~75%, 0.3 mmol) was added in portions. The reaction was allowed to stir at room temperature overnight. After the reaction completed, the solution was condensed and precipitated from methanol three times to give a white polymer **PE-SO<sub>2</sub>** (158 mg, 99.9%).

GPC:  $M_n = 54.1$  kDa, PDI = 1.478,  $dn/dc = 0.091$ .  $^1\text{H NMR}$  (500 MHz,  $\text{CDCl}_3$ )  $\delta$ : 4.37-4.16 (m, 10H), 3.40 (t, 2H), 2.94 (t, 2H), 2.45 (t, 8H), 2.20-2.06 (m, 5H), 1.99 (p, 4H). Calculated sulfone content:  $2/10 \times 100\% = 20$  mol%.

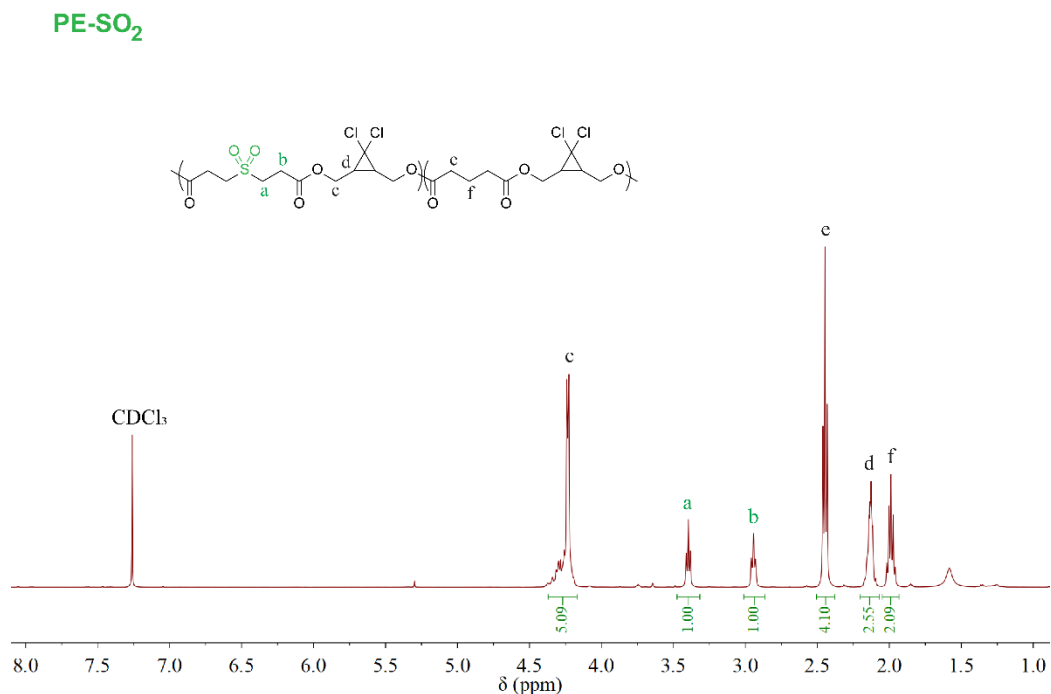


**Figure 82 :  $^1\text{H NMR}$  ( $\text{CDCl}_3$ , 500 MHz) spectrum of PE-S polymer**

### 2.3.3.3 Sonication experiment

General sonication procedures: A solution of 36 mg polymer (**PE-S**, **PE-SO** or **PE-SO<sub>2</sub>**) in 18 mL dry THF ( $c = 2$  mg/mL) was transferred into a Suslick cell. The solution was purged with  $\text{N}_2$  for 10 min while cooled with ice bath. Pulsed ultrasound was applied (1s on, 1s off) at 30% amplitude. An aliquot of 0.8 mL sample was taken out for GPC analysis at time points: 0, 3, 6, 10, 15, 20, 30, 45 min. Each of these samples were further rotavaped in a 10 ml scintillation vial to give a thin layer of polymer at the bottom. The polymer was

washed with methanol and further dried under high vacuum. Obtained dry polymers were further subjected to  $^1\text{H}$  NMR analysis.

### 2.3.3.3.1 Sonication of PE-S polymer

Calculation of PE-S polymer chain scission cycle:

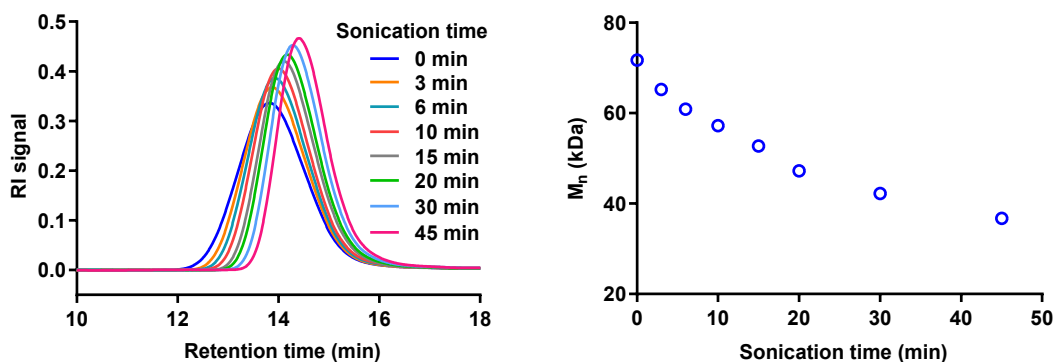


**Figure 83 : Evolution of GPC traces during sonication of PE-S polymer (left) and corresponding plot of molecular weight versus sonication (right).**

The chain scission cycle (SC) describes the average number of times a polymer has undergone chain scission. SC of PE-S polymer at each sonication time was obtained from the following equation:

$$\text{SC} = \frac{\ln M_{n(0)} - \ln M_{n(t)}}{\ln 2}$$

Where  $M_{n(0)}$  is the initial molecular weight;  $M_{n(t)}$  is molecular weight at sonication time  $t$ .

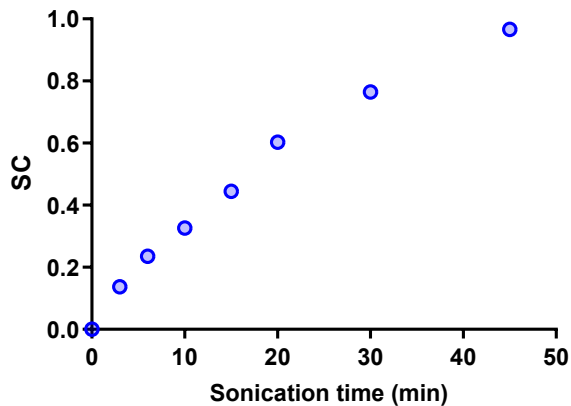


Figure 84 : Scission cycle (SC) of PE-S polymer at various sonication time

Determination of ring-opening percentage of gDCC in PE-S polymer:

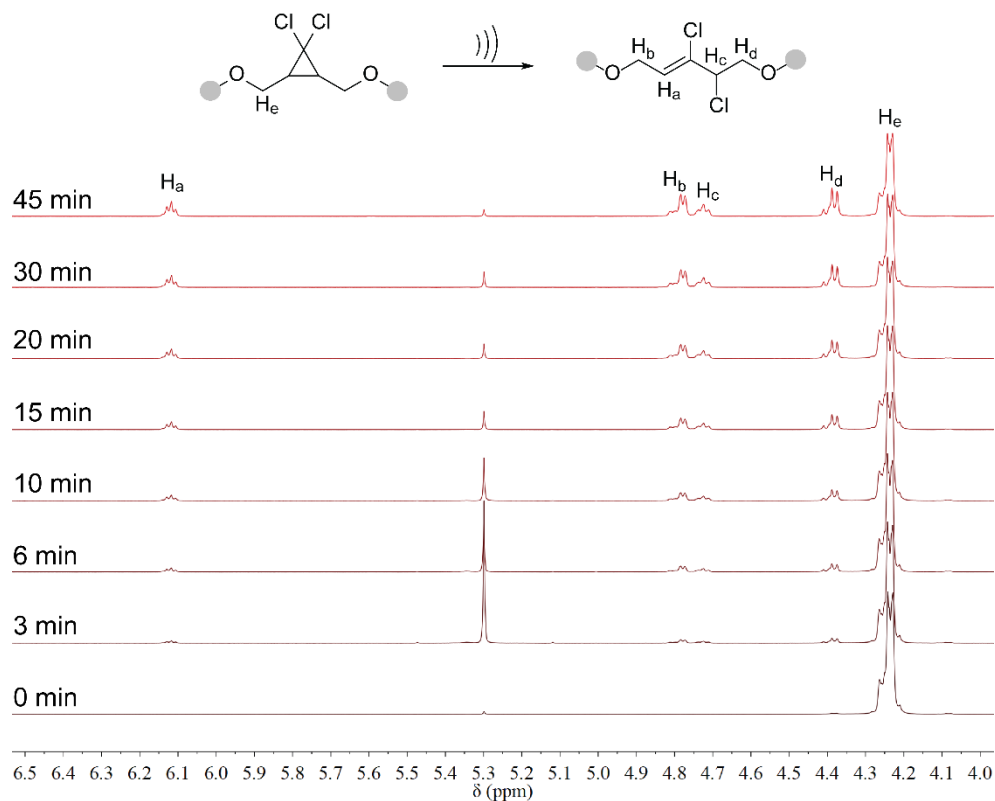


Figure 85 : Stack of <sup>1</sup>H-NMR (CDCl<sub>3</sub>, 500 MHz) spectra of sonicated PE-S polymer at various sonication time.

In the  $^1\text{H NMR}$ , the peak at 5.32~5.56 ppm ( $\text{H}_c$ ) corresponds to pristine total alkenes of polymer as prepared. The peak at 5.84 ppm ( $\text{H}_a$ ) and 4.48 ppm ( $\text{H}_b$ ) are new generated alkene after sonication. The ring-opening percentage can be obtained:

$$\text{Ring opening \%} = \frac{4 * \int \text{H}_a}{\int \text{H}_b + \int \text{H}_d + \int \text{H}_e} \times 100\%$$

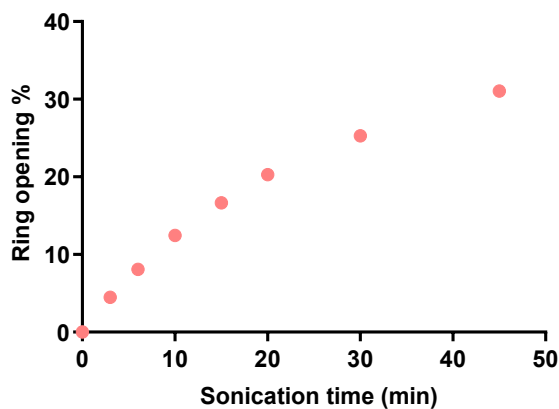


Figure 86 : Ring-opening percentage of gDCC in PE-S polymer versus sonication time.

Evaluation of  $\Phi$  value:

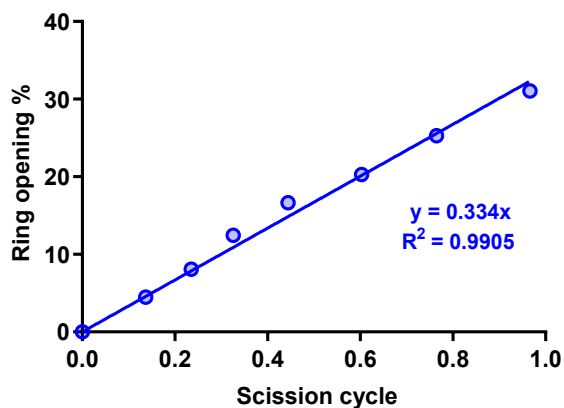


Figure 87 : Percentage of gDCC ring opening versus scission cycle plot for PE-S polymer. The slope of linear fitting through origin gives  $\Phi = 0.334$ .

### 2.3.3.3.2 Sonication of PE-SO polymer

The procedure of analyzing PE-SO polymer is the same as PE-S polymer.

Calculation of PE-SO polymer chain scission cycle:

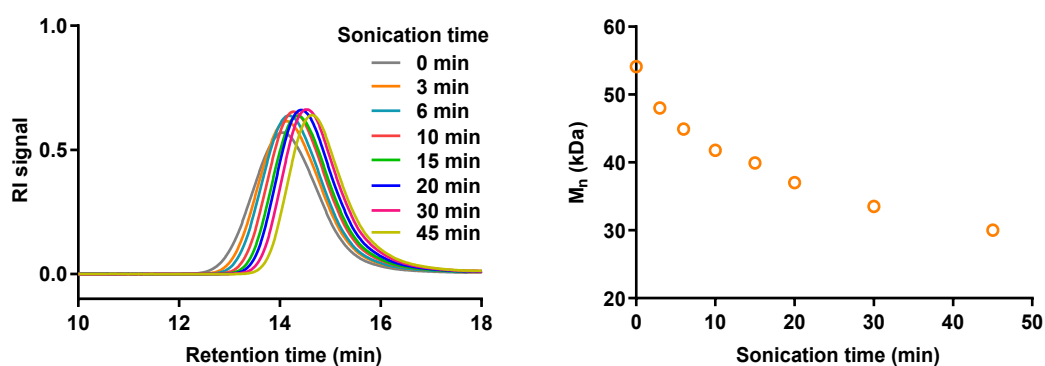


Figure 88 : Evolution of GPC traces during sonication of PE-SO polymer (left) and corresponding plot of molecular weight versus sonication (right).

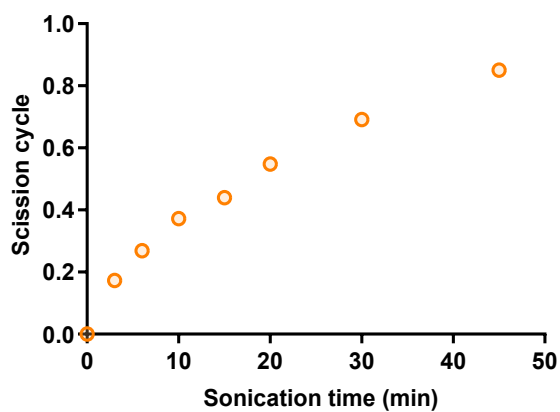
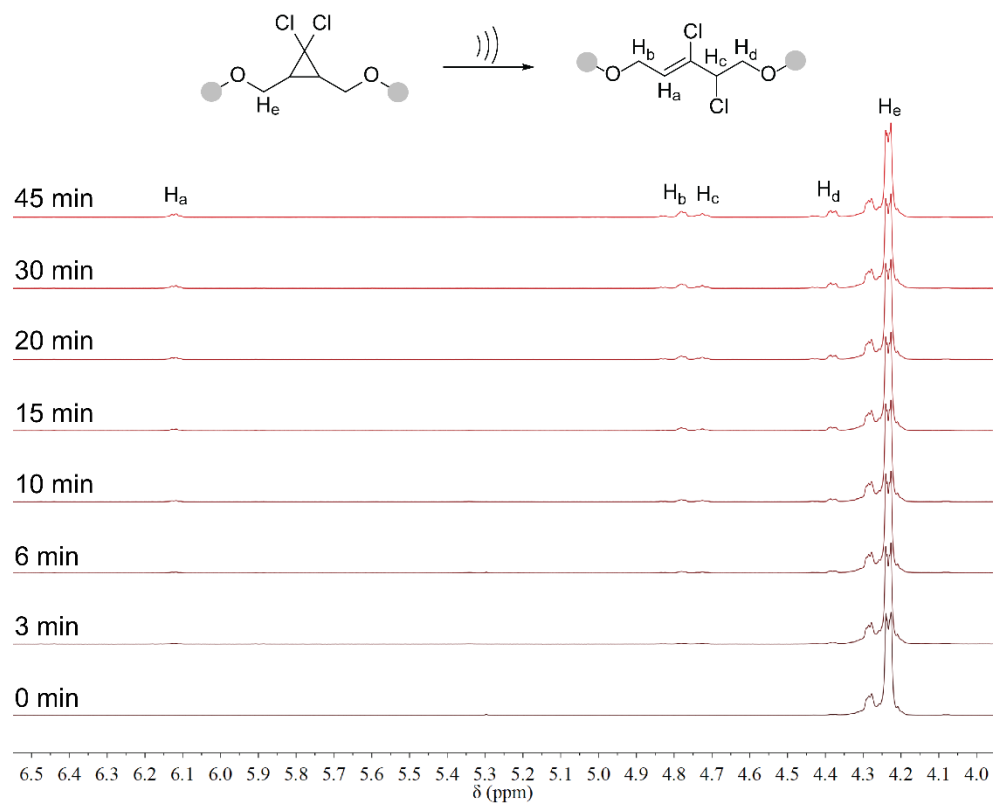


Figure 89 : Scission cycle (SC) of PE-SO polymer at various sonication time

Determination of ring-opening percentage of gDCC in PE-SO polymer:



**Figure 90 : Stack of <sup>1</sup>H-NMR (CDCl<sub>3</sub>, 500 MHz) spectra of sonicated PE-SO polymer at various sonication time.**

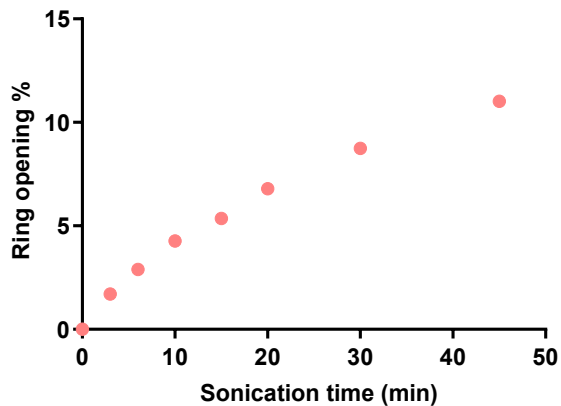


Figure 91 : Ring-opening percentage of gDCC in PE-SO polymer versus sonication time.

Evaluation of  $\Phi$  value:

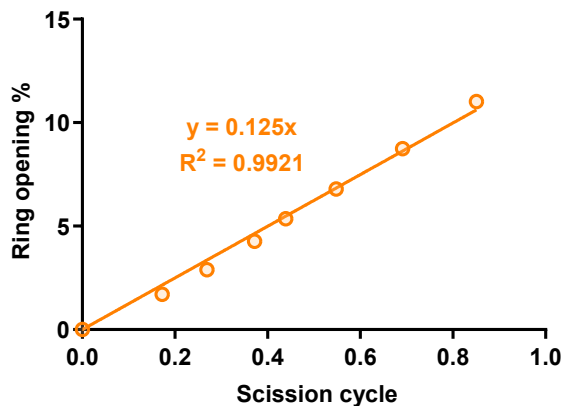


Figure 92 : Percentage of gDCC ring opening versus scission cycle plot for PE-SO polymer. The slope of linear fitting through origin gives  $\Phi = 0.125$ .

### 2.3.3.3.3 Sonication of PE-SO<sub>2</sub> polymer

The procedure of analyzing PE-SO<sub>2</sub> polymer is the same as PE-S polymer.

Calculation of PE-SO<sub>2</sub> polymer chain scission cycle:

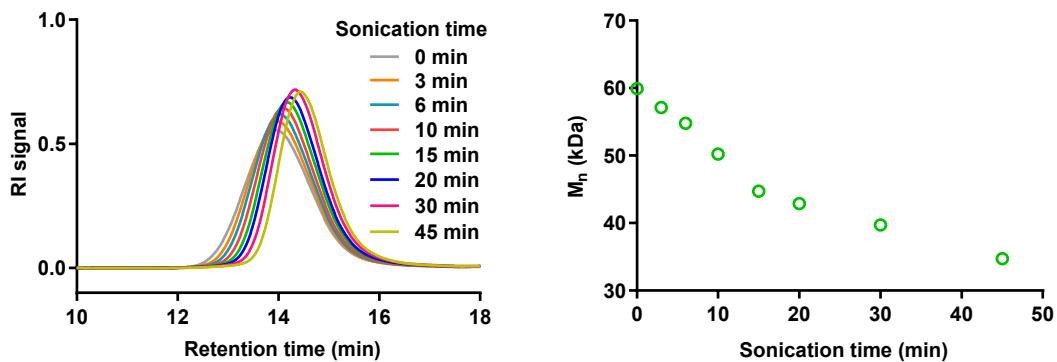


Figure 93 : Evolution of GPC traces during sonication of PE-SO polymer (left) and corresponding plot of molecular weight versus sonication (right).

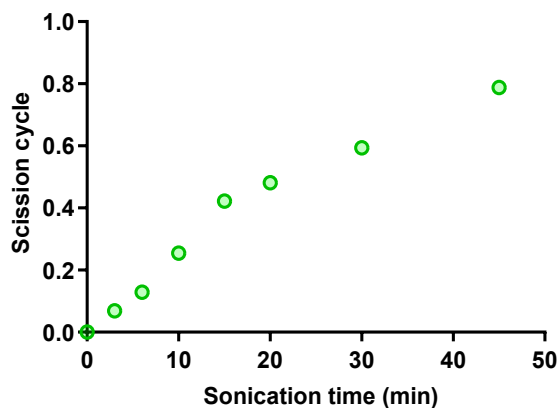


Figure 94 : Scission cycle (SC) of PE-SO polymer at various sonication time

Determination of ring-opening percentage of gDCC in PE-SO<sub>2</sub> polymer:

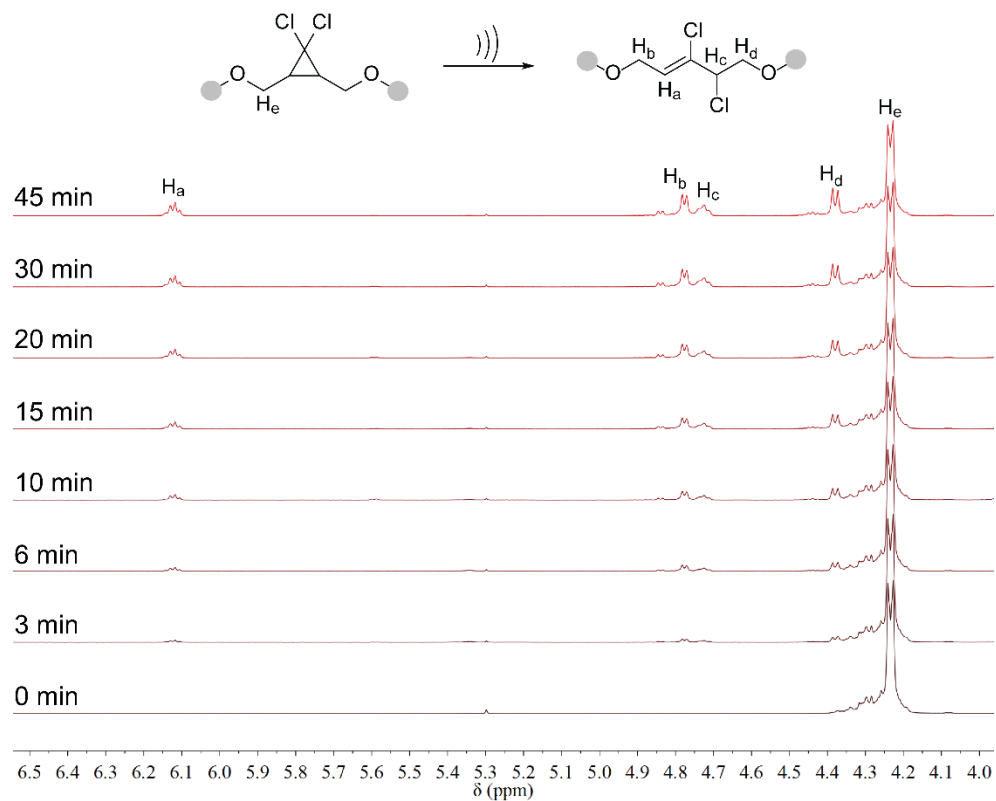


Figure 95 : Stack of  $^1\text{H-NMR}$  ( $\text{CDCl}_3$ , 500 MHz) spectra of sonicated PE-SO<sub>2</sub> polymer at various sonication time.

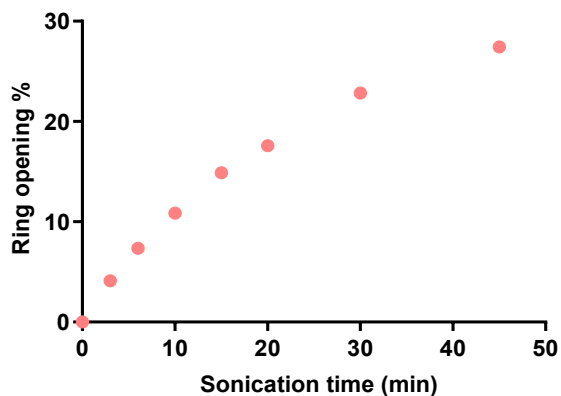
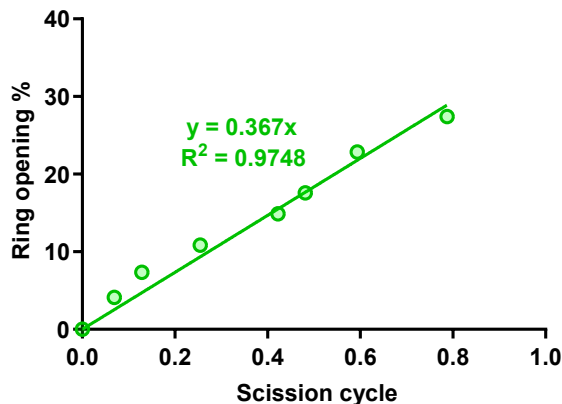


Figure 96 : Ring-opening percentage of gDCC in PE-SO<sub>2</sub> polymer versus sonication time.

Evaluation of  $\Phi$  value:



**Figure S15.** Percentage of gDCC ring opening versus scission cycle plot for **PE-SO<sub>2</sub>** polymer. The slope of linear fitting through origin gives  $\Phi = 0.367$ .

### 2.3.3.4 Relative mechanical strength analysis

The force distribution on the polymer chain is known to be parabolic under pulsed ultrasound.<sup>170-171</sup> The force for gDCC activation is calculated to be 2042 pN ( $F_{open}$ ) on the timescale of the sonication experiment ( $k = 10^6 \text{ s}^{-1}$ ) according to the Cusp model. The maximum force ( $F_{max}$ ) achieved on the polymer backbone, which corresponds to the mechanical strength of C-S bond, can be calculated.

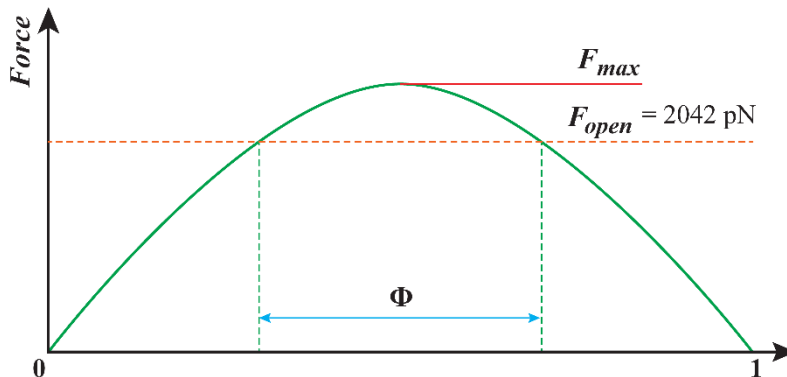


**Figure 97 :** Force distribution of polymer backbone under sonication.

The function of the parabolic distribution of force on polymer backbone in above figure is assumed as:  $y = ax(x-1)$ . Given the  $\Phi$  value have been obtained from sonication analysis, the corresponding parameter  $a$  can be calculated.

Mechanical strength of C-S bond in PE-S polymer:

The  $x$  value can be calculated from  $\Phi$  value:  $x = (1 - \Phi)/2 = (1-0.33)/2 = 0.34$

$F = a*0.34*(0.34-1) = 2042$  ;  $a = -9100$  ;  $F_{\max}(\text{PE-S}) = -9100*0.5*(0.5-1) = 2275$  pN

Mechanical strength of C-S bond in PE-SO polymer:

The  $x$  value can be calculated from  $\Phi$  value:  $x = (1 - \Phi)/2 = (1-0.12)/2 = 0.44$

$F = a*0.44*(0.44-1) = 2042$  ;  $a = -8214$  ;  $F_{\max}(\text{PE-SO}) = -8214*0.5*(0.5-1) = 2054$  pN

Mechanical strength of C-S bond in PE-SO<sub>2</sub> polymer:

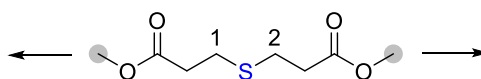
The  $x$  value can be calculated from  $\Phi$  value:  $x = (1 - \Phi)/2 = (1-0.37)/2 = 0.32$

$F = a*0.32*(0.32-1) = 2042$  ;  $a = -9301$  ;  $F_{\max}(\text{PE-SO}_2) = -9301*0.5*(0.5-1) = 2325$  pN

### 2.3.3.5 GoGEF modeling

The methyl ester form of each sulfide, sulfoxide or sulfone containing repeating unit was subjected to CoGEF modeling using DFT method on the theory level of B3YLP/61G\*. The ground state geometry was first optimized, and then its end-to-end distance was constrained with step increasement of 0.1 Å. The optimized energy was plotted as a function of end-to-end distance.

CoGEF modeling of sulfide repeating unit:



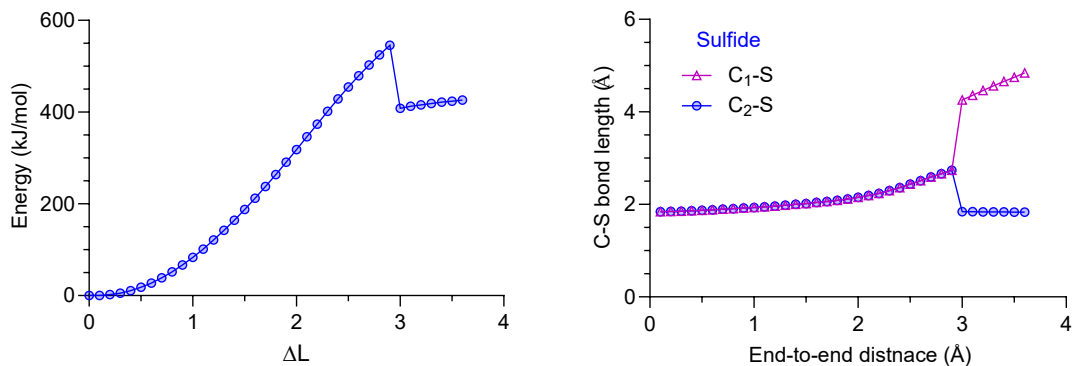


Figure 98 : CoGEF modeling of sulfide containing unit. Left: the evolution of energy over increasement in end-to-end distance. Right: the length of two C-S bonds at different constrained distance.

CoGEF modeling of sulfoxide repeating unit:

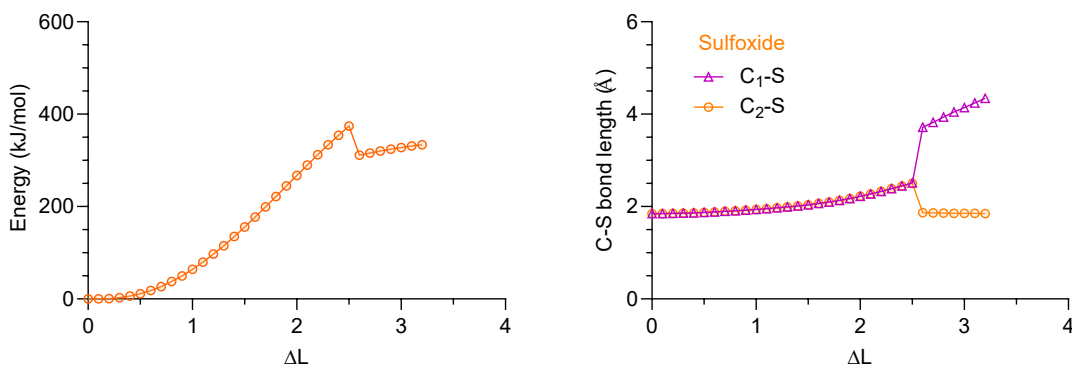
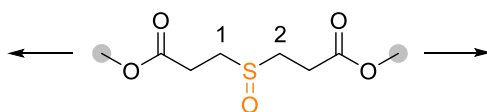
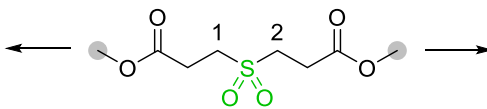


Figure 99 : CoGEF modeling of sulfoxide containing unit. Left: the evolution of energy over increasement in end-to-end distance. Right: the length of two C-S bonds at different constrained distance.

CoGEF modeling of sulfone repeating unit:



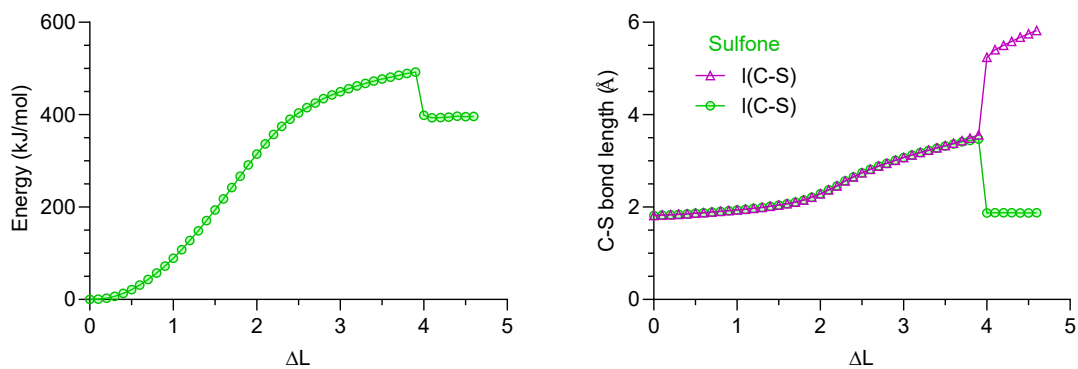


Figure 100 : CoGEF modeling of sulfone containing unit. Left: the evolution of energy over increasement in end-to-end distance. Right: the length of two C-S bonds at different constrained distance.

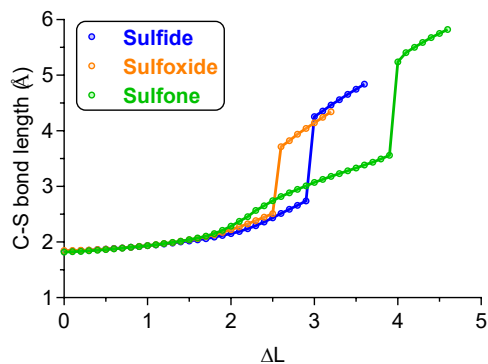


Figure 101 : Overlay of lengths of breaking C-S bonds for at various constrained distance.

## 2.4 Dynamic memory effects in the mechanochemistry of cyclic polymers <sup>II</sup>

Cyclic polymers containing multiple *gem*-dichlorocyclopropane (gDCC) mechanophores along their backbone were prepared using ring expansion metathesis polymerization (REMP). The mechanochemistry of the cyclic polymers was investigated using pulsed ultrasonication. The fraction of gDCC mechanophores that are activated per chain halving event ( $\Phi$ ) was compared to that of linear analogs. For 167 kDa cyclic polymer,  $\Phi = 0.38$ , which is substantially lower than that observed in linear polymers ( $\Phi = 0.62$  for 158 kDa) even though cyclic chain fragmentation necessarily proceeds through a linear intermediate of comparable composition to the initially linear systems. Ozonolysis of the mechanochemical products further shows that the mechanochemical “activation zone” in the cyclic polymer is less continuous than that in the linear polymer. These results suggest that the linear intermediate in cyclic polymer fragmentation undergoes subsequent scission during the same high strain rate extensional event in which it is formed and furthermore retains at least a partial dynamic memory of its original cyclic conformation at the time of fragmentation.

### 2.4.1 Introduction

Progress in covalent polymer mechanochemistry has revealed a range of fundamental insights into the dynamics of mechanically coupled chemical reactions. Force-coupled kinetics and dynamics within mechanophores has received considerable

---

<sup>II</sup> This chapter is adopted from: Lin, Y.; Zhang, Y.; Wang, Z.; Craig, S. L. Dynamic Memory Effects in the Mechanochemistry of Cyclic Polymers. *J. Am. Chem. Soc.* **2019**, *141*, 10943-10947.

attention, with insights into stereochemical,<sup>53, 83-84, 86, 107, 179</sup> regiochemical,<sup>33, 87, 90, 116-117, 180</sup> and substituent<sup>109, 181</sup> effects, including the impact of mechanical bonds<sup>182-183</sup> on mechanophore activation, mechanically accelerated and suppressed chemical reactions,<sup>55, 89</sup> and force stabilized maleimide–thiol adducts.<sup>184</sup> Studies of the influence of polymer chain structure have disclosed the interplay of scissile and non-scissile events,<sup>171</sup> the impact of chain branching in star<sup>185</sup> and bottlebrush<sup>186</sup> architectures, and the influence of micellar assembly.<sup>187-188</sup> More recently, Diesendruck<sup>189</sup> has shown that collapsing a single linear chain into a cross-linked nanoparticle enhances shear resistance, while Peterson and co-workers<sup>190</sup> reported multiple ruptures of denpols in a single extension event, due to higher hydrodynamic drag. The single chain dynamics in question arise in the context of high strain rate extensional strains, such as those generated by pulsed ultrasonication. A critical feature of extensional strain is that the polymer experiences a peak force near its midpoint. We wondered about the consequences of removing a fixed midpoint, specifically by embedding mechanophores in a cyclic polymer.

The mechanochemistry of cyclic polymers has been considered previously,<sup>191</sup> but to the best of our knowledge there is only a single experimental report on the subject, in which Moore and Boydston showed that sonomechanical scission of self-immolative cyclic poly(phthalaldehyde) triggered a cascade depolymerization to *o*-phthalaldehyde monomer.<sup>192</sup> Dynamics specific to the cyclic architecture were not addressed. In particular, cyclic polymers (other than self-immolative ones) differ from linear analogs in that initial chain scission does not reduce molecular weight; fragmentation only occurs *via* a second

and subsequent chain scission event (Figure 102). Moreover, the evolution of strain in cyclic polymers likely differs from that in linear polymers.<sup>193</sup> Here, we report the mechanochemistry of cyclic polymers with multiple non-scissile mechanophores embedded along the polymer backbone. Comparison of their behavior to that of linear analogs reveals unanticipated conformational memory effects and insights into the dynamics of polymer mechanochemistry in high strain rate extensional flow fields.

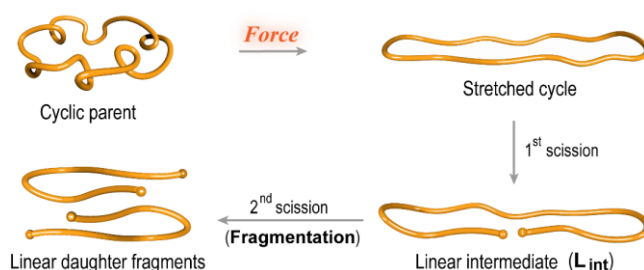


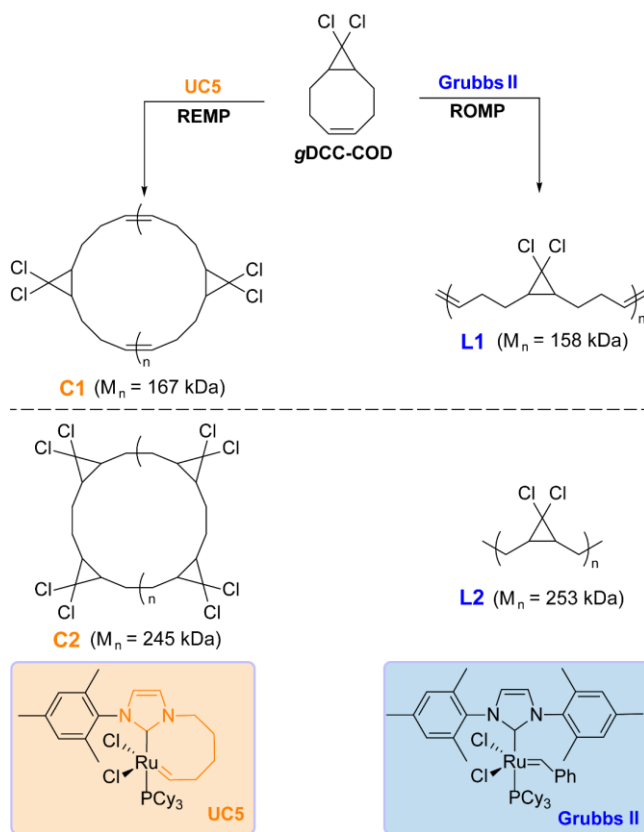
**Figure 102 : Depiction of mechanical scission of a cyclic polymer to give a linear intermediate that subsequently fragments into two linear daughter polymers**

## 2.4.2 Results and discussion

From the synthetic strategies available to prepare cyclic polymers,<sup>194-195</sup> we chose cyclic ruthenium-alkylidene catalyzed ring expansion metathesis polymerization (REMP), which has been used to produce cyclic polymers (Scheme 3) with high molecular weight and purity<sup>196-198</sup> and is more compatible with previous cyclooctene-based mechanophore monomers than other ring-expansion techniques (e.g. zwitterionic ring-opening polymerization<sup>199</sup>). Catalyst UC5, bearing an unsaturated N-heterocyclic carbene (NHC) and 5 carbons in the ruthenium-alkylidene ring, was selected for REMP because its favorable catalyst releasing process<sup>200-201</sup> minimizes residual ruthenium complexes on the polymer backbone that may serve as weak bonds in the chain.<sup>40</sup> A representative

REMP of *gem*-dichlorocyclopropanated cyclooctadiene (gDCC-COD) at 40 °C for 12 h gave a cyclic polybutadiene-based gDCC polymer (**C1**,  $M_n = 167$  kDa). For comparison, a linear polymer analog **L1** ( $M_n = 158$  kDa) was prepared *via* ring opening metathesis polymerization (ROMP) using Grubbs II catalyst (Scheme 3).<sup>202</sup> The large  $M_n$  challenged our ability to directly characterize the linear vs. cyclic content of **C1**, for example by end group analysis, but we observed relative lower intrinsic viscosity of **C1** ( $M_n = 154$  kDa,  $[\eta] = 0.098$  mL/mg) than **L1** ( $M_n = 141$  kDa,  $[\eta] = 0.108$  mL/mg), as expected of a cyclic polymers (see Figures 105 and 106, section 2.4.3.3). We of course cannot rule out the possible presence of linear impurities in **C1**, but any such impurities would mean that the differences in behavior observed here underreport, if anything, the true differences in these two topologies.

**Scheme 3 : Top: synthesis of multi-mechanophore containing cyclic and linear polymers *via* REMP and ROMP, respectively; Bottom: structures of catalysts and other polymers used in this study**



Solutions (2 mg/mL, THF) of **C1** and **L1** were subjected to pulsed ultrasonication (8.7 W/cm<sup>2</sup>, 0 °C, 1s on/1s off, N<sub>2</sub>) to assess the extent of two different mechanochemical responses: the non-scissile ring opening of **gDCC** to 2,3-dichloroalkene, and the fragmentation of the parent polymers to daughter fragments through one (linear) or two (cyclic, see Figure 102) chain scission events. In both cases, fragmentation into two daughter polymers of lower  $M_n$  is observed: **C1** reduces from 167 kDa to 90 kDa and **L1** degrades from 158 kDa to 103 kDa after 20 min sonication. At the same time, **gDCC** mechanophores along the backbone react in response to the force along the polymer main chain (Figure 103b).

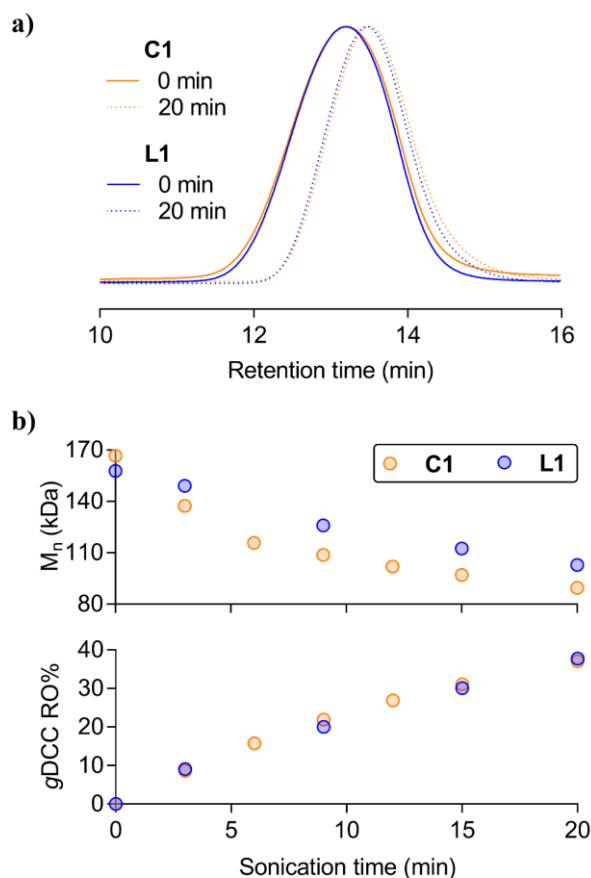


**Figure 103 : a) Overlay of normalized GPC traces of C1 (orange) and L1 (blue). Solid lines are for nascent polymers, dotted lines denote to polymers after 20 min sonication. b) Evolution of  $M_n$  (top) and gDCC ring opening (bottom) at various sonication time in C1 (orange) and L1 (blue).**

Figure 104 shows the extent of gDCC ring opening (quantified by  $^1\text{H}$  NMR) as a function of what we have defined previously as scission cycle, although here we refer to it as fragmentation cycle (FC, eq 1), since the first scission event of a cyclic polymer does not reduce molecular weight.

$$\text{FC} = \frac{\ln M_{n(0)} - \ln M_n}{\ln 2} \quad (2)$$

In eq. 2,  $M_{n(0)}$  and  $M_n$  are initial and sonicated number-average molecular weight (GPC-MALS), respectively. The competition between gDCC ring opening and fragmentation can be quantified by the slope  $\Phi$  of the plot of ring opening vs. FC.<sup>170</sup>

We anticipated a greater extent of ring opening with fragmentation in **C1** than **L1** for three reasons. First, fragmentation of **C1** requires two different scission events in which the tension is focused in two different regions of the polymer, whereas only a single region of tension focusing is required for the fragmentation of **L1**. Second, if there were substantial gDCC ring opening without scission, subsequent stretching events in **L1** would presumably focus tension in the same middle portion of the polymer where gDCCs have already been activated, whereas **C1** has no midpoint and subsequent stretching would likely focus tension on unopened gDCC mechanophores. Third, and most significantly, the fragmentation of **C1** proceeds through a linear intermediate (**L<sub>int</sub>**) (Figure 102) that is effectively chemical identical to **L1**, and so the total gDCC activation observed following its subsequent scission was expected to be at least that observed in **L1**, plus any non-overlapping gDCCs that were activated in the first **C1**-to-**L<sub>int</sub>** scission event.

Remarkably, the opposite is observed: less gDCC ring opening is observed per **C1** fragmentation ( $\Phi = 0.38$ ) than per **L1** fragmentation ( $\Phi = 0.62$ ). This observation cannot be ascribed to lower forces acting on the cyclic polymer (for example, because of a smaller contour length), because the use of FC means that we are comparing the extent of gDCC activation that occurs during stretching events at which the force necessary to induce bond scission is reached.<sup>171</sup> Here, we compare polymers that have the same composition

along their backbone, and so this normalization means that we are comparing gDCC activation against events that reach on average the same peak force, regardless of any differences in the probability of reaching that peak force due to, e.g., differences in hydrodynamic volume between **C1** and **L1**.

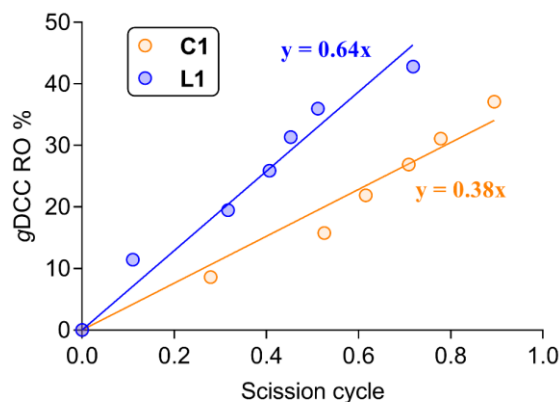


**Figure 104 : gDCC ring opening as a function of fragmentation cycle (FC) for C1 and L1 polymers in this study. Solid lines are linear fits through the origin; slope =  $\Phi$ .**

Another potential explanation is that residual catalyst in **C1** might be responsible, by creating a “weak link” along the polymer backbone. Prior work has established that the UC5 catalyst favors a released state<sup>200-201</sup> that precludes residual main-chain ruthenium-carbene bonds serving as weak points along the chain.<sup>40</sup> Nonetheless, we independently established that the difference in **C1** and **L1** cannot be accounted for by residual catalyst on the **C1** backbone as follows: 1) The amount of residual ruthenium in **C1** is determined from ICP-MS to be 166 ppm, which is similar to previously reported result of 230 ppm<sup>201</sup> and indicates that there is only 0.27 mol UC5 per mol **C1** (see Table 12). If we assume that all of the UC5 is contained in the polymer main chain and that

scission of **C1** with embedded UC5 occurs without any accompanying gDCC ring opening, an identical  $\Phi$  value of the remaining **C1** devoid of UC5 and **L1** gives an anticipated  $\Phi$  value of 0.45 ( $0.73 \times 0.62$ ), which is still well above the observed value of  $\Phi = 0.38$ . 2) This analysis surely overestimates the amount of UC5 that might be embedded in the polymer, as the majority is likely physically absorbed, as noted previously.<sup>201</sup> 3) In support of the latter point, removing residual catalyst in 98 kDa **C1** with QuadraSil®Mercaptopropyl lowers the residual ruthenium to 130 ppm (0.13 Ru per polymer), but the resulting  $\Phi = 0.44$  is still much less than that of 94 kDa **L1** ( $\Phi = 0.70$ ) (see Figure 111). 4) Finally, as the differences in **C1** and **L1** further confirm the predominance of cyclic architecture in **C1**, we note that the fragmentation of **C1** requires two scissions, and the fraction of polymer chains with two or more embedded UC5 is negligible relative to the magnitude of the effects observed.

We conclude, therefore, that **L<sub>int</sub>** formed *via* initial **C1** scission is not identical to **L1**. As **L<sub>int</sub>** and **L1** are structurally indistinguishable (except for any prior ring-opened gDCC in **L<sub>int</sub>**), their differences are likely a consequence of their conformational history. In other words, **L<sub>int</sub>** retains a “memory” that it was formed *via* **C1** scission, and that memory persists (on average) through its subsequent scission/fragmentation.

Any conformational memory would disappear rapidly once the polymer relaxes, and so fragmentation of **L<sub>int</sub>** must occur in the same extension event as initial scission. Furthermore, fragmentation of **L<sub>int</sub>** occurs before **L<sub>int</sub>** can fully extend from its as-formed pseudo-cyclized conformation. Our hypothesis is that initial **C1** scission occurs at

sufficiently high strain rate and tension that  $L_{int}$  fractures before substantial uncoiling can occur. Metastable, partially coiled intermediates in chain extension have been observed by Chu and co-workers in the extensional unwinding of DNA,<sup>203</sup> but to the best of our knowledge evidence for similar conformational dynamics in the sonication of synthetic polymers has yet to be reported. To verify our hypothesis, a **C1** ( $M_n = 181$  kDa) polymer was subjected to sonication in the presence of a radical scavenger coumarin-2,2,6,6-tetramethylpiperidine-1-oxyl (CT). Addition of UV active CT to polymer was observed at low molecular weight region (Figure 114). This highly suggests that **C1** polymer underwent scission and subsequent fragmentation in the same elongation flow.

**Table 11 : Effect of sonication and subsequent ozonolysis on L2 and C2 homopolymers**

| Polymer   | $M_n$<br>(kDa) | Post-sonication |                |           |                       |                     | Post-ozonolysis |           |
|-----------|----------------|-----------------|----------------|-----------|-----------------------|---------------------|-----------------|-----------|
|           |                | Time<br>(min)   | $M_n$<br>(kDa) | $\bar{D}$ | gDCC ring<br>opening% | gDCC/chain<br>(kDa) | $M_n$<br>(kDa)  | $\bar{D}$ |
| <b>L2</b> | 253            | 10              | 122            | 1.37      | 56%                   | 57                  | 60              | 1.61      |
| <b>C2</b> | 245            | 12              | 122            | 1.31      | 40%                   | 73                  | 41              | 1.62      |

As tension is distributed differently during **C1** fragmentation relative to that in **L1**, we sought other manifestations of that distribution. We have observed previously that the activation of non-scissile gDCC mechanophores in linear poly(gDCC) occurs in nearly perfect blocks along the polymer main chain.<sup>204</sup> We performed dichlorocyclopropanation of **L1** to give polymer **L2** ( $M_n = 253$  kDa) with no detectable backbone alkenes. Subsequent sonication gave daughter fragments of  $M_n = 122$  kDa with 56% gDCC repeats ring-opened to 2,3-dichloroalkenes, while 44% (accounting for on average 57 kDa per chain) remain unreacted. Further ozonolysis cleaves all alkenes, and leaves pure (by <sup>1</sup>H NMR, Figure

122) poly(gDCC) of  $M_n = 60$  kDa (Table 11). In other words, the unactivated gDCCs are almost entirely continuous, consistent with our previous observations. Similar treatment of **C2** ( $M_n = 245$  kDa, prepared from dichlorocyclopropanation of **C1**), however, produced different results. For **C2**, daughter fragments were produced with  $M_n = 122$  kDa and 60% (73 kDa) of unreacted gDCC repeats per chain, but ozonolysis produced pure poly(gDCC) polymer of only  $M_n = 41$  kDa. The fragmentation of **C2** involves the production of (on average) more than one region of gDCC ring opening per daughter. A reasonable possibility would be two different regions, each extending from one of the two sites of scission.

The sonication of a cyclic polymer leads to an initial increase in tension and resultant chain scission event. The data presented here suggest that cyclic polymer fragmentation through a second scission rapidly follows the initial scission during the same extensional event, and the increased tension and second scission event occur in positions that are remote to the first scission. Prior to this second scission, the linear intermediate of the primary cyclic scission does not explore the same conformational space available to nascent linear polymers during identical sonication conditions – with at least one end presumably remaining partially “folded” back toward itself. Such restricted dynamics are reasonable, given that the strain rates necessary to extend the polymer to the point of its first break must exceed the rates of conformational relaxation (else the chain would relax before extending and breaking).<sup>205-206</sup> We note that the extreme limit of this dynamic conformational trapping would be an extremely short lifetime for

$L_{int}$ , to the extent that the two scission events might be considered effectively simultaneous.

This picture suggests the potential importance of conformational dynamics in the very high strain rate environment of pulsed ultrasonication, which exceed those employed in previous studies of cyclic polymers.<sup>207-210</sup> The consequences of such dynamics might be exaggerated here due to the initial pseudo-cyclic conformation of  $L_{int}$ , but these results raise the possibility that conformations that are similarly “trapped” during high strain rate processes<sup>203</sup> might also play a role in the mechanochemistry of linear polymers. Furthermore, these results suggest the intriguing possibility of conformational memory effects in other high strain rate processes, such as the propagation of shock waves in polymeric materials.<sup>100</sup> Cyclic and other topologically complex polymers might therefore provide potential opportunities to tune mechanochemical response in bulk materials as well as sonochemical environments. The role of such architectures and influence of (for example) molecular weight, chain stiffness, and solvent quality on dynamic behavior seems to us to be a promising area for further inquiry.

## **2.4.3 Experimental section**

### **2.4.3.1 Materials and characterization**

Materials: Lab general solvents (dichloromethane, chloroform, hexane, ethyl acetate, acetone, toluene, tetrahydrofuran, methanol) were purchased from VWR or Sigma Aldrich. Cyclooctadiene, 6-bromo-1-hexene, potassium *t*-butoxide, Grubbs I

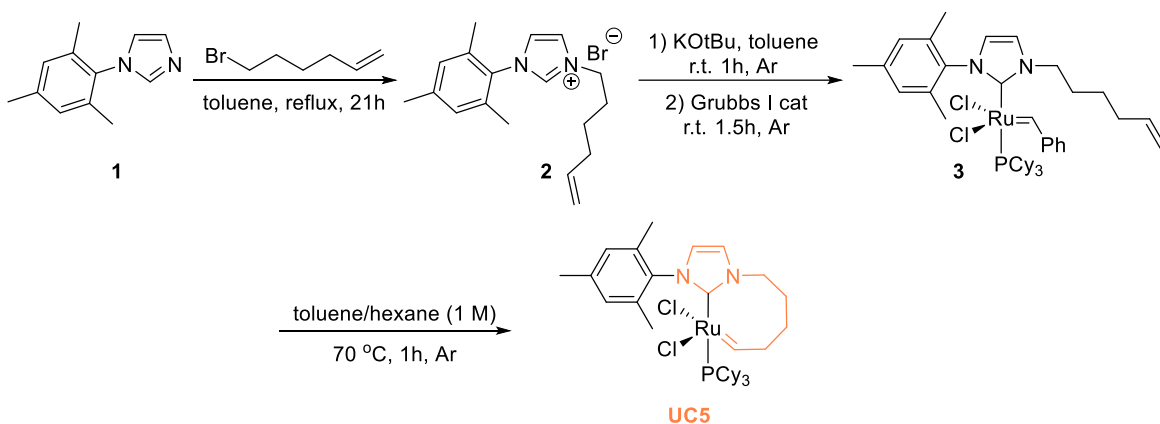
catalyst, Grubbs II catalyst, NaOH powder and PEG400 were purchased from Sigma Aldrich or Alfa Aesar and used without further purification.

Characterizations:  $^1\text{H}$  NMR spectra were collected on a 400 MHz Varian INOVA spectrometer and  $^{13}\text{C}$  NMR spectra were obtained on a 500 MHz Varian UNITY spectrometer. Chemical shifts are given in *ppm* ( $\delta$ ) and referenced to the residual  $^1\text{H}$  peak at 7.26 ppm or  $^{13}\text{C}$  peak at 77.16 ppm in  $\text{CDCl}_3$ .  $^1\text{H}$  shifts are reported as chemical shift, multiplicity, coupling constant if applicable, and relative integral. Multiplicities are reported as: singlet (s), doublet (d), doublet of doublets (dd), doublet of triplets (dt), doublet of doublet of doublets (ddd), doublet of doublet of triplets (ddt), triplet (t), triplet of doublets (td), quartet (q), multiplet (m), or broad (br). Coupling constants (J) are reported in Hertz. High-resolution mass spectra were collected on an Agilent LCMS-TOF-DART at Duke University's Mass Spectrometry Facility. Gel permeation chromatography (GPC) was performed on two Agilent PLgel mixed-C columns ( $10^5 \text{ \AA}$ , 7.5x300 mm, 5  $\mu\text{m}$ , part number PL1110-6500) using THF (stabilized with 100 ppm BHT) as the eluent. Molecular weights were calculated using a Wyatt Dawn EOS multi-angle light scattering (MALS) detector and Wyatt Optilab DSP Interferometric Refractometer (RI). The refractive index increment ( $dn/dc$ ) values were determined by online calculation based on injections of known concentration and mass.

## 2.4.3.2 Synthetic procedures

### 2.4.3.2.1 Synthesis of cyclic ruthenium catalyst UC5

UC5 catalyst was prepared using a modified procedure according to previous literature<sup>200, 211</sup>.



### Synthesis of imidazolium salt 2

*N*-mesitylimidazole **1** was synthesized according to reported procedure.<sup>212</sup>

To a solution of *N*-mesitylimidazole **1** (1.86 g, 10 mmol) in 25 mL toluene, added 6-bromo-1-hexene (1.603 mL, 12 mmol). The solution was heated to reflux under N<sub>2</sub> for 21 h. After the reaction was cooled down to room temperature, toluene was removed under reduce pressure. The waxy residual was dissolved with 2 mL DCM and precipitated from Et<sub>2</sub>O. This precipitation procedure was performed twice. Obtained waxy solid was further dried under high vacuum to give product **2** as a light-yellow foam solid (1.786 g, 51.2%). This solid turned to a sticky wax upon bring to contact with air. <sup>1</sup>H NMR is consistent with reported value.<sup>211</sup> <sup>1</sup>H NMR (400 MHz, CDCl<sub>3</sub>): δ = 10.51 (s, 1H), 7.68 (t, J = 1.6 Hz, 1H), 7.17 (t, J = 1.6 Hz, 1H), 6.99 (s, 2H), 5.74 (ddt, J = 16.9, 10.2, 6.7 Hz, 1H), 5.09 – 4.91 (m, 2H),

4.76 (t,  $J = 7.3$  Hz, 2H), 2.33 (s, 3H), 2.17 – 2.09 (m, 2H), 2.07 (s, 6H), 2.05 – 1.94 (m, 2H), 1.55 – 1.43 (m, 2H).

### Synthesis of acyclic ruthenium catalyst **3**

Imidazolium salt **2** (175 mg, 0.5 mmol) was weighed in a 25 mL Schlenk flask. Given the easily liquidified nature of salt **2** when contacted with air during the weighting process, the sticky wax was weighed in a scintillation vial and dissolved with minimum amount of DCM and further transferred to the Schlenk flask. After DCM was removed, the residual oil at the bottom of the flask was further dried under high vacuum. After solvent was completely removed, a light yellow foam solid formed at the bottom of the flask. The flask was then filled with Ar. KO $t$ Bu (56 mg, 0.5 mmol) was then weighed and added to the flask followed by 3 mL dry toluene. The foam salt **2** became a waxy oil upon adding the toluene. The flask was then put into a sonication bath and shaken to help disperse the mixture while kept under Ar. After the waxy solid disappeared and a homogenous suspension formed, the mixture was removed from sonication bath and stirred at room temperature for 1 h. Grubbs I catalyst (205 mg, 0.25 mmol) was added to the flask under an Ar steam. The flask was then sealed and stirred for additional 1.5 h under Ar. TLC (25% EtOAc/Hexane) indicated complete conversion of Grubbs I and a new spot appeared at  $R_f = 0.7$ . After completion, the mixture was run through a thin silica pad and eluted with dry Et $_2$ O. Solvent was removed with rotavapor to give a pink brown solid. The solid was further dried under high vacuum. This crude product was directly used in the next step without further purification. An analytical product was obtained by

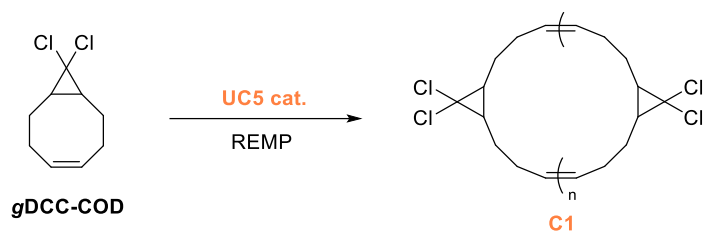
tritulating the solid with dried hexane to give product **3** as a pink solid.  $^1\text{H}$  NMR was consist with reported data.<sup>200, 211</sup>  $^1\text{H}$  NMR (400 MHz,  $\text{CDCl}_3$ ):  $\delta$  = 19.23 (s, 1H), 7.86 (br, 2H), 7.38 (t,  $J$  = 7.3 Hz, 1H), 7.19 (d,  $J$  = 2.0 Hz, 1H), 7.10 (t,  $J$  = 8.0 Hz, 2H), 6.79 (d,  $J$  = 1.9 Hz, 1H), 6.28 (br, 2H), 5.84 (ddt,  $J$  = 17.1, 10.4, 6.7 Hz, 1H), 5.17 – 4.93 (m, 2H), 4.71 (t,  $J$  = 7.7 Hz, 2H), 2.50 – 2.24 (m, 5H), 2.20 (q,  $J$  = 7.9, 7.4 Hz, 3H), 2.00 – 1.78 (m, 8H), 1.77 – 1.55 (m, 15H), 1.39 – 1.23 (m,  $J$  = 12.2 Hz, 6H), 1.23 – 0.99 (m, 11H). Tautomer (1/10 ratio) appeared at:  $\delta$  = 20.15 (d,  $J$  = 11.6 Hz, 1H).

### Synthesis of cyclic ruthenium catalyst UC5

In a 250 mL Schlenk flask, crude solid **3** was dissolved with 3 mL dry toluene under Ar. The solution was diluted with 200 mL dry hexane. The pink suspension was then heated to 70 °C under Ar. The suspension became clear after 5 min and turned brown after 10 min. After 1 h, a brown suspension was obtained. The mixture was cooled downed to room temperature and filtered. The filtrate was condensed to give a brown solid. The solid was further triturated with 10 mL 20% Et<sub>2</sub>O/Hexane. After filtration and dry under high vacuum, product **UC5** was obtained as a brown green solid (93 mg, 52.7% in two steps).  $^1\text{H}$  NMR was consist with reported data.<sup>200, 211</sup>  $^1\text{H}$  NMR (400 MHz,  $\text{CDCl}_3$ ):  $\delta$  = 20.25 (dt,  $J$  = 9.5, 4.9 Hz, 1H), 7.03 (dm,  $J$  = 1.8 Hz, 1H), 7.00 (s, 2H), 6.81 (s, 1H), 3.59 (t,  $J$  = 5.8 Hz, 2H), 3.00 (m, 2H), 2.44 – 2.06 (m, 14H), 1.83 – 1.59 (m, 17H), 1.44 – 1.03 (m, 15H).

### 2.4.3.2.2 Synthesis of cyclic polymers *via* ring expansion metathesis polymerization (REMP)

Representative synthesis of high molecular weight cyclic gDCC polymer:

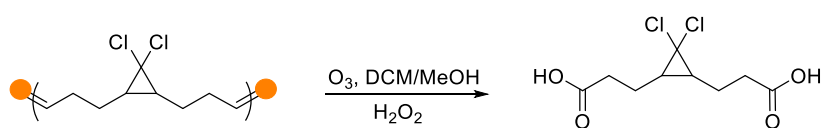


A 10 mL dried ampoule vial was purged with Ar, then **gDCC-COD** monomer<sup>170</sup> (191 mg, 1 mmol) was added. The vial was kept under Ar. To a separate Ar purged vial, **UC5** catalyst (0.7 mg,  $1 \times 10^{-3}$  mmol) was dissolved with 2 mL dried DCM under Ar. The catalyst solution was then transfer to the monomer vial. The reaction vial was then sealed and heated at 40 °C for 12 h. After cooled down to room temperature, the solution was precipitated in MeOH or Et<sub>2</sub>O. Polymer was redissolved with 2 mL DCM and precipitated from MeOH. Precipitation was repeated twice to give an off white polymer. Obtained polymer was further dried under high vacuum (143 mg, 70%).  $dn/dc = 0.121$ ,  $M_n = 167$ ,  $M_w = 233$  kDa, PDI = 1.40.

Removing residual ruthenium in **C1** using QuadraSil®Mercaptopropyl silica:

To a 20 mL scintillation vial, 80 mg **C1** polymer (98 kDa, PDI = 1.82) was dissolved in 5 mL DCM, 200 mg QuadraSil®Mercaptopropyl silica (extent of labeling: 1.0-1.5 mmol/g loading) was added. After the mixture was stirred overnight, silica was filtered and the solution was condensed. A white polymer was obtained after precipitation from MeOH (76 mg). This polymer was further subjected to sonication and ICP-MS analysis.

#### ICP-MS analysis of residual ruthenium amount in **C1** polymer



To a 10 mL scintillation vial, added 8.6 mg **C1** ( $M_n = 167$  kDa). The polymer was then dissolved with 5 mL DCM/MeOH (v/v, 5/1). The solution was then cooled to  $-78$  °C and sparged with  $O_3$ . After the solution turned blue,  $O_3$  was further sparged for 10 min.  $O_2$  was then used to removed excess  $O_3$  until the solution turned colorless. 0.2 mL 30%  $H_2O_2$  was then added to the solution, the solution was slowly warmed to r.t. and stirred overnight. Volatile solvent was removed and resulting residual was digested with 2 mL HCl/ $H_2O_2$  (v/v, 1/1). The solution was then subjected to ICP-MS analysis. In a different batch, 8.9 mg 98 kDa **C1** polymer was digested using the same method as described above. Obtained results are summarized in the following table.

**Table 12 : Summary of residual ruthenium amounts in C1 polymer**

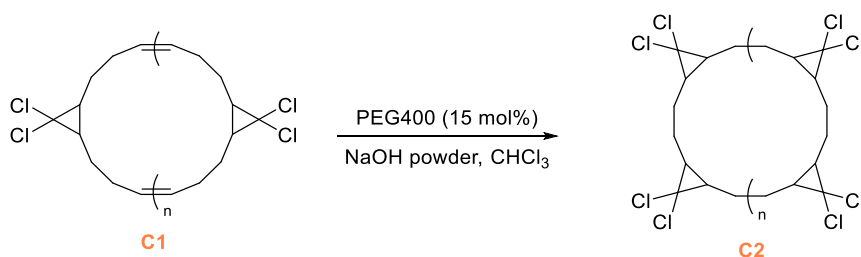
| $M_n$ (kDa) | m (mg) | $^{101}Ru$ (ppm) | n ( $^{101}Ru$ ) (mol) | n ( <b>C1</b> polymer) (mol) | Ru per polymer |
|-------------|--------|------------------|------------------------|------------------------------|----------------|
| 167         | 8.6    | 166              | $1.41 \times 10^{-8}$  | $5.16 \times 10^{-8}$        | 0.27           |
| 98 kDa      | 8.9    | 130              | $1.14 \times 10^{-8}$  | $8.80 \times 10^{-8}$        | 0.13           |

Synthesis of low molecular weight cyclic *g*DCC polymer:

In a 10 mL Ar purged ampule vial, *g*DCC-COD monomer (573 mg, 3 mmol) was added. The vial was kept under Ar. To a separate Ar purged vial, **UC5** catalyst (1.0 mg,  $1.5 \times 10^{-3}$  mmol) was dissolved with 3 mL dried DCM under Ar. The catalyst solution was then transfer to the monomer vial. The vial was then sealed and heated at  $40$  °C for 12 h. After the solution was cooled down to r.t., the solution was added dropwise into a stirring Et<sub>2</sub>O. Resulting suspension was set for 10 min. A waxy precipitate formed at the bottom. The upper suspension was then decant. Precipitate was washed with MeOH to give a

white gummy polymer (30 mg, 5.2%). Decant suspension was then rotavaped to give an oil. This oil was then loaded on a thin silica pad. Elute with hexane by gravity to give a clear liquid (285 mg, 49.7%, **gDCC-COD** monomer). Elute with Et<sub>2</sub>O by gravity to give a thick oil (28 mg, 4.4%, cyclic gDCC oligomer, dn/dc = 0.121, M<sub>n</sub> = 9 kDa, M<sub>w</sub> = 19 kDa, PDI = 2.06).

Cyclopropanation of cyclic gDCC polymer:

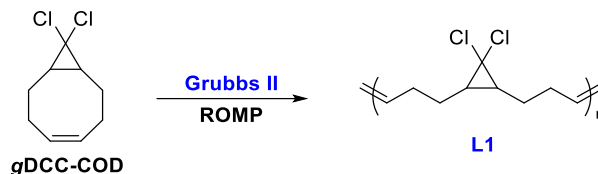


Cyclopropanation was performed using reported protocol<sup>213</sup>.

In a 20 mL scintillation vial, **C1** polymer (282 mg, 1.48 mmol monomer, M<sub>n</sub> = 151 kDa, PDI = 1.39) and PEG400 (120 mg, 0.3 mmol) were dissolved with 4 mL dry chloroform. NaOH powder (240 mg, 6 mmol) was then added in portions. The mixture was allowed to stir at r.t. for overnight. Additional NaOH powder (80 mg, 2 mmol) and 2 mL chloroform were added. The mixture was further stirred for 1 day to achieve full conversion of alkene. After the reaction completed, the mixture was diluted with 20 mL DCM, washed with 4×20 mL brine and 2×20 mL DI water. Organic phase was then condensed and precipitated from MeOH three time to give a white **C2** polymer (379 mg, 93%). dn/dc = 0.108, M<sub>n</sub> = 245 kDa, M<sub>w</sub> = 296 kDa, PDI = 1.21.

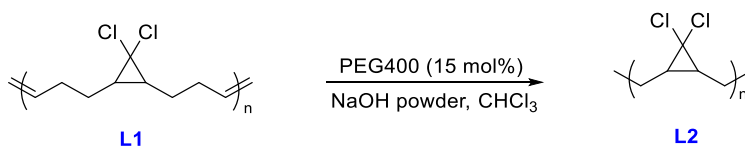
### 2.4.3.2.3 Synthesis of linear polymer *via* ring opening metathesis polymerization (ROMP)

Representative synthesis of linear gDCC polymer:



A flame dried vial was purged with  $N_2$ , gDCC-COD (191 mg, 1 mmol) was then added to the vial. Grubbs II catalyst (0.85 mg,  $1 \times 10^{-3}$  mmol) was weighted in another vial and kept under  $N_2$ . 0.4 mL DCM was added to dissolve the catalyst. The catalyst solution was then transferred to the monomer vial. The polymerization was stirred at r.t. for 3 h. Several drops of ethyl vinyl ether were added to quench to polymerization. The viscous solution was further stirred for 30 min. The solution was then dilute with DCM and precipitated from MeOH or Et<sub>2</sub>O. Obtained polymer was redissolved in DCM and precipitate from MeOH. Precipitation procedure was repeated twice. After dried under high vacuum, a white polymer L1 was obtained (136 mg, 71%).  $dn/dc = 0.121$ ,  $M_n = 158$  kDa,  $M_w = 230$  kDa, PDI = 1.46.

Full cyclopropanation of linear gDCC polymer:



A 101.7 kDa L1 polymer (191 mg, 1 mmol monomer) and PEG400 (60 mg, 0.15 mmol) were dissolved in 5 mL  $CHCl_3$ . NaOH powder (240 mg, 6 mmol) was then added in portions. The mixture was stirred overnight. After the reaction completed, the mixture

was diluted with 20 mL DCM, washed with 4×20 mL brine and 2×20 mL DI water. Organic phase was then condensed, precipitated from MeOH three time to give a white polymer **L2** (260 mg, 95%).  $dn/dc = 0.099$ ,  $M_n = 253$  kDa,  $M_w = 326$  kDa, PDI = 1.29.

### 2.4.3.3 Intrinsic viscosity

The intrinsic viscosity  $[\eta]$  of **C1** ( $M_n = 154$  kDa) and **L1** ( $M_n = 141$  kDa) were characterized using an Ubbelohde capillary viscometer. Measurements were performed at ambient temperature. Four different concentrations (1.0, 2.0, 3.0, 4.0, 5.0 mg/mL) were carried out for each polymer and the flow time at each concentration was measured 3 times and averaged.

**Table 13 : List of data for measurement of intrinsic viscosity.**

|           | c(mg/mL) | t (s) |       |       |       | $\eta_r$ | $\ln(\eta_r)/c$<br>(mL/mg) | $\eta_{SP}$ | $\eta_{SP}/c$<br>(mL/mg) |
|-----------|----------|-------|-------|-------|-------|----------|----------------------------|-------------|--------------------------|
|           |          | 1     | 2     | 3     | Avg.  |          |                            |             |                          |
| THF       | /        | 126.3 | 127.3 | 127.9 | 127.1 | /        | /                          | /           | /                        |
| <b>C1</b> | 2.0      | 154.1 | 154.2 | 154.1 | 154.1 | 1.212    | 0.096                      | 0.212       | 0.106                    |
|           | 3.0      | 169.4 | 168.8 | 168.9 | 169.0 | 1.330    | 0.095                      | 0.330       | 0.110                    |
|           | 4.0      | 185.3 | 185.1 | 185.0 | 185.2 | 1.457    | 0.094                      | 0.457       | 0.114                    |
|           | 5.0      | 203.2 | 203.0 | 203.2 | 203.2 | 1.598    | 0.094                      | 0.598       | 0.120                    |
| <b>L1</b> | 2.0      | 160.1 | 160.3 | 159.5 | 160.0 | 1.258    | 0.115                      | 0.258       | 0.129                    |
|           | 3.0      | 177.9 | 178.0 | 177.5 | 177.8 | 1.399    | 0.112                      | 0.399       | 0.133                    |
|           | 4.0      | 199.9 | 200.0 | 199.9 | 199.9 | 1.573    | 0.113                      | 0.573       | 0.143                    |
|           | 5.0      | 229.9 | 229.2 | 229.5 | 229.5 | 1.806    | 0.118                      | 0.806       | 0.161                    |

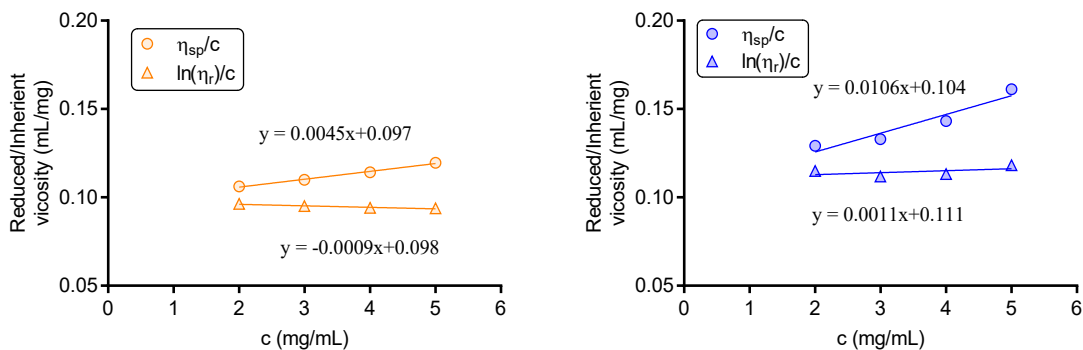


Figure 105 : Huggins-Kraemer plot for C1 (left) and L1 (right).

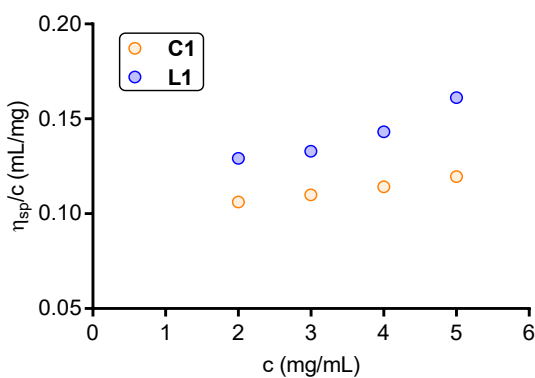


Figure 106 : Overlay of Huggins plot for C1 and L1.

#### 2.4.3.4 Sonication experiment

Representative procedure for sonication of gDCC polymer: 36 mg C1 or L1 polymer was dissolved with 18 mL dry THF to give a 2 mg/mL polymer solution. The solution was then transferred into a Suslick cell and sparged with N<sub>2</sub> for 10 min. Sonication was performed with a Sonics VC750 at 20% amplitude (1s on, 1s off) under N<sub>2</sub> atmosphere in ice bath. Aliquot of 1 mL was taken out from the solution at 0, 3, 6, 10, 15, 20, 30 min sonication time. GPC test and <sup>1</sup>H NMR analysis were performed for each sample.

#### 2.4.3.4.1 Analysis of gDCC ring opening in C1 polymer

Calculation of polymer chain fragmentation cycle:

The shift of retention time in GPC traces indicates the degradation of C1 polymer during sonication. The  $M_n$  was obtained using MALS detector.

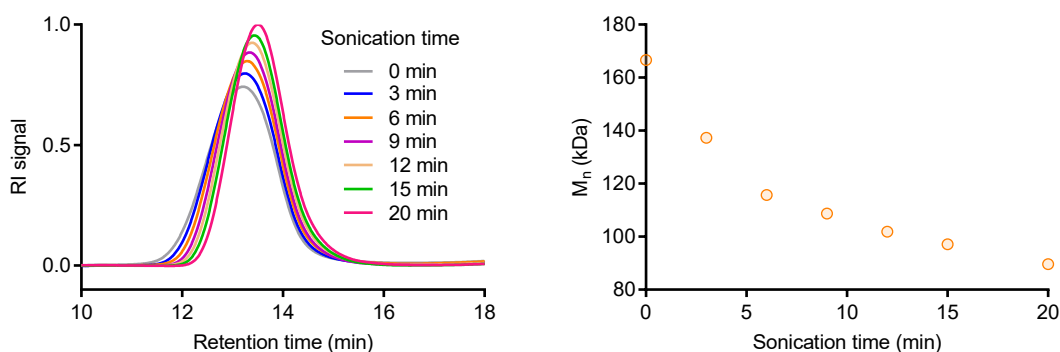


**Figure 107 : Sonication of C1 polymer: evolution of GPC traces during sonication (left); molecular weight vs. sonication time plot (right) indicates that molecular weight decreases from 167 kDa to 90 kDa after 20 min sonication.**

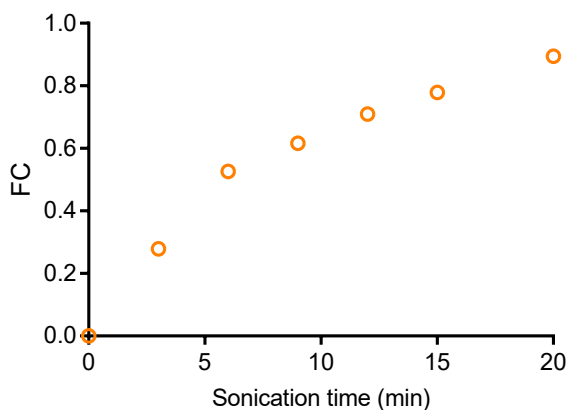


**Figure 108 : Fragmentation cycle (FC) of 167 kDa C1 vs. sonication time**

The fragmentation cycle (FC) of C1 polymer at each sonication time was calculated using the following equation:

$$FC = \frac{\ln M_{n(0)} - \ln M_n}{\ln 2}$$

Where  $M_{n(o)}$  is the initial molecular weight;  $M_n$  is after sonication. SC describes the average number of times a polymer has undergone chain scission. (Notice: one fragmentation cycle corresponds to 2 bond breaks for cyclic polymer.)

Determination of ring opening percentage of gDCC:

The ring opening of gDCC during sonication was analyzed using previous reported method<sup>170</sup>. In the  $^1\text{H}$  NMR, the peak at 5.32~5.56 ppm ( $\text{H}_c$ ) corresponds to pristine total alkenes of polymer as prepared. The peak at 5.84 ppm ( $\text{H}_a$ ) and 4.48 ppm ( $\text{H}_b$ ) are new generated alkene after sonication. The ring opening percentage can be obtained:

$$\text{Ring opening \%} = \frac{(\int \text{H}_a + \int \text{H}_b)}{\int \text{H}_c} \times 100\%$$

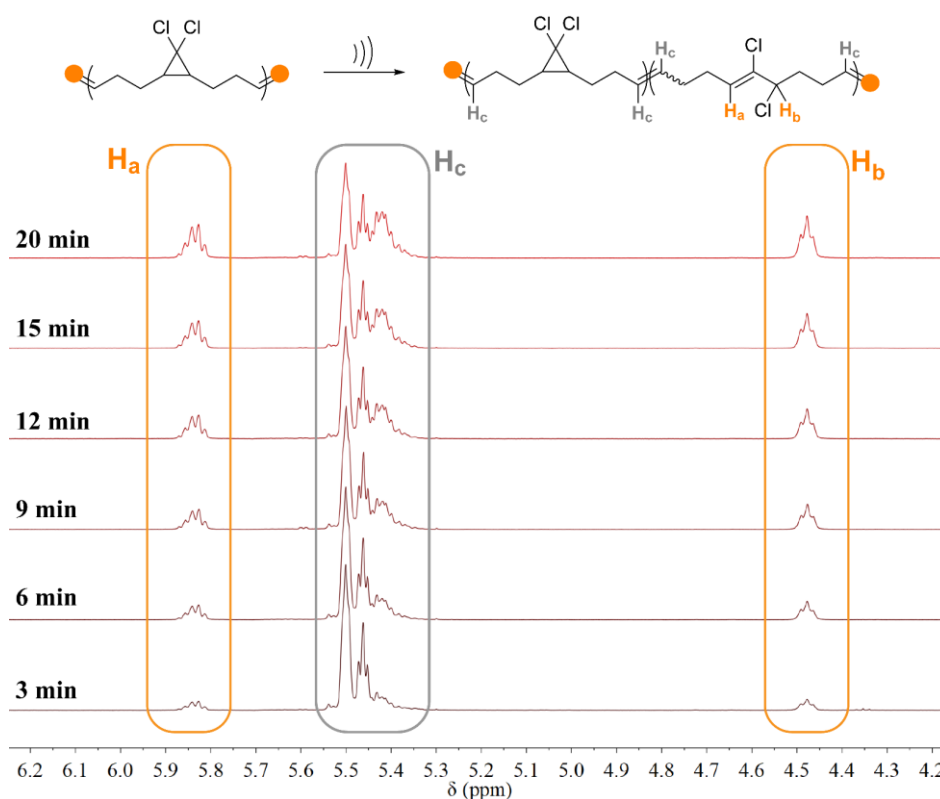
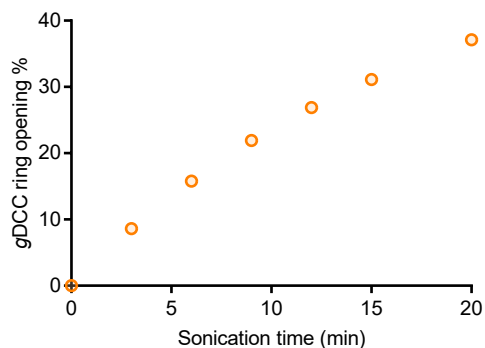


Figure 109 : .  $^1\text{H}$ -NMR ( $\text{CDCl}_3$ , 400 MHz) spectra stack of sonicated 167 kDa C1 at various sonication time.



**Figure 110 : Ring opening percentage of gDCC in 167 kDa C1 at different sonication time.**

Evaluation of  $\Phi$  value:

According to previous report,  $\Phi$  value, defined as the slope of ring opening vs. fragmentation cycle (FC) plot, is used to evaluate the relative strength of weak bonds. Here,  $\Phi$  value is used to differentiate the mechanical activation of gDCC along the polymer backbone between cyclic and linear polymers. A 98 kDa C1 polymer that has been subjected to removing residual ruthenium is also analyzed.

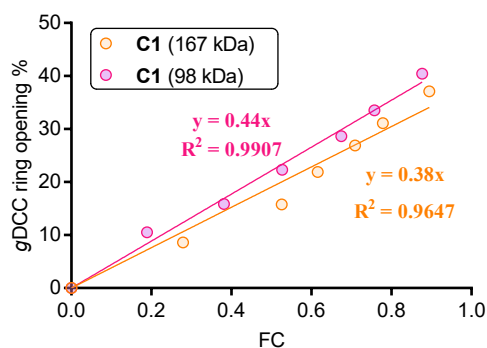


**Figure 111 : gDCC ring opening vs. fragmentation cycle (FC) plot of 167 kDa and 98 kDa C1 polymers. The slope of linear fitting through origin gives  $\Phi = 0.38$  and  $0.44$ , respectively.**

Sonication of low molecular weight C1 polymer:

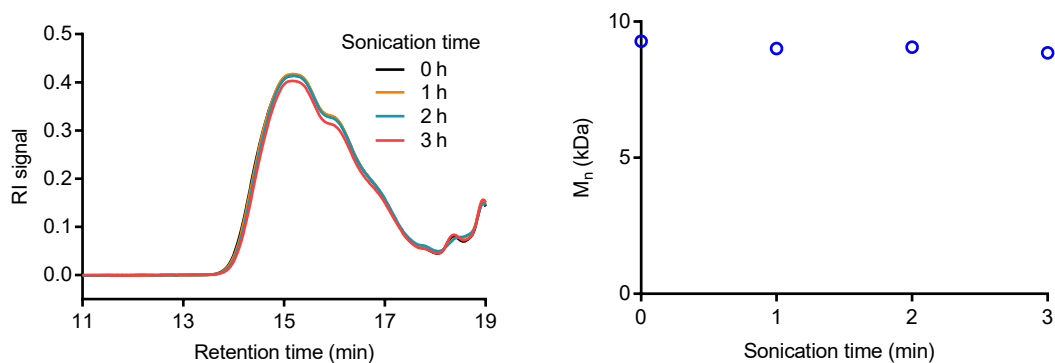


**Figure 112 : Sonication of a 9 kDa C1: evolution of GPC traces during sonication (left); molecular weight vs. sonication time plot (right).**

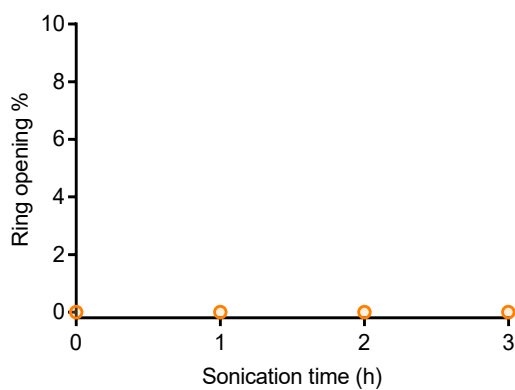


**Figure 113 : gDCC ring opening percentage of 9 kDa C1 polymer at different sonication time.**

Radical trapping:

C1 (181 kDa) was subjected to sonication in the presence of radical scavenger CT (32 mM). Radical was generated after C-C bond cleavage and further trapped by CT, which is UV active.

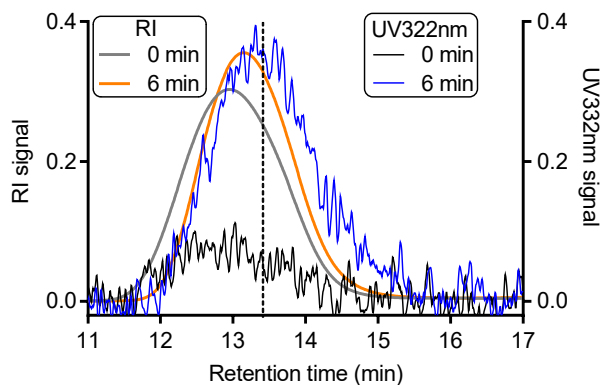


**Figure 114 : CT labeling of C1 polymer under sonication.  $M_n$  reduced from 181 kDa to 164 kDa after 6 min sonication.**

#### 2.4.3.4.2 Analysis of gDCC ring opening in L1 polymer

Calculation of polymer chain fragmentation cycle:

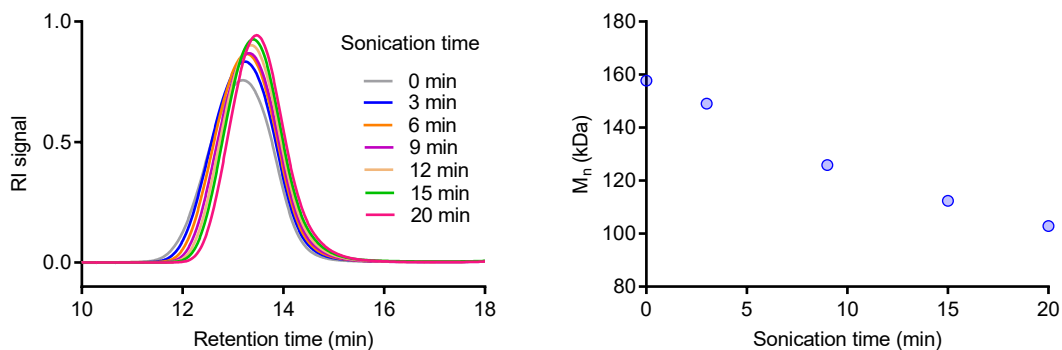


**Figure 115 : g Sonication of L1: evolution of GPC traces during sonication (left); molecular weight vs. sonication time plot (right) indicates that molecular weight decreases from 158 kDa to 103 kDa after 20 min sonication.**

The fragmentation cycle (FC) of L1 polymer was determined using the same method as that of C1.

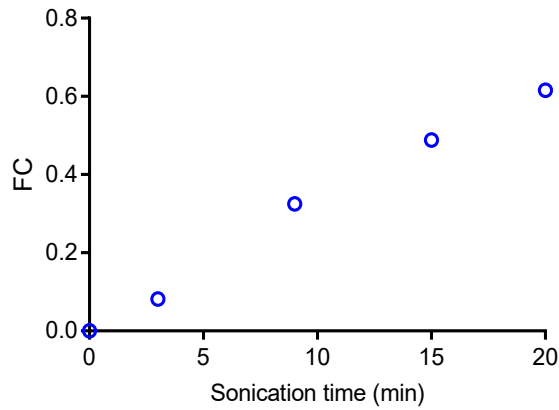


**Figure 116 : Fragmentation cycle (FC) of 158 kDa L1 vs. sonication time.**

Determination of ring opening percentage of gDCC:

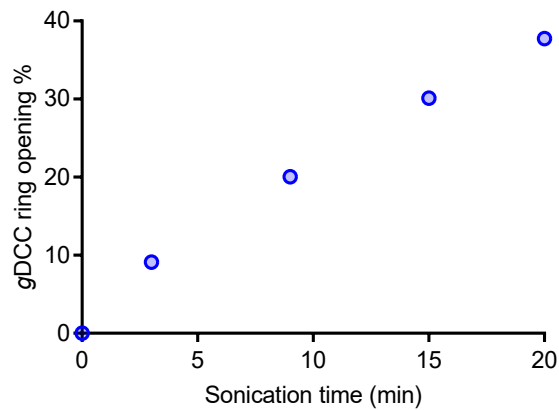


**Figure 117 : Ring opening percentage of gDCC in 158 kDa L1 at different sonication time.**

Evaluation of  $\Phi$  value:

The  $\Phi$  value analysis of L1 is the same as C1 polymer. The  $\Phi$  values for 94 kDa and 158 kDa L1 polymer are 0.70 and 0.64, respectively. Both  $\Phi$  values are higher than that of 98 kDa and 167 kDa C1 polymer (0.44 and 0.38).

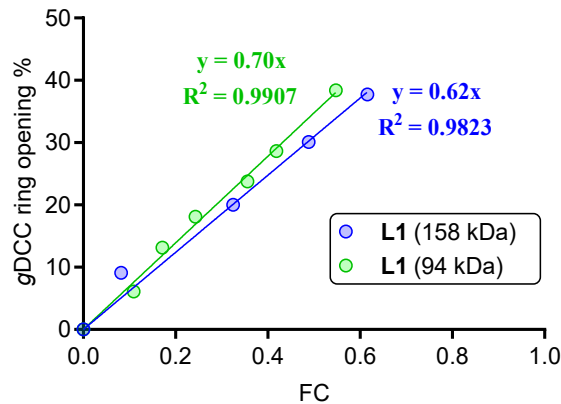
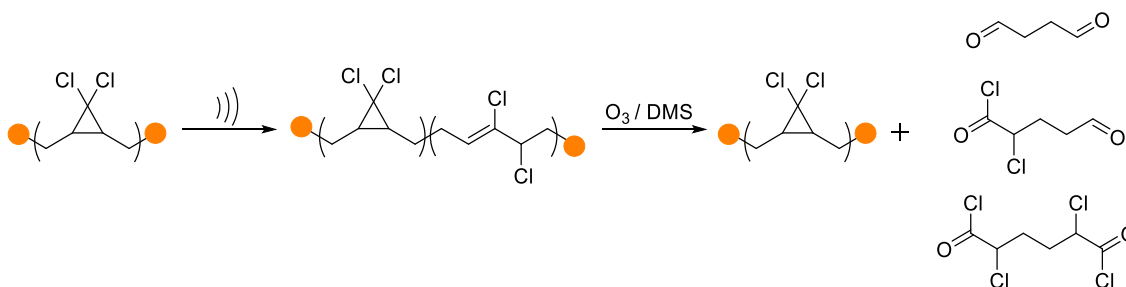


**Figure 118 : gDCC ring opening vs. fragmentation cycle plot of 158 kDa and 94 kDa L1. The slope of linear fitting through origin gives  $\Phi = 0.62$  and  $0.70$ , respectively.**

#### 2.4.3.5 Ozonolysis experiment



Sonication of poly(gDCC) homopolymer for ozonolysis:

Using described sonication procedure in section III.1. 36 mg 245 kDa **C2** was dissolved in dry THF and subjected to sonication for 12 min. Sonicated polymer was analyzed from GPC and  $^1\text{H}$  NMR. 36 mg 253 kDa **L2** was sonicated for 10 min and analyzed with GPC and  $^1\text{H}$  NMR.

Ozonolysis of sonicated gDCC polymer:

Sonicated poly(gDCC) homopolymer polymer was dissolved in 5 mL DCM. The solution was cooled to  $-78\text{ }^\circ\text{C}$  and sparged with  $\text{O}_3$  for about 10 min, when the solution turned blue.  $\text{O}_3$  was sparged through for additional 10 min.  $\text{O}_2$  was then bubbled to

remove excess O<sub>3</sub> in the solution till the solution turned colorless, and 2 mL dimethylsulfide (DMS) was added to the solution. The solution was then slowly warmed to room temperature and stirred for overnight. After condensation, the polymer was precipitated from MeOH and dry under high vacuum.

#### 2.4.3.5.1 Ozonolysis analysis of C2 homopolymer

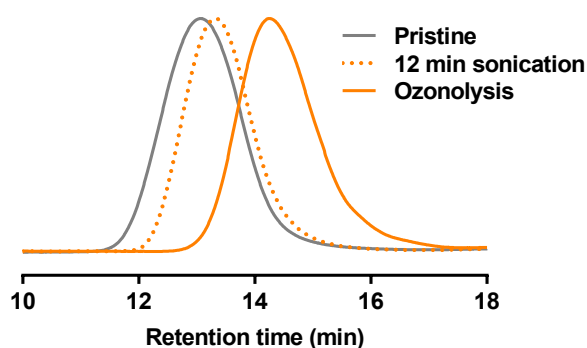


Figure 119 : GPC traces of C2 ( $M_n = 245$  kDa, PDI = 1.21) before (gray) and after (dotted orange) 12 min sonication and ozonolyzed polymer (solid orange) (12 min sonication:  $M_n = 122$  kDa, PDI = 1.31; ozonolysis:  $M_n = 41$  kDa, PDI = 1.62).

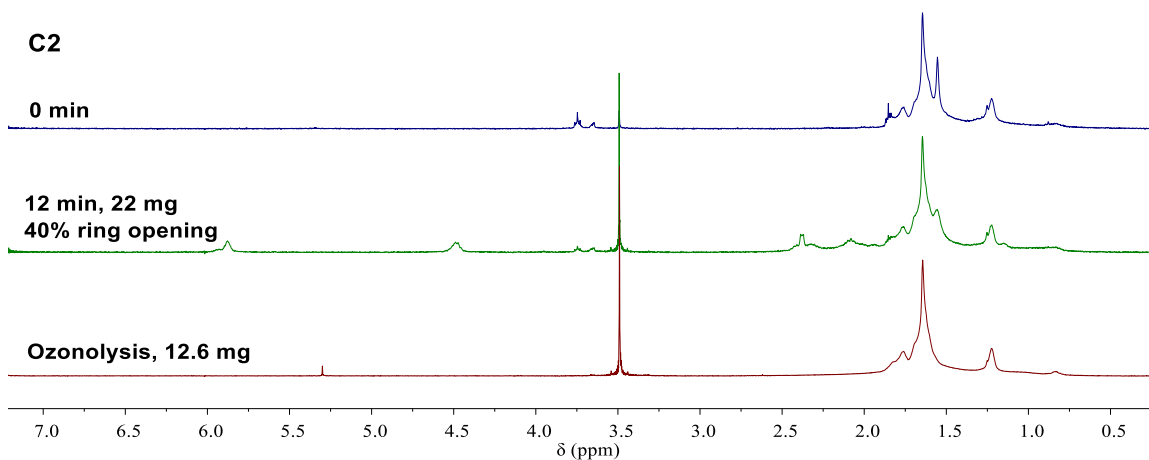
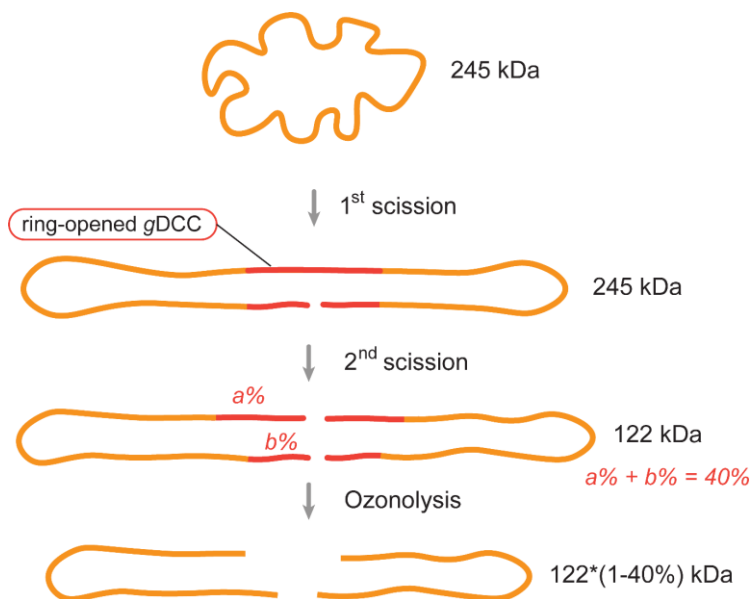


Figure 120 : <sup>1</sup>H NMR overlay of C2 polymer before and after 12 min sonication and subsequent ozonolysis.

Analysis:

245 kDa C2 polymer degraded to 122 kDa with 40% gDCC ring opening. The fragmentation cycle is:  $FC = \ln(245/122)/\ln 2 = 1.00$  (Notice: first fragmentation breaks two bonds in cyclic polymer). The  $\Phi = 40\%/1.00 = 0.40$ .



The ring opening in linear polymers, such as L1 above, occurs in what is consistent with a single region of activation. The average distribution of ring opening in C1, however, is not consistent with the same behavior observed in linear polymers. Sonication of 255 kDa C1 leads to a final  $M_n$  of 122 kDa, at which point 40% of gDCC has been activated. The activated gDCC is removed by ozonolysis, leaving a total mass of unreacted gDCC per sonicated chain of

$$M_n(\text{cal.}) = 122 \times (1 - 40\%) = 73 \text{ kDa}$$

The mass of the post-ozonolyzed polymer fragments obtained from GPC/MALS, however, is  $M_n = 41 \text{ kDa}$ .

Note that the observed  $M_n$  is not consistent with the simplest picture of cyclic activation/scission shown in the figure above, in which each chain scission event occurs within a region of activated gDCC and no gDCC activation occurs outside of those regions. For example, in the 1<sup>st</sup> scission, gDCC near the breaking bond get activated while gDCC on the parallel chain could also get activated. After the 2<sup>nd</sup> scission, additional gDCC could get activated near the breaking bond. Hence, gDCC on two parallel chains get activated when cyclic chain fragments into two daughter chains. The total amount of activated gDCC on the cyclic chain is calculated as:  $(a\%+b\%) = 40\%$ . Two daughter chains with activated gDCC on chain ends, forming a triblock polymer ( $M_n = 122$  kDa) with 40% ring opened gDCC. After ozonolysis, activated gDCC is present only on the chain ends and its removal by ozonolysis leaves the remaining gDCC on the daughter fragment in one continuous block that would have a mass of 73 kDa, as opposed to the observed mass of 41 kDa.

The data are not sufficient to give a more detailed picture of what is happening, but one possible contributor could be a scenario in which the first scission leads to activation in nearly parallel regions of the polymer (as shown in the first step of the above figure), but then the region of stress concentration, subsequent gDCC activation and the second scission event occur in a different and non-overlapping region of the chain than has been activated previously.

#### 2.4.3.5.2 Ozonolysis analysis of L2 homopolymer

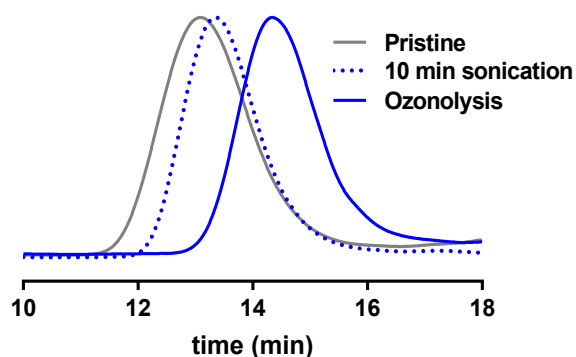


Figure 121 : GPC traces of L2 homopolymer ( $M_n = 253$  kDa, PDI = 1.29) before (gray) and after (dotted blue) 10 min sonication and ozonolyzed polymer (solid blue) (10 min sonication:  $M_n = 122$  kDa, PDI = 1.37; ozonolysis:  $M_n = 60$  kDa, PDI = 1.61).

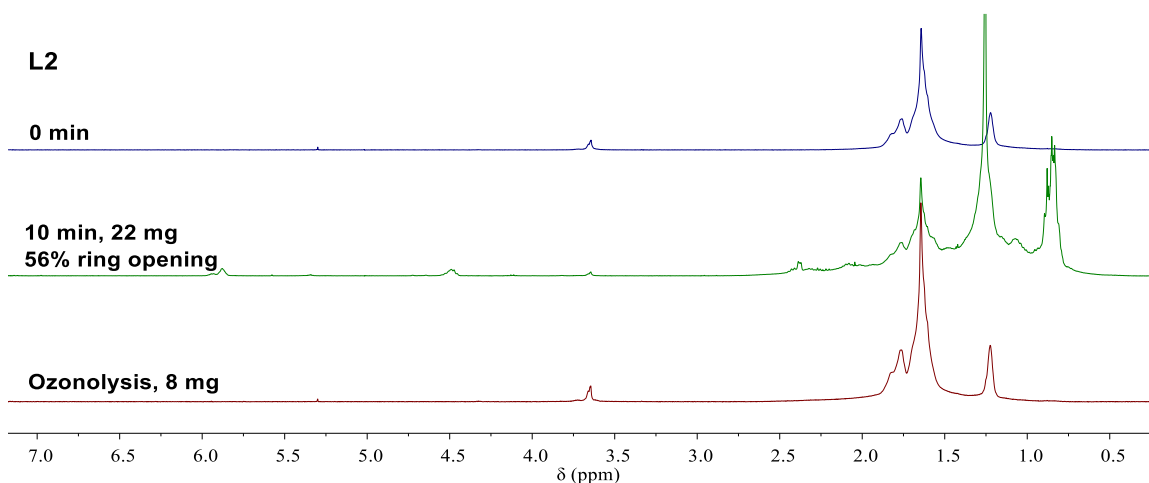
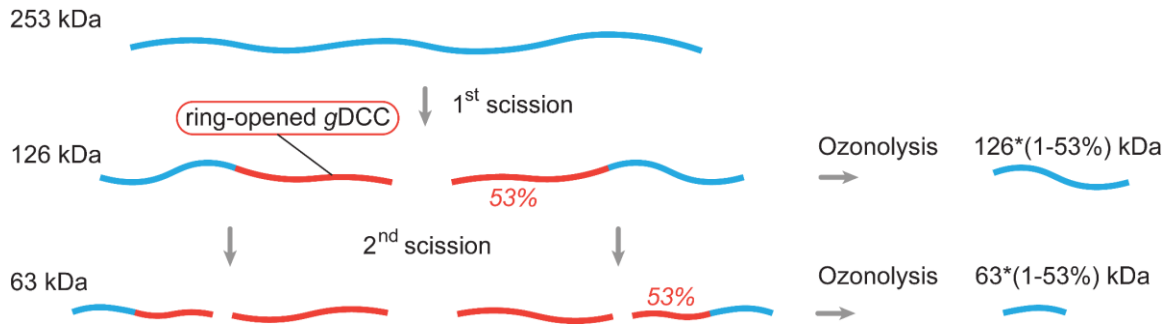


Figure 122 :  $^1\text{H}$  NMR overlay of L2 polymer before and after 10 min sonication and subsequent ozonolysis.

Analysis:

253 kDa L2 polymer degraded to 122 kDa with 56% gDCC ring opening. The fragmentation cycle is:  $\text{FC} = \ln(253/122)/\ln 2 = 1.05$ .  $\Phi = 56\%/1.05 = 0.53$ , i.e. each polymer chain activated 53% gDCC per scission.



Since  $FC > 1$ , there must exist secondary chain fragmentation, i.e. some of the  $M_n = 126$  kDa daughter chains undergo secondary chain scission to form “granddaughter” chains of average  $M_n = \sim 63$  kDa. The average number of bond breaks per initial chain can be calculated:  $\#B = 2^{FC} - 1 = 1.07$ .

The exact distribution of non-fragmenting, single fragmenting, and doubly fragmenting chains is not known, but we can approximate that expected  $M_n$  of polymer after ozonolysis by assuming that first all parent chains undergo one scission, and then 7% of the daughter chains undergo a second scission:

1) the number of final “daughter” chains that result from a single scission:  $2 \times (2 - 1.07) = 1.86$

2) the number of final “granddaughter” chains than result from two sequential scissions:  $4 \times 0.07 = 0.28$

Chains that result from a single scission contains on average 53% activated gDCC each, and chains that undergo two scissions contain half chains with all activated gDCC and half chains with an unknown amount of activated gDCC, but for purposes of this exercise we estimate at 53% (this leads to a total activated gDCC of around 55%, and therefore should underestimate by a few % the ultimate  $M_n$  expected of the polymer after

ozonolysis. After ozonolysis, the activated gDCC will be removed. Therefore, the  $M_n$  of polymer after ozonolysis can be calculated:

$$M_n(\text{cal.}) = \frac{1.86 \times 126 \times (1 - 53\%) + (50\% \times 0.28 \times 63 \times (1 - 0.53\%))}{1.86 + (50\% \times 0.28)} = 57 \text{ kDa}$$

Observed from GPC:  $M_n(\text{expt.}) = 60 \text{ kDa}$

Summary: Not to be lost in the details of the analyses is that cyclic and linear polymers of very similar MW are treated similarly in terms of dichlorocyclopropanation, sonication, and subsequent ozonolysis. There is *less activation (ring opening)* in the cyclic polymer, but *smaller* regions of continuous, unactivated gDCC along the backbones of the sonication products. In other words, in the products from the sonication of the cyclic polymer, there are regions of activated gDCC that interrupt sequences of unactivated gDCC to an extent that is not present in the sonicated, linear polymer.

### 3. Development of mechanophores with novel stress-responsive behaviors

#### ***3.1 Mechanical Generation of Isocyanate by Mechanically Induced Retro [2+2] Cycloaddition of a 1,2-Diazetidione Mechanophore<sup>III</sup>***

The encapsulation of guests in supramolecular capsules has long been used to trap reactive intermediates and enhance or reduce the kinetic stability of reactants, and alter the products of chemical reactions that occur within the capsule interior. In recent years, multiple studies have shown that variations of normal reactivity patterns can be induced by trapping reactants under tension, for example along a backbone of an overextended polymer chain, in a manner that is fundamentally very different from, but reminiscent of, encapsulation. Here, we describe the formation of a mechanochemically generated isocyanate via a mechanical retro [2+2] cycloaddition of a 1,2-diazetidione (DAO) mechanophore. A single DAO mechanophore is incorporated into the chain center of a poly(methyl acrylate) (PMA) backbone via single electron transfer-living radical polymerization (SET-LRP). Mechanical activation of the DAO via ultrasonic sonication leads to the formation of isocyanate and imine products, as supported by trapping experiments using 9-(methylaminomethyl)anthracene labelling and <sup>1</sup>H NMR spectroscopy. Further, we examine the relative mechanical susceptibility of chain-

---

<sup>III</sup> This chapter is adopted from: Lin, Y. J.; Chang, C. C.; Craig, S. L. Mechanical Generation of Isocyanate by Mechanically Induced Retro [2+2] Cycloaddition of a 1,2-Diazetidione Mechanophore. *Organic Chemistry Frontiers* **2019**, *6*, 1052-1057.

centered DAO mechanophores through a variety of methods, and evaluate the advantage and disadvantages of each.

### 3.1.1 Introduction

A similar mix of new and useful molecular behaviours with additional opportunities to study the fundamental underpinnings of chemical reactivity in new ways can be found in the area of covalent polymer mechanochemistry, where recent advances have demonstrated the potential of force-responsive motifs (mechanophores) to signal the onset of high material strains,<sup>29, 31, 72</sup> report molecular level damage in materials,<sup>38, 54, 214-216</sup> and respond to high stresses with triggered bond forming reactions that enhance mechanical properties (i.e., stress-strengthening).<sup>36, 50-51, 53, 122-123</sup> The latter is facilitated by mechanically unveiled reactive functional groups (e.g. *ortho*-quinodimethide,<sup>10, 51</sup> cyanoacrylate/acrylate,<sup>48, 50</sup> ruthenium/platinum catalyst,<sup>40, 121</sup> NHC carbene,<sup>217</sup> ketene<sup>49</sup>) that can participate in subsequent reactions at overloaded/damaged regions to promote self-healing/strengthening. The development of new mechanophores in which can undergo facile generation of reactive functionalities remains as a challenging and yet a charming research topic.

Here, we explore mechanically assisted reactivity in the context of the generation of isocyanates. Isocyanates and related reactive functional groups<sup>218-220</sup> have been extensively exploited as essential building blocks for industrial products including polyurethane elastomers, foams, polymer modification<sup>221</sup> and waterborne paints.<sup>222</sup> They are therefore appealing targets for mechanochemistry, but to the best of our knowledge

the mechanically assisted activation of latent isocyanate functionality has yet to be reported. To that end, we were inspired by recent work by Robb and Moore, who reported the mechanochemical cycloreversion of a  $\beta$ -lactam-based mechanophore (Figure 123a, pulling handles at  $R_1$  and  $R_2$ ) to produce a ketene that was subsequently trapped with *iso*-butanol in situ.<sup>49</sup> A low trapping efficiency was observed, probably due to the highly reactive nature of ketene. We hypothesized that a mechanochemical cycloreversion of the same mechanophore by pulling handles through  $R_2$  and  $R_3$  would lead to an isocyanate product (Figure 123a). The preparation of the requisitely substituted  $\beta$ -lactam, however, is somewhat arduous. We were therefore gratified to notice that an analogous 1,2-diazetidione (DAO) can be synthesized from facile addition of ketene to *cis*-azobenzene<sup>223-224</sup>, which we expected could be used to generate isocyanate through mechanical force applied to substituents on the two N atoms (Figure 123b).

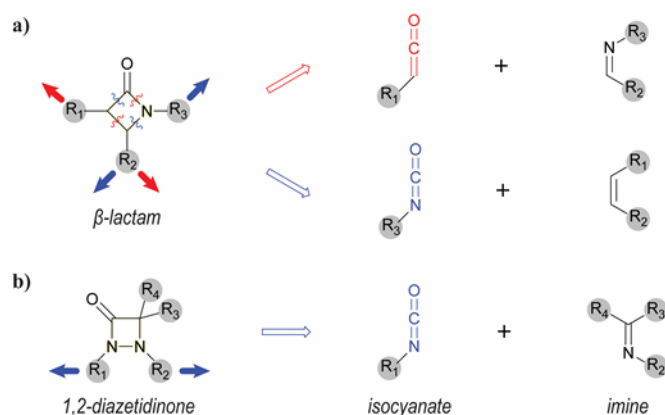
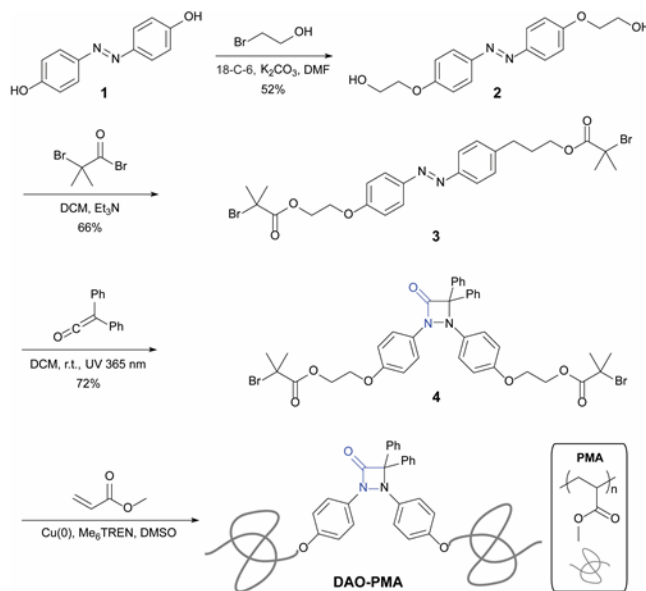


**Figure 123 :** a) Mechanical generation of ketene or isocyanate from  $\beta$ -lactam mechanophore by altering pulling handles on the four-member ring; b) 1,2-diazetidione as mechanophore to produce isocyanate.

### 3.1.2 Results and discussion

To test out hypothesis, we employed a chain-centered, single mechanophore polymer strategy, as has been widely applied with a wide range of mechanophores. The synthesis of the desired polymer is shown in Scheme 4. Bisphenol azobenzene **1** was prepared using variations of reported procedures (see section 3.1.3.2) and modified in two steps to give **3** in moderate yield. The [2+2] cycloaddition of *cis*-azobenzene with diphenyl ketene (generated *in situ*)<sup>224-225</sup> gave the desired DAO mechanophore **4**. Subsequent single electron transfer-living radical polymerization (SET-LRP) provided polymer **DAO-PMA** (number average molecular weight  $M_n = 98.0$  kDa, polydispersity  $D = 1.13$ ).

**Scheme 4 : Synthetic route for poly(methyl acrylate) with chain-centered single 1,2-diazetidione mechanophore**



We tested the mechanical reactivity of DAO by pulsed ultrasonication. **DAO-PMA** was subjected to ultrasonic irradiation (2 mg/mL, THF, 9.8 W/cm<sup>2</sup>) and monitored by gel-permeation chromatography (GPC) coupled to refractive index (RI), multi-angle light

scattering (MALS), and UV-vis photodiode array (PDA) detectors. As shown in Figure 124b, GPC traces reveal a gradual decrease of the incipient polymer peak and concomitant emergence of a daughter polymer peak with increasing sonication time. After 60 min sonication, the incipient polymer peak has effectively disappeared, and several pieces of evidence (*vide infra*) indicate that chain scission occurs *via* the expected cycloreversion shown in Figure 123b.

The formation of imine species under sonication is supported by increasing absorbance at 356 nm (Figure 124c) since generated imine has a characteristic shoulder absorption peak at 356 nm (Figure 124d), consistent that expected based on the UV-vis spectrum of small molecule model SMM1 (Figure 129). Moreover, the signal from GPC-coupled PDA detector shows the characteristic shoulder peak in the absorption spectrum around 356 nm (Figure 124e) at retention times that correspond to the elution of the daughter fragment. Further evidence from <sup>1</sup>H NMR is consistent with the mechanical activation of DAO and formation of the imine functionality (Figure 129).

The desired formation of phenyl isocyanate is more difficult to detect, due to its transience as a result of its reactivity with water and any other protic and/or nucleophilic species that might be either present in trace amounts or generated during sonication. We therefore used 9-(methylaminomethyl)anthracene (MAMA) as a labelled trapping molecule. **DAO-PMA** polymer was subjected to sonication in the presence of MAMA (1000 equivalent) and 5  $\mu$ L dibutyltin dilaurate (DBTDL) as catalyst. After 60 min

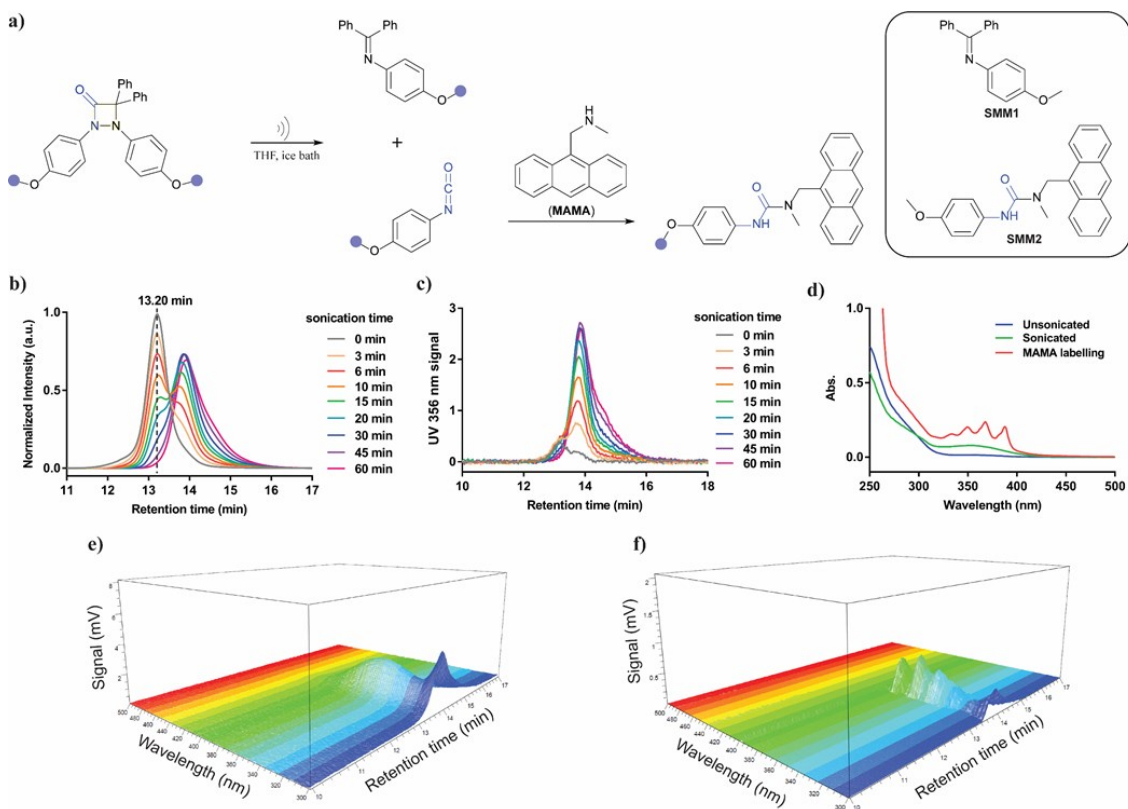


**Figure 124 :** a) Schematic illustration of mechanical activation of DAO mechanophore under sonication to generate imine and isocyanate and generated isocyanate can further react with labelling molecule MAMA; two small model molecules are given in the right box; b) GPC-RI traces of DAO-PMA polymer at various sonication time; c) GPC-UV356nm traces of DAO-PMA polymer at various sonication time; d) UV-vis spectra of raw (blue), sonicated (green) and MAMA labelled (red) DAO-PMA polymer in THF (3 mg/mL); e) 3D UV-vis GPC signal of sonicated DAO-PMA polymer; f) 3D UV-vis GPC signal of MAMA labelled DAO-PMA polymer.

sonication, the  $M_n$  of the polymer is reduced from 98 to 35 kDa. The PDA signal of the GPC trace reveals absorption at retention times of 13-16 min, which correspond to the elution of the daughter fragments (Figure 124f). The UV-vis absorption spectrum in the range of 320-420 nm is consistent with a MAMA adduct of the expected isocyanate, as confirmed by spectroscopy of the model molecule SMM2 (Figure 129). To further confirm that MAMA is covalently attached to the daughter polymer, the sonicated polymer was

purified by five rounds of methanol precipitation to completely remove any excess MAMA. The resulting polymer was dissolved and characterized by UV-vis and  $^1\text{H}$  NMR spectroscopy. The UV-vis of MAMA labeled polymer (Figure 124d) presents a same absorption pattern as model molecule SMM2 (Figure 129), while the  $^1\text{H}$  NMR spectrum shows a mixture of peaks that are characteristic of the expected products, as confirmed by spectroscopy of model compounds SMM1 and SMM2 (Figure 125). Integration of the product  $^1\text{H}$  NMR peaks provides an estimate that ~80% of the DAO mechanophore is converted to isocyanate and trapped by MAMA (Figure 128). As a control, an identical solution of **DAO-PMA**, MMAA and DBTDL was allowed to sit without sonication for 60 min before analysis; no evidence for activation or MAMA binding is observed in the UV-vis signal associated with the elution of the polymer (Figure 130, 131).

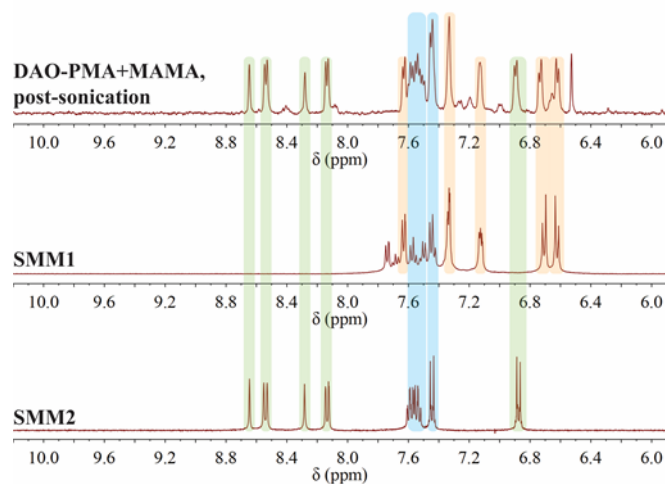


**Figure 125 :  $^1\text{H}$  NMR spectra (DMSO- $d_6$ , 500 MHz) comparison of model molecules SMM1 and SMM2 and MAMA labelled DAO-PMA polymer after purification.**

The fact that the molecular weight is reduced by more than 50% means that the average chain is broken more than once, and yet the scission of DAO is not quantitative.

This raises an interesting question as to how best quantify the mechanochemical susceptibility of the DAO mechanophore. Typically, single mechanophore polymers such as **DAO-PMA** are characterized by the reaction kinetics, and in particular the kinetics of chain scission, during sonication. Here, we applied several kinetic models to quantify the ultrasonication-mediated degradation behaviors of **DAO-PMA**. The most commonly applied framework for chain scission kinetics is given by equation (3),

$$\frac{1}{M_{n(t)}} - \frac{1}{M_{n(0)}} = kt \quad (3)$$

Where  $M_{n(t)}$  is the molecular weight at time  $t$ ;  $M_{n(0)}$  is the initial molecular weight and  $k$  is the rate constant.

Eq. (3) can be traced back to Casassa's theory in 1949.<sup>226</sup> It was cited by Jellinek and Haward in 1950<sup>227-228</sup> and then, for the first time, used by Nelapa to analyze the degradation of cellulose under shear force in 1977.<sup>229</sup> Later, it was used by Malhotra<sup>230</sup> in extensive studies of polymer degradation under sonication through presumably nonspecific homolytic scission. In 2011, Kryger et al. applied eq. (3) to the kinetics of scission in single mechanophore paper<sup>181</sup> providing a quantitative basis upon which to evaluate the relative mechanical susceptibility within a family of mechanophores.

The fact that eq. (3) is based on  $M_n$  raises an interesting question, in that, as noted previously, not all events that reduce  $M_n$  involve the scission of the mechanophore whose behavior we are trying to quantify.<sup>68</sup> Therefore, the kinetics of chain scission do not necessarily match the kinetics of mechanophore activation.

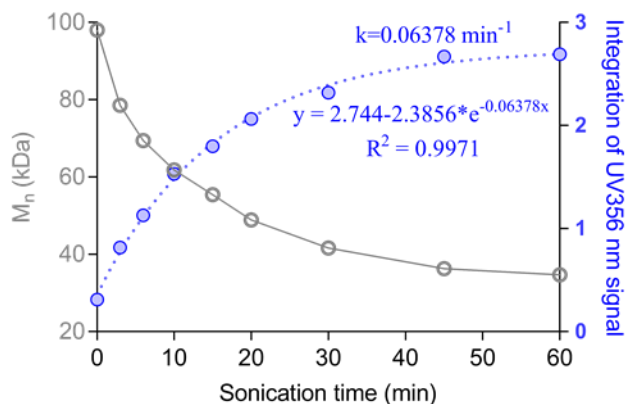


**Figure 126 : The evolution of molecular weight ( $M_n$ ) and integration of GPC-UV356nm signal of DAO-PMA polymer during sonication.**

Because DAO provides a UV signal of activation that is independent of change in molecular weight, the system at hand provides an opportunity to evaluate the suitability of eq. (3) for this polymer and mechanophore combination. We can obtain a direct measure of DAO scission from the UV-vis absorption signal of the imine by fitting the change in absorption at 356 nm to a first-order exponential decay. We denote the resulting rate constant  $k_{\text{product}}$  as it results from quantifying the products of DAO scission.

We also considered a third method, based on the change in peak height of the parent polymer peak in the GPC data, to calculate the mechanical degradation rate. This method was reported by Florea<sup>231</sup> and later used by Boydston to compare the chain scission rates of linear and star polymers.<sup>185</sup> Because we have adequate resolution of our parent and daughter peaks, we also performed a kinetic analysis of the change in peak height of the RI signal that is attributed to the parent polymer (retention time at 13.20 min, Figure 124b) to obtain what we denote  $k_{\text{RI}}$ . Finally, a variant of this method was employed, in which we deconvoluted the GPC traces into overlaying parent and daughter peaks, as

previously performed by Boydston (for details, see section 3.1.3.4).<sup>185</sup> The degradation rate constants were then calculated from peak intensity ( $k_{\text{peak}}$ ) and area ( $k_{\text{area}}$ ) of the resolved parent polymer peak (Figure 137).

**Table 14 : DAO-PMA activation rate constants obtained from various methods**

| Casassa  | Product   | Florea                                     | Deconvolution                                |  |
|--|---|--|--|--|
| $k_{\text{MW}}*10^5$<br>( $\text{Da}^{-1} \text{min}^{-1}$ ) | $k_{\text{product}}*10^2$ ( $\text{min}^{-1}$ ) | $k_{\text{RI}}*10^2$ ( $\text{min}^{-1}$ ) | $k_{\text{peak}}*10^2$ ( $\text{min}^{-1}$ ) | $k_{\text{area}}*10^2$ ( $\text{min}^{-1}$ ) |
| $4.6 \pm 0.25$   | $6.4 \pm 0.36$                                  | $5.6 \pm 0.23$                             | $5.4 \pm 0.12$                               | $5.0 \pm 0.07$                               |

The mechanophore activation rates obtained from the various methods are shown in Table 14. Notably, the rate constant retrieved from Casassa’s method involves the possibility of multiple events per chain, rather than a 1:1 conversion of reactant (parent polymer) to product (daughter fragment). The intrinsic difference in its meaning is reflected in the units of the rate constant, and we put aside discussion of  $k_{\text{MW}}$  for the moment. A comparison of the remaining kinetic parameters is more revealing. The values of the other four rate constants are generally consistent, with a maximum difference of only 30%, but the apparent rate constant for product formation ( $k_{\text{product}}$ ) is slightly, yet statistically significantly, greater than the rate constants inferred from changes in molecular weight ( $k_{\text{peak}}$ ,  $k_{\text{area}}$ , and  $k_{\text{RI}}$ ). It is tempting to simply ascribe the admittedly modest difference to experimental uncertainty, but given that the data are obtained from the same reaction, and all rate constants depend only on the relative (and not absolute) signal as a function of time, we consider the possibility that the difference is real and its likely implications.

In particular, the difference in rate constants boils down to the idea that DAO scission comes to completion prior to the end of chain scission chemistry. The relative extent of DAO scission vs. overall chain scission makes clear that there is some off-target rupture taking place. If non-DAO scission occurred only in direct competition with DAO scission, however, and each chain broke only up to a single time, then the half-life for each process would be identical and the measured rate constants should match. A shorter half-life (greater  $k$ ) for DAO scission instead implies that the chain scission reactions continue to occur even as the DAO scission has effectively stopped. In other words, some population of the parent polymers might be cleaved first at the DAO, and then subsequently undergo a second scission within a daughter fragment.

As the data in Table 14 suggest, the implications of such processes might often be modest, or even barely detectable, but these possibilities are worth bearing in mind, especially since they might be hidden by dispersity even for fairly well controlled polymerizations such as those employed here. Since rate constants of chain scission are often used to compare different mechanophores, and since those mechanophores are necessarily in different polymers, slight differences in polymer molecular weight and/or dispersity might contribute to differential behavior that complicates the desired comparison. It therefore seems prudent to monitor the scission of single mechanophore polymers by multiple methods whenever possible, using techniques that are specific to the mechanochemical reaction of interest as well as to the scission of the polymer chain in general.

Conclusions. The use of mechanophore-specific signals is reminiscent of the ability to distinguish  $^1\text{H}$  NMR signals of host, encapsulated guest, and unencapsulated guest that so empowered the thermodynamic, kinetic, and mechanistic investigations in those systems. While the ideas presented here are unlikely to surprise anyone working in the field of polymer mechanochemistry, we are not aware that they have been spelled out previously in the literature, and the new DAO mechanophore disclosed here presented a valuable opportunity to do so. In addition, the mechanochemical reactivity of DAO itself might be quite useful, as the isocyanate and, to a lesser extent, imine products formed from DAO cycloreversion are potentially useful as building blocks in stress-adaptive materials.

### **3.1.3 Experimental section**

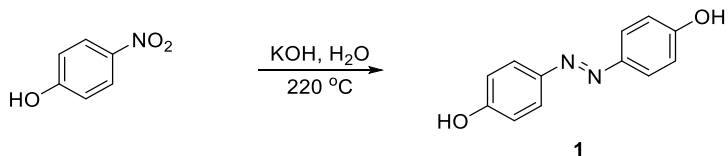
#### **3.1.3.1 Materials and characterization**

Materials: Lab general solvents (dichloromethane, chloroform, hexane, ethyl acetate, acetone, toluene, tetrahydrofuran, methanol, DMSO) were purchased from VWR or Sigma Aldrich. 4-nitrophenol, 2-bromo-ethanol, triethyl amine, 2-Bromo-isobutyrate bromide, diphenylacetyl chloride, Me<sub>6</sub>TREN, methyl acrylate, benzophenone, AlCl<sub>3</sub>, 4-Methoxyaniline, 9-(Methylaminomethyl)anthracene, DBTDL, 4-Methoxyphenyl isocyanate, KOH and K<sub>2</sub>CO<sub>3</sub> were purchased from Sigma Aldrich, Alfa Aesar or TCI and used without further purification. Flash chromatography was performed on CombiFlash®200 auto-column system from Teledyne ISCO.

Characterizations:  $^1\text{H}$  NMR spectra were collected on a 400 MHz Varian INOVA spectrometer and  $^{13}\text{C}$  NMR spectra were collected on a 500 MHz Varian UNITY spectrometer. Chemical shifts are provided in *ppm* ( $\delta$ ) and referenced to the residual  $^1\text{H}$  peak at 7.26 ppm or  $^{13}\text{C}$  peak at 77.16 ppm in  $\text{CDCl}_3$ , or to the residual  $^1\text{H}$  peak at 2.50 ppm or  $^{13}\text{C}$  peak at 39.52 ppm in  $\text{DMSO-}d_6$ .  $^1\text{H}$  shifts are reported as chemical shift, multiplicity, coupling constant if applicable, and relative integral. Multiplicities are reported as: singlet (s), doublet (d), doublet of doublets (dd), doublet of triplets (dt), doublet of doublet of doublets (ddd), doublet of doublet of triplets (ddt), triplet (t), triplet of doublets (td), quartet (q), multiplet (m), or broad (br). Coupling constants (J) are reported in Hertz. High-resolution mass spectra were collected on an Agilent LCMS-TOF-DART at Duke University's Mass Spectrometry Facility. Gel permeation chromatography (GPC) was performed on two Agilent PLgel mixed-C columns ( $10^5 \text{ \AA}$ , 7.5x300 mm, 5  $\mu\text{m}$ , part number PL1110-6500) using THF (stabilized with 100 ppm BHT) as the eluent. Molecular weights were calculated using a Wyatt Dawn EOS multi-angle light scattering (MALS) detector and Wyatt Optilab DSP Interferometric Refractometer (RI). The refractive index increment (dn/dc) values were determined by online calculation based on injections of known concentration and mass. UV-vis spectra were collected on a Varian Cary 500 UV-Vis Spectrophotometer.

### 3.1.3.2 Synthetic procedures

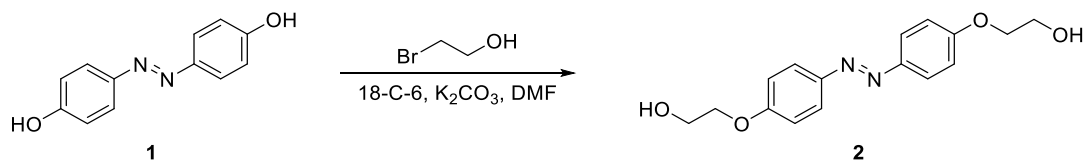
Synthesis of 4,4'-bis(hydroxy)-azobenzene 1:



The 4, 4'-bis(hydroxy)-azobenzene **1** was synthesized according to previous procedure<sup>232</sup>.

4-nitrophenol (10 g, 72 mmol) and KOH (50 g, 893 mmol) were weighted in a 250 mL round bottom flask. 12 mL DI water was then added to the mixture. The flask was then heated to 120 °C, the mixture turned orange but still cannot be stirred. After 1 h, the temperature was raised to 200 °C, the mixture slowly turned dark red and started to melt. The viscous mixture was then vigorously stirred until a lot of foam evolved. The mixture was then cooled down to room temperature. The solid was then dissolved with DI water and acidified to pH equals to 3 with HCl. Then obtained dark red aqueous solution was extracted with 3×100 mL ether. Combined ether was dried with MgSO<sub>4</sub> and further removed. The residual was recrystallized with 140 mL 50% EtOH/H<sub>2</sub>O to give pure 4, 4'-bis(hydroxy)-azobenzene **1** as dark red solid (3.547 g, 46.1%). The <sup>1</sup>H NMR data is in agreement with previous reported<sup>232</sup>.

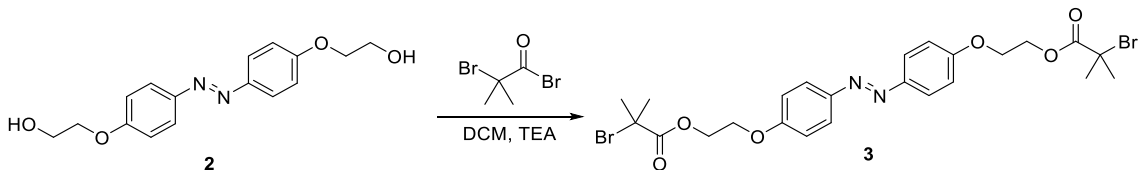
Synthesis of azobenzene diol **2**:



The azobenzene diol **2** was synthesized according to previous procedure<sup>233</sup>.

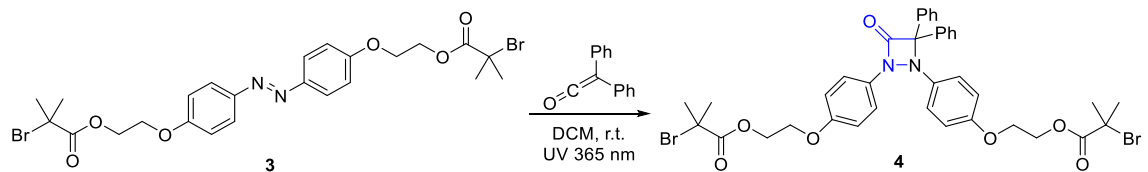
Compound **1** (1.0 g, 4.67 mmol), 2-bromo-ethanol (1.46 g, 11.68 mmol) and 18-Crown-6 (62 mg, 0.23 mmol) were dissolved in 10 mL DMF. Then, K<sub>2</sub>CO<sub>3</sub> (2.58 g, 18.68 mmol) was added to the solution. The mixture was then heated at 100 °C for 2 days. The mixture was cooled down and poured into 100 mL DI water. The yellow precipitation was filtered and recrystallized in EtOH to give pure azobenzene diol **2** as yellow solid (0.74 g, 52.4%). The <sup>1</sup>H NMR data is in agreement with previous reported<sup>233</sup>.

Synthesis of azobenzene initiator **3**:



Azobenzene diol **2** (650 mg, 2.15 mmol, 1.0eq.) and triethyl amine (0.9 mL, 6.5 mmol) was dissolved in 25 mL DCM. The solution was cooled with ice bath. 2-Bromo-isobutyrate bromide (638  $\mu$ L, 5.2 mmol) was then added dropwise. The reaction was slowly warmed to room temperature and allow to stir for overnight. After the reaction completed, solvent was removed. Residual was further purified by flash chromatography (0% to 25 % EtOAc/hexane gradient eluent). Pure azobenzene initiator **3** was obtained as a yellow solid (853 mg, 66.0%). <sup>1</sup>H NMR (CDCl<sub>3</sub>, 400MHz)  $\delta$ : 7.88 (d, J = 8.97 Hz, 4H), 7.02 (d, J = 8.99, 4H), 4.56 (t, 4H), 4.31 (t, 4H), 1.95 (s, 12H). <sup>13</sup>C NMR (125 MHz, CDCl<sub>3</sub>)  $\delta$ : 171.74, 160.55, 147.43, 124.51, 115.00, 65.93 64.16, 55.57, 30.82. HRMS-ESI (m/z): [M + H]<sup>+</sup> calculated for C<sub>24</sub>H<sub>29</sub>Br<sub>2</sub>N<sub>2</sub>O<sub>6</sub>, 601.31145; found 601.03690.

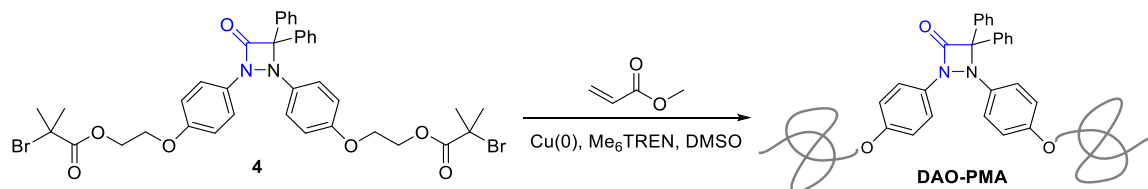
Synthesis of 1, 2-diazetidione (DAO) mechanophore containing initiator **4**:



The DAO mechanophore was synthesized using in situ generated diphenyl ketene according to previous procedure<sup>224</sup>.

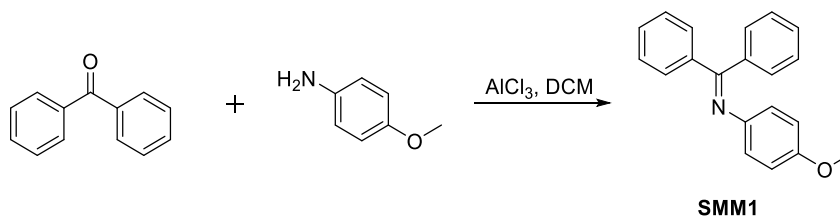
Compound **3** (400 mg, 0.66 mmol) was dissolved in 5 mL DCM. The solution was irradiated with a UV 365 nm LED light. Diphenylacetyl chloride (184 mg, 0.8 mmol) was then added to the solution and stirred to dissolve. Dried triethyl amine (120  $\mu$ L, 0.86 mmol) was then added to the solution. The solution was kept under irradiation with UV 365 nm light. The reaction was monitored by TLC. After the reaction completed, the mixture was purified by flash chromatography (0% to 25 % EtOAc/hexane gradient eluent). The DAO mechanophore containing initiator **4** was obtained as a light yellow solid (383 mg, 72.4%). <sup>1</sup>H NMR (CDCl<sub>3</sub>, 400MHz)  $\delta$ : 7.50~6.95 (m & br, 12 H), 6.85 (q, 4H), 6.58 (d, 2H), 4.48 (t, 2H), 4.40 (t, 2H), 4.17 (t, 2H), 4.04 (t, 2H), 1.91 (s, 6H), 1.90 (s, 6H). <sup>13</sup>C NMR (125 MHz, CDCl<sub>3</sub>)  $\delta$ : 171.61, 165.64, 155.47, 155.41, 138.77, 131.99, 130.08, 128.73, 128.60, 128.32, 122.34, 117.92, 115.33, 114.75, 94.04, 66.08, 65.85, 64.17, 64.08, 55.18, 30.74. HRMS-ESI (m/z): [M + H]<sup>+</sup> calculated for C<sub>38</sub>H<sub>39</sub>Br<sub>2</sub>N<sub>2</sub>O<sub>7</sub>, 795.54445; found 795.11041.

Synthesis of DAO mechanophore centered PMA polymer (DAO-PMA):



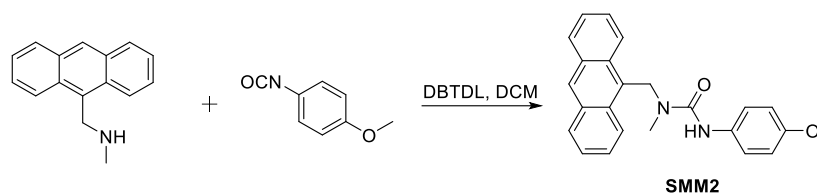
Mechanophore initiator **4** (20 mg, 0.025 mmol), Me<sub>6</sub>TREN (1.3 μL, 0.005 mmol) and methyl acrylate (3.76 mL, 41.5 mmol) monomer were weighted in a 50 mL Schlenk flask. 3.76 mL DMOS was then added and stirred to mix completely. A ~2.0 cm copper wire was firstly polished with sand paper and added to the solution. The flask was then capped and subjected to freeze-pump-thaw cycle to remove dissolved oxygen. The polymerization was proceeded for 3 h. The polymerization was terminated by connecting the Schlenk flask to air. The viscous solution was diluted with DCM and precipitated form methanol. The polymer was redissolved in DCM and precipitated from methanol. This procedure was repeated twice. The polymer was further dried under high vacuum. Obtained polymer was characterized by GPC ( $M_n = 98.0$  kDa,  $M_w = 110.5$  kDa, PDI = 1.128).

Synthesis of small molecule model (SMM):



To a solution of benzophenone (243 mg, 1.33 mmol) in 12 DCM, added AlCl<sub>3</sub> (302 mg, 2.26 mmol). 4-Methoxyaniline (246 μL, 2.14 mmol) and triethyl amine (954 μL, 6.84 mmol) was added to a 20 mL scintillation vial and dissolved with 3 mL DCM. The solution was then added dropwise to the previous mixture. The reaction was allowed to stir at room temperature for 5 h. After the reaction completed, it was quenched with 20 mL DI water and extracted with 3×10 mL DCM. DCM was combined and dried with MgSO<sub>4</sub>. Pure product was obtained as light oil (332 mg, 86.7%) after column chromatography (0

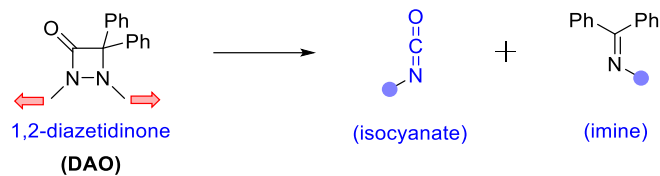
~25% EtOAc/Hexane gradient eluent).  $^1\text{H}$  NMR (DMSO- $d_6$ , 400MHz)  $\delta$ : 7.80~7.28 (m, 8H), 7.12 (m, 2H), 6.71 (d,  $J = 8.8$  Hz, 2H), 6.62 (d,  $J = 8.8$  Hz, 2H), 3.64 (s, 3H).  $^{13}\text{C}$  NMR (125 MHz, DMSO- $d_3$ )  $\delta$ : 166.93, 155.29, 143.98, 139.14, 136.99, 136.20, 132.63, 130.65, 129.59, 128.85, 128.60, 128.54, 128.41, 128.25, 128.14, 121.96, 113.65, 54.96. HRMS-ESI (m/z): [M + H] $^+$  calculated for  $\text{C}_{20}\text{H}_{18}\text{NO}$ , 288.36945; found 288.13860.



9-(Methylaminomethyl)anthracene (MAMA) (221 mg, 1 mmol) was dissolved in 4 mL DCM. A drop of DBTDL catalyst was added to the solution. Then 4-Methoxyphenyl isocyanate (129  $\mu\text{L}$ , 1 mmol) was added. The reaction was stirred at room temperature for 0.5 h, precipitated formed. The reaction was further stirred for 0.5 h. The mixture was then added dropwise to a stirring hexane. The white solid was filtered and dried under vacuum (360 mg, 97.3%).  $^1\text{H}$  NMR (DMSO- $d_6$ , 400MHz)  $\delta$ : 8.65 (s, 1H), 8.54 (d, 2H), 8.28 (s, 1H), 8.13 (d, 2H), 7.56 (m, 4H), 7.45 (d, 2H), 6.88 (d, 2H), 5.58 (s, 2H), 3.73 (s, 3H), 2.60 (s, 3H).  $^{13}\text{C}$  NMR (DMSO- $d_6$ , 125MHz)  $\delta$ : 155.92, 154.60, 133.62, 131.02, 130.86, 129.13, 127.82, 126.49, 125.18, 124.36, 121.98, 113.56, 55.17, 41.78, 32.15. HRMS-ESI (m/z): [M + H] $^+$  calculated for  $\text{C}_{24}\text{H}_{23}\text{N}_2\text{O}_2$ , 371.45945; found 371.17562.

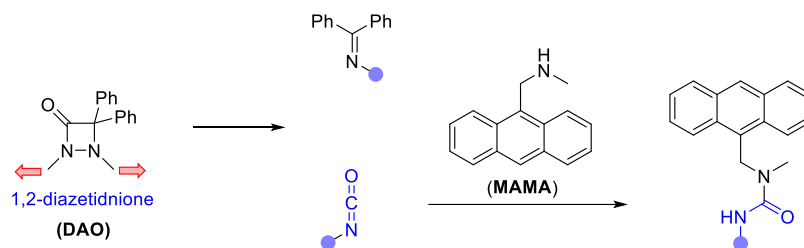
### 3.1.3.3 Sonication experiment

Sonication of DAO-PMA for GPC analysis:



A solution of 32 mg **DAO-PMA** polymer in 16 mL dry THF ( $c = 2$  mg/mL) was transferred into a Suslick cell. The solution was purged with  $N_2$  for 10 min and then cooled with ice bath. Ultrasound impulse was applied (1s on, 1s off) at 30% amplitude. An aliquot of 0.2 mL sample were taken out for GPC analysis at time points: 0, 3, 6, 10, 15, 20, 30, 45, 60 min. After sonication, the remained solution was condensed and precipitated from MeOH. The obtained polymer was dried and analyzed from  $^1H$  NMR and UV-vis.

Labeling of DAO-PMA under sonication:



A solution of 32 mg **DAO-PMA** polymer in 16 mL dry THF ( $c = 2$  mg/mL) was transferred into a Suslick cell. Then, 9-(Methylaminomethyl)anthracene (MAMA) (71 mg, 1000 eq.) and DBTDL (1  $\mu$ L) was added to the solution. The solution was purged with  $N_2$  for 10 min and then cooled with ice bath. Ultrasound impulse was applied (1s on, 1s off) at 30% amplitude for 60 min. After sonication, the solution was condensed and precipitated from MeOH. The polymer was then redissolved in 0.2 mL DCM and precipitated from MeOH. This procedure was repeated 4 times. The polymer was dried under vacuum and subjected to GPC, UV-vis and  $^1H$  NMR analysis.

Determination of mechanically activated product:

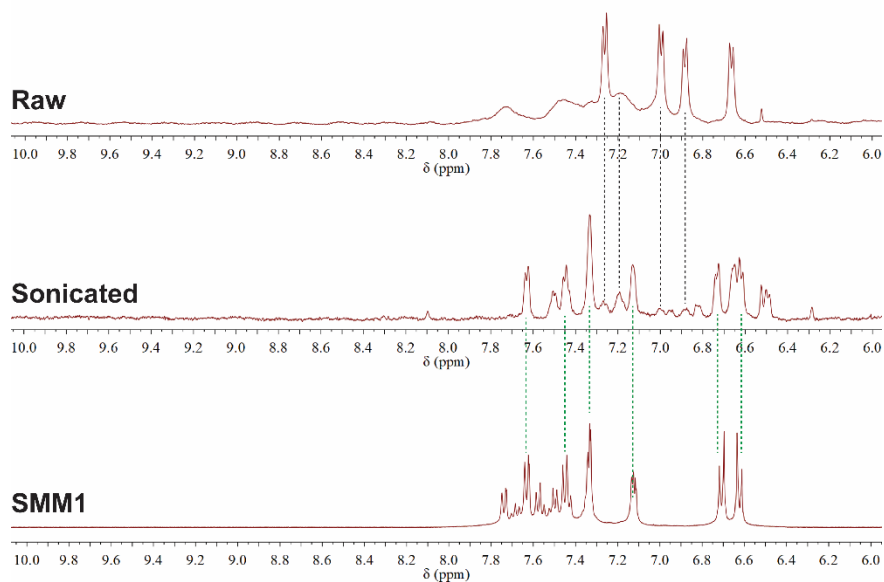


Figure 127 :  $^1\text{H}$  NMR (400 MHz,  $\text{DMSO-}d_6$ ) overlay of raw and sonicated DAO-PMA polymer and compound SMM1.

UV-vis spectra:

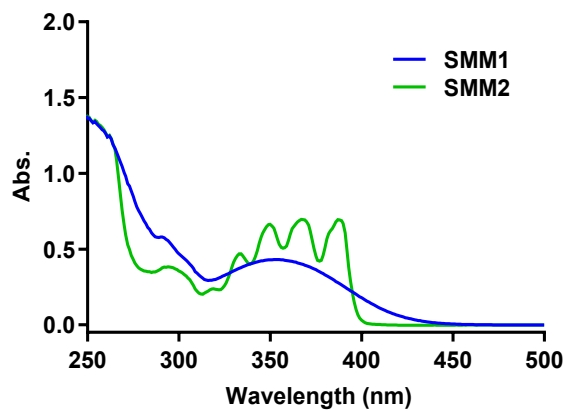
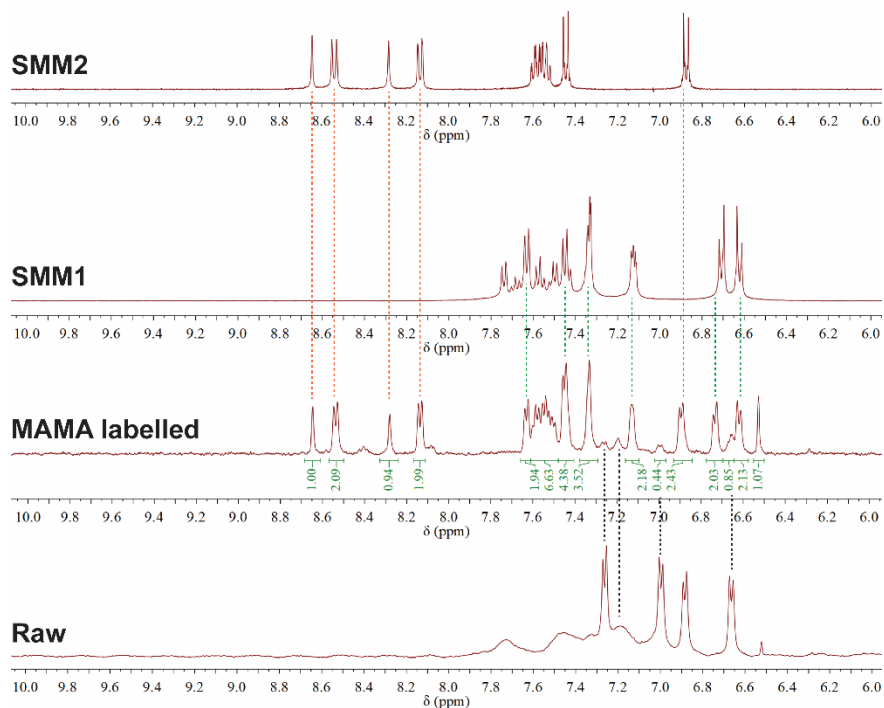


Figure 128 : UV-vis spectra of SMM1 and SMM2 in THF



**Figure 129 :  $^1\text{H}$  NMR (400 MHz,  $\text{DMSO-}d_6$ ) overlay of raw and MAMA labelled DAO-PMA polymer, compound SMM1 and SMM2. The activation percentage was estimated from remaining DAO peak and formed imine:  $2.03/(0.44+2.03)*100\% = 82\%$ ; the ratio of formed imine to trapped MAMA is near  $2.03:2.09 \sim 1$ ; therefore, the isocyanate reacted quantitatively with MAMA.**

Control experiment for MAMA labelling:

DAO-PMA polymer was mixed with 1000 eq. MAMA and 5 uL DBTDL catalyst for 60 min, the mixture was then subjected to GPC analysis.

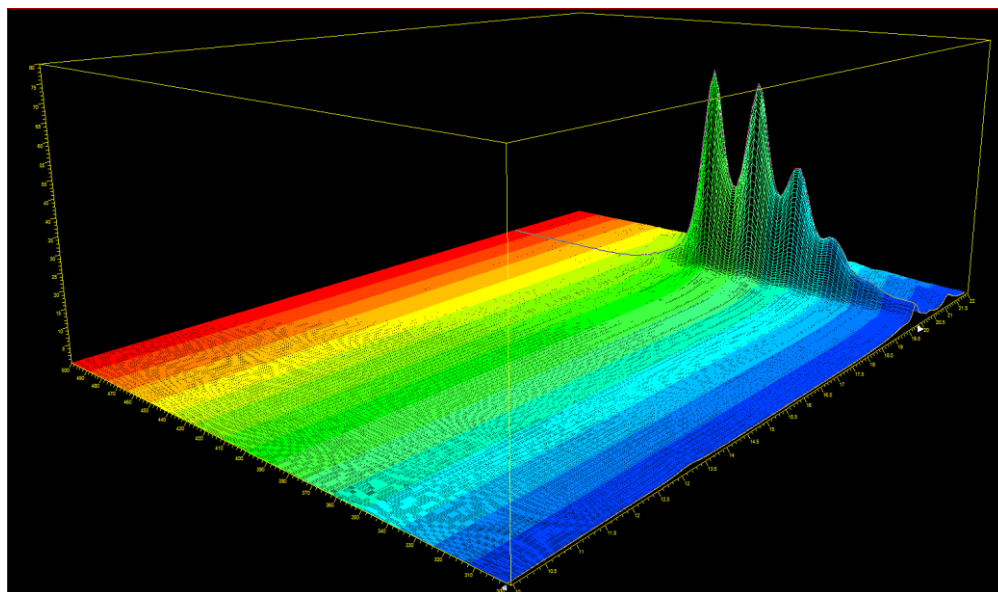


Figure 130 : 3D UV-vis signal of DAO-PMA, MAMA and DBTDL after 60 min physical mixing. The strong UV-vis signal appeared at retention time of 19.5~20.5 min that corresponds to excess small molecule MAMA.

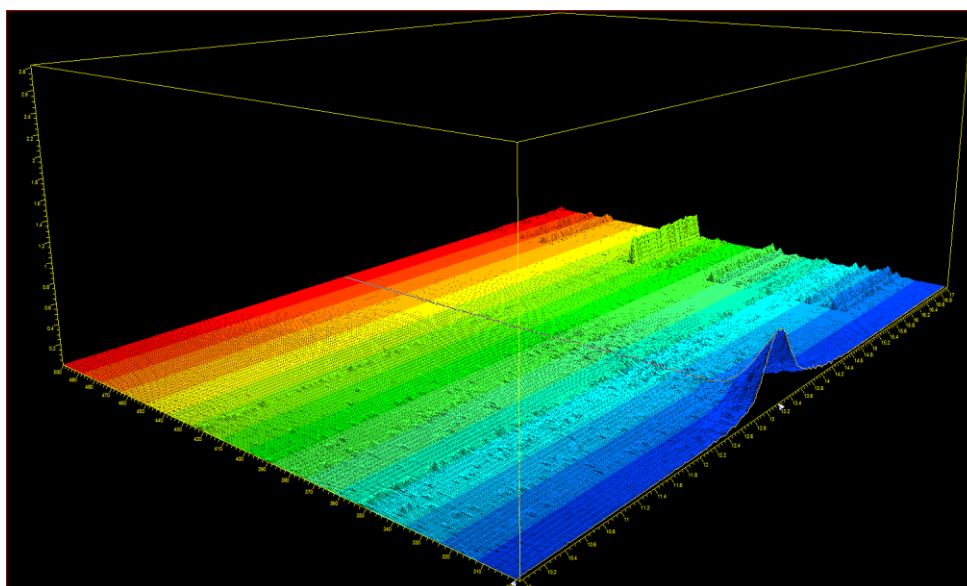


Figure 131 : Zoom-in view of Figure 130 shows 12~14 min polymer retention time region presents 3D UV-vis signal appeared only at the range of 300~320 nm, which is consistent with UV-vis absorption of raw polymer.

#### 3.1.3.4 Determination of mechanophore activation rate under sonication

Polymer degradation kinetics:

The molecular degradation rate was calculated from the following equation (4):

$$\frac{1}{M_t} - \frac{1}{M_i} = \frac{kt}{M_0}$$

Where  $M_t$  is the number average molecular weight at time  $t$ ,  $M_i$  stands for the initial number average molecular weight,  $M_0$  represents for the molecular weight of repeating unit and  $k$  refers to the degradation rate. Table 15 provides a representative number average molecular weight of sonicated polymer at time  $t$ . The corresponding polymer degradation rate was determined.

**Table 15 : A representative data set of molecular degradation during sonication**

| Sonication time<br>/ min | $M_n$<br>/ kDa | $M_w$<br>/ kDa | PDI   | $(1/M_t - 1/M_i) * M_0 * 1000$ | Rate / $\text{min}^{-1}$ |
|--------------------------|----------------|----------------|-------|--------------------------------|--------------------------|
| 0                        | 98.0           | 110.5          | 1.128 | 0.0426                         |                          |
| 3                        | 78.6           | 93.4           | 1.189 | 0.2592                         |                          |
| 6                        | 69.4           | 84.1           | 1.211 | 0.4042                         |                          |
| 10                       | 61.8           | 74.1           | 1.199 | 0.5566                         |                          |
| 15                       | 55.4           | 65.8           | 1.187 | 0.7174                         | 5.152*10 <sup>-5</sup>   |
| 20                       | 48.9           | 59.0           | 1.207 | 0.9237                         |                          |
| 30                       | 41.6           | 51.1           | 1.228 | 1.2323                         |                          |
| 45                       | 36.3           | 44.9           | 1.236 | 1.5342                         |                          |
| 60                       | 34.7           | 41.6           | 1.200 | 1.6434                         |                          |

As shown in Figure 132, the whole data set presents a poor linearity. Therefore, the data points from the first 20 min sonication were used for linear fitting since the molecular weight reduced from 98.0 kDa to 48.9 kDa that lies in the first scission cycle.

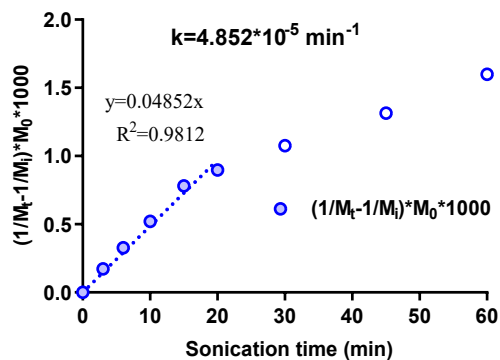
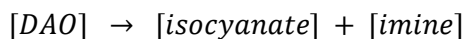


**Figure 132 :** Analyzing the molecular degradation rate using equation (4). The linear fitting was applied on first 15 min sonication that lies in the first scission cycle. The obtained molecular degradation rate is  $4.852 \times 10^{-5} \text{ min}^{-1}$ .

Determination of mechanophore activation rate from UV 356 nm signal:

The increase at UV 365 nm signal from GPC trace corresponds to the generation of imine during the sonication. The mechanical activation of DAO mechanophore can be treated as a first order reaction:



$$-\frac{d[DAO]}{dt} = k[DAO]$$

$$\ln[DAO]_t - \ln[DAO]_0 = kt$$

Since,  $[DAO]_0 = [DAO]_t + [imine]$ :

$$\ln \frac{[DAO]_0 - [imine]}{[DAO]_0} = kt$$

The concentration of generated imine species is proportional to the UV 356 nm absorption. Hence, the activation rate can be obtained from integration of UV 356 nm signal using the following equation:

$$[imine] = [DAO]_0 - [DAO]_0 e^{-kt}$$

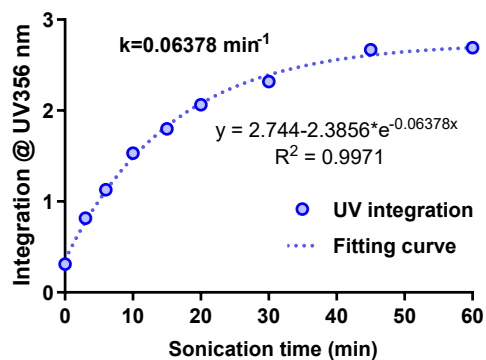


**Figure 133 : Mechanophore activation rate was obtained using integration of UV 356 nm signal form GPC traces. The data was fitted with one-phase association.**

Determination of mechanophore activation rate from RI signal before deconvolution:

Given the narrow PDI of prepared DAO-PMA polymer (PDI = 1.13), the activated polymer that reduces to near half molecular weight can be resolved from our two column GPC. Hence, the activation rate of DAO mechanophore can be determined using the method reported by Boydston group. The RI intensity at 13.20 min was applied to calculate the activation rate.

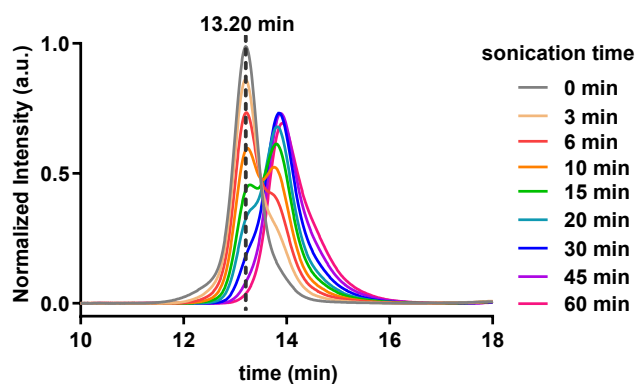


**Figure 134 : GPC RI signal of parent polymer at 13.20 min retention time decreased when subjected to sonication.**

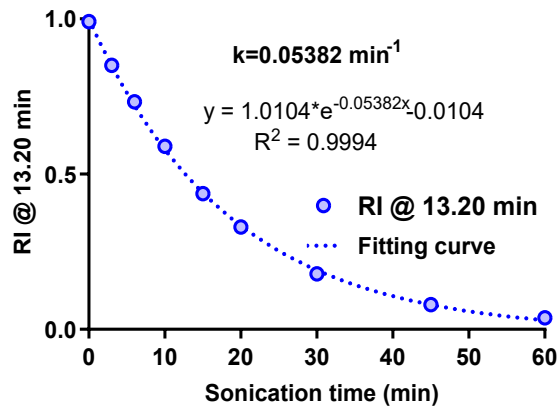


Figure 135 : Mechanophore activation rate was obtained by fitting the evolution of RI signal at 13.20 min retention time.

Determination of mechanophore activation rate from RI signal after deconvolution:

In order to verify that the activation rate of mechanophore in our narrow disperse polymer can be correctly valued from the evolution of RI intensity at initial peak, we performed the deconvolution of GPC traces to analyze the activation rate by using microsoft excel solver according to previous reported method<sup>185, 234</sup>.

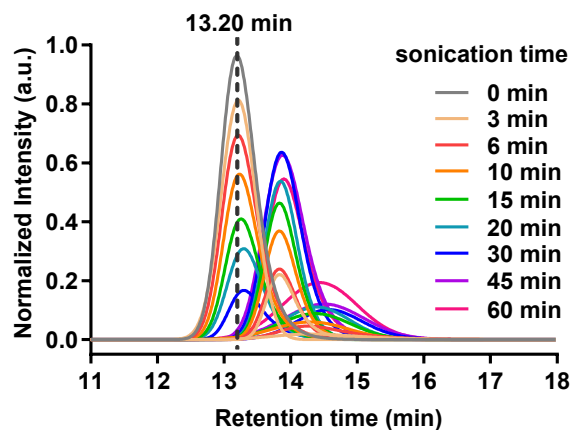


Figure 136 : Deconvolution of GPC RI traces using Microsoft excel solver.

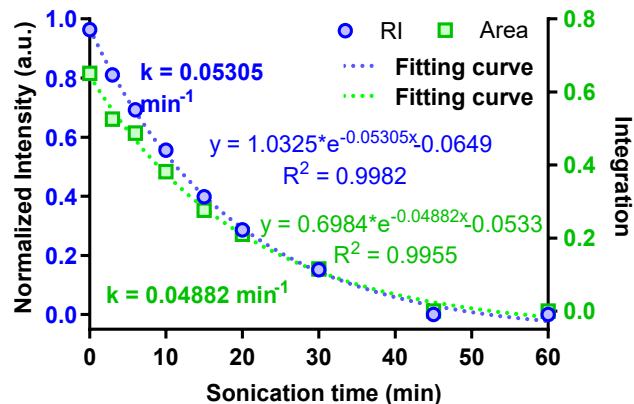


Figure 137 : Mechanophore activation rate was evaluated from deconvolution of GPC RI traces. Fitting the RI signal of parent polymer at 13.20 min retention time with one-phase decay (Blue circle); fitting the RI signal integration of parent polymer with one-phase decay (Green square).

Comparison of activation rate evaluation:

Table 16 : Summary of obtained activation rate from different reported method.

| Method                | Activation rate (min <sup>-1</sup> ) |                       |                       |                       |                       |                       |
|-----------------------|--------------------------------------|-----------------------|-----------------------|-----------------------|-----------------------|-----------------------|
|                       | Trial 1                              | Trial 2               | Trial 3               | Average               | SD.                   |                       |
| Cassasa's theory      | 4.85×10 <sup>-5</sup>                | 4.64×10 <sup>-5</sup> | 4.35×10 <sup>-5</sup> | 4.61×10 <sup>-5</sup> | 2.52×10 <sup>-6</sup> |                       |
| UV 356 nm integration | 6.38×10 <sup>-2</sup>                | 6.95×10 <sup>-2</sup> | 7.03×10 <sup>-2</sup> | 6.79×10 <sup>-2</sup> | 3.55×10 <sup>-3</sup> |                       |
| RI @ 13.20 min        | 5.38×10 <sup>-2</sup>                | 5.78×10 <sup>-2</sup> | 5.77×10 <sup>-2</sup> | 5.64×10 <sup>-2</sup> | 2.27×10 <sup>-3</sup> |                       |
| Deconvolution         | RI@13.20min                          | 5.31×10 <sup>-2</sup> | 5.55×10 <sup>-2</sup> | 5.47×10 <sup>-2</sup> | 5.44×10 <sup>-2</sup> | 1.24×10 <sup>-3</sup> |
|                       | Area                                 | 4.88×10 <sup>-2</sup> | 5.02×10 <sup>-2</sup> | 5.00×10 <sup>-2</sup> | 4.97×10 <sup>-2</sup> | 7.36×10 <sup>-4</sup> |

### **3.2 A Latent Mechanoacid for Time-Stamped Mechanochromism and Chemical Signaling in Polymeric Materials <sup>IV</sup>**

Mechanically coupled proton transduction offers potential for stress-responsive polymeric materials whose properties can be switched via acid triggered coloration, polymerization/crosslinking, or degradation. The utility of currently available mechanoacids, however, is limited by modest force-free stability or a scissile response that caps mechanoacid generation at one proton per strained polymer chain. Here, we report a new mechanoacid based on 2-methoxy-substituted *gem*-dichlorocyclopropane (MeO-gDCC). Pulsed ultrasonication leads to the mechanochemical ring opening of the MeO-gDCC and the subsequent elimination of either HCl or MeCl, with ~0.58 equivalents of HCl released per mechanophore activation, and ~67 protons per chain scission event. Single molecule force spectroscopy reveals that, the methoxy substituent lowers the force required for rapid ( $k_{\text{open}} \sim 10^2 \text{ s}^{-1}$ ) ring opening to ca. 900 pN, vs. 1300 pN required for the parent gDCC. The utility of the mechanoacid is demonstrated in silicone elastomers, where its mechanical activation leads to a strain-triggered color change prior to fracture of the elastomer. The post-activation kinetics of coloration are used to demonstrate a new concept in mechanochromism, namely not only a spectroscopic indicator of whether and where a mechanical event has occurred, but when it occurred.

---

<sup>IV</sup> This chapter is adopted from: Lin, Y.; Kouznetsova, T. B.; Craig, S. L. A Latent Mechanoacid for Time-Stamped Mechanochromism and Chemical Signaling in Polymeric Materials. *J. Am. Chem. Soc.* **2020**, *142*, 99-103.

### 3.2.1 Introduction

The strategic introduction of mechanophores can transduce typically destructive mechanical loads into constructive chemical responses,<sup>20-21, 58, 60</sup> including stress-responsive polymer properties such as stress-reporting,<sup>31, 35, 116-118</sup> mechanocatalysis,<sup>40</sup> the release of chemical cargo,<sup>42, 44-45, 47, 115</sup> and stress-strengthening.<sup>36, 51, 123</sup> One of the most broadly useful chemical species remains the proton, and applications of acids in polymer modification include polymerization/crosslinking reactions,<sup>235-237</sup> polymer degradation,<sup>238-239</sup> and pH-sensitive phase transitions.<sup>240</sup> For this reason, there is considerable interest in developing latent, force-triggered acids (mechanoacids) for multipurpose stress-responsive materials.

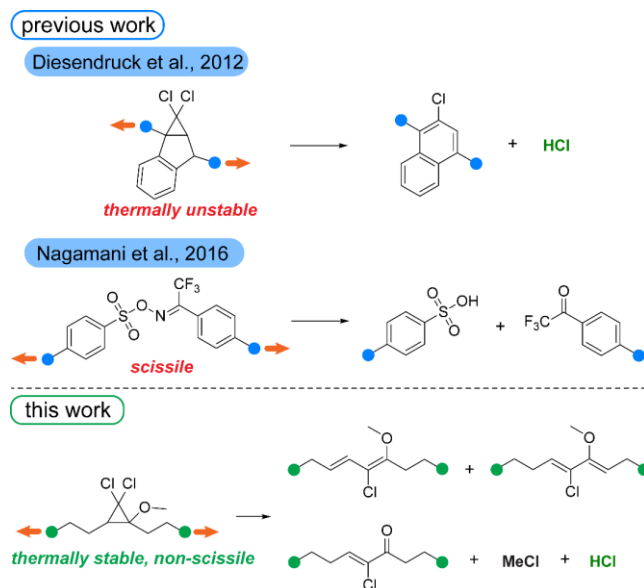


**Figure 138 : Previously reported mechanoacids and new design in this work.**

The current mechanoacid toolkit, however, is rather limited (Figure 138). Diesendruck et al.<sup>43</sup> reported a *gem*-dichlorocyclopropane (gDCC) based mechanoacid that combines an initial, mechanically triggered ring-opening reaction with a subsequent

force-free aromatization to that liberates HCl. The utility of this elegant design is limited somewhat, however, by the modest thermal stability of the mechanophore. Subsequent work by Nagamani<sup>241</sup> creatively repurposed a known oxime photoacid<sup>242</sup> as a stable mechanoacid with efficient acid release upon mechanophore scission. The fact that acid generation is coupled to scission, however, limits acid generation to a single proton per breaking chain.

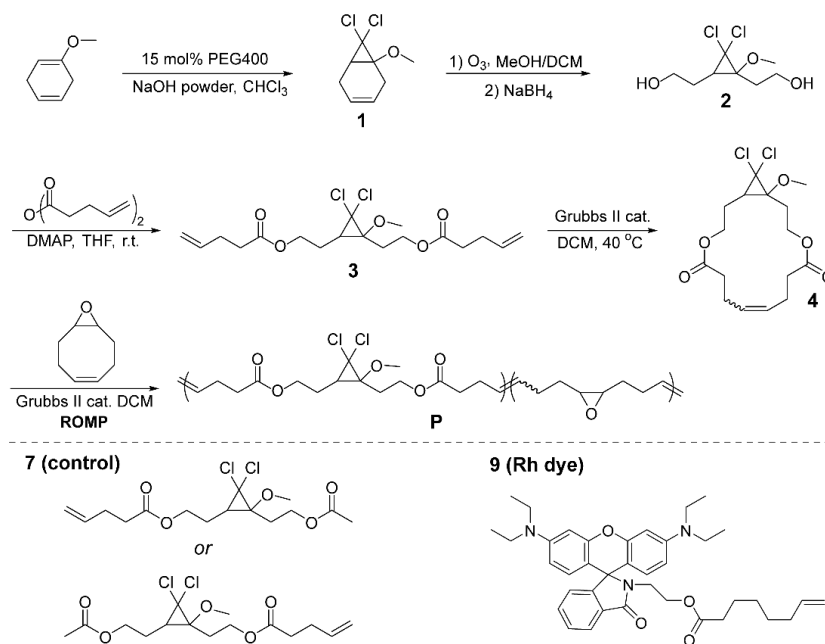
Against this backdrop, we were delighted to find in the course of other work that gDCC derivatives that contain an alkoxy substituent on the cyclopropane core, as shown in Figure 138, spontaneously eliminate HCl from the 2,3-dichloroalkene product of thermally driven ring opening, leading to the production of chlorodienes.<sup>243-247</sup> This behavior is not observed in unsubstituted gDCC analogs, and is attributed to the alkoxy substituent stabilizing developing cationic character during chloride dissociation from the ring-opened product.<sup>243, 248</sup> Subsequent deprotonation accounts for the chlorodiene product.<sup>243, 246</sup> We hypothesized that coupling mechanical force to a similar methoxy substituted gDCC derivative (MeO-gDCC) would lead to mechanical generation of HCl.

### 3.2.2 Results and discussion

Our synthetic strategy is shown in Scheme 5. MeO-gDCC containing **1** was prepared from the selective cyclopropanation of the electron-rich alkene of commercially available 1-methoxyl-1,4-cyclohexadiene using a protocol<sup>213</sup> that avoids the tedious workup involved with conventional phase transfer agents (e.g., tetrabutylammonium salts). Subsequent ozonolysis and reduction produces diol **2** as a colorless oil. The diacetic

ester of **2** is quite stable, with no reaction observed by  $^1\text{H}$  NMR after heating in toluene-*d*<sub>8</sub> at 110 °C for one day (Figure 143). Even at 138 °C, ring opening occurs on the timescale of hours in diphenyl ether (Figure 144), establishing that MeO-gDCC has sufficient thermal stability for a range of potential applications.

**Scheme 5 : Top: Mechanoaphore and polymer synthesis. Bottom: control molecule and rhodamine dye used in this study.**



To test its mechanochemical activity, we incorporated multiple repeats of MeO-gDCC into a polymer backbone using strategies employed previously in other systems.<sup>45, 109, 170</sup> Briefly, **2** was esterified to diene **3** with 4-pentenoic anhydride, and ring closing metathesis (RCM) yielded macrocycle **4**. Ring opening metathesis co-polymerization (ROMP) of **4** with 9-oxabicyclo[6.1.0]non-4-ene gave multi-mechanoaphore containing polymer **P** ( $M_n = 99$  kDa, 47 mol% MeO-gDCC) (Scheme 5). This copolymer is suitable for

both ultrasonication and single molecule force spectroscopy (SMFS) studies using previously reported procedures.<sup>84, 87-88, 109</sup>

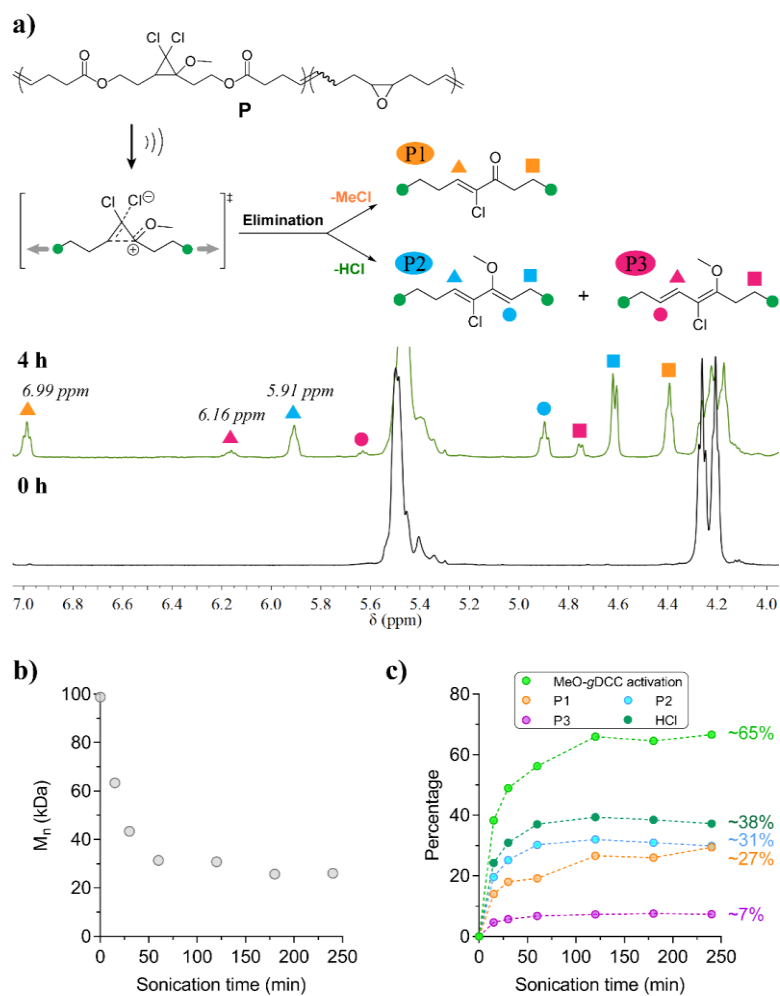


**Figure 139 :** a) <sup>1</sup>H NMR spectra (CDCl<sub>3</sub>, 500 MHz) of polymer P before and after 4 h sonication and peaks assigned to products P1, P2 and P3; relative peak integration 27:31:7; b) Change in  $M_n$  with sonication time; c) Fractional MeO-gDCC activation and product abundance as a function of sonication time.

As shown in Figure 139, pulsed ultrasonication of polymer P for 4 h reduces  $M_n$  from 99 kDa to 26 kDa and generates three new species with corresponding characteristic peaks at  $\delta = 6.99$  ppm, 6.16 ppm, and 5.91 ppm in the <sup>1</sup>H NMR spectrum. These species were identified as P1, P2, and P3, respectively (Figure 139a), as has been reported

previously in a related system.<sup>243, 248</sup> The mechanochemical generation of HCl was confirmed by adding pH indicator rhodamine B to the sonicated polymer solution. As expected, the solution turned pink immediately, signaling the protonation of rhodamine B (Fig. S3).

The consumption of MeO-gDCC plateaus at ~65% activation after 2 h sonication, and the production of **P1**, **P2**, and **P3** saturates on a similar timescale at 27%, 31%, and 7% relative to initial MeO-gDCC, respectively (Figure 139c). The product ratio corresponds to ~0.58 equivalents of HCl per MeO-gDCC activation. The accumulation of HCl during ongoing MeO-gDCC activation is evidenced by an increase in the characteristic UV-vis absorption spectrum of protonated rhodamine B when indicator is added to the sonicated solutions (Figure 146). The ring opening competes well with chain scission of **P**; 67 protons are released on average per chain scission event.

We used SMFS protocols developed in our lab<sup>84, 87, 109</sup> to quantify the mechanochemical response of MeO-gDCC. A typical SMFS curve of **P** is shown in Figure 140. The key feature is a characteristic plateau that corresponds to the force-coupled ring opening of the mechanophores, which lead to a longer polymer product. The observed extension matches determined from CoGEF calculations based on the product distribution observed from sonication (see section 3.2.3.7).

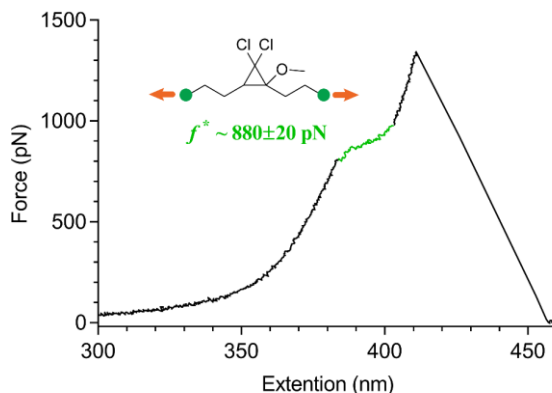


**Figure 140 : Representative force-extension curve of MeO-gDCC containing ROMP copolymer P in toluene (MeO-gDCC content: 47 mol%); retraction velocity = 300 nm/s.**

The transition force for MeO-gDCC occurs at  $880 \pm 20$  pN, which is the force necessary to increase the rate constant of ring opening to  $\sim 10^2$  s<sup>-1</sup>. This force is substantially lower than that of the unsubstituted parent gDCC ( $1330 \pm 70$  pN),<sup>84</sup> which we attribute to stabilization of the ring opening transition state by the methoxy substituent. In support of this conclusion, the calculated activation energy of MeO-gDCC is  $\sim 9$  kcal/mol lower than that of unsubstituted gDCC (Figure 149). One would expect that greater dissociative character in the mechanism would translate to an earlier transition state, and fitting the SMFS curves with kinetic models based on a cusp-like potential energy surface gives a  $\Delta x^\ddagger$  value of  $1.07 \pm 0.02$  Å that is  $\sim 0.2$  Å less than that of the parent gDCC ( $1.28 \pm 0.05$  Å). In other words, the transition state of the MeO-gDCC occurs earlier on the disrotatory torsional reaction coordinate than that of unsubstituted gDCC. Computational transition state geometries of the two systems are qualitatively and quantitatively consistent with the difference in activation lengths inferred from the SMFS data (Figure 149). The derived

force-rate relationships translate to the ring opening of MeO-gDCC being  $\sim 10^6$  fold faster than unsubstituted gDCC at 880 pN force (see section 3.2.3.5.2).

**Table 17 : Force-free activation energies, mechanical coupling  $\Delta x^\ddagger$ , and transition force of gDCC and MeO-gDCC.**

| Mechanophore | $\Delta G^\ddagger$ (kcal/mol) | $\Delta x^\ddagger$<br>(Cusp) (Å) | f (pN)        |
|--------------|--------------------------------|-----------------------------------|---------------|
| gDCC*        | 36.2                           | 1.28 $\pm$ 0.05                   | 1330 $\pm$ 70 |
| MeO-gDCC     | 27.2                           | 1.07 $\pm$ 0.02                   | 880 $\pm$ 20  |

\*Data from Wang et al.<sup>84</sup>

We wondered if the enhanced activity from the methoxy substituent would allow the mechanophore to be activated in detectable amounts in bulk materials prior to the onset of irreversible mechanical damage. Mechanoacid diene **3** (0.5 wt% of polymer) and rhodamine dye **9** (proton indicator, 10 mol% of **3**) were covalently embedded into a poly(dimethylsiloxane) (PDMS) network using reported procedures (Figure 141a),<sup>115</sup> producing a clear pale-pink elastomer. The same color appears in samples made without **3**, and so is not due to acid generation but might result from platinum induced ring-opening as observed with some rhodamine derivatives.<sup>249-250</sup> As seen in Figure 141b, applying a tensile strain to a rectangular film leads to the expected pink color in the deformed region. The contrast is more dramatic in fluorescent images, where the bright yellow fluorescence of protonated rhodamine under 365 nm irradiation is evident. The mechanochromic and fluorescence responses are also observed under both global and local compression of PDMS cylinders. Quantitative analysis from UV-vis measurement reveals that compression of a PDMS cylinder leads to  $\sim 0.2\%$  activation of mechanoacid (Figure 153).

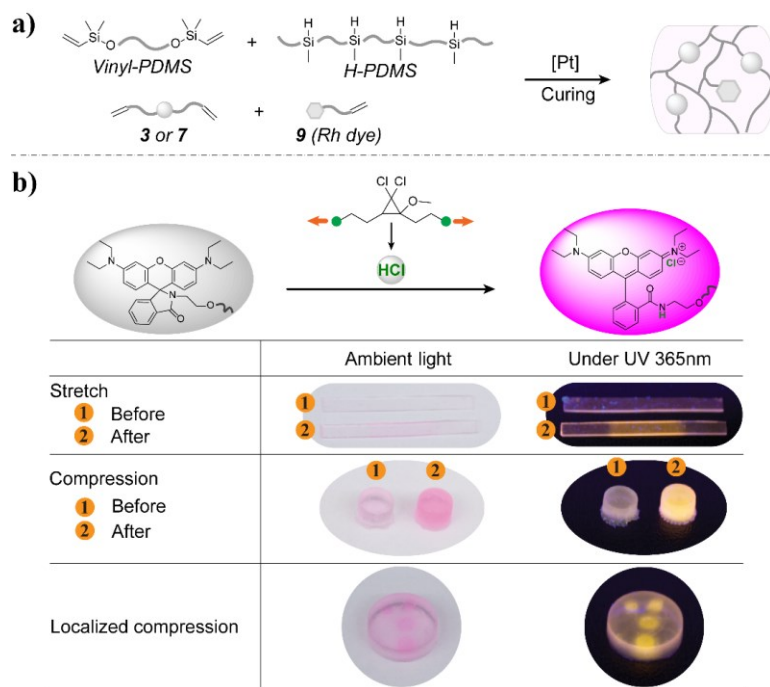


**Figure 141 : a) Preparation of PDMS elastomer containing active/control mechanoacid and rhodamine indicator. b) Demonstration of using mechanoacid to indicate mechanical load under stretch, compression and localized compression in PDMS elastomer. Protonated rhodamine shows pink color under ambient light and yellow fluorescence under UV 365nm light.**

To confirm that the acid is generated by direct mechanochemical coupling, we prepared two control samples: one incorporating the same amount of **9** but no **3**, and the other incorporating **9** and control molecule **7** (0.5 wt% of polymer). Neither control material exhibits a detectable change in color or fluorescence after the same tensile strain, compression, or localized compression used to activate the material with **3** (Figure 154, 155).

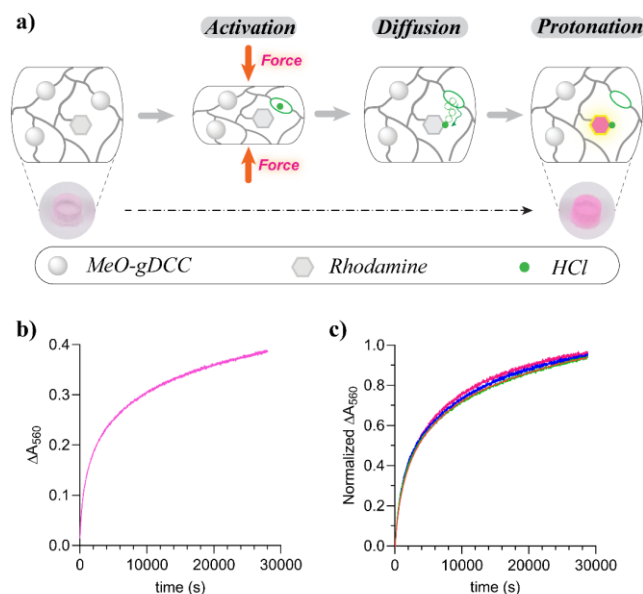


**Figure 142 : a) Schematic of mechanoacid activation, acid diffusion, and rhodamine protonation in a silicone matrix. b) Representative kinetics of absorption at 560 nm ( $A_{560}$ ) after hammer strike. c) Overlay of four normalized coloration kinetics. The average rate constant of the empirical fast ( $k_f = (8.9 \pm 1.3) \times 10^{-4} \text{ s}^{-1}$ ) and slow ( $k_s = (8.2 \pm 0.8) \times 10^{-5} \text{ s}^{-1}$ ) phases and relative contribution of the fast phase ( $f\% = (39 \pm 1)\%$ ) are retrieved.**

Unlike existing mechanophore based signaling, the mechanochromic and fluorescence response in this system involves a bimolecular reaction between the mechanochemical product (the acid) and the indicator (rhodamine).<sup>251</sup> Thus, the color change is not instantaneous but develops over time following the activation event. We reasoned that, if the post-activation kinetics of rhodamine response were reproducible, the time-dependent change in signal could be extrapolated back to give the time at which the signal initiated – a sort of kinetic “time change in absorbance of a PDMS cylinder in response to a hammer strike (Figure 142b) is not consistent with a first order kinetic process, but can be reasonably fit with a two-phase exponential function. More importantly, the general features of the temporal response are well preserved across

several individual measurements (Figure 142c), even though the absolute magnitude of the response varies from one triggering event to the next.

**Table 18 : Kinetically regulated “time stamp” calculations of the occurrence of a triggering mechanical event.**

|                   | 1     | 2      | 3      |
|-------------------|-------|--------|--------|
| $t_{\text{wait}}$ | 6 min | 12 min | 26 min |
| $t_{\text{calc}}$ | 8 min | 18 min | 31 min |

The reproducibility in the normalized response allows us to take late time points and extrapolate the evolution in signal back to the time of the triggering event, without having observed the triggering event itself. This approach was tested by using the full average time-dependent response of four systems to extrapolate an apparent activation point from the late-time behavior in another sample, as follows. A sample was struck by a hammer, and absorbance was measured as a function of time following an interval  $t_{\text{wait}}$ . The collected kinetics data were fit to the form of the average empirical two exponential fit of the control sample data, using the delay time  $t_{\text{wait}}$  as the only adjustable parameter (see section 3.2.3.6.2 for details). The delay time that provides the best fit is termed  $t_{\text{calc}}$ , and it is compared to the corresponding values of  $t_{\text{wait}}$  in Table 18. While there is some deviation between the actual and extrapolated time points, this simple concept and as yet unoptimized methodology correctly identify the most recent and most distant past events, and provide reasonable but rough estimates of the actual times at which the triggering events occurred.

The mechanochromic response in a bulk elastomer reported here is, to the best of our knowledge, the first demonstration of a mechanoacid in a bulk material. That advance is empowered by a MeO-gDCC mechanophore that is both thermally stable enough to be cured into the network with minimal activation, and mechanically active enough to produce a response that is easily detected. The ease of synthesis further bodes well for the use of MeO-gDCC in future applications where mechanoacids are desirable. Among the possibilities is the simple but potentially empowering concept of “time stamping” reported here. The ability to report not only whether and where a mechanical event occurred, but *when* it occurred, offers a potentially useful capability for stress-responsive materials based on mechanophores, and careful study of the governing kinetics and optimization of the system design are likely to improve the resolution and reproducibility of the method. It is notable that the diffusive nature of the kinetics necessary for time stamping do not come at the expense of all spatial resolution, and the position of localized events is also discernable. Because protons are such highly functional species, we foresee additional opportunities in a range of mechanically adaptive contexts, including (but not limited to) mechanically degradable, self-healing and stress-strengthening polymeric materials.

### **3.2.3 Experimental section**

#### **3.2.3.1 Materials and characterization**

Materials: Lab general solvents (dichloromethane, chloroform, hexane, ethyl acetate, acetone, toluene, tetrahydrofuran, methanol) were purchased from VWR or

Sigma Aldrich. 1-methoxy-1, 4-cyclohexadiene, NaOH powder, sodium borohydride, 4-pentenoic anhydride, dimethyl aminopyridine (DMAP), rhodamine B base, p-Toluenesulfonyl chloride, aminoethanol, 7-octenoic acid, 1, 2-epoxy-5-cyclooctene, Grubbs 2 catalyst were purchased from Sigma Aldrich or Alfa Aesar and used without further purification. Sylgard®184 was purchased from Ellsworth Adhesives, Germantown, WI. Flash chromatography was performed on CombiFlash®200 auto-column system from Teledyne ISCO.

Characterizations: <sup>1</sup>H NMR spectra were collected on a 400 MHz Varian INOVA spectrometer and <sup>13</sup>C NMR spectra were collected on a 500 MHz Varian UNITY spectrometer. Chemical shifts are given in *ppm* ( $\delta$ ) and referenced to the residual <sup>1</sup>H peak at 7.26 ppm or <sup>13</sup>C peak at 77.16 ppm in CDCl<sub>3</sub>. <sup>1</sup>H shifts are reported as chemical shift, multiplicity, coupling constant if applicable, and relative integral. Multiplicities are reported as: singlet (s), doublet (d), doublet of doublets (dd), doublet of triplets (dt), doublet of doublet of doublets (ddd), doublet of doublet of triplets (ddt), triplet (t), triplet of doublets (td), quartet (q), multiplet (m), or broad (br). Coupling constants (J) are reported in Hertz. High-resolution mass spectra were collected on an Agilent LCMS-TOF-DART at Duke University's Mass Spectrometry Facility. Gel permeation chromatography (GPC) was performed on two Agilent PLgel mixed-C columns (10<sup>5</sup> Å, 7.5x300 mm, 5  $\mu$ m, part number PL1110-6500) using THF (stabilized with 100 ppm BHT) as the eluent. Molecular weights were calculated using a Wyatt Dawn EOS multi-angle light scattering (MALS) detector and Wyatt Optilab DSP Interferometric Refractometer (RI). The

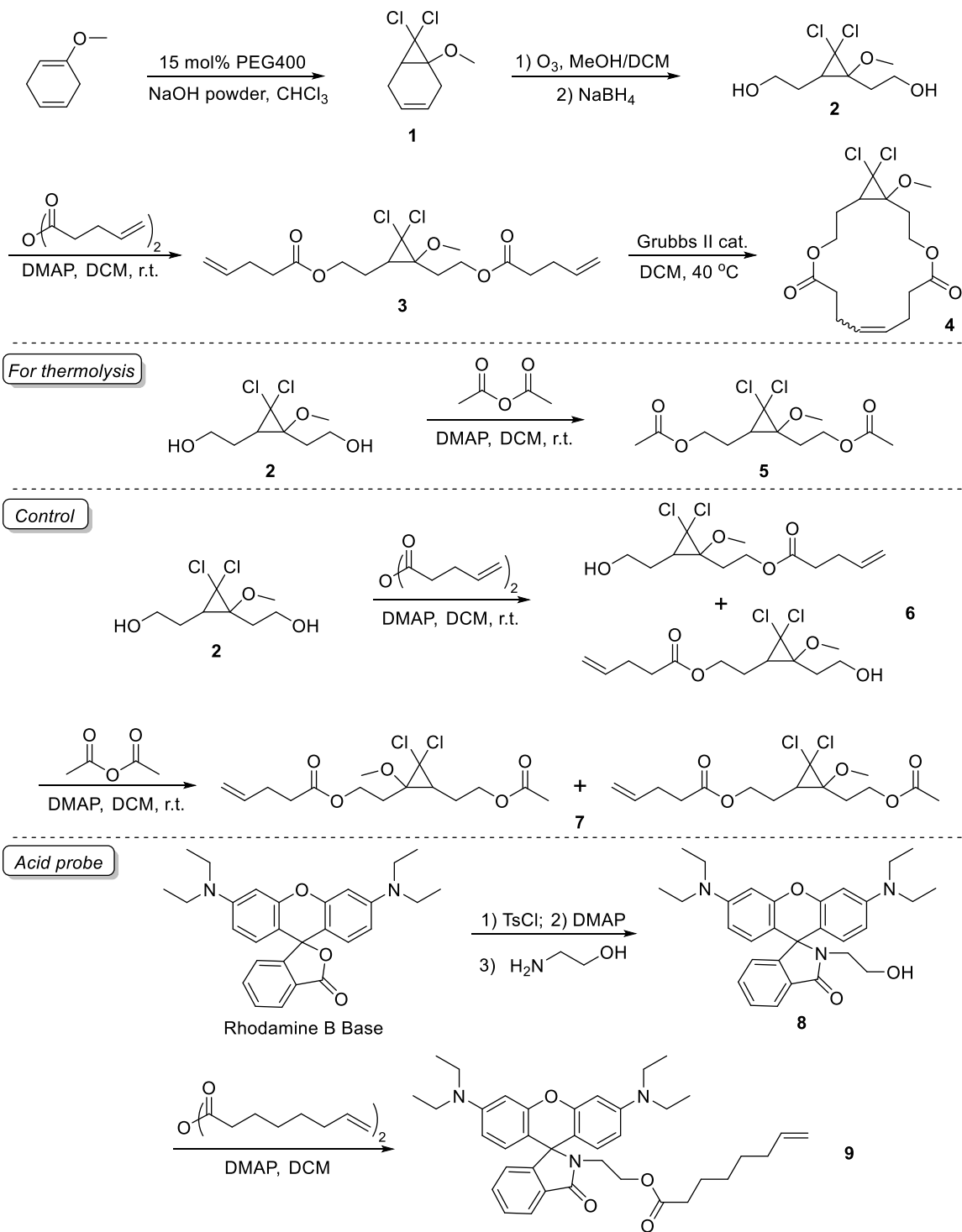
refractive index increment ( $dn/dc$ ) values were determined by online calculation based on injections of known concentration and mass. UV-vis spectra were collected on a Varian Cary 500 UV-Vis Spectrophotometer.

Single molecule force spectroscopy: Sharp Microlever silicon probes (MSNL) and Silicon Nitride AFM Probes (PNP-DB) were correspondingly purchased from Bruker (Camarillo, CA) and NanoAndMore(Watsonville, CA). All of the SMFS studies were conducted at ambient temperature ( $\sim 23$  °C) using a homemade AFM, which was constructed using a Digital Instruments scanning head mounted on top of a piezoelectric positioner, similar to the one described in detail previously.<sup>82, 84</sup> The AFM pulling experiments were conducted in a solution of toluene. The spring constant of each cantilever was calibrated in air, using the thermal noise method, based on the energy equipartition theorem as described previously.<sup>82, 84</sup> Measurements were carried out in a closed fluid cell with a scanning set for a series of approaching/retracting cycles. Probes were prepared by immersing in piranha solution ( $H_2SO_4$ :  $H_2O_2$  = 3:1) for 15 minutes at room temperature and then immersing in deionized water and dried by touching them against a borohydride. Silicon substrates were prepared by first allowing each to soak in hot piranha solution for 30 minutes and then washed with deionized water and dried under a stream of nitrogen. Caution should be used when handling piranha solution: it has been reported to detonate unexpectedly. The substrate and the cantilever were then placed in a UVO cleaner (ozone produced through UV light) for 15 minutes. After ozonolysis, the cantilever was mounted in the fluid cell. 20  $\mu$ L of a 0.05-0.1 mg/mL

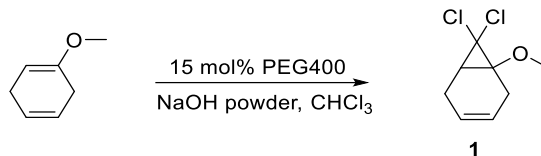
polymer solution was added to the silicon substrate surface and allowed to dry. The silicon substrate was then placed on the piezoelectric stage of the AFM. Force curves were collected in dSPACE (dSPACE Inc. Wixom, MI) and analyzed using Matlab (The MathWorks, Inc., Natick, MA). All data were filtered during acquisition at 500 Hz. After acquisition, the data were calibrated and plotted by using homemade software written in Matlab language.

### 3.2.3.2 Synthetic procedures

#### 3.2.3.2.1 Synthesis of small molecules



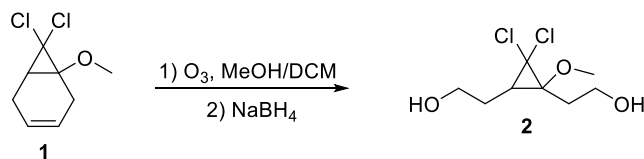
Synthesis of compound 1:



The synthesis of methoxyl substituted *gem*-dichlorocyclopropane (MeO-gDCC) was performed using reported protocol.<sup>213</sup>

To a solution of 1-methoxy-1, 4-cyclohexadiene (1.10 g, 10 mmol) in 20 mL of chloroform, added PEG400 ( $M_n = 400$ , 600 mg, 1.5 mmol) as phase transfer catalyst. The solution was cooled with an ice bath. NaOH powder (1.2 g, 30 mmol) was then added in portions. The solution turned dark green. After stirred for 30 min, 100 mL of Et<sub>2</sub>O was added to the mixture. Insoluble solid was filtered, and the filtrate was washed with 25 mL 1 N HCl, 5 × 25 mL DI water and then 25 mL brine. The organic phase was further dried with MgSO<sub>4</sub>. After filtration, the solvent was removed under reduced pressure, a colorless liquid was obtained (1.90 g, 98%). <sup>1</sup>H and <sup>13</sup>C NMR indicated > 90% purity of compound 1. This liquid was used without further purification. <sup>1</sup>H NMR (400 MHz, CDCl<sub>3</sub>): δ 5.54 (m, 2H), 3.49 (s, 3H), 2.74 – 2.49 (m, 3H), 2.30 – 2.16 (m, 1H), 1.84 (d,  $J = 7.93$  Hz, 1H). <sup>13</sup>C NMR (125 MHz, CDCl<sub>3</sub>): δ 122.60, 122.17, 67.37, 63.62, 54.56, 31.52, 24.13, 21.09.

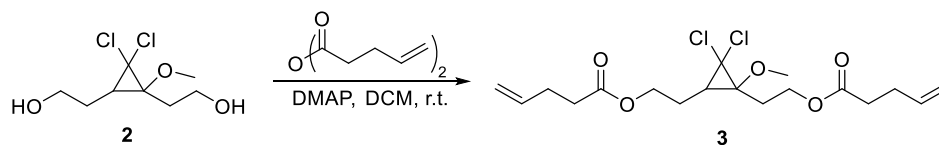
Synthesis of compound 2:



Compound 1 (0.965 g, 5 mmol) was dissolved in 15 mL of methanol/DCM (2:1). The solution was cooled to -78 °C and O<sub>3</sub> was then bubbled through. The solution turned

blue after 10 min. TLC (25% EtOAc/Hexane) indicated that the reactant had been completely consumed. O<sub>2</sub> was then bubbled through to remove excess O<sub>3</sub>. The solution turned colorless after 15 min. NaBH<sub>4</sub> solid (950 mg, 50 mmol) was then added in portions at -78 °C. The mixture was slowly warmed to r.t. and stirred for overnight. After the reaction completed, MeOH was removed and 25 mL DI water was added to the residual. The mixture was extracted with 3×25 mL Et<sub>2</sub>O. The combined organic phase was dried with MgSO<sub>4</sub> and condensed. Residual was purified with flash chromatography (0~100% EtOAc/Hexane gradient elution) to give compound **2** as a colorless oil (867 mg, 77.8%). <sup>1</sup>H NMR (400 MHz, CDCl<sub>3</sub>): δ 3.96 – 3.73 (m, 4H), 3.46. (s, 3H), 2.20-2.10 (m, 2H), 2.02 – 1.91 (m, 1H), 1.75 (m, 2H). <sup>13</sup>C NMR (125 MHz, CDCl<sub>3</sub>): δ 68.26, 67.34, 61.02, 58.86, 54.83, 37.13, 28.94, 28.20. HRMS-ESI (*m/z*): [M+H]<sup>+</sup> calculated for C<sub>8</sub>H<sub>14</sub>Cl<sub>2</sub>O<sub>3</sub>, 229.03928; observed, 229.03865.

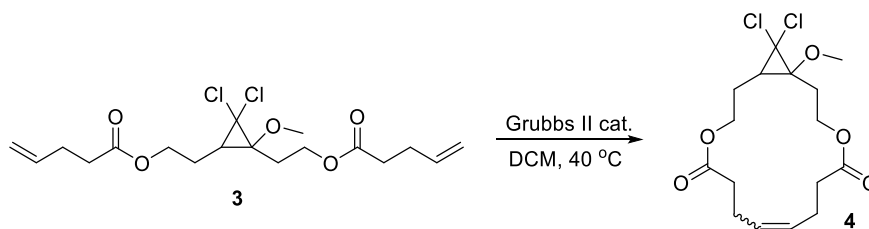
### Synthesis of compound **3**



To a solution of compound **2** (458 mg, 2 mmol) in 10 mL of DCM, added DMAP (24.4 mg, 0.2 mmol). Pentenoic anhydride (766 μL, 4.2 mmol) was then added dropwise to the solution. After stirred at room temperature for overnight, DMC was removed. The residual was purified by flash chromatography (0~25% EtOAc/Hexane gradient elution) to give product **3** as a colorless oil (716 mg, 91.1%). <sup>1</sup>H NMR (400 MHz, CDCl<sub>3</sub>): δ 5.92 – 5.69 (m, 2H), 5.16 – 4.94 (m, 4H), 4.27 (t, *J* = 7.1 Hz, 2H), 4.21 (t, *J* = 6.3 Hz, 2H), 3.43 (s, 3H),

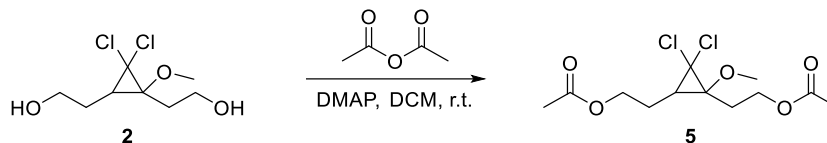
2.51 – 2.32 (m, 8H), 2.23 (m, 1H), 2.04 – 1.92 (m, 1H), 1.92 – 1.71 (m, 2H), 1.67 (dd,  $J = 8.3$ , 5.7 Hz, 1H).  $^{13}\text{C}$  NMR (125 MHz,  $\text{CDCl}_3$ ):  $\delta$  172.85, 136.58, 115.64, 67.34, 67.22, 62.47, 60.16, 54.66, 36.40, 33.49, 28.81, 25.38, 24.98. HRMS-ESI ( $m/z$ ):  $[\text{M}+\text{H}]^+$  calculated for  $\text{C}_{18}\text{H}_{26}\text{Cl}_2\text{O}_5$ , 393.12301; observed, 393.12223.

Synthesis of macrocycle 4:



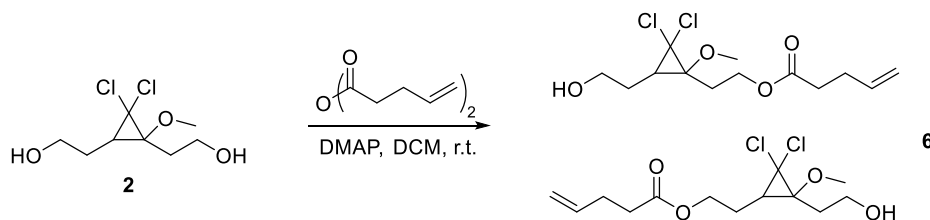
Compound 3 (393 mg, 1 mmol) was dissolved in 500 mL of  $\text{DCM}$ , and the solution was bubbled with  $\text{N}_2$  for 10 min. Grubbs catalyst 2 (85 mg, 0.1 mmol) was added in one portion. The solution was heated at  $40\text{ }^\circ\text{C}$  for overnight. After completion, solution was condensed onto silica. Pure macrocycle 4 was obtained as a colorless oil (343 mg, 94.0%) after flash chromatography (0~25%  $\text{EtOAc}$ /Hexane gradient elution). The oil solidified after standing for several days.  $^1\text{H}$  NMR (400 MHz,  $\text{CDCl}_3$ ):  $\delta$  5.56 – 5.35 (m, 2H), 4.54 – 4.42 (m, 1H), 4.54 – 4.27 (m, 2H), 4.16 – 3.97 (m, 1H), 3.47 (s, 3H), 2.56 – 2.18 (m, 8H), 2.15 – 2.06 (m, 1H), 2.02 – 1.91 (m, 1H), 1.89 – 1.75 (m, 1H), 1.73 – 1.60 (m, 2H).  $^{13}\text{C}$  NMR (125 MHz,  $\text{CDCl}_3$ ):  $\delta$  172.80, 172.33, 130.10, 129.80, 67.08, 66.46, 62.06, 59.52, 54.65, 37.00, 34.69, 34.52, 28.21, 26.63, 25.81. HRMS-ESI ( $m/z$ ):  $[\text{M}+\text{H}]^+$  calculated for  $\text{C}_{16}\text{H}_{22}\text{Cl}_2\text{O}_5$ , 365.09171; observed, 365.09145.

Synthesis of compound 5:



To a solution of **2** (229 mg, 1mmol) in 3 mL of DCM, added DMAP (6.1 mg, 0.05 mmol). Acetic anhydride (284  $\mu$ L, 3 mmol) was then added dropwise to the solution. The reaction was stirred at r.t. for overnight. After the reaction completed, the solvent was removed and product was purified by flash chromatography (0~25% EtOAc/hexane gradient). A colorless liquid **5** was obtained (215 mg, 68.6%).  $^1\text{H}$  NMR (400 MHz,  $\text{CDCl}_3$ ):  $\delta$  4.26 (td,  $J = 7.0, 1.2$  Hz, 2H), 4.20 (td,  $J = 6.4, 0.9$  Hz, 2H), 3.43 (s, 3H), 2.24 (m, 1H), 2.09 (s, 3H), 2.07 (s, 3H), 2.03 – 1.92 (m, 1H), 1.91 – 1.71 (m, 2H), 1.67 (dd,  $J = 8.1, 6.0$  Hz, 1H).  $^{13}\text{C}$  NMR (125 MHz,  $\text{CDCl}_3$ ):  $\delta$  171.02, 67.41, 67.26, 62.62, 60.25, 54.72, 36.50, 25.41, 25.00, 21.09, 21.02. HRMS-ESI ( $m/z$ ):  $[\text{M}+\text{H}]^+$  calculated for  $\text{C}_{12}\text{H}_{18}\text{Cl}_2\text{O}_5$ , 313.06041; observed, 313.06007.

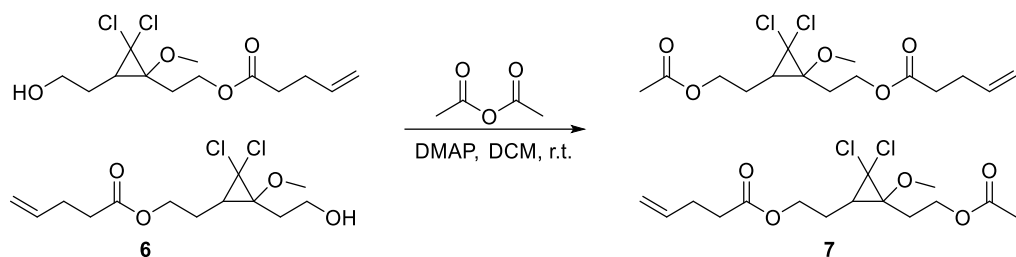
Synthesis of compound **6**:



In a 20 mL scintillation vial, added compound **2** (140 mg, 0.6 mmol), DMAP (7.3 mg, 0.06 mmol) and 3 mL DCM. Then, 4-pentenoic anhydride (110  $\mu$ L, 0.6 mmol) was then added dropwise to the solution. The reaction was stirred overnight. After the reaction completed, 100  $\mu$ L triethylamine was then added. DCM was removed and residual was subjected to flash chromatography (0~50% EtOAc/hexane eluent). Compound **6** was

obtained as a colorless liquid (82 mg, 43.9%).  $^1\text{H}$  NMR (400 MHz,  $\text{CDCl}_3$ ):  $\delta$  = 5.83 (ddt,  $J$  = 16.5, 10.1, 6.1 Hz, 1H), 5.14 – 4.95 (m, 2H), 4.36 – 4.19 (m, 2H), 3.93 – 3.81 (m, 2H), 3.44&2.97 (s, 3H), 2.50 – 2.34 (m, 4H), 2.23 – 1.96 (m, 1H), 1.96 – 1.63&1.52 (m&t,  $J$  = 5.2 Hz, 4H).  $^{13}\text{C}$  NMR (125 MHz,  $\text{CDCl}_3$ ):  $\delta$  173.17, 173.11, 136.75, 136.69, 115.81, 115.74, 68.56, 67.63, 67.60, 62.67, 61.32, 60.45, 59.60, 54.91, 54.81, 36.70, 36.56, 33.68, 33.65, 29.11, 28.95, 28.93, 28.22, 25.62, 25.21. HRMS-ESI ( $m/z$ ):  $[\text{M}+\text{H}]^+$  calculated for  $\text{C}_{13}\text{H}_{20}\text{Cl}_2\text{O}_4$ , 311.08114; observed, 311.08078.

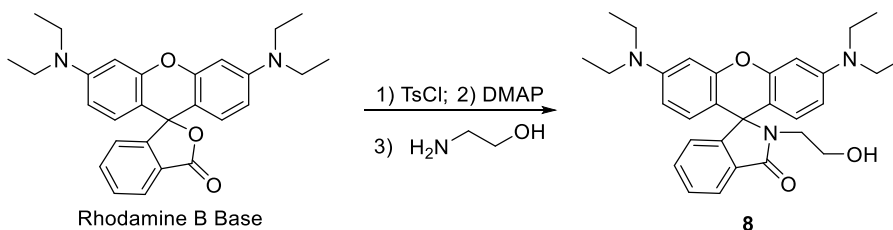
#### Synthesis of compound 7:



To a solution of compound **6** (66 mg, 0.21 mmol) and DMAP (2.5 mg, 0.02 mmol) in 2 mL DCM, added acetic anhydride (40 mg, 0.42 mmol) dropwise. The reaction was stirred overnight. The product was purified by flash chromatography (0~30% EtOAc/hexane gradient). Compound **7** was obtained as a colorless oil (65.5 mg, 88.4%).  $^1\text{H}$  NMR (400 MHz,  $\text{CDCl}_3$ ):  $\delta$  = 5.82 (ddtd,  $J$  = 16.3, 10.3, 6.2, 1.4 Hz, 1H), 5.13 – 4.94 (m, 2H), 4.32 – 4.15 (m, 4H), 3.42 (s, 3H), 2.51 – 2.32 (m, 4H), 2.23 (dtd,  $J$  = 16.4, 7.0, 2.3 Hz, 1H), 2.08&2.07 (s, 3H), 1.97 (m, 1H), 1.90 – 1.82 (m, 1H), 1.82 – 1.72 (m, 1H), 1.66 (m, 1H).  $^{13}\text{C}$  NMR (125 MHz,  $\text{CDCl}_3$ ):  $\delta$  = 173.03, 171.02, 136.71, 136.68, 115.79, 115.73, 67.46, 67.31, 62.65, 62.59, 60.29, 60.28, 54.78, 36.55, 36.52, 33.63, 33.61, 28.93, 28.90, 25.50, 25.45, 25.09,

25.05, 21.13, 21.07. HRMS-ESI ( $m/z$ ):  $[M+H]^+$  calculated for  $C_{15}H_{22}Cl_2O_5$ , 353.09171; observed, 353.09155.

Synthesis of compound 8:

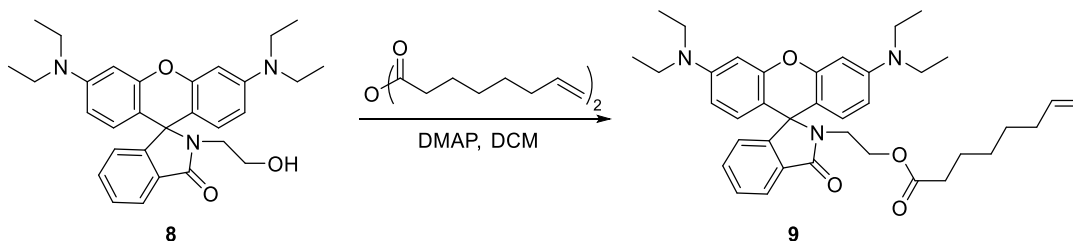


The synthetic procedure was adopted according to reported literature.<sup>252</sup>

Rhodamine B base (2.21 g, 5 mmol) was dissolved in 20 mL  $CH_3CN$ . Tosyl chloride (1.62 g, 8.5 mmol) was then added to the solution and the solution was stirred for 15 min. After DMAP (1.40 g, 11.5 mmol) was added, the solution was stirred for additional 15 min. A solution of enthanolamine (604  $\mu$ L, 10 mmol) in 20 mL  $CH_3CN$  was then added. The reaction was further stirred for overnight. After the reaction completed, insoluble solid was filtered.  $CH_3CN$  was removed under reduced pressure and the resulting residual was dissolved with 150 mL  $Et_2O$ . Washed with 2 $\times$ 50 mL brine. After  $Et_2O$  was removed, product was purified by flash chromatography (50%  $EtOAc$ /hexane). Compound 8 was obtained as an off-white solid (1.73 g, 71.5%).  $^1H$  NMR (500 MHz,  $CDCl_3$ ):  $\delta$  7.94 – 7.86 (m, 1H), 7.48 – 7.39 (m, 2H), 7.07 (m, 1H), 6.49 (d,  $J$  = 8.8 Hz, 2H), 6.38 (d,  $J$  = 2.6 Hz, 2H), 6.29 (dd,  $J$  = 8.9, 2.6 Hz, 2H), 4.21 – 4.13 (m, 1H), 3.47 (q,  $J$  = 5.2 Hz, 2H), 3.33 (q,  $J$  = 7.1 Hz, 8H), 3.30 – 3.24 (t,  $J$  = 4.9 Hz, 2H), 1.16 (t,  $J$  = 7.0 Hz, 12H).  $^{13}C$  NMR (125 MHz,  $CDCl_3$ ):  $\delta$  170.23, 154.04, 153.39, 149.01, 132.82, 130.56, 128.63, 128.26, 123.93, 123.03, 108.35, 104.90, 97.90,

66.00, 62.83, 62.82, 44.79, 44.49, 12.72. HRMS-ESI ( $m/z$ ):  $[M+H]^+$  calculated for  $C_{30}H_{35}N_3O_3$ , 486.27512; observed, 486.27573.

Synthesis of compound 9:

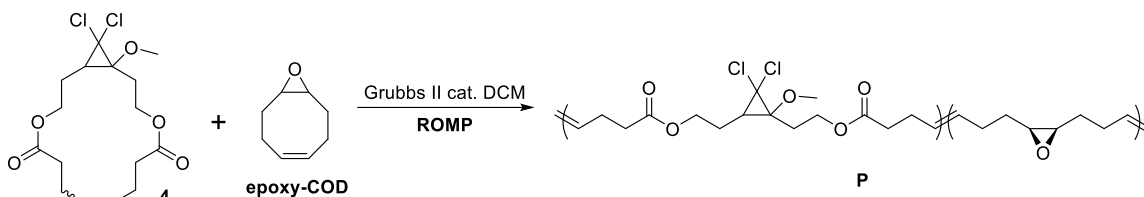


7-Octenoic anhydride was prepared using adopted procedures from previous paper.<sup>87</sup> To a solution of 7-Octanoic acid (1.54 mL, 10 mmol) in 25 ml DCM, added *N,N'*-dicyclohexylcarbodiimide (1.07 g, 5.2 mmol). The reaction was stirred overnight and the resulting insoluble solid was filtered. DCM was removed and 30 mL hexane was added to dissolve the residual. Insoluble solid was further filtered and collected filtrate was condensed under reduced pressure. The resulting liquid was used without further purification.

To a 20 mL scintillation vial, compound 7 (485 mg, 1 mmol) and DMAP (12 mg, 0.1 mmol) were dissolved with 10 mL THF. Octanoic anhydride (319 mg, 1.2 mmol) was then added dropwise. After the reaction was stirred overnight, solvent was removed and the residual was subjected to flash chromatography to give compound 9 as a white solid (600 mg, 95.8%). <sup>1</sup>H NMR (500 MHz, CDCl<sub>3</sub>):  $\delta$  7.94 – 7.85 (m, 1H), 7.46 – 7.38 (m, 2H), 7.11 – 7.00 (m, 1H), 6.45 (d,  $J$  = 8.8 Hz, 2H), 6.38 (d,  $J$  = 2.6 Hz, 2H), 6.26 (dd,  $J$  = 8.9, 2.6 Hz, 2H), 5.77 (ddt,  $J$  = 17.0, 10.2, 6.7 Hz, 1H), 5.02 – 4.87 (m, 2H), 3.80 (t,  $J$  = 6.4 Hz, 2H), 3.40 (t,  $J$  = 6.4 Hz, 2H), 3.33 (q,  $J$  = 7.1 Hz, 8H), 2.11 (t,  $J$  = 7.6 Hz, 2H), 2.01 (q,  $J$  = 7.1 Hz, 2H), 1.51 (p,  $J$  =

7.6 Hz, 2H), 1.35 (p,  $J = 7.2$  Hz, 2H), 1.29 – 1.21 (m, 2H), 1.16 (t,  $J = 7.1$  Hz, 12H).  $^{13}\text{C}$  NMR (125 MHz,  $\text{CDCl}_3$ ):  $\delta$  173.41, 168.68, 154.06, 153.36, 148.93, 139.00, 132.61, 130.79, 128.94, 128.09, 123.93, 122.97, 114.48, 108.25, 105.54, 97.88, 64.98, 61.56, 44.48, 39.11, 34.08, 33.70, 28.72, 28.69, 24.73, 12.75. HRMS-ESI ( $m/z$ ):  $[\text{M}+\text{H}]^+$ calculated for  $\text{C}_{38}\text{H}_{47}\text{N}_3\text{O}_4$ , 610.36393; observed, 610.36461.

### 3.2.3.2.2 Synthesis of ROMP polymers



In a 5 mL frame dried scintillation vial, added compound 4 (36.5 mg, 0.1 mmol) and epoxy-COD (12.4 mg, 0.1 mmol). The vial was kept under Ar. To another frame dried scintillation vial, added Grubbs II catalyst (1.4 mg,  $1.67 \times 10^{-3}$  mmol). 2 mL dry DCM was added to dissolve the catalyst and the resulting solution was bubbled with Ar for 3 min. 0.2 mL of the catalyst solution ( $0.14$  mg,  $1.67 \times 10^{-3}$  mmol) was then added to the monomer containing vial. The vial was then sealed and stirred for overnight. Several drops of ethyl vinyl ether were added to quench the polymerization. The viscous solution was further stirred for 30 min. A white polymer was obtained after three times precipitation from MeOH. The polymer was then dissolved in 2 mL DCM, MeOH was slowly added to the solution until the solution turned cloudy. The cloudy suspension was then subjected to centrifuge to separate out a thin layer of polymer at the bottom of the vial. This polymer was collected and further dried under high vacuum and used for single molecule force

spectroscopy test. The molar content of compound **4** was determined to be 47% from  $^1\text{H}$  NMR.

### 3.2.3.2.3 Preparation of PDMS materials

To a 10 mL scintillation vial, added the following small molecules for each sample.

Active: mechanophore **3** (11 mg, 0.5 wt%) and rhodamine **9** (1.7 mg, 10 mol% of **3**)

Control 1: rhodamine **9** (1.7 mg)

Control 2: control mechanophore **7** (11 mg, 0.5 wt%) and rhodamine **9** (1.7 mg, 10 mol% of **3**)

250  $\mu\text{L}$  xylene was then added to the vial to dissolve the small molecule. Sylgard<sup>®</sup> 184 PDMS base part (2.0 g) was added and mixed completely using Vortex. PDMS curing (0.2 g) was then added and further mixed to give a clear mixture and it turned pale pink after a few minutes. This viscous mixture was then degassed and cast on a PP board or a PS dish. Curing at 65  $^{\circ}\text{C}$  for overnight gave a pale pink clear pale-pink material. The pale-pink background color is due to the platinum catalyst induced ring opening of rhodamine dye.

### 3.2.3.3 Thermal stability of mechanoacid

In a dried NMR tube, ~5 mg of compound **5** was dissolved with 0.5 ml toluene- $d_6$ . The NMR tube was then sealed and heated at 110  $^{\circ}\text{C}$  for 0 h, 2 h, 4 h and 25.5 h.  $^1\text{H}$  NMR spectroscopy was collected at each time point. No thermally activated ring-opening product was observed even after 25.5 h.

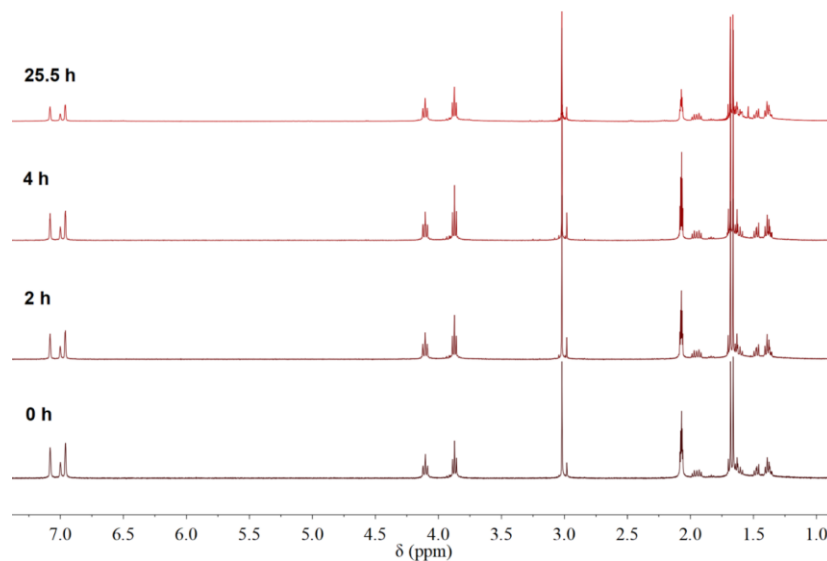


**Figure 143 : Thermal stability test:  $^1\text{H}$  NMR of compound 5 in toluene- $d_6$  heated at 110 °C for different periods of time.**

To a 25 mL dried Schlenk flask, added 100 mg compound 5 and 0.5 mL of diphenyl ether. The flask was heated at 138 °C under  $\text{N}_2$ . Aliquot of 20  $\mu\text{L}$  solution was taken out for  $^1\text{H}$  NMR analysis at each time point (0, 1, 2, 3, 5 h).

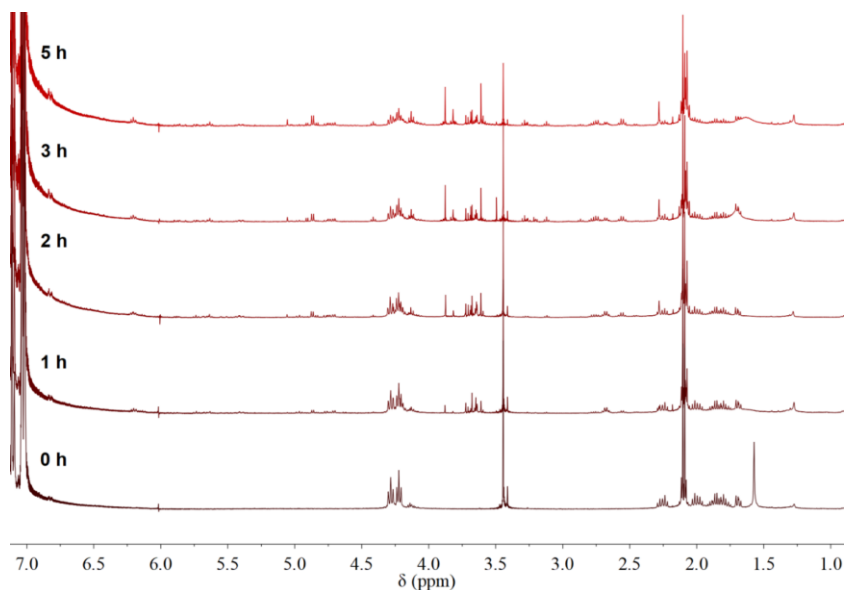


**Figure 144 : New species appeared after thermolysis of compound 5 in diphenyl ether at 138.5 $\pm$ 0.5 °C.**

### 3.2.3.4 Sonication experiment

#### 3.2.3.4.1 Study of mechanophore activation under sonication

A solution of 32 mg polymer **P** in 16 mL dry THF was transferred to a Suslick cell. The solution was cooled with an ice bath and bubbled with N<sub>2</sub> for 5 min. Sonication was performed with a Sonics VC750 at 30% amplitude (1s on, 1s off) under ice bath. Aliquots of 0.9 ml solution at each time point (0, 15, 30, 60, 120, 180, 240 min) were taken out from the cell and subjected to GPC-MALS analysis. Remained solution samples were condensed and the resulting thin layer of polymer was rinsed with MeOH twice to remove byproduct from sonication. The obtained polymer was further dried under high vacuum and analyzed from <sup>1</sup>H NMR.

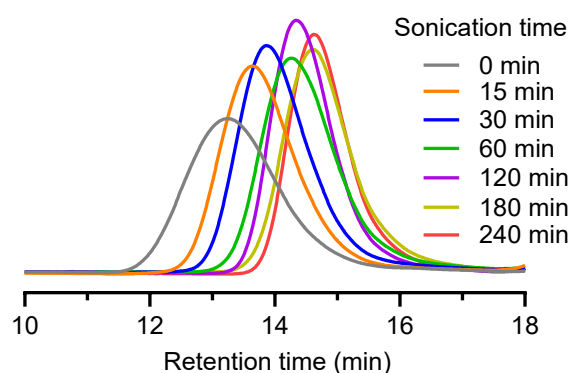


**Figure 145 : Primary GPC elugrams of polymer P as a function of sonication time.**

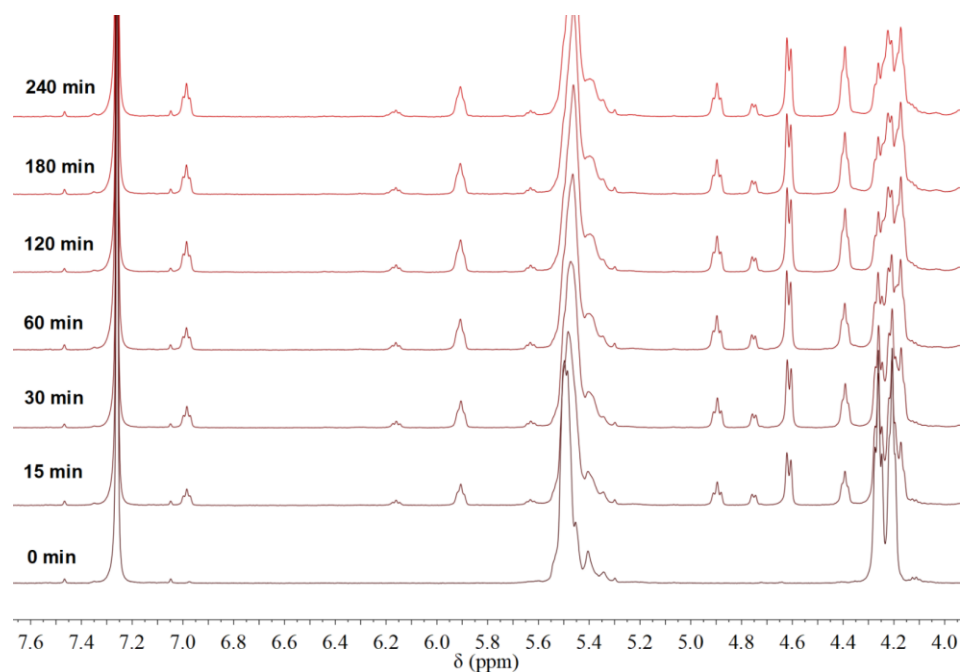


**Figure 146 : Overlay of  $^1\text{H}$  NMR ( $\text{CDCl}_3$ , 500 MHz) spectra of sonicated polymer **P** at various sonication times.**

#### 3.2.3.4.2 Probing mechanoacid

A solution of 42 mg polymer **P** in 21 mL dry THF (2 mg/mL) was transferred to a Suslick cell. The solution was cooled and bubbled with  $\text{N}_2$  for 5 min. Pulsed ultrasound was then applied (30% amplitude, 1s on/1s off). Aliquots of 1.0 mL solution at each time point (0, 15, 30, 60, 120, 180, 240 min) was taken out from the cell. A solution of 38 mg Rhodamine B base in 21 mL dry THF was prepared. 0.1 mL of solution mixture (1 mL sonicated solution + 1 mL Rhodamine B solution) and 0.9 mL THF were then mixed to give a solution with 0.1 mg/mL polymer **P** and 0.09 mg/mL rhodamine B base. The sonicated solution turned pink instantly upon adding rhodamine solution. These samples were further subjected to UV-vis analysis.



**Figure 147 :** Polymer P solution was subjected to sonication for various times (0, 15, 30, 60, 120, 180, 240 min) and added with rhodamine B base solution. (The pink color appeared instantly after adding rhodamine B base solution.)

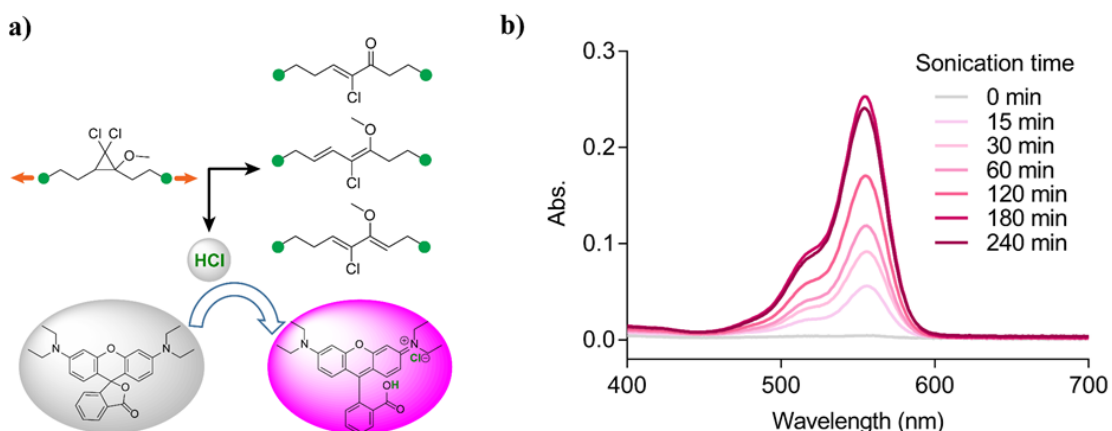


**Figure 148 :** a) Schematic protonation of rhodamine by generated mechanoacid. b) UV-vis spectra of sonicated polymer solution with rhodamine dye at various sonication times.

### 3.2.3.5 SMFS analysis

#### 3.2.3.5.1 Calculation of transition state

We calculated the transition state of ring opening reaction for parent gDCC and MeO-gDCC using GaussView 5.0.9 software. The ground state and ring-opened product of parent gDCC and MeO-gDCC were first optimized using DFT method on the theory level of B3YLP/61G\*(d). The transition state of each was then calculated on the same theory level using QST3 method with force constant calculated for once.

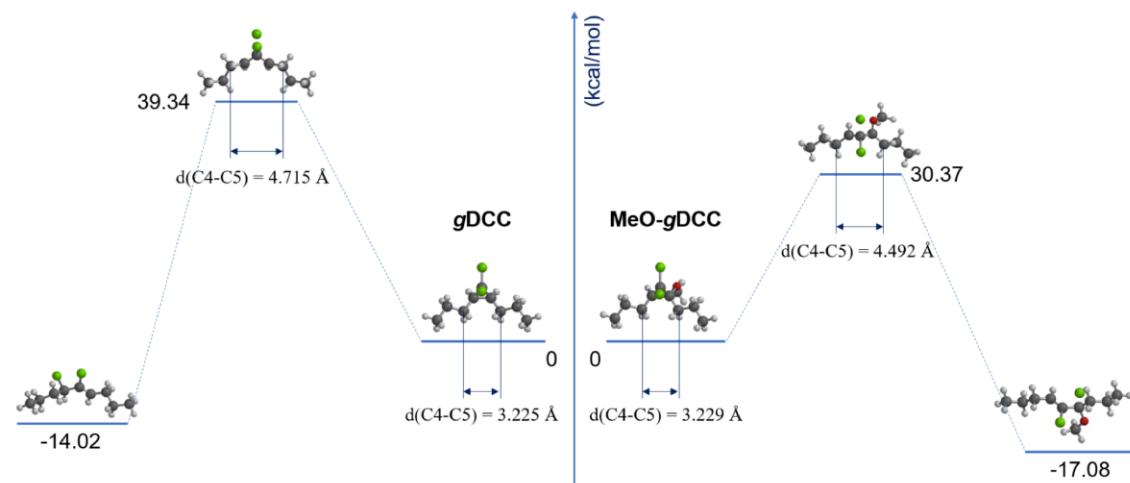


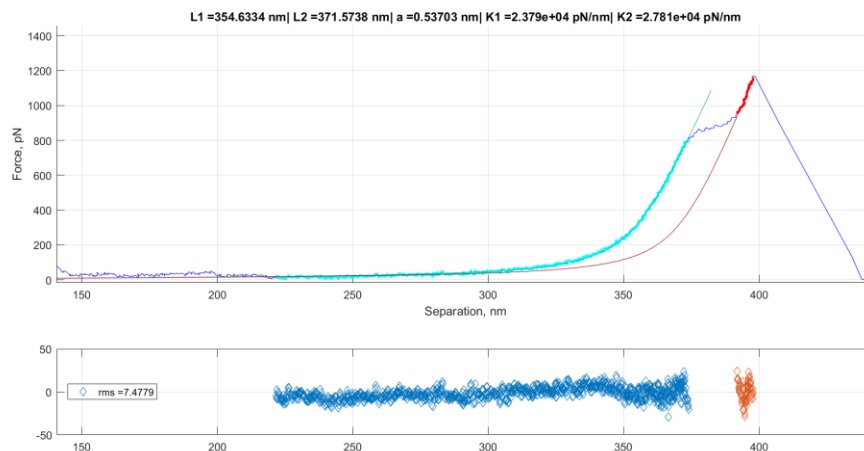
Figure 149 : Calculation of transition state for gDCC and MeO-gDCC. The activation energy of MeO-gDCC is  $\sim 9$  kcal/mol less than that of gDCC. The absolute mechanical coupling of the reaction should take into account the effects of connection to the polymer chain, but the relative mechanical coupling of the two systems is roughly estimated by the distance changes shown:  $\Delta x^\ddagger(\text{gDCC}) = 4.715 - 3.225 = 1.49 \text{ \AA}$ ,  $\Delta x^\ddagger(\text{MeO-gDCC}) = 4.492 - 3.229 = 1.263 \text{ \AA}$ . Thus the  $\Delta\Delta x^\ddagger$  of MeO-gDCC vs. gDCC is  $\sim (1.49 \text{ \AA} - 1.26) = 0.23 \text{ \AA}$ , consistent with the difference derived from SMFS curve fitting.

### 3.2.3.5.2 SMFS curve analysis

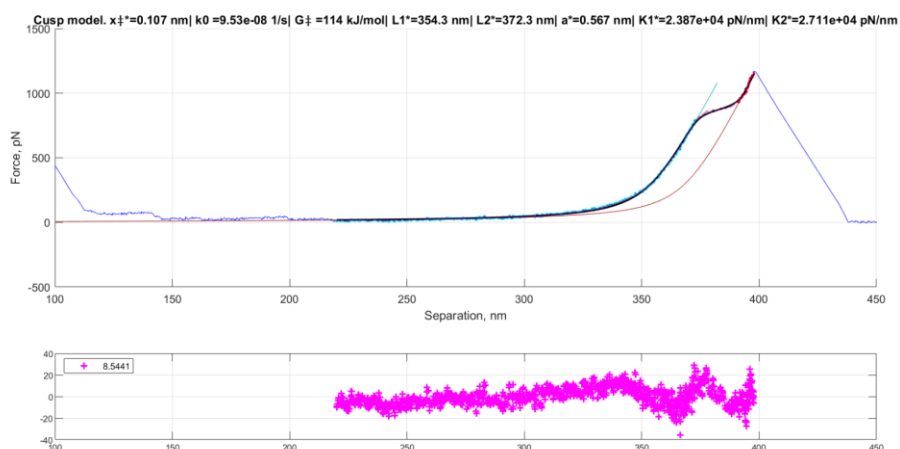
Force-extension curves were analyzed using method described in section 2.2.3.4.2.

Pre- and post-transition force curves were fitted with an extended freely jointed chain (FJC) model to give the contour lengths of polymers before and after transition. Further analysis with a Cusp models provided mechanical coupling ( $\Delta x^\ddagger$ ) information.

SMFS curve fitting:

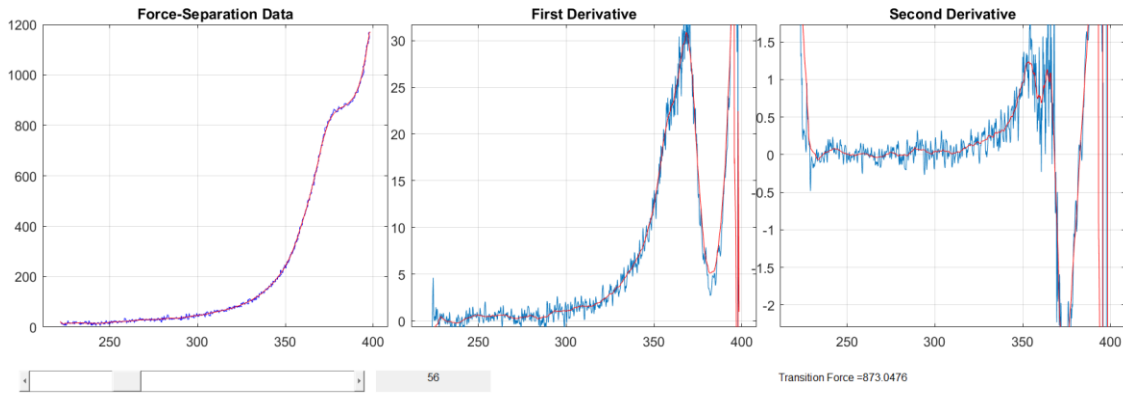


**Figure 150 : Representative fitting of pre- and post-transition curves using an extended-FJC model.**



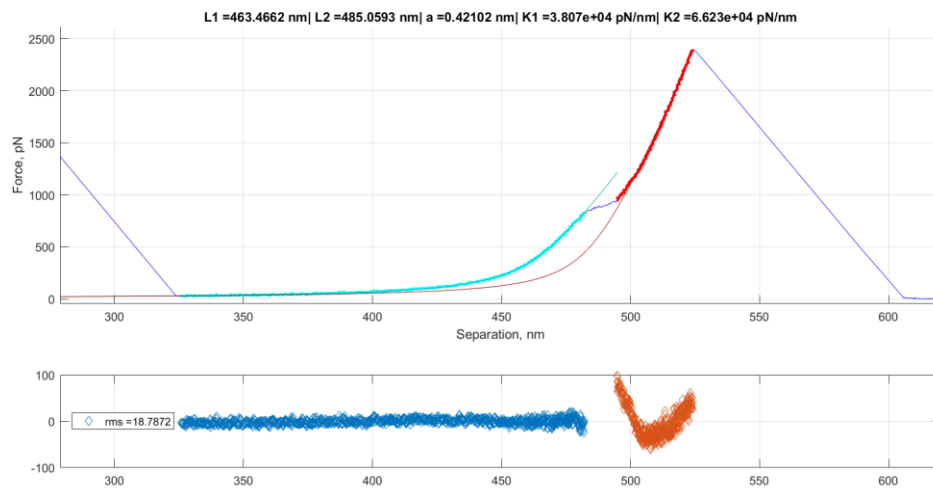
**Figure 151 : Representative fitting of SMFS curve using a Cusp model. The mechanical coupling was retrieved:  $\Delta x^\ddagger = 1.07 \text{ \AA}$ .**

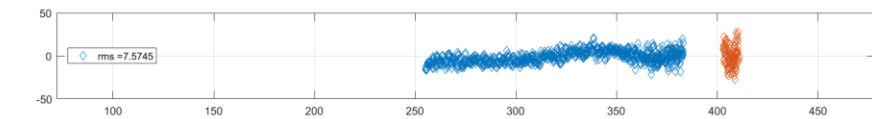
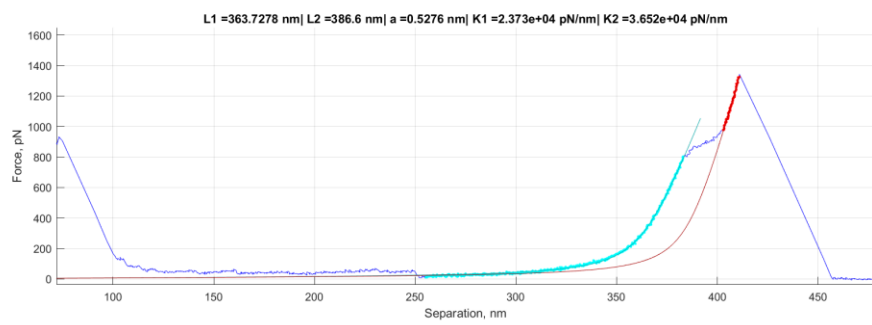
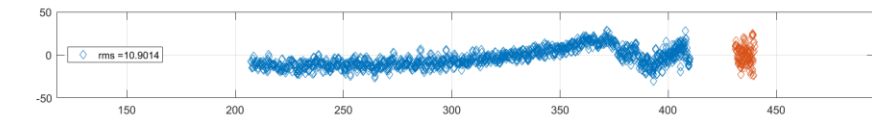
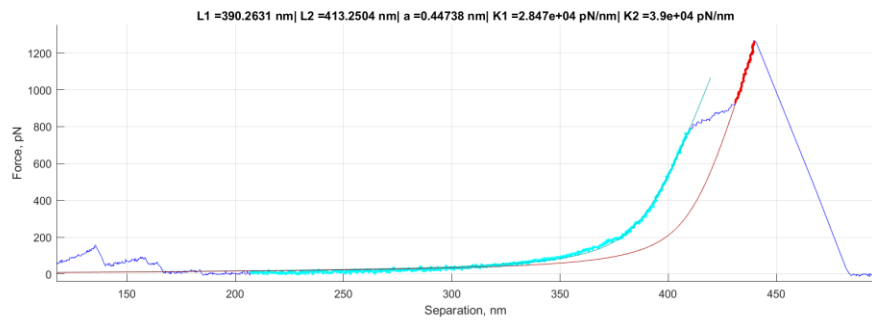
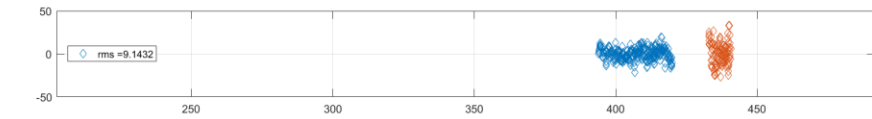
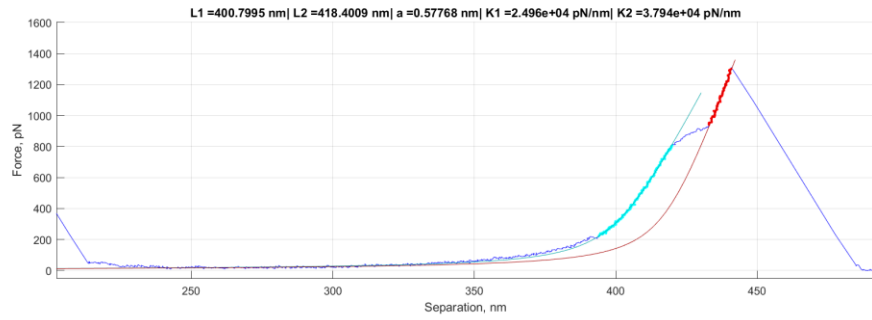
The characteristic transition force was determined by deriving the first and second derivative of force-extension curves. The characteristic force point on the plateau corresponds to the zero point in the second derivative and minimum point in the first derivative.

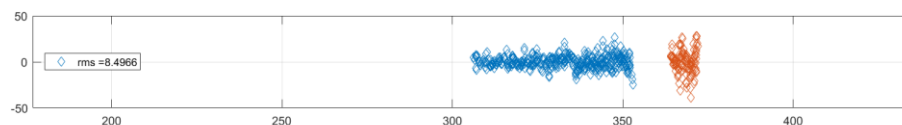
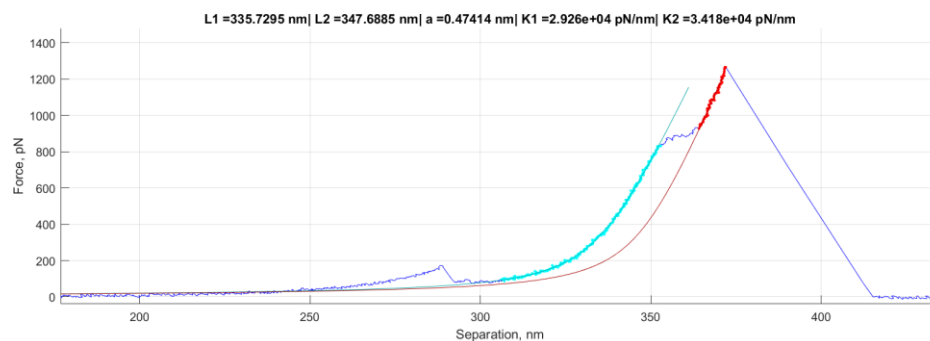
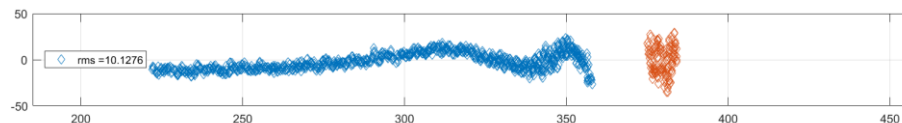
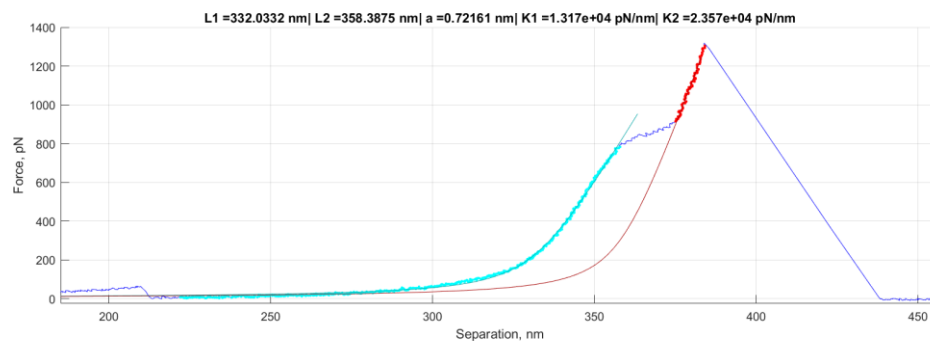


**Figure 152 : Determination of characteristic transition force using first and second derivative of SMFS curve.**

Additional SMFS curves:







SMFS data list:

**Table 19 : List of results from SMFS curves analysis**

| # | $L_i$ (nm) | $L_f$ (nm) | $L_f/L_i$ | Kuhn length (nm) | $K_1$ (pN/nm) | $K_2$ (pN/nm) | $\frac{\Delta x^\ddagger (\text{\AA})}{\text{Cusp}}$ | $f^*$ (pN) |
|---|------------|------------|-----------|------------------|---------------|---------------|--|------------|
| 1 | 332.0      | 358.4      | 1.079     | 0.722            | 1.3E+04       | 2.4E+04       | 1.09   | 850        |
| 2 | 134.3      | 143.8      | 1.071     | 0.565            | 1.7E+04       | 2.7E+04       | 1.07   | 850        |
| 3 | 162.7      | 166.2      | 1.021     | 0.625            | 1.3E+04       | 1.1E+04       | 1.11   | 864        |
| 4 | 179.2      | 187.8      | 1.048     | 0.569            | 2.7E+04       | 3.3E+04       | 1.08   | 872        |
| 5 | 166.0      | 179.3      | 1.080     | 0.763            | 1.8E+04       | 4.8E+04       | 1.09   | 853        |
| 6 | 188.2      | 198.2      | 1.053     | 0.542            | 1.9E+04       | 2.4E+04       | 1.08   | 878        |
| 7 | 224.0      | 232.8      | 1.039     | 0.575            | 2.2E+04       | 2.2E+04       | 1.07   | 870        |

|               |       |       |              |       |         |         |              |            |
|---------------|-------|-------|--------------|-------|---------|---------|--------------|------------|
| 8             | 234.6 | 254.5 | 1.085        | 0.721 | 1.5E+04 | 3.4E+04 | 1.05         | 852        |
| 9             | 133.5 | 145.1 | 1.087        | 0.568 | 2.0E+04 | 5.1E+04 | 1.07         | 888        |
| 10            | 240.9 | 260.6 | 1.082        | 0.518 | 2.4E+04 | 5.6E+04 | 1.05         | 875        |
| 11            | 377.5 | 406.9 | 1.078        | 0.505 | 2.6E+04 | 5.1E+04 | 1.05         | 910        |
| 12            | 195.1 | 206.7 | 1.060        | 0.457 | 3.3E+04 | 4.6E+04 | 1.05         | 905        |
| 13            | 340.5 | 360.6 | 1.059        | 0.536 | 2.6E+04 | 3.5E+04 | 1.05         | 888        |
| 14            | 390.3 | 413.3 | 1.059        | 0.447 | 2.8E+04 | 3.9E+04 | 1.08         | 856        |
| 15            | 472.1 | 490.5 | 1.039        | 0.385 | 4.6E+04 | 6.5E+04 | 1.06         | 869        |
| 16            | 185.4 | 193.4 | 1.043        | 0.485 | 2.6E+04 | 2.9E+04 | 1.01         | 890        |
| 17            | 335.7 | 347.7 | 1.036        | 0.474 | 2.9E+04 | 3.4E+04 | 1.07         | 885        |
| 18            | 354.6 | 371.6 | 1.048        | 0.537 | 2.4E+04 | 2.9E+04 | 1.07         | 873        |
| 19            | 463.5 | 485.1 | 1.047        | 0.421 | 3.8E+04 | 6.6E+04 | 1.02         | 882        |
| 20            | 268.2 | 284.1 | 1.059        | 0.409 | 3.6E+04 | 5.1E+04 | 1.07         | 880        |
| 21            | 527.9 | 548.9 | 1.040        | 0.544 | 2.4E+04 | 2.8E+04 | 1.07         | 870        |
| 22            | 152.4 | 159.8 | 1.049        | 0.381 | 3.6E+04 | 4.0E+04 | 1.06         | 912        |
| 23            | 400.8 | 418.4 | 1.044        | 0.578 | 2.5E+04 | 3.8E+04 | 1.08         | 888        |
| 24            | 363.7 | 386.6 | 1.063        | 0.528 | 2.4E+04 | 3.7E+04 | 1.05         | 886        |
| 25            | 189.3 | 200.4 | 1.059        | 0.461 | 7.7E+03 | 9.8E+03 | 1.07         | 890        |
| <b>Avg.</b>   | /     | /     | 1.057        | /     | /       | /       | 1.068        | 877        |
| <b>SD.</b>    | /     | /     | 0.018        | /     | /       | /       | 0.023        | 18         |
| <b>Report</b> | /     | /     | <b>1.06</b>  | /     | /       | /       | <b>1.07</b>  | <b>880</b> |
|               |       |       | <b>±0.02</b> |       |         |         | <b>±0.02</b> | <b>±20</b> |

Relative reaction rate:

The Arrhenius equation modified by Bell<sup>12</sup> provides the following rate-force relation:

$$k(F) = Ae^{\frac{F\Delta x^\ddagger - \Delta G^\ddagger/N_A}{k_B T}}$$

The relative ring-opening rate of MeO-gDCC to gDCC at force of 880 pN can be calculated:

$$\frac{k(\text{MeO-gDCC})}{k(\text{gDCC})} = e^{\frac{F\Delta\Delta x^\ddagger - \Delta\Delta G^\ddagger/N_A}{k_B T}} = e^{\frac{880*(1.07-1.28)*10^{-22} - (27.2-36.2)*4184/(6.02*10^{23})}{1.38*10^{-23}*298}}$$

$$= 2,647,165 = \sim 10^6$$

### 3.2.3.6 Generation and labeling of mechanoacid in PDMS elastomer

#### 3.2.3.6.1 Mechanical activation of mechanoacid

Qualitative evaluation of mechanoacid activation in PDMS elastomer was performed by stretch, compression, and localized compression.

Prepared PDMS elastomer film is about 0.3~0.4 mm in thickness. The film was manually stretched to near maximum strain and relaxed. For PDMS cylinders, the thickness is around ~0.3 cm. The cylinder was applied with a hammer strike. In turns of localized compression, the cylinder was manually compressed with an iron rod.

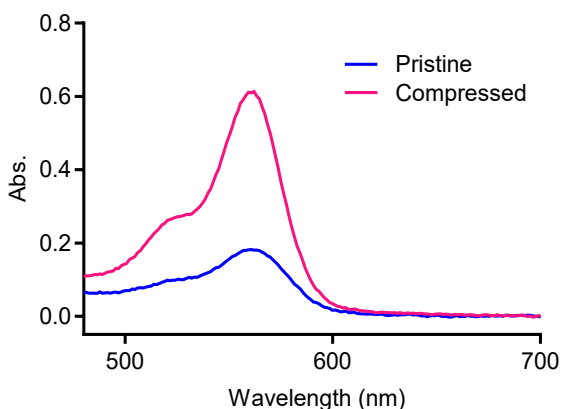


**Figure 153 : UV-vis spectra of active PDMS cylinder before and after compression. The corresponding absorption at 560 nm is 0.182 and 0.610.**

The amount of activated MeO-gDCC can be estimated using Beer-Lambert law:

$$A = \epsilon lc$$

Where  $\epsilon = 106000 \text{ L}/(\text{mol}\cdot\text{cm})$  is the extinction coefficient of rhodamine B,  $l$  is the length (the thickness of PDMS cylinder in our case) and  $c$  is the concentration in the matrix.

Assuming each released HCl protonated one rhodamine dye, we can calculate the concentration of released HCl:

$$c = \frac{A}{\epsilon l} = \frac{0.610 - 0.182}{106000 * 0.3} = 1.342 \times 10^{-5} \text{ mol/L}$$

We incorporated 11 mg MeO-gDCC into 2.2 g PDMS material ( $\rho=0.965$ ). If we assumed the volume of PDMS does not change after curing, the total concentration of MeO-gDCC in the matrix could be obtained:

$$c_0 = \frac{m}{MV} = \frac{11 \times 10^{-3}}{395 * (2.2/0.965 \times 10^{-3})} = 1.266 \times 10^{-3} \text{ mol/L}$$

Since  $\sim 0.58$  equivalents of HCl is generated per MeO-gDCC, the activation percentage is:  $c/0.58/c_0 * 100\% = 0.18\%$

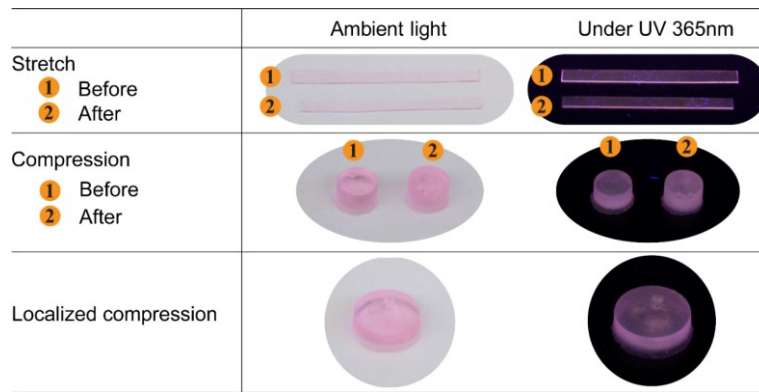


**Figure 154 : Results of control 1 sample (rhodamine 9) under different models of mechanical load.**

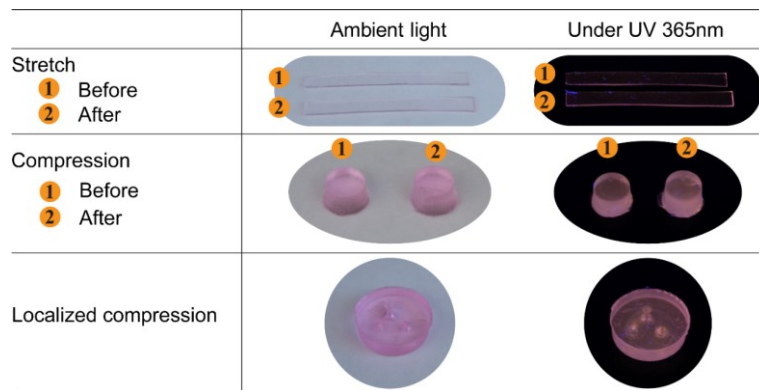


**Figure 155 : Results of control 2 sample (rhodamine 9 and control 7) under different models of mechanical load.**

### 3.2.3.6.2 Time-dependent mechanochromism

An active PDMS cylinder (diameter: ~6 mm, thickness: ~3 mm) was struck with a hammer, and the evolution in UV-vis absorbance at 560 nm ( $A_{560}$ ) was recorded as a function of time over 8 h. Several runs were performed, and recorded results were shown in the following:

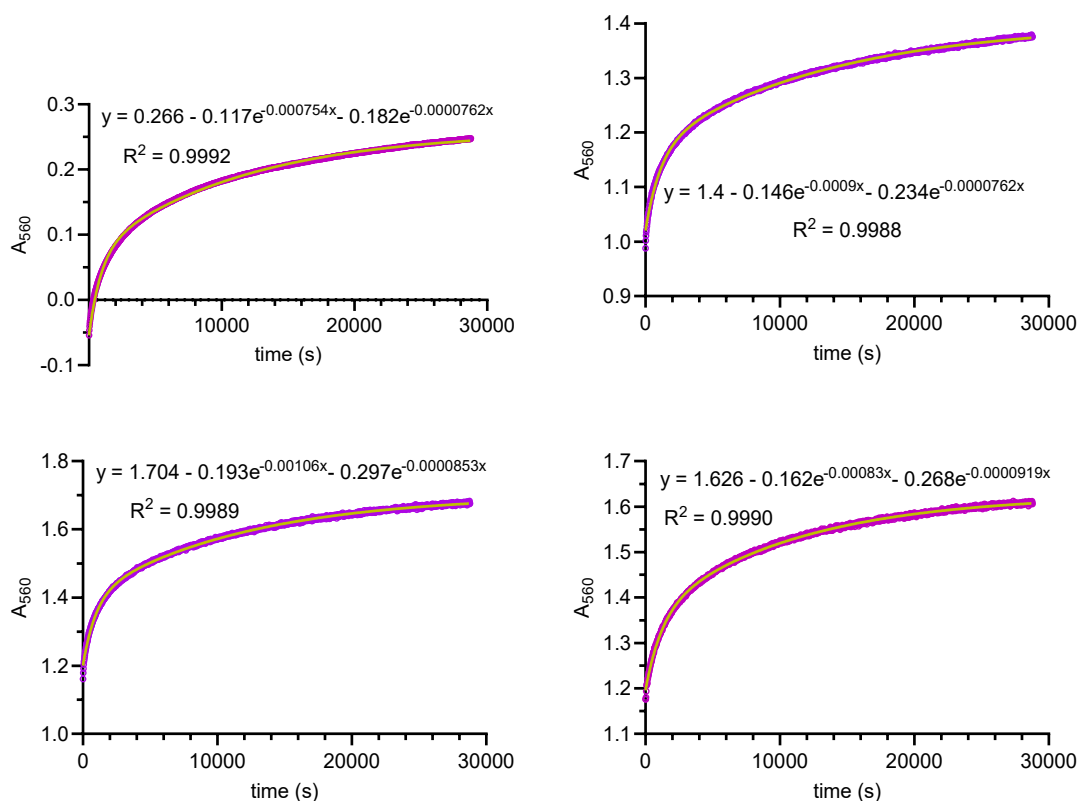


**Figure 156 : Four different runs of  $A_{560}$  evolution in active PDMS cylinder after hammer strike. The data were fitted with a two-phase association (yellow line, fitting results are shown in the figure).**

These curves are fitted with the following two-phase association equation (5):

$$A = A_{\infty} - A_f e^{-k_f t} - A_s e^{-k_s t} \quad (6)$$

$$A_f = (A_{\infty} - A_0) * f\% \quad (7)$$

$$A_s = (A_{\infty} - A_0) * (1 - f\%) \quad (8)$$

$A$  is absorption as measured;  $A_0$  and  $A_\infty$  are initial and final absorption; while  $k_f$  and  $k_s$  stand for rate constant of fast and slow phases, respectively;  $f\%$  refers to contribution of fast phase.

These four runs are normalized using the following equation:

$$I = A/(A_\infty - A_0) \quad (9)$$

Where  $A$  is the recorded absorption,  $A_\infty$  and  $A_0$  are final and initial absorption.

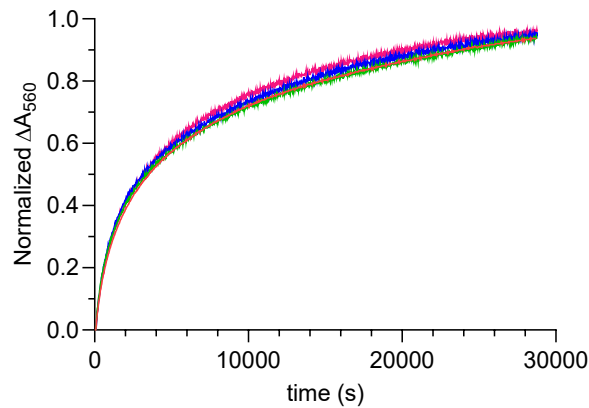


**Figure 157 : Overlay of normalized turn-on kinetics. These data are treated as standard curves and provide:  $k_f = (8.86 \pm 1.30) \times 10^{-4} \text{ s}^{-1}$ ,  $k_s = (8.24 \pm 0.76) \times 10^{-5} \text{ s}^{-1}$ , and  $f\% = (38.7 \pm 0.7)\%$ .**

For a sample with an unknown mechanical load time point, we anticipated that recorded kinetics would allow to extrapolate back the time point. To test this concept, we recorded the initial absorption ( $A_0$ ) of samples and subjected the sample to hammer strike. The kinetics data at  $A_{560}$  was recorded for different samples and various times (6, 12, 26 min) after hammer strike. These kinetics results were then fitted with the empirical two-phase association (10) using parameters constraints obtained from standard curves in Figure 157.

$$A = A_{\infty} - A_f e^{-k_f(t-t_{\text{wait}})} - A_s e^{-k_s(t-t_{\text{wait}})} \quad (10)$$

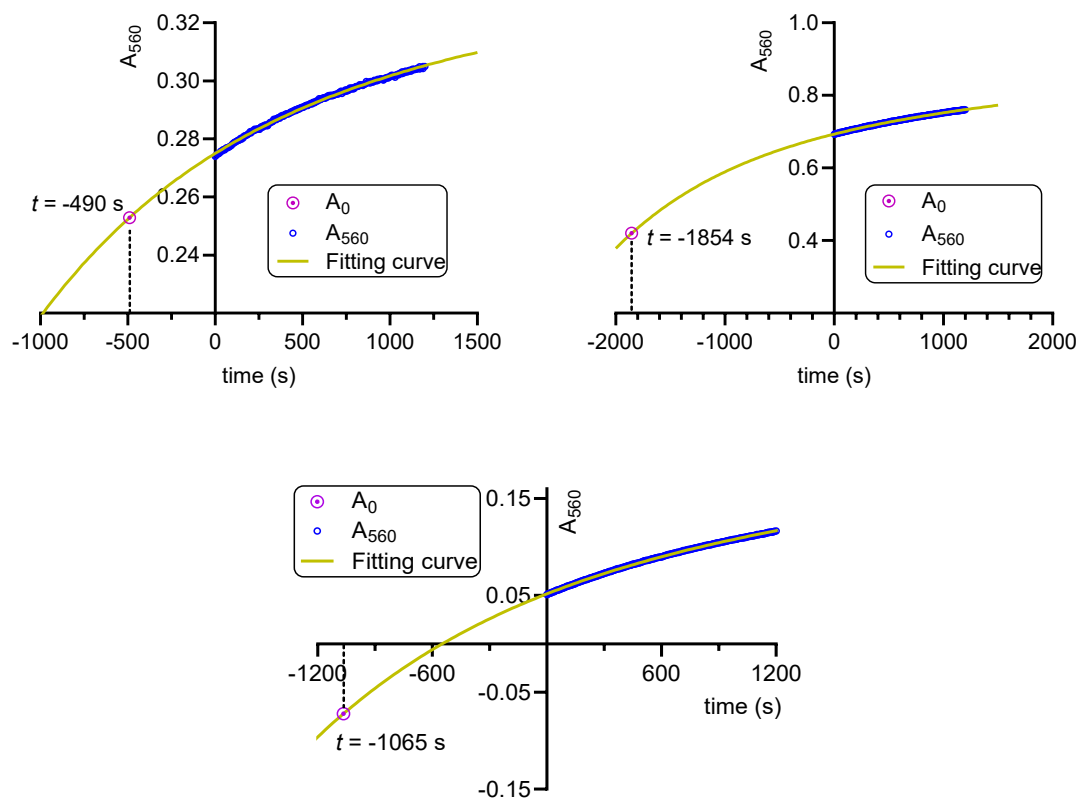
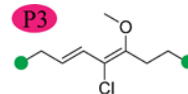
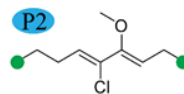
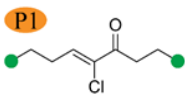
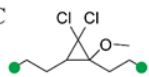


**Figure 158 :** The time point of mechanical load was extrapolated by fitting of kinetics data. The actual time for each sample is 6, 26, 12 min, respectively.

### 3.2.3.7 CoGEF modeling

CoGEF modeling of MeO-gDCC and corresponding three species generated after mechanical activation were performed on Spartan'16 V2.0.7 version at Molecular Mechanics/MMFF theory level. The end-to-end distance was constrained and relaxed using the same procedure in reported literature.<sup>84, 87, 109, 117</sup> The energy at each relaxed step was plotted as a function of distance. Following fitting with a quadratic equation and further analysis from the first derivative gave force vs. extension as a linear relation. Extrapolation of linear curve at zero force provided the contour length ( $x_0$ ).

MeO-gDCC



CoGEF modeling of MeO-gDCC:

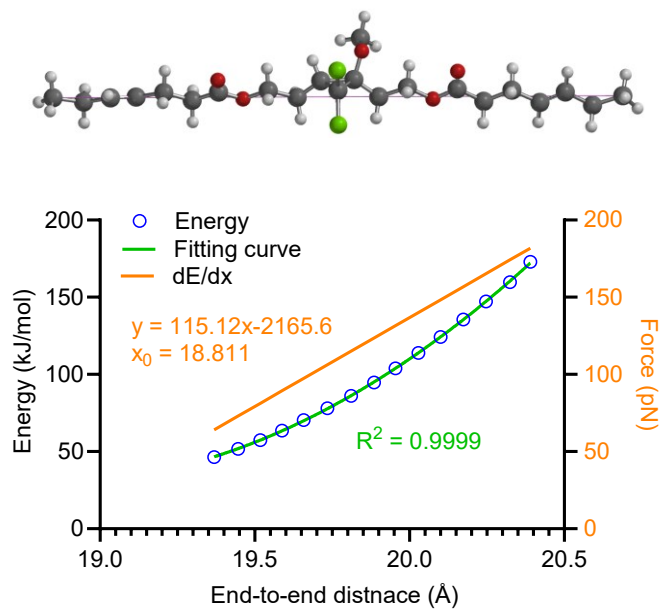


Figure 159 : Quadratic fit of energy vs. distance curve (green); force vs. distance plot (orange). End-to-end distance of MeO-gDCC: 18.811 Å

CoGEF modeling of P1:



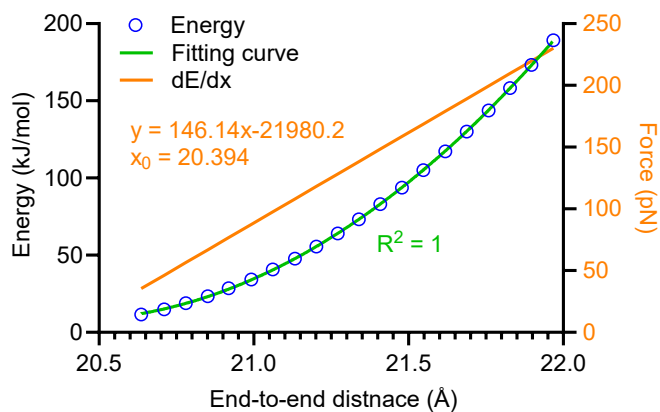


Figure 160 : Quadratic fit of energy vs. distance curve (green); force vs. distance plot (orange). End-to-end distance of P1: 20.394 Å

### CoGEF modeling of P2

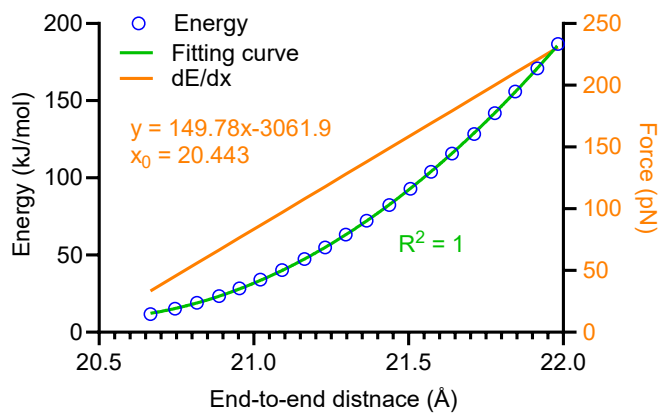
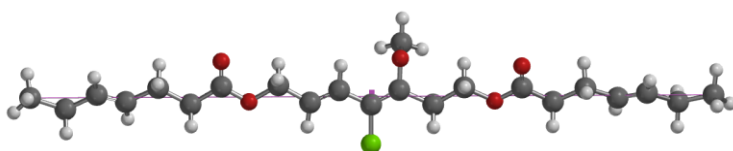


Figure 161 : Quadratic fit of energy vs. distance curve (green); force vs. distance plot (orange). End-to-end distance of P2: 20.443 Å

### CoGEF modeling of P3:

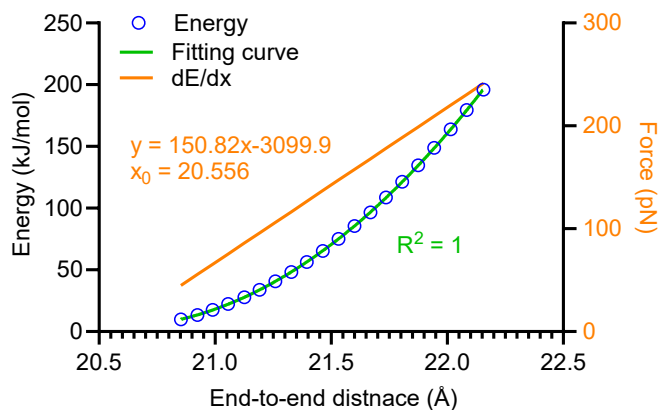
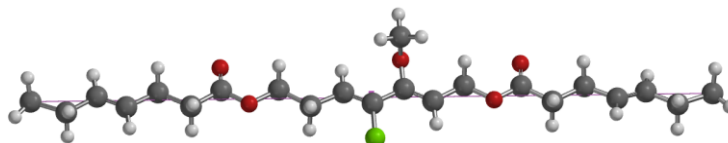


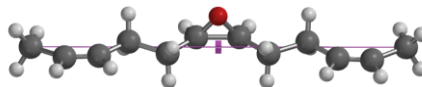
Figure 162 : Quadratic fit of energy vs. distance curve (green); force vs. distance plot (orange). End-to-end distance of P3: 20.556 Å

Table 20 : Summary of modeling contour length (unit: Å)

|            | MeO-gDCC | P1     | P2     | P3     |
|------------|----------|--------|--------|--------|
| Trial 1    | 18.810   | 20.397 | 20.446 | 25.556 |
| Trial 2    | 18.811   | 20.393 | 20.443 | 25.553 |
| Trial 3    | 18.836   | 20.394 | 20.441 | 25.556 |
| Avg.       | 18.819   | 20.394 | 20.443 | 25.555 |
| SD.        | 0.015    | 0.002  | 0.003  | 0.002  |
| $\Delta L$ | /        | 1.575  | 1.624  | 1.736  |

Modeling contour length of epoxide repeating unit:

Epoxide repeating unit with *cis*-olefin



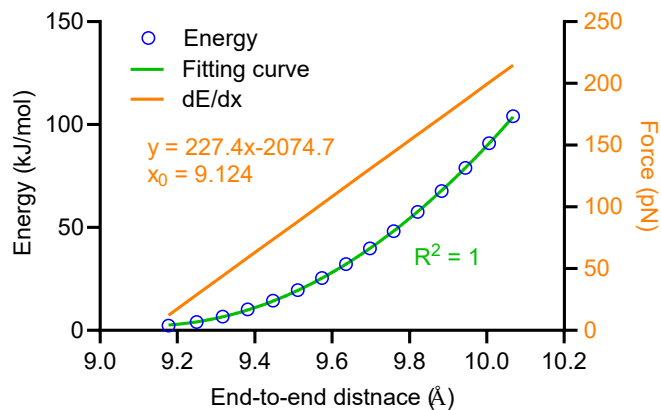


Figure 163 : Quadratic fit of energy vs. distance curve (green); force vs. distance plot (orange). End-to-end distance of epoxide repeating unit with *cis*-olefin: 9.124 Å

Epoxide repeating unit with *trans*-olefin

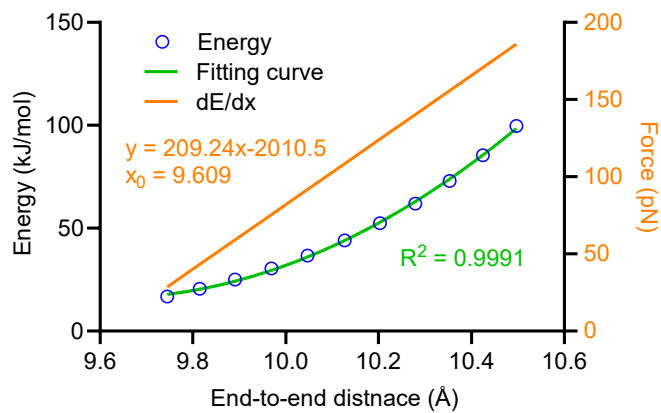
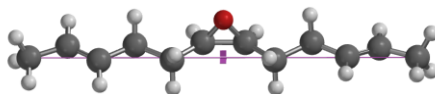


Figure 164 : Quadratic fit of energy vs. distance curve (green); force vs. distance plot (orange). End-to-end distance of epoxide repeating unit with *trans*-olefin: 9.609 Å

**Table 21 : Summary of contour length for epoxide repeating unit (unit: Å)**

|                | <i>Cis</i> | <i>Trans</i> | Average |
|----------------|------------|--------------|---------|
| <b>Trial 1</b> | 9.124      | 9.583        |         |
| <b>Trial 2</b> | 9.126      | 9.609        | /       |
| <b>Trial 3</b> | 9.126      | 9.628        |         |
| <b>Avg.</b>    | 9.125      | 9.607        | 9.366   |
| <b>SD.</b>     | 0.004      | 0.001        | /       |

The ratio of final contour length ( $L_f$ ) to initial contour length ( $L_i$ ) was calculated according to the following equation:

$$\frac{L_f}{L_i} = \frac{x \cdot l_f + (1-x) \cdot l_{COD}}{x \cdot l_i + (1-x) \cdot l_{COD}}$$

$L_i$ ,  $l_i$  represent for initial contour lengths of polymer and mechanophore repeating unit;  $L_f$ ,  $l_f$  refer to final contour lengths of polymer and mechanophore repeating unit;  $l_{COD}$  stands for contour length of epoxide repeating unit;  $x$  denotes the molar fraction of mechanophore in the polymer.  $l_i$ ,  $l_f$  and  $l_{COD}$  were determined from CoGEF modeling and  $x$  was calculated from  $^1\text{H}$  NMR spectrum.

For 47 mol% MeO-gDCC containing ROMP copolymer, the ratio of product **P1**: **P2**: **P3** is 27:31:7, we have:

$$\frac{L_f}{L_i} = \frac{0.47 \cdot (27 \cdot 20.394 + 31 \cdot 20.443 + 7 \cdot 20.555) / 65 + 0.53 \cdot 9.366}{0.47 \cdot 18.819 + 0.53 \cdot 9.366} = 1.063$$

This number agrees well with results observed from SMFS experiment.

## 4. Force distribution in the strained bulk materials

### 4.1 Strain-dependent Kinetics in the *cis-to-trans* Isomerization of Azobenzene in Bulk Elastomers <sup>v</sup>

The *cis-to-trans* isomerization of azobenzene is accelerated in a bulk PDMS elastomer under uniaxial tension. The kinetics are cleanly described by a single exponential first order process ( $k = 2.7 \times 10^{-5} \text{ s}^{-1}$ ) in the absence of tension but become multi-exponential under constant strains of 40-90%. The complex kinetics can be reasonably modeled as a two-component process. The majority (~92%) process is slower and occurs with a rate constant that is similar to that of the unstrained system ( $k = 2.3\text{-}2.7 \times 10^{-5} \text{ s}^{-1}$ ), whereas the rate constant of the minority (~8%) process increases from  $k = 10.1 \times 10^{-5} \text{ s}^{-1}$  at 40% strain to  $k = 21.3 \times 10^{-5} \text{ s}^{-1}$  at 90% strain. Simple models of expected force-rate relationships suggest that the average force of tension per strand in the minority component ranges from 28 pN to 44 pN across strains of 40-90%.

#### 4.1.1 Introduction

The well-known ability to photoswitch azobenzene (AB) (Figure 165a) between its *cis* and *trans* isomers has empowered a range of optically adaptive systems, including: tunable surface tension in solutions<sup>253</sup>, adjustable surface wettability<sup>254-257</sup>, molecular devices<sup>258</sup>, photoresponsive liquid crystals<sup>259-260</sup>, smart biological systems<sup>261-262</sup>, optical actuators/devices<sup>263-267</sup> and triggered elasticity changes in polymer strands<sup>268-270</sup>. Switching

---

<sup>v</sup> This chapter is adopted from: Lin, Y.; Hansen, H. R.; Brittain, W. J.; Craig, S. L. Strain-Dependent Kinetics in the *Cis-to-Trans* Isomerization of Azobenzene in Bulk Elastomers. *J. Phys. Chem. B* **2019**, *123*, 8492-8498.

is typically enabled by light and heat, but additional forms of energy transduction provide opportunities to further generalize the switchable properties that have already been reported.<sup>271</sup> In particular, mechanical force is an intriguing stimulus, as it has been utilized to transform force-responsive functional groups (mechanophores) in strained polymer strands to access forbidden reaction pathways that conventional conditions (light or heat) are not able to achieve<sup>10, 83-84</sup> and to construct stress-responsive materials that are capable of self-reporting damage or overload<sup>29, 72</sup>, chemiluminescence<sup>38, 74, 217</sup>, catalyzing reactions<sup>40, 120-121</sup>, releasing small molecules<sup>42-43, 78, 115</sup> and strengthening polymeric materials<sup>36, 50-51, 53, 123, 272</sup>. Recently, the force-induced isomerization of the shorter *cis* azobenzene to its longer *trans* isomer has been observed under the large forces generated by pulsed ultrasound in solution<sup>273</sup>, but the mechanical isomerization of azobenzene in bulk materials has not yet been reported.

To date, the predominant focus of polymer mechanochemistry research has been on solution-based systems, often those that utilize ultrasound to generate high forces of tension that are able to activate a variety of mechanophores. Less attention has been paid to activating mechanophores in bulk materials, with notable studies focused on spiropyran (SP), diarylbibenzofuranone (DABBF) and dioxetane based mechanochromic materials<sup>30, 72-73, 96-99, 102, 115, 274-275</sup>. Quantitative studies of the relationship between molecular-level tension and mechanophore activation in strained bulk materials are less plentiful. One bulk materials system of interest is that of siloxane elastomers such as Sylgard 184<sup>®</sup>,<sup>115</sup> because strains sufficient to drive measurable mechanochemical response can be

obtained with minimal plastic deformation, enabling insights into the high strain behavior of the elastomer<sup>116-117, 180</sup> as well as a growing range of soft device applications.<sup>113, 276-277</sup> Here, we report the mechanically accelerated *cis*-to-*trans* isomerization of AB in bulk Sylgard 184® polydimethylsiloxane (PDMS) elastomer at lower strains (40-90%) than have been examined in the majority of PDMS-mechanophore studies to date. Simple, single-exponential first-order kinetics in the unstrained PDMS become multi-exponential at the strains investigated, and kinetic models are used to estimate the population of high force strands in the networks as a function of strain.

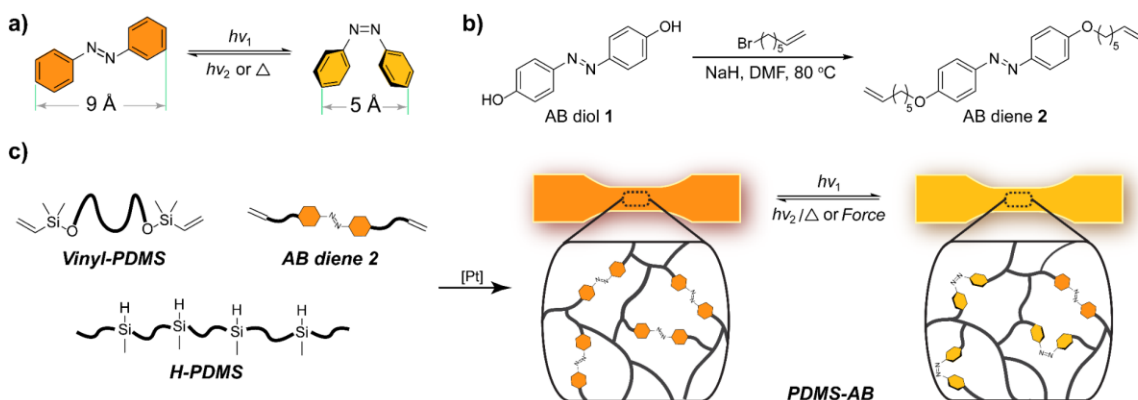


**Figure 165 :** a) Isomerization of azobenzene between *trans* and *cis* form; distance between para carbon atoms is indicated. b) Synthesis of AB diene from AB diol. c) Preparation of azobenzene embedded PDMS elastomer via platinum catalyzed hydrosilylation using commercially available Sylgard 184® kit and depiction of azobenzene isomerization in PDMS network.

#### 4.1.2 Experimental section

Synthesis of azobenzene diene 2. To a 50 mL dry round bottom flask, azobenzene diol<sup>232</sup> (0.71 g, 3.32 mmol) and sodium hydride (60%, 0.29 g, 7.30 mmol) were added. 15 mL dry dimethylformamide was then added to the flask and gas generation was observed. The mixture was heated to 80 °C and 7-bromoheptene (1.07 mL, 6.97 mmol) was

added. The reaction was allowed to proceed under N<sub>2</sub> for 16 h. After the reaction mixture was cooled to room temperature, 30 mL dichloromethane was added. The organic phase was washed with 3×20 mL DI water and then 20 mL brine. The organic phase was further dried with MgSO<sub>4</sub> and condensed to give orange solid as crude product. Column chromatography was performed (0% to 25% EtOAc/Hexane gradient eluent) to give pure product as yellow solid (1.06 g, 87.6%). <sup>1</sup>H NMR (CDCl<sub>3</sub>, 400MHz) δ: 7.86 (d, J = 8.97 Hz, 4H), 6.99 (d, J = 8.97 Hz, 4H), 5.83 (ddt, J = 16.96, 10.18, 6.68 Hz, 2 H), 5.00 (m, 4H), 4.03 (t, J = 6.51 Hz, 4H), 2.11 (m, 4H), 1.82 (td, J = 8.55, 7.79, 5.52 Hz, 4H), 1.49 (dt, J = 6.92, 2.74 Hz, 8H). <sup>13</sup>C NMR (125 MHz, CDCl<sub>3</sub>) δ: 161.21, 147.03, 138.85, 124.41, 114.73, 114.62, 68.28, 33.78, 29.18, 28.75, 25.63. HRMS-ESI (m/z): calcd [M + H]<sup>+</sup> for C<sub>26</sub>H<sub>34</sub>N<sub>2</sub>O<sub>2</sub>, 407.26930; found, 407.26965.

Curing of PDMS-AB film. The commercially available Sylgard 184® silicone elastomer kit was used to prepare azobenzene incorporated PDMS (PDMS-AB). To a 20 mL scintillation vial, 1.1 mg azobenzene diene was dissolved with 200 μL xylene. Then, 2 g Sylgard 184 base was added and mixed with Vortex for 3 min. A clear and homogenous pale yellow mixture was obtained. After adding 0.2 g Sylgard 184 curing, the mixture was further well mixed and casted on a flat PP board. Further curing at 65 °C for overnight gave a yellow clear film with 0.05 wt% azobenzene. For UV-vis and tensile tests, the PDMS film was cut into strips.

Photoswitching of PDMS-AB film. The photodynamics of PDMS-AB was examined via UV-vis. A PDMS-AB strip was adhered to the inner wall of UV-vis cuvette.

The PDMS-AB film was exposed to UV 365 nm from a handheld lamp followed by white light. The UV-vis spectrum was recorded on a Varian Cary 500 UV-Vis Spectrometer at each irradiation time interval.

Tensile test coupled with UV-vis measurement. PDMS-AB film strip was irradiated with a UV365nm handheld lamp for 30s and then subjected to tensile test using a TA Instruments RSA III Dynamic Mechanical Analyzer, and the corresponding 318 nm and 355 nm UV-vis signal at various time points were recorded with a Photonics CCD array UV-vis Spectrometer.

Strain-dependent kinetics. PDMS-AB film was irradiated with a UV365nm handheld lamp for 30 s. The film was then stretched to 0%, 40%, 60%, 80%, 90% or 100% strain with a homebuilt stretcher. The cis-to-trans evolution kinetics was traced from UV-vis absorption at 318 nm (isosbestic point) and 355 nm. The absorption was measured every 2 min and 500 data points were collected.

#### **4.1.3 Results and discussion**

The AB diene **2** (Figure 165b) was obtained *via* a one-step functionalization of diol **1**. Diene **2** was incorporated into Sylgard 184 using conditions previously reported for analogous spiropyran mechanophores (Figure 165c). The content of **2** in the cured network was kept at 0.05 wt% to avoid oversaturation in the UV-vis measurements. The obtained pale yellow AB embedded PDMS film (PDMS-AB) was cut into strips (40 mm × 8 mm × 0.4 mm) for subsequent mechanical manipulation.

We next tested the photoswitching of PDMS-AB film. Like other azobenzene derivatives, **2** exists as either of two geometric isomers: the more extended *trans* isomer and a more compact *cis* isomer. The *trans* isomer is more stable by 10-12 kcal mol<sup>-1</sup>,<sup>278</sup> and is the predominant isomer in the dark. Differential absorbance spectra of the two isomers, however, means that the stationary state of the system can be perturbed by light.<sup>258, 279</sup> The *trans* form is selectively converted to *cis* form by short UV (<400nm) irradiation whereas the rate to of *cis*-to-*trans* isomerization is faster than *trans*-to-*cis* under visible or no irradiation.<sup>280</sup> These characteristic behaviors are observed in PDMS-AB. After curing at 65 °C overnight, the UV-vis spectrum of PDMS-AB is consistent with nearly quantitative (> 99.9%) *trans* **2** content (Figure 169). The PDMS-AB films maintain the photoswitching properties of azobenzene. Upon irradiation with UV 365 nm light, the intensity at 355 nm decreases while a shoulder peak at 450 nm slightly increases, indicating the expected *trans*-to-*cis* isomerization. In our hands, the photostationary state of the PDMS-AB film was reached within 20 s irradiation; an isosbestic point at 318 nm indicated the effectively one-to-one conversion between the two isomers. The *cis* isomer can be converted back to *trans* by white light irradiation (Figure 169).

There is a significant difference in end-to-end distance between the isomers, as characterized by the distance between *para* carbon atoms in *trans* and *cis* azobenzene (9 Å and 5.5 Å, respectively, Figure 165a).<sup>258, 281</sup> We therefore anticipated that the *cis*-to-*trans* isomerization could be accelerated mechanically in the strained bulk materials. We prepared PDMS-AB in a predominantly *cis* state in order to compare its isomerization in

a film under tension to that in a relaxed film. A PDMS-AB film was irradiated with 365 nm light for 30 s to reach a photostationary state of 75% *cis* and 25% *trans* azobenzene (as determined by  $^1\text{H}$  NMR, Figure 174). Then, UV-vis absorption intensities at 355 nm ( $A_{355}$ ) and 318 nm ( $A_{318}$ , isosbestic point) were recorded as a function of time while the PDMS-AB film was subjected to uniaxial strain (strain rate  $5\% \text{ s}^{-1}$ ). Instead of evaluating the absolute intensity at 355 nm ( $A_{355}$ ), we normalized against the absorbance at the 318 nm isosbestic point ( $A_{355}/A_{318}$ ) to account for any variation due to changes in film thickness during strain and fluctuations in lighting. As shown in Figure 166, under these conditions  $A_{355}/A_{318}$  stays relatively constant from 0 to 70% strain, at which point further increase in strain leads to an increase in  $A_{355}/A_{318}$  up to a value of 0.50 at 160% strain, at which point the film breaks. The onset strain for detectable *cis*-to-*trans* isomerization is  $\sim 70\%$ , which corresponds to the onset of strain-hardening observed in the stress-strain curve. A control experiment with  $A_{355}/A_{318}$  of unstrained PDMS-AB recorded under ambient light revealed that the  $A_{355}/A_{318}$  value slightly increases from 0.15 to 0.24 within the same  $\sim 90$  s time period as for tensile test (Figure 170). We conclude that the application of tension has led to a mechanically induced *cis*-to-*trans* isomerization of azobenzene in PDMS elastomer under these conditions.

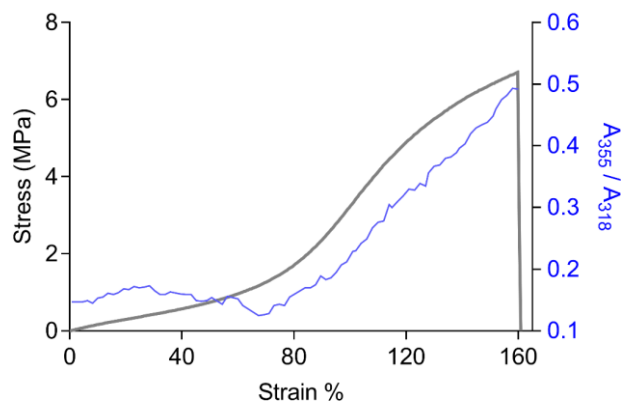


**Figure 166 : A representative stress-strain curve (gray curve, left axis) of PDMS-AB elastomer and corresponding evolution in  $A_{355}/A_{318}$  value (blue curve, right axis).**

The force-coupled *cis-to-trans* isomerization of AB is reminiscent of previous work by Sottos and coworkers,<sup>282</sup> who characterized the influence of stress and strain on the kinetics of spiropyran-to-merocyanine isomerization in bulk materials. They further interpreted the effect of mechanical stress in terms of a force-coupled change in activation energy. In order to draw quantitative insights into molecular behavior in PDMS-AB, we studied the effect of constant strain on the *cis-to-trans* isomerization kinetics. As with the constant strain rate experiment, we first irradiated PDMS-AB film with 365 nm light for 30 s to obtain a predominance of *cis*-AB. We then uniaxially stretched the film to different, fixed strains and monitored the evolution of  $A_{355}$  and  $A_{318}$ . Representative kinetic results are shown in Figure 174. As expected,  $A_{318}$  (isosbestic point) remains constant, while  $A_{355}$  grows with time. To better compare the strain coupled and force-free isomerization kinetics, the absorbance values were normalized and overlaid in Figure 167a. Consistent with the experiments under constant strain rate, the rate of  $A_{355}$  increase is greater in strained PDMS-AB than in unstrained PDMS-AB.

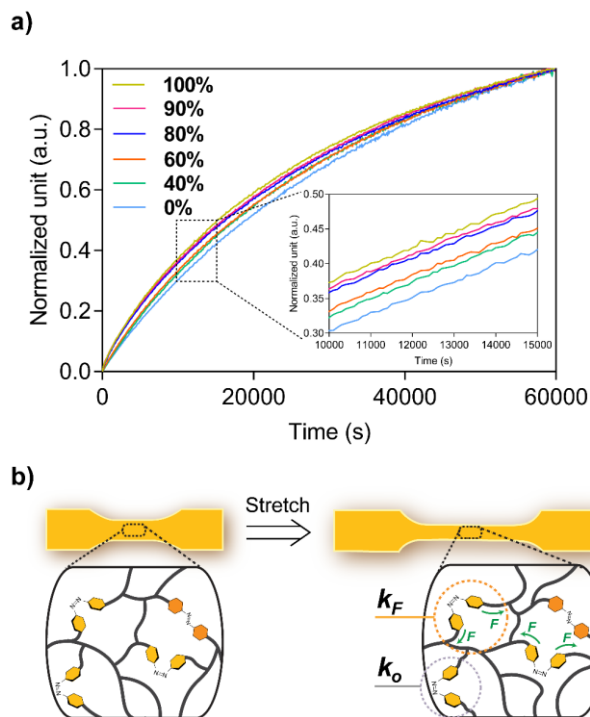


**Figure 167 : a) Overlay of normalized kinetics of PDMS-AB film under various strains. b) Illustration of force-coupled ( $k_F$ , orange circle) and force-free ( $k_0$ , gray circle) *cis-to-trans* isomerization kinetics in the stretched PDMS-AB film**

As illustrated in Figure 167b, we anticipated a distribution of strand tensions in the behavior of the networks.<sup>111, 283</sup> Consistent with this expectation, the kinetics of the strain free film are fit well with a single, first-order exponential; strain coupled kinetics appear to be multi-exponential. We therefore fit the kinetics data of strained PDMS-AB with a two-phase exponential rate law:

$$A = A_\infty - A_F e^{-k_F t} - A_0 e^{-k_0 t} \quad (11)$$

Where  $A$  is the absorbance measured;  $A_\infty$  is the extrapolated plateau in the absorbance;  $A_F$  and  $A_0$  are prefactors that determine the relative contributions of kinetic processes with respective rate constants  $k_F$  and  $k_0$ . All terms are treated as adjustable parameters, and duplicate runs were conducted to account for experimental uncertainty.

The obtained kinetic parameters are summarized in Table 22. As can be seen, the two-phase fitting of strained PDMS-AB kinetics gives one slow rate constant  $k_0$  that is similar to force-free relaxation (i.e. rate constant at 0% strain) and one larger rate constant which is 4-8 fold greater than  $k_0$ . The two-phase approximation is surely an oversimplification of a more complex distribution, but within its limits we therefore interpret the two processes to represent contributions from a minority component of force-coupled ( $A_F$  and  $k_F$ ) and majority component of effectively strain-free ( $A_0$  and  $k_0$ ) AB strands.

**Table 22 : Summary of rate constants obtained from two-phase fitting of strained PDMS-AB film**

| Strain                                    | 0%            | 40%            | 60%            | 80%            | 90%            | 100%           |
|---|---------------|----------------|----------------|----------------|----------------|----------------|
| $k_0$ ( $\times 10^{-5} \text{ s}^{-1}$ ) | 2.7 $\pm$ 0.1 | 2.3 $\pm$ 0.2  | 2.5 $\pm$ 0.1  | 2.7 $\pm$ 0.2  | 2.7 $\pm$ 0.1  | 2.5 $\pm$ 0.5  |
| $k_F$ ( $\times 10^{-5} \text{ s}^{-1}$ ) | /             | 10.1 $\pm$ 1.7 | 13.3 $\pm$ 1.8 | 19.5 $\pm$ 5.4 | 21.3 $\pm$ 1.5 | 12.8 $\pm$ 5.6 |

The relationship between  $k_F$  and strain is shown in Figure 168. At a strain of 40%,  $k_F = 10.1 \times 10^{-5} \text{ s}^{-1}$ , i.e. the force-coupled isomerization rate increases  $\sim 4$  fold from the unstrained value. The rate constant increases monotonically up to a strain of 90%, at which point  $k_F = 21.3 \times 10^{-5} \text{ s}^{-1}$ , or a factor of  $\sim 8$  greater than  $k_0$  ( $2.3\text{-}2.7 \times 10^{-5} \text{ s}^{-1}$ , in agreement with prior force-free measurements of similarly AB derivatives<sup>284</sup>). Increasing the strain further to 100%, however, results in a drop in the derived  $k_F = 12.8 \times 10^{-5} \text{ s}^{-1}$  while, interestingly, the percentage of force-coupled component increases from  $\sim 8\%$  to  $\sim 15\%$ . This drop in  $k_F$  was unexpected, and we hypothesize it might result at least in part from the well-known Mullins effect<sup>285</sup> of the Sylgard 184® elastomer, which occurs at around 90% strain and

involves processes that relieve stress, generate hysteresis, and redistribute tension in the remaining active strands.

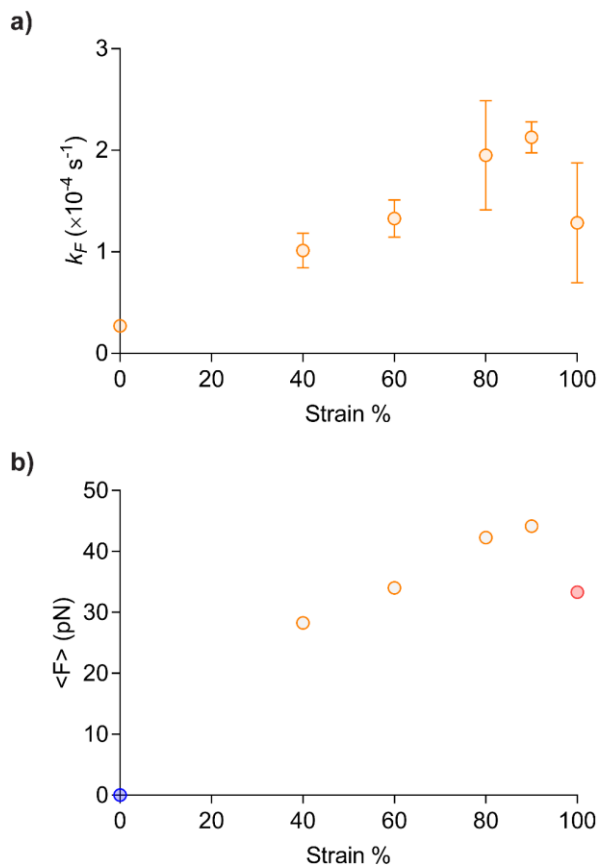


**Figure 168 : a) Derived values of  $k_F$  for the *cis*-to-*trans* isomerization in PDMS-AB at different uniaxial strains. b) Apparent average force  $\langle F \rangle$  of force-coupled component in PDMS-AB as a function of strains.**

The magnitude of  $k_F$  can be used to estimate an average force within the highly stressed sub-population. We emphasize that analyses based on  $k_F$  in this way are highly approximate, since distribution of force in a strained polymer network is likely to be very broad<sup>11</sup> and the two-phase model is undoubtedly an oversimplification. Nonetheless, back-of-the-envelope type insights can be obtained by interpreting  $k_F$  in terms of the Bell-Evans model for mechanically assisted processes:<sup>12</sup>

$$k_F = k_0 e^{\langle F \rangle \Delta x^\ddagger / k_B T} \quad (12)$$

And the average molecular-level force  $\langle F \rangle$  is obtained by rearranging the prior equation:

$$\langle F \rangle = \frac{k_B T}{\Delta x^\ddagger} \ln(k_F / k_0) \quad (13)$$

Where  $k_B$  is the Boltzmann constant;  $T$  is the temperature; and  $\Delta x^\ddagger$  stands for the change in end-to-end distance between ground and transition state coupled to the vector of applied force. Values of  $k_0$  and  $k_F$  are taken from the strain-dependent kinetics of AB isomerization (Figure 168a), but  $\Delta x^\ddagger$  cannot be obtained from these experiments. Instead, we employed CoGEF modeling<sup>82, 86-87</sup> to obtain value of  $\Delta x^\ddagger$  that is associated with the commonly accepted inversion mechanism of AB isomerization<sup>273, 286-288</sup> (see section 4.1.4.7 for details). The obtained  $\Delta x^\ddagger$  value (1.92 Å) was then used to calculate  $\langle F \rangle$  at different strains. As shown in Figure 168b, the derived value of  $\langle F \rangle$  at 40% strain is around 28 pN and this number increases to 44 pN at a strain of 90%.

A comparison of  $A_F$  and  $A_0$  suggests that the strain-affected component of the distribution is ~8% of the total. Within the (considerable) limits of the two-phase model, negligible tension is within the remaining 92%, and so the average force per chain at 90% strain is  $(0.08 \times 44 \text{ pN}) + (0.92 \times 0 \text{ pN}) = 3.5 \text{ pN}$ . By comparison, the average tension of a freely jointed chain at 90% extension ( $\lambda = 1.9$ ) is given by:<sup>111</sup>

$$\langle F \rangle = \frac{k_B T}{b} L^{-1} \left( \sqrt{\frac{\lambda^2 + 2}{3n\lambda}} \right) \quad (4)$$

Where  $b$  is the Kuhn length per segment and  $n$  is the number of Kuhn lengths between cross-links in the network.  $L^{-1}$  is the inverse Langevin function ( $L(x) = \coth x -$

$\frac{1}{x}$ ). For PDMS-AB,  $b$  is  $1.3 \text{ nm}^{289}$  and  $n$  is 12, so for  $\lambda = 1.9$  the average force per chain is expected to be 3.7 pN. A direct comparison of this value and the 3.5 pN obtained from the kinetics analysis assumes that all AB is doubly reacted into the network to form a stress-bearing crosslinker and that the network is deformed affinely. Similar average forces are obtained if we treated the kinetics data with one-phase fitting (Figure 177). Hence, our two-phase model is reasonable. The breadth of force distribution in bulk materials would increase with increasing strain,<sup>111</sup> and so models beyond single exponential are likely to be even more important at higher stresses/strains.

Conclusion. The point of the above analysis is that, despite the number of simplifying assumptions involved, the magnitude of the effect on AB isomerization kinetics is reasonable and in line with first principles expectations. A more comprehensive analysis of expected force distributions in polymer networks, including the exponential distributions uncovered by Makarov and co-workers,<sup>111</sup> might provide even greater insights, and the PDMS-AB system and methodology employed here should be useful in testing those theories. To that end, we are especially encouraged by the ability to probe the effects of strains that are lower than those we have previously studied in PDMS-mechanophore networks using spiropyran mechanochromism. We also believe that it is likely, as observed here, that the kinetics of mechanochemical processes in strained networks will in general not be adequately captured by a single rate constant. We are encouraged, however, by the empirical utility of the simple, two-phase kinetic model employed here and suspect that it might be used to make similar analyses and to draw

comparisons across mechanophore and material systems in similar strain ranges. Finally, the fact that the state of azobenzene can be perturbed mechanically offers potential utility in creating, for example, films with surface energies that are strain-dependent as well as (and in combination with) photo-responsive.

#### **4.1.4 Synthetic and general procedures**

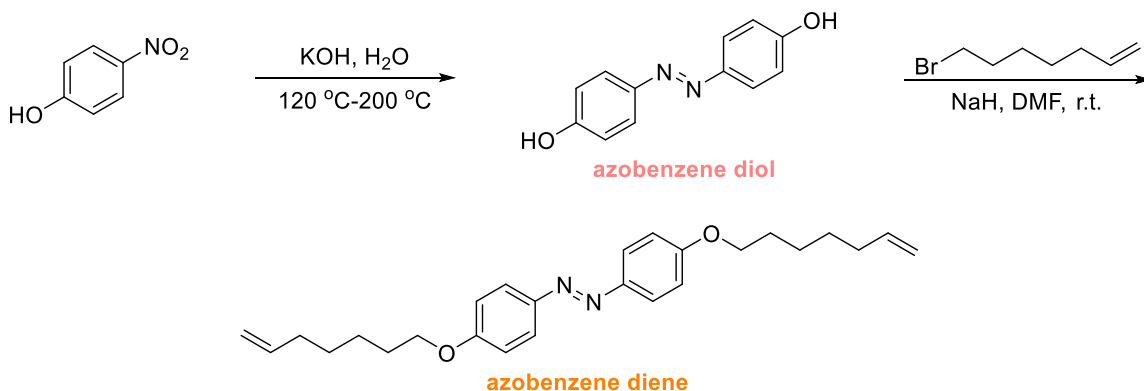
##### **4.1.4.1 Materials and characterization**

Materials: General solvents including dichloromethane, chloroform, hexane, ethyl acetate, acetone, xylene and *N,N*-dimethylformamide were purchased from VWR or Sigma Aldrich. Sodium hydroxide, 4-nitrophenol, sodium hydride and 7-bromoheptene were purchased from Sigma Aldrich and used without further purification. Sylgard®184 was purchased from Ellsworth Adhesives, Germantown, WI. Flash chromatography was performed on CombiFlash®200 auto-column system from Teledyne ISCO.

Characterizations: <sup>1</sup>H NMR spectra were collected on a 400 MHz Varian INOVA spectrometer and <sup>13</sup>C NMR spectra were collected on a 500 MHz Varian UNITY spectrometer. Chemical shifts are given in *ppm* ( $\delta$ ) and referenced to the residual <sup>1</sup>H peak at 7.26 ppm or <sup>13</sup>C peak at 77.16 ppm in CDCl<sub>3</sub>. <sup>1</sup>H shifts are reported as chemical shift, multiplicity, coupling constant if applicable, and relative integral. Multiplicities are reported as: singlet (s), doublet (d), doublet of doublets (dd), doublet of triplets (dt), doublet of doublet of doublets (ddd), doublet of doublet of triplets (ddt), triplet (t), triplet of doublets (td), quartet (q), multiplet (m), or broad (br). Coupling constants (J) are reported in Hertz. High-resolution mass spectra were collected on an Agilent LCMS-TOF-

DART at Duke University's Mass Spectrometry Facility. UV-vis spectra were collected on a Varian Cary 500 UV-Vis Spectrophotometer or a Photonics CCD Array UV-vis Spectrophotometer. Tensile test was performed on a TA Instruments RSA III Dynamic Mechanical Analyzer.

#### 4.1.4.2 Small molecule synthesis



Synthesis of azobenzene diol:

The synthesis of azobenzene diol was performed according to reported procedure.<sup>232</sup>

Synthesis of azobenzene diene:

To a 50 mL dry round bottom flask, azobenzene diol (0.71 g, 3.32 mmol) and sodium hydride (60%, 0.29 g, 7.30 mmol) were added. 15 mL dry dimethylformamide was then added to the flask and gas generation was observed. The mixture was heated to 80 °C and 7-bromoheptene (1.07 mL, 6.97 mmol) was added. The reaction was allowed to proceed under N<sub>2</sub> for 16 h. After the reaction mixture was cooled to room temperature, 30 mL dichloromethane was added. The organic phase was washed with 3×20 mL DI water and then 20 mL brine. The organic phase was further dried with MgSO<sub>4</sub> and condensed

to give orange solid as crude product. Column chromatography was performed (0% to 25% EtOAc/Hexane gradient eluent) to give pure product as yellow solid (1.06 g, 87.6%).  $^1\text{H}$  NMR ( $\text{CDCl}_3$ , 400MHz)  $\delta$ : 7.86 (d,  $J = 8.97$  Hz 4H), 6.99 (d,  $J = 8.97$  Hz, 4H), 5.83 (ddt,  $J = 16.96, 10.18, 6.68$  Hz, 2 H), 5.00 (m, 4H), 4.03 (t,  $J = 6.51$  Hz, 4H), 2.11 (m, 4H), 1.82 (td,  $J = 8.55, 7.79, 5.52$  Hz, 4H), 1.49 (dt,  $J = 6.92, 2.74$  Hz 8H).  $^{13}\text{C}$  NMR (125 MHz,  $\text{CDCl}_3$ )  $\delta$ : 161.21, 147.03, 138.85, 124.41, 114.73, 114.62, 68.28, 33.78, 29.18, 28.75, 25.63. HRMS-ESI ( $m/z$ ): calcd  $[\text{M} + \text{H}]^+$  for  $\text{C}_{26}\text{H}_{34}\text{N}_2\text{O}_2$ , 407.26930; found, 407.26965.

#### 4.1.4.3 Preparation of azobenzene incorporated PDMS bulk material

The commercially available Sylgard 184 silicone elastomer kit was used to prepare azobenzene incorporated PDMS (PDMS-AB). To a 20 mL scintillation vial, 1.1 mg azobenzene diene was dissolved with 200  $\mu\text{L}$  xylene. Then, 2 g Sylgard 184 base was added and mixed with Vortex for 3 min. A clear and homogenous pale yellow mixture was obtained. After adding 0.2 g Sylgard 184 curing, the mixture was further mixed and casted on a flat PP board. Further curing at 65  $^\circ\text{C}$  for overnight gave a yellow clear film with 0.05 wt% azobenzene. For UV-vis and tensile tests, the PDMS film was cut into strips.

#### 4.1.4.4 UV-vis characterization

Photo-switch of PDMS-AB film:

The photodynamics of PDMS-AB was examined via UV-vis. A PDMS-AB strip was adhered to the inner wall of UV-vis cuvette. The PDMS-AB film was exposed to UV 365 nm from a handheld lamp followed by white light. The UV-vis spectrum was recorded on a Varian Cary 500 UV-Vis spectrometer at each irradiation time interval.

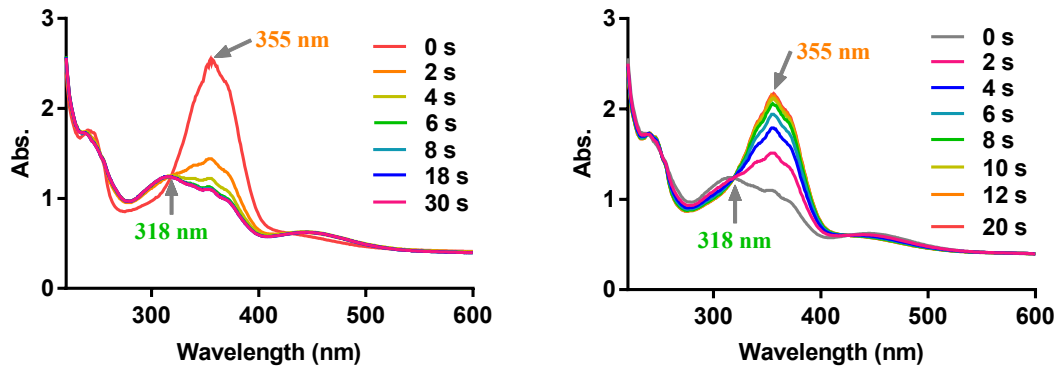


Figure 169 : Photoswitch of PDMS-AB film under UV 365 nm (left) and white light (right). An isosbestic point at 318 nm was observed during photoswitching.

Force-induced cis-to-trans isomerization of azobenzene in PDMS-AB film:

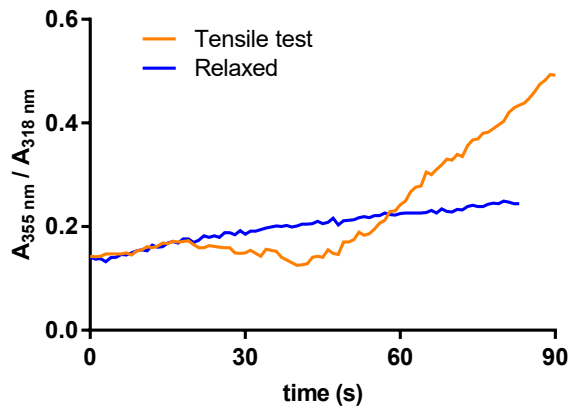


Figure 170 :  $A_{355} / A_{318}$  evolution of PDMS-AB film that was stretched on a TA Instruments RSA III Dynamic Mechanical Analyzer under ambient light (orange line):  $A_{355} / A_{318}$  value increases from 0.147 to 0.492;  $A_{355} / A_{318}$  evolution of unstrained PDMS-AB film under ambient light (blue line):  $A_{355} / A_{318}$  value increases from 0.141 to 0.244. The  $A_{355} / A_{318}$  increase under tension (0.345) is 3.3 times greater than unstrained thermal relaxation (0.103).

Thermal relaxation:

Thermal relaxation experiments were performed to study the cis-to-trans isomerization under ambient temperature in relaxed PDMS-AB. The PDMS-AB film was

irradiated with UV 365 nm LED light for 30 s and was allowed to thermally relax for 5 min and 10 min in the dark.

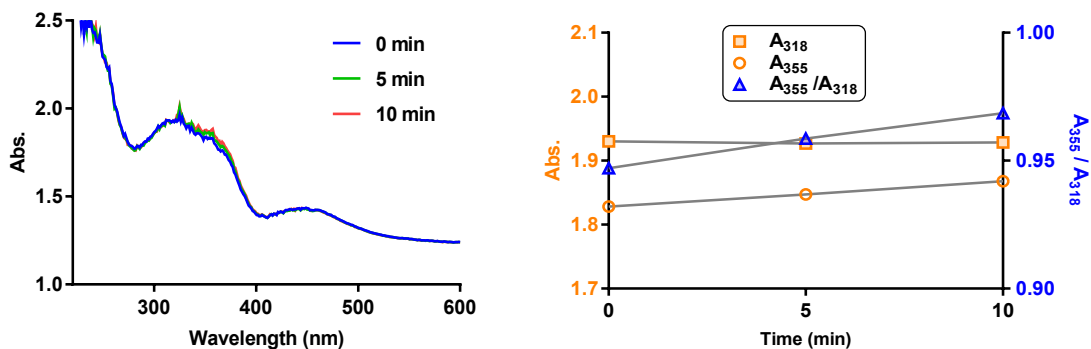


Figure 171 : *cis*-azobenzene predominant PDMS-AB film was set in dark at rt for 5 and 10 min (left). The  $A_{318}$  value did not change (from 1.930 to 1.928), the  $A_{355}$  value increased slightly from 1.828 to 1.868 and the  $A_{355}/A_{318}$  ratio increased slightly from 0.947 to 0.968.

#### 4.1.4.5 $^1\text{H}$ NMR determination of the photostationary state

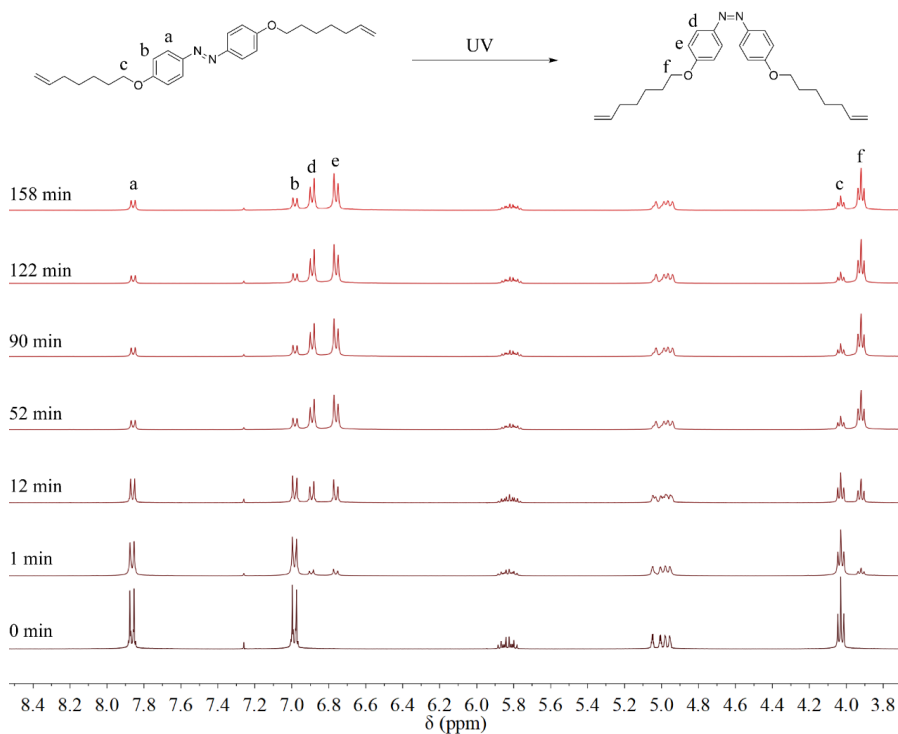
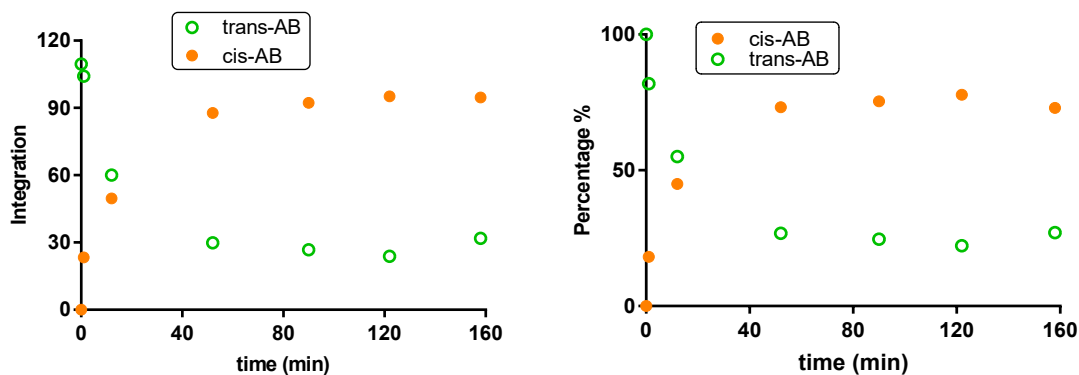


Figure 172 :  $^1\text{H}$  NMR overlay of UV 365 nm irradiated solution of azobenzene diene in  $\text{CDCl}_3$ . The  $^1\text{H}$  NMR at each time interval was recorded.



**Figure 173 : Evolution of integration of chemical shifts from *trans*- and *cis*-azobenzene (left). Percentage of *cis*- and *trans*- azobenzene changed with increasing UV irradiation time. The photostationary state contains ~75% *cis*-azobenzene and ~25% *trans*-azobenzene.**

#### 4.1.4.6 Kinetic study of strained PDMS-AB film

For all kinetic experiments, PDMS-AB film was irradiated with a UV365nm handheld lamp for 30 s. The film was then stretched to 0%, 40%, 60%, 80%, 90% or 100% strain with a homebuilt stretcher. The *cis*-to-*trans* evolution kinetics was traced from UV-vis absorption at 318 nm (isosbestic point) and 355 nm. The absorption was measured every 2 min and 500 data points were collected. Kinetic data at 0% were fitted with one-phase association, while the other data were fitted with two-phase and one-phase association correlation.

For two-phase fitting, the summation of contribution in fast and slow phase is 100%. We did not constrain the  $k_0$  to the value obtained from 0% stain kinetics due to the fact that each kinetics measurement takes 17 h so that they are performed on different days. And the temperature variation depends on day to day. We performed the following

calculation to demonstrate that, ~2 K difference in temperature could lead to change of  $0.65 \times 10^{-5} \text{ s}^{-1}$  in 0 % strain rate constant.

According to the transition state theory:  $k_0 = \frac{k_B T}{h} e^{\frac{-\Delta G^\ddagger}{RT}}$

If  $k_0 = 2.70 \times 10^{-5} \text{ s}^{-1}$  at  $T = 298 \text{ K}$ , then we have:  $\Delta G^\ddagger = 99.04 \text{ kJ/mol}$

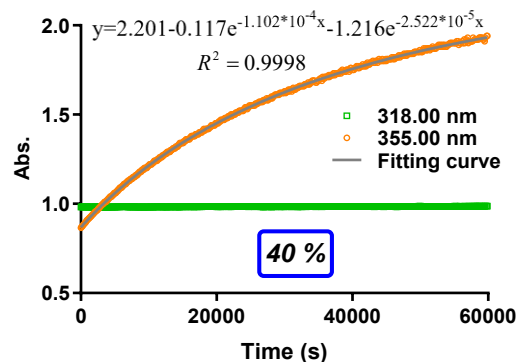
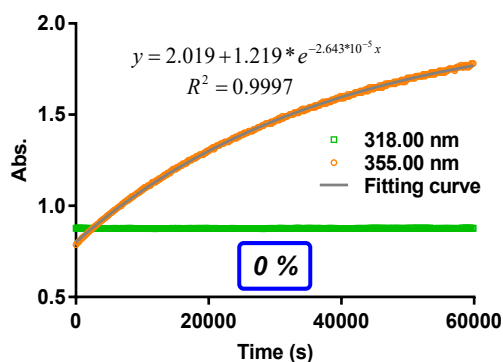
When  $T = 296 \text{ K}$ , we have  $k_0 = 2.05 \times 10^{-5} \text{ s}^{-1}$ .

In addition, there is no significant difference between fitting with and without constraining  $A_0, A_\infty$  (Table 23). Therefore, fittings were performed without constraint.

**Table 23 : Fitting result with  $A_0$  and  $A_\infty$  constrained/unconstrained**

|               | Constraint      | $A_0$ | $A_\infty$ | $k_0$                 | $k_F$                 | Fast% | $R^2$  |
|---------------|-----------------|-------|------------|-----------------------|-----------------------|-------|--------|
| Constrained   | $A_0, A_\infty$ | 0.344 | 1.370      | $1.82 \times 10^{-5}$ | $8.13 \times 10^{-5}$ | 14    | 0.9999 |
| Unconstrained | /               | 0.346 | 1.323      | $2.06 \times 10^{-5}$ | $8.66 \times 10^{-5}$ | 11    | 0.9999 |

A representative set of kinetic data at each strain are shown here (fitting were performed without constraint):



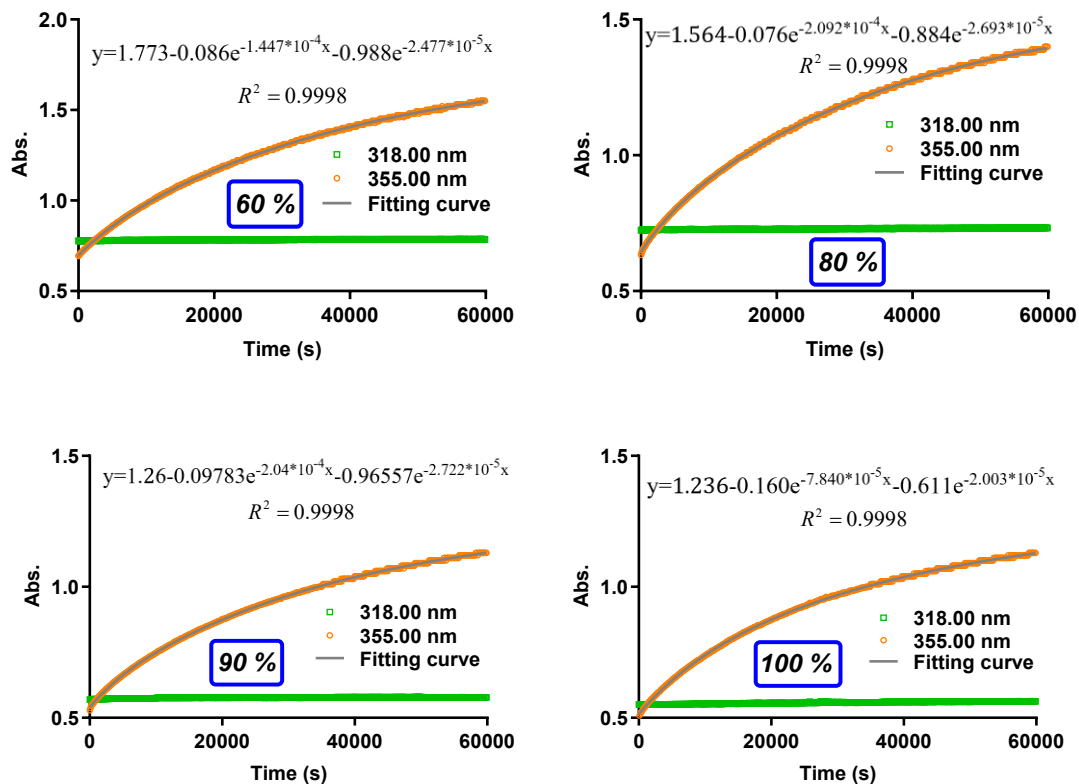


**Figure 174 : Representative kinetics of cis-to-trans isomerization in PDMS-AB film at various strains. 0% strain curve was fitted with one-phase association, strained kinetics were analyzed with two-phase association.**

To visualize the force accelerated cis-to-trans isomerization in the kinetics data, the absorbance at 355 nm data was normalized using the following equation:

$$I = A_t / (A_f - A_i)$$

Where  $A_t$  is the absorbance at time  $t$ ,  $A_f$  and  $A_i$  are final and initial absorbance.

**Table 24 : Two-phase fitting of obtained isomerization rate constants under various strains.**

| Strain             | 0%                   |                      |                      | 40%                   |                       |                      |
|--------------------|----------------------|----------------------|----------------------|-----------------------|-----------------------|----------------------|
|                    | 1                    | 2                    | 3                    | 1                     | 2                     | 3                    |
| $k_1$ ( $s^{-1}$ ) | $2.7 \times 10^{-5}$ | $2.8 \times 10^{-5}$ | $2.6 \times 10^{-5}$ | $2.4 \times 10^{-5}$  | $2.5 \times 10^{-5}$  | $2.0 \times 10^{-5}$ |
| $k_2$ ( $s^{-1}$ ) | /                    | /                    | /                    | $11.8 \times 10^{-5}$ | $10.2 \times 10^{-5}$ | $8.4 \times 10^{-5}$ |
| Fast%              | /                    | /                    | /                    | 6.2                   | 8.8                   | 15.6                 |
| $R^2$              | 0.9997               | 0.9997               | 0.9997               | 0.9998                | 0.9998                | 0.9998               |

|                              |                      |                       |
|------------------------------|----------------------|-----------------------|
| <b>Avg. (s<sup>-1</sup>)</b> | 2.7×10 <sup>-5</sup> | 10.1×10 <sup>-5</sup> |
| <b>SD.</b>                   | 0.1×10 <sup>-5</sup> | 1.7×10 <sup>-5</sup>  |

| <b>Strain</b>                         | <b>60%</b>            |                       |                       | <b>80%</b>            |                       |                       |                       |
|---------------------------------------|-----------------------|-----------------------|-----------------------|-----------------------|-----------------------|-----------------------|-----------------------|
|                                       | 1                     | 2                     | 3                     | 1                     | 2                     | 3                     | 4                     |
| <b>k<sub>1</sub> (s<sup>-1</sup>)</b> | 2.5×10 <sup>-5</sup>  | 2.5×10 <sup>-5</sup>  | 2.4×10 <sup>-5</sup>  | 2.7×10 <sup>-5</sup>  | 2.6×10 <sup>-5</sup>  | 3.0×10 <sup>-5</sup>  | 2.5×10 <sup>-5</sup>  |
| <b>k<sub>2</sub> (s<sup>-1</sup>)</b> | 14.5×10 <sup>-5</sup> | 14.2×10 <sup>-5</sup> | 11.2×10 <sup>-5</sup> | 20.9×10 <sup>-5</sup> | 15.1×10 <sup>-5</sup> | 26.5×10 <sup>-5</sup> | 15.6×10 <sup>-5</sup> |
| <b>Fast%</b>                          | 8.1                   | 7.1                   | 8.8                   | 8.3                   | 8.6                   | 6.0                   | 10.0                  |
| <b>R<sup>2</sup></b>                  | 0.9998                | 1                     | 0.9998                | 0.9998                | 0.9999                | 0.9998                | 0.9999                |
| <b>Avg. (s<sup>-1</sup>)</b>          | 21.3×10 <sup>-5</sup> |                       |                       | 19.5×10 <sup>-5</sup> |                       |                       |                       |
| <b>SD.</b>                            | 1.5×10 <sup>-5</sup>  |                       |                       | 5.4×10 <sup>-5</sup>  |                       |                       |                       |

| <b>Strain</b>                         | <b>90%</b>            |                       |                       | <b>100%</b>           |                       |                      |
|---------------------------------------|-----------------------|-----------------------|-----------------------|-----------------------|-----------------------|----------------------|
|                                       | 1                     | 2                     | 3                     | 1                     | 2                     | 3                    |
| <b>k<sub>1</sub> (s<sup>-1</sup>)</b> | 2.6×10 <sup>-5</sup>  | 2.7×10 <sup>-5</sup>  | 2.7×10 <sup>-5</sup>  | 2.9×10 <sup>-5</sup>  | 2.5×10 <sup>-5</sup>  | 2.0×10 <sup>-5</sup> |
| <b>k<sub>2</sub> (s<sup>-1</sup>)</b> | 20.4×10 <sup>-5</sup> | 23.1×10 <sup>-5</sup> | 20.4×10 <sup>-5</sup> | 19.4×10 <sup>-5</sup> | 11.3×10 <sup>-5</sup> | 7.8×10 <sup>-5</sup> |
| <b>Fast%</b>                          | 8.4                   | 7.9                   | 9.2                   | 8.9                   | 16.5                  | 20.7                 |
| <b>R<sup>2</sup></b>                  | 0.9998                | 0.9998                | 0.9998                | 0.9999                | 0.9998                | 0.9999               |
| <b>Avg. (s<sup>-1</sup>)</b>          | 21.3×10 <sup>-5</sup> |                       |                       | 12.8×10 <sup>-5</sup> |                       |                      |
| <b>SD.</b>                            | 1.5×10 <sup>-5</sup>  |                       |                       | 5.9×10 <sup>-5</sup>  |                       |                      |

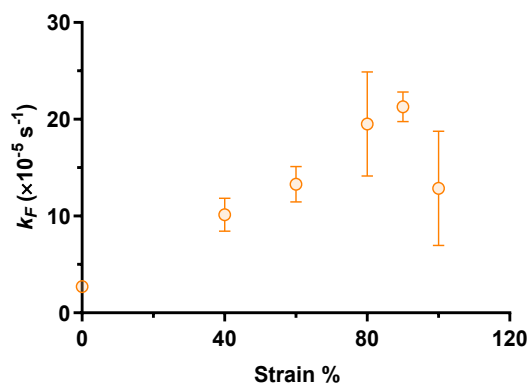


Figure 175 : Cis-to-trans isomerization rate of fast-phase azobenzene in PDMS-AB film at various strains.

Table 25 : Parameters obtained from one-phase fitting

| <b>Strain</b> | <b>0%</b> |   |   | <b>40%</b> |   |   |
|---------------|-----------|---|---|------------|---|---|
|               | 1         | 2 | 3 | 1          | 2 | 3 |

|                                |                      |                      |                      |                       |                       |                       |
|--------------------------------|----------------------|----------------------|----------------------|-----------------------|-----------------------|-----------------------|
| <b>k</b> (s <sup>-1</sup> )    | 2.7×10 <sup>-5</sup> | 2.8×10 <sup>-5</sup> | 2.6×10 <sup>-5</sup> | 2.78×10 <sup>-5</sup> | 3.05×10 <sup>-5</sup> | 3.00×10 <sup>-5</sup> |
| <b>R<sup>2</sup></b>           | 0.9997               | 0.9997               | 0.9997               | 0.9997                | 0.9996                | 0.9995                |
| <b>Avg.</b> (s <sup>-1</sup> ) | 2.7×10 <sup>-5</sup> |                      |                      |                       | 2.94×10 <sup>-5</sup> |                       |
| <b>SD.</b>                     | 0.1×10 <sup>-5</sup> |                      |                      |                       | 0.14×10 <sup>-5</sup> |                       |

| <b>Strain</b>                           | <b>60%</b>            |                       |                       | <b>80%</b>            |                       |                       |                       |
|---|-----------------------|-----------------------|-----------------------|-----------------------|-----------------------|-----------------------|-----------------------|
|   | 1                     | 2                     | 3                     | 1                     | 2                     | 3                     | 4                     |
| <b>k<sub>1</sub></b> (s <sup>-1</sup> ) | 3.03×10 <sup>-5</sup> | 3.01×10 <sup>-5</sup> | 3.01×10 <sup>-5</sup> | 3.24×10 <sup>-5</sup> | 3.16×10 <sup>-5</sup> | 3.31×10 <sup>-5</sup> | 3.22×10 <sup>-5</sup> |
| <b>R<sup>2</sup></b>                    | 0.9995                | 0.9996                | 0.9995                | 0.9991                | 0.9994                | 0.9994                | 0.9993                |
| <b>Avg.</b> (s <sup>-1</sup> )          | 3.25×10 <sup>-5</sup> |                       |                       | 3.41×10 <sup>-5</sup> |                       |                       |                       |
| <b>SD.</b>                              | 0.75×10 <sup>-6</sup> |                       |                       | 0.78×10 <sup>-6</sup> |                       |                       |                       |

| <b>Strain</b>                           | <b>90%</b>            |                       |                       | <b>100%</b>           |                       |                       |
|---|-----------------------|-----------------------|-----------------------|-----------------------|-----------------------|-----------------------|
|   | 1                     | 2                     | 3                     | 1                     | 2                     | 3                     |
| <b>k<sub>1</sub></b> (s <sup>-1</sup> ) | 3.19×10 <sup>-5</sup> | 3.22×10 <sup>-5</sup> | 3.33×10 <sup>-5</sup> | 3.51×10 <sup>-5</sup> | 3.62×10 <sup>-5</sup> | 3.11×10 <sup>-5</sup> |
| <b>R<sup>2</sup></b>                    | 0.9991                | 0.9991                | 0.9990                | 0.9993                | 0.9991                | 0.9996                |
| <b>Avg.</b> (s <sup>-1</sup> )          | 3.25×10 <sup>-5</sup> |                       |                       | 3.41×10 <sup>-5</sup> |                       |                       |
| <b>SD.</b>                              | 0.75×10 <sup>-6</sup> |                       |                       | 0.78×10 <sup>-6</sup> |                       |                       |

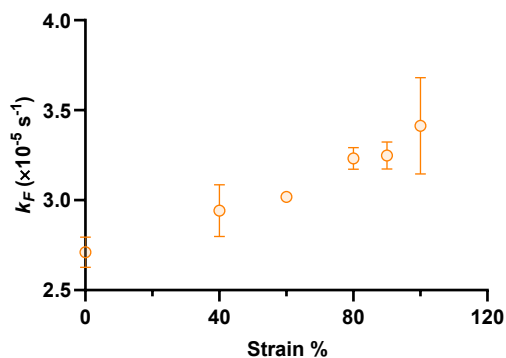


**Figure 176 : Cis-to-trans isomerization rate of azobenzene in PDMS-AB film at various strains.**

We further compared the evolution of average force in the bulk materials retrieved from one- and two-phase fitting analysis. For one-phase fitting, we estimated the average force by simplifying the force assisted isomerization with Bell-Evan model:

$$\langle F \rangle = \frac{k_B T}{\Delta x^\ddagger} \ln(k_F/k_0)$$

In two-phase fitting analysis, we assumed zero force on slow (unstrained) azobenzene stands. The average force in the bulk is estimated as the product of average force of fast-phase component and percentage of fast phase:  $\langle F \rangle = \langle F \rangle_{fast} \times \langle fast\% \rangle$

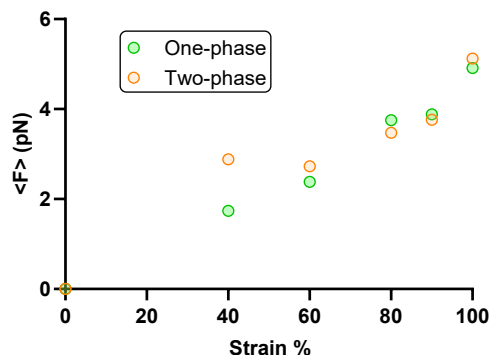


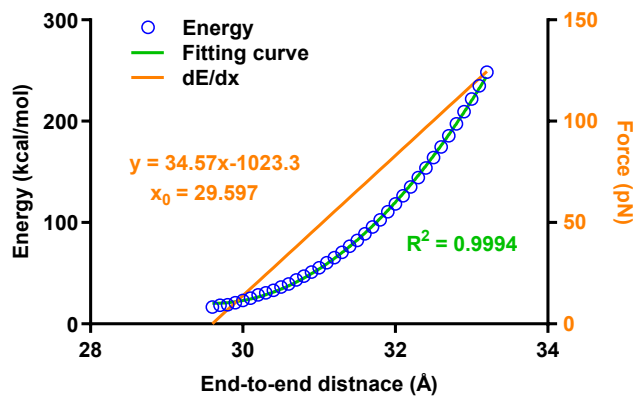
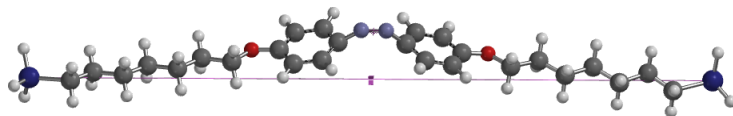
**Figure 177 : Average force calculated from one- and two-phase fitting analysis**

#### 4.1.4.7 CoGEF modeling

The CoGEF modeling was performed on Spartan station according to previous literature.<sup>82,86</sup> The ground states of both *cis*- and *trans*- azobenzene were optimized using Semi-empirical at the PM6 level. We adopted the transition state for the inversion mechanism. GoGEF were performed using Molecular Mechanics at MMFF level.

CoGEF modeling of *cis*-AB:

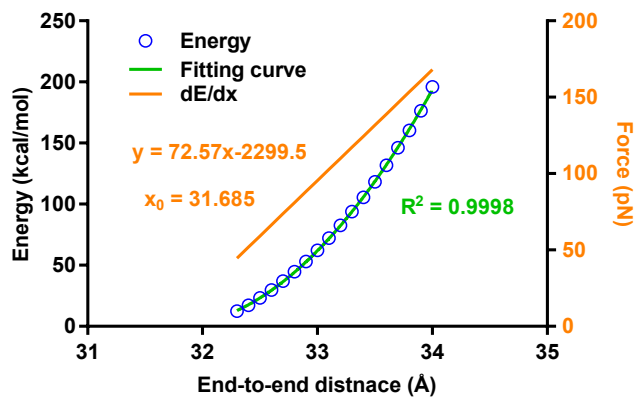
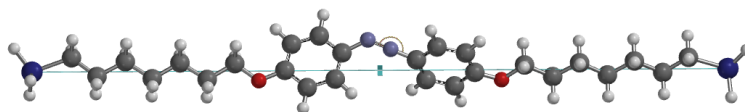
The C-N=N-C dihedral angle was held constant while the distance between terminal Si atoms was decreased from 34 Å to 26 Å in 81 steps. The energy profile was plotted against end-to-end distance. First derivative of energy-distance curve provides the force-distance relation. Extrapolation to zero force give the force free end-to-end distance of *cis*-AB.



**Figure 178 : CoGEF modeling of *cis*-AB**

### CoGEF modeling of transition state (TS)

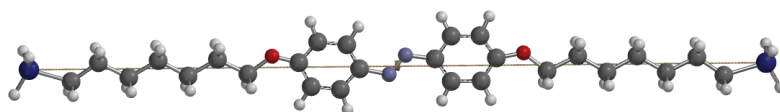
We assumed the *cis*-to-*trans* isomerization of AB proceeds via an inversion mechanism.<sup>288</sup> The plane of one phenyl substituent was fixed perpendicular to the second phenyl ring that has a N=N-C angle of 180°. The N=N-C angle was then constrained to 180° while the distance between terminal Si atoms were stepped from 34 Å to 26 Å in 81 steps of equal increments. The energy profile was plotted against end-to-end distance. First derivative of energy-distance curve provides the force-distance relation. Extrapolation to zero force give the force free end-to-end distance of TS.



**Figure 179 :s CoGEF modeling of TS**

CoGEF modeling of *trans*-AB:

The end Si atoms of *trans*-AB were constrained from 38 Å to 30 Å in 81 steps. The energy profile was plotted against end-to-end distance. First derivative of energy-distance curve provides the force-distance relation. Extrapolation to zero force give the force free end-to-end distance of *trans*-AB.



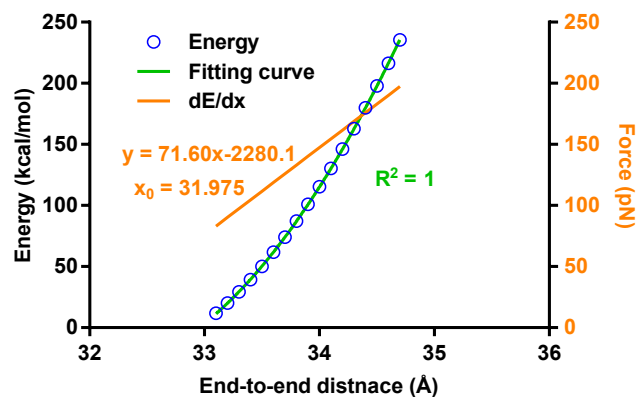


Figure 180 : CoGEF modeling of *trans*-AB

Table 26 : Summary of CoGEF modeling if azobenzene

|         | <i>cis</i> -AB | TS      | <i>trans</i> -AB | $\Delta x^\ddagger$ | $\Delta L$ |
|---------|----------------|---------|------------------|---------------------|------------|
| Trial 1 | 29.597         | 31.785  | 31.936           |                     |            |
| Trial 2 | 29.676         | 31.685  | 31.975           | /                   | /          |
| Trial 3 | 29.976         | 31.5496 | 31.976           |                     |            |
| Avg.    | 29.750         | 31.673  | 31.963           | 1.923               | 2.213      |
| SD.     | 0.200          | 0.118   | 0.023            |                     |            |

## 5. Mechanically integrated degradable polymers

### 5.1 Mechanically gated degradable polymers <sup>vi</sup>

Degradable polymers are desirable for the replacement of conventional organic polymers that persist in the environment, but they often suffer from the unintentional scission of the degradable functionalities on the polymer backbone, which diminishes polymer properties during storage and regular use. Herein, we report a strategy that combats unintended degradation in polymers by combining two common degradation stimuli—mechanical and acid triggers—in an “AND gate” fashion. A cyclobutane (CB) mechanophore is used as a mechanical gate to regulate an acid-sensitive ketal that has been widely employed in acid degradable polymers. This gated ketal is further incorporated into the polymer backbone. In the presence of acid trigger alone, the pristine polymer retains its backbone integrity, and delivering high mechanical forces alone by ultrasonication degrades the polymer to an apparent limiting molecular weight of 28 kDa. The sequential treatment of ultrasonication followed by acid, however, leads to a further 11-fold decrease in molecular weight to 2.5 kDa. Experimental and computational evidence further indicate that the ungated ketal possesses mechanical strength that is commensurate with the conventional polymer backbones. Single molecule force spectroscopy (SMFS) reveals that the force necessary to activate the CB molecular gate on the timescale of 100 ms is approximately 2 nN.

---

<sup>vi</sup> This chapter is adopted from: Lin, Y.; Kouznetsova, T. B.; Craig, S. L. Mechanically Gated Degradable Polymers. *J. Am. Chem. Soc.* **2020**, *142*, 2105-2109.

### 5.1.1 Introduction

Degradable polymers, including biodegradable polymers<sup>290</sup> and stimuli-degradable polymers,<sup>291-292</sup> are highly desirable targets for the purpose of alleviating plastic pollution that results from poor recycling and improper disposal of typically 'long-lived' synthetic organic polymers.<sup>293-294</sup> Typical degradable polymers contain degradable functionalities (e.g. ester,<sup>295</sup> azo,<sup>296-297</sup> ketal,<sup>298</sup>, disulfide,<sup>299</sup> diselenium<sup>154</sup> and other cleavable functionalities<sup>151</sup>) on the polymer backbone that cleave under an external trigger, thus leading to the fragmentation of the polymer main chain (Figure 181). Depending on the reactivities of the embedded functionalities, polymers that degrade in response to heat,<sup>300-301</sup> light,<sup>302</sup> force,<sup>192</sup> acid<sup>298</sup> and redox species<sup>151</sup> have been created. These degradable polymers have proven to be useful in drug delivery,<sup>292, 303</sup> biomedical surgery,<sup>304</sup> and designing transient electronics.<sup>305-306</sup> Despite exhibiting desirable degradability in response to mild triggers (e.g., orthoester or ketal containing polymers degrade in the presence of catalytic amount of acid), the instability that originates from the same degradable functionality increases the risk of diminished polymer properties under storage or in regular service. Therefore, polymers that are increasingly resistant to unintended degradation under storage or use conditions, while still responding to mild triggers for degradation, would be advantageous.

One strategy to achieving higher fidelity in triggered degradation is to combine existing degradation methods in an "AND gate" fashion (Figure 181), so that either stimulus alone leads to less degradation than the two in combination. The concept of gated

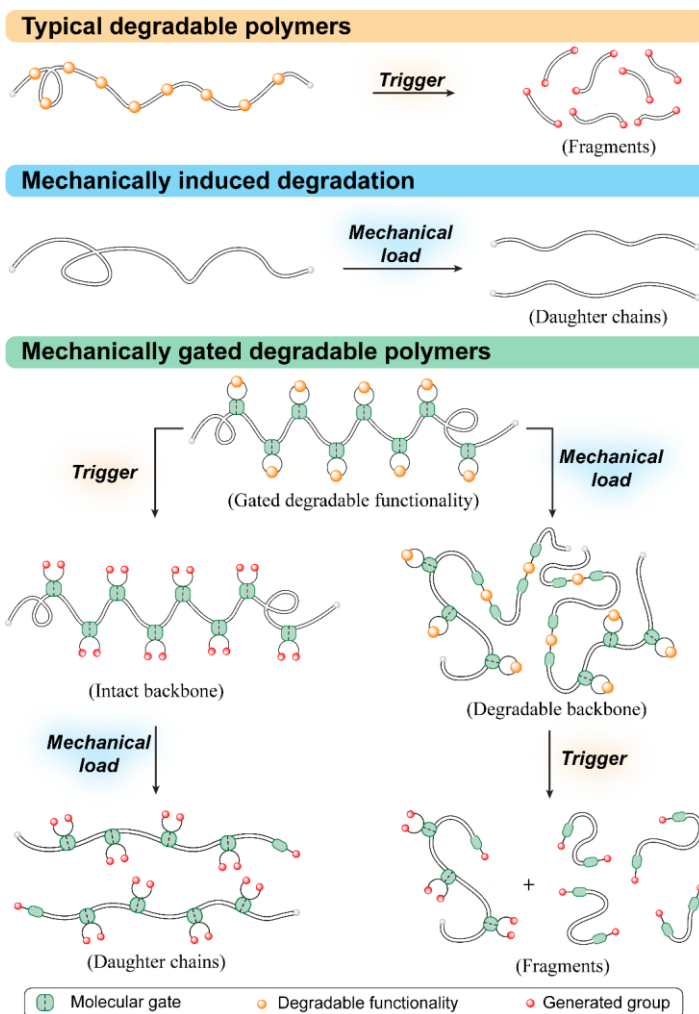


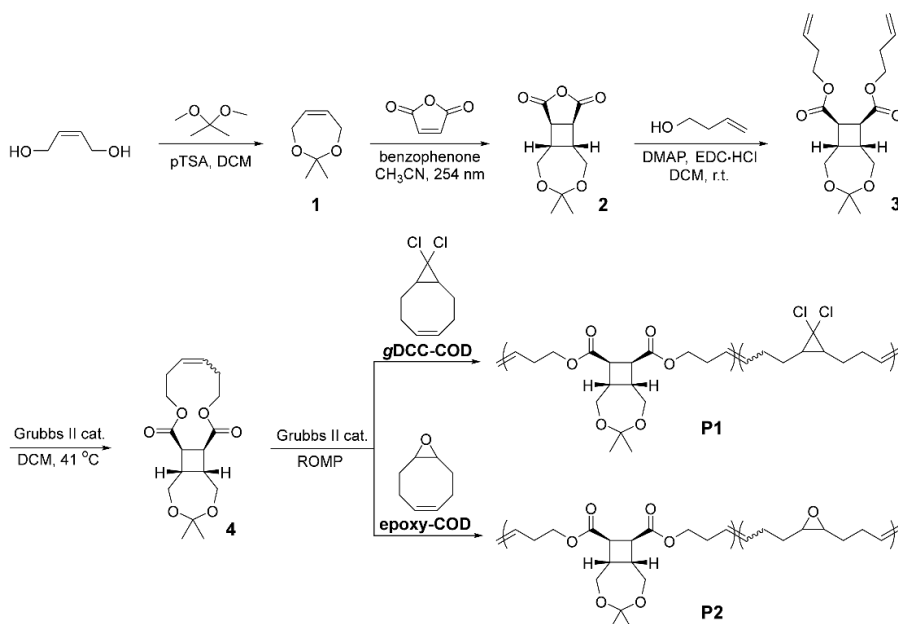
**Figure 181 : Typical degradable polymers decompose to fragments/oligomers due to cleavage of degradable functionalities. Subjection of polymer to mechanical force produces fragmented daughter chains. Mechanically gated degradable polymers retain intact backbone under an external trigger and chain cleaves after subsequent mechanical load, while sequential treatment of mechanical load and an external trigger allows polymers to fragment.**

function has been widely applied in regulable molecular systems. For example, regulation of chemical reactions underlies photochemically controlled self-healing and adhesion in polymers,<sup>307-308</sup> photo-regulable catalytic activity,<sup>309</sup> paralysis in living organs,<sup>310</sup> chemical or mechanochemical reactions,<sup>91, 311-312</sup> and chemically controlled photochromism<sup>313</sup>.

Subjection of polymer to mechanical force produces fragmented daughter chains. Mechanically gated degradable polymers retain intact backbone under an external trigger and chain cleaves after subsequent mechanical load, while sequential treatment of mechanical load and an external trigger allows polymers to fragment.

Mechanical force is a common trigger for degrading polymer molecular weight, and we were inspired by the recent use of a cyclobutane as a mechanochemical gate for the tandem activation of a *gem*-dichlorocyclopropane (gDCC) mechanophore.<sup>314</sup> The concept of mechanochemical gating was further exploited by Robb and co-workers to regulate photochromism<sup>315</sup> and small molecule release,<sup>44</sup> and Otsuka has similarly used photochemistry to gate mechanochemical reactivity.<sup>27</sup> In these latter examples, the “AND gating” is limited to a single event per chain. Here, we demonstrate that a similar mechanochemical gating concept (Figure 181) is also a viable strategy for degradable polymers. Broadly, we envisioned polymers in which a chemically triggered degradable functionality is gated in a side-chain loop by a mechanophore that is positioned along the polymer main chain. Thus, application of the chemical trigger alone would not lead to molecular weight degradation. On the other hand, subjecting the polymer to high mechanical loads would open the non-scissile gate, leading to many chemically degradable functionalities along the main chain. Because mechanochemical gating allows many degradable functionalities to be exposed per mechanical chain scission event, the combination of mechanical and chemical triggers would lead to greater degradation than either stimulus alone.

### Scheme 6 : Synthesis of mechanically gated degradable polymers **P1** and **P2**.



#### 5.1.2 Results and discussion

Our synthetic design is described in Scheme 6. Cyclic alkene **1** with acid-cleavable ketal group is subjected to photo [2+2] cycloaddition with maleic anhydride to provide cyclobutane (CB) containing molecule **2**. Esterification of **2** yields diene **3**, and subsequent ring-closing metathesis gives polymerizable macrocycle **4**. Further entropy-driven ring-opening metathesis polymerization (ED-ROMP)<sup>316</sup> of **4** with gDCC-COD and epoxy-COD co-monomers gives polymers **P1** and **P2**, respectively. These co-monomers were chosen for their respective demonstrated utility as internal standards of mechanochemical activity (gDCC in **P1**)<sup>84, 171, 317</sup> and as a means to promote high forces of adhesion to cantilevers in single molecule force spectroscopy (SMFS) studies (epoxide in **P2**).<sup>82</sup>

To verify that our design is resilient to acid alone, a THF solution of **P1** ( $M_n = 129$  kDa,  $D = 1.49$ ; 1.2 mg mL<sup>-1</sup>) was treated with trifluoroacetic acid (TFA) at room

temperature overnight to yield **P3**. GPC analysis reveals that the retention time shifts slightly from 13.38 min to 13.48 min, and multi-angle light scattering shows a decrease in number average molecular weight ( $M_n$ ) to 120 kDa (Figure 182b), which is attributed to the cleavage of the ketal ( $^1\text{H}$  NMR, Figure 182c) without main chain scission. Thus, the main chain of **P1** is resistant to acidic degradation.

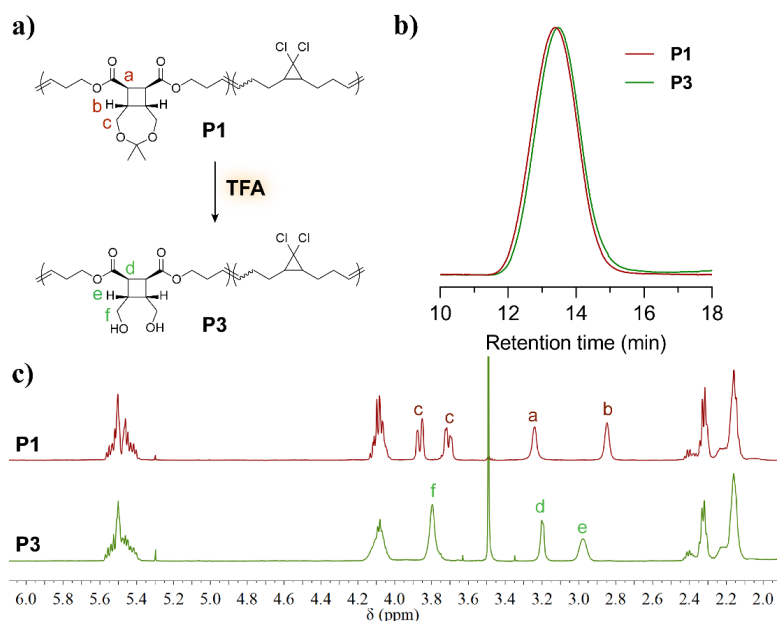


**Figure 182.** a) Treatment of **P1** polymer with TFA cleaves the ketal functionality but preserves the polymer backbone; b) Normalized GPC traces of **P1** and **P3**; c)  $^1\text{H}$  NMR spectrum of **P1** and **P3**.

If, however, **P1** ( $M_n = 154$  kDa,  $D = 1.53$ , 34 mol% **4**, 66 mol% gDCC-COD) is first subjected to pulsed ultrasonication ( $1 \text{ mg mL}^{-1}$  in THF, 1s on/1s off, ice bath,  $\text{N}_2$ ) for 240 min,  $^1\text{H}$  NMR indicates that the product **P4** comprises pristine and activated CB and gDCC mechanophores on the backbone (Figure 183a). The  $^1\text{H}$  NMR integrations show that 58% of CB and 85% of the gDCC internal standard are activated under these conditions. Notably, activation of CB produces E/Z alkenes in a ratio of  $\sim 2/1$  that is substantially

higher than 1.14/1 observed previously with a similar cyclohexane-fused CB mechanophore.<sup>50</sup> We hypothesize that the increased *E* content from the ketal-fused CB here is due to the more strained seven-member ring,<sup>318</sup> relative to the cyclohexyl ring reported previously, that is fused to the CB. Following initial C1-C2 bond scission, the greater ring strain in the current design might promote the rate of C3-C4 bond scission, so that it occurs more quickly relative to C1-C4 bond rotation in the diradical intermediate. Such dynamic competition has previously been implicated in determining the product stereochemistry, with rapid C3-C4 scission facilitating the formation of *EE* product.

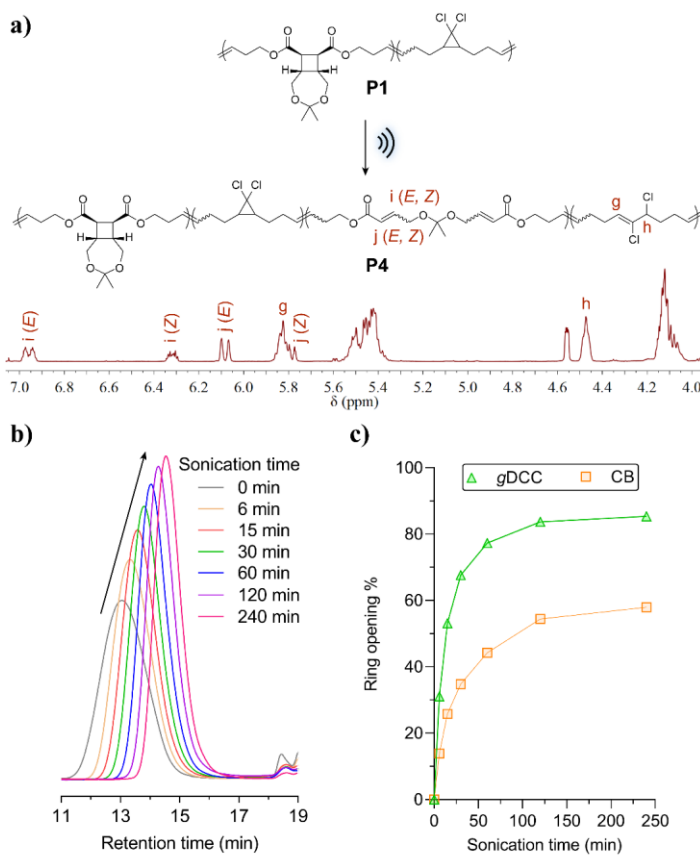


**Figure 183.** a) Mechanical conversion of P1 into P4; <sup>1</sup>H NMR spectrum of P4 after 30 min sonication. The relative integration of i(E) and i(Z) protons gives E:Z = 2:1; b) GPC traces of P4 as a function of sonication time; c) Ring-opening percentage of CB and gDCC over sonication time.

With increasing sonication time, GPC traces show a continuous shift to longer retention time (Figure 183b), as expected for typical polymer chain scission under pulsed ultrasonication. Meanwhile,  $^1\text{H}$  NMR indicates the activation of both CB and gDCC mechanophores due to sonication, with more ring opening observed for gDCC than CB (Figure 183c). The greater activity of gDCC relative to CB is consistent with prior reports on similar substrates.<sup>314</sup> The activation of CB results in unveiled ketals along the polymer backbone. To assess the mechanical stability of the ketals, we followed the procedure of previous studies that have shown that mechanically weak bonds on polymer backbones lead to less activation of gDCC internal standard per chain scission event.<sup>45, 170, 173</sup> After 15 min sonication, where the  $M_n$  reaches to half of initial value (from 154 kDa to 78 kDa, Figure 184d), the activation of gDCC reaches 53%. This gives 54% gDCC activation per average scission event, which is comparable to previous results on C-C bond containing polymers<sup>171</sup> and suggests that the ketal is mechanically robust relative to conventional hydrocarbon polymers. This experimental result is supported computationally by CoGEF<sup>135</sup> calculations that show that it is the C-O bond adjacent to the ester group, rather than the ketal, that breaks at high extension (Figure 204).

The mechanically activated **P4** was then treated with TFA. As seen in Figure 184a, TFA treatment of **P4** generates CB and gDCC containing polymer **P3'**, along with activated gDCC fragments/oligomers that are consistent with acid catalyzed hydrolysis of the ketals. The  $^1\text{H}$  NMR spectrum of the **P4** + TFA products shows activated CB and gDCC proton signals and, remarkably, signals from furanone. The formation of furanone is

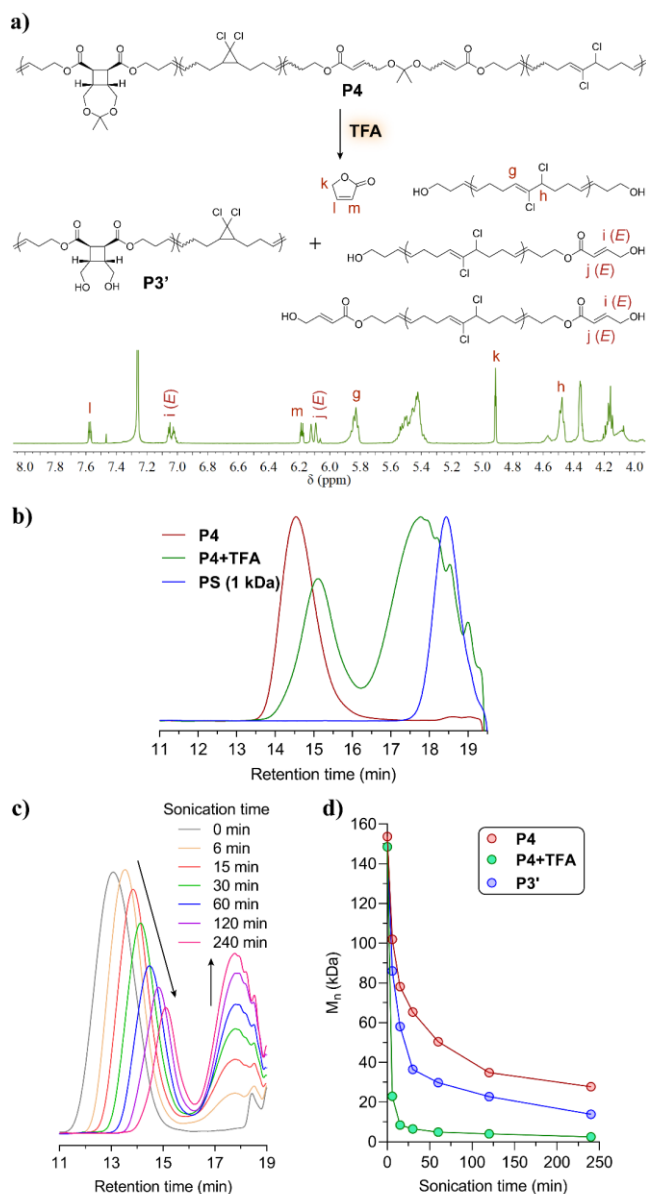


**Figure 184.** a) Schematic illustration of generated fragments and furanone after TFA treatment of P4 and its  $^1\text{H}$  NMR spectrum in  $\text{CDCl}_3$ . The molar ratio of furanone to E alkene species is 1/2. b) Overlay of normalized GPC traces of P4 polymer before (maroon) and after (green) TFA treatment. Blue trace is PS standard ( $M_n = 1000$  Da). c) GPC overlay of TFA treated P4 polymer with various sonication times. The arrows indicate the shift of polymer peak and increase of oligomer peak over sonication time. d) Comparison of  $M_n$  for P4 before (red dots) and after (green dots) TFA treatment and high molecular weight fragment P3' (blue dots).

attributed to quantitative conversion of the mechanically generated *Z* alkene, as supported by <sup>1</sup>H NMR integration. The GPC of the **P4** + TFA products is bimodal, with a higher molecular weight (MW) peak (**P3'**) that is shifted to longer retention times (lower MW) than untreated **P4**, and a new peak at even longer (~17-19 min) retention times that corresponds to low MW fragments and oligomers of ~1 kDa (Figure 184b). As sonication time increases, the GPC peak of **P3'** consistently shifts to longer retention time and the relative RI intensity of the oligomer region increases (Figure 184c). After 4 h of mechanical treatment followed by acid degradation, the gated system reaches an ultimate  $M_n$  of 2.5 kDa, in comparison to 28 kDa for the mechanical treatment alone and effectively no backbone degradation for acid treatment alone. Interestingly, the order of the combined treatment matters; reaction with TFA followed by 4 h of mechanical treatment leads to  $M_n$  = 22 kDa (Figure 187), because treatment with TFA converts the CB into a scissile “weak bond” whose activation now breaks the polymer main chain. That scission event prevents the activation of multiple CB mechanophores in the daughter fragments, and the associated <sup>1</sup>H NMR spectra are consistent with a single CB activation per chain scission event (Figure 190).

The gated cyclic ketal provides additional extension of the polymer upon mechanical activation of the CB gate, and so the design is well suited for quantitative studies of kinetics using previously reported SMFS techniques.<sup>87, 109</sup> A representative force-extension curve of **P2** (48 mol% **4**, 52 mol% epoxy-COD) is shown in Figure 185a. The mechanical activation of CB and subsequent release of reserved length give a

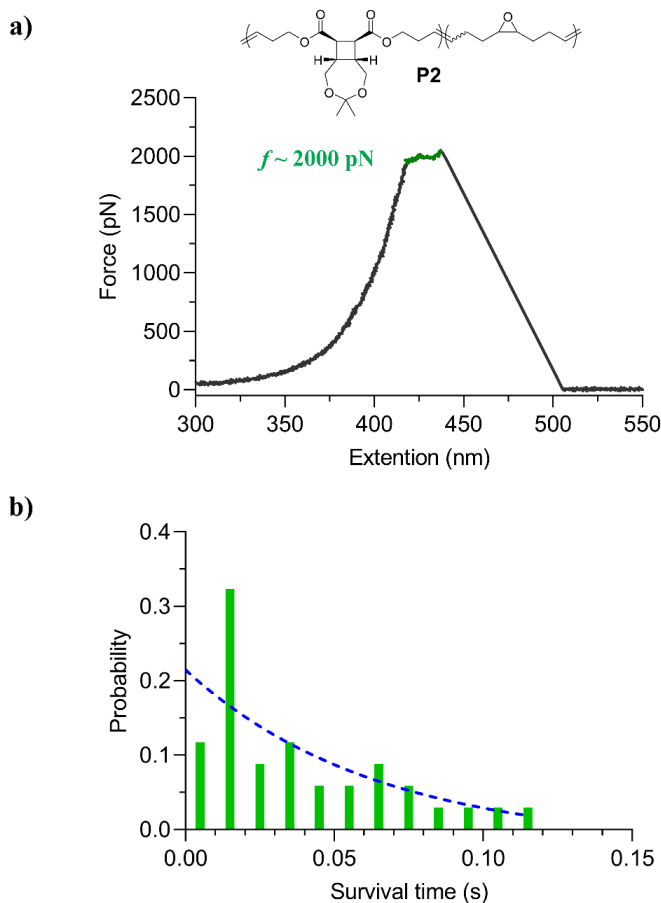


**Figure 185 : a) Representative force-extension curve of P2 polymer (pulling velocity: 300 nm/s). b) Probability distribution of survival time at transition force (green histogram) and corresponding one-phase fitting (blue dotted line,  $k = 16 \text{ s}^{-1}$ ). Note that very short survival times might be easily missed by visual inspection, artificially limiting the population of the lowest bin.**

characteristic plateau transition at  $f \sim 2000 \text{ pN}$ , which is about 200 pN lower than observed for a similar CB molecular gate fused to an eight-membered ring.<sup>314</sup> We attribute this minor difference in force to the greater ring strain in the fused CB in the present bicyclic design (see 5.1.3.6.1). Despite our best efforts, we were unable to obtain a force-extension curve in which the polymer completed the ring-opening transition. An analysis of the polymer survival times in the plateau region (Figure 185b) is consistent with an effective

(but approximate) rate constant for chain detachment of  $16 \text{ s}^{-1}$  at the plateau force of ca. 2000 pN. The competition with chain detachment limits the average fractional extension observed to only  $\sim 1.5\%$ , far less than the 34% extension expected from modeling (see section 5.1.3.6.3).

In summary, we have demonstrated that gated backbones provide access to polymers that are efficiently degraded by combinations of triggers used commonly in polymer degradation (here, mechanical force and acid), but that are resistant to degradation from either trigger alone. If similar concepts (e.g., combinations of degradable functionalities with other photo/chemical gates) could be applied to scale, it might lead to new degradable polymer systems that are increasingly (if not perfectly) robust and more reliably maintain their properties during regular service. Beyond degradability, we also envision that the cleavable, gated ketal functionality provides a mechanism to chemically regulate the stress-relieving behavior (turning extensible mechanophores into scissile mechanophores). We are currently applying this concept to the study of stress-relief and fracture behavior in mechanophore-enriched polymer networks.

## **5.1.3 Experimental section**

### **5.1.3.1 Materials and characterization**

Materials: Lab general solvents (dichloromethane, acetonitrile, hexane, ethyl acetate, acetone, tetrahydrofuran, methanol) were purchased from VWR or Sigma Aldrich. Maleic anhydride, cis-buten-1,4-diol, 2,2-dimethoxypropane, *p*-toluenesulfonic

acid (pTSA), benzophenone, 3-buten-1-ol, 4-(dimethylamino)pyridine (DMAP), N-(3-dimethylaminopropyl)-N'-ethylcarbodiimide hydrochloride (EDC·HCl), Grubbs II catalyst, 9-oxabicyclo[6.1.0]non-4-ene and trifluoroacetic acid (TFA) were purchased from Sigma Aldrich or Alfa Aesar and used without further purification.

Characterizations:  $^1\text{H}$  NMR and  $^{13}\text{C}$  NMR spectra were collected on a 400 MHz Varian INOVA spectrometer or a 500 MHz Bruker spectrometer. Chemical shifts are given in *ppm* ( $\delta$ ) and referenced to the residual  $^1\text{H}$  peak at 7.26 ppm or  $^{13}\text{C}$  peak at 77.16 ppm in  $\text{CDCl}_3$ .  $^1\text{H}$  shifts are reported as chemical shift, multiplicity, coupling constant if applicable, and relative integral. Multiplicities are reported as: singlet (s), doublet (d), doublet of doublets (dd), doublet of triplets (dt), doublet of doublet of doublets (ddd), doublet of doublet of triplets (ddt), triplet (t), triplet of doublets (td), quartet (q), multiplet (m), or broad (br). Coupling constants (J) are reported in Hertz. High-resolution mass spectra were collected on an Agilent LCMS-TOF-DART at Duke University's Mass Spectrometry Facility.

Ultrasonication was performed with a Sonics VCX 750 generator using a 13 mm tip. Pulsed ultrasound (1s on, 1s off) was applied under  $\text{N}_2$  atmosphere while cooled with an ice bath. Aliquot was taken from the solution and subjected to GPC and  $^1\text{H}$  NMR analysis.

Gel permeation chromatography (GPC) was performed on two Agilent PLgel mixed-C columns ( $10^5 \text{ \AA}$ , 7.5x300 mm, 5  $\mu\text{m}$ , part number PL1110-6500) using THF (stabilized with 100 ppm BHT) as the eluent. Molecular weights were calculated using a

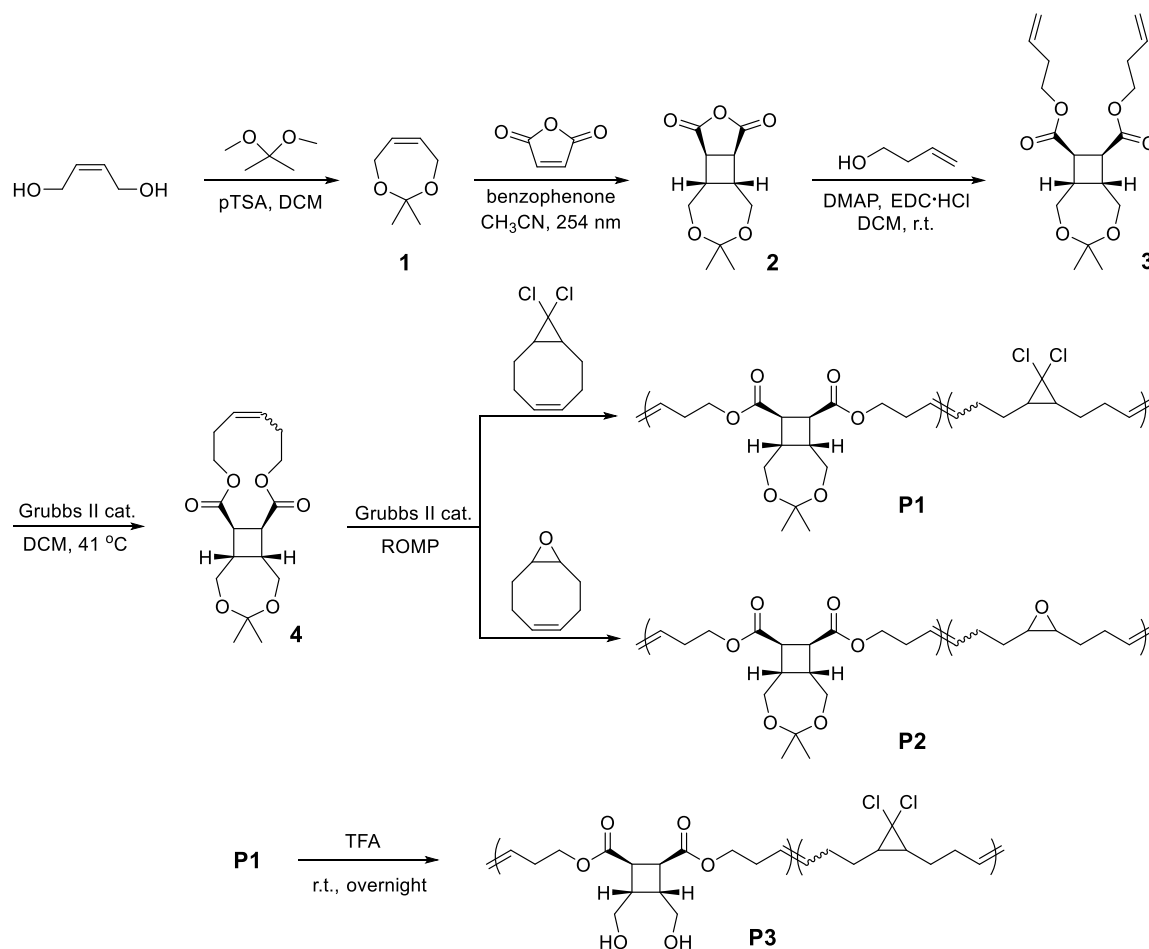
Wyatt Dawn EOS multi-angle light scattering (MALS) detector and Wyatt Optilab DSP Interferometric Refractometer (RI). The refractive index increment ( $dn/dc$ ) values were determined by online calculation based on injections of known concentration and mass.

Single molecule force spectroscopy (SMFS) characterization: Sharp Microlever silicon probes (MSNL) and Silicon Nitride AFM Probes (PNP-DB) were correspondingly purchased from Bruker (Camarillo, CA) and NanoAndMore (Watsonville, CA). All of the SMFS studies were conducted at ambient temperature ( $\sim 23$  °C) using a homemade AFM, which was constructed using a Digital Instruments scanning head mounted on top of a piezoelectric positioner, similar to the one described in detail previously.<sup>1</sup> The AFM pulling experiments were conducted in a solution of toluene. The spring constant of each cantilever was calibrated in air, using the thermal noise method, based on the energy equipartition theorem as described previously.<sup>2</sup> Measurements were carried out in a closed fluid cell with scanning set for a series of approaching/retracting cycles. Probes were prepared by immersing in piranha solution (3:1  $H_2SO_4$  :  $H_2O_2$ ) for 15 minutes at room temperature and then immersing in deionized water and dried by touching them against a kimwipe. Silicon substrates were prepared by first allowing each to soak in hot piranha solution for 30 minutes and then washed with deionized water and dried under a stream of nitrogen. Caution should be used when handling piranha solution: it has been reported to detonate unexpectedly. The substrate and the cantilever were then placed in a UVO cleaner (ozone produced through UV light) for 15 minutes. After ozonolysis, the cantilever was mounted in the fluid cell. 20  $\mu$ L of a 0.05-0.1 mg/mL polymer solution was

added to the silicon substrate surface and allowed to dry. The silicon substrate was then placed on the piezoelectric stage of the AFM. Force curves were collected in dSPACE (dSPACE Inc. Wixom, MI) and analyzed using Matlab (The MathWorks, Inc., Natick, MA). All data were filtered during acquisition at 500 Hz. After acquisition, the data was calibrated and plotted by using homemade software written in Matlab language.

### 5.1.3.2 Synthesis

#### Synthetic scheme



#### Synthetic procedures

2,2-Dimethyl-1,3-dioxep-5-ene (1) was prepared according to reported literature<sup>319</sup>

Synthesis of compound 3:

To a 250 mL quartz flask, added compound **1** (2.56 g, 20 mmol), maleic anhydride (2.156 g, 22 mmol) and benzophenone (1.0 g) photosensitizer. 100 mL acetonitrile was then added and resulting solution was sparged with N<sub>2</sub> for 10 min. The flask was then sealed and subjected to UV 254 nm irradiation using a photochemical reactor from The Southern New England Ultraviolet Company (Model #RPR-100, RPR2537A/254 nm bulb). After 54 h irradiation, <sup>1</sup>H NMR of reaction mixture indicated ~65% conversion of reactant. The reaction was stop and solvent was then removed to give a yellow solid. 50 mL dry ethyl ether was added to disperse the solid. After stirred at r.t. for 10 min, insoluble solid was filtered and washed with diethyl ether. Ethyl ether was then removed to give a pale yellow solid (2.225 g). <sup>1</sup>H NMR suggested this solid contains mainly benzophenone, maleic anhydride and product **2**. This solid was then used in next step reaction without further purification. <sup>1</sup>H NMR (400 MHz, CDCl<sub>3</sub>): δ 3.98 (m, 2H), 3.76 (m, 2H), 2.90 (m, 2H), 1.41 (s, 3H), 1.39 (s, 3H).

To a 50 mL flask, crude product **2** (452 mg) and 3-buten-1-ol (516 μL, 6 mmol) were dissolved with 15 mL DCM. DMAP (24.4 mg, 0.2 mmol) was then added to the solution. The solution turned dark brown in a few seconds. EDC·HCl (764 mg, mmol) was then added in portions. The reaction was stirred at r.t. for overnight. After the reaction completed, the solution was diluted with 20 mL DCM and washed with 20 mL Na<sub>2</sub>CO<sub>3</sub> solution, 20 mL DI water and 20 mL brine. DCM phase was then dried with MgSO<sub>4</sub>. After filtration, the dark brown solution was then concentrated onto silica. Column

chromatography (0~25% EtOAc/hexane gradient eluent) gave compound **3** as a colorless oil (205 mg, 14.3% yield in two steps).

$^1\text{H}$  NMR (500 MHz,  $\text{CDCl}_3$ ):  $\delta$  5.77 (ddt,  $J = 17.0, 10.3, 6.7$  Hz, 2H), 5.18 – 4.99 (m, 4H), 4.13 (qt,  $J = 10.8, 6.8$  Hz, 4H), 3.92 – 3.81 (m, 2H), 3.76 – 3.64 (m, 2H), 3.24 (s, 2H), 2.86 (s, 2H), 2.37 (qt,  $J = 6.7, 1.4$  Hz, 4H), 1.38 (s, 3H), 1.37 (s, 3H).  $^{13}\text{C}$  NMR (125 MHz,  $\text{CDCl}_3$ ):  $\delta$  172.74, 134.06, 117.39, 102.63, 63.90, 61.96, 40.33, 39.32, 33.13, 25.58, 23.87. HRMS-ESI ( $m/z$ ):  $[\text{M} + \text{H}]^+$  calculated for  $\text{C}_{19}\text{H}_{29}\text{O}_6$ , 353.19587; observed 353.19651.

Synthesis of macrocycle **4**:

To a solution of compound **3** (205 mg, 0.57 mmol) in 300 mL DCM, added Grubbs II catalyst (51 mg, 0.057 mol). The solution was then refluxed at 41 °C for overnight. After the reaction was cooled down to r.t., 0.2 mL ethyl vinyl ether was added. The reaction was stirred for additional 30 min before concentrated on to silica. Macrocycle **4** was isolated by column chromatography (0~30% EtOAc/hexane gradient eluent) as a white solid (153 mg, 82.8%). This solid was further recrystallized from hexane and used for polymerization.  $^1\text{H}$  NMR (500 MHz,  $\text{CDCl}_3$ ):  $\delta$  5.57 – 5.32 (m, 2H), 4.43 (ddd,  $J = 10.7, 8.2, 4.4$  Hz, 2H), 4.09 – 3.96 (m, 2H), 3.91 – 3.79 (m, 2H), 3.75 – 3.60 (m, 2H), 3.24 (s, 2H), 2.90 (s, 2H), 2.60 – 2.19 (m, 4H), 1.36 (d,  $J = 2.1$  Hz, 6H).  $^{13}\text{C}$  NMR (125 MHz,  $\text{CDCl}_3$ ):  $\delta$  172.55, 172.42, 129.11, 128.73, 102.58, 63.69, 62.80, 62.01, 61.96, 40.85, 39.21, 38.86, 32.14, 31.74, 27.42, 25.56, 23.86, 22.80, 14.26. HRMS-ESI ( $m/z$ ):  $[\text{M} + \text{Na}]^+$  calculated for  $\text{C}_{17}\text{H}_{26}\text{O}_6\text{Na}$ , 347.14651; observed 347.14703.

Preparation of **P1** polymer:

To a 10 mL dried scintillation vial, added monomer macrocycle **4** (32.4 mg, 0.1 mmol) and gDCC-COD (19.1 mg, 0.1 mmol). The vial was then purged with argon. A solution of Grubbs II catalyst (1.4 mg,  $1.67 \times 10^{-3}$  mmol) in 2 mL dry DCM was prepared in another vial. This catalyst solution was then sparged with argon for 3 min. 200  $\mu$ L catalyst solution was then added to the monomer containing vial. The vial was then sealed, and polymerization underwent overnight. 200  $\mu$ L ethyl vinyl ether was then added to quench the polymerization, and the viscous solution was stirred for additional 30 min. The solution was then diluted with 0.2 mL DCM and precipitated from MeOH. This procedure was repeated twice to give a white polymer **P1**. (26 mg, 50%). This polymer was dried under high vacuum and further analyzed from GPC:  $dn/dc = 0.105$ ,  $M_n = 128.9$  kDa, PDI = 1.49.  $^1\text{H}$  NMR indicated 38 mol% incorporation of molecule **4**.

Preparation of **P2** polymer:

The preparation procedure of **P2** is similar to that of **P1**. Monomer macrocycle **4** (16.2 mg, 0.05 mmol) and gDCC-COD (19.1 mg, 0.1 mmol) were added to a 10 mL dried scintillation vial, followed by 100  $\mu$ L sparged Grubbs II catalyst solution (1.4 mg in 2 mL). After the polymerization was performed overnight, resulting viscous solution was quenched with 100  $\mu$ L ethyl vinyl ether and precipitated from MeOH. Obtained white polymer was then dissolved with 2 mL DCM, MeOH was then added dropwise to the solution under stirring. When the solution turned cloudy, addition was stopped. The cloudy solution was centrifuged at 4500 rpm for 5 min to give a thin layer of polymer at the bottom of vial. Upper clear solution was decanted and polymer was rinsed with MeOH. This

isolated polymer was then subjected to  $^1\text{H}$  NMR analysis and SMFS characterization.  $^1\text{H}$  NMR indicated 48 mol% incorporation of molecule 4.

### 5.1.3.3 Ultrasonication

TFA treatment followed by ultrasonication:

To a solution of **P1** polymer in THF (0.76 mg/mL), added 100  $\mu\text{L}$  MeOH and 100  $\mu\text{L}$  TFA. The solution was stirred at r.t. to give polymer **P3**. Full cleavage of ketal functionalities is confirmed by  $^1\text{H}$  NMR. The solution was then directly subjected to pulsed ultrasonication conditions. The solution was first degassed with  $\text{N}_2$  under ice-bath for 10 min. Next, pulsed ultrasound was applied (1s on, 1s off, 20 % amplitude) under  $\text{N}_2$  atmosphere. Aliquot (0.8 mL) at various sonication time (0, 15, 30, 60, 120, 240 min) was withdrawn from the solution and subjected to GPC and then  $^1\text{H}$  NMR analysis.

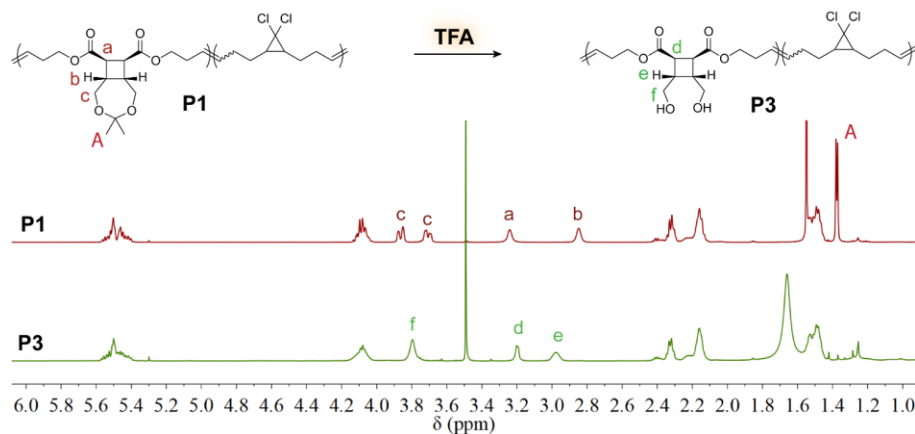


**Figure 186 :**  $^1\text{H}$  NMR ( $\text{CDCl}_3$ , 500 MHz) of **P1** and **P3** polymers. The disappearance of proton A signals and shifts of a, b and c protons suggest full cleavage of ketal functionalities.

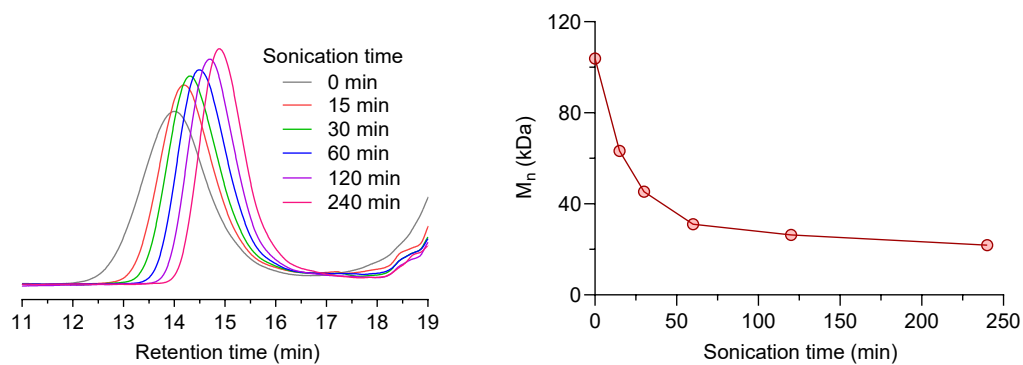


**Figure 187 : GPC RI signals (Left) and molecular weight (right) of P3 polymer ( $M_n = 153.7$  kDa) at various sonication times. The apparent limiting  $M_n$  of P3 polymer after 4 h sonication is 21.8 kDa.**

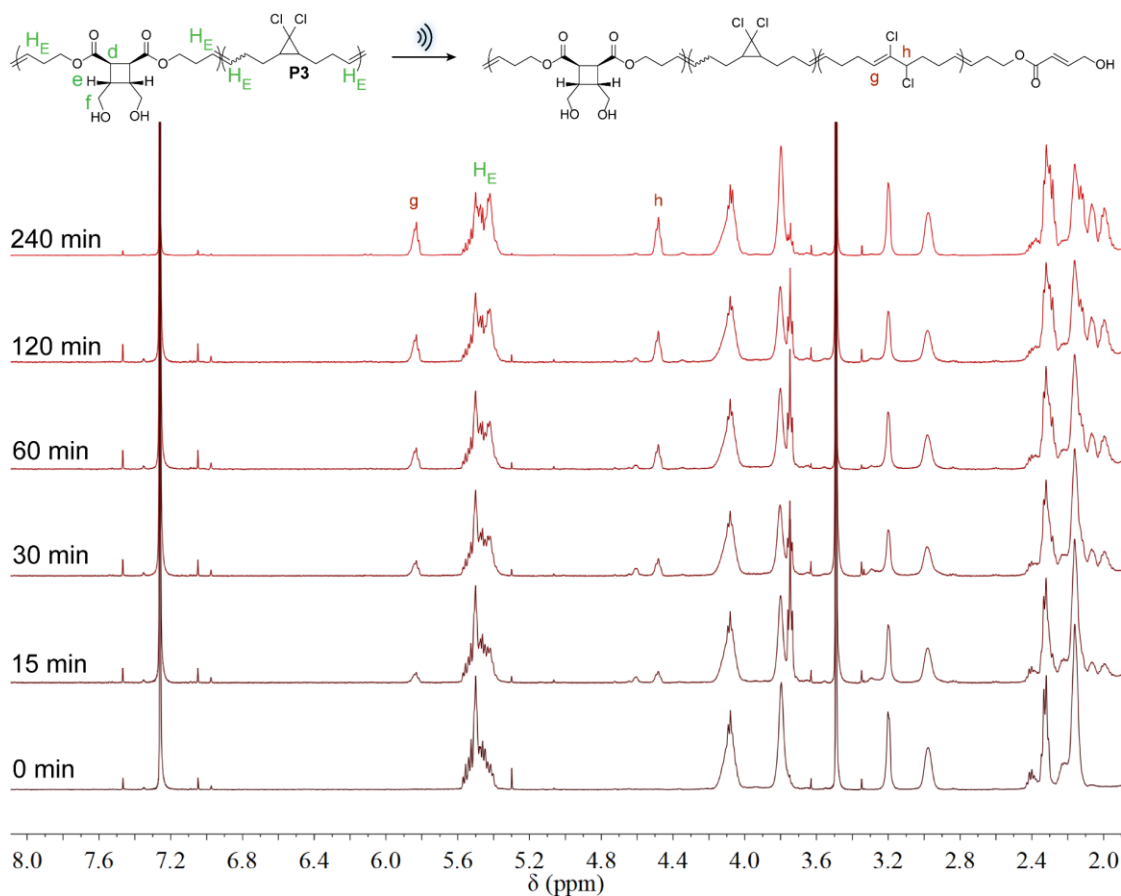


**Figure 188 :  $^1\text{H}$  NMR ( $\text{CDCl}_3$ ) spectrum overlay of P3 polymer with various sonication times.**

The amount of gDCC activation was analyzed using the following equation:

$$RO(gDCC)\% = \frac{2 \times \int H_g}{gDCC\% \times \int H_E} \times 100\%$$

$H_g$  is proton  $g$  from activated  $gDCC$  and  $H_E$  is alkene proton in the initial polymer;  $gDCC\%$  refers to the molar percentage of incorporated  $gDCC$  internal standard in the **P3** polymer.

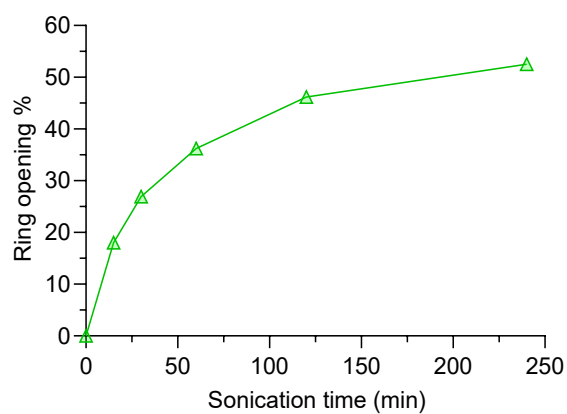


**Figure 189 : Percentage of  $gDCC$  ring opening in **P3** polymer at different sonication times.**

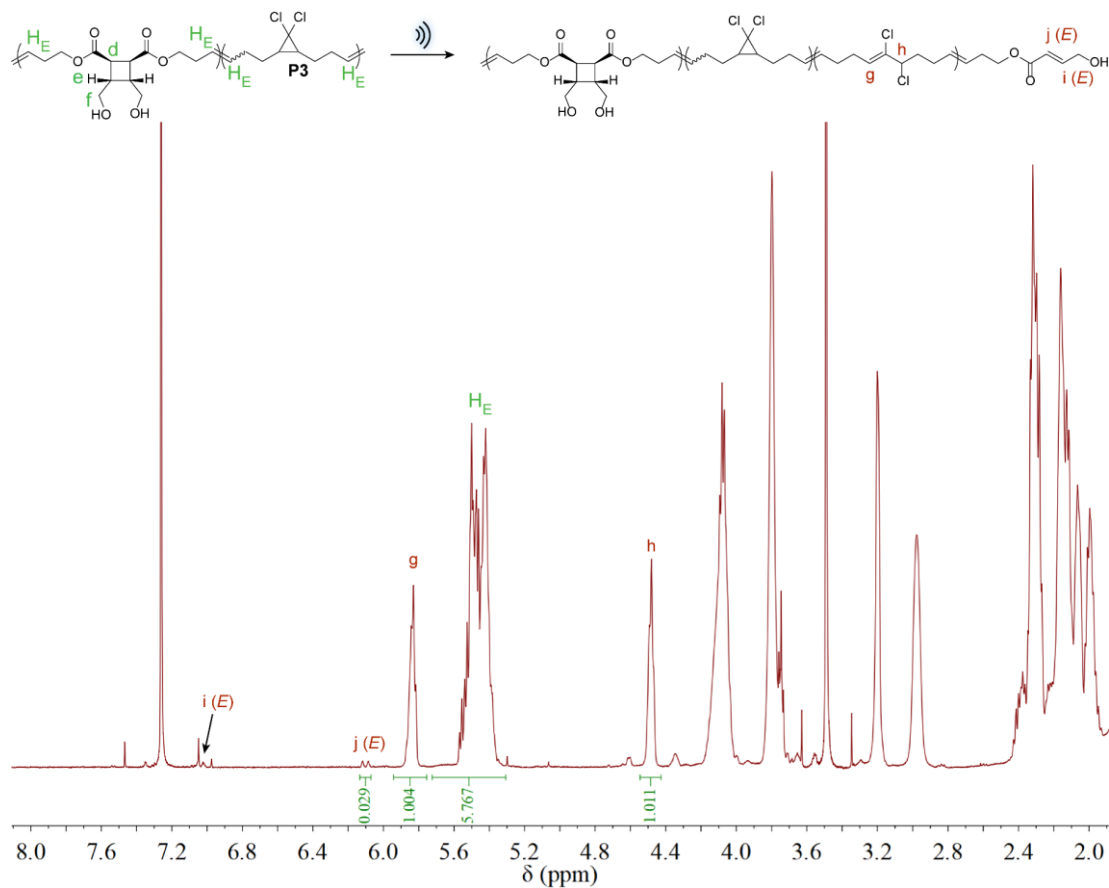


**Figure 190 :**  $^1\text{H}$  NMR ( $\text{CDCl}_3$ ) spectrum analysis of CB activation in P3 polymer after 4 h sonication.

To quantify the amount of cyclobutane (CB) activation, the  $^1\text{H}$  NMR spectrum of P3 polymer after 4 h sonication was further zoomed in to visualize the proton signals of activated CB ( $i(E)$  and  $j(E)$  in Figure 190). The activation percentage of CB can be calculated:

$$RO(\text{CB})\% = \frac{2 \times \int H_{(j(E))}}{\text{CB}\% \times \int H_E} \times 100\% = \frac{2 \times 0.029}{0.34 \times 5.767} \times 100\% = \sim 3\%$$

The initial P3 polymer has  $M_n = 103.8$  kDa. Therefore, the number of CB on polymer backbone can be calculated:

$$N(CB) = \frac{103800}{284 \times 0.34 + 191 \times 0.66} \times 34\% = 158$$

The number of activated CB after 4 h sonication can be obtained:  $158 \times 3\% = 4.7$

The molecular weight of **P3** polymer reduces from 103.8 kDa to 21.8 kDa after 4 h sonication. Hence, the scission cycle is:

$$SC = \frac{\ln(103.8/21.8)}{\ln 2} = 2.25$$

For the first scission cycle, polymer chain undergoes 1 scission event to generate two new chains. These two new chains further cleave to generate four chains in the second scission cycle, which accounts for 2 scission events. While in the third scission cycle, four chains break into eight chains with 4 scission events occur. Because CB is mechanical weak site compared to other covalent bond on backbone, if we assumed that each scission event would selectively occur on activating scissile CB mechanophores.

The theoretical number of activated CB after 4 h sonication is:  $1 + 2 + 0.25 \times 4 = 4$

This number agrees reasonably with value obtained from  $^1\text{H}$  NMR integration. Note that the error in  $^1\text{H}$  NMR integration could be significant for very small peak signals and would count for this slight difference.

### **Ultrasonication followed by TFA treatment**

For a typical pulsed ultrasonication experiment, a solution of **P1** polymer (1.0 mg/mL in dry THF) was degassed with  $\text{N}_2$  under ice-bath for 10 min. Pulsed ultrasound was applied (1s on, 1s off, 20 % amplitude) with solution kept under  $\text{N}_2$  atmosphere. At each (0, 6, 15, 30, 60, 120 and 240 min) sonication time, aliquot (1.0 mL) was taken from

the solution. 0.6 mL of withdrew solution was directly subjected to GPC and subsequent  $^1\text{H}$  NMR analysis. On the other hand, 0.4 mL of withdrew solution was added 10  $\mu\text{L}$  TFA. After overnight, the TFA treated solution was further analyzed from GPC and  $^1\text{H}$  NMR.

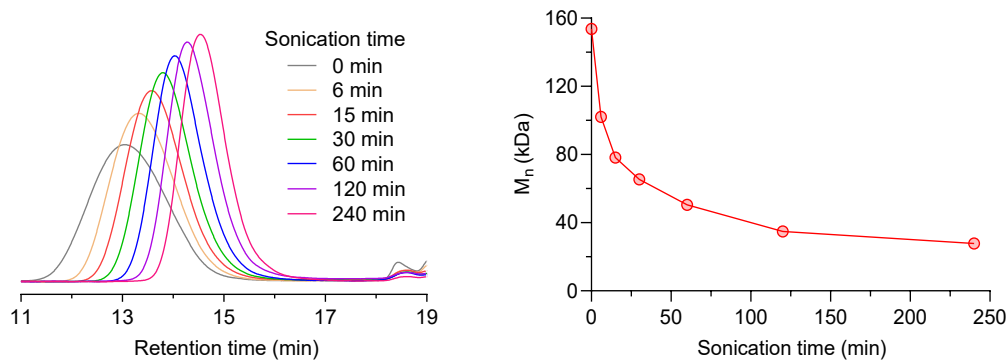


**Figure 191 : GPC RI signals (Left) and molecular weight (right) of P1 polymer ( $M_n = 153.7$  kDa) at various sonication times. The apparent limiting  $M_n$  of P1 polymer after 4 h sonication is 27.8 kDa.**

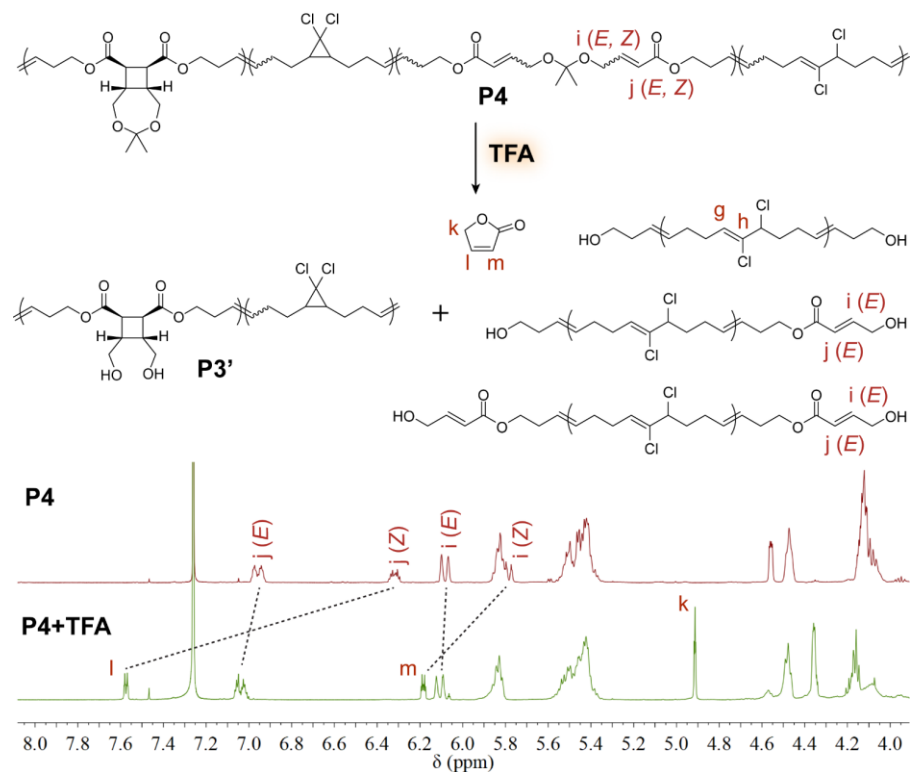


**Figure 192 :**  $^1\text{H}$  NMR ( $\text{CDCl}_3$ ) spectrum evolution of TFA treated P4 polymer (P1 polymer after 4 h sonication). The formation of furanone is ascribed to the rearrangement of generated *E* akene from CB.

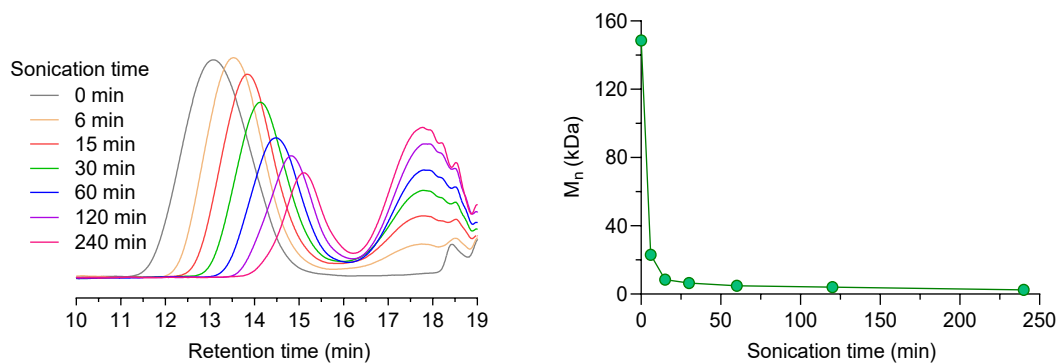


**Figure 193 :** GPC RI signals (Left) and molecular weight (right) of TFA treated P4 polymer.

The percentages of gDCC ring opening and CB activation were calculated from integration of  $^1\text{H}$  NMR.

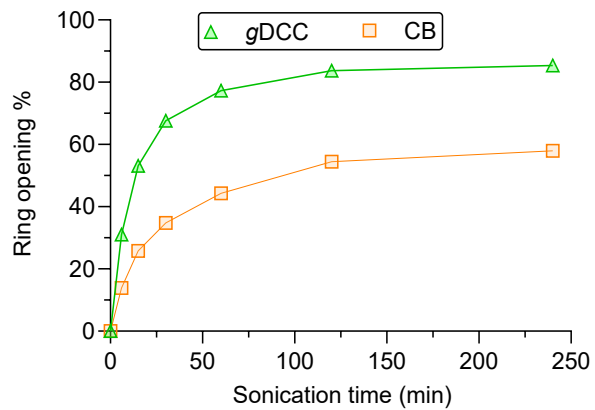


**Figure 194 : Percentages of gDCC ring opening and CB activation in P4 at different sonication times.**

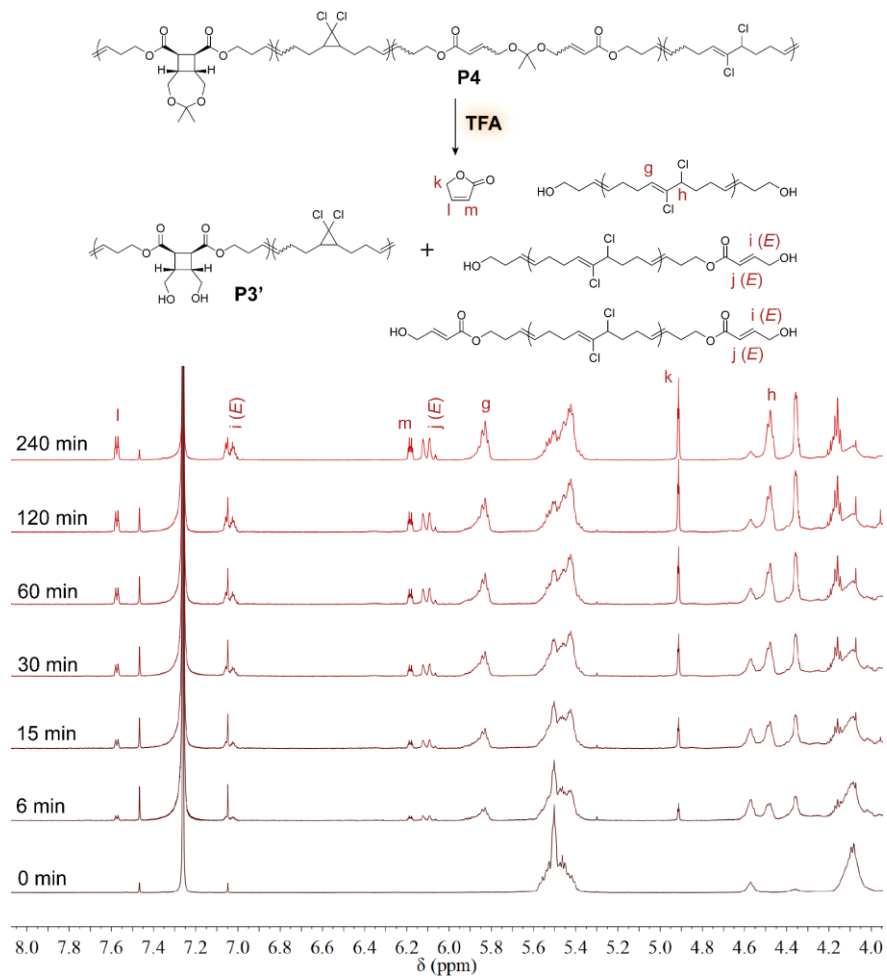


**Figure 195 : <sup>1</sup>H NMR spectrum (CDCl<sub>3</sub>) overlay of TFA treated P4 polymer with various sonication times.**

Ultrasonication within first scission cycle:

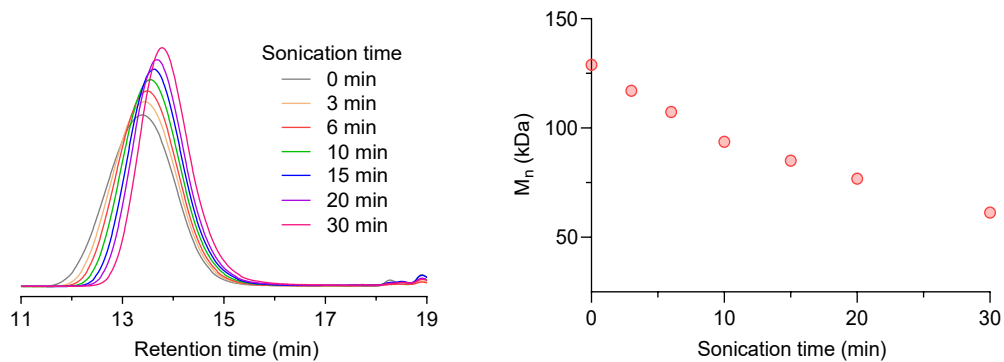


**Figure 196 : GPC RI signals (Left) and molecular weight (right) of P1 polymer ( $M_n = 128.9$  kDa) at various sonication time. The  $M_n$  reduces to 61.3 kDa after 30 min sonication.**

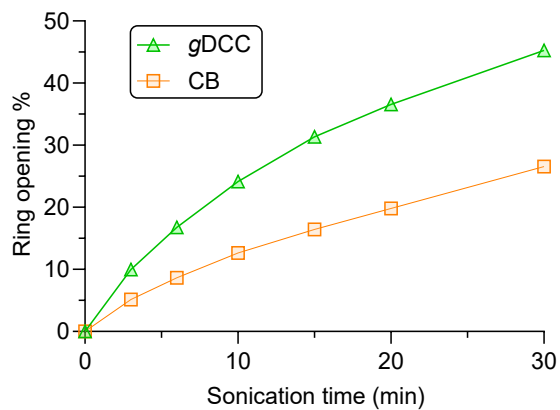


**Figure 197 : Percentages of gDCC ring opening and CB activation in P1 polymer at different sonication times.**

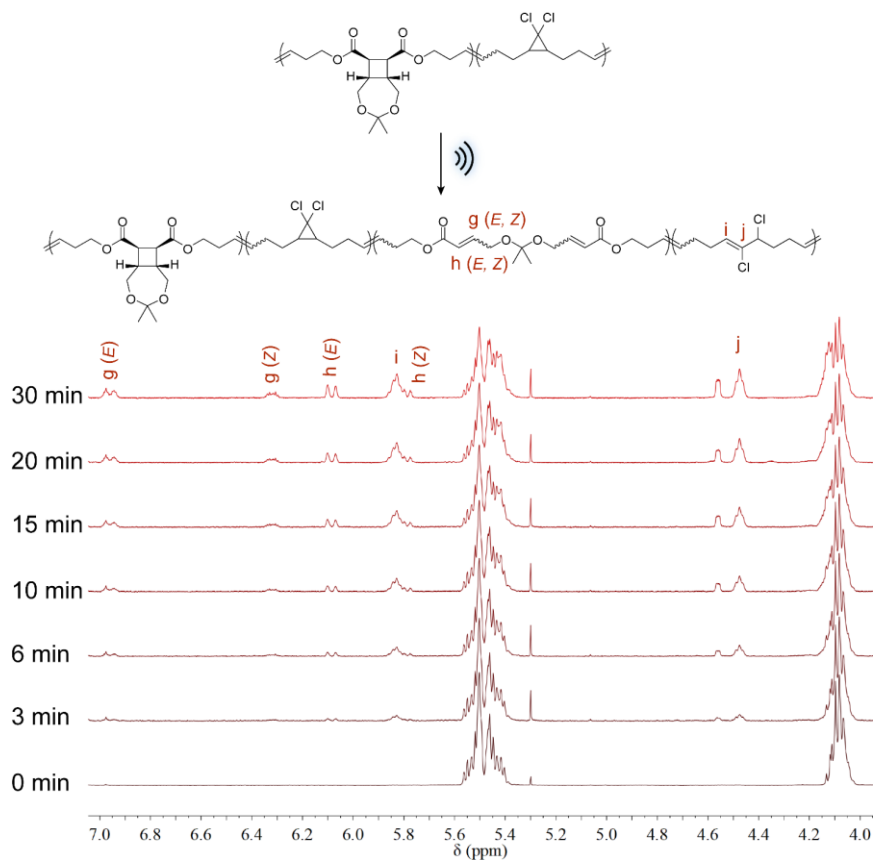


Figure 198 :  $^1\text{H}$  NMR ( $\text{CDCl}_3$ ) of P1 polymer after subjection to sonication for various time.

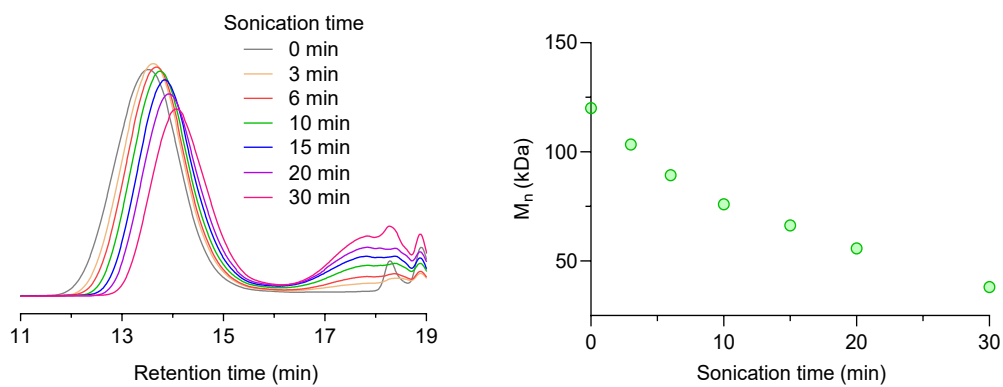
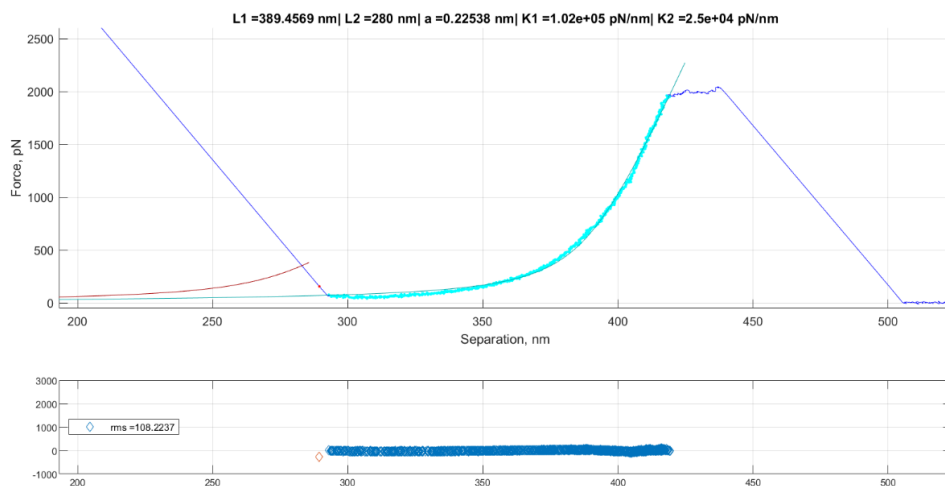


Figure 199 : Evolution of GPC RI signals (Left) and molecular weight (right) for sonicated P1 polymer after treated with TFA.

### 5.1.3.4 SMFS analysis

Force-extension curves were analyzed using method described in section 2.2.3.4.2. Pretransition curves were fitted with extended freely jointed chain (FJC) model to give the contour lengths of polymers before transition ( $L_i$ ). Due to the detachment of polymer chain at the high transition force, which is a very typical phenomenon in SMFS measurement, only part of cyclobutane mechanophores on the polymer backbone underwent ring opening. The length of extra extension was estimated by measure the length of observed plateau ( $\Delta x = x_2 - x_1$ ). The percentage of extra extension (EE%) was calculated by  $EE\% = \Delta x / L_i * 100\%$ . This value was summarized and further compared with that of theoretical calculation obtained assuming full cyclobutene ring-opening on polymer backbone (calculation details see section V. CoGEF modeling).



**Figure 200 : Fitting of force-extension curve with extended FJC model to give polymer contour length before transition ( $L_i = 389.4$  nm).**

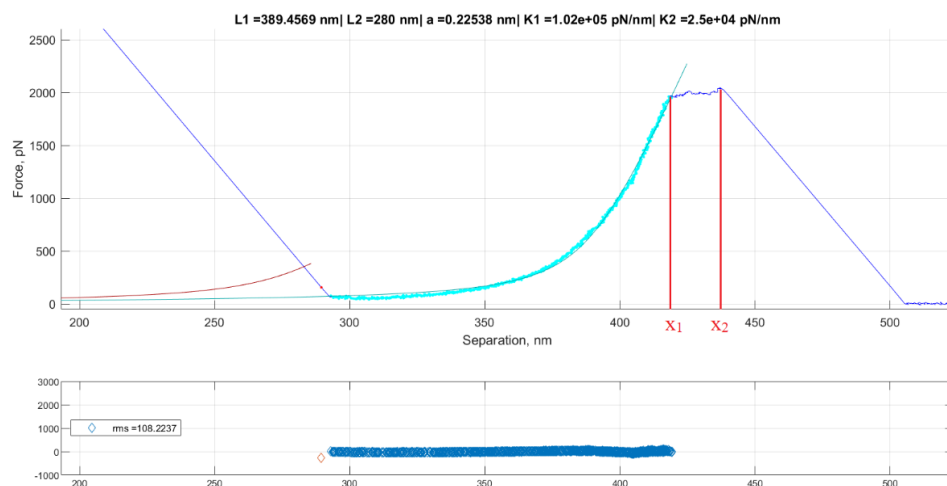
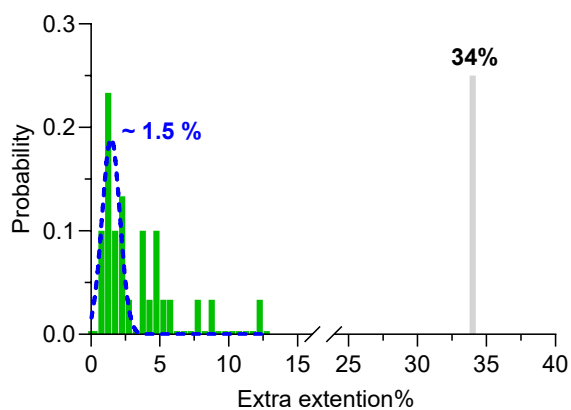


**Figure 201 : Estimation of extra extension from plateau ( $\Delta x = x_2 - x_1 = 438.4 - 417.8 = 20.6$  nm).**

**Table 27 : List of results from SMFS analysis**

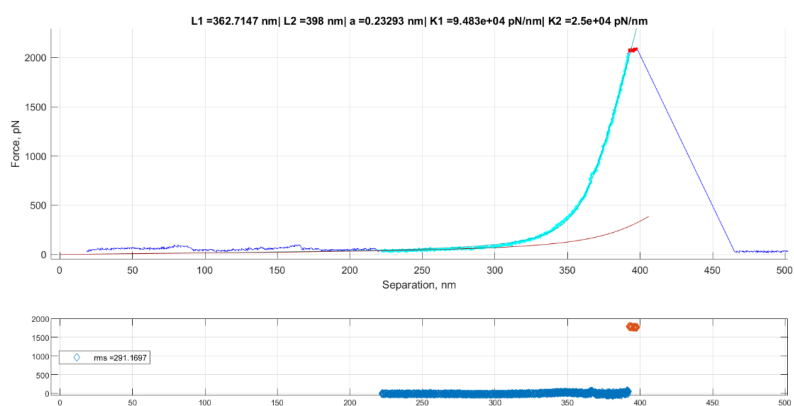
| #  | $L_i$ (nm) | $x_1$ (nm) | $x_2$ (nm) | $\Delta x$ (nm) | Survival time (s) | EE%  | $f$ (pN) |
|----|------------|------------|------------|-----------------|-------------------|------|----------|
| 1  | 483.7      | 524.7      | 546.6      | 21.9            | 0.0730            | 4.5  | 1995     |
| 2  | 410.9      | 454.7      | 458.9      | 4.2             | 0.0140            | 1.0  | 1991     |
| 3  | 662.9      | 718.8      | 723.3      | 4.5             | 0.0150            | 0.7  | 2052     |
| 4  | 411.99     | 436.3      | 452.1      | 15.8            | 0.0527            | 3.8  | 2059     |
| 5  | 573.3      | 622.2      | 643.2      | 21.0            | 0.0700            | 3.7  | 2030     |
| 6  | 363.4      | 392.4      | 397.8      | 5.4             | 0.0180            | 1.5  | 2077     |
| 7  | 592.1      | 638.2      | 660.1      | 21.9            | 0.0730            | 3.7  | 1983     |
| 8  | 827.4      | 892.5      | 901.4      | 8.9             | 0.0297            | 1.1  | 1974     |
| 9  | 371.9      | 387.3      | 396.2      | 8.9             | 0.0297            | 2.4  | 2077     |
| 10 | 437.5      | 458.0      | 467.7      | 9.7             | 0.0323            | 2.2  | 1983     |
| 11 | 297.9      | 319.7      | 331.7      | 12.0            | 0.0400            | 4.0  | 1974     |
| 12 | 666.8      | 715.9      | 747.0      | 31.1            | 0.1037            | 4.7  | 2045     |
| 13 | 372.0      | 403.6      | 432.1      | 28.5            | 0.0950            | 7.7  | 2033     |
| 14 | 215.8      | 226.7      | 253.1      | 26.4            | 0.0880            | 12.2 | 2084     |
| 15 | 803.5      | 867.2      | 876.6      | 9.4             | 0.0313            | 1.2  | 2070     |
| 16 | 324.1      | 345.9      | 351.7      | 5.8             | 0.0193            | 1.8  | 2078     |
| 17 | 386.0      | 417.7      | 423.7      | 6.0             | 0.0200            | 1.6  | 2105     |
| 18 | 232.5      | 252.2      | 257.6      | 5.4             | 0.0180            | 2.3  | 1994     |
| 19 | 389.4      | 417.8      | 438.4      | 20.6            | 0.0687            | 5.3  | 2000     |
| 20 | 813.7      | 882.5      | 899.1      | 16.6            | 0.0553            | 2.0  | 1989     |
| 21 | 485.8      | 518.3      | 521.1      | 2.8             | 0.0093            | 0.6  | 1993     |
| 22 | 392.6      | 411.9      | 446.1      | 34.2            | 0.1140            | 8.7  | 1987     |

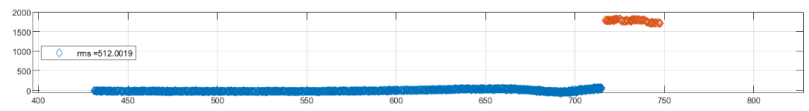
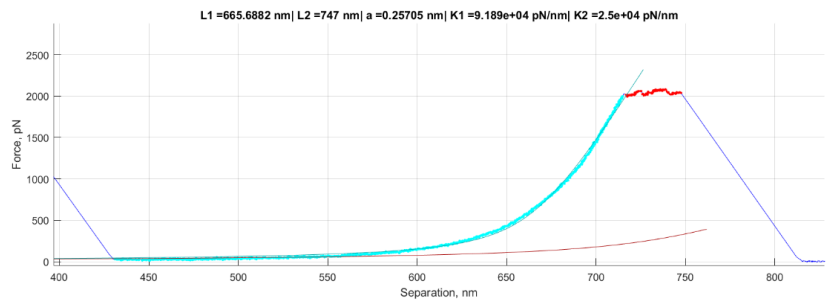
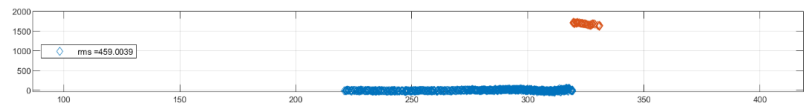
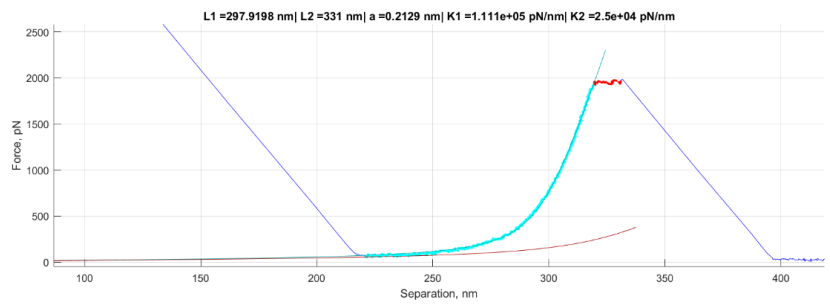
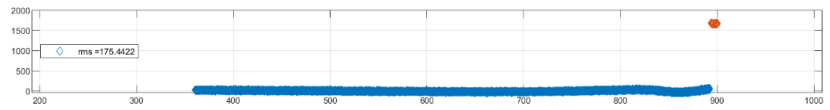
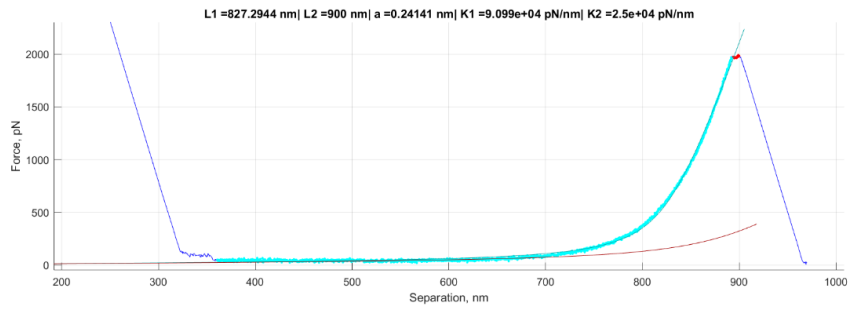
|    |       |       |       |      |        |     |      |
|----|-------|-------|-------|------|--------|-----|------|
| 23 | 250.9 | 263.2 | 277.9 | 14.7 | 0.0490 | 5.8 | 2061 |
| 24 | 307.9 | 327.9 | 342.9 | 15.0 | 0.0500 | 4.9 | 2038 |
| 25 | 381.5 | 410.3 | 415.1 | 4.8  | 0.0160 | 1.2 | 1996 |
| 26 | 326.8 | 348.8 | 354.7 | 5.9  | 0.0197 | 1.8 | 1930 |
| 27 | 592.5 | 635.3 | 638.9 | 3.6  | 0.0120 | 0.6 | 1965 |
| 28 | 311.7 | 334.3 | 338.3 | 4.0  | 0.0133 | 1.3 | 1953 |
| 29 | 576.4 | 620.2 | 626.7 | 6.5  | 0.0217 | 1.1 | 1967 |

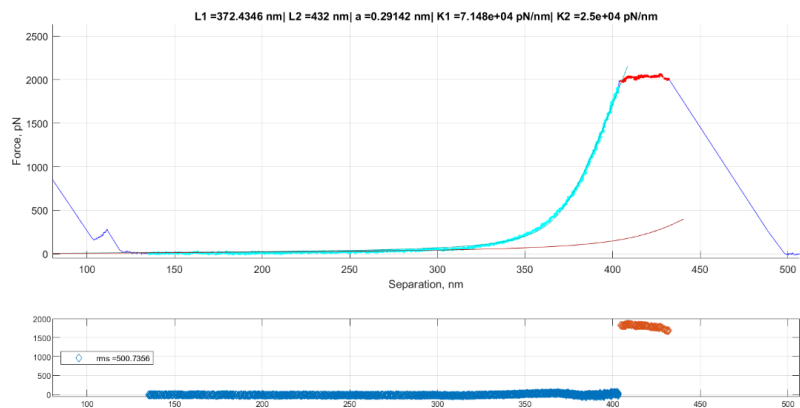


**Figure 202 : Probability distribution of extra extension% (EE%) observed from SMFS experiment. Grey histogram of at 34% is theoretical value of full transition obtained from GoGEF.**

Additional SMFS curves:

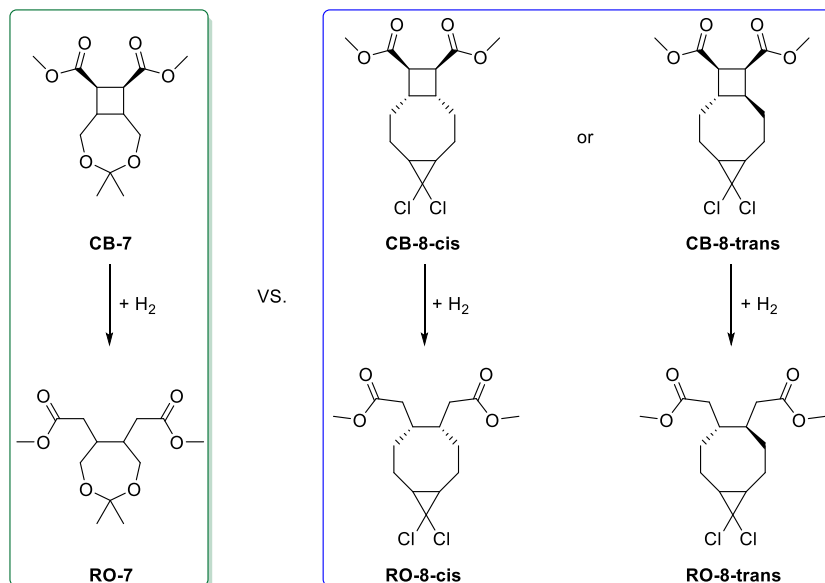






### 5.1.3.5 Comparison of ring strain

To rationalize the difference in transition force between our design here and previous CB-fused 8-member ring systems, the relative fused CB ring strain was estimated by calculating the energy difference between CB and its derivative shown as follows. The calculation was performed in Spartan '18 using DFT method on the theory level of B3LYP/6-31G\*.



The rate of force-induced ring opening of CB is determined by the generation of diradical intermediate, releasing the release of ring strain. Therefore, the ring strain of fused CB can be applied to estimate relative mechanical reactivities. We evaluated the relative ring strain of fused CB by comparing the energy difference ( $\Delta E$ ) between CB and RO species:

$$\Delta E(\text{CB-7}) = E(\text{CB-7}) + E(\text{H}_2) - E(\text{RO-7}) = 36.3 \text{ kcal/mol}$$

$$\Delta E(\text{CB-8- cis}) = E(\text{CB-8- cis}) + E(\text{H}_2) - E(\text{RO-8- cis}) = 34.0 \text{ kcal/mol}$$

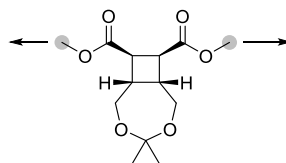
$$\Delta E(\text{CB-8- trans}) = E(\text{CB-8- trans}) + E(\text{H}_2) - E(\text{RO-8- trans}) = 27.9 \text{ kcal/mol}$$

Hence, the relative ring strain of fused CB: **CB-7 > CB-8-cis > CB-8-trans**

### 5.1.3.6 CoGEF modeling

#### 5.1.3.6.1 Modeling of cyclobutane ring opening

CoGEF modeling was performed on a methyl ester form of compound **2** using DFT method on the theory level of B3YLP/61G\* according to reported procedures.<sup>44, 315</sup> The ground state geometry was optimized, and its end-to-end distance was constrained and increased with step increasement of 0.1 Å.



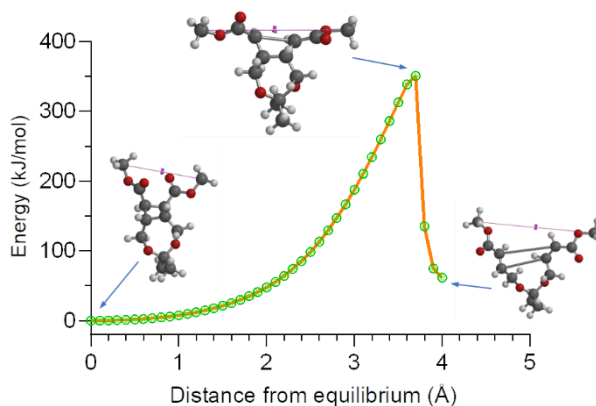


**Figure 203 : CoGEF modeling of cyclobutane indicates retro-[2+2] cycloaddition under extension.**

#### 5.1.3.6.2 Modeling of ring opened cyclobutane

To study the mechanical strength of ketal functional group on mechanically activated polymer backbone, CoGEF was also performed on a ring opened product using the same calculation setting.

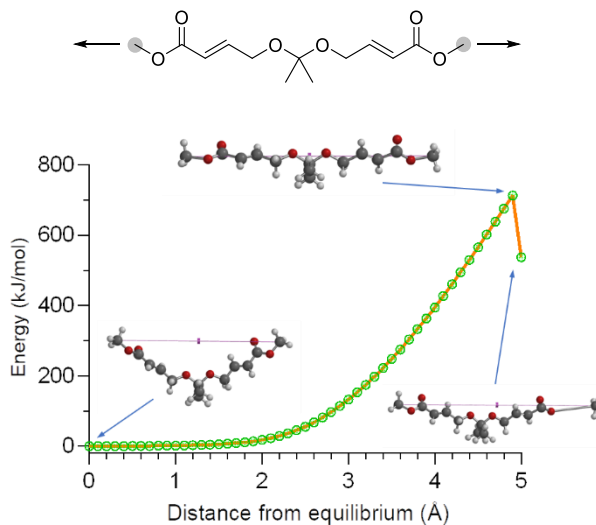


**Figure 204 : CoGEF modeling of ketal containing product under extension. The C-O bond of methyl ester cleaves under high extension suggests high mechanical strength of ketal functional group.**

### 5.1.3.6.3 Modeling of polymer contour length

The change in polymer contour length before and after transition was modelled by CoGEF using previous reported method.<sup>87, 117</sup> The calculation was performed using molecular mechanics method on the theory level of MMFF.

Contour length of cyclobutane repeating segment:

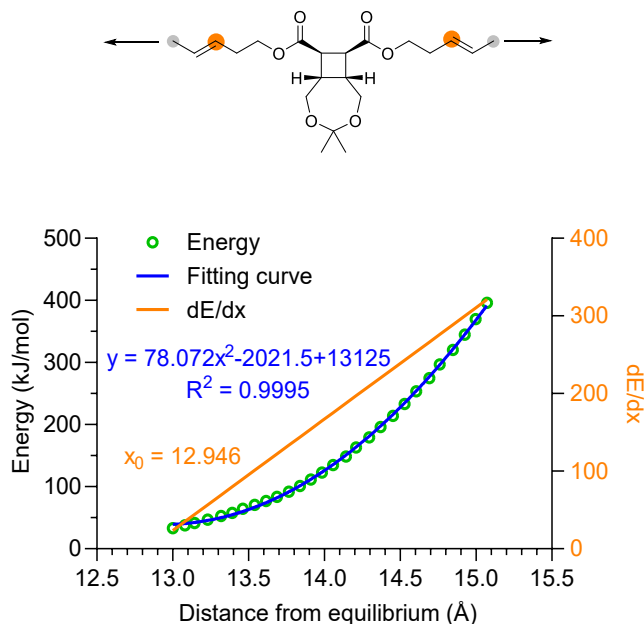
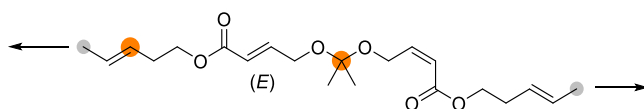


Figure 205 : First derivative of quadratic fitting gives force-distance relation. The contour length of cyclobutane repeating unit (indicated between two orange dots) is the intercept at x axis ( $x_0 = 12.946$  Å)

Contour length of ring opened cyclobutane repeating segment:



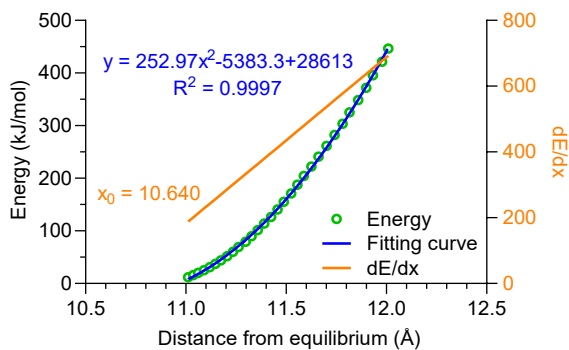


Figure 206 : First derivative of quadratic fitting gives force-distance relation. The contour length of *E* alkene segment in ring-opened cyclobutane (indicated between two orange dots) is the intercept at x axis ( $x_0 = 10.640 \text{ \AA}$ )

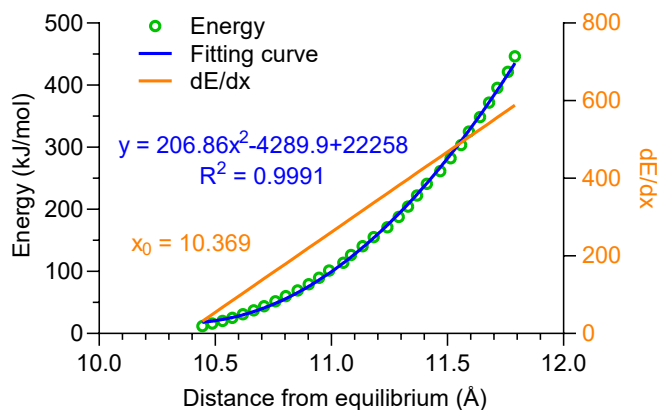
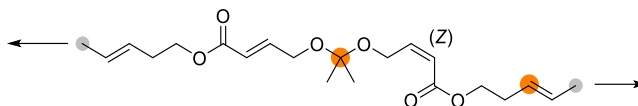
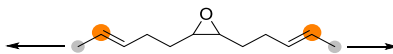


Figure 207 : First derivative of quadratic fitting gives force-distance relation. The contour length of *Z* alkene segment in ring-opened cyclobutane (indicated between two orange dots) is the intercept at x axis ( $x_0 = 10.369 \text{ \AA}$ )

Contour length of epoxide repeating segment:



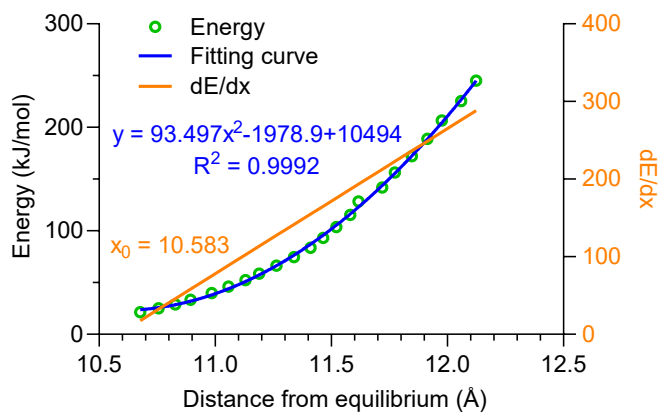


Figure 208 : First derivative of quadratic fitting gives force-distance relation. The contour length of *trans* alkene containing epoxide repeating unit (indicated between two orange dots) is the intercept at x axis ( $x_0 = 10.583 \text{ \AA}$ )

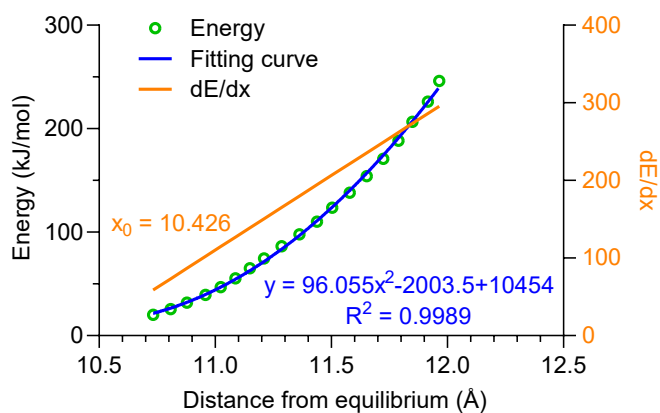


Figure 209 : First derivative of quadratic fitting gives force-distance relation. The contour length of *cis* alkene containing epoxide repeating unit (indicated between two orange dots) is the intercept at x axis ( $x_0 = 10.426 \text{ \AA}$ )

**Table 28 : Contour length of each repeating unit obtained from CoGEF modeling**

|         | CB     | Ring-opened CB   |                  | Epoxide      |            |
|---------|--------|------------------|------------------|--------------|------------|
|         |        | <i>E</i> segment | <i>Z</i> segment | <i>trans</i> | <i>cis</i> |
| Trial 1 | 12.951 | 10.640           | 10.369           | 10.370       | 10.526     |
| Trial 2 | 12.957 | 10.660           | 10.361           | 10.426       | 10.583     |
| Trial 3 | 12.946 | 10.682           | 10.358           | 10.443       | 10.617     |
| Avg.    | 12.952 | 10.661           | 10.363           | 10.413       | 10.576     |
| SD.     | 0.005  | 0.021            | 0.006            | 0.038        | 0.046      |

The ratio of **P2** polymer contour length before and after activation can be calculated using the following equation:

$$\frac{L_f}{L_i} = \frac{x \times 2 \times (y \times l_E + (1 - y) \times l_Z) + (1 - x) \times l_{epoxide}}{x \times l_{CB} + (1 - x) \times l_{epoxide}}$$

$L_i$  and  $L_f$  refer to initial and final contour lengths of polymer chain;  $l_{CB}$  and  $l_{epoxide}$  stand for the contour length of cyclobutane and epoxide repeating units ( $l_{epoxide} = (10.413 + 10.576)/2 = 10.494 \text{ \AA}$ );  $l_E$  and  $l_Z$  are contour length of *E* and *Z* alkene segments in ring-opened cyclobutane products;  $x$  is the molar fraction of cyclobutane on polymer backbone and  $y$  is the percentage of *E* alkene segment in activated cyclobutane.  $l_{CB}$ ,  $l_{epoxide}$ ,  $l_E$  and  $l_Z$  were determined from CoGEF modelling and  $x$  and  $y$  were calculated from  $^1\text{H}$  NMR spectrum.

For a **P2** polymer with  $x = 48 \%$  cyclobutane, there are  $y = 63\%$  *E* alkene segment generated after mechanical activation, we have:

$$\frac{L_f}{L_i} = \frac{0.48 \times 2 \times (0.63 \times 10.661 + (1 - 0.63) \times 10.363) + (1 - 0.48) \times 10.494}{0.48 \times 12.952 + (1 - 0.48) \times 10.494} = 1.335$$

The theoretical percentage of extra extension (EE%) after activation is: ~34%

## ***5.2 Enhanced polymer mechanical degradation through mechanochemically unveiled lactonization***

The mechanical degradation of polymers is typically limited to a single chain scission per triggering chain stretching event, and the loss of stress transfer that results from the scission limits the extent of degradation that can be achieved. Here, we report a mechanically triggered, delayed scission strategy that allows many eventual scission events to be initiated within a single polymer chain. The strategy is demonstrated via a mechanophore with a [4.2.0]bicyclooctene (BCOE) core that leverages a mechanochemical, orbital symmetry-forbidden 4p-electron disrotatory ring-opening reaction to set up a subsequent, force-free and thermodynamically favorable lactonization. Ultrasonication of a 120 kDa BCOE copolymer triggers the desired mechanical remodeling of the polymer backbone, and the resulting lactonization leads to a gradual decrease in molecular weight over the course of 9 days to a final value of 4.4 kDa, more than an order of magnitude smaller than control polymers in which the ring-opened BCOE is protected from lactonizing. The force-coupled activity of the ring-opening reaction is probed by single molecule force spectroscopy and through the use of internal standards in sonication, and the forces required for activation are far smaller than is typically required for the mechanical chain scission of conventional covalent polymers.

### **5.2.1 Introduction**

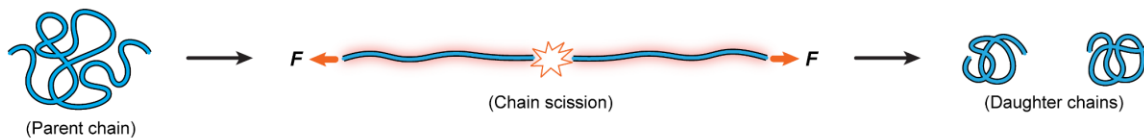
Synthetic polymers have brought tremendous benefits to daily life, but the same structural stability that makes them so useful leads to a major challenge: they are often difficult to break down. Depending on the type of plastic, disposed plastics persist for ~

$10^2 - 10^3$  years in landfills and oceans with far reaching environmental consequences. Strategies for dealing with this challenge include biodegradable/degradable polymers,<sup>320-</sup><sup>321</sup> recyclable/reprocessable polymers,<sup>322-325</sup> and polymers made from renewable sources.<sup>326</sup> The advance of degradable polymers has been facilitated by the tactical introduction of a rich range of biodegradable or stimuli-degradable motifs into the polymer backbone, the degradation of which often occurs in the presence of an external stimulus (e.g., heat, light, chemical, electricity).

Nearly a century ago,<sup>327</sup> mechanical forces were recognized as being capable of breaking down polymer chains and networks. But while mastication and other mechanical processing techniques are capable of triggering polymer degradation to an extent that changes mechanical properties, the utility of mechanical force for extensive polymer degradation is limited by the fact that the tension in a parent polymer chain relaxes after a single scission event (Figure 210a), and the ability to recapture the chain in a high stress event drops with its molecular weight. In mechanical processing environments such as extrusion or sonication, therefore, polymer degradation plateaus at an apparent limiting molecular weight<sup>61</sup> that is not sufficiently low to meet desired degradation targets. Moore and Boydston et al.<sup>192</sup> reported a clever strategy to amplify a single triggering event through the scission-induced cascade depolymerization of a self-immolative cyclic poly(phthalaldehyde). This strategy, however, is not likely to be suitable for all degradation purposes, as the mechanically depolymerizable system relies on a metastable polymer backbone, and cascade degradation happens instantaneously

upon activation, which might reduce stress transfer and limit the ability to trigger events throughout all strands in a bulk material.

**a. Mechanically induced chain scission**



**b. Enhanced mechanical degradation**

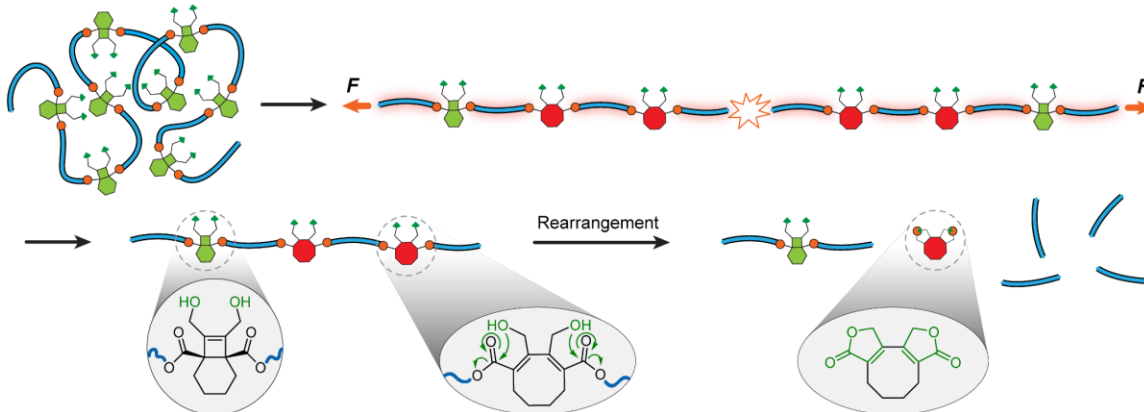


**Figure 210 : Illustration of mechanically induced chain scission and design of enhanced mechanical degradation. a) Subjection of polymer chain to mechanical force leads to chain scission at near midchain region and produces two daughter chains. b) A polymer bearing BCOE mechanophores undergoes mechanically induced forbidden ring opening and subsequent lactonization rearrangement, leading to enhanced degradation.**

We therefore sought a system in which mechanical force could trigger a delayed degradation, allowing polymer topology and mechanical properties to be retained so that many such initiating events could be induced. In particular, mechanophores<sup>21</sup> have been used in recent years to create a wide range of stress-coupled responses in polymer materials,<sup>21, 26-28</sup> including the extensive “remodeling” of polymers under processing conditions that might be suitable to large scale degradation.<sup>26, 204, 328-331</sup> Inspired by these successes, we considered designs in which mechanical forces that would normally lead to a single scission event might instead convert multiple copies of a mechanophore into

products that undergo spontaneous but slow chain scission reactions. Herein, we report that mechanophores based on a [4.2.0]bicyclooctene (BCOE) core provide the desired functionality. Mechanical activation of BCOE leads to a disrotatory,  $4\pi$ -electron ring-opening reaction, the product of which is set up for spontaneous, intramolecular lactonization (Figure 210b) that, over the course of days, leads to order-of-magnitude enhancements in the extent of mechanically triggered degradation relative to controls in which the lactonization is blocked.

## 5.2.2 Results and discussion

Thermodynamics of lactonization. The design of BCOE mechanophore is inspired by the beautiful work of Booker-Milburn and coworkers<sup>332-333</sup> on the preparation of pachylactone from a hydroxy-substituted BCOE derivative **A** (Figure 211a). When refluxed in xylenes, sequential disrotatory ring opening and lactonization of **A** affords the target lactone product **E**. Based on prior work on mechanically triggered, disrotatory  $4p$ -electron processes,<sup>10, 18, 84, 107</sup> we reasoned that a similar reaction cascade could be mechanically induced as long as the subsequent lactonization remains thermodynamically favorable. Computations supported the viability of ring-opened dihydroxy BCOE derivative **F**. As seen in Figure 211b, the first intramolecular lactonization of **F** to **G** is exothermic by 9.4 kcal/mol, and a subsequent second lactonization to bis-lactone **H** gains an additional 2.8 kcal/mol. Based on these calculations, we hypothesized that polymers with the appropriate BCOE mechanophore

precursor in the backbone would spontaneously release **H** following mechanical activation.

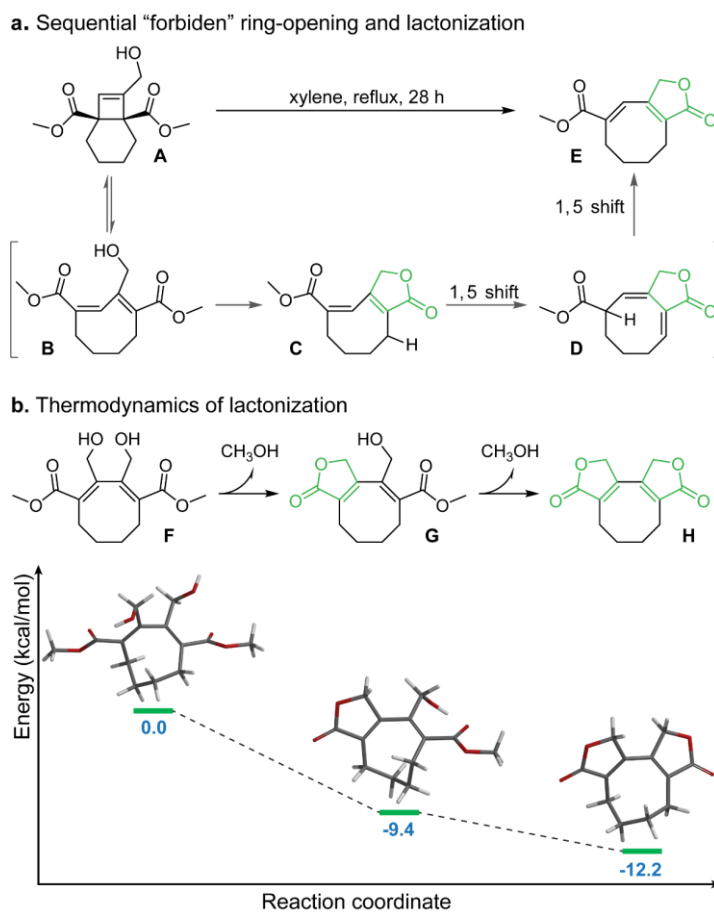
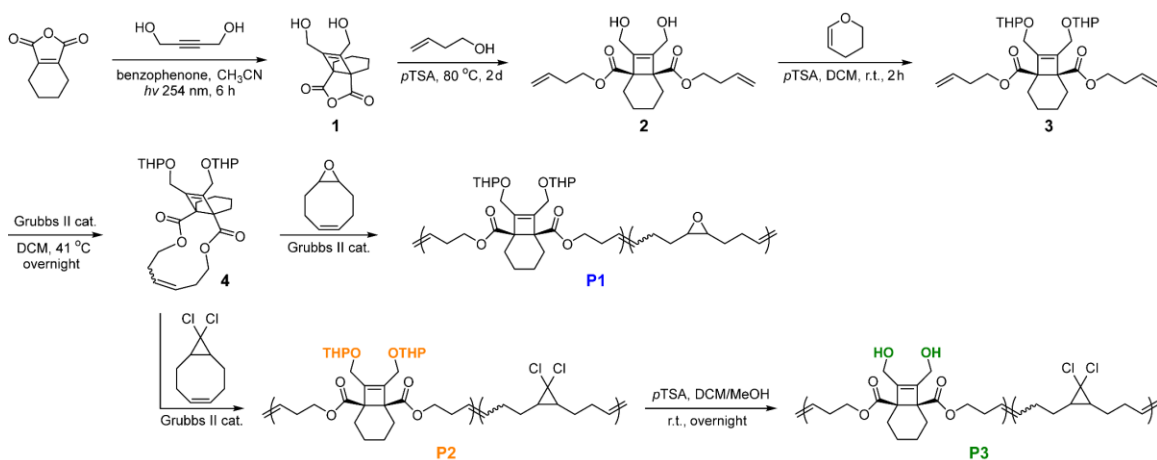


**Figure 211 : Synthesis of pachylactone from a BCOE derivative and thermodynamics of lactonization. a) Thermally induced sequential "forbidden" ring opening and lactonization reported by Booker-Milburn and coworkers. b) Computational study of the lactonization thermodynamics of a ring opened BCOE species.**

Synthetic design. The BCOE mechanophore was synthesized as shown in Scheme 7, using a slightly modified procedure based on reports by Booker-Milburn and coworkers.<sup>334-337</sup> BCOE anhydride **1** was prepared from the photochemical [2+2] cycloaddition of 3,4,5,6-tetrahydrophthalic anhydride and but-2-yne-1,4-diol. Subsequent

acid-catalyzed esterification with 4-buten-1-ol gave the diene derivative **2**, of which the hydroxyls were protected with tetrahydropyran (THP) groups to yield **3**. Macrocycle **4** was obtained from ring-closing metathesis (RCM) of **3**, and **4** was further subjected to entropy-driven ring-opening metathesis polymerization (ED-ROMP) with comonomer 9-oxabicyclo[6.1.0]non-4-ene (epoxy-COD) and 9,9-dichlorobicyclo[6.1.0]non-4-ene (gDCC-COD) to provide polymers **P1** (26 mol% **4**) and **P2** ( $M_n = 128$  kDa,  $D = 1.39$ , 14 mol% **4**), respectively. The epoxide-containing **P1** was employed in single molecule force spectroscopy (SMFS) studies, following previous reports in which the epoxide comonomer was used to enhance adhesion to the cantilever.<sup>82</sup> Polymer **P2** was cleanly converted to **P3** ( $M_n = 120$  kDa,  $D = 1.62$ , 14 mol% **4**) through the selective removal of THP protecting groups. **P2** and **P3** were employed in sonication studies, with **P2** serving as a control for the role of lactonization, which is blocked by the presence of THP protecting groups.

**Scheme 7 : Synthetic design of BCOE mechanophore and preparation of polymers P1, P2 and P3.**



Mechanical degradation. The mechanical degradation of the polymers was investigated through pulsed ultrasonication of their tetrahydrofuran (THF) solutions. As shown in Figure 212a and 212c, ultrasonication of **P2** leads to three mechanochemical outcomes: (1) a reduction in polymer molecular weight (MW), as indicated by the steady

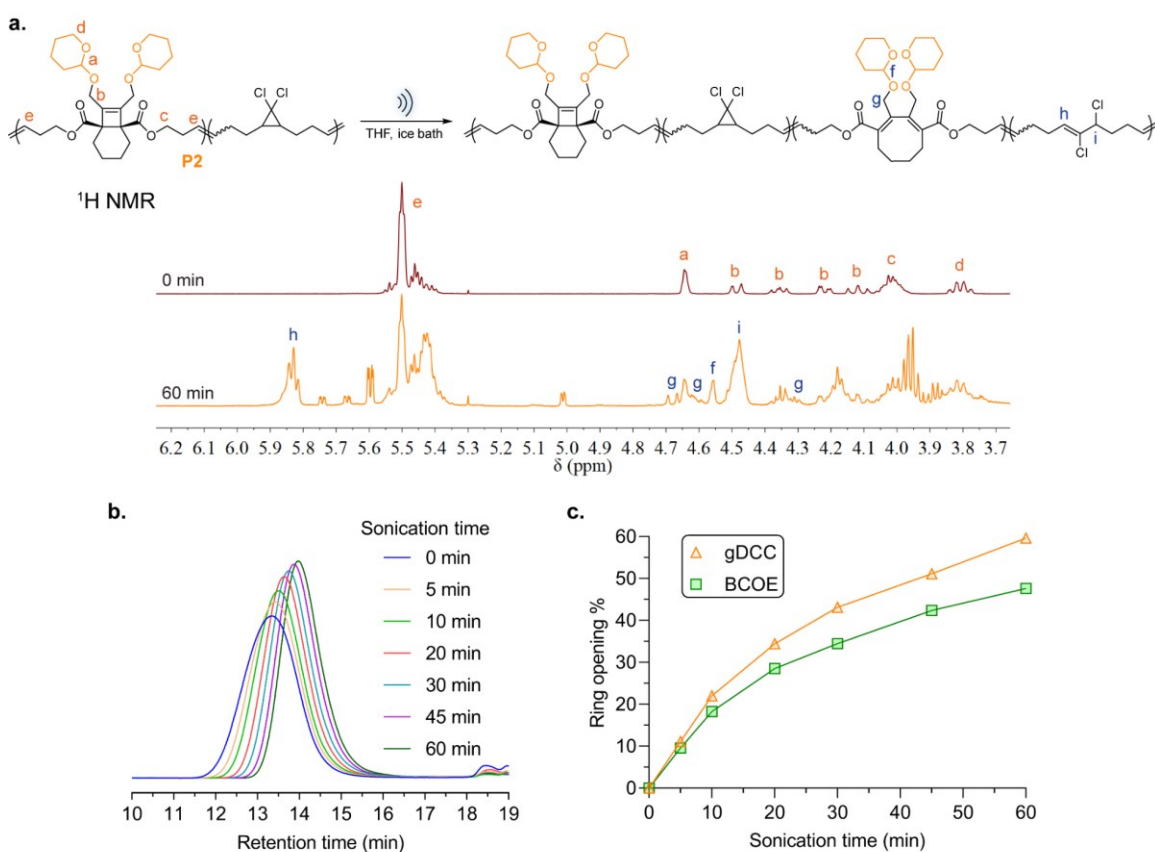


**Figure 212 : Ultrasonication study of polymer P2. a) Schematic presentation of ultrasonication induced mechanical activation of BCOE and gDCC in P2, and the  $^1\text{H NMR}$  characterization of activated species in P2. b) Evolution of GPC traces of P2 over ongoing sonication time. c) Fraction of activated BCOE and gDCC at various sonication time.**

shift of GPC traces to longer retention time (Figure 212b); (2) the conversion of gDCC mechanophores into their respective 2,3-dichloroalkene products (as previously reported<sup>170, 317</sup>); and (3) the ring opening of BCOE to the corresponding diene species. All

three processes increase with increasing sonication time, but the rates of all gradually drop off with decreasing MW, as expected for mechanochemical processes. After 60 min of sonication, the MW of **P2** drops from 128 kDa to 51 kDa, and this reduction is consistent with a typical outcome of polymer degradation under ultrasonication, where preferential force-induced scissions tend to occur at the near chain-center region.<sup>338</sup> Over that same sonication time, the conversion of gDCC and BCOE mechanophores is 60% and 48%, respectively. This suggests that BCOE is similar to, but slightly less mechanically reactive than, the well-known gDCC mechanophore. Single molecule force spectroscopy experiments confirm this conclusion (see below).

We anticipated similar extents of each of the three primary mechanochemical responses (homolytic chain scission, gDCC activation, and BCOE activation) in **P3** as were observed in **P2**, for the following reasons: (1) the rates of mechanochemical response are primarily determined by polymer contour length,<sup>171, 339-340</sup> which is effectively unchanged on going from **P2** to **P3**; (2) any differences in solvation of the BCOE alcohols and THP groups in THF have a negligible effect on sonochemical response, as suggested by a previous study;<sup>340</sup> and (3) the electrocyclic ring opening of the cyclobutene core is electronically decoupled from the OH/OTHP groups. As expected, <sup>1</sup>H NMR spectra confirm that the amount of activated gDCC internal standard at 60 min is effectively identical in **P3** (62 %, Figure 213a) to that observed for **P2** (60 %), but slightly greater shifts in retention time in the associated GPC traces are observed for **P3** as a function of sonication time (Figure 213d). These slight differences in shifted retention time suggest

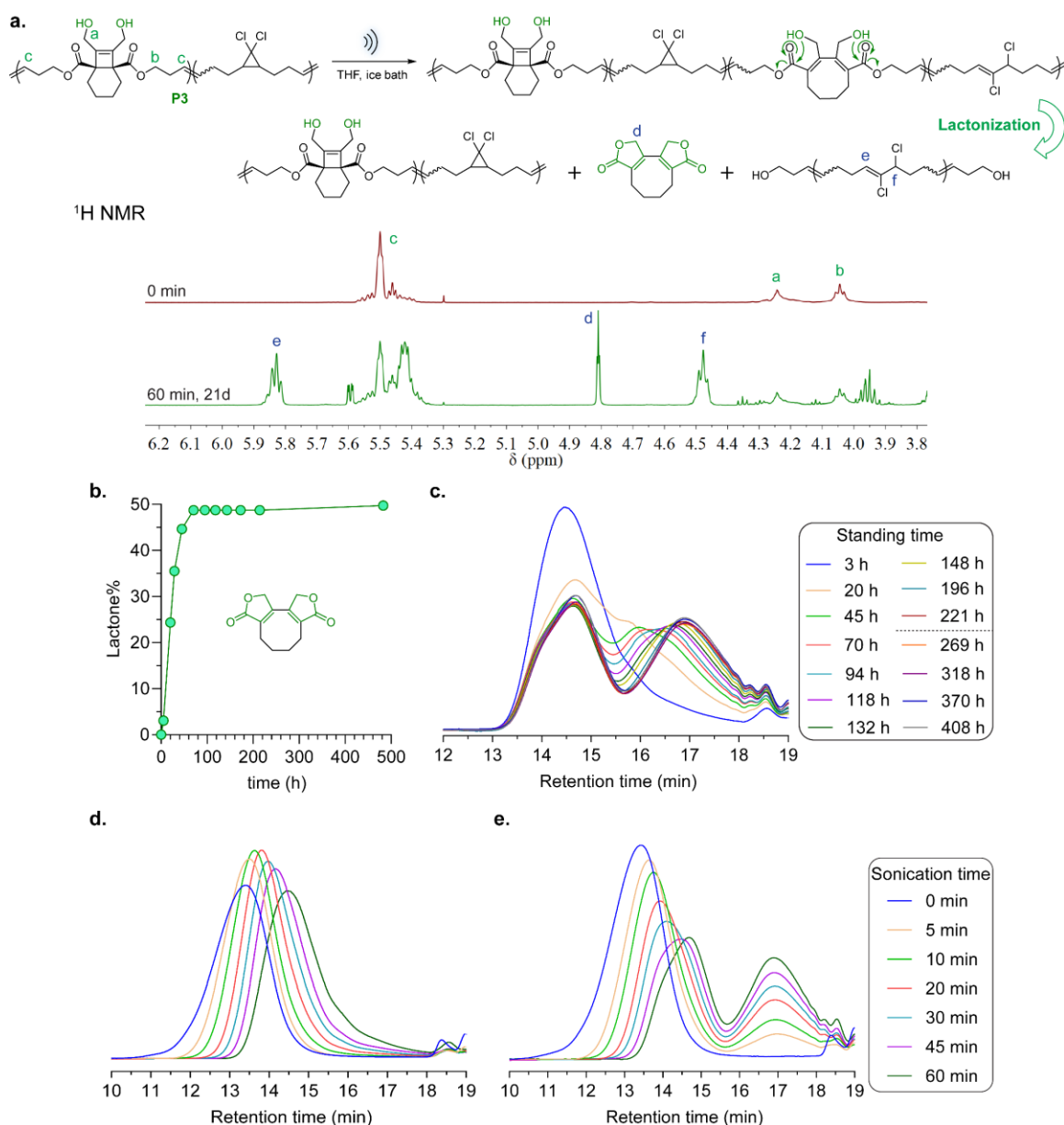


**Figure 213 : Ultrasonication study of polymer P3. a) Scheme of mechanical activation of BCOE and gDCC in P3 and following spontaneously lactonization. <sup>1</sup>H NMR characterization of activated gDCC and generated lactone in a P3 polymer that was sonicated for 60 min and set for 21 days to reach full lactonization. b) <sup>1</sup>H NMR (CDCl<sub>3</sub>) quantification of lactone formation over standing time in a P3 polymer post 60 min sonication. c) GPC trace evolution of P3 polymer after 60 min sonication over various standing time in THF. GPC analysis of sonicated P3 immediately after sonication (d) and after 17 days standing time (e). The legends for (d) and (e) are indicated on the right.**

that small amounts of post-activation lactonization (and the associated chain scission) are occurring during the ongoing sonication and GPC analysis, and the  $^1\text{H}$  NMR spectra of sonicated **P3** reveal ~3% lactone after 60 min sonication and an additional 5 h standing time (Figure 213b, 226).

The post-sonication kinetics of lactonization were then studied in greater detail, using **P3** that had been sonicated for 60 min. The conversion of the lactone was quantified by integrating the  $^1\text{H}$  NMR spectra, and it increases gradually over a couple of days until it plateaus at  $49 \pm 2\%$ , within experimental uncertainty of the  $48 \pm 2\%$  BCOE ring opening observed in **P2** under identical sonication conditions. The production of the intended bis-lactone was further confirmed by mass spectroscopy (Figure 227). The generation of the lactone further correlates with an ongoing decrease in MW. As shown in Figure 213c, the GPC traces of post-sonicated **P3** gradually evolve to reveal a bimodal distribution over ~45 h of standing time. This evolution in MW distribution continues for days and eventually reaches an apparent steady state after 221 h, in contrast to the 70 h observed in  $^1\text{H}$  NMR studies of lactonization. We attribute this three-fold difference in apparent lactonization rate to the different solvent environments of the two studies (i.e.,  $^1\text{H}$  NMR experiments were conducted in  $\text{CDCl}_3$ , GPC experiments in THF).

To ensure “complete” lactonization, each of the sonicated **P3** samples was allowed to sit under ambient conditions until a total of 17 d had passed since sonication. Subsequent characterization by GPC (Figure 213e) shows a clean bimodal distribution, with a new and distinct low-MW peak centered at ~17 min retention time that increases

as a function of initial sonication time. The MW of this peak, as determined by multi-angle static light scattering (MALS), is  $\sim 1.4$  kDa. Coincident with the growth in this oligomer peak, the higher MW peak decreases in intensity and gradually shifts to longer retention time. The MW of **P3** (combination of both peaks) following 60 min sonication and 17 d of

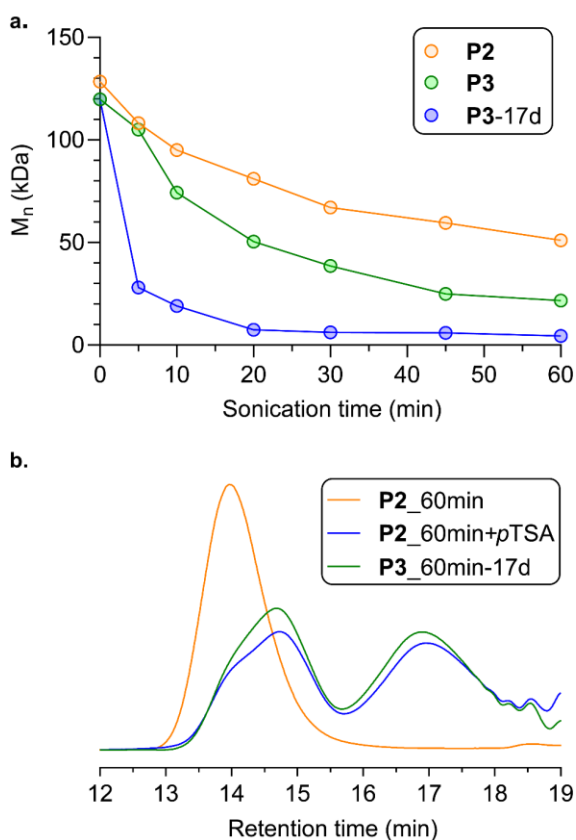


**Figure 214 : Mechanical degradation of P2 and P3, and mechanically regulated degradability of P2. a) Comparison of  $M_n$  evolution over sonication time. Orange dot: P2 polymer; blue dots: P3 polymer analyzed immediately after sonication; green dots: P3 polymer analyzed after sonication and further 17 days standing time. b) GPC overlay of P2 polymer after sonication, P2 polymer after sonication and further *p*TSA treatment, and P3 polymer after sonication and additional 17 days standing time.**

subsequent lactonization has decreased from an initial value of 120 kDa to an ultimate value of 4.4 kDa. In contrast, the MW of **P2** (control polymer) plateaus at only 51 kDa (from an initial value of 128 kDa) under identical conditions (Figure 214a), because the

THP protecting groups block subsequent lactonization. When *p*-toluenesulfonic acid is added to sonicated **P2**, it catalyzes the removal of the THPs and unveils the hydroxy groups. Following lactonization, the MW distribution of “sonicated + acid” **P2** is indistinguishable from that of sonicated **P3** (Figure 214b). This sequential ultrasonication and acid treatment suggests a mechanically regulated degradability that complements previous designs of mechanically gated degradable polymers.<sup>330-331</sup>

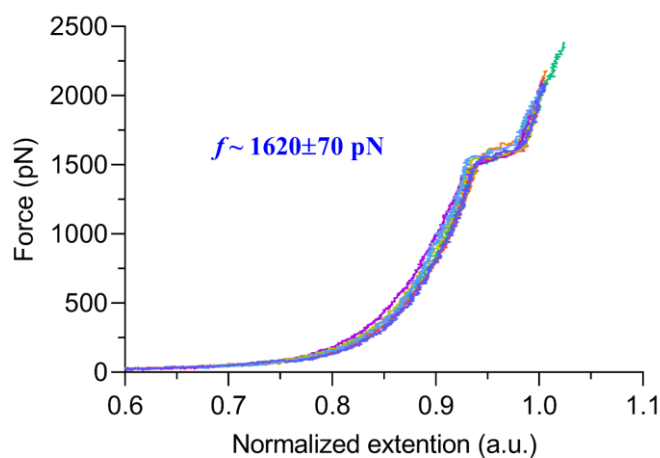


**Figure 215 : Representative force-extension curves of P1. SMFS study was performed in toluene with a pulling velocity of 300 nm/s. Seven force-extension curves are normalized at the extension related to 2 nN force and overlaid in the figure.**

Single molecule force spectroscopy. SMFS was performed using techniques based on those reported previously by Craig and co-workers.<sup>82, 84, 87-88, 109</sup> Representative force-extension curves of **P1** is presented in Figure 215. The characteristic plateau at average force of  $\sim 1620 \pm 70$  pN is a consequence of rapid BCOE ring opening ( $\sim 10^2$  s<sup>-1</sup>) along the polymer backbone, and the resulting extra extension ( $6 \pm 2\%$ ) in the polymer chain is consistent with that calculated from CoGEF modeling (6%, see details provided in the section 5.2.3.5). To facilitate comparison with related systems, the force-coupled kinetics

of BCOE ring opening were analyzed using a force-coupled cusp (truncated quadratic) function for the potential energy as a function of position along the reaction coordinate.<sup>15</sup> This analysis provides an estimate of the activation length,  $\Delta x^\ddagger = 1.09 \pm 0.05 \text{ \AA}$ , which refers to force-free limit of the change in contour length of the stretched polymer chain at the reaction transition state relative to the ground state.

The behavior of the system is consistent with the designed delayed-fracture mechanism, each of two factors is required to be present simultaneously. First, the BCOE mechanophore must be opened to the corresponding diene, as pristine **P3** shows no evidence of spontaneous molecular weight degradation (Figure 225). Second, the diene product of ring opening must be able to undergo subsequent lactonization, as mechanically activated **P2**, which comprises of ring opened BCOE but no unveiled hydroxy groups, shows no evidence of fragmented oligomers beyond single-event bond breaking in the GPC traces (Figure 212b, 221). Thus, we conclude that the intended scheme shown in Figure 210 is indeed operative.

A key consequence of this design is that once the BCOE is activated, its subsequent lactonization proceeds slowly (time scale of days) and does not require additional mechanical input. Therefore, the lactonization rearrangement is the rate-limiting step in the chain fragmentation process. Because BCOE activation is non-scissile with respect to the polymer backbone, this allows many BCOE mechanophores to open prior to chain scission in ultrasonication (as many as ~31 BCOE per mechanically triggered chain scission event; see section 5.2.3.3). The extent of BCOE activation during sonication is

limited by the uneven force distribution along the polymer backbone that is generated by the extensional flow fields produced in this experimental setup. Large forces that are sufficient for chain scission are produced near the center of the chain even as the ends of the chain are under modest tension, leaving BCOE in the terminal regions unactivated. When the chains are stretched under constant tension via SMFS, in fact, the changes in polymer contour length are consistent with the quantitative activation of all BCOE mechanophores along the backbone prior to chain scission or detachment from the probe. Consistent with this observation, the force required for BCOE activation (2.1 nN for a rate constant of  $3.2 \times 10^7 \text{ s}^{-1}$ ) is much lower than that required for homolytic scission of the backbone (likely 4-5 nN<sup>135, 170</sup>).

The statistics of chain fragmentation are also consistent with the statistic of BCOE activation. Black Ramirez et al. showed that the sonomechanochemical activation of a multi-mechanophore polymer resulted in largely continuous blocks of activated and unactivated mechanophore. If we assume the same behavior here, the activated blocks of BCOE would eventually degrade through lactonization to oligomers of average MW comparable to the average MW between BCOE repeats in **P3**. Given the 14 mol% of BCOE incorporated into **P3**, the average composition is 1 BCOE repeat + (0.86/0.14) gDCC repeat, which, once the mass of the bis-lactone product is subtracted, leads an expected average MW of 1.2 kDa in the low-mass 2,3-dichloroalkene oligomer fragments following full lactonization (note that ring opening of the gDCC mechanophore to the corresponding 2,3-dichloroalkene product does not change MW). The observed MW of ~2 kDa is within

experimental uncertainty of the theoretical value. Similarly, the MW of the putative block of unreacted BCOE depends on the extent of BCOE activation. In a specific case, we separately analyzed the high MW peak of **P3** following 20 min ultrasonication and 17 d lactonization (extent of BCOE activation taken from studies of **P2**; see section 5.2.3.3). The MW of the high MW fraction was determined by GPC-MALS to be 59 kDa, in similarly good agreement with the theoretical value of 58 kDa.

Finally, the presence of two separate non-scissile mechanophores along the same polymer backbone provides an opportunity to probe simple, quantitative models of force distribution in polymer chains during sonication. Ultrasonication of **P2** show leads to slightly less BCOE activation than gDCC activation, about 48% gDCC and 39% BCOE activation per average chain scission event ( $\Phi$  value, Figure 220). This relative activation can be analyzed from a quadratic model,<sup>170-171</sup> which describes the force-distribution along the polymer chain under ultrasonication. The quadratic model is expressed using the following equation:

$$F = a * \frac{1 - \Phi}{2} * \left( \frac{1 - \Phi}{2} - 1 \right)$$

To perform the comparison, the force of gDCC activation obtained from SMFS (1330 pN at  $10^{-1}$  s time scale) is extrapolated to microsecond ( $F_{\text{open}} = 2040$  pN),<sup>170</sup> which is the time scale of stretching event under ultrasonication. From the gDCC internal standard, we know that a  $\Phi$  value of 0.48 gives  $F = F_{\text{open}} = 2040$  pN. Therefore, a  $\Phi$  value of 0.39 in BCOE yields  $F_{\text{open}} = 2370$  pN, which is  $\sim 300$  pN more than gDCC and is consistent with results from SMFS.

The strategy reported here, of delayed degradation enabled by mechanochemically unveiled functionality, stands in contrast to existing mechanical degradation schemes in that it enables multiple chain scissions to occur under conditions that would normally result in a single scission event. Looking ahead, this and related strategies might find use in mechanically degraded polymers, for example in materials that could be extruded or otherwise mechanically worked to degrade into much smaller components than would be possible if the fragmentation were limited to instantaneous single scission events. In addition, delayed degradation provides a potential route to materials with programmed obsolescence, in which a part subjected to early stage damage events would continue to function until its immediate tasks were completed, but then would subsequently fall apart in order to signal that a change was needed prior to redeployment. Finally, the kinetics of the unveiled degradation (here, lactonization) might be useful as time-dependent chemical signals whose evolution can be used to retroactively determine when a damaging event occurred, complementing a similar “time stamping” strategy reported recently.<sup>46</sup> Whether through lactonization or entirely new designs, these opportunities motivate further studies into tandem reaction cascades that are triggered by a mechanical stimulus.

## **5.2.3 Experimental section**

### **5.2.3.1 Materials and characterization**

Materials: Lab general solvents (hexane, ethyl acetate, dichloromethane, toluene, tetrahydrofuran, acetonitrile, methanol) were purchased from VWR or Sigma Aldrich.

Tetrahydrophthalic anhydride (THPA), 2-butyne-1,4-diol, 3-buten-1-ol, benzophenone, *p*-toluenesulfonic acid (pTSA), 3,4-Dihydro-2*H*-pyran, 9-oxabicyclo[6.1.0]non-4-ene and Grubbs II catalyst were purchased from Sigma Aldrich, Alfa Aesar, Acros or TCI and used without further purification.

Characterizations: <sup>1</sup>H NMR spectra were collected on a Bruker Advance Neo-500 MHz multinuclear NMR spectrometer. Chemical shifts are provided in *ppm* ( $\delta$ ) and referenced to the residual <sup>1</sup>H peak at 7.26 ppm in CDCl<sub>3</sub>. <sup>1</sup>H shifts are reported as chemical shift, multiplicity, coupling constant if applicable, and relative integral. Multiplicities are reported as: singlet (s), doublet (d), doublet of doublets (dd), doublet of triplets (dt), doublet of doublet of doublets (ddd), doublet of doublet of triplets (ddt), triplet (t), triplet of doublets (td), quartet (q), pentet (p), multiplet (m), or broad (br). Coupling constants (J) are reported in Hertz. High-resolution mass spectra were collected on an Agilent LCMS-TOF-DART at Duke University's Mass Spectrometry Facility.

Photoreaction was conducted using a photochemical reactor from The Southern New England Ultraviolet Company (Model #RPR-100, RPR2537A/254 nm bulb).

Ultrasonication was performed with a Sonics VCX 750 generator using a 13 mm tip. Pulsed ultrasound (1s on, 1s off) was applied under N<sub>2</sub> atmosphere while cooled with an ice bath. Aliquot was taken from the solution and subjected to GPC and <sup>1</sup>H NMR analysis.

Gel permeation chromatography (GPC) was performed on two Agilent PLgel mixed-C columns (10<sup>5</sup> Å, 7.5x300 mm, 5  $\mu$ m, part number PL1110-6500) using THF

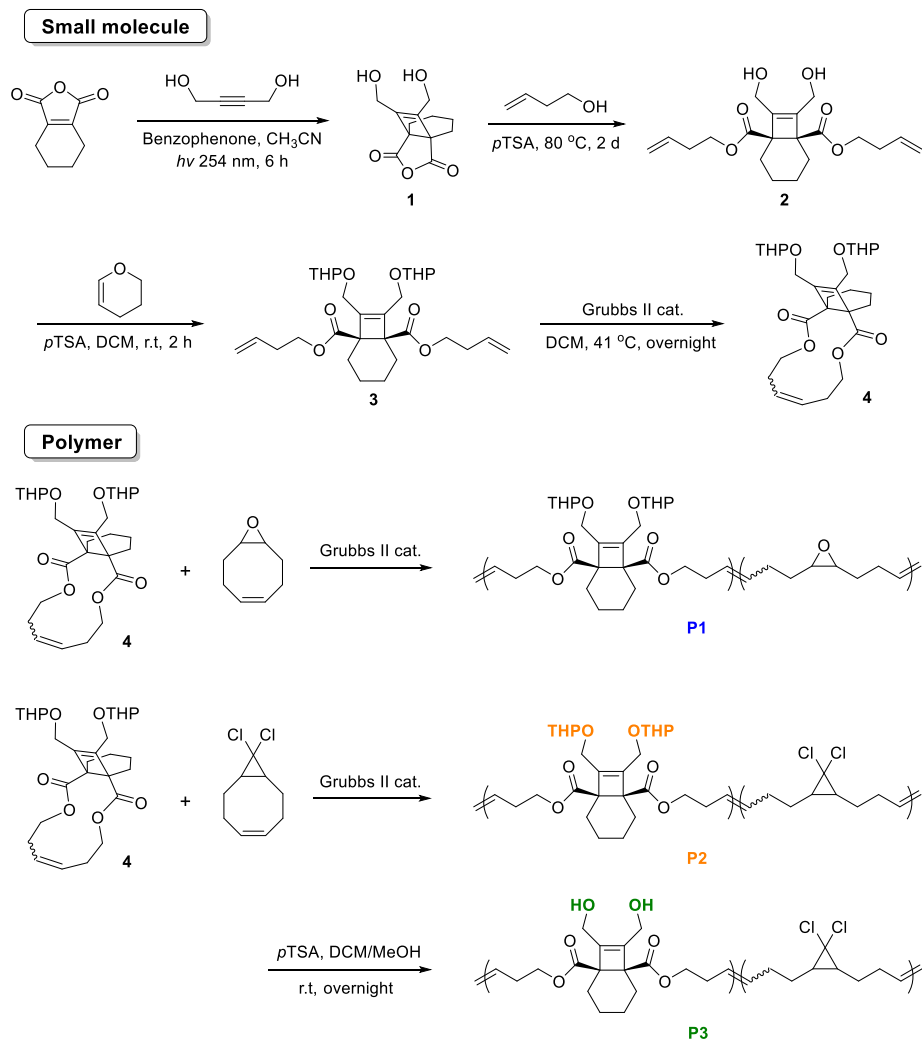
(stabilized with 100 ppm BHT) as the eluent. Molecular weights were calculated using a Wyatt Dawn EOS multi-angle light scattering (MALS) detector and Wyatt Optilab DSP Interferometric Refractometer (RI). The refractive index increment ( $dn/dc$ ) values were determined by online calculation based on injections of known concentration and mass.

Sharp Microlever silicon probes (MSNL) and Silicon Nitride AFM Probes (PNP-DB) were correspondingly purchased from Bruker (Camarillo, CA) and NanoAndMore (Watsonville, CA). All of the SMFS studies were conducted at ambient temperature ( $\sim 23$  °C) using a homemade AFM, which was constructed using a Digital Instruments scanning head mounted on top of a piezoelectric positioner, similar to the one described in detail previously.<sup>82, 84</sup> The AFM pulling experiments were conducted in a solution of toluene. The spring constant of each cantilever was calibrated in air, using the thermal noise method, based on the energy equipartition theorem as described previously.<sup>82, 84</sup> Measurements were carried out in a closed fluid cell with a scanning set for a series of approaching/retracting cycles. Probes were prepared by immersing in piranha solution ( $H_2SO_4:H_2O_2 = 3:1$ ) for 15 minutes at room temperature and then immersing in deionized water and dried by touching them against a borohydride. Silicon substrates were prepared by first allowing each to soak in hot piranha solution for 30 minutes and then washed with deionized water and dried under a stream of nitrogen. Caution should be used when handling piranha solution: it has been reported to detonate unexpectedly. The substrate and the cantilever were then placed in a UVO cleaner (ozone produced through UV light) for 15 minutes. After ozonolysis, the cantilever was mounted

in the fluid cell. 20  $\mu\text{L}$  of a 0.05-0.1 mg/mL polymer solution was added to the silicon substrate surface and allowed to dry. The silicon substrate was then placed on the piezoelectric stage of the AFM. Force curves were collected in dSPACE (dSPACE Inc. Wixom, MI) and analyzed using Matlab (The MathWorks, Inc., Natick, MA). All data were filtered during acquisition at 500 Hz. After acquisition, the data were calibrated and plotted by using homemade software written in Matlab language.

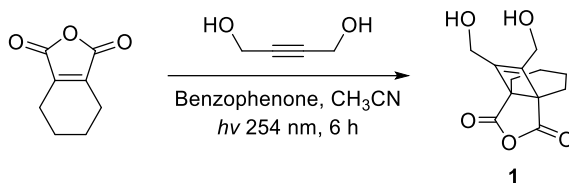
### 5.2.3.2 Synthesis details

Synthesis scheme:



### 5.2.3.2.1 Synthesis of small molecules

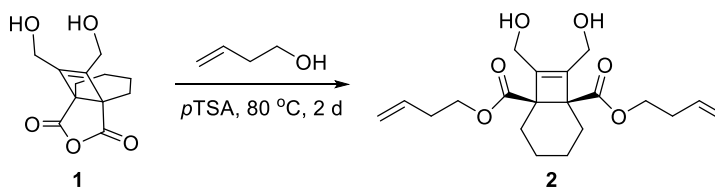
Synthesis of compound 1:



The synthesis of compound **1** was performed using adapted procedures according to previous literature.<sup>334-337</sup>

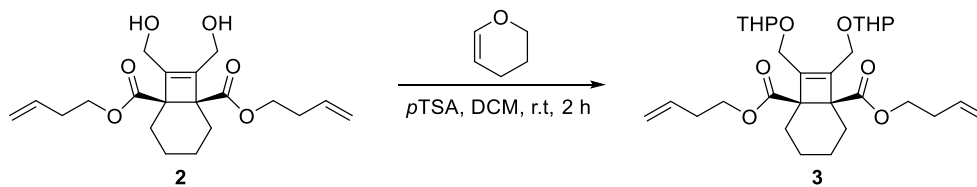
To a 500 mL quartz flask, added tetrahydrophthalic anhydride (THPA) (2.28 g, 15 mmol), 2-butyne-1,4-diol (1.835 g, 22.5 mmol) and benzophenone (900 mg). 188 mL CH<sub>3</sub>CN was then added to dissolve the compounds and the solution was sparged with N<sub>2</sub> for 10 min. The flask was capped and irradiated with UV 254 nm light for 6 h. The resulting pale-orange solution was condensed. Product was purified by chromatography using 0~70% EtOAc/hexane gradient eluent. Compound **1** was isolated as a pale-yellow solid (2.536 g, <sup>1</sup>H NMR indicates 1:1 molar ratio of product **1** to 2-butyne-1,4-diol, 52.2% yield). <sup>1</sup>H NMR (500 MHz, CDCl<sub>3</sub>) δ: 4.31 (s, 4H), 2.14 – 1.91 (m, 4H), 1.72 – 1.59 (m, 2H), 1.59 – 1.45 (m, 2H). <sup>13</sup>C NMR (125 MHz, CDCl<sub>3</sub>) <sup>13</sup>C NMR (125 MHz, CDCl<sub>3</sub>) δ: 171.77, 145.08, 57.73, 51.27, 24.21, 19.45. HRMS-ESI (*m/z*): [M+H]<sup>+</sup> calculated for C<sub>12</sub>H<sub>15</sub>O<sub>5</sub>, 239.09140; observed, 239.09204.

Synthesis of compound 2:



To a 50 mL round bottom flask, added compound **1** (1.19 g, 3.67 mmol compound **1**), *p*TSA (47 mg, 0.25 mmol) and 20 mL 3-buten-1-ol. The solution was then heated at 80 °C for 2d. The excess 3-buten-1-ol was then distilled under reduced pressure. Resulting yellow viscous mixture was purified by chromatography (0~50% EtOAc/hexane) to give compound **2** as a pale-yellow oil (659 mg, 49.3%). <sup>1</sup>H NMR (500 MHz, CDCl<sub>3</sub>) δ: 5.76 (ddt, *J* = 17.0, 10.2, 6.7 Hz, 2H), 5.18 – 5.03 (m, 4H), 4.32 – 4.17 (m, 4H), 4.08 (t, *J* = 6.7 Hz, 4H), 2.36 (qt, *J* = 6.7, 1.4 Hz, 4H), 2.21 – 2.06 (m, 2H), 1.87 – 1.76 (m, 2H), 1.69 – 1.59 (m, 2H), 1.56 – 1.44 (m, 2H). <sup>13</sup>C NMR (125 MHz, CDCl<sub>3</sub>) δ: 173.75, 143.13, 134.08, 117.57, 64.14, 58.06, 55.98, 33.09, 25.18, 16.10. HRMS-ESI (*m/z*): [M+H]<sup>+</sup> calculated for C<sub>20</sub>H<sub>29</sub>O<sub>6</sub>, 365.19587; observed, 365.19625.

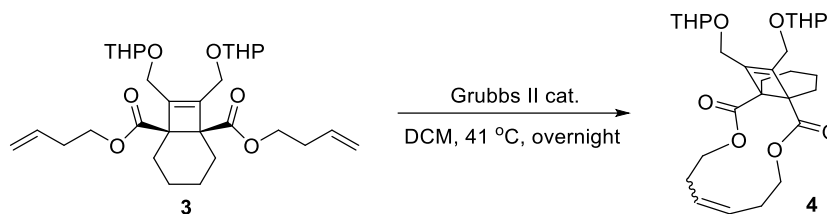
#### Synthesis of compound **3**:



To a solution of compound **2** (364 mg, 1 mmol) in 10 mL DCM, added 3,4-dihydropyran (364 mg, 4 mmol) and *p*TSA (17 mg, 0.1 mmol). The solution was stirred at room temperature for 2 h. DCM was then removed and resulting oil was subjected to chromatography (0~30% EtOAc/hexane) to give compound **3** as a clear oil (322 mg, 60.5%). <sup>1</sup>H NMR (500 MHz, CDCl<sub>3</sub>) δ: 5.77 (ddt, *J* = 17.0, 10.2, 6.9 Hz, 2H), 5.15 – 5.00 (m, 4H), 4.64 (t, *J* = 3.3 Hz, 2H), 4.53 – 4.45 (m, 1H), 4.36 (dd, *J* = 13.2, 9.0 Hz, 1H), 4.26 – 4.18 (m, 1H), 4.16 – 4.11 (m, 1H), 4.11 – 3.99 (m, 4H), 3.87 – 3.74 (m, 2H), 3.55 – 3.46 (m, 2H),

2.35 (dddd,  $J = 9.0, 7.7, 4.7, 1.6$  Hz, 2H), 2.18 – 2.07 (m, 2H), 1.93 – 1.83 (m, 2H), 1.83 – 1.72 (m, 2H), 1.72 – 1.45 (m, 14H)..  $^{13}\text{C}$  NMR (125 MHz,  $\text{CDCl}_3$ )  $\delta$ : 173.52, 141.58, 141.51, 134.25, 134.22, 117.30, 117.27, 98.13, 98.02, 63.80, 63.78, 63.75, 62.51, 62.47, 62.28, 62.26, 61.66, 61.62, 61.53, 61.51, 56.04, 56.01, 55.94, 33.17, 33.15, 31.74, 30.55, 30.53, 30.52, 26.13, 26.00, 25.92, 25.74, 25.63, 22.80, 19.10, 19.09, 19.07, 19.04, 16.13, 16.11, 16.08, 16.05, 14.27. HRMS-ESI ( $m/z$ ):  $[\text{M}+\text{Na}]^+$  calculated for  $\text{C}_{30}\text{H}_{44}\text{O}_8\text{Na}$ , 555.29284; observed, 555.29235.

#### Synthesis of compound 4:

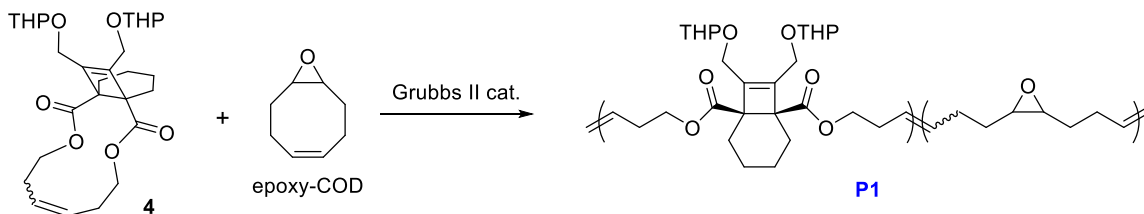


A solution of compound 3 (112 mg, 0.23 mmol) in 115 mL DCM was sparged with  $\text{N}_2$  for 10 min, Grubbs II catalyst (20 mg, 0.023 mmol) was then added in one portion. The solution was heated at 41 °C for overnight. After the reaction completed, 0.2 mL of ethyl vinyl ether was added to quench the reaction and the solution was further stirred for 30 min. Resulting solution was rotavaped onto silica and purified by chromatography (0~30% EtOAc/hexane) to give compound 4 as an off-white solid (107 mg, 93%). Compound 4 was further recrystallized from hexane.  $^1\text{H}$  NMR (500 MHz,  $\text{CDCl}_3$ )  $\delta$ : 5.55 – 5.37 (m, 2H), 4.71 – 4.58 (m, 2H), 4.52 – 3.94 (m, 6H), 3.87 – 3.74 (m, 2H), 3.57 – 3.44 (m, 2H), 2.50 – 2.31 (m, 2H), 2.31 – 2.20 (m, 2H), 2.19 – 2.06 (m, 2H), 1.91 – 1.82 (m, 2H), 1.82 – 1.73 (m, 2H), 1.73 – 1.43 (m, 12H).  $^{13}\text{C}$  NMR (125 MHz,  $\text{CDCl}_3$ )  $\delta$ : 173.67, 173.52, 141.56, 141.22, 129.11, 129.08, 129.06, 128.61, 98.01, 97.95, 97.85, 63.42, 63.37, 63.31, 62.49, 62.23,

62.18, 61.65, 61.61, 61.31, 56.26, 56.22, 56.19, 31.15, 31.11, 31.08, 31.06, 30.52, 30.50, 27.54, 26.51, 26.28, 26.07, 25.78, 25.64, 19.09, 18.96, 18.93, 16.09, 16.05. HRMS-ESI ( $m/z$ ):  $[M+NH_4]^+$  calculated for  $C_{28}H_{44}NO_8$ , 522.30614; observed, 522.30747.

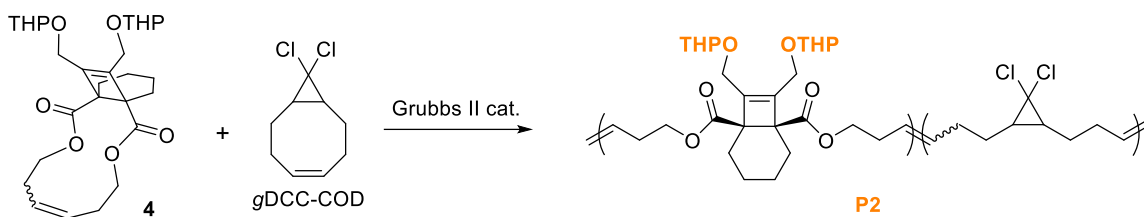
### 5.2.3.2.2 Synthesis of polymers

Synthesis of polymer P1:



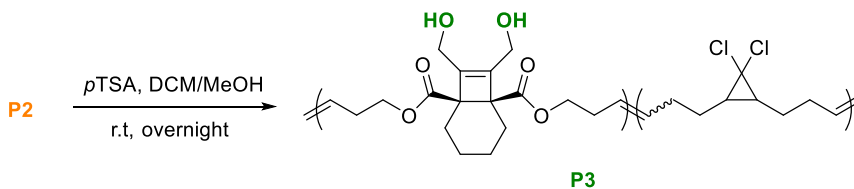
Monomer **4** (15.1 mg, 0.03 mmol) and 9-oxabicyclo[6.1.0]non-4-ene (epoxy-COD, 8.7 mg, 0.07 mmol) was weighted in a 10 mL flame-dried scintillation vial and kept under  $N_2$ . 0.1 mL of  $N_2$  sparged Grubbs II catalyst solution (1.4 mg in 2 mL toluene) was added to the monomers. The polymerization was performed overnight, after which several drops of ethyl vinyl ether were added. The viscous solution was further stirred for 30 min. After two rounds of precipitation from methanol, the resulting white polymer was dissolved in 1 mL DCM under stirring, and MeOH was added dropwise into the solution until it turned cloudy. The vial was capped and subjected to centrifuge at 4500 rpm for 10 min. The upper clear solution was decanted and the bottom polymer was washed with MeOH and dried under high vacuum. This high molecular weight portion polymer was further used for SMFS study.

Synthesis of polymer P2:



To a 10 mL frame-dried scintillation vial, added monomer **4** (25 mg, 0.05 mmol) and 9,9-dichlorobicyclo[6.1.0]non-4-ene<sup>45, 170, 172</sup> (gDCC-COD, 38.2 mg, 0.2 mmol). The vial was purged and kept under N<sub>2</sub>. 0.25 mL of N<sub>2</sub> sparged Grubbs II catalyst solution (1.6 mg in 2 mL DCM) was added. After the polymerization was stirred for overnight, several drops of ethyl vinyl ether were added, and the solution was further stirred for 30 min to quench the catalyst. After three rounds of precipitation from methanol, a white polymer was obtained (52 mg, 82%). <sup>1</sup>H NMR spectra indicated 14 mol% incorporation of monomer **4**. GPC-MALS: M<sub>n</sub> = 128.4 kDa. PDI = 1.39, dn/dc = 0.114.

Synthesis of polymer P3:



To a solution of 25 mg **P2** polymer in 1.5 mL DCM/MeOH (2:1), added 1 mg pTSA catalyst. After stirred for overnight, the solution was condensed and precipitated from MeOH. Obtained white polymer was dried under high vacuum (20 mg, ). <sup>1</sup>H NMR indicated selective removal of THP protecting group. The polymer was analyzed from GPC-MALS: M<sub>n</sub> = 119.8 kDa. PDI = 1.69, dn/dc = 0.124.

### 5.2.3.3 Sonication experiment

General sonication procedures: A solution of polymer **P2** (1.2 mg/mL) and **P3** (1.0 mg/mL) in dry THF was transferred into a dry Suslick cell. The solution was sparged with N<sub>2</sub> for 10 min while cooled with ice bath. Pulsed ultrasound was applied (1s on, 1s off) at 30% amplitude. Aliquots of 0.8 mL sample at various sonication times (0, 5, 10, 20, 30, 45, 60 min) were taken from the cell and analyzed by GPC. After GPC analysis, each remaining sample was transferred into a 10 ml scintillation vial and condensed. Resulting polymer was further dried under high vacuum and then subjected to <sup>1</sup>H NMR analysis to quantify the amount of ring opened BCOE and gDCC mechanophores.

Analysis of mechanical activation of **P2** polymer:

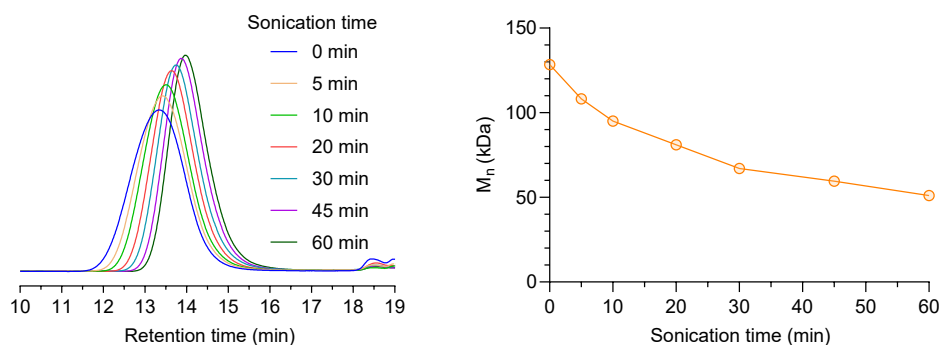


**Figure 216 : GPC traces of P2 polymer (left) and corresponding M<sub>n</sub> evolution (right) at various sonication time.**

The number of chain scission cycle (SC) was calculated according to the following equation:

$$SC = \frac{\ln(M_n^{(0)} / M_n^{(t)})}{\ln 2}$$

$M_n^{(0)}$  is the initial molecular weight and  $M_n^{(t)}$  is the sonicated molecular weight.

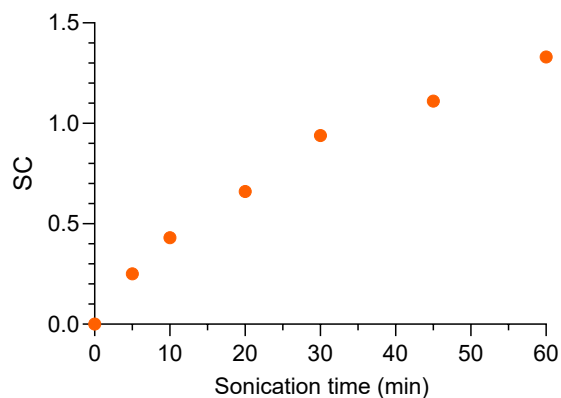


Figure 217 : Scission cycles of P2 polymer at various sonication times.

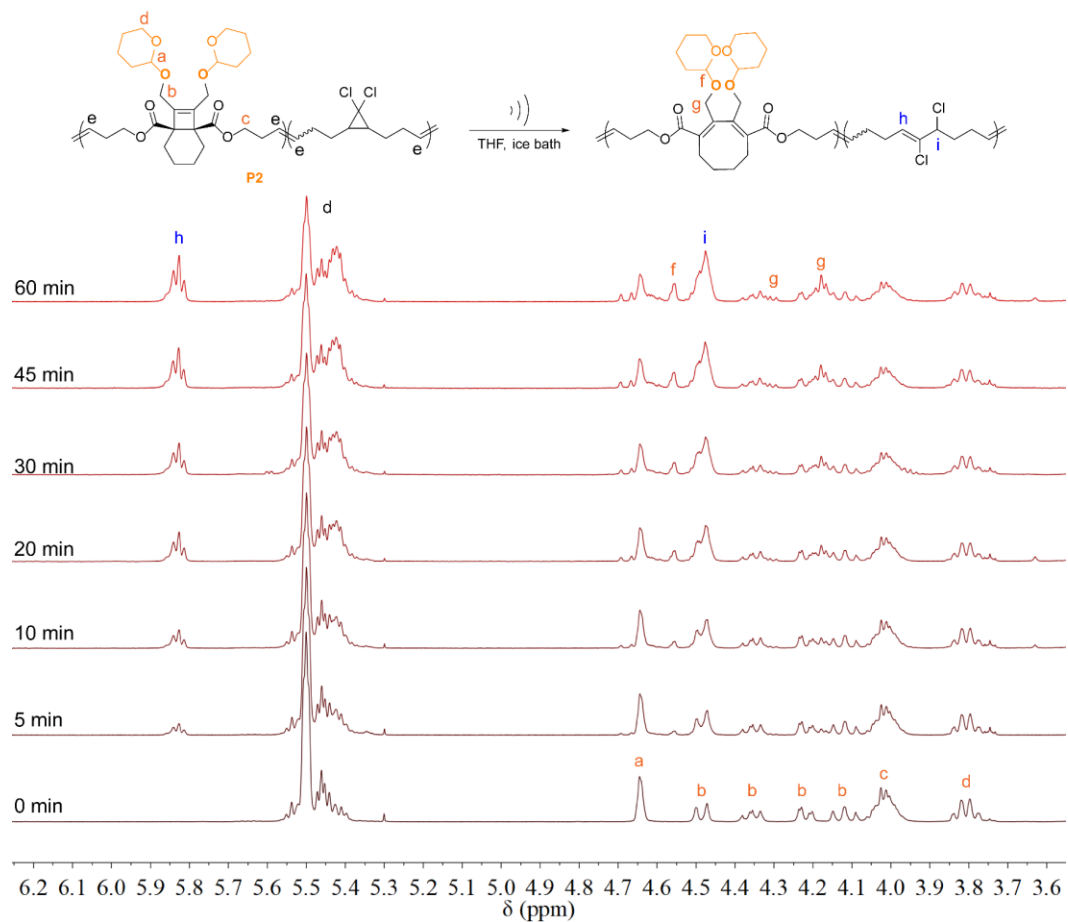


Figure 218 : Stack of  $^1\text{H}$ -NMR ( $\text{CDCl}_3$ , 500 MHz) spectra of sonicated P2 polymer at various sonication time.

The activation of gDCC and BCOE mechanophores were analyzed from  $^1\text{H}$  NMR spectrum. The ring-opening (RO) percentage of gDCC and BCOE are calculated from the following equations:

$$\text{RO}(g\text{DCC})\% = \frac{2 \cdot \int H_h}{\int H_d \cdot 86\%} \times 100\% ; \text{RO}(\text{BCOE})\% = \frac{\int H_f}{\int H_d \cdot 14\%} \times 100\%$$

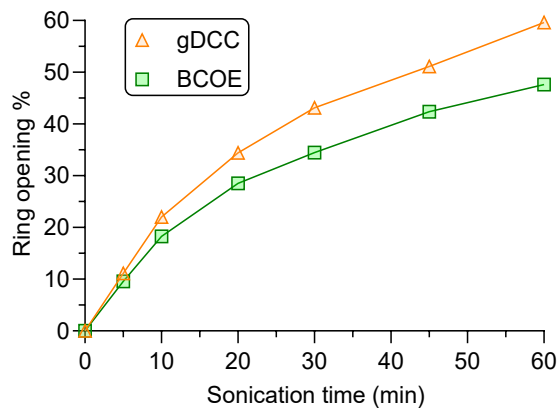


Figure 219 : Ring-opening percentage of gMCC (left) and HCl release (right) in polymer 3 at various sonication time.

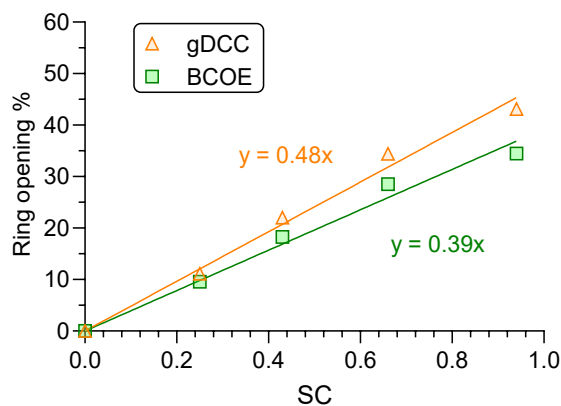
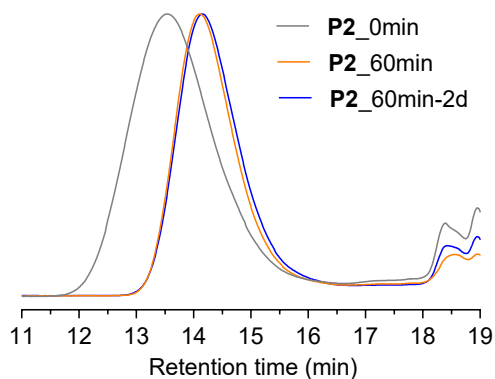
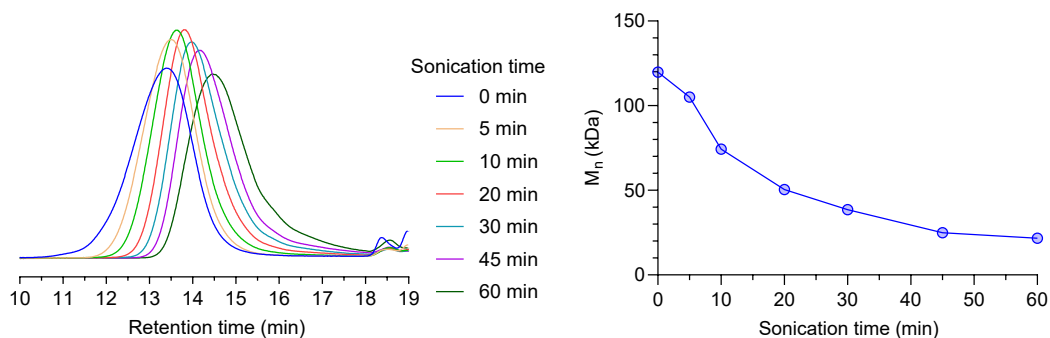


Figure 220 : Ring opening% of gDCC and BCOE vs. scission cycles. The slope (or  $\Phi$  value) of linear fitting indicates the activation of mechanophore per chain scission. gDCC:  $\Phi = 0.48$ ; BCOE:  $\Phi = 0.39$ .



**Figure 221 :  $M_n$  of a P2 polymer decreased from 83.5 kDa ( $\bar{D} = 1.56$ ) to 43.8 kDa ( $\bar{D} = 1.22$ ) after 60 min ultrasonication treatment, and the  $M_n$  of sonicated P2 remained nearly unchanged (42.5 kDa,  $\bar{D} = 1.27$ ) after 2d standing time.**

Analysis of mechanical activation of P3 polymer:



**Figure 222 : GPC traces of P3 polymer (left) and corresponding  $M_n$  evolution (right) at various sonication time. GPC analysis was performed right after sonication.**

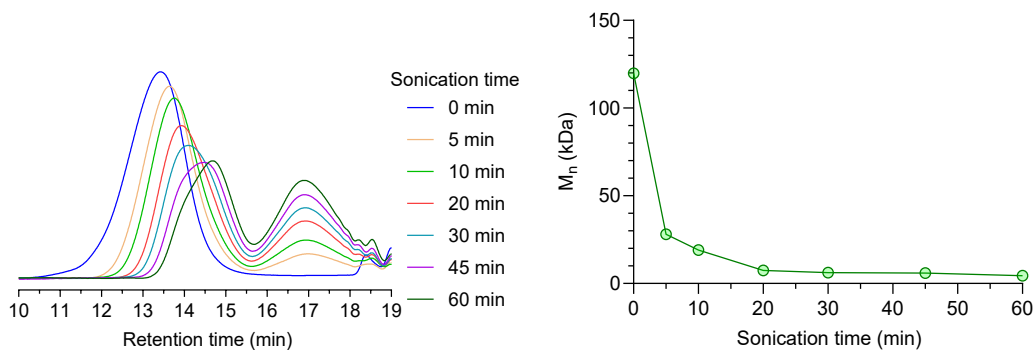


**Figure 223 : GPC traces of P3 polymer (left) and corresponding  $M_n$  evolution (right) at various sonication time. GPC analysis was performed after 17d of standing.**

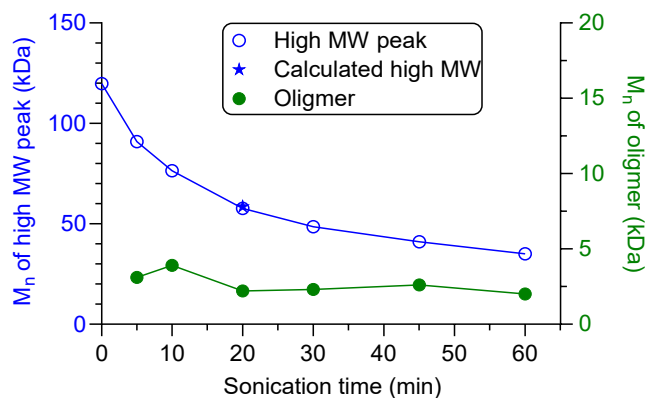


**Figure 224 : Molecular weight (MW) analysis of P3-17d polymer. The  $M_n$  of high MW peak and oligomer peak were analyzed separately. The theoretical  $M_n$  of high MW fraction at 20 min sonication time was calculated assuming the same scission cycle as P2 ( $SC = \ln(128.4/81.1)/\ln 2 = 0.66$ ). The polymer has broken  $2^{SC}-1 = 0.58$  times. After one time of chain break, a 120 kDa polymer produces two 60 kDa daughter chains comprised of 39% activated BCOE (Figure SX) along the chain. According to reported method,<sup>204</sup> after removal of activated BCOE block, the theoretical  $M_n$  after 0.58 times of chain break is:  $M_n = (120 \cdot 0.42 + 2 \cdot 60 \cdot 0.61 \cdot 0.58) / (0.42 + 0.58 \cdot 2) = 58.6$  kDa.**

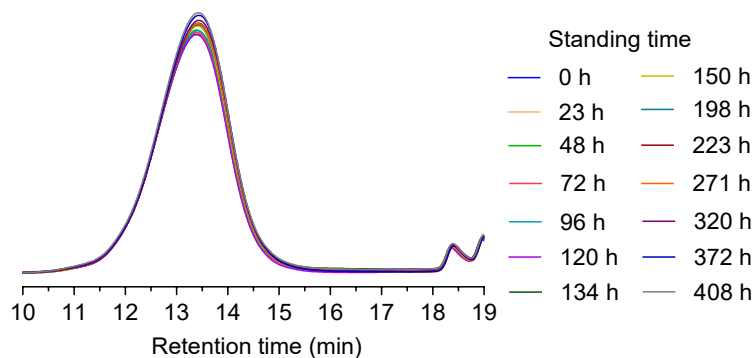


Figure 225 : GPC traces of pristine P3 polymer at various standing time.

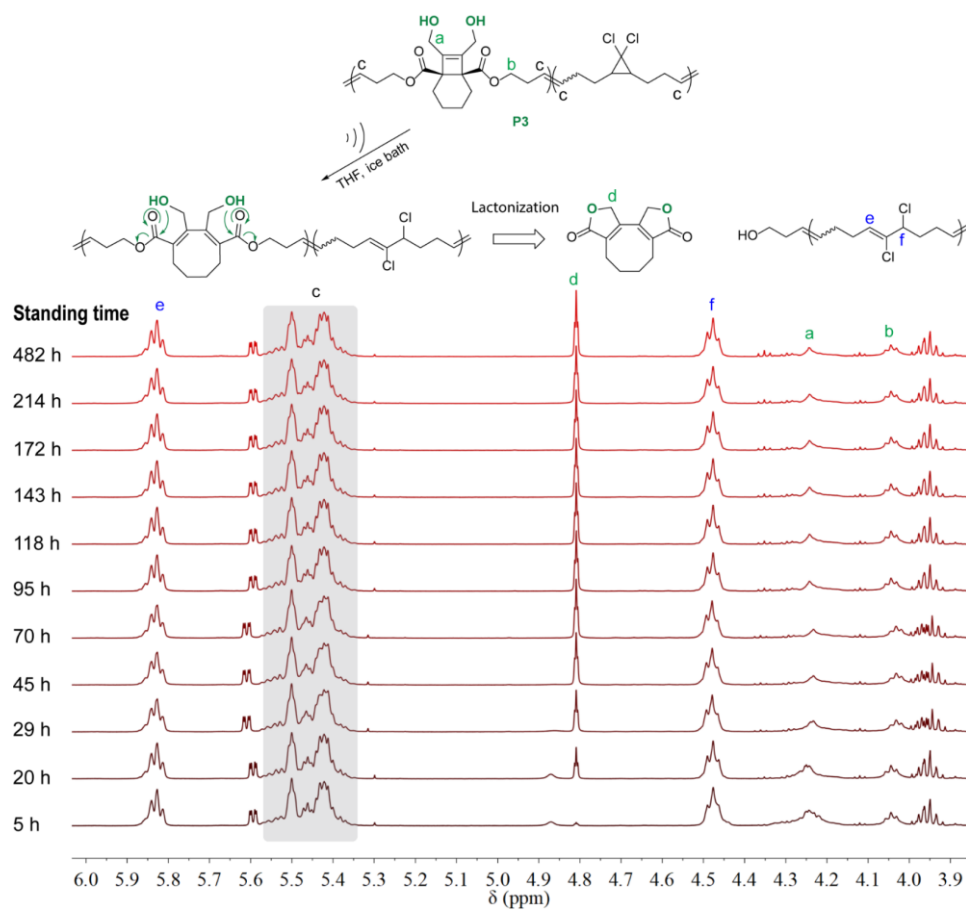
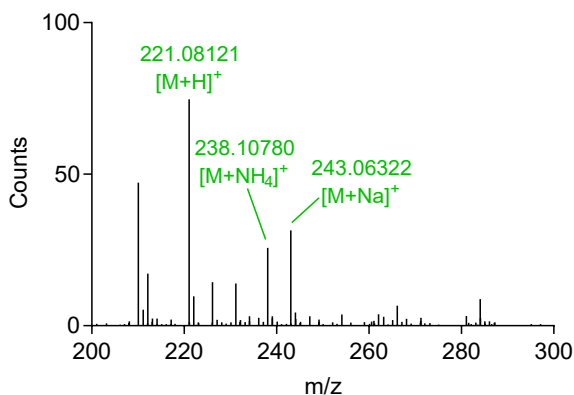


Figure 226 :  $^1\text{H-NMR}$  ( $\text{CDCl}_3$ , 500 MHz) spectra stack of sonicated P3 polymer at various standing time. P3 polymer was subjected to ultrasonication for 60 min before  $^1\text{H NMR}$  analysis.

The percentage of lactone specie relative to initial content of BCOE mechanophore is calculated from the following equations:

$$\text{Lactone\%} = \frac{\int H_d}{2 * \int H_c * 14\%} \times 100\%$$

There is about  $12000 / (0.14 * 336 + 0.86 * 191) * 0.14 = 80$  BCOE along P3 polymer. If we assumed that P3 has a same value as P2. There will be 39% BCOE ring open per chain scission, that is, ~31 BCOE activation per chain stretching event.



**Figure 227 : HRMS analysis of P3 polymer after 60 min sonication and further 20 days of standing.**

#### 5.2.3.4 SMFS analysis

##### 5.2.3.4.1 Determination of the thermal activation energy

In a 25 mL dry Shlenk flask, 20 mg of BCOE diene derivative **3** was dissolved in 2 mL diphenyl ether. The flask was then heated to 150 °C under N<sub>2</sub>. Aliquots of 0.1 mL solution at time point (0, 30, 60, 160, 270, 360 min) was took from the flask and dilute with CDCl<sub>3</sub> for <sup>1</sup>H NMR analysis. Note: Due to the more strained 8-member ring in the ring opened product and presence of THP protecting groups, the ring opened (RO) compound **3** can undergo reversible ring closing to give pristine ring closed (RC) form without

producing lactone.<sup>332-333</sup> The percentage of ring closed from in the system can be calculated using the following equation:

$$RC \% = \frac{\int H_a + \int H_b}{\int H_c} \times 100\%$$

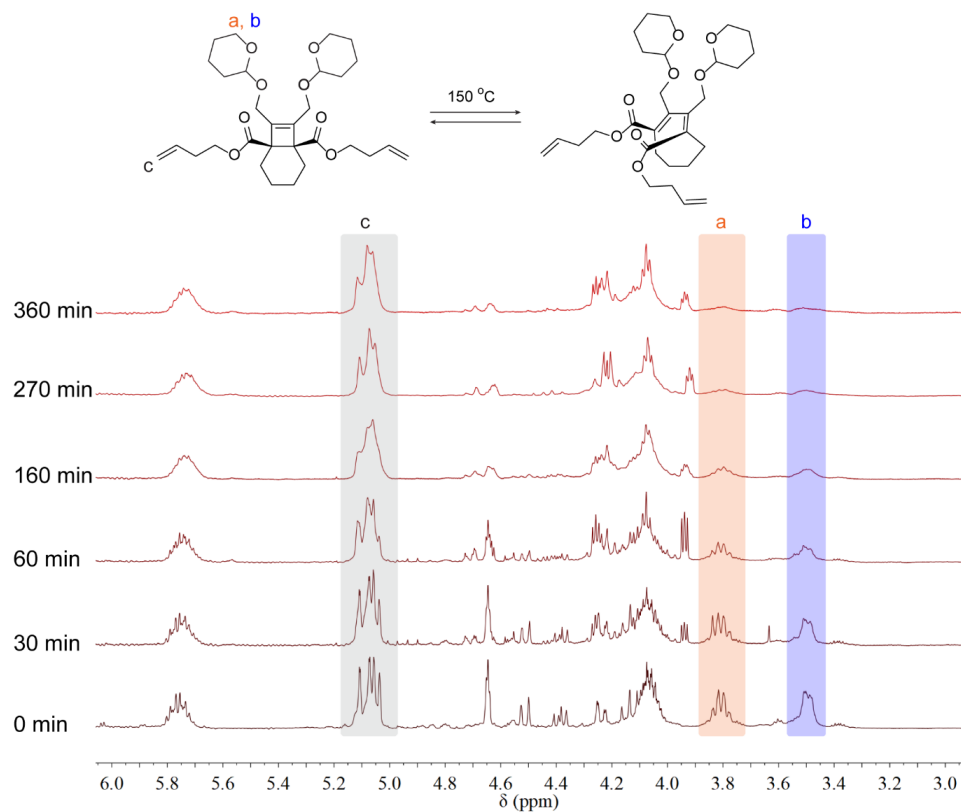


**Figure 228 :** <sup>1</sup>H NMR (CDCl<sub>3</sub>, 500 MHz) spectra stack of compound 3 in diphenyl ether after heated at 150 °C for various time.

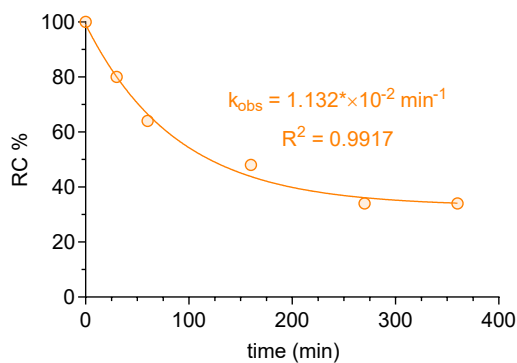


**Figure 229 : Percentage of ring closed BCOE over time at 150 °C in diphenyl ether.**

The equilibrium at 150 °C can be estimated from the plateau (33%) of fitting:

$$K_{eq} = \frac{k_1}{k_{-1}} = \frac{[RO]}{[RC]} \approx 2$$

The observed rate constants is:  $k_{obs} = k_1 - k_{-1} = 1.132 \times 10^{-2} \text{ min}^{-1}$

Therefore, the ring-opening rate constant is:  $k_1 = 2k_{-1} = 2k_{obs} = 2.264 \times 10^{-2} \text{ min}^{-1} = 3.77 \times 10^{-4} \text{ s}^{-1}$

According to the transition state theory, the thermal activation energy can be estimated:

$$\begin{aligned} \Delta G^\ddagger &= -RT \ln \frac{k_1 h}{k_B T} = -8.314 \times 423 \times \ln \frac{3.77 \times 10^{-4} \times 6.626 \times 10^{-34}}{1.38 \times 10^{-24} \times 423} \text{ J/mol} \\ &= 132550 \text{ J/mol} = 31.7 \text{ kcal/mol} \end{aligned}$$

Mechanically induced disrotatory ring opening of BCOE is a forbidden pathway. Hence, the activation energy of forbidden reaction would be at least 4 kcal/mol more than thermal allowed path way.<sup>83</sup> The activation energy of disrotatory ring opening of BCOE is:  $\Delta G^\ddagger > 31.7 + 4 \text{ kcal/mol} = 35.7 \text{ kcal/mol}$

#### 5.2.3.4.2 SMFS curve analysis

Force-extension curves were analyzed using method described in section 2.2.3.4.2. Pre- and post- transition force curves were fitted with extended freely jointed chain (FJC) model to give the contour lengths of polymers before and after transition. Further analysis with Bell-Evans (BE) or Cusp models provided  $\Delta x^\ddagger$  information.

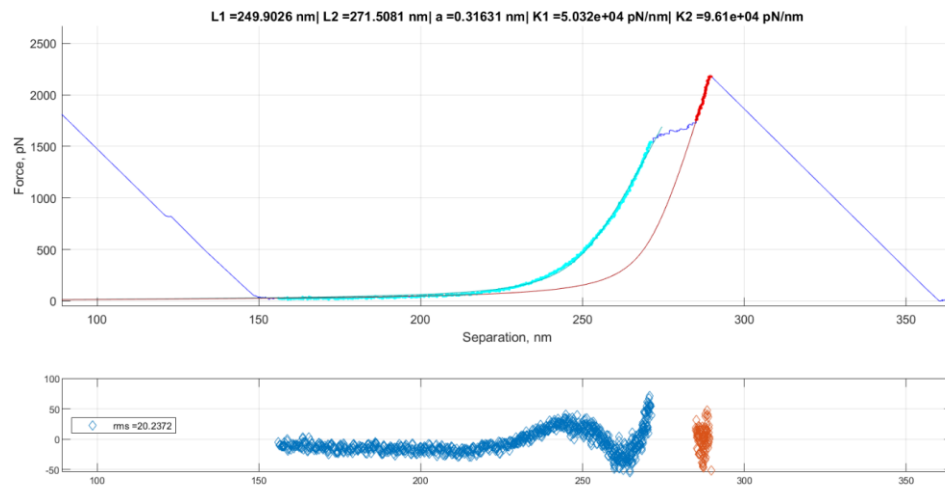


**Figure 230 : Fitting of pre and post transition in force-extension curve with extended FJC model. The contour before and after transition are obtained: before,  $L_i = 249.9$  nm; after,  $L_f = 271.5$  nm.**

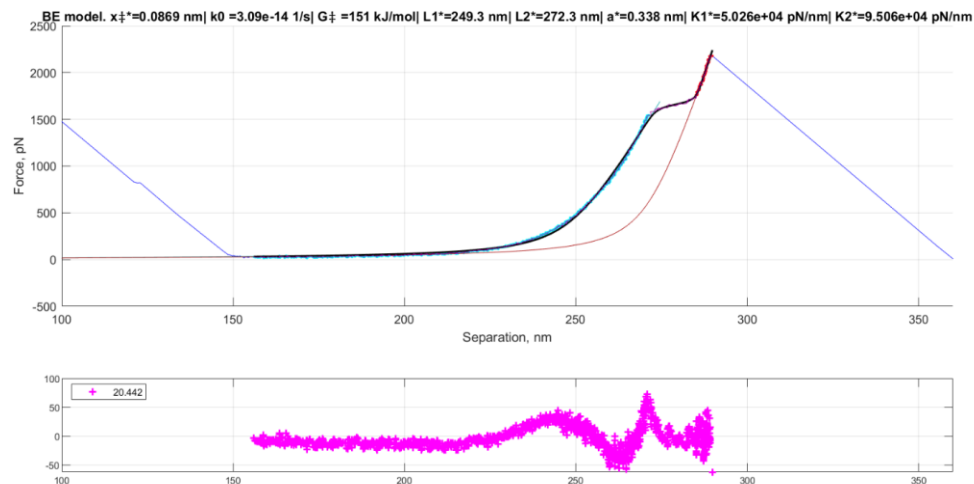


Figure 231 : Fitting of force-extension curve with BE model. Mechanical coupling  $\Delta x^\ddagger = 0.87$  Å.

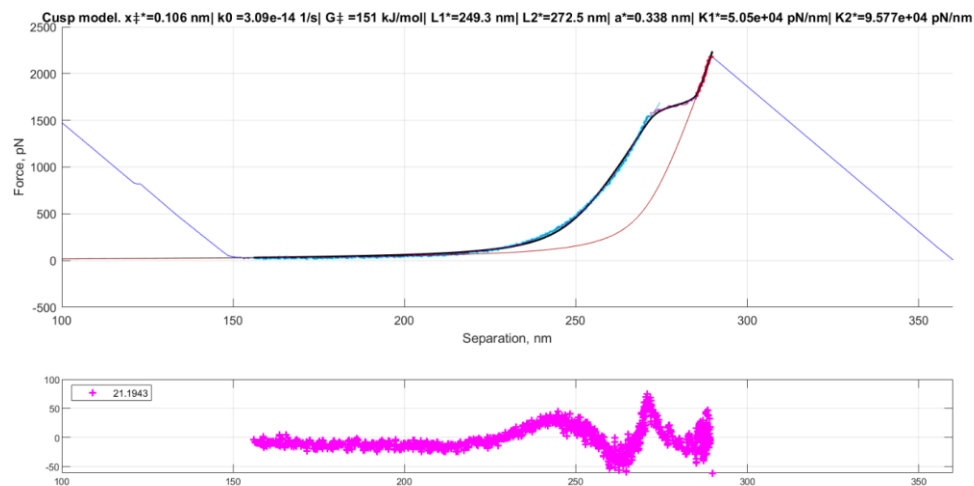
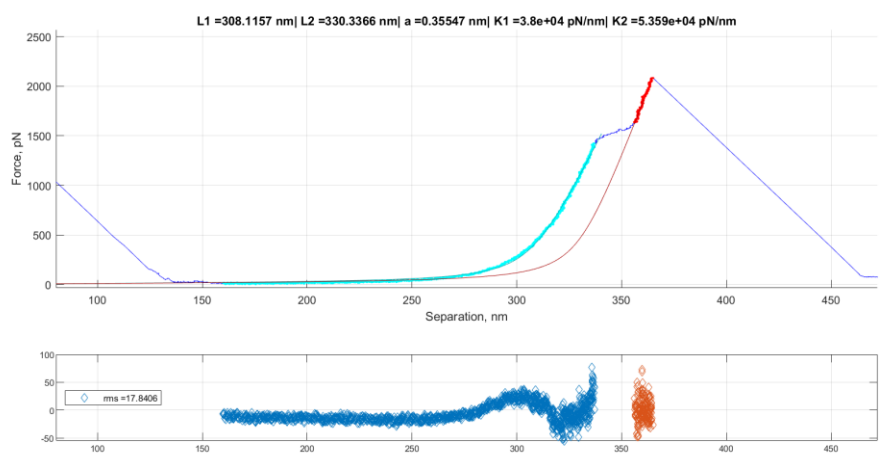
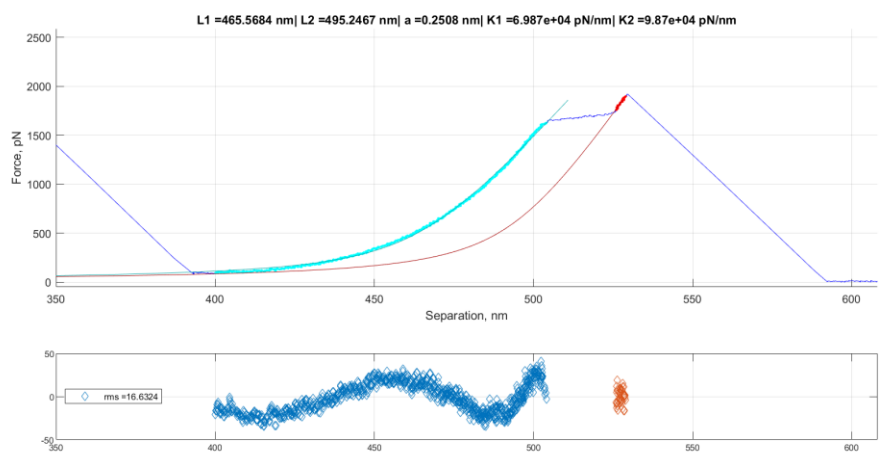
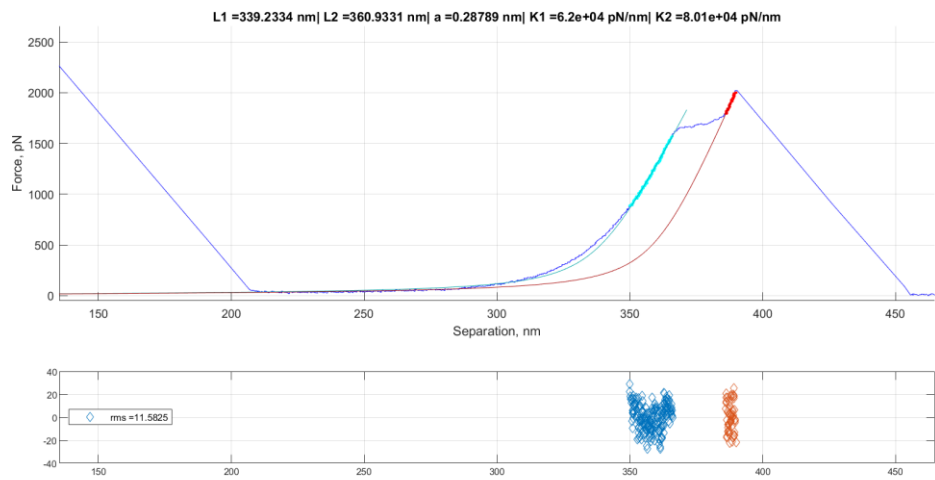
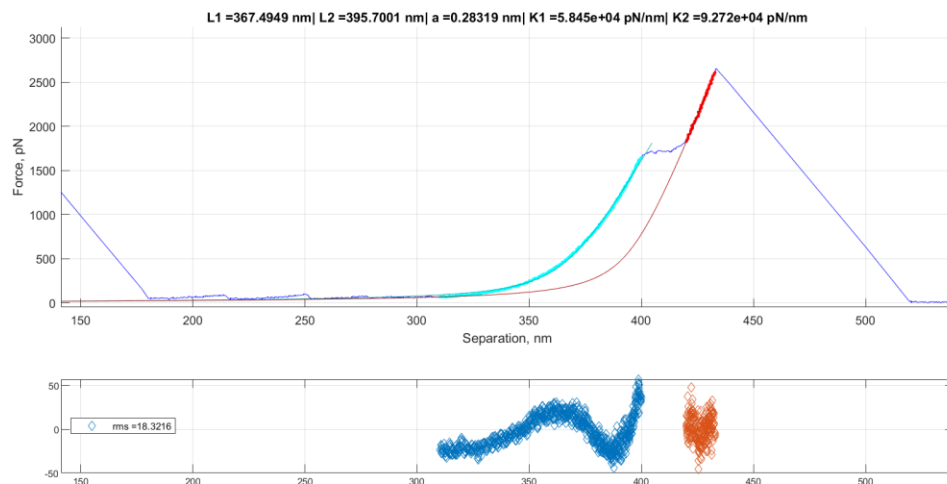


Figure 232 : Fitting of force-extension curve with Cusp model. Mechanical coupling  $\Delta x^\ddagger = 1.06$  Å.

Additional SMFS curves





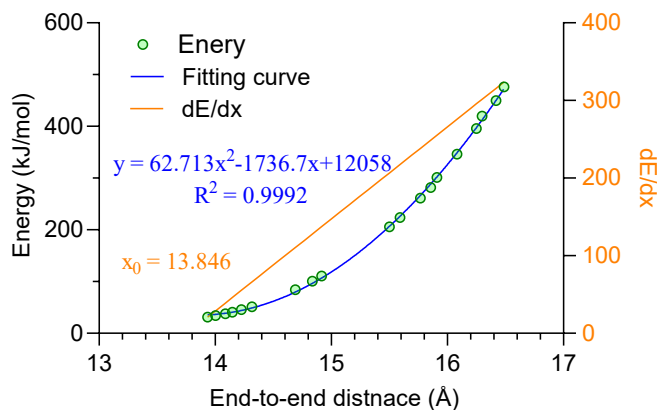
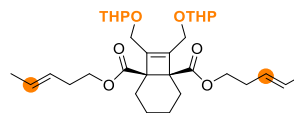
**Table 29 : List of results from SMFS curves analysis**

| #             | L <sub>i</sub><br>(nm) | L <sub>f</sub><br>(nm) | L <sub>f</sub> /L <sub>i</sub> | Kuhn<br>length<br>(nm) | K <sub>1</sub><br>(pN/nm) | K <sub>2</sub><br>(pN/nm) | Δx <sup>‡</sup> |              | F*<br>(pN)  |
|---------------|------------------------|------------------------|--------------------------------|------------------------|---------------------------|---------------------------|-----------------|--------------|-------------|
|               |                        |                        |                                |                        |                           |                           | BE              | Cusp         |             |
| 1             | 99.5                   | 105.0                  | 1.056                          | 0.225                  | 7.51×10 <sup>4</sup>      | 8.31×10 <sup>4</sup>      | 0.94            | 1.15         | 1539        |
| 2             | 186.8                  | 190.4                  | 1.020                          | 0.237                  | 7.43×10 <sup>4</sup>      | 6.50×10 <sup>4</sup>      | 0.94            | 1.15         | 1557        |
| 3             | 198.4                  | 209.7                  | 1.057                          | 0.279                  | 6.45×10 <sup>4</sup>      | 8.19×10 <sup>4</sup>      | 0.91            | 1.11         | 1594        |
| 4             | 308.1                  | 330.3                  | 1.072                          | 0.355                  | 3.80×10 <sup>4</sup>      | 5.36×10 <sup>4</sup>      | 0.92            | 1.13         | 1529        |
| 5             | 339.2                  | 360.9                  | 1.064                          | 0.288                  | 6.20×10 <sup>4</sup>      | 8.01×10 <sup>4</sup>      | 0.84            | 1.03         | 1690        |
| 6             | 249.9                  | 271.5                  | 1.086                          | 0.316                  | 5.03×10 <sup>4</sup>      | 9.61×10 <sup>4</sup>      | 0.87            | 1.06         | 1645        |
| 7             | 465.6                  | 495.2                  | 1.064                          | 0.251                  | 6.99×10 <sup>4</sup>      | 9.87×10 <sup>4</sup>      | 0.84            | 1.03         | 1690        |
| 8             | 367.5                  | 395.7                  | 1.077                          | 0.283                  | 5.85×10 <sup>4</sup>      | 9.27×10 <sup>4</sup>      | 0.82            | 1.01         | 1716        |
| 9             | 138.9                  | 147.7                  | 1.063                          | 0.199                  | 1.12×10 <sup>4</sup>      | 1.53×10 <sup>4</sup>      | 0.93            | 1.14         | 1566        |
| 10            | 265.6                  | 280.5                  | 1.056                          | 0.298                  | 5.57×10 <sup>4</sup>      | 8.49×10 <sup>4</sup>      | 0.85            | 1.04         | 1704        |
| 11            | 129.6                  | 139.8                  | 1.078                          | 0.263                  | 6.45×10 <sup>4</sup>      | 9.78×10 <sup>4</sup>      | 0.92            | 1.13         | 1570        |
| 12            | 89.6                   | 95.5                   | 1.066                          | 0.308                  | 5.46×10 <sup>4</sup>      | 7.48×10 <sup>4</sup>      | 0.90            | 1.10         | 1609        |
| Avg.          |                        |                        | 1.063                          |                        |                           |                           | 0.89            | 1.09         | 1617        |
| SD.           |                        |                        | 0.017                          |                        |                           |                           | 0.04            | 0.05         | 68          |
| <b>Report</b> |                        |                        | <b>1.063</b>                   |                        |                           |                           | <b>0.89</b>     | <b>1.09</b>  | <b>1620</b> |
|               |                        |                        | <b>±0.017</b>                  |                        |                           |                           | <b>±0.04</b>    | <b>±0.05</b> | <b>±70</b>  |

### 5.2.3.5 CoGEF modeling

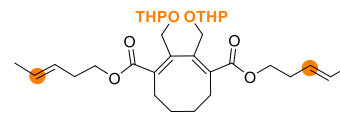
CoGEF modeling of BCOE repeating unit and corresponding forbidden ring opening product were performed on Spartan'16 V2.0.7 version at Molecular Mechanics/MMFF theory level. The end-to-end distance was constrained and relaxed with step interval of 0.1 Å. The obtained energy at each relaxed step was plotted as a function of distance. Further quadratic fitting and subsequent analysis from the first derivative gave force vs. extension relation, from which the contour length ( $x_0$ ) at zero force can be extrapolated.

End-to-end distance modeling of ring closed BCOE:



**Figure 233 : Quadratic fit of energy vs. distance curve (blue); force vs. distance plot (orange). End-to-end distance of ring closed BCOE:  $x_0 = 13.846$  Å.**

End-to-end distance modeling of ring opened BCOE:



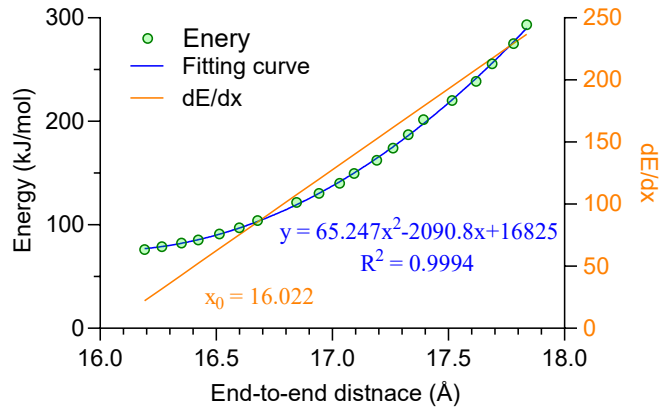


**Figure 234 : Quadratic fit of energy vs. distance curve (blue); force vs. distance plot (orange). End-to-end distance of ring closed BCOE:  $x_0 = 16.022 \text{ \AA}$ .**

The ratio of final contour length ( $L_f$ ) to initial contour length ( $L_i$ ) can be calculated:

$$\frac{L_f}{L_i} = \frac{x \times l_f + (1-x) \times l_{COD}}{x \times l_i + (1-x) \times l_{COD}} = \frac{0.26 \times 16.022 + 0.74 \times 9.366}{0.26 \times 13.846 + 0.74 \times 9.366} = 1.054$$

$x$  is the incorporation percentage of BCOE;  $l_{COD}$  is the contour length of epoxy-COD repeating unit.<sup>46</sup>

## 6. Conclusions

We have applied molecular-level engineering tools to extend the scope of stress-responsive materials and addressed four aspects: structure-reactivity relationships, novel behaviors, extrapolation of force distribution in the bulk materials, and mechanochemically regulated degradable polymers. Three techniques, i.e., ultrasonication, SMFS, and bulk tests, have been applied to approach the mechanochemical responses. Ultrasonication study provides fundamental and mechanistic understanding of mechanochemical reactions and related outcomes, while the SMFS analysis offers quantitative evaluation of mechanochemical reactivities. Lastly, the insertion of mechanophores into bulk materials allows for examination of mechanochemical reactivities, which in turn provides feedback to the molecular design. The combination of ultrasonication, SMFS, and bulk studies forms a closed study loop and potentially correlates the molecular-level mechanochemical reactivity and macroscopic response, promoting the rational design of stress-responsive materials.

The mechanical properties of polymeric materials gradually diminish after subjecting to continuous loads, which causes polymer fatigue, formation of microcracks, and, eventually, polymer failure. When scrutinized from the molecular level, a typical crosslinked polymeric material exhibits mechanical elasticity owing to the entropic formation of 'coiled' and entangled polymer strands in the polymer network, and high strains associated with mechanical load depletes the chain entropy and enthalpically stretches the polymer chains. Overstretching of polymer chains leads to chain scissions

and polymer failure. However, subjecting a polymer network to strain usually results in a nonaffine deformation of polymer chains, due to the intrinsic polydispersity of chain links and network defects. As a result, there is a force distribution in the strained network. While a considerable fraction of chains stays at the entropic region, some experience force that is sufficiently high to break C-C bonds. In terms of a single polymer chain, the entropic extension of 'coiled' chain requires a low force ( $\times 10$  pN), but provides a great strain; in contrast, a small increase in strain at the entropic region significantly increase the force ( $\times 100$  pN to  $> \text{nN}$ ). Therefore, the nonaffine deformation and so force distribution in the strained polymer network limits the direct correlation between single-chain mechanical properties and macroscopic mechanical performance. Although the nonaffine deformation of polymer network and corresponding force distribution have been probed computationally, the knowledge of detailed force distribution in strained polymer network has yet been realized experimentally.

The study loop of polymer mechanochemistry (i.e., ultrasonication, SMFS, and bulk tests) presented in this dissertation provides a means to correlation the molecular reactivities to the macroscopic responses. We reasoned that a similar systematic investigation of some mechanochromic force probes would help disclose the real force distribution in the strained bulk materials and, in turn, guide the design of stress-responsive polymer networks. In other words, the molecular mechanochemical response of force probes can be correlated to their macroscopic mechanochromic behaviors. Specifically, we can use SMFS technique to quantify force probes and further exam their

relative activation in the bulk materials. Moreover, different force probes comprised of distinct mechanochemical reactivities, which are known from SMFS quantification, exhibit different levels of activation in the bulk materials. Then, the relative activation can be applied to draw some insights into the force distribution. Bridging the molecular and bulk level behaviors would help understand the material mechanics, guide the design of stress-responsive materials, which could benefit not only the industry but also our life.

## 7. Reference

1. Staudinger, H. Über Polymerisation. *Ber. Dtsch. Chem. Ges.* **1920**, *53*, 1073–1085.
2. Staudinger, H.; Bondy, H. F. Isoprene and Rubber. Xix. The Molecular Size of Rubber and Balata. *Ber. Dtsch. Chem. Ges. B* **1930**, *63*, 734–736.
3. Staudinger, H.; Leupold, E. O. Isoprene and Rubber. Xviii. Studies of the Viscosity of Balata. . *Ber. Dtsch. Chem. Ges. B* **1930**, *63*, 730–733.
4. Staudinger, H.; Hener, W. Highly Polymerized Compounds. Xciii. The Breaking up Ofthe Molecular Fibers Ofthe Polystyrenes. *Ber. Dtsch. Chem. Ges. B* **1934**, *67*, 1159–1164.
5. Sohma, J. Mechanochemistry of Polymers. *Prog. Polym. Sci.* **1989**, *14*, 451-596.
6. Koda, S.; Mori, H.; Matsumoto, K.; Nomura, H. Ultrasonic Degradation of Water-Soluble Polymers. *Polymer* **1994**, *35*, 30-33.
7. Encina, M. V.; Lissi, E.; Sarasua, M.; Gargallo, L.; Radic, D. Ultrasonic Degradation of Polyvinylpyrrolidone - Effect of Peroxide Linkages. *J Polym Sci Pol Lett* **1980**, *18*, 757-760.
8. Paulusse, J. M.; Sijbesma, R. P. Reversible Mechanochemistry of a Pd(Ii) Coordination Polymer. *Angew Chem Int Ed Engl* **2004**, *43*, 4460-4462.
9. Kimberly L. Berkowski; Stephanie L. Potisek; Charles R. Hickenboth; Moore\*, J. S. Ultrasound-Induced Site-Specific Cleavage of Azo-Functionalized Poly(Ethylene Glycol). *Macromolecules* **2005**, *38* 8975-8978.
10. Hickenboth, C. R.; Moore, J. S.; White, S. R.; Sottos, N. R.; Baudry, J.; Wilson, S. R. Biasing Reaction Pathways with Mechanical Force. *Nature* **2007**, *446*, 423-427.
11. Kauzmann, W.; Eyring, H. The Viscous Flow of Large Molecules. *J. Am. Chem. Soc.* **1940**, *62*, 3113-3125.

12. Bell, G. I. Models for the Specific Adhesion of Cells to Cells. *Science* **1978**, *200*, 618-627.
13. Evans, E.; Ritchie, K. Dynamic Strength of Molecular Adhesion Bonds. *Biophys. J.* **1997**, *72*, 1541-1555.
14. Evans, E. Probing the Relation between Force - Lifetime - and Chemistry in Single Molecular Bonds. *Annu. Rev. Biophys. Biomol. Struct.* **2001**, *30*, 105-128.
15. Dudko, O. K.; Hummer, G.; Szabo, A. Intrinsic Rates and Activation Free Energies from Single-Molecule Pulling Experiments. *Phys. Rev. Lett.* **2006**, *96*, 108101.
16. Konda, S. S.; Brantley, J. N.; Bielawski, C. W.; Makarov, D. E. Chemical Reactions Modulated by Mechanical Stress: Extended Bell Theory. *J. Chem. Phys.* **2011**, *135*, 164103.
17. Boulatov, R. Reaction Dynamics in the Formidable Gap. *Pure Appl. Chem.* **2010**, *83*.
18. Ong, M. T.; Leiding, J.; Tao, H.; Virshup, A. M.; Martinez, T. J. First Principles Dynamics and Minimum Energy Pathways for Mechanochemical Ring Opening of Cyclobutene. *J. Am. Chem. Soc.* **2009**, *131*, 6377-6379.
19. Ribas-Arino, J.; Shiga, M.; Marx, D. Understanding Covalent Mechanochemistry. *Angew Chem Int Ed Engl* **2009**, *48*, 4190-4193.
20. Li, J.; Nagamani, C.; Moore, J. S. Polymer Mechanochemistry: From Destructive to Productive. *Acc. Chem. Res.* **2015**, *48*, 2181-2190.
21. Boulatov, R., *Polymer Mechanochemistry*. Springer: Berlin: 2015; Vol. 369.
22. Akbulatov, S.; Boulatov, R. Experimental Polymer Mechanochemistry and Its Interpretational Frameworks. *Chemphyschem* **2017**, *18*, 1422-1450.
23. Boulatov, R. The Challenges and Opportunities of Contemporary Polymer Mechanochemistry. *Chemphyschem* **2017**, *18*, 1419-1421.

24. Anderson, L.; Boulatov, R., Polymer Mechanochemistry: A New Frontier for Physical Organic Chemistry. In *Advances in Physical Organic Chemistry*, Elsevier: 2018; Vol. 52, pp 87-143.
25. De Bo, G. Mechanochemistry of the Mechanical Bond. *Chem. Sci.* **2018**, *9*, 15-21.
26. Bowser, B. H.; Craig, S. L. Empowering Mechanochemistry with Multi-Mechanophore Polymer Architectures. *Poly. Chem.* **2018**, *9*, 3583-3593.
27. Izak-Nau, E.; Campagna, D.; Baumann, C.; Göstl, R. Polymer Mechanochemistry-Enabled Pericyclic Reactions. *Poly. Chem.* **2020**, *11*, 2274-2299.
28. Stratigaki, M.; Gostl, R. Methods for Exerting and Sensing Force in Polymer Materials Using Mechanophores. *Chempluschem* **2020**, *85*, 1-10.
29. Davis, D. A.; Hamilton, A.; Yang, J.; Cremar, L. D.; Van Gough, D.; Potisek, S. L.; Ong, M. T.; Braun, P. V.; Martinez, T. J.; White, S. R.; Moore, J. S.; Sottos, N. R. Force-Induced Activation of Covalent Bonds in Mechanoresponsive Polymeric Materials. *Nature* **2009**, *459*, 68-72.
30. Imato, K.; Irie, A.; Kosuge, T.; Ohishi, T.; Nishihara, M.; Takahara, A.; Otsuka, H. Mechanophores with a Reversible Radical System and Freezing-Induced Mechanochemistry in Polymer Solutions and Gels. *Angew. Chem. Int. Ed.* **2015**, *54*, 6168-6172.
31. Sagara, Y.; Karman, M.; Verde-Sesto, E.; Matsuo, K.; Kim, Y.; Tamaoki, N.; Weder, C. Rotaxanes as Mechanochromic Fluorescent Force Transducers in Polymers. *J. Am. Chem. Soc.* **2018**, *140*, 1584-1587.
32. Filonenko, G. A.; Lugger, J. A. M.; Liu, C.; van Heeswijk, E. P. A.; Hendrix, M.; Weber, M.; Muller, C.; Hensen, E. J. M.; Sijbesma, R. P.; Pidko, E. A. Tracking Local Mechanical Impact in Heterogeneous Polymers with Direct Optical Imaging. *Angew Chem Int Ed Engl* **2018**, *57*, 16385-16390.
33. Robb, M. J.; Kim, T. A.; Halmes, A. J.; White, S. R.; Sottos, N. R.; Moore, J. S. Regioisomer-Specific Mechanochromism of Naphthopyran in Polymeric Materials. *J. Am. Chem. Soc.* **2016**, *138*, 12328-12331.

34. McFadden, M. E.; Robb, M. J. Force-Dependent Multicolor Mechanochromism from a Single Mechanophore. *J. Am. Chem. Soc.* **2019**.
35. Yildiz, D.; Baumann, C.; Mikosch, A.; Kuehne, A. J. C.; Herrmann, A.; Gostl, R. Anti-Stokes Stress Sensing: Mechanochemical Activation of Triplet-Triplet Annihilation Photon Upconversion. *Angew Chem Int Ed Engl* **2019**, *58*, 12919-12923.
36. Zhang, H.; Gao, F.; Cao, X.; Li, Y.; Xu, Y.; Weng, W.; Boulatov, R. Mechanochromism and Mechanical-Force-Triggered Cross-Linking from a Single Reactive Moiety Incorporated into Polymer Chains. *Angew. Chem. Int. Ed.* **2016**, *55*, 3040-3044.
37. Zhang, H.; Zeng, D.; Pan, Y.; Chen, Y.; Ruan, Y.; Xu, Y.; Boulatov, R.; Creton, C.; Weng, W. Mechanochromism and Optical Remodeling of Multi-Network Elastomers Containing Anthracene Dimers. *Chem. Sci.* **2019**.
38. Chen, Y.; Spiering, A. J.; Karthikeyan, S.; Peters, G. W.; Meijer, E. W.; Sijbesma, R. P. Mechanically Induced Chemiluminescence from Polymers Incorporating a 1,2-Dioxetane Unit in the Main Chain. *Nat. Chem.* **2012**, *4*, 559-562.
39. Yang, F.; Yuan, Y.; Sijbesma, R. P.; Chen, Y. Sensitized Mechanoluminescence Design toward Mechanically Induced Intense Red Emission from Transparent Polymer Films. *Macromolecules* **2020**, *53*, 905-912.
40. Piermattei, A.; Karthikeyan, S.; Sijbesma, R. P. Activating Catalysts with Mechanical Force. *Nat. Chem.* **2009**, *1*, 133-137.
41. Michael, P.; Binder, W. H. A Mechanochemically Triggered "Click" Catalyst. *Angew Chem Int Ed Engl* **2015**, *54*, 13918-13922.
42. Larsen, M. B.; Boydston, A. J. "Flex-Activated" Mechanophores: Using Polymer Mechanochemistry to Direct Bond Bending Activation. *J. Am. Chem. Soc.* **2013**, *135*, 8189-8192.
43. Diesendruck, C. E.; Steinberg, B. D.; Sugai, N.; Silberstein, M. N.; Sottos, N. R.; White, S. R.; Braun, P. V.; Moore, J. S. Proton-Coupled Mechanochemical Transduction: A Mechanogenerated Acid. *J. Am. Chem. Soc.* **2012**, *134*, 12446-12449.

44. Hu, X.; Zeng, T.; Husic, C. C.; Robb, M. J. Mechanically Triggered Small Molecule Release from a Masked Furfuryl Carbonate. *J. Am. Chem. Soc.* **2019**, *141*, 15018-15023.
45. Sha, Y.; Zhang, Y. D.; Xu, E. H.; Wang, Z.; Zhu, T. Y.; Craig, S. L.; Tang, C. B. Quantitative and Mechanistic Mechanochemistry in Ferrocene Dissociation. *ACS Macro. Lett.* **2018**, *7*, 1174-1179.
46. Lin, Y.; Kouznetsova, T. B.; Craig, S. L. A Latent Mechanoacid for Time-Stamped Mechanochromism and Chemical Signaling in Polymeric Materials. *J. Am. Chem. Soc.* **2020**, *142*, 99-103.
47. Di Giannantonio, M.; Ayer, M. A.; Verde-Sesto, E.; Lattuada, M.; Weder, C.; Fromm, K. M. Triggered Metal Ion Release and Oxidation: Ferrocene as a Mechanophore in Polymers. *Angew Chem Int Ed Engl* **2018**, *57*, 11445-11450.
48. Kryger, M. J.; Ong, M. T.; Odom, S. A.; Sottos, N. R.; White, S. R.; Martinez, T. J.; Moore, J. S. Masked Cyanoacrylates Unveiled by Mechanical Force. *J. Am. Chem. Soc.* **2010**, *132*, 4558-4559.
49. Robb, M. J.; Moore, J. S. A Retro-Staudinger Cycloaddition: Mechanochemical Cycloelimination of a Beta-Lactam Mechanophore. *J. Am. Chem. Soc.* **2015**, *137*, 10946-10949.
50. Kean, Z. S.; Niu, Z.; Hewage, G. B.; Rheingold, A. L.; Craig, S. L. Stress-Responsive Polymers Containing Cyclobutane Core Mechanophores: Reactivity and Mechanistic Insights. *J. Am. Chem. Soc.* **2013**, *135*, 13598-13604.
51. Wang, J. P.; Piskun, I.; Craig, S. L. Mechanochemical Strengthening of a Multi-Mechanophore Benzocyclobutene Polymer. *ACS Macro. Lett.* **2015**, *4*, 834-837.
52. Lin, Y. J.; Chang, C. C.; Craig, S. L. Mechanical Generation of Isocyanate by Mechanically Induced Retro [2+2] Cycloaddition of a 1,2-Diazetidione Mechanophore. *Organic Chemistry Frontiers* **2019**, *6*, 1052-1057.
53. Zhang, H.; Li, X.; Lin, Y.; Gao, F.; Tang, Z.; Su, P.; Zhang, W.; Xu, Y.; Weng, W.; Boulatov, R. Multi-Modal Mechanophores Based on Cinnamate Dimers. *Nat. Commun.* **2017**, *8*, 1147.

54. Göstl, R.; Sijbesma, R. P.  $\Pi$ -Extended Anthracenes as Sensitive Probes for Mechanical Stress. *Chem. Sci.* **2016**, *7*, 370-375.
55. Akbulatov, S.; Tian, Y.; Huang, Z.; Kucharski, T. J.; Yang, Q. Z.; Boulatov, R. Experimentally Realized Mechanochemistry Distinct from Force-Accelerated Scission of Loaded Bonds. *Science* **2017**, *357*, 299-303.
56. Sha, Y.; Zhang, Y.; Xu, E.; McAlister, C. W.; Zhu, T.; Craig, Stephen L.; Tang, C. Generalizing Metallocene Mechanochemistry to Ruthenocene Mechanophores. *Chem. Sci.* **2019**.
57. Sagara, Y.; Karman, M.; Seki, A.; Pannipara, M.; Tamaoki, N.; Weder, C. Rotaxane-Based Mechanophores Enable Polymers with Mechanically Switchable White Photoluminescence. *ACS Central Science* **2019**.
58. Willis-Fox, N.; Rognin, E.; Aljohani, T. A.; Daly, R. Polymer Mechanochemistry: Manufacturing Is Now a Force to Be Reckoned With. *Chem* **2018**, *4*, 2499-2537.
59. Lenhardt, J. M.; Ong, M. T.; Choe, R.; Evenhuis, C. R.; Martinez, T. J.; Craig, S. L. Trapping a Diradical Transition State by Mechanochemical Polymer Extension. *Science* **2010**, *329*, 1057-1060.
60. Caruso, M. M.; Davis, D. A.; Shen, Q.; Odom, S. A.; Sottos, N. R.; White, S. R.; Moore, J. S. Mechanically-Induced Chemical Changes in Polymeric Materials. *Chem. Rev.* **2009**, *109*, 5755-5798.
61. May, P. A.; Moore, J. S. Polymer Mechanochemistry: Techniques to Generate Molecular Force Via Elongational Flows. *Chem. Soc. Rev.* **2013**, *42*, 7497-7506.
62. Rief, M.; Gautel, M.; Oesterhelt, F.; Fernandez, J. M.; Gaub, H. E. Reversible Unfolding of Individual Titin Immunoglobulin Domains by Afm. *Science* **1997**, *276*, 1109-1112.
63. Smith, S. B.; Cui, Y.; Bustamante, C. Overstretching B-DNA: The Elastic Response of Individual Double-Stranded and Single-Stranded DNA Molecules. *Science* **1996**, *271*, 795-799.

64. Rief, M.; Oesterhelt, F.; Heymann, B.; Gaub, H. E. Single Molecule Force Spectroscopy on Polysaccharides by Atomic Force Microscopy. *Science* **1997**, *275*, 1295-1297.
65. Marszalek, P. E.; Oberhauser, A. F.; Pang, Y. P.; Fernandez, J. M. Polysaccharide Elasticity Governed by Chair-Boat Transitions of the Glucopyranose Ring. *Nature* **1998**, *396*, 661-664.
66. Lavrenova, A.; Balkenende, D. W. R.; Sagara, Y.; Schrettl, S.; Simon, Y. C.; Weder, C. Mechano- and Thermoresponsive Photoluminescent Supramolecular Polymer. *Journal of the American Chemical Society* **2017**, *139*, 4302-4305.
67. Colom, A.; Derivery, E.; Soleimanpour, S.; Tomba, C.; Molin, M. D.; Sakai, N.; González-Gaitán, M.; Matile, S.; Roux, A. A Fluorescent Membrane Tension Probe. *Nature Chemistry* **2018**, *10*, 1118-1125.
68. Kean, Z. S.; Gossweiler, G. R.; Kouznetsova, T. B.; Hewage, G. B.; Craig, S. L. A Coumarin Dimer Probe of Mechanochemical Scission Efficiency in the Sonochemical Activation of Chain-Centered Mechanophore Polymers. *Chem Commun (Camb)* **2015**, *51*, 9157-9160.
69. Zhang, H.; Gao, F.; Cao, X.; Li, Y.; Xu, Y.; Weng, W.; Boulatov, R. Mechanochromism and Mechanical-Force-Triggered Cross-Linking from a Single Reactive Moiety Incorporated into Polymer Chains. *Angew Chem Int Ed Engl* **2016**, *55*, 3040-3044.
70. Verstraeten, F.; Gostl, R.; Sijbesma, R. P. Stress-Induced Colouration and Crosslinking of Polymeric Materials by Mechanochemical Formation of Triphenylimidazolyl Radicals. *Chem Commun (Camb)* **2016**, *52*, 8608-8611.
71. Imato, K.; Irie, A.; Kosuge, T.; Ohishi, T.; Nishihara, M.; Takahara, A.; Otsuka, H. Mechanophores with a Reversible Radical System and Freezing-Induced Mechanochemistry in Polymer Solutions and Gels. *Angew Chem Int Ed Engl* **2015**, *54*, 6168-6172.

72. Imato, K.; Kanehara, T.; Ohishi, T.; Nishihara, M.; Yajima, H.; Ito, M.; Takahara, A.; Otsuka, H. Mechanochromic Dynamic Covalent Elastomers: Quantitative Stress Evaluation and Autonomous Recovery. *ACS Macro. Lett.* **2015**, *4*, 1307-1311.
73. Kosuge, T.; Imato, K.; Goseki, R.; Otsuka, H. Polymer-Inorganic Composites with Dynamic Covalent Mechanochromophore. *Macromolecules* **2016**, *49*, 5903-5911.
74. Chen, Y.; Sijbesma, R. P. Dioxetanes as Mechanoluminescent Probes in Thermoplastic Elastomers. *Macromolecules* **2014**, *47*, 3797-3805.
75. Kean, Z. S.; Hawk, J. L.; Lin, S.; Zhao, X.; Sijbesma, R. P.; Craig, S. L. Increasing the Maximum Achievable Strain of a Covalent Polymer Gel through the Addition of Mechanically Invisible Cross-Links. *Adv. Mater.* **2014**, *26*, 6013-6018.
76. Groote, R.; Jakobs, R. T. M.; Sijbesma, R. P. Mechanocatalysis: Forcing Latent Catalysts into Action. *Polymer Chemistry* **2013**, *4*, 4846.
77. Clough, J. M.; Balan, A.; van Daal, T. L.; Sijbesma, R. P. Probing Force with Mechanobase-Induced Chemiluminescence. *Angew Chem Int Ed Engl* **2016**, *55*, 1445-1449.
78. Larsen, M. B.; Boydston, A. J. Successive Mechanochemical Activation and Small Molecule Release in an Elastomeric Material. *J. Am. Chem. Soc.* **2014**, *136*, 1276-1279.
79. Gossweiler, G. R.; Hewage, G. B.; Soriano, G.; Wang, Q.; Welshofer, G. W.; Zhao, X.; Craig, S. L. Mechanochemical Activation of Covalent Bonds in Polymers with Full and Repeatable Macroscopic Shape Recovery. *ACS Macro Letters* **2014**, *3*, 216-219.
80. Lenhardt, J. M.; Ong, M. T.; Choe, R.; Evenhuis, C. R.; Martinez, T. J.; Craig, S. L. Trapping a Diradical Transition State by Mechanochemical Polymer Extension. *Science* **2010**, *329*, 1057-1060.
81. Lenhardt, J. M.; Ogle, J. W.; Ong, M. T.; Choe, R.; Martinez, T. J.; Craig, S. L. Reactive Cross-Talk between Adjacent Tension-Trapped Transition States. *J. Am. Chem. Soc.* **2011**, *133*, 3222-3225.

82. Klukovich, H. M.; Kouznetsova, T. B.; Kean, Z. S.; Lenhardt, J. M.; Craig, S. L. A Backbone Lever-Arm Effect Enhances Polymer Mechanochemistry. *Nat. Chem.* **2013**, *5*, 110-114.
83. Wang, J.; Kouznetsova, T. B.; Craig, S. L. Reactivity and Mechanism of a Mechanically Activated Anti-Woodward-Hoffmann-Depuy Reaction. *J. Am. Chem. Soc.* **2015**, *137*, 11554-11557.
84. Wang, J.; Kouznetsova, T. B.; Niu, Z.; Ong, M. T.; Klukovich, H. M.; Rheingold, A. L.; Martinez, T. J.; Craig, S. L. Inducing and Quantifying Forbidden Reactivity with Single-Molecule Polymer Mechanochemistry. *Nat. Chem.* **2015**, *7*, 323-327.
85. Wang, J.; Ong, M. T.; Kouznetsova, T. B.; Lenhardt, J. M.; Martinez, T. J.; Craig, S. L. Catch and Release: Orbital Symmetry Guided Reaction Dynamics from a Freed "Tension Trapped Transition State". *J. Org. Chem.* **2015**, *80*, 11773-11778.
86. Wang, J.; Kouznetsova, T. B.; Kean, Z. S.; Fan, L.; Mar, B. D.; Martinez, T. J.; Craig, S. L. A Remote Stereochemical Lever Arm Effect in Polymer Mechanochemistry. *J. Am. Chem. Soc.* **2014**, *136*, 15162-15165.
87. Gossweiler, G. R.; Kouznetsova, T. B.; Craig, S. L. Force-Rate Characterization of Two Spiropyran-Based Molecular Force Probes. *J. Am. Chem. Soc.* **2015**, *137*, 6148-6151.
88. Wang, J.; Kouznetsova, T. B.; Craig, S. L. Single-Molecule Observation of a Mechanically Activated Cis-to-Trans Cyclopropane Isomerization. *J. Am. Chem. Soc.* **2016**, *138*, 10410-10412.
89. Konda, S. S.; Brantley, J. N.; Varghese, B. T.; Wiggins, K. M.; Bielawski, C. W.; Makarov, D. E. Molecular Catch Bonds and the Anti-Hammond Effect in Polymer Mechanochemistry. *J. Am. Chem. Soc.* **2013**, *135*, 12722-12729.
90. Stevenson, R.; De Bo, G. Controlling Reactivity by Geometry in Retro-Diels-Alder Reactions under Tension. *J. Am. Chem. Soc.* **2017**, *139*, 16768-16771.
91. Kida, J.; Imato, K.; Goseki, R.; Aoki, D.; Morimoto, M.; Otsuka, H. The Photoregulation of a Mechanochemical Polymer Scission. *Nat. Commun.* **2018**, *9*, 3504.

92. Robb, M. J.; Kim, T. A.; Halmes, A. J.; White, S. R.; Sottos, N. R.; Moore, J. S. Regioisomer-Specific Mechanochromism of Naphthopyran in Polymeric Materials. *J Am Chem Soc* **2016**.
93. Fang, X.; Zhang, H.; Chen, Y.; Lin, Y.; Xu, Y.; Weng, W. Biomimetic Modular Polymer with Tough and Stress Sensing Properties. *Macromolecules* **2013**, *46*, 6566-6574.
94. Hong, G.; Zhang, H.; Lin, Y.; Chen, Y.; Xu, Y.; Weng, W.; Xia, H. Mechanoresponsive Healable Metallosupramolecular Polymers. *Macromolecules* **2013**, *46*, 8649-8656.
95. Beiermann, B. A.; Davis, D. A.; Kramer, S. L. B.; Moore, J. S.; Sottos, N. R.; White, S. R. Environmental Effects on Mechanochemical Activation of Spiropyran in Linear Pmma. *Journal of Materials Chemistry* **2011**, *21*, 8443.
96. Beiermann, B. A.; Kramer, S. L. B.; Moore, J. S.; White, S. R.; Sottos, N. R. Role of Mechanophore Orientation in Mechanochemical Reactions. *ACS Macro. Lett.* **2012**, *1*, 163-166.
97. Lee, C. K.; Beiermann, B. A.; Silberstein, M. N.; Wang, J.; Moore, J. S.; Sottos, N. R.; Braun, P. V. Exploiting Force Sensitive Spiropyrans as Molecular Level Probes. *Macromolecules* **2013**, *46*, 3746-3752.
98. Beiermann, B. A.; Kramer, S. L. B.; May, P. A.; Moore, J. S.; White, S. R.; Sottos, N. R. The Effect of Polymer Chain Alignment and Relaxation on Force-Induced Chemical Reactions in an Elastomer. *Adv. Funct. Mater.* **2014**, *24*, 1529-1537.
99. Degen, C. M.; May, P. A.; Moore, J. S.; White, S. R.; Sottos, N. R. Time-Dependent Mechanochemical Response of Sp-Cross-Linked Pmma. *Macromolecules* **2013**, *46*, 8917-8921.
100. Grady, M. E.; Beiermann, B. A.; Moore, J. S.; Sottos, N. R. Shockwave Loading of Mechanochemically Active Polymer Coatings. *ACS Appl. Mater. Interfaces* **2014**, *6*, 5350-5355.

101. O'Bryan, G.; Wong, B. M.; McElhanon, J. R. Stress Sensing in Polycaprolactone Films Via an Embedded Photochromic Compound. *ACS Appl. Mater. Interfaces* **2010**, *2*, 1594-1600.
102. Corissa K. Lee; Douglas A. Davis; Scott R. White; Jeffrey S. Moore; Nancy R. Sottos; Braun, P. V. Force-Induced Redistribution of a Chemical Equilibrium. *J. Am. Chem. Soc.* **2010**, *132*, 16107-16111.
103. Chen, H.; Yang, F.; Chen, Q.; Zheng, J. A Novel Design of Multi-Mechanoresponsive and Mechanically Strong Hydrogels. *Adv. Mater.* **2017**, *29*.
104. Li, M.; Liu, W.; Zhu, S. Smart Polyolefins Feeling the Force: Color Changeable Poly(Ethylene-Vinyl Acetate) and Poly(Ethylene-Octene) in Response to Mechanical Force. *Polymer* **2017**, *112*, 219-227.
105. Cho, Y. J.; Lee, S. H.; Bae, J. W.; Kim, S. H.; Keum, S. R.; Yoon, C. M. Synthesis of 7-Hydroxyspiropyran. *Synth. Commun.* **2000**, *30*, 2205-2211.
106. Aishah Hasbullah, S.; Rohadi, A.; Mat Lazim, A.; Nordin, R. Improving the Synthesis of Spiropyran Derivatives Using Microwave Irradiation Method. *Heterocycles* **2014**, *89*.
107. Wang, J.; Kouznetsova, T. B.; Niu, Z.; Rheingold, A. L.; Craig, S. L. Accelerating a Mechanically Driven Anti-Woodward-Hoffmann Ring Opening with a Polymer Lever Arm Effect. *J. Org. Chem.* **2015**, *80*, 11895-11898.
108. Brown, C. L.; Craig, S. L. Molecular Engineering of Mechanophore Activity for Stress-Responsive Polymeric Materials. *Chem. Sci.* **2015**, *6*, 2158-2165.
109. Barbee, M. H.; Kouznetsova, T.; Barrett, S. L.; Gossweiler, G. R.; Lin, Y.; Rastogi, S. K.; Brittain, W. J.; Craig, S. L. Substituent Effects and Mechanism in a Mechanochemical Reaction. *J. Am. Chem. Soc.* **2018**, *140*, 12746-12750.
110. Kim, T. A.; Robb, M. J.; Moore, J. S.; White, S. R.; Sottos, N. R. Mechanical Reactivity of Two Different Spiropyran Mechanophores in Polydimethylsiloxane. *Macromolecules*, submitted.

111. Adhikari, R.; Makarov, D. E. Mechanochemical Kinetics in Elastomeric Polymer Networks: Heterogeneity of Local Forces Results in Nonexponential Kinetics. *J. Phys. Chem. B* **2017**, *121*, 2359-2365.
112. Clough, J. M.; Creton, C.; Craig, S. L.; Sijbesma, R. P. Covalent Bond Scission in the Mullins Effect of a Filled Elastomer: Real-Time Visualization with Mechanoluminescence. *Adv. Funct. Mater.* **2016**, *26*, 9063-9074.
113. Barbee, M. H.; Mondal, K.; Deng, J. Z.; Bharambe, V.; Neumann, T. V.; Adams, J. J.; Boechler, N.; Dickey, M. D.; Craig, S. L. Mechanochromic Stretchable Electronics. *ACS Appl. Mater. Interfaces* **2018**, *10*, 29918-29924.
114. Achard, T. R. J.; Clegg, W.; Harrington, R. W.; North, M. Chiral Salen Ligands Designed to Form Polymetallic Complexes. *Tetrahedron* **2012**, *68*, 133-144.
115. Gossweiler, G. R.; Hewage, G. B.; Soriano, G.; Wang, Q. M.; Welshofer, G. W.; Zhao, X. H.; Craig, S. L. Mechanochemical Activation of Covalent Bonds in Polymers with Full and Repeatable Macroscopic Shape Recovery. *ACS Macro. Lett.* **2014**, *3*, 216-219.
116. Kim, T. A.; Robb, M. J.; Moore, J. S.; White, S. R.; Sottos, N. R. Mechanical Reactivity of Two Different Spiropyran Mechanophores in Polydimethylsiloxane. *Macromolecules* **2018**, *51*, 9177-9183.
117. Lin, Y.; Barbee, M. H.; Chang, C. C.; Craig, S. L. Regiochemical Effects on Mechanophore Activation in Bulk Materials. *J. Am. Chem. Soc.* **2018**, *140*, 15969-15975.
118. Kosuge, T.; Zhu, X.; Lau, V. M.; Aoki, D.; Martinez, T. J.; Moore, J. S.; Otsuka, H. Multicolor Mechanochromism of a Polymer/Silica Composite with Dual Distinct Mechanophores. *J. Am. Chem. Soc.* **2019**, *141*, 1898-1902.
119. Kabb, C. P.; O'Bryan, C. S.; Morley, C. D.; Angelini, T. E.; Sumerlin, B. S. Anthracene-Based Mechanophores for Compression-Activated Fluorescence in Polymeric Networks. *Chem. Sci.* **2019**.
120. Groote, R.; Jakobs, R. T. M.; Sijbesma, R. P. Mechanocatalysis: Forcing Latent Catalysts into Action. *Poly. Chem.* **2013**, *4*, 4846-4859.

121. Wei, K.; Gao, Z.; Liu, H.; Wu, X.; Wang, F.; Xu, H. Mechanical Activation of Platinum–Acetylide Complex for Olefin Hydrosilylation. *ACS Macro. Lett.* **2017**, *6*, 1146-1150.
122. Jakobs, R. T. M.; Ma, S.; Sijbesma, R. P. Mechanocatalytic Polymerization and Cross-Linking in a Polymeric Matrix. *ACS Macro. Lett.* **2013**, *2*, 613-616.
123. Ramirez, A. L.; Kean, Z. S.; Orlicki, J. A.; Champhekar, M.; Elsagr, S. M.; Krause, W. E.; Craig, S. L. Mechanochemical Strengthening of a Synthetic Polymer in Response to Typically Destructive Shear Forces. *Nat. Chem.* **2013**, *5*, 757-761.
124. Yang, Q. Z.; Huang, Z.; Kucharski, T. J.; Khvostichenko, D.; Chen, J.; Boulatov, R. A Molecular Force Probe. *Nat Nanotechnol* **2009**, *4*, 302-306.
125. Timothy J. Kucharski; Qing-Zheng Yang; Yancong Tian; Boulatov, R. Strain-Dependent Acceleration of a Paradigmatic Sn2 Reaction Accurately Predicted by the Force Formalism. *J Phys Chem Lett* **2010**, *1*, 2820–2825.
126. Pill, M. F.; East, A. L. L.; Marx, D.; Beyer, M. K.; Clausen-Schaumann, H. Mechanical Activation Drastically Accelerates Amide Bond Hydrolysis, Matching Enzyme Activity. *Angew Chem Int Ed Engl* **2019**.
127. Chen, Z.; Zhu, X.; Yang, J.; Mercer, J. A. M.; Burns, N. Z.; Martinez, T. J.; Xia, Y. The Cascade Unzipping of Ladderane Reveals Dynamic Effects in Mechanochemistry. *Nat. Chem.* **2020**, *12*, 302-309.
128. Klukovich, H. M.; Kean, Z. S.; Black Ramirez, A. L.; Lenhardt, J. M.; Lin, J.; Hu, X.; Craig, S. L. Tension Trapping of Carbonyl Ylides Facilitated by a Change in Polymer Backbone. *J. Am. Chem. Soc.* **2012**, *134*, 9577-9580.
129. Ribas-Arino, J.; Shiga, M.; Marx, D. Unravelling the Mechanism of Force-Induced Ring-Opening of Benzocyclobutenes. *Chemistry - A European Journal* **2009**, *15*, 13331-13335.
130. Woodward, R. B.; Hoffmann, R. The Conservation of Orbital Symmetry. *Angewandte Chemie International Edition in English* **1969**, *8*, 781-853.

131. Brauman, J. I.; Archie, W. C. Energies of Alternate Electrocyclic Pathways. Pyrolysis of Cis-3,4-Dimethylcyclobutene. *J. Am. Chem. Soc.* **1972**, *94*, 4262-4265.
132. DePuy, C. H. Cyclopropanols. *Acc. Chem. Res.* **2002**, *1*, 33-41.
133. Parham, W. E.; Yong, K. S. Steric and Electronic Effects in the Solvolysis of Cis- and Trans- Mono- and Dihalocyclopropanes. *J. Org. Chem.* **1970**, *35*, 683-685.
134. Baird, M. S.; Reese, C. B. Exo- and Endo-6-Chlorobicyclo[3.1.0]Hexanes. *Tetrahedron Lett.* **1967**, *8*, 1379-1382.
135. Beyer, M. K. The Mechanical Strength of a Covalent Bond Calculated by Density Functional Theory. *J. Chem. Phys.* **2000**, *112*, 7307-7312.
136. Baird, M. S.; Reese, C. B. Thermal Rearrangement of 9,9-Dibromobicyclo[6,1,0]Non-4-Ene and Related Compounds. *J Chem Soc C* **1969**, 1808-&.
137. Klukovich, H. M.; Kean, Z. S.; Iacono, S. T.; Craig, S. L. Mechanically Induced Scission and Subsequent Thermal Remending of Perfluorocyclobutane Polymers. *J. Am. Chem. Soc.* **2011**, *133*, 17882-17888.
138. Wu D; Lenhardt, J. M.; Black, A. L.; Akhremitchev, B. B.; Craig, S. L. Molecular Stress Relief through a Force-Induced Irreversible Extension in Polymer Contour Length. *J. Am. Chem. Soc.* **2010**, *132*, 15936–15938.
139. Wang, S.; Panyukov, S.; Rubinstein, M.; Craig, S. L. Quantitative Adjustment to the Molecular Energy Parameter in the Lake–Thomas Theory of Polymer Fracture Energy. *Macromolecules* **2019**, *52*, 2772-2777.
140. Lake, G. J.; Thomas, A. G. The Strength of Highly Elastic Materials. *Proc. R. Soc. London, Ser. A: Math. Phys. Sci.* **1967**, *300*, 108–119.
141. Bertrand, O.; Gohy, J.-F. Photo-Responsive Polymers: Synthesis and Applications. *Poly. Chem.* **2017**, *8*, 52-73.

142. Roy, D.; Brooks, W. L.; Sumerlin, B. S. New Directions in Thermoresponsive Polymers. *Chem. Soc. Rev.* **2013**, *42*, 7214-7243.
143. Kocak, G.; Tuncer, C.; Bütün, V. Ph-Responsive Polymers. *Poly. Chem.* **2017**, *8*, 144-176.
144. Stuart, M. A.; Huck, W. T.; Genzer, J.; Muller, M.; Ober, C.; Stamm, M.; Sukhorukov, G. B.; Szleifer, I.; Tsukruk, V. V.; Urban, M.; Winnik, F.; Zauscher, S.; Luzinov, I.; Minko, S. Emerging Applications of Stimuli-Responsive Polymer Materials. *Nat. Mater.* **2010**, *9*, 101-113.
145. Hu, J.; Zhang, G.; Liu, S. Enzyme-Responsive Polymeric Assemblies, Nanoparticles and Hydrogels. *Chem. Soc. Rev.* **2012**, *41*, 5933-5949.
146. Wei, M.; Gao, Y.; Li, X.; Serpe, M. J. Stimuli-Responsive Polymers and Their Applications. *Poly. Chem.* **2017**, *8*, 127-143.
147. Liu, L.; Rui, L.; Gao, Y.; Zhang, W. Self-Assembly and Disassembly of a Redox-Responsive Ferrocene-Containing Amphiphilic Block Copolymer for Controlled Release. *Poly. Chem.* **2015**, *6*, 1817-1829.
148. Nakahata, M.; Takashima, Y.; Yamaguchi, H.; Harada, A. Redox-Responsive Self-Healing Materials Formed from Host-Guest Polymers. *Nat. Commun.* **2011**, *2*, 511.
149. Nakahata, M.; Takashima, Y.; Hashidzume, A.; Harada, A. Redox-Generated Mechanical Motion of a Supramolecular Polymeric Actuator Based on Host-Guest Interactions. *Angew Chem Int Ed Engl* **2013**, *52*, 5731-5735.
150. Huo, M.; Yuan, J.; Tao, L.; Wei, Y. Redox-Responsive Polymers for Drug Delivery: From Molecular Design to Applications. *Polym. Chem.* **2014**, *5*, 1519-1528.
151. Song, C.-C.; Du, F.-S.; Li, Z.-C. Oxidation-Responsive Polymers for Biomedical Applications. *J. Mater. Chem. B* **2014**, *2*, 3413-3426.

152. Zhang, X.; Han, L.; Liu, M.; Wang, K.; Tao, L.; Wan, Q.; Wei, Y. Recent Progress and Advances in Redox-Responsive Polymers as Controlled Delivery Nanoplatfoms. *Materials Chemistry Frontiers* **2017**, *1*, 807-822.
153. Wu, J.; Wang, L.; Yu, H.; Zain ul, A.; Khan, R. U.; Haroon, M. Ferrocene-Based Redox-Responsive Polymer Gels: Synthesis, Structures and Applications. *J. Organomet. Chem.* **2017**, *828*, 38-51.
154. Xia, J.; Li, T.; Lu, C.; Xu, H. Selenium-Containing Polymers: Perspectives toward Diverse Applications in Both Adaptive and Biomedical Materials. *Macromolecules* **2018**, *51*, 7435-7455.
155. Wang, L.; Zhu, K.; Cao, W.; Sun, C.; Lu, C.; Xu, H. Ros-Triggered Degradation of Selenide-Containing Polymers Based on Selenoxide Elimination. *Poly. Chem.* **2019**, *10*, 2039-2046.
156. Sarapas, J. M.; Tew, G. N. Thiol-Ene Step-Growth as a Versatile Route to Functional Polymers. *Angew Chem Int Ed Engl* **2016**, *55*, 15860-15863.
157. Nair, D. P.; Podgórski, M.; Chatani, S.; Gong, T.; Xi, W.; Fenoli, C. R.; Bowman, C. N. The Thiol-Michael Addition Click Reaction: A Powerful and Widely Used Tool in Materials Chemistry. *Chem. Mater.* **2013**, *26*, 724-744.
158. Kilcher, G.; Duckham, C.; Tirelli, N. Emulsion Macromonomer Cross-Linking. A Preparative Method for Oxidation-Responsive Nanoparticles with a Controlled Network Structure. *Langmuir* **2007**, *23*, 12309-12317.
159. Khutoryanskiy, V. V.; Tirelli, N. Oxidation-Responsiveness of Nanomaterials for Targeting Inflammatory Reactions. *Pure Appl. Chem.* **2008**, *80*, 1703-1718.
160. Wu, W.-X.; Yang, X.-L.; Liu, B.-Y.; Deng, Q.-F.; Xun, M.-M.; Wang, N.; Yu, X.-Q. Lipase-Catalyzed Synthesis of Oxidation-Responsive Poly(Ethylene Glycol)-B-Poly(B-Thioether Ester) Amphiphilic Block Copolymers. *RSC Advances* **2016**, *6*, 11870-11879.
161. Herzberger, J.; Fischer, K.; Leibig, D.; Bros, M.; Thiermann, R.; Frey, H. Oxidation-Responsive and "Clickable" Poly(Ethylene Glycol) Via Copolymerization of 2-(Methylthio)Ethyl Glycidyl Ether. *J. Am. Chem. Soc.* **2016**, *138*, 9212-9223.

162. Napoli, A.; Valentini, M.; Tirelli, N.; Muller, M.; Hubbell, J. A. Oxidation-Responsive Polymeric Vesicles. *Nat. Mater.* **2004**, *3*, 183-189.
163. Fu, X.; Ma, Y.; Shen, Y.; Fu, W.; Li, Z. Oxidation-Responsive Oegylated Poly-L-Cysteine and Solution Properties Studies. *Biomacromolecules* **2014**, *15*, 1055-1061.
164. Jeanmaire, D.; Laliturai, J.; Almalik, A.; Carampin, P.; Richard, d. A.; Lallana, E.; Evans, R.; Winpenny, R. E. P.; Tirelli, N. Chemical Specificity in Redox-Responsive Materials: The Diverse Effects of Different Reactive Oxygen Species (Ros) on Polysulfide Nanoparticles. *Poly. Chem.* **2014**, *5*.
165. El-Mohtadi, F.; d'Arcy, R.; Tirelli, N. Oxidation-Responsive Materials: Biological Rationale, State of the Art, Multiple Responsiveness, and Open Issues. *Macromol. Rapid Commun.* **2019**, *40*, e1800699.
166. Podgórski, M.; Wang, C.; Yuan, Y.; Konetski, D.; Smalyukh, I.; Bowman, C. N. Pristine Polysulfone Networks as a Class of Polysulfide-Derived High-Performance Functional Materials. *Chem. Mater.* **2016**, *28*, 5102-5109.
167. Sarapas, J. M.; Tew, G. N. Poly(Ether–Thioethers) by Thiol–Ene Click and Their Oxidized Analogues as Lithium Polymer Electrolytes. *Macromolecules* **2016**, *49*, 1154-1162.
168. d'Arcy, R.; Tirelli, N. Fishing for Fire: Strategies for Biological Targeting and Criteria for Material Design in Anti-Inflammatory Therapies. *Polym. Adv. Technol.* **2014**, *25*, 478-498.
169. Benson, S. W. Thermochemistry and Kinetics of Sulfur-Containing Molecules and Radicals. *Chem. Rev.* **1978**, *78*, 23-35.
170. Lee, B.; Niu, Z.; Wang, J.; Slobodnick, C.; Craig, S. L. Relative Mechanical Strengths of Weak Bonds in Sonochemical Polymer Mechanochemistry. *J. Am. Chem. Soc.* **2015**, *137*, 10826-10832.
171. Lenhardt, J. M.; Ramirez, A. L. B.; Lee, B.; Kouznetsova, T. B.; Craig, S. L. Mechanistic Insights into the Sonochemical Activation of Multimechanophore Cyclopropanated Polybutadiene Polymers. *Macromolecules* **2015**, *48*, 6396-6403.

172. Lin, Y.; Zhang, Y.; Wang, Z.; Craig, S. L. Dynamic Memory Effects in the Mechanochemistry of Cyclic Polymers. *J. Am. Chem. Soc.* **2019**, *141*, 10943-10947.
173. Wang, Z.; Craig, S. L. Stereochemical Effects on the Mechanochemical Scission of Furan-Maleimide Diels-Alder Adducts. *Chem Commun (Camb)* **2019**, *55*, 12263-12266.
174. Kim, S. S.; Nehru, K.; Kim, S. S.; Kim, D. W.; Jung, H. C. A Mild and Highly Efficient Oxidation of Sulfides to Sulfoxides with Periodic Acid Catalyzed by FeCl<sub>3</sub>. *Synthesis-Stuttgart* **2002**, 2484-2486.
175. Levy, A.; Goldstein, H.; Brenman, D.; Diesendruck, C. E. Effect of Intramolecular Crosslinker Properties on the Mechanochemical Fragmentation of Covalently Folded Polymers. *J. Polym. Sci.* **2020**.
176. Kean, Z. S.; Black Ramirez, A. L.; Craig, S. L. High Mechanophore Content Polyester-Acrylate ABA Block Copolymers: Synthesis and Sonochemical Activation. *J Polym Sci B Polym Phys* **2012**, *50*, 3481-3484.
177. Moore, J. S.; Stupp, S. I. Room-Temperature Polyesterification. *Macromolecules* **1990**, *23*, 65-70.
178. Kakarla, R.; Dulina, R. G.; Hatzenbuehler, N. T.; Hui, Y. W.; Sofia, M. J. Simple and Efficient Method for the Oxidation of Sulfides to Sulfoxides: Application to the Preparation of Glycosyl Sulfoxides. *J. Org. Chem.* **1996**, *61*, 8347-8349.
179. Brown, C. L.; Craig, S. L. Molecular Engineering of Mechanophore Activity for Stress-Responsive Polymeric Materials. *Chem. Sci.* **2015**, *6*, 2158-2165.
180. Qiu, W. L.; Gurr, P. A.; da Silva, G.; Qiao, G. G. Insights into the Mechanochromism of Spiropyran Elastomers. *Poly. Chem.* **2019**, *10*, 1650-1659.
181. Kryger, M. J.; Munaretto, A. M.; Moore, J. S. Structure-Mechanochemical Activity Relationships for Cyclobutane Mechanophores. *J. Am. Chem. Soc.* **2011**, *133*, 18992-18998.
182. Zhang, M.; De Bo, G. Impact of a Mechanical Bond on the Activation of a Mechanophore. *J. Am. Chem. Soc.* **2018**, *140*, 12724-12727.

183. Lee, B.; Niu, Z.; Craig, S. L. The Mechanical Strength of a Mechanical Bond: Sonochemical Polymer Mechanochemistry of Poly(Catenane) Copolymers. *Angew. Chem. Int. Ed.* **2016**, *55*, 13086-13089.
184. Huang, W.; Wu, X.; Gao, X.; Yu, Y.; Lei, H.; Zhu, Z.; Shi, Y.; Chen, Y.; Qin, M.; Wang, W.; Cao, Y. Maleimide–Thiol Adducts Stabilized through Stretching. *Nature Chemistry* **2019**, *11*, 310-319.
185. Church, D. C.; Peterson, G. I.; Boydston, A. J. Comparison of Mechanochemical Chain Scission Rates for Linear Versus Three-Arm Star Polymers in Strong Acoustic Fields. *ACS Macro. Lett.* **2014**, *3*, 648-651.
186. Li, Y.; Niu, Z.; Burdyńska, J.; Nese, A.; Zhou, Y.; Kean, Z. S.; Dobrynin, A. V.; Matyjaszewski, K.; Craig, S. L.; Sheiko, S. S. Sonication-Induced Scission of Molecular Bottlebrushes: Implications of the “Hairy” Architecture. *Polymer* **2016**, *84*, 178-184.
187. Wang, L.-J.; Zhou, X.-J.; Zhang, X.-H.; Du, B.-Y. Enhanced Mechanophore Activation within Micelles. *Macromolecules* **2015**, *49*, 98-104.
188. Li, H.; Göstl, R.; Delgove, M.; Sweeck, J.; Zhang, Q.; Sijbesma, R. P.; Heuts, J. P. A. Promoting Mechanochemistry of Covalent Bonds by Noncovalent Micellar Aggregation. *ACS Macro. Lett.* **2016**, 995-998.
189. Levy, A.; Wang, F.; Lang, A.; Galant, O.; Diesendruck, C. E. Intramolecular Cross-Linking: Addressing Mechanochemistry with a Bioinspired Approach. *Angew Chem Int Ed Engl* **2017**, *56*, 6431-6434.
190. Peterson, G. I.; Bang, K. T.; Choi, T. L. Mechanochemical Degradation of Denpols: Synthesis and Ultrasound-Induced Chain Scission of Polyphenylene-Based Dendronized Polymers. *J. Am. Chem. Soc.* **2018**, *140*, 8599-8608.
191. Zhang, H.; Lin, Y.; Xu, Y.; Weng, W. Mechanochemistry of Topological Complex Polymer Systems. *Top. Curr. Chem.* **2015**, *369*, 135-207.
192. Diesendruck, C. E.; Peterson, G. I.; Kulik, H. J.; Kaitz, J. A.; Mar, B. D.; May, P. A.; White, S. R.; Martinez, T. J.; Boydston, A. J.; Moore, J. S. Mechanically Triggered

Heterolytic Unzipping of a Low-Ceiling-Temperature Polymer. *Nat. Chem.* **2014**, *6*, 623-628.

193. Li, Y.; Hsiao, K.-W.; Brockman, C. A.; Yates, D. Y.; Robertson-Anderson, R. M.; Kornfield, J. A.; San Francisco, M. J.; Schroeder, C. M.; McKenna, G. B. When Ends Meet: Circular DNA Stretches Differently in Elongational Flows. *Macromolecules* **2015**, *48*, 5997-6001.

194. Laurent, B. A.; Grayson, S. M. Synthetic Approaches for the Preparation of Cyclic Polymers. *Chem. Soc. Rev.* **2009**, *38*, 2202-2213.

195. Zhu, Y.; Hosmane, N. S. Advanced Developments in Cyclic Polymers: Synthesis, Applications, and Perspectives. *ChemistryOpen* **2015**, *4*, 408-417.

196. Bielawski, C. W.; Benitez, D.; Grubbs, R. H. An "Endless" Route to Cyclic Polymers. *Science* **2002**, *297*, 2041-2044.

197. Bielawski, C. W.; Benitez, D.; Grubbs, R. H. Synthesis of Cyclic Polybutadiene Via Ring-Opening Metathesis Polymerization: The Importance of Removing Trace Linear Contaminants. *J. Am. Chem. Soc.* **2003**, *125*, 8424-8425.

198. Zhang, K.; Tew, G. N. Cyclic Polymers as a Building Block for Cyclic Brush Polymers and Gels. *React. Funct. Polym.* **2014**, *80*, 40-47.

199. Brown, H. A.; Waymouth, R. M. Zwitterionic Ring-Opening Polymerization for the Synthesis of High Molecular Weight Cyclic Polymers. *Acc. Chem. Res.* **2013**, *46*, 2585-2596.

200. Boydston, A. J.; Xia, Y.; Kornfield, J. A.; Gorodetskaya, I. A.; Grubbs, R. H. Cyclic Ruthenium-Alkylidene Catalysts for Ring-Expansion Metathesis Polymerization. *J. Am. Chem. Soc.* **2008**, *130*, 12775-12782.

201. Xia, Y.; Boydston, A. J.; Yao, Y.; Kornfield, J. A.; Gorodetskaya, I. A.; Spiess, H. W.; Grubbs, R. H. Ring-Expansion Metathesis Polymerization: Catalyst-Dependent Polymerization Profiles. *J. Am. Chem. Soc.* **2009**, *131*, 2670-2677.

202. Sutthasupa, S.; Shiotsuki, M.; Sanda, F. Recent Advances in Ring-Opening Metathesis Polymerization and Application to Synthesis of Functional Materials. *Polym. J.* **2010**, *42*, 905-915.
203. Schroeder, C. M.; Babcock, H. P.; Shaqfeh, E. S.; Chu, S. Observation of Polymer Conformation Hysteresis in Extensional Flow. *Science* **2003**, *301*, 1515-1519.
204. Black Ramirez, A. L.; Ogle, J. W.; Schmitt, A. L.; Lenhardt, J. M.; Cashion, M. P.; Mahanthappa, M. K.; Craig, S. L. Microstructure of Copolymers Formed by the Reagentless, Mechanochemical Remodeling of Homopolymers Via Pulsed Ultrasound. *ACS Macro. Lett.* **2011**, *1*, 23-27.
205. Perkins, T. T.; Smith, D. E.; Chu, S. Single Polymer Dynamics in an Elongational Flow. *Science* **1997**, *276*, 2016-2021.
206. Smith, D. E.; Chu, S. Response of Flexible Polymers to a Sudden Elongational Flow. *Science* **1998**, *281*, 1335-1340.
207. Lang, P. S.; Obermayer, B.; Frey, E. Dynamics of a Semiflexible Polymer or Polymer Ring in Shear Flow. *Phys Rev E Stat Nonlin Soft Matter Phys* **2014**, *89*, 022606.
208. Chen, W.; Chen, J.; Liu, L.; Xu, X.; An, L. Effects of Chain Stiffness on Conformational and Dynamical Properties of Individual Ring Polymers in Shear Flow. *Macromolecules* **2013**, *46*, 7542-7549.
209. Chen, W.; Chen, J.; An, L. Tumbling and Tank-Treading Dynamics of Individual Ring Polymers in Shear Flow. *Soft Matter* **2013**, *9*.
210. Hernández Cifre, J. G.; Pamies, R.; López Martínez, M. C.; García de la Torre, J. Steady-State Behavior of Ring Polymers in Dilute Flowing Solutions Via Brownian Dynamics. *Polymer* **2005**, *46*, 267-274.
211. Furstner, A.; Ackermann, L.; Gabor, B.; Goddard, R.; Lehmann, C. W.; Mynott, R.; Stelzer, F.; Thiel, O. R. Comparative Investigation of Ruthenium-Based Metathesis Catalysts Bearing N-Heterocyclic Carbene (Nhc) Ligands. *Chemistry* **2001**, *7*, 3236-3253.

212. Lee, D. H.; Kim, J. H.; Jun, B. H.; Kang, H.; Park, J.; Lee, Y. S. Macroporous Polystyrene-Supported Palladium Catalyst Containing a Bulky N-Heterocyclic Carbene Ligand for Suzuki Reaction of Aryl Chlorides. *Org. Lett.* **2008**, *10*, 1609-1612.
213. Song, Q.-W.; Yu, B.; Liu, A.-H.; He, Y.; Yang, Z.-Z.; Diao, Z.-F.; Song, Q.-C.; Li, X.-D.; He, L.-N. Peg400-Enhanced Synthesis of Gem-Dichloroaziridines and Gem-Dichlorocyclopropanes Via in Situ Generated Dichlorocarbene. *RSC Advances* **2013**, *3*, 19009-19014.
214. Ishizuki, K.; Aoki, D.; Goseki, R.; Otsuka, H. Multicolor Mechanochromic Polymer Blends That Can Discriminate between Stretching and Grinding. *ACS Macro. Lett.* **2018**, *7*, 556-560.
215. Celestine, A.-D. N.; Beiermann, B. A.; May, P. A.; Moore, J. S.; Sottos, N. R.; White, S. R. Fracture-Induced Activation in Mechanophore-Linked, Rubber Toughened Pmma. *Polymer* **2014**, *55*, 4164-4171.
216. Zhang, H.; Chen, Y. J.; Lin, Y. J.; Fang, X. L.; Xu, Y. Z.; Ruan, Y. H.; Weng, W. G. Spiropyran as a Mechanochromic Probe in Dual Cross-Linked Elastomers. *Macromolecules* **2014**, *47*, 6783-6790.
217. Clough, J. M.; Balan, A.; van Daal, T. L.; Sijbesma, R. P. Probing Force with Mechanobase-Induced Chemiluminescence. *Angew. Chem. Int. Ed.* **2016**, *55*, 1445-1449.
218. Saunders, J. H.; Slocombe, R. J. The Chemistry of the Organic Isocyanates. *Chem. Rev.* **1948**, *43*, 203-218.
219. Ozaki, S. Recent Advances in Isocyanate Chemistry. *Chem. Rev.* **1972**, *72*, 457-496.
220. Delebecq, E.; Pascault, J. P.; Boutevin, B.; Ganachaud, F. On the Versatility of Urethane/Urea Bonds: Reversibility, Blocked Isocyanate, and Non-Isocyanate Polyurethane. *Chem. Rev.* **2013**, *113*, 80-118.
221. R. G. Arnold; J. A. Nelson; Verbanc, J. J. Recent Advances in Isocyanate Chemistry. *Chem. Rev.* **1957**, *57*, 47-76.

222. Panda, S. S.; Panda, B. P.; Nayak, S. K.; Mohanty, S. A Review on Waterborne Thermosetting Polyurethane Coatings Based on Castor Oil: Synthesis, Characterization, and Application. *Polymer-Plastics Technology and Engineering* **2018**, *57*, 500-522.
223. A. H. Cook; Jones, D. G. Cis-Azo-Compounds. Part Iv. Some Reactions with Diphenylketene. *J. Chem. Soc.* **1941**, *0*, 184-187.
224. Hall, J. H.; Kellogg, R. Synthesis and Thermal Stability of 1,2-Diazetidiones. Reaction of Diphenylketene with Substituted Azobenzenes. *J. Org. Chem.* **1966**, *31*, 1079-1082.
225. Schweizer, E. E.; Evans, S. Cyclization of Conjugated Azines. Synthesis and Thermal Rearrangements of L-Oxo-3,4-Diaza-2,4,6,7-Octatetraenes (Allenyl Azines). *J. Org. Chem.* **1978**, *43*, 4328-4334.
226. Casassa, E. F. Degradation of High Polymers. *J. Polym. Sci.* **1949**, *4*, 405-407.
227. Jellinek, H. H. G. Degradation of High Polymers. *J. Polym. Sci.* **1950**, *5*, 264-265.
228. Haward, R. N. Degradation of Ethyl Cellulose in Solution. *J. Polym. Sci.* **1950**, *5*, 635-636.
229. Sato, T.; Nalepa, D. E. Shear Degradation of Cellulose Derivatives. *J. Appl. Polym. Sci.* **1978**, *22*, 865-867.
230. Malhotra, S. L. Ultrasonic Solution Degradations of Poly(Alkyl Methacrylates). *Journal of Macromolecular Science: Part A - Chemistry* **1986**, *23*, 729-748.
231. Florea, M. New Use of Size-Exclusion Chromatography in Kinetics of Mechanical Degradation of Polymers in Solution. *J. Appl. Polym. Sci.* **1993**, *50*, 2039-2045.
232. Li, S. H.; Zhou, Y. F.; Yu, C. W.; Chen, F. R.; Xu, J. G. Switching the Ligand-Exchange Reactivities of Chloro-Bridged Cyclopalladated Azobenzenes for the Colorimetric Sensing of Thiocyanate. *New J. Chem.* **2009**, *33*, 1462-1465.

233. Akiyama\*, H.; Tamaoki\*, N. Synthesis and Photoinduced Phase Transitions of Poly(N-Isopropylacrylamide) Derivative Functionalized with Terminal Azobenzene Units. *Macromolecules* **2007**, *40*, 5129-5132.
234. Nikitas, P.; Pappa-Louisi, A.; Papageorgiou, A. On the Equations Describing Chromatographic Peaks and the Problem of the Deconvolution of Overlapped Peaks. *J. Chromatogr. A* **2001**, *912*, 13-29.
235. Lee, S. M.; Frechet, J. M. J.; Willson, C. G. Photo-Cross-Linking of Poly(4-Hydroxystyrene) Via Electrophilic Aromatic-Substitution - Use of Polyfunctional Benzylic Alcohols in the Design of Chemically Amplified Resist Materials with Tunable Sensitivities. *Macromolecules* **1994**, *27*, 5154-5159.
236. Shirai, M.; Morishita, S.; Okamura, H.; Tsunooka, M. Photo-Cross-Linkable Polymers with Thermally Degradable Property. *Chem. Mater.* **2002**, *14*, 334-340.
237. Fu, C.; Xu, J.; Boyer, C. Photoacid-Mediated Ring Opening Polymerization Driven by Visible Light. *Chem Commun (Camb)* **2016**, *52*, 7126-7129.
238. Binauld, S.; Stenzel, M. H. Acid-Degradable Polymers for Drug Delivery: A Decade of Innovation. *Chem Commun (Camb)* **2013**, *49*, 2082-2102.
239. Miller, K. A.; Morado, E. G.; Samanta, S. R.; Walker, B. A.; Nelson, A. Z.; Sen, S.; Tran, D. T.; Whitaker, D. J.; Ewoldt, R. H.; Braun, P. V.; Zimmerman, S. C. Acid-Triggered, Acid-Generating, and Self-Amplifying Degradable Polymers. *J. Am. Chem. Soc.* **2019**, *141*, 2838-2842.
240. Lee, S. Y.; Lee, Y.; Kim, J. E.; Park, T. G.; Ahn, C.-H. A Novel Ph-Sensitive Peg-Ppg-Peg Copolymer Displaying a Closed-Loop Sol-Gel-Sol Transition. *J. Mater. Chem.* **2009**, *19*, 8198-8201.
241. Nagamani, C.; Liu, H.; Moore, J. S. Mechanogeneration of Acid from Oxime Sulfonates. *J. Am. Chem. Soc.* **2016**, *138*, 2540-2543.
242. Zivic, N.; Kuroishi, P. K.; Dumur, F.; Gigmès, D.; Dove, A. P.; Sardon, H. Recent Advances and Challenges in the Design of Organic Photoacid and Photobase Generators for Polymerizations. *Angew Chem Int Ed Engl* **2019**, *58*, 10410-10422.

243. Schweizer, E. E.; Parham, W. E. Oxepines. I. Preparation of 2,3-Dihydroöxepine and 2,3-Dihydro-6-Chloroöxepine. *J. Am. Chem. Soc.* **1960**, *82*, 4085-4087.
244. Parham, W. E.; Soeder, R. W.; Dodson, R. M. A Convenient Synthesis of 3,5-Cycloheptadienone. *J. Am. Chem. Soc.* **1962**, *84*, 1755-1756.
245. Anderson, J. C.; Lindsay, D. G.; Reese, C. B. The Reaction between 2,3-Dihydrofuran and Dihalocarbenes: An Attempted 2h-Pyran Synthesis. *Tetrahedron* **1964**, *20*, 2091-2096.
246. Parham, W. E.; Soeder, R. W.; Throckmorton, J. R.; Kuncl, K.; Dodson, R. M. Reactions of Enol Ethers with Carbenes. V. Rearrangements of Dihalocyclopropanes Derived from Six-, Seven-, and Eight-Membered Cyclic Enol Ethers. *J. Am. Chem. Soc.* **1965**, *87*, 321-328.
247. Parham, W. E.; Parham, F. M.; Dooley, J. F.; Meilahn, M. K. Reaction of Dichlorocarbene with Enol Ethers. IX. Ethoxycycloheptadiene. *J. Org. Chem.* **1968**, *33*, 3651-3653.
248. McElvain, S. M.; Weyna, P. L. Ketene Acetals. Xxxvii. Cyclopropanone Acetals from Ketene Acetals and Carbenes. *J. Am. Chem. Soc.* **1959**, *81*, 2579-2588.
249. Zhang, J. F.; Zhou, Y.; Yoon, J.; Kim, J. S. Recent Progress in Fluorescent and Colorimetric Chemosensors for Detection of Precious Metal Ions (Silver, Gold and Platinum Ions). *Chem. Soc. Rev.* **2011**, *40*, 3416-3429.
250. Tracey, M. P.; Pham, D.; Koide, K. Fluorometric Imaging Methods for Palladium and Platinum and the Use of Palladium for Imaging Biomolecules. *Chem. Soc. Rev.* **2015**, *44*, 4769-4791.
251. Czaplyski, W. L.; Purnell, G. E.; Roberts, C. A.; Allred, R. M.; Harbron, E. J. Substituent Effects on the Turn-on Kinetics of Rhodamine-Based Fluorescent Ph Probes. *Org. Biomol. Chem.* **2014**, *12*, 526-533.
252. Lee, M. K.; Rai, P.; Williams, J.; Twieg, R. J.; Moerner, W. E. Small-Molecule Labeling of Live Cell Surfaces for Three-Dimensional Super-Resolution Microscopy. *J. Am. Chem. Soc.* **2014**, *136*, 14003-14006.

253. Shin, J. Y.; Abbott, N. L. Using Light to Control Dynamic Surface Tensions of Aqueous Solutions of Water Soluble Surfactants. *Langmuir* **1999**, *15*, 4404-4410.
254. Delorme, N.; Bardeau, J. F.; Bulou, A.; Poncin-Epaillard, F. Azobenzene-Containing Monolayer with Photoswitchable Wettability. *Langmuir* **2005**, *21*, 12278-12282.
255. Yang, D.; Piech, M.; Bell, N. S.; Gust, D.; Vail, S.; Garcia, A. A.; Schneider, J.; Park, C. D.; Hayes, M. A.; Picraux, S. T. Photon Control of Liquid Motion on Reversibly Photoresponsive Surfaces. *Langmuir* **2007**, *23*, 10864-10872.
256. Pei, X.; Fernandes, A.; Mathy, B.; Laloyaux, X.; Nysten, B.; Riant, O.; Jonas, A. M. Correlation between the Structure and Wettability of Photoswitchable Hydrophilic Azobenzene Monolayers on Silicon. *Langmuir* **2011**, *27*, 9403-9412.
257. Siewierski, L. M.; Brittain, W. J.; Petrash, S.; Foster, M. D. Photoresponsive Monolayers Containing in-Chain Azobenzene. *Langmuir* **1996**, *12*, 5838-5844.
258. Merino, E.; Ribagorda, M. Control over Molecular Motion Using the Cis-Trans Photoisomerization of the Azo Group. *Beilstein J. Org. Chem.* **2012**, *8*, 1071-1090.
259. Ichimura, K. Photoalignment of Liquid-Crystal Systems. *Chem. Rev.* **2000**, *100*, 1847-1874.
260. Ikeda, T. Photomodulation of Liquid Crystal Orientations for Photonic Applications. *J. Mater. Chem.* **2003**, *13*, 2037-2057.
261. Shimoboji, T.; Larenas, E.; Fowler, T.; Kulkarni, S.; Hoffman, A. S.; Stayton, P. S. Photoresponsive Polymer-Enzyme Switches. *Proc Natl Acad Sci U S A* **2002**, *99*, 16592-16596.
262. Kamiya, Y.; Asanuma, H. Light-Driven DNA Nanomachine with a Photoresponsive Molecular Engine. *Acc. Chem. Res.* **2014**, *47*, 1663-1672.
263. Oh, S.-K.; Nakagawa, M.; Ichimura, K. Photocontrol of Liquid Motion on an Azobenzene Monolayer. *J. Mater. Chem.* **2002**, *12*, 2262-2269.

264. Yu, Y.; Nakano, M.; Ikeda, T. Photomechanics: Directed Bending of a Polymer Film by Light. *Nature* **2003**, *425*, 145.
265. White, T. J.; Tabiryany, N. V.; Serak, S. V.; Hrozhyk, U. A.; Tondiglia, V. P.; Koerner, H.; Vaia, R. A.; Bunning, T. J. A High Frequency Photodriven Polymer Oscillator. *Soft Matter* **2008**, *4*, 1796-1798.
266. Yamada, M.; Kondo, M.; Mamiya, J.; Yu, Y.; Kinoshita, M.; Barrett, C. J.; Ikeda, T. Photomobile Polymer Materials: Towards Light-Driven Plastic Motors. *Angew. Chem. Int. Ed.* **2008**, *47*, 4986-4988.
267. Yamada, M.; Kondo, M.; Miyasato, R.; Naka, Y.; Mamiya, J.-i.; Kinoshita, M.; Shishido, A.; Yu, Y.; Barrett, C. J.; Ikeda, T. Photomobile Polymer Materials—Various Three-Dimensional Movements. *J. Mater. Chem.* **2009**, *19*, 60-62.
268. Hugel, T.; Holland, N. B.; Cattani, A.; Moroder, L.; Seitz, M.; Gaub, H. E. Single-Molecule Optomechanical Cycle. *Science* **2002**, *296*, 1103-1106.
269. Neuert, G.; Hugel, T.; Netz, R. R.; Gaub, H. E. Elasticity of Poly(Azobenzene-Peptides). *Macromolecules* **2006**, *39*, 789-797.
270. Schafer, L. V.; Muller, E. M.; Gaub, H. E.; Grubmuller, H. Elastic Properties of Photoswitchable Azobenzene Polymers from Molecular Dynamics Simulations. *Angew. Chem. Int. Ed.* **2007**, *46*, 2232-2237.
271. Goulet-Hanssens, A.; Rietze, C.; Titov, E.; Abdullahu, L.; Grubert, L.; Saalfrank, P.; Hecht, S. Hole Catalysis as a General Mechanism for Efficient and Wavelength-Independent Z → E Azobenzene Isomerization. *Chem* **2018**, *4*, 1740-1755.
272. Gordon, M. B.; Wang, S.; Knappe, G. A.; Wagner, N. J.; Epps, T. H.; Kloxin, C. J. Force-Induced Cleavage of a Labile Bond for Enhanced Mechanochemical Crosslinking. *Poly. Chem.* **2017**, *8*, 6485-6489.
273. Surampudi, S. K.; Patel, H. R.; Nagarjuna, G.; Venkataraman, D. Mechano-Isomerization of Azobenzene. *Chem Commun (Camb)* **2013**, *49*, 7519-7521.

274. Kingsbury, C. M.; May, P. A.; Davis, D. A.; White, S. R.; Moore, J. S.; Sottos, N. R. Shear Activation of Mechanophore-Crosslinked Polymers. *J. Mater. Chem.* **2011**, *21*, 8381-8388.
275. Oka, H.; Imato, K.; Sato, T.; Ohishi, T.; Goseki, R.; Otsuka, H. Enhancing Mechanochemical Activation in the Bulk State by Designing Polymer Architectures. *ACS Macro. Lett.* **2016**, 1124-1127.
276. Wang, Q.; Gossweiler, G. R.; Craig, S. L.; Zhao, X. Cephalopod-Inspired Design of Electro-Mechano-Chemically Responsive Elastomers for on-Demand Fluorescent Patterning. *Nat. Commun.* **2014**, *5*, 4899.
277. Gossweiler, G. R.; Brown, C. L.; Hewage, G. B.; Sapiro-Gheiler, E.; Trautman, W. J.; Welshofer, G. W.; Craig, S. L. Mechanochemically Active Soft Robots. *ACS Appl. Mater. Interfaces* **2015**, *7*, 22431-22435.
278. Beharry, A. A.; Woolley, G. A. Azobenzene Photoswitches for Biomolecules. *Chem. Soc. Rev.* **2011**, *40*, 4422-4437.
279. Garcia-Amoros, J.; Velasco, D. Recent Advances Towards Azobenzene-Based Light-Driven Real-Time Information-Transmitting Materials. *Beilstein J. Org. Chem.* **2012**, *8*, 1003-1017.
280. Bandara, H. M.; Burdette, S. C. Photoisomerization in Different Classes of Azobenzene. *Chem. Soc. Rev.* **2012**, *41*, 1809-1825.
281. Hamon, F.; Djedaini-Pilard, F.; Barbot, F.; Len, C. Azobenzenes—Synthesis and Carbohydrate Applications. *Tetrahedron* **2009**, *65*, 10105-10123.
282. Kim, T. A.; Beiermann, B. A.; White, S. R.; Sottos, N. R. Effect of Mechanical Stress on Spiropyran-Merocyanine Reaction Kinetics in a Thermoplastic Polymer. *ACS Macro. Lett.* **2016**, 1312-1316.
283. Rubinstein, M.; Panyukov, S. Nonaffine Deformation and Elasticity of Polymer Networks. *Macromolecules* **1997**, *30*, 8036-8044.

284. Garcia-Amoros, J.; Sanchez-Ferrer, A.; Massad, W. A.; Nonell, S.; Velasco, D. Kinetic Study of the Fast Thermal Cis-to-Trans Isomerisation of Para-, Ortho- and Polyhydroxyazobenzenes. *Phys. Chem. Chem. Phys.* **2010**, *12*, 13238-13242.
285. Schmoller, K. M.; Bausch, A. R. Similar Nonlinear Mechanical Responses in Hard and Soft Materials. *Nat. Mater.* **2013**, *12*, 278-281.
286. Asano, T.; Okada, T.; Shinkai, S.; Shigematsu, K.; Kusano, Y.; Manabe, O. Temperature and Pressure Dependences of Thermal Cis-to-Trans Isomerization of Azobenzenes Which Evidence an Inversion Mechanism. *J. Am. Chem. Soc.* **1981**, *103*, 5161-5165.
287. Samai, S.; Bradley, D. J.; Choi, T. L. Y.; Yan, Y. Q.; Ginger, D. S. Temperature-Dependent Photoisomerization Quantum Yields for Azobenzene-Modified DNA. *J Phys Chem C* **2017**, *121*, 6997-7004.
288. Tavadze, P.; Avendano Franco, G.; Ren, P.; Wen, X.; Li, Y.; Lewis, J. P. A Machine-Driven Hunt for Global Reaction Coordinates of Azobenzene Photoisomerization. *J. Am. Chem. Soc.* **2018**, *140*, 285-290.
289. Rubinstein, M.; Colby, R. H., *Polymer Physics*. Oxford University Press: UK, 2003.
290. Leja, K.; Lewandowicz, G. Polymer Biodegradation and Biodegradable Polymers - a Review. *Pol J Environ Stud* **2010**, *19*, 255-266.
291. Zhang, Q.; Ko, N. R.; Oh, J. K. Recent Advances in Stimuli-Responsive Degradable Block Copolymer Micelles: Synthesis and Controlled Drug Delivery Applications. *Chem Commun (Camb)* **2012**, *48*, 7542-7552.
292. Bawa, K. K.; Oh, J. K. Stimulus-Responsive Degradable Polylactide-Based Block Copolymer Nanoassemblies for Controlled/Enhanced Drug Delivery. *Mol. Pharm.* **2017**, *14*, 2460-2474.
293. Siracusa, V.; Rocculi, P.; Romani, S.; Rosa, M. D. Biodegradable Polymers for Food Packaging: A Review. *Trends Food Sci. Technol.* **2008**, *19*, 634-643.

294. Schneiderman, D. K.; Hillmyer, M. A. 50th Anniversary Perspective: There Is a Great Future in Sustainable Polymers. *Macromolecules* **2017**, *50*, 3733-3749.
295. Kricheldorf, H. R. Syntheses of Biodegradable and Biocompatible Polymers by Means of Bismuth Catalysts. *Chem. Rev.* **2009**, *109*, 5579-5594.
296. Kenley, R. A.; Manser, G. E. Degradable Polymers - Incorporating a Difunctional Azo Compound into a Polymer Network to Produce Thermally Degradable Polyurethanes. *Macromolecules* **1985**, *18*, 127-131.
297. Mutlu, H.; Geiselhart, C. M.; Barner-Kowollik, C. Untapped Potential for Debonding on Demand: The Wonderful World of Azo-Compounds. *Materials Horizons* **2018**, *5*, 162-183.
298. Paramonov, S. E.; Bachelder, E. M.; Beaudette, T. T.; Standley, S. M.; Lee, C. C.; Dashe, J.; Frechet, J. M. Fully Acid-Degradable Biocompatible Polyacetal Microparticles for Drug Delivery. *Bioconjug Chem* **2008**, *19*, 911-919.
299. Tachibana, Y.; Baba, T.; Kasuya, K.-i. Environmental Biodegradation Control of Polymers by Cleavage of Disulfide Bonds. *Polym. Degrad. Stab.* **2017**, *137*, 67-74.
300. Peterson, G. I.; Church, D. C.; Yakelis, N. A.; Boydston, A. J. 1,2-Oxazine Linker as a Thermal Trigger for Self-Immolative Polymers. *Polymer* **2014**, *55*, 5980-5985.
301. Yardley, R. E.; Kenaree, A. R.; Gillies, E. R. Triggering Depolymerization: Progress and Opportunities for Self-Immolative Polymers. *Macromolecules* **2019**, *52*, 6342-6360.
302. Ayer, M. A.; Schrettl, S.; Balog, S.; Simon, Y. C.; Weder, C. Light-Responsive Azo-Containing Organogels. *Soft Matter* **2017**, *13*, 4017-4023.
303. Li, Y.; Maciel, D.; Rodrigues, J.; Shi, X.; Tomas, H. Biodegradable Polymer Nanogels for Drug/Nucleic Acid Delivery. *Chem. Rev.* **2015**, *115*, 8564-8608.
304. Cai, Z.; Wan, Y.; Becker, M. L.; Long, Y. Z.; Dean, D. Poly(Propylene Fumarate)-Based Materials: Synthesis, Functionalization, Properties, Device Fabrication and Biomedical Applications. *Biomaterials* **2019**, *208*, 45-71.

305. Hernandez, H. L.; Kang, S. K.; Lee, O. P.; Hwang, S. W.; Kaitz, J. A.; Inci, B.; Park, C. W.; Chung, S.; Sottos, N. R.; Moore, J. S.; Rogers, J. A.; White, S. R. Triggered Transience of Metastable Poly(Phthalaldehyde) for Transient Electronics. *Adv. Mater.* **2014**, *26*, 7637-7642.
306. Tan, M. J.; Owh, C.; Chee, P. L.; Kyaw, A. K. K.; Kai, D.; Loh, X. J. Biodegradable Electronics: Cornerstone for Sustainable Electronics and Transient Applications. *Journal of Materials Chemistry C* **2016**, *4*, 5531-5558.
307. Fuhrmann, A.; Gostl, R.; Wendt, R.; Kotteritzsch, J.; Hager, M. D.; Schubert, U. S.; Brademann-Jock, K.; Thunemann, A. F.; Nochel, U.; Behl, M.; Hecht, S. Conditional Repair by Locally Switching the Thermal Healing Capability of Dynamic Covalent Polymers with Light. *Nat. Commun.* **2016**, *7*, 13623.
308. Asadirad, A. M.; Boutault, S.; Erno, Z.; Branda, N. R. Controlling a Polymer Adhesive Using Light and a Molecular Switch. *J. Am. Chem. Soc.* **2014**, *136*, 3024-3027.
309. Kaur, B.; Raza, R.; Stashick, M. J.; Branda, N. R. Using Light to Control the Inhibition of Karstedt's Catalyst. *Organic Chemistry Frontiers* **2019**, *6*, 1253-1256.
310. Al-Atar, U.; Fernandes, R.; Johnsen, B.; Baillie, D.; Branda, N. R. A Photocontrolled Molecular Switch Regulates Paralysis in a Living Organism. *J. Am. Chem. Soc.* **2009**, *131*, 15966-15967.
311. Erno, Z.; Asadirad, A. M.; Lemieux, V.; Branda, N. R. Using Light and a Molecular Switch to 'Lock' and 'Unlock' the Diels-Alder Reaction. *Org. Biomol. Chem.* **2012**, *10*, 2787-2792.
312. Warford, C. C.; Carling, C. J.; Branda, N. R. From Slow to Fast--the User Controls the Rate of the Release of Molecules from Masked Forms Using a Photoswitch and Different Types of Light. *Chem Commun (Camb)* **2015**, *51*, 7039-7042.
313. Nourmohammadian, F.; Wu, T.; Branda, N. R. A 'Chemically-Gated' Photoresponsive Compound as a Visible Detector for Organophosphorus Nerve Agents. *Chem Commun (Camb)* **2011**, *47*, 10954-10956.

314. Wang, J.; Kouznetsova, T. B.; Boulatov, R.; Craig, S. L. Mechanical Gating of a Mechanochemical Reaction Cascade. *Nat. Commun.* **2016**, *7*, 13433.
315. Hu, X.; McFadden, M. E.; Barber, R. W.; Robb, M. J. Mechanochemical Regulation of a Photochemical Reaction. *J. Am. Chem. Soc.* **2018**, *140*, 14073-14077.
316. Marsella, M. J.; Maynard, H. D.; Grubbs, R. H. Template-Directed Ring-Closing Metathesis: Synthesis and Polymerization of Unsaturated Crown Ether Analogs. *Angew Chem Int Ed Engl* **1997**, *36*, 1101-1103.
317. Lenhardt, J. M.; Black, A. L.; Craig, S. L. Gem-Dichlorocyclopropanes as Abundant and Efficient Mechanophores in Polybutadiene Copolymers under Mechanical Stress. *J. Am. Chem. Soc.* **2009**, *131*, 10818-10819.
318. Neary, W. J.; Kennemur, J. G. Polypentenamer Renaissance: Challenges and Opportunities. *ACS Macro. Lett.* **2018**, *8*, 46-56.
319. Szpera, R.; Kovalenko, N.; Natarajan, K.; Paillard, N.; Linclau, B. The Synthesis of the 2,3-Difluorobutan-1,4-Diol Diastereomers. *Beilstein J. Org. Chem.* **2017**, *13*, 2883-2887.
320. Albertsson, A. C.; Hakkarainen, M. Designed to Degrade. *Science* **2017**, *358*, 872-873.
321. Kamaly, N.; Yameen, B.; Wu, J.; Farokhzad, O. C. Degradable Controlled-Release Polymers and Polymeric Nanoparticles: Mechanisms of Controlling Drug Release. *Chem. Rev.* **2016**, *116*, 2602-2663.
322. Sangroniz, A.; Zhu, J. B.; Tang, X.; Etxeberria, A.; Chen, E. Y.; Sardon, H. Packaging Materials with Desired Mechanical and Barrier Properties and Full Chemical Recyclability. *Nat. Commun.* **2019**, *10*, 3559.
323. Fortman, D. J.; Brutman, J. P.; De Hoe, G. X.; Snyder, R. L.; Dichtel, W. R.; Hillmyer, M. A. Approaches to Sustainable and Continually Recyclable Cross-Linked Polymers. *ACS Sustainable Chemistry & Engineering* **2018**, *6*, 11145-11159.

324. Denissen, W.; Winne, J. M.; Du Prez, F. E. Vitrimers: Permanent Organic Networks with Glass-Like Fluidity. *Chem. Sci.* **2016**, *7*, 30-38.
325. Scheutz, G. M.; Lessard, J. J.; Sims, M. B.; Sumerlin, B. S. Adaptable Crosslinks in Polymeric Materials: Resolving the Intersection of Thermoplastics and Thermosets. *J. Am. Chem. Soc.* **2019**, *141*, 16181-16196.
326. Zhu, Y.; Romain, C.; Williams, C. K. Sustainable Polymers from Renewable Resources. *Nature* **2016**, *540*, 354-362.
327. Staudinger, H.; Leupold, E. O. Über Isopren Und Kautschuk, 18. Mitteil.: Viscositäts-Untersuchungen an Balata. *Berichte der deutschen chemischen Gesellschaft (A and B Series)* **1930**, *63*, 730-733.
328. Chen, Z.; Mercer, J. A. M.; Zhu, X.; Romaniuk, J. A. H.; Pfattner, R.; Cegelski, L.; Martinez, T. J.; Burns, N. Z.; Xia, Y. Mechanochemical Unzipping of Insulating Polyadderene to Semiconducting Polyacetylene. *Science* **2017**, *357*, 475-479.
329. Su, J. K.; Feist, J. D.; Yang, J.; Mercer, J. A. M.; Romaniuk, J. A. H.; Chen, Z.; Cegelski, L.; Burns, N. Z.; Xia, Y. Synthesis and Mechanochemical Activation of Ladderene-Norbornene Block Copolymers. *J. Am. Chem. Soc.* **2018**, *140*, 12388-12391.
330. Hsu, T. G.; Zhou, J.; Su, H. W.; Schrage, B. R.; Ziegler, C. J.; Wang, J. A Polymer with "Locked" Degradability: Superior Backbone Stability and Accessible Degradability Enabled by Mechanophore Installation. *J. Am. Chem. Soc.* **2020**.
331. Lin, Y.; Kouznetsova, T. B.; Craig, S. L. Mechanically Gated Degradable Polymers. *J. Am. Chem. Soc.* **2020**, *142*, 2105-2109.
332. Booker-Milburn, K. I.; Delgado Jiménez, F.; Sharpe, A. Sequential Ring-Opening/Cyclisation Reactions of Bicyclo[4.2.0]Oct-7-Enes for the Synthesis of Cyclooctadiene Fused Lactones: Model Studies Towards the Total Synthesis of Pachylactone. *Tetrahedron* **1999**, *55*, 5889-5902.
333. Ralph, M. J.; Harrowven, D. C.; Gaulier, S.; Ng, S.; Booker-Milburn, K. I. The Profound Effect of the Ring Size in the Electrocyclic Opening of Cyclobutene-Fused Bicyclic Systems. *Angew Chem Int Ed Engl* **2015**, *54*, 1527-1531.

334. Booker-Milburn, K. I.; Cowell, J. K.; Harris, L. J. Model Studies Towards the Total Synthesis of Asteriscanolide. *Tetrahedron Lett.* **1994**, *35*, 3883-3886.
335. Booker-Milburn, K. I.; Cowell, J. K.; Sharpe, A.; Jiménez, F. D. Tetrahydrophthalic Anhydride and Imide: Remarkably Efficient Partners in Photochemical [2 + 2] Cycloaddition Reactions with Alkenols and Alkynols. *Chem. Commun.* **1996**, 249-251.
336. Booker-Milburn, K. I.; Cowell, J. K.; Harris, L. J. A Concise Synthesis of 7-Desmethyasteriscanolide and the Discovery of an Unusual Fragmentation Reaction to the Related Asteriscunolide Skeleton. *Tetrahedron* **1997**, *53*, 12319-12338.
337. Booker-Milburn, K. I.; Cowell, J. K.; Delgado Jiménez, F.; Sharpe, A.; White, A. J. Stereoselective Intermolecular [2+2] Photocycloaddition Reactions of Tetrahydrophthalic Anhydride and Derivatives with Alkenols and Alkynols. *Tetrahedron* **1999**, *55*, 5875-5888.
338. Suslick, K. S.; Price, G. J. Application of Ultrasound to Materials Chemistry. *Annu. Rev. Mater. Sci.* **1999**, *29*, 295-326.
339. May, P. A.; Munaretto, N. F.; Hamoy, M. B.; Robb, M. J.; Moore, J. S. Is Molecular Weight or Degree of Polymerization a Better Descriptor of Ultrasound-Induced Mechanochemical Transduction? *ACS Macro. Lett.* **2016**, *5*, 177-180.
340. Schaefer, M.; Icli, B.; Weder, C.; Lattuada, M.; Kilbinger, A. F. M.; Simon, Y. C. The Role of Mass and Length in the Sonochemistry of Polymers. *Macromolecules* **2016**, *49*, 1630-1636.

## Biography

Yangju Lin graduated from Xianyou #1 Private Middle School in 2008 and received his Bachelors' degree in chemistry from Xiamen University in 2012. He later devoted to polymer mechanochemistry and self-healing polymer and earned a Master's degree in polymer engineering and chemistry under the guidance of Prof. Wengui Weng from Xiamen University in 2015. In the same year, he was enrolled in Duke University and continued exploring polymer mechanochemistry in Craig Lab, where he received spiritual guidance from Prof. Stephen L. Craig and obtained degree of Doctor of Philosophy in chemistry in 2020.

### Publication

1. **Yangju Lin**, Tatiana B. Kouznetsouva and Stephen L. Craig. Mechanically Gated Degradable Polymers. *J. Am. Chem. Soc.* **2020**, *142*, 2105-2109.
2. **Yangju Lin**, Tatiana B. Kouznetsouva and Stephen L. Craig. A Latent Mechanoacid for Time-Stamped Mechanochromism and Chemical Signaling in Polymeric Materials. *J. Am. Chem. Soc.* **2020**, *142*, 99-103.
3. **Yangju Lin**, Heather R. Hansen, William J. Brittain and Stephen L. Craig. Strain-dependent Kinetics in the cis-to-trans Isomerization of Azobenzene in Bulk Elastomers. *J. Phys. Chem. B* **2019**, *123*, 8492-8498.
4. **Yangju Lin**, Yudi Zhang, Zi Wang and Stephen L. Craig. Dynamic Memory Effect in the Mechanochemistry of Cyclic Polymers. *J. Am. Chem. Soc.* **2019**, *141* (28), 10943-10947.

5. **Yangju Lin**, Chia-chi Chang, Stephen L. Craig. Mechanical Generation of Isocyanate by Mechanically Induced Retro [2 + 2] Cycloaddition of a 1,2-Diazetidione Mechanophore. *Organic Chemistry Frontiers* **2019**, *6*, 1052-1057.
6. **Yangju Lin**, Meredith H. Barbee, Chia-chi Chang, Stephen L. Craig. Regiochemical Effects on Mechanophore Activation in Bulk Materials. *J. Am. Chem. Soc.* **2018**, *140* (46), 15969-15975.
7. Meredith H. Barbee, Tatiana B. Kouznetsova, Scott L. Barrett, Gossweiler, G. R.; **Yangju Lin**, Shiva K. Rastogi, William J. Brittain, Stephen L. Craig. Substituent Effects and Mechanism in a Mechanochemical Reaction. *J. Am. Chem. Soc.* **2018**, *140*, 12746-12750.
8. Huan Zhang, Linxing Zhang, Yinjun Chen, **Yangju Lin** and Wengui Weng. Chapter 5: Tailoring Mechanochemical Reactivity of Covalent Bonds in Polymers by Non-covalent Interactions. *Mechanochemistry in Materials*. **2017**, DOI: 10.1039/9781782623885-00119
9. Huan Zhang, Xun Li, **Yangju Lin (co-1<sup>st</sup> author)**, Fei Gao, Zhen Tang, Peifeng Su, Wenke Zhang, Yuanze Xu, Wengui Weng, Roman Boulatov. Multi-modal mechanophores based on cinnamate dimers. *Nat. Comm.* **2017**, *8* (1), 1147.
10. Huan Zhang, **Yangju Lin**, Yuanze Xu and Wengui Weng. Mechanochemistry of Topological Complex Polymer Systems. *Topics in Current Chemistry* pp 1-73.
11. Tingwan Xie, Huan Zhang, **Yangju Lin**, Yuanze Xu, Yonghong Ruan, Wengui Weng and Haiping Xia. *RSC Adv.*, **2015**, *5*, 13261.
12. Huan Zhang, Yinjun Chen, **Yangju Lin**, Xiuli Fang, Yuanze Xu, Yonghong Ruan and Wengui Weng. Mechanoresponsive Dual Cross-Linked Elastomers with Strong and Tough Mechanical Properties. *Macromolecules* **2014**, *47*, 6783.

13. Yinjun Chen, Huan Zhang, Yangju Lin, Xiuli Fang, Yuanze Xu and Wengui Weng. Mechanical Activation of Mechanophore Enhanced by Strong Hydrogen Bonding Interactions. *ACS Macro Lett.* **2014**, 3, 141.
14. Guangning Hong, Huan Zhang, Yangju Lin, Yinjun Chen, Yuanze Xu, Wengui Weng\* and Haiping Xia\*. Mechanoresponsive Healable Metallosupramolecular Polymers. *Macromolecules* **2013**, 46, 8649.
15. Xiuli Fang, Huan Zhang, Yinjun Chen, Yangju Lin, Yuanze Xu and Wengui Weng\*. Biomimetic Modular Polymer with Tough and Stress Sensing Properties. *Macromolecules* **2013**, 46, 6566.
16. Wengui Weng, Xiuli Fang, Huan Zhang, Huiying Peng, Yangju Lin and Yinjun Chen. Multiresponsive Supramolecular Gels Constructed by Orthogonal Metal-ligand Coordination and Hydrogen Bonding. *Eur. Polym. J.* **2013**, 49, 4062.
17. Shengchao Jiang, Lingxing Zhan, Tingwan Xie, Yangju Lin, Huan Zhang, Yuanze Xu, Wengui Weng\* and Lizong Dai. Mechanoresponsive PS-PnBA-PS Triblock Copolymers via Covalently Embedding Mechanophore. *ACS Macro Lett.* **2013**, 2, 705.
18. Jinchun Yuan, Xiuli Fang, Lingxing Zhang, Guangning Hong, Yangju Lin, Qifeng Zheng, Yuanze Xu, Yonghong Ruan, Wengui Weng, Haiping Xia and Guohua Chen. Multi-responsive Self-healing Metallo-supramolecular Gels Based on "Click" Ligand. *J. Mater. Chem.* **2012**, 22, 11515.